Plasma Physics and Controlled Nuclear Fusion Research 1984 Vol. 2

TENTH CONFERENCE PROCEEDINGS, LONDON, 12–19 SEPTEMBER 1984

Nuclear Fusion, Supplement 1985

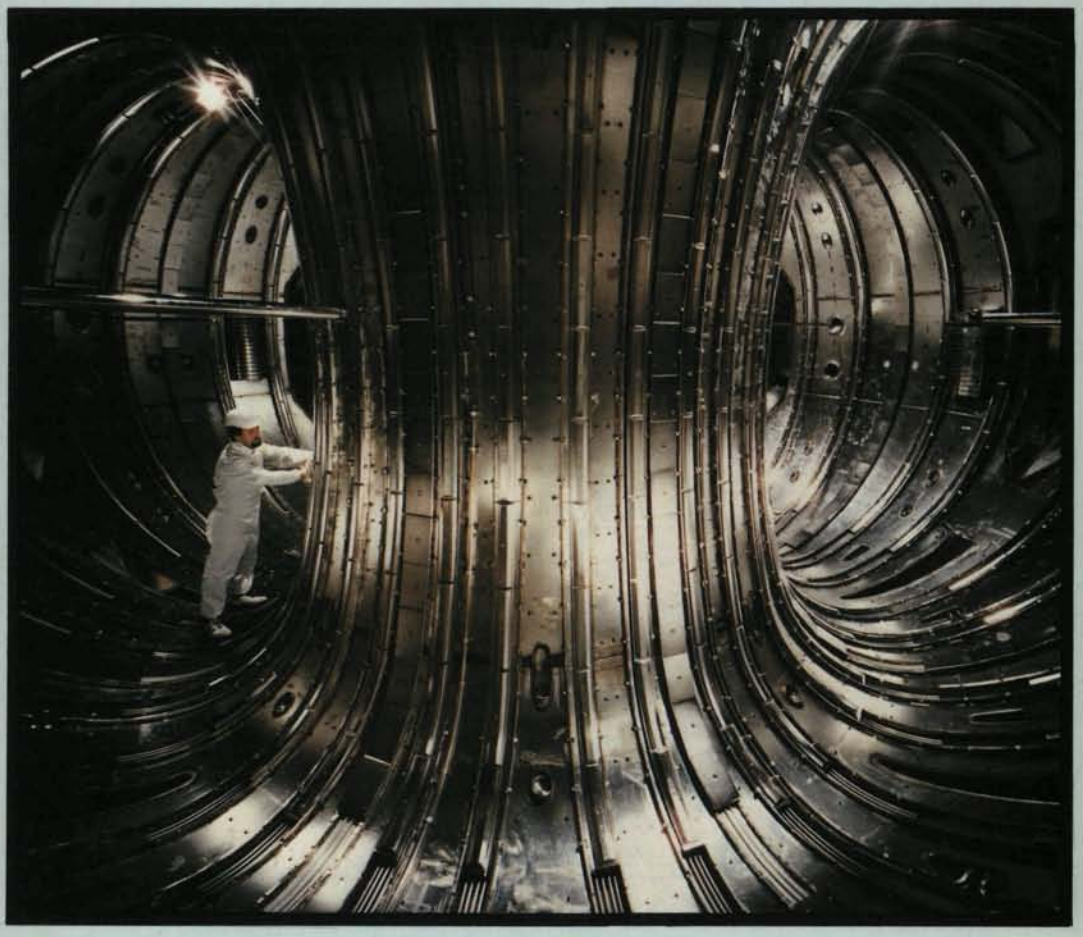

INTERNATIONAL ATOMIC ENERGY AGENCY, VIENNA, 1985

PLASMA PHYSICS AND CONTROLLED NUCLEAR FUSION RESEARCH 1984

VOLUME 2

The following States are Members of the International Atomic Energy Agency:

AFGHANISTAN
ALBANIA
ALGERIA
ARGENTINA
AUSTRALIA
AUSTRIA
BANGLADESH
BELGIUM
BOLIVIA
BRAZIL
BULGARIA
BURMA
BYELORUSSIAN SOVIET SOCIALIST REPUBLIC
CAMEROON
CANADA
CHILE
CHINA
COLOMBIA
COSTA RICA
CUBA
CYPRUS
CZECHOSLOVAKIA
DEMOCRATIC KAMPUCHEA
DEMOCRATIC PEOPLE'S REPUBLIC OF KOREA
DENMARK
DOMINICAN REPUBLIC
ECUADOR
EGYPT
EL SALVADOR
ETHIOPIA
FINLAND
FRANCE
GABON
GERMAN DEMOCRATIC REPUBLIC
GERMANY, FEDERAL REPUBLIC OF
GHANA
GREECE
GUATEMALA
HAITI
HOLY SEE
HUNGARY
ICELAND
INDIA
INDONESIA
IRAN, ISLAMIC REPUBLIC OF
IRAQ
IRELAND
ISRAEL
ITALY
IVORY COAST
JAMAICA
JAPAN
JORDAN
KENYA
KOREA, REPUBLIC OF
KUWAIT
LEBANON
LIBERIA
LIBYAN ARAB JAMAHIRIYA
LIECHTENSTEIN
LUXEMBOURG
MADAGASCAR
MALAYSIA
MALI
MAURITIUS
MEXICO
MONACO
MONGOLIA
MOROCCO
NAMIBIA
NETHERLANDS
NEW ZEALAND
NICARAGUA
NIGER
NIGERIA
NORWAY
PAKISTAN
PANAMA
PARAGUAY
PERU
PHILIPPINES
POLAND
PORTUGAL
QATAR
ROMANIA
SAUDI ARABIA
SENEGAL
SIERRA LEONE
SINGAPORE
SOUTH AFRICA
SPAIN
SRI LANKA
SUDAN
SWEDEN
SWITZERLAND
SYRIAN ARAB REPUBLIC
THAILAND
TUNISIA
TURKEY
UGANDA
UKRAINIAN SOVIET SOCIALIST REPUBLIC
UNION OF SOVIET SOCIALIST REPUBLICS
UNITED ARAB EMIRATES
UNITED KINGDOM OF GREAT BRITAIN AND NORTHERN IRELAND
UNITED REPUBLIC OF TANZANIA
UNITED STATES OF AMERICA
URUGUAY
VENEZUELA
VIET NAM
YUGOSLAVIA
ZAIRE
ZAMBIA

The Agency's Statute was approved on 23 October 1956 by the Conference on the Statute of the IAEA held at United Nations Headquarters, New York; it entered into force on 29 July 1957. The Headquarters of the Agency are situated in Vienna. Its principal objective is "to accelerate and enlarge the contribution of atomic energy to peace, health and prosperity throughout the world".

© IAEA, 1985

Permission to reproduce or translate the information contained in this publication may be obtained by writing to the International Atomic Energy Agency, Wagramerstrasse 5, P.O. Box 100, A-1400 Vienna, Austria.

Printed by the IAEA in Austria
March 1985

NUCLEAR FUSION SUPPLEMENT 1985

PLASMA PHYSICS AND CONTROLLED NUCLEAR FUSION RESEARCH 1984

PROCEEDINGS OF THE
TENTH INTERNATIONAL CONFERENCE ON PLASMA PHYSICS
AND CONTROLLED NUCLEAR FUSION RESEARCH
HELD BY THE
INTERNATIONAL ATOMIC ENERGY AGENCY
IN LONDON, 12–19 SEPTEMBER 1984

In three volumes

VOLUME 2

INTERNATIONAL ATOMIC ENERGY AGENCY
VIENNA, 1985

PLASMA PHYSICS AND CONTROLLED NUCLEAR FUSION RESEARCH 1984
IAEA, VIENNA, 1985
STI/PUB/670
ISBN 92–0–130185–5

FOREWORD

The continuing progress of fusion research towards its ultimate goal of commercially viable power was reported at the Tenth IAEA International Conference on Plasma Physics and Controlled Nuclear Fusion Research. This progress extends to all approaches to controlled fusion and fusion technology, particularly in the area of tokamak experiments. The first results reported by the two new-generation tokamaks, the Joint European Torus (JET) and the Tokamak Fusion Test Reactor (TFTR) in the United States of America exceeded expectations.

This series of conferences is organized bienially by the IAEA. The Tenth Conference was held from 12 to 19 September 1984 at the Imperial College of Science and Technology in London. It was organized by the Agency in co-operation with the United Kingdom Atomic Energy Authority's Culham Laboratory and the JET Joint Undertaking, to whom the Agency wishes to express its gratitude. The conference was attended by 531 participants and 46 observers from 37 countries and 5 international organizations. At the technical sessions, which included 6 poster sessions, 171 papers were presented. Contributions were made on theory, magnetic and inertial confinement systems and related technology. The conference opened with the traditional Artsimovich Memorial Lecture.

These Proceedings, which include all the technical papers and five conference summaries, are published in English as a supplement to the IAEA journal, *Nuclear Fusion.*

The Agency promotes close international co-operation among plasma and fusion physicists and engineers of all countries by organizing these regular conferences on controlled nuclear fusion and by holding seminars, workshops and specialists meetings on appropriate topics. It is hoped that the present publication, as part of these activities, will contribute to the rapid demonstration of fusion power as one of the world's future energy resources.

EDITORIAL NOTE

The papers and discussions have been edited by the editorial staff of the International Atomic Energy Agency to the extent considered necessary for the reader's assistance. The views expressed and the general style adopted remain, however, the responsibility of the named authors or participants. In addition, the views are not necessarily those of the governments of the nominating Member States or of the nominating organizations.

Where papers have been incorporated into these Proceedings without resetting by the Agency, this has been done with the knowledge of the authors and their government authorities, and their cooperation is gratefully acknowledged. The Proceedings have been printed by composition typing and photo-offset lithography. Within the limitations imposed by this method, every effort has been made to maintain a high editorial standard, in particular to achieve, wherever practicable, consistency of units and symbols and conformity to the standards recommended by competent international bodies.

The use in these Proceedings of particular designations of countries or territories does not imply any judgement by the publisher, the IAEA, as to the legal status of such countries or territories, of their authorities and institutions or of the delimitation of their boundaries.

The mention of specific companies or of their products or brand names does not imply any endorsement or recommendation on the part of the IAEA.

Authors are themselves responsible for obtaining the necessary permission to reproduce copyright material from other sources.

CONTENTS OF VOLUME 2

MAGNETIC CONFINEMENT THEORY (Session E)

Physics of the H-mode (IAEA-CN-44/E-I-1) 3
F.L. Hinton, M.S. Chu, R.R. Dominguez, R.W. Harvey, L.L. Lao, J.K. Lee, C.S. Liu, R.W. Moore, T. Ohkawa, S.K. Wong, Y.C. Lee
Discussion 10

Resistive fluid turbulence and energy confinement (IAEA-CN-44/E-I-2) 13
J.W. Connor, J.B. Taylor
Discussion 22

Tokamak disruptions (IAEA-CN-44/E-I-3) 23
J.A. Wesson, A. Sykes, M.F. Turner
Discussion 28

MHD equilibrium and stability for stellarator/torsatron configurations (IAEA-CN-44/E-I-4-1) 31
B.A. Carreras, J.L. Cantrell, L.A. Charlton, L. Garcia, J.H. Harris, T.C. Hender, H.R. Hicks, J.A. Holmes, J.A. Rome, V.E. Lynch

Study of stellarator devices by expansion techniques (IAEA-CN-44/E-I-4-2) 41
J.L. Johnson, A.H. Boozer, A.E. Koniges, G. Kuo-Petravic, J. Manickam, D.A. Monticello, H. Mynick, W. Park, A. Reiman, G. Rewoldt

Neoclassical energy balance in stellarators (IAEA-CN-44/E-I-5) 47
K.S. Dyabilin, L.M. Kovrizhnykh
Discussion 56

Theory and simulation of fishbone-type instabilities in beam-heated tokamaks (IAEA-CN-44/E-II-1) 59
L. Chen, R.B. White, C.Z. Cheng, F. Romanelli, J. Weiland, R. Hay, J.W. Van Dam, M.N. Rosenbluth, S.T. Tsai, D.C. Barnes
Discussion 66

Self-consistent transport theory in tokamak plasmas (IAEA-CN-44/E-II-2). 69
B.B. Kadomtsev, O.P. Pogutse
Discussion 79

Studies of major disruptions and tearing and ballooning modes (IAEA-CN-44/E-II-3) 81
T.M. Antonsen Jr., J.F. Drake, J.M. Finn, A.B. Hassam, R.G. Kleva, B.D. Scott

Physics of plasmas close to the Lawson limit and under burn conditions (IAEA-CN-44/E-II-4) 93
B. Coppi, S. Cowley, P. Detragiache, R. Kulsrud, F. Pegoraro, W. Tang

Modelling analyses of tokamaks with divertors and pumped limiters (IAEA-CN-44/E-II-5-1) 103
M. Petravic, D. Heifetz, D. Post
Advanced two-dimensional simulation of edge plasma in a poloidal divertor (IAEA-CN-44/E-II-5-2) 113
Yu.L. Igitkhanov, A.S. Kukushkin, A.Yu. Pigarov, V.I. Pistunovich, V.A. Pozharov
Application of two-dimensional modelling to scrape-off and single-null poloidal divertor plasma of INTOR (IAEA-CN-44/E-II-5-3) 125
B.J. Braams, M.F.A. Harrison, E.S. Hotston, J.G. Morgan
Performance analysis of JT-60 plasma with poloidal divertor (IAEA-CN-44/E-II-5-4) 131
M. Azumi, K. Shimizu, T. Hirayama, T. Takizuka, M. Sugihara, S. Saito, H. Shirai, K. Tani, M. Nakanishi, H. Kimura, T. Imai, Y. Shimomura
Discussion on Papers IAEA-CN-44/E-II-5-1 to E-II-5-4 137
Drift wave transport, sawtooth relaxations, heat pulse propagation and density limit (IAEA-CN-44/E-III-1) 139
A. Rogister, G. Hasselberg, A. Kaleck, F.Waelbroeck
On limiting plasma pressures and MHD stability in tokamaks (IAEA-CN-44/E-III-2) 147
L.M. Degtyarev, V.V. Drozdov, A.A. Martynov, S.Yu. Medvedev, A.G. Kirov, M.A. Stotland
Investigation of high-beta tokamak stability with the program HBT (IAEA-CN-44/E-III-3) 165
J.P. Goedbloed, G.M.D. Hogeweij, R. Kleibergen, J. Rem, R.M.O. Galvão, P.H. Sakanaka
Accessible beta value of tokamaks (IAEA-CN-44/E-III-4) 173
T. Tuda, M. Azumi, K. Itoh, G. Kurita, T. Takeda, T. Takizuka, S. Tokuda, T. Tsunematsu, M. Adachi, Y. Tanaka, M. Watanabe, S.-I. Itoh
Influence of magnetic field ripple on plasma rotation in tokamaks (IAEA-CN-44/E-III-5) 179
V.Ya. Goloborod'ko, Ya.I. Kolesnichenko, V.A. Yavorskij
The radial electric field in a non-axisymmetric torus (IAEA-CN-44/E-III-6) 189
K.C. Shaing, R.H. Fowler, D.E. Hastings, W.A. Houlberg, E.F. Jaeger, J.F. Lyon, J.A. Rome, J.S. Tolliver, J.D. Callen
Thermal instability and disruptions in a tokamak (IAEA-CN-44/E-III-7) 197
P.H. Rebut, M. Hugon
Anomalous transport and confinement scaling studies in tokamaks (IAEA-CN-44/E-III-8) 213
W.M. Tang, C.Z. Cheng, J.A. Krommes, W.W. Lee, C.R. Oberman, F.W. Perkins, G. Rewoldt, R. Smith, B. Bonoli, B. Coppi, R. Englade, J. Martinelli, L. Sugiyama

Magnetic islands in toroidally confined plasma (IAEA-CN-44/E-III-9) 223
M. Kotschenreuther, A.Y. Aydemir, D.C. Barnes, J.R. Cary, J.D. Hanson, R.D. Hazeltine, P.J. Morrison
Role of multiple helicity non-linear interaction of tearing modes in dynamo and anomalous thermal transport in reversed-field pinch (IAEA-CN-44/E-III-10) 231
Z.G. An, P.H. Diamond, R.D. Hazeltine, J.N. Leboeuf, M.N. Rosenbluth, R.D. Sydora, T. Tajima, B.A. Carreras, L. Garcia, T.C. Hender, H.R. Hicks, J.A. Holmes, V.E. Lynch, H.R. Strauss
Resistive spectrum of configurations without magnetic shear (IAEA-CN-44/E-III-11) 245
D. Lortz, G. Spies

OPEN CONFINEMENT SYSTEMS (Session C)

Thermal barrier confinement experiments in the TMX-U tandem mirror (IAEA-CN-44/C-I-1) 255
T.C. Simonen, S.L. Allen, D.E. Baldwin, T.A. Casper, J.F. Clauser, F.H. Coensgen, R.H. Cohen, D.L. Correll, W.F. Cummins, C.C. Damm, J.H. Foote, T.K. Fowler, R.K. Goodman, D.P. Grubb, D.N. Hill, E.B. Hooper, R.S. Hornady, A.L. Hunt, R.G. Kerr, G.W. Leppelmeier, J. Marilleau, J.M. Moller, A.W. Molvik, W.E. Nexsen, J.E. Osher, W.L. Pickles, P. Poulsen, G.D. Porter, E.H. Silver, B.W. Stallard, J. Taska, W.C. Turner, J.D. Barter, T.W. Christensen, G. Dimonte, T.E. Romesser, R.F. Ellis, R.A. James, C.J. Lasnier, T.L. Yu, L.V. Berzins, M.R. Carter, C.A. Clower, B.H. Failor, S. Falabella, M. Flammer, T. Nash, W.L. Hsu
Discussion 263
Plasma potential control and MHD stability experiments in the Phaedrus tandem mirror (IAEA-CN-44/C-I-2) 265
N. Hershkowitz, R.A. Breun, D.A. Brouchous, J.D. Callen, C. Chan, J.R. Conrad, J.R. Ferron, S.N. Golovato, R. Goulding, S. Horne, S. Kidwell, B. Nelson, H. Persing, J. Pew, S. Ross, G. Severn, D. Sing
Discussion 273
Potential formation in axisymmetrized tandem mirror GAMMA 10 (IAEA-CN-44/C-I-3) 275
T. Cho, M. Ichimura, M. Inutake, K. Ishii, A. Itakura, I. Katanuma, T. Kawabe, Y. Kiwamoto, A. Mase, S. Miyoshi, Y. Nakashima, T. Saito, K. Sawada, D. Tsubouchi, N. Yamaguchi, K. Yatsu
TARA and Constance B mirror confinement experiments and theory (IAEA-CN-44/C-I-4) 285
R.S. Post, M. Gerver, J. Kesner, J.H. Irby, B.G. Lane, M.E. Mauel, B.D. McVey, A. Ram, E. Sevillano, D.L. Smatlak, D.K. Smith,

J.D. Sullivan, J. Trulsen, A. Bers, J.W. Coleman, M.P.J. Gaudreau, R.E. Klinkowstein, R.P. Torti, X. Chen, R.C. Garner, D.L. Goodman, P. Goodrich, S.A. Hokin
Discussion 295

Theoretical studies in tandem mirror physics (IAEA-CN-44/C-I-5) 297
R.H. Cohen, S.P. Auerbach, D.E. Baldwin, J.A. Byers, Y.-J. Chen, B.I. Cohen, R.P. Freis, J.M. Gilmore, J.H. Hammer, T.B. Kaiser, L.L. Lodestro, B. McNamara, Y. Matsuda, W.A. Newcomb, W.M. Nevins, L.D. Pearlstein, T.D. Rognlien, J.W. Shearer, G.R. Smith, J.J. Stewart, I.B. Bernstein, M.W. Phillips
Discussion 307

New results of gas-dynamic trap research (IAEA-CN-44/C-II-1) 309
I.A. Kotel'nikov, V.V. Mirnov, V.P. Nagornyj, D.D. Ryutov
Discussion 319

Stabilization of an axisymmetric mirror cell and trapped particle modes (IAEA-CN-44/C-II-2) 321
H.L. Berk, C.W. Horton Jr., M.N. Rosenbluth, H.V. Wong, J. Kesner, B. Lane, T.M. Antonsen Jr., K.T. Tsang, X.S. Lee, B. Hafizi, J.A. Byers, R.H. Cohen, J.H. Hammer, W.M. Nevins, T.B. Kaiser, L. Lodestro, L.D. Pearlstein, G.R. Smith, R. Ramachandran, W.M. Tang

Plasma heating, confinement and stabilization experiments in an axisymmetric mirror-cusp device (IAEA-CN-44/C-II-3) 337
S. Okamura, R. Kumazawa, K. Adati, T. Aoki, H. Fujita, K. Hattori, S. Hidekuma, T. Kawamoto, Y. Okubo, T. Sato, T. Hatori, K. Muraoka, K. Uchino, M. Maeda, M. Hamamoto, K. Sunako, K. Takayama, D.R. Baker, H.R. Garner, H.D. Price, P.B. Parks, A.M. Sleeper, R. Itatani, Y. Yasaka
Discussion 346

Beam heating of plasma in solenoids (IAEA-CN-44/C-II-4) 347
A.V. Arzhannikov, B.N. Brejzman, A.V. Burdakov, V.S. Burmasov, S.G. Voropaev, L.N. Vyacheslavov, V.I. Erofeev, A.M. Iskol'dskij, B.A. Knyazev, V.S. Kojdan, V.V. Konyukhov, Eh.P. Kruglyakov, S.V. Lebedev, V.N. Luk'yanov, K.I. Mekler, O.I. Meshkov, A.A. Podyminogin, V.V. Postupaev, A.I. Rogozin, D.D. Ryutov, S.L. Sinitskij, A.D. Khil'chenko, Yu.A. Tsidulko, V.V. Chikunov, M.A. Shcheglov
Discussion 358

Plasma end loss confinement studies in a linear theta pinch with magnetic mirrors (IAEA-CN-44/C-II-5) 359
G.G. Zukakishvili, V.N. Ryzhkov, R.G. Salukvadze, Eh.K. Tikhanov, Z.D. Chkuaseli, P.P. Volosevich, I.I. Galigusova, N.A. Dar'in, V.Ya. Karpov, E.I. Levanov

ALTERNATIVE AND SUPPORTING SYSTEMS (Session D)

Plasma confinement and the effect of rotational transform in the Wendelstein VII-A stellarator (IAEA-CN-44/D-I-1) 371
G. Cattanei, D. Dorst, A. Elsner, V. Erckmann, G. Grieger, P. Grigull, H. Hacker, H.J. Hartfuss, M.A. Hellberg, H. Jäckel, R. Jaenicke, J. Junker, M. Kick, H. Kroiss, G. Kuehner, H. Maassberg, C. Mahn, S. Marlier, G. Müller, W. Ohlendorf, F. Rau, H. Renner, H. Ringler, F. Sardei, M. Tutter, A. Weller, H. Wobig, E. Würsching, M. Zippe, K. Freudenberger, W. Ott, F.-P. Penningsfeld, E. Speth, H. Büchl

NBI heating of currentless plasma in Heliotron E (IAEA-CN-44/D-I-2) 383
K. Uo, A. Iiyoshi, T. Obiki, O. Motojima, S. Morimoto, M. Wakatani, A. Sasaki, K. Kondo, M. Sato, K. Hanatani, T. Mutoh, H. Zushi, H. Kaneko, S. Besshou, M. Nakasuga, F. Sano, T. Mizuuchi, S. Sudo, J. Harris, I. Ohtake, M. Iima, H. Okada, Y. Nakashima
Discussion 395

Currentless plasma production and heating in the torsatron Uragan-3 by RF waves (IAEA-CN-44/D-I-3) 397
V.V. Bakaev, S.P. Bondarenko, V.V. Bronnikov, V.S. Vojtsenya, M.P. Vasil'ev, A.Yu. Voloshko, Yu.V. Gutarev, A.G. Dikij, I.A. Dikij, Yu.K. Kuznetsov, A.E. Kulaga, M.S. Kulak, V.B. Korovin, B.V. Kravchin, S.S. Kalinichenko, E.M. Lats'ko, A.P. Litvinov, A.I. Lysojvan, Yu.K. Mironov, N.I. Nazarov, G.P. Opaleva, O.S. Pavlichenko, V.K. Pashnev, V.V. Plyusnin, N.F. Perepelkin, N.P. Ponomarenko, A.S. Slavnyj, A.I. Skibenko, S.I. Solodovchenko, K.N. Stepanov, V.S. Taran, V.T. Tolok, V.M. Tonkopryad, I.P. Fomin, O.M. Shvets, A.F. Shtan'
Discussion 407

First results on currentless plasma production and heating by ECR waves in the L-2 stellarator (IAEA-CN-44/D-I-4) 409
E.D. Andryukhina, G.M. Batanov, M.S. Berezhetskij, M.A. Blokh, G.S. Voronov, N.P. Donskaya, K.S. Dyabilin, S.V. Kladov, L.M. Kovrizhnykh, L.V. Kolik, N.F. Larionova, A.I. Meshcheryakov, A.V. Novikova, S.N. Popov, A.V. Sapozhnikov, K.A. Sarksyan, I.S. Sbitnikova, A.D. Smirnova, V.N. Sukhodolskij, A.E. Petrov, O.I. Fedyanin, Yu.V. Kholnov, M.G. Shats, I.S. Shpigel', E.F. Gippius, V.N. Kolesnikov, B.I. Ilyukhin, A.V. Paramonov, A.G. Litvak, O.B. Smolyakova, E.V. Suvorov, A.A. Frajman
Discussion 417

Wave absorption and transport studies on ECR-heated stellarator plasmas in W VII-A (IAEA-CN-44/D-I-5) 419
V. Erckmann, G. Janzen, W. Kasparek, G. Müller, E. Räuchle, P.G. Schüller, K. Schwörer, M. Thumm, R. Wilhelm, W VII-A Team
Discussion 429

High-current high-beta toroidal pinch experiments on OHTE (IAEA-CN-44/D-II-1) 431
T. Tamano, W.D. Bard, T.N. Carlstrom, C.Chu, B. Curwen, R.K. Fisher, D.W. Graumann, R.R. Goforth, G.L. Jackson, R.J. La Haye, T. Ohkawa, M.J. Schaffer, M.T. Saito, P.L. Taylor, T.S. Taylor, D.F. Register, S.E. Walker
Discussion 437

Experimental and theoretical studies of the ZT-40M reversed-field pinch (IAEA-CN-44/D-II-2) 439
D.A. Baker, C.J. Buchenauer, L.C. Burkhardt, E.J. Caramana, J.N. DiMarco, J.N. Downing, R.M. Erickson, R.F. Gribble, A. Haberstich, R.B. Howell, J.C. Ingraham, A.R. Jacobson, K.A. Klare, E.M. Little, R.S. Massey, J.G. Melton, G. Miller, R.W. Moses, C.P. Munson, J.A. Phillips, M.M. Pickrell, R.A. Nebel, A.E. Schofield, K.F. Schoenberg, R.G. Watt, P.G. Weber, D.M. Weldon, K.A. Werley, R.W. Wilkins, G.A. Wurden, D.D. Schnack, D.C. Baxter, A.Y. Aydemir, D.C. Barnes
Discussion 447

New results from HBTX1A reversed-field pinch (IAEA-CN-44/D-II-3) 449
P.G. Carolan, B. Alper, M.K. Bevir, H.A.B. Bodin, C.A. Bunting, D.R. Brotherton-Ratcliffe, H. Ahmed, D.E. Evans, D. Evans, A.R. Field, L. Firth, M.J. Forrest, C.G. Gimblett, N.C. Hawkes, I.H. Hutchinson, M. Malacarne, A. Manley, A.A. Newton, P.G. Noonan, A. Patel, N.J. Peacock, D.P. Storey, H. Tsui, P.D. Wilcock
Discussion 460

3D MHD studies of dynamic processes in the reversed-field pinch (IAEA-CN-44/D-II-4-1) 461
T. Sato, K. Kusano

MHD behaviour of a reversed-field pinch plasma in the setting-up phase (IAEA-CN-44/D-II-4-2) 467
Z. Yoshida, N. Inoue, H. Yamada, S. Hamaguchi, K. Itami, N. Suzuki, K. Hattori, Y. Kamada, K. Okano, J. Morikawa, H. Nihei, K. Miyamoto, T. Uchida, T. Sato
Discussion on Papers IAEA-CN-44/D-II-4-1 and D-II-4-2 473

Reversed-field pinch experiment on TPE-1R(M) (IAEA-CN-44/D-II-5) 475
Y. Hirano, Y. Kondoh, Y. Maejima, Y. Nogi, K. Ogawa, M. Sato, T. Shimada, Y. Yagi, H. Yoshimura

Reversed-field pinch plasmas with current flat-top in ETA-BETA II (IAEA-CN-44/D-II-6) 487
V. Antoni, M. Bassan, A. Buffa, S. Costa, L. Giudicotti, W. Grossmann, S. Martini, S. Ortolani, R. Paccagnella, M.E. Puiatti, P. Scarin, M. Valisa, E. Zilli
Discussion 498
Spheromak studies on CTX (IAEA-CN-44/D-III-1) 501
T.R. Jarboe, C.W. Barnes, I. Henins, H.W. Hoida, S.O. Knox, R.K. Linford, G.J. Marklin, D.A. Platts, A.G. Sgro, A.R. Sherwood, B.L. Wright, A.A. Mirin, D.E. Shumaker
Discussion 509
Theoretical studies of field-reversed configurations (FRC) and experimental study of the FRC during translation (IAEA-CN-44/D-III-2-1) 511
R.E. Siemon, W.T. Armstrong, R.E. Chrien, P.L. Klingner, R.K. Linford, K.F. McKenna, D.J. Rej, J.L. Schwarzmeier, A. Sgro, E.G. Sherwood, R.L. Spencer, M. Tuszewski, N.T. Gladd, D.S. Harned, D. Shumaker, C.E. Seyler
Stabilization and translation of a plasma with field-reversed configuration (IAEA-CN-44/D-III-2-2) 523
M. Tanjyo, S. Okada, Y. Ito, M. Kako, S. Ohi, S. Goto, T. Ishimura, H. Itô, Y. Nogi, S. Shimamura, T. Ikawa, S. Hamada
Discussion on Papers IAEA-CN-44/D-III-2-1 and D-III-2-2 533
Initial results from S-1 spheromak (IAEA-CN-44/D-III-3) 535
M. Yamada, R. Ellis Jr., H.P. Furth, G. Hart, A. Janos, S. Jardin, F. Levinton, D. Meyerhofer, M. Mimura, C.H. Nam, S. Paul, A. Sperduti, S. Von Goeler, F. Wysocki, P. Young
Discussion 544
Recent advances in confinement and heating physics on EBT-S (IAEA-CN-44/D-III-4) 545
L.A. Berry, F.W. Baity, D.B. Batchelor, F.M. Bieniosek, T.S. Bigelow, J.A. Cobble, R.J. Colchin, W.A. Davis, J.C. Glowienka, J.R. Goyer, G.R. Haste, D.L. Hillis, S. Hiroe, H.D. Kimrey, L.W. Owen, T.L. Owens, R.K. Richards, L. Solensten, D.W. Swain, N.A. Uckan, T. Uckan, J.B. Wilgen
Characteristics of high-density and high-temperature plasmas in the Nagoya Bumpy Torus (IAEA-CN-44/D-III-5) 551
M. Fujiwara, T. Kamimura, M. Hosokawa, T. Shoji, H. Iguchi, H. Sanuki, K. Takasugi, F. Tsuboi, H. Tsuchidate, K. Kadota, K. Sato, K. Tsuchida, A. Tsushima, H. Ikegami
Discussion 559
Non-hydrodynamic model of plasma structure (IAEA-CN-44/D-III-6-1) 561
V.S. Imshennik, N.M. Zueva, O.V. Lokutsievskij, M.S. Mikhajlova

Correlation between charged-particle beams and neutron emission in a dense plasma focus (IAEA-CN-44/D-III-6-2) 569
K. Hirano, T. Yamamoto, K. Shimoda, K. Kobayashi, M. Yokoyama, Y. Yamamoto, A. Kisoda, Y. Yamada, Y. Kitagawa, M. Yamanaka, C. Yamanaka
Two phases of neutron production in the Poseidon plasma focus (IAEA-CN-44/D-III-6-3) 579
H. Herold, L. Bertalot, K. Hirano, U. Jäger, H.J. Kaeppeler, M. Sadowski, H. Schmidt, R. Schmidt, M. Shakhatre, A. Shyam, G. Böckle, K. Matl, N. Wenzel, R. Wolf, R. Bätzner, H. Hinsch, K. Hübner
Neutron, ion and X-ray emission from a 360 kJ plasma focus device (IAEA-CN-44/D-III-6-4) 591
A. Jerzykiewicz, M. Bielik, L. Jakubowski, Z. Jankowicz, K. Kocięcka, J. Kuciński, E. Rydygier, M. Sadowski, J. Żebrowski, M. Borowiecki, S. Czekaj, S. Denus, A. Kasperczuk, M. Paduch, T. Pisarczyk, W. Skrzeczanowski
Discussion on Papers IAEA-CN-44/D-III-6-1 to D-III-6-4 599
Lifetime scaling of field-reversed configurations (IAEA-CN-44/D-IV-1) 601
A.L. Hoffman, D.G. Harding, R.D. Milroy, J.T. Slough, L.C. Steinhauer, G.C. Vlases
Z-pinch fusion research (IAEA-CN-44/D-IV-2) 611
J.D. Sethian, K.A. Gerber, A.E. Robson, A.W. DeSilva, J.E. Hammel, D.W. Scudder, J.S. Shlachter
Drift instabilities and the dynamo effect in the reversed-field pinch (IAEA-CN-44/D-IV-3) 619
N.T. Gladd, N.A. Krall, R.W. Moses, A.R. Jacobson
Coupled transport and heating in EBT and EBS (IAEA-CN-44/D-IV-4) 627
C.L. Hedrick, D.B. Batchelor, G.L. Chen, R.C. Goldfinger, D.E. Hastings, E.F. Jaeger, D.K. Lee, L.W. Owen, D.A. Spong, J.S. Tolliver, N.A. Uckan, N. Krall, S. Hamasaki, J. Sperling
Impurity transport in the Wendelstein VII-A stellarator (IAEA-CN-44/D-IV-5) 635
G. Cattanei, D. Dorst, A. Elsner, V. Erckmann, G. Grieger, P. Grigull, H. Hacker, H.J. Hartfuss, H. Jäckel, R. Jaenicke, J. Junker, M. Kick, H. Kroiss, G. Kuehner, H. Maassberg, C. Mahn, S. Marlier, G. Müller, W. Ohlendorf, F. Rau, H. Renner, H. Ringler, F. Sardei, M. Tutter, A. Weller, H. Wobig, E. Würsching, M. Zippe, K. Freudenberger, G.G. Lister, W. Ott, F.-P. Penningsfeld, E. Speth
Z-pinch experiments and theory (IAEA-CN-44/D-IV-6) 647
M.G. Haines, A.E. Dangor, A. Folkierski, P. Baldock, W.G. Bessell, D.J. Bond, C.D. Challis, P. Choi, M. Coppins, M.B. Favre-Dominguez, D.A. Hammer, E.L. Lindman, J.R. Liu, G. Nave, O.G. Parfenov, G. Rickard, J. Westlake

Shear stabilizing experiment of gun-spheromak plasma (CTCC-I) (IAEA-CN-44/D-IV-7) 655
M. Nagata, Y. Honda, K. Ikegami, M. Nishikawa, A. Ozaki, N. Satomi, T. Uyama, K. Watanabe

Chairmen of Sessions 667
Secretariat of the Conference 667

Session E

MAGNETIC CONFINEMENT THEORY

Chairmen of Sessions

Session E-I	P.H. RUTHERFORD	(USA)
Session E-II	L.M. KOVRIZHNYKH	(USSR)

Session E-III (Posters)

PHYSICS OF THE H-MODE*

F.L. HINTON, M.S. CHU, R.R. DOMINGUEZ,
R.W. HARVEY, L.L. LAO, J.K. LEE, C.S. LIU,
R.W. MOORE, T. OHKAWA, S.K. WONG, Y.C. LEE**
GA Technologies Inc.,
San Diego, California,
United States of America

Abstract

PHYSICS OF THE H-MODE.

A theoretical picture of the H-mode is proposed which explains some of the most important features of this good confinement mode in neutral beam heated plasmas with divertors. From consideration of the transport through the separatrix and along the open field lines outside the separatrix, as well as the stability of the plasma inside the separatrix, we show that a bifurcation in the operating parameters is possible. At high edge temperatures, very large particle confinement times are possible because of the Ware pinch. The transport of particles and heat along the open field lines to the divertor region depends on temperature in a non-monotonic way, and the bifurcation of the thermal equilibrium which is implied may correspond to the L- to H-mode transition. The improvement of the interior confinement in the H-mode, when the edge temperature is higher, is shown to follow from the tearing mode stability properties of current profiles with pedestals.

1. INTRODUCTION

A good confinement regime in neutral beam heated plasmas has been found in the ASDEX, PDX and Doublet III tokamaks [1,2,3]. The particle and energy confinement in the *H*-mode are considerably better than in the *L*-mode. The *H*-mode is characterized by a high electron temperature near the separatrix, with a steep gradient there, indicating very much reduced radial transport compared with the *L*-mode. The main requirement in obtaining the *H*-mode [1,2] is that the electron temperature near the separatrix must be at least several hundred electron volts. The *L*- to *H*-mode transition [1,2] is often triggered by a sawtooth heat pulse.

Because the particle confinement is so good (much more than 100 ms, in the absence of the edge-localized instabilities which ultimately limit it) the transport may be neoclassical. In fact, the observed central

* Work supported by US Department of Energy Contract No.DE-AT03-84ER53158.
** University of Maryland, College Park, MD, USA.

accumulation of impurities is consistent with that predicted by neoclassical theory [4].

Related to the radial transport properties is the confinement on the open field lines outside the separatrix. The electrons must be electrostatically confined there, so this is essentially a mirror confinement region, with the magnetic field playing the main role in confining ions. We have considered the physics which determines the temperature drop between the edge of the plasma and the divertor region, and its dependence on the heat flux. A bifurcation in the thermal equilibrium appears to be possible.

Finally, the tearing mode stability of the L- and H-modes has been investigated. A reason is given for the reduction in the electron thermal conductivity in the plasma interior when the edge temperature is increased, in the H-mode.

2. NEOCLASSICAL TRANSPORT ACROSS THE SEPARATRIX

Previous work on neoclassical transport needs to be modified in order to be applied to divertor tokamaks. Near the separatrix, the ion guiding center orbit excursion, or banana width, cannot be treated as small compared to the radial scale length. Also, the electrostatic trapping of most of the electrons outside the separatrix and the drift due to the trapping potential must be taken into account.

Assuming the ions to be nearly collisionless near the separatrix, the dominant ion loss is by scattering into velocity space loss regions, corresponding to diverted drift surfaces. In order to treat this problem, we have solved the orbit-averaged drift kinetic equation with the boundary condition that the ion distribution function be zero on the loss region boundaries. The result shows that the ion loss from a layer within a few banana widths of the separatrix is at the ion-ion collision rate, as in a mirror device. This efficient energy loss mechanism at the plasma edge must match the ion neoclassical heat flow from the plasma interior. We have, approximately,

$$n_i T_i \nu_i S \Delta = q_i S$$

where S is the plasma surface area and Δ is an ion banana width, and q_i is the ion neoclassical heat flux,

$$q_i = -n_i \Delta^2 \nu_i \frac{\partial T_i}{\partial r}$$

Thus, the ion temperature gradient length must be about one ion banana width:

$$\frac{\partial T_i}{\partial r} = -\frac{T_i}{\Delta}$$

The ion temperature gradient would then be typically several hundred electron volt per centimeter, which is approximately the same as the measured electron temperature gradients in the H-mode.

When the gradient length is comparable to the banana width, the ion flux due to ion-ion collisions is much larger than that due to electron-ion collisions. The ion loss rate would then be much larger than the neoclassical electron loss rate. One possible way to achieve equal fluxes is for the electron flux to be anomalous and easily adjustable to match the ion flux. Since the ion neoclassical diffusivity is typically around 10^3 cm^2/s, the empirical electron transport rates are more than sufficient.

We consider here the alternative possibility that the electron transport in the H-mode is neoclassical, with no anomalous contribution, and that a negative radial electric field effectively contains the ions. The confining potential is required to increase in the radial direction by a few T_i/e, over a distance of one ion banana width. This effectively eliminates the ion loss regions. The ion diamagnetic flow in the presence of the large ion pressure gradient near the separatrix would be comparable to the ion thermal speed, and in the same direction as the toroidal current. However, the flow due to the negative radial electric field would be counter to the current and of approximately the same magnitude, tending to cancel the diamagnetic flow. Thus, a large shear in the toroidal flow near the separatrix is not expected. The magnitude of the toroidal flow may still be large, however.

The density and temperature gradients near the separatrix in the H-mode are sufficiently large that the electron neoclassical fluxes of particles and heat may be approximately balanced by the Ware pinch velocity [5,6,7]. Both diffusion and pinch are enhanced near the separatrix because of the fact that the poloidal magnetic field is zero at the x-point on the separatrix [8]. The long mean-free path condition for the banana regime is violated very close to the separatrix, where the connection length becomes infinite. However, because of the fact that most of the electrons just outside the separatrix are electrostatically trapped, their effective collisionality is not enhanced in the usual

way for large aspect ratio, so the banana regime applies closer to the separatrix than without electrostatic trapping. Also, there is no distinction between banana and plateau regimes, when the fraction of trapped electrons is not small. For typical parameters, we find that the balance occurs when the electron density and temperature gradient lengths are a few centimeters, which is what they are found to be, in the H-mode.

The possibility of balancing the fluxes implies that the particle confinement time may be essentially infinite when instabilities responsible for transport in the L-mode are suppressed. The requirement of a high temperature near the separatrix can be understood as the condition for the banana regime, since the Ware pinch is much weaker in the collisional regime. The effect of the edge temperature on stability will be addressed in Sec. 4.

3. DETERMINATION OF THE EDGE TEMPERATURE

We note that a high edge temperature may eliminate some of the cooling mechanisms which operate at lower temperature. Among these is turbulence associated with collisional drift waves. Also, a higher edge temperature and the high density near the divertor plate which exists in the H-mode are expected to improve the line-tying of MHD modes outside the separatrix. When these cooling mechanisms are eliminated, the edge temperature is determined by the electron heat flow along the field lines.

It has been pointed out [9] that Spitzer heat conduction along the open field lines from the plasma edge to the divertor plate is too fast to allow edge temperatures as high as 100 eV. Allowing for experimental uncertainties, it is possible that such temperatures exist outside the separatrix in the H-mode. We assume that plasma with a temperature of this order of magnitude is connected by field lines to the divertor region, possibly because of the disturbance in the magnetic field due to saturated magnetic islands inside the separatrix. When the electron collisionality is sufficiently low, the electron heat flow can be strongly reduced from the Spitzer value by a thermal barrier, in the form of a potential minimum along the open field lines between the plasma edge and the divertor plate. This can effectively prevent cool electrons produced by recycling from moving to the plasma edge and replacing hot electrons, which is the long mean-free path version of heat conduction.

At low temperature, the heat conduction is determined by Spitzer's law, so that [10] the heat flux is $Q_e \propto T_e^{7/2}$. At higher temperatures, where the electrons escape from the mirror confinement region by collisional scattering out of the potential well, the heat flow consists of the sum of two contributions. The first part is the convective heat loss, due to electrons scattering out of the potential well at the same rate as the ions scatter into the loss regions, $Q_{e1} = L_m(n_i/\tau_{ii})\,T_e$, where L_m is the effective length of the mirror region. Assuming $T_i = T_e$, this is proportional to $T_e^{-1/2}$. The second part is the conductive loss, due to the replacement of hot electrons by cool ones which come in over the thermal barrier from the divertor plate region, at a rate determined by the temperature there, $Q_{e2} = n_{e,b} v_{e,b} T_e$, where $n_{e,b}$ and $v_{e,b}$ are the density and thermal speed of the cool electrons which pass over the thermal barrier. The sum of these, in terms of the hot electron temperature T_e, is

$$Q_e = k_1\, T_e^{-1/2} + k_2\, T_e$$

At sufficiently high electron temperatures, the second (conductive) term dominates. At somewhat lower temperatures, the convective term dominates and the heat flow *decreases* with an increase in electron temperature. This is clearly a thermally unstable range of temperature, which implies a bifurcation in the thermal equilibrium. Estimates of the numerical factors give this temperature range as 100 to 250 eV. In Fig. 1(a) we show the form of the heat flow as a function of the edge electron temperature. When the heat flow is increased above the value Q_e^* (even for a short time, as from a sawtooth heat pulse), the edge temperature must jump from the value T_L to the value T_H.

This is the *L*- to *H*-mode transition, assuming that the radial transport also allows this type of bifurcation, so that the radial and parallel transport can be matched. A bifurcation in the perpendicular transport appears possible because of the presence of the Ware pinch at higher temperatures, as discussed in Sec. 2, and also because of tearing mode stability, as will be shown in Sec. 4.

The corresponding curve for the particle flux, Fig. 1(b), shows the ion-sound limited flow $n_e\, c_s$ for low temperatures, proportional to $T_e^{1/2}$, and the mirror-confinement loss for higher temperatures, proportional to $T_e^{-3/2}$. The particle flux clearly drops significantly at the *L*-*H* transition, which agrees with the sudden drop in recycling in the divertor chamber seen experimentally.

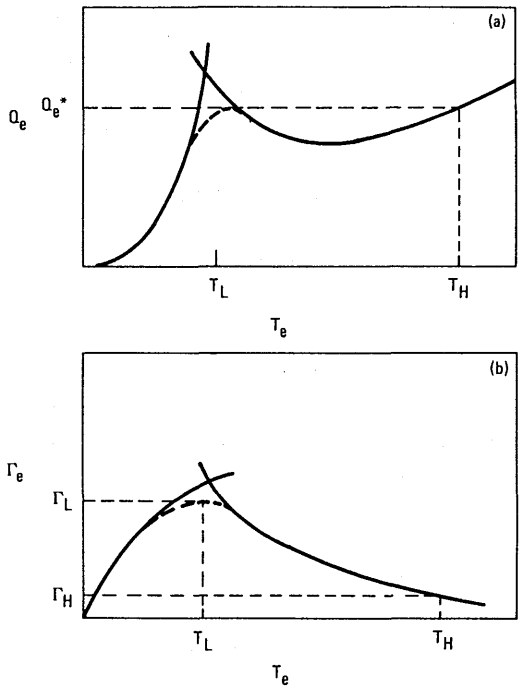

FIG. 1. Fluxes of (a) heat and (b) particles through the divertor channel as a function of edge temperature. The heat flux Q_e^* is the critical value for transition from the L- to H-mode.

4. EFFECT OF HIGH EDGE TEMPERATURE ON INTERIOR CONFINEMENT

Raising the temperature, and therefore the conductivity, at the plasma edge has the effect of raising the pedestal on the current density profile. That such a pedestal is effective in stabilizing low-m tearing modes was shown by Glasser, Furth and Rutherford [11]. We have extended their work to show the trend of tearing mode stabilization with increasing current pedestal values, for different values of $q(a)$, the circular equivalent safety factor at the plasma edge. We have used profiles which are stable to the (1,1) and (2,1) modes which have their largest gradients between the $q=1$ and $q=2$ surfaces. For simplicity, we have chosen to use the step profile [11]

$$\begin{aligned} j(r) &= j_1 , & r \leq c \\ &= p j_1 , & c < r \leq a \\ &= 0 , & r > a \end{aligned}$$

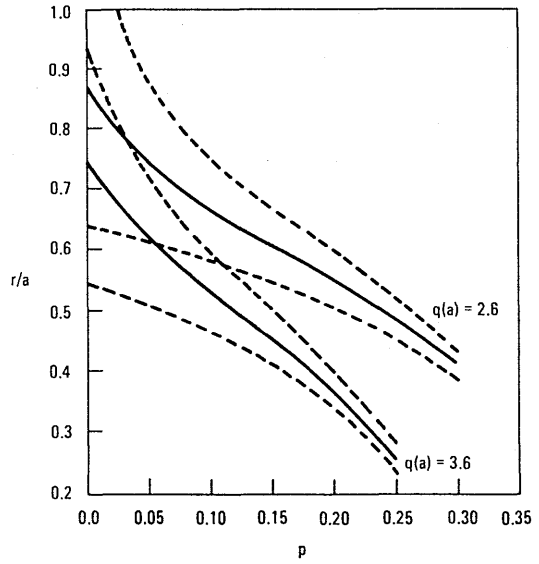

FIG.2. Minor radius of the most unstable mode's singular surface (solid curves) and the outer and inner edges of the stochastic regions (dashed curves), as a function of the current pedestal parameter, for two values of the safety factor (circular equivalent) at the plasma edge, $q(a) = 2.6$ and $q(a) = 3.6$.

where p is the pedestal parameter. The value j_1 is determined by setting $q = 1.05$ for $r \leq c$. The stability of (m,n) modes with $1 \leq m$, $n \leq 20$ was determined from the discontinuity in the slopes of the ideal MHD eigenfunctions at the singular surface. Only modes with singular surfaces inside the plasma were included. The saturated island widths were determined by the condition of equal slopes at the two sides of the island.

Figure 2 shows the minor radius position of the singular surface of the most unstable mode and the inner and outer edges of the region of stochastic field lines due to overlap of the saturated islands, as functions of the pedestal parameter p. In this model, the current gradient is zero outside the position of the current gradient, $r = c$, and the island of the most unstable mode grows until it touches $r = c$. Since other modes are also unstable within the region spanned by this island, all of the islands overlap and we expect the magnetic fields to be stochastic. The electron thermal transport is expected to be large in this stochastic region.

Figure 2 shows that, as the pedestal value is increased, the stochastic region moves inward away from the edge and becomes smaller, which

corresponds to a reduction of thermal conductivity, especially near the edge. This reduction is even more dramatic for larger values of $q(a)$; in Fig. 2 we have compared $q(a) = 2.6$ and 3.6. As the pedestal value is increased, the lower mode numbers become stable. The most unstable mode and the one with the largest island for $p = 0$ is the (2,1), while for $p = 0.05$ it is the (3,2), for $p = 0.1$ it is the (4,3), for $p = 0.15$ it is the (5,4), etc.

At some limiting value of the current pedestal, the current gradient at the plasma boundary r=a would destabilize surface kinks, which might correspond to the onset of the edge-localized modes which ultimately limit the confinement in the H-mode. This implies that optimization of confinement may require careful control of the temperature near the separatrix.

REFERENCES

[1] WAGNER, F., *et al.*, Phys. Rev. Lett. **49** (1982) 1408.
[2] KAYE, S.M., *et al.*, Attainment of High Confinement in Neutral Beam Heated Divertor Discharges in the PDX Tokamak, Princeton Plasma Physics Laboratory Rep. PPPL-2056 (1983).
[3] OHYABU, N., *et al.*, A regime of Improved Energy Confinement in Beam-Heated Expanded-Boundary Discharges in Doublet III, GA Technologies Rep. GA-A17108 (1984).
[4] HINTON, F.L., HAZELTINE, R.D., Rev. Mod. Phys. **4** (1976) 239.
[5] WARE, A.A., Phys. Rev. Lett. **25** (1970) 916.
[6] GALEEV, A.A., Sov. Phys.-JETP **32** (1971) 752.
[7] RUTHERFORD, P.H., *et al.*, Phys. Rev. Lett. **25** (1970) 1090.
[8] GLASSER, A.H., THOMPSON, W.B., Phys. Fluids **16** (1973) 95.
[9] OHKAWA, T., *et al.*, Phys. Rev. Lett. **51** (1983) 2101.
[10] MAHDAVI, M.A., *et al.*, Phys. Rev. Lett. **47** (1981) 1602.
[11] GLASSER, A.H., FURTH, H.P., RUTHERFORD, P.H., Phys. Rev. Lett. **38** (1977) 234.

DISCUSSION

R.J. GOLDSTON: A unifying feature of all enhanced confinement mode results – H-mode, Z-mode, scoop and pellets – is the reduction in edge recycling of neutral hydrogen. It seems that enhanced confinement requires neither low

edge radiation nor high edge *electron* temperature, nor divertor geometry. The key element is then perhaps high edge *ion* temperature. Can your theory help in the effort to unify our understanding of the different enhanced confinement modes?

F.L. HINTON: Although I do not share your faith that all improved confinement modes are equivalent, it does seem that a common feature is the reduction in edge recycling, which degrades confinement. In the H-mode, refuelling occurs by cold plasma inflow in a thin layer near the separatrix. The importance of this may lie in the fact that the electron temperature is held down in a narrower layer and can then have a steep gradient, as is found in the ASDEX H-mode.

G. FUSSMANN: You argue that the accumulation of impurities observed in the experiments supports the assumption of neoclassical transport during the (quiescent) H-phase. It is found, however, that under conditions of insertion of the n_e and T_e profiles actually measured in ASDEX, neoclassical theory predicts an outward rather than an inward drift of the impurities. The reason is the high T_e gradient obtained at the boundary which, in the collisionless regime, leads to an effective temperature screening.

RESISTIVE FLUID TURBULENCE AND ENERGY CONFINEMENT

J.W. CONNOR, J.B. TAYLOR
Culham Laboratory, Abingdon, Oxfordshire,
(Euratom/UKAEA Fusion Association),
United Kingdom

Abstract

RESISTIVE FLUID TURBULENCE AND ENERGY CONFINEMENT.

The invariance properties of the underlying equations under scale transformations provide information about plasma transport. By applying this argument to specific models, in which the magnetic configuration and the physical mechanism of transport are identified, sufficient information may be obtained to specify completely the transport coefficients in a turbulent plasma. In this way the electron energy transport due to resistive fluid turbulence is determined in tokamak and reverse field pinch configurations.

1. INTRODUCTION

This paper is concerned with anomalous energy loss in toroidal confinement systems and the relation between energy confinement time and the parameters of the system - the so-called "scaling law" for confinement. In previous work[1] we showed that the invariance properties of the basic plasma equations led to constraints on the possible confinement laws. Here we show that much more information can be obtained by applying the argument not to the basic plasma equations, but to more specific models which incorporate some knowledge of the configuration or of the mechanism of turbulence. For resistive fluid turbulence, which we discuss in detail, invariance properties alone determine the diffusion coefficient completely.

2. SCALE INVARIANCE IN THE TOKAMAK LIMIT

Strauss[2] has discussed the resistive mhd equations for a tokamak in the large aspect ratio limit, with the ordering

$\varepsilon = a/R \sim B_p/B_t \sim p/B_t^2$. The poloidal field and the fluid velocity are expressed as

$$\vec{B}_p = \frac{\nabla\Psi \times \vec{e}}{R_0} \quad , \quad \vec{v}_p = \frac{\vec{e} \times \nabla\phi}{B_0}$$

Then the reduced equations are

$$\frac{\partial\Psi}{\partial t} = -\frac{R_0}{B_0}\vec{B}\cdot\nabla\phi + \eta\nabla_\perp^2\Psi \tag{1}$$

$$\frac{\rho R_0}{B_0}\frac{d}{dt}\nabla_\perp^2\phi = -(\vec{B}\cdot\nabla)\nabla_\perp^2\Psi - \frac{\vec{e}\cdot\nabla \times (R^2\nabla p)}{R_0} \tag{2}$$

$$\frac{dp}{dt} = 0 \tag{3}$$

These equations provide a model of a large aspect ratio tokamak. Following Ref. 1 we first seek all the scale transformations which leave the full set of equations invariant. Then the confinement law must transform appropriately under such tranformations.

The scale transformations which leave (1)-(3) invariant are

A_1 $\quad t \to \lambda_1 t, \quad \phi \to \lambda_1^{-1}\phi, \quad \eta \to \lambda_1^{-1}\eta, \quad \rho \to \lambda_1^2\rho$

A_2 $\quad B_0 \to \lambda_2 B_0, \quad \phi \to \lambda_2\phi, \quad \Psi \to \lambda_2\Psi, \quad \rho \to \lambda_2^2\rho, \quad p \to \lambda_2^2 p$

A_3 $\quad a \to \lambda_3 a, \quad \phi \to \lambda_3^2\phi, \quad \Psi \to \lambda_3^2\Psi, \quad \eta \to \lambda_3^2\eta, \quad p \to \lambda_3 p$

A_4 $\quad R_0 \to \lambda_4 R_0, \quad \rho \to \lambda_4^{-2}\rho, \quad p \to \lambda_4^{-1}p$

To conform with invariance under these transformations any confinement time τ , expressed as a function of the plasma parameters p, B_0, η and ρ, and the geometrical parameters a, R_0 and $q \equiv aB_0/R_0B_p$, must be of the form

$$\tau = \tau_R F\left(\frac{\beta q^2}{\varepsilon} \ , \ S \ , \ q\right) \tag{4}$$

where $\beta \equiv 2p/B_0^2$, $\tau_R = a^2/\eta$, $\tau_A \equiv \rho^{1/2}R_0 q/B_0$ and $S \equiv \tau_R/\tau_A$ is the magnetic Reynolds number.

If, as in Ref. 1, we had considered the full resistive fluid equations we would have found only that

$$\tau = \tau_R \, F(\beta, S, q, \varepsilon)$$

We see, therefore, that geometrical information inherent in the reduced equations is reflected as an extra constraint on the confinement law. [Note that the result (4) is incompatible with both classical ($\tau \sim \tau_R/\beta$) and Pfirsch-Schlüter ($\tau \sim \tau_R/\beta q^2$) transport; these processes are not described by the reduced equations.]

3. LOCAL RESISTIVE FLUID TURBULENCE IN TOKAMAKS

We now turn to a more detailed discussion of turbulent transport and to an important extension of the invariance argument. In the limit of large S the turbulence involves fluctuations whose scale length is small compared to the plasma dimensions across the magnetic field but is comparable to plasma dimensions along the field. We therefore write $\Psi = \Psi_0 + \Psi_1$, $p = p_0 + p_1$, $\phi = \phi_1$, where Ψ_1, p_1, ϕ_1 are the non-linear fluctuations, and introduce local variables $x \equiv (r - r_0)dq/dr$, $y \equiv \zeta - q\theta$. Then the fluctuating quantities vary rapidly in x and y but slowly in θ, while the background quantities vary slowly in all directions. We express this formally by a systematic ordering with $\delta \sim S^{-1/2}$ and

$$\frac{p_1}{p_0} = \delta \tilde{p}\left(\frac{x}{\delta}, \frac{y}{\delta}, \theta, \tau\right)$$

$$\frac{q\Psi_1}{r^2 B_0} = \delta^2 \tilde{\Psi}\left(\frac{x}{\delta}, \frac{y}{\delta}, \theta, \tau\right)$$

$$\frac{qR_0\rho^{1/2}\phi_1}{r^2 B_0^2} = \delta^2 \tilde{\phi}\left(\frac{x}{\delta}, \frac{y}{\delta}, \theta, \tau\right)$$

where $\tau = B_0 t/R_0 q \rho^{1/2}$. This ordering retains the appropriate linear and non-linear terms. Then the fluctuations are governed by

$$\frac{d\tilde{\Psi}}{d\tau} = -\frac{\partial\tilde{\phi}}{\partial\theta} + \frac{q^2}{s}\nabla_\perp^2\tilde{\Psi} \tag{5}$$

$$\frac{d}{d\tau}\nabla_\perp^2\tilde{\phi} = -\frac{\partial}{\partial\theta}\nabla_\perp^2\tilde{\Psi} - q^2 s\left\{\frac{\partial\tilde{\Psi}}{\partial x}\frac{\partial}{\partial y}\nabla_\perp^2\tilde{\Psi} - \frac{\partial\tilde{\Psi}}{\partial y}\frac{\partial}{\partial x}\nabla_\perp^2\tilde{\Psi}\right\} + \frac{\beta^*}{q}\left\{s\sin\theta\left(\frac{\partial\tilde{p}}{\partial x} - \theta\frac{\partial\tilde{p}}{\partial y}\right) - \cos\theta\frac{\partial\tilde{p}}{\partial y}\right\} \tag{6}$$

$$\frac{d\tilde{p}}{d\tau} + Kq\frac{\partial\tilde{\phi}}{\partial y} = 0 \tag{7}$$

where

$$\frac{d}{d\tau} = \frac{\partial}{\partial\tau} - q^2 s\left\{\frac{\partial\tilde{\phi}}{\partial x}\frac{\partial}{\partial y} - \frac{\partial\tilde{\phi}}{\partial y}\frac{\partial}{\partial x}\right\}$$

$$\nabla_\perp^2 = s^2\left(\frac{\partial}{\partial x} - \theta\frac{\partial}{\partial y}\right)^2 + \frac{\partial^2}{\partial y^2}$$

This set of equations describes local turbulence. In addition to q it depends on the parameters

$$s = \frac{r}{q}\frac{dq}{dr}\quad,\quad K = \frac{r}{p_0}\frac{\partial p_0}{\partial r}$$

$$S = \frac{r^2 B_0}{\eta\rho^{1/2}R_0 q}\quad,\quad \beta^* = \frac{2R_0 q^2}{r}\frac{p_0}{B_0{}^2}$$

Equations (5)-(7) already incorporate invariance under the transformations A1-A4. However, they are also invariant under additional transformations because a new characteristic length, independent of the size of the system, has been introduced. These new transformations are

B_1 $\quad x \to \mu_1 x,\quad y \to \mu_1 y,\quad q \to \mu_1 q$

B_2 $\quad x \to \mu_2 x,\quad y \to \mu_2 y,\quad \tilde{\phi} \to \mu_2{}^2\tilde{\phi},\quad \tilde{\Psi} \to \mu_2{}^2\tilde{\Psi},\quad \tilde{p} \to \mu_2{}^2\tilde{p}$

$\quad S \to \mu_2{}^{-2}S$

B_3 $\quad \tilde{p} \to \mu_3\tilde{p},\quad K \to \mu_3 K,\quad \beta^* \to \mu_3{}^{-1}\beta^*$

To conform with invariance under the transformations B1-B3, any local convective diffusion coefficient must be of the form

$$D_0 = \eta F_0(\alpha,s)$$

where $$\alpha \equiv -2 \frac{R_0}{B_0^2} \frac{dp_0}{dr} q^2 \quad \text{and} \quad s \equiv \frac{r}{q} \frac{dq}{dr}$$

4. TRANSPORT ALONG STOCHASTIC FIELDS IN TOKAMAKS

Energy loss by transport along a stochastic magnetic field lies outside the simple resistive fluid model. Nevertheless, when the stochastic field is created by fluid turbulence the invariance properties of the fluid equations can still be used indirectly.

Usually high temperature plasmas are in the collisionless regime where the diffusion coefficient representing loss along a stochastic field is[3] $D_s \sim v_e D_m$ where D_m is the magnetic field diffusion coefficient

$$D_m = \left(\frac{\delta B_r}{B}\right)^2 L_c$$

Here L_c is the correlation length of the fluctuations. The calculation of this correlation length is difficult but we require only that it be determined by the turbulence. First we need to know how it transforms under the scale transformations. [As it is not a characterstic length perpendicular to the field its transformation properties cannot be inferred directly from those of the local coordinates x and y.] To determine the transformation properties of L_c we observe that diffusion of the field lines can be viewed as a random walk with perpendicular step length

$$\Delta r = \left(\frac{\delta B_r}{B}\right) L_c$$

This step length transforms as other cross-field lengths and must therefore be of the form

$$\Delta r = \frac{r}{s^{1/2}} F(\alpha,s)$$

The transformation of the fluctuation amplitude is straightforward and requires

$$\left(\frac{\delta B_r}{B}\right)^2 = \frac{r^2}{q^2 R_0^2 S} F(\alpha,s)$$

so that L_c is of the form

$$L_c = qR_0 F(\alpha,s)$$

and the diffusion coefficient for energy loss in a stochastic field is

$$D_s = \eta\left(\frac{M}{m}\beta\right)^{1/2} F_s(\alpha,s) \qquad (8)$$

5. RESISTIVE BALLOONING MODE TURBULENCE

So far we have shown that the invariance properties severely constrain the turbulent diffusion coefficient for a tokamak plasma and that its form is determined up to functions $F(\alpha,s)$. This is already a valuable result. However, the functions $F(\alpha,s)$ can themselves be determined from invariance properties alone if the nature of the turbulence is more closely specified.

For turbulence due to resistive ballooning modes with small n^2/S , $\partial\tilde{\Psi}/\partial t$ may be neglected and the fluctuations vary more rapidly in the (radial) x-direction than in the (poloidal) y-direction. For such fluctuations convection of pressure is the dominant non-linear process and others may be neglected. [These are the customary assumptions in renormalised plasma turbulence calculations[4].] Then the equations of local turbulence reduce to

$$\frac{\partial\tilde{\phi}}{\partial\theta} = \frac{q^2 s^2}{S}\frac{\partial^2}{\partial x^2}\tilde{\Psi} \qquad (9)$$

$$\frac{d}{d\tau}\frac{\partial^2\tilde{\phi}}{\partial x^2} = -\frac{\partial}{\partial\theta}\frac{\partial^2\tilde{\Psi}}{\partial x^2} + \frac{\beta^*}{qs}\sin\theta\frac{\partial\tilde{p}}{\partial x} \qquad (10)$$

$$\frac{\partial \tilde{p}}{\partial \tau} - q^2 s \left[\frac{\partial \tilde{\phi}}{\partial x}\frac{\partial \tilde{p}}{\partial y} - \frac{\partial \tilde{\phi}}{\partial y}\frac{\partial \tilde{p}}{\partial x}\right] + Kq \frac{\partial \tilde{\phi}}{\partial y} = 0 \qquad (11)$$

In addition to the transformations B1-B3, these equations are invariant under two further scale transformations,

C_1 $\tau \to \nu_1 \tau$, $x \to \nu_1^{-1/2} x$, $y \to \nu_1^{-1/2} y$, $\tilde{\phi} \to \nu_1^{-2}\tilde{\phi}$

$\tilde{\Psi} \to \nu_1^{-3}\tilde{\Psi}$, $\tilde{p} \to \nu_1^{-5/2}\tilde{p}$, $K \to \nu_1^{-2} K$

C_2 $x \to \nu_2 x$, $y \to \nu_2 y$, $\tilde{\phi} \to \nu_2 \tilde{\phi}$, $\tilde{\Psi} \to \nu_2 \tilde{\Psi}$, $\tilde{p} \to \nu_2 \tilde{p}$

$s \to \nu_2 s$, $K \to \nu_2 K$

which impose further constraints on the diffusion coefficient. These additional contraints are just sufficient to determine the functions $F(\alpha,s)$, and hence the diffusion coefficient, completely (up to a constant multiplier). For convective diffusion we find

$$D_c = c \frac{Rq^2\eta}{sB_0^2}\left(\frac{-dp}{dr}\right) \qquad (12)$$

and for collisionless diffusion in stochastic fields

$$D_s = c\eta \left(\frac{M\beta}{m}\right)^{1/2} \left(\frac{R}{r}\frac{q^3}{B_0^2}\frac{p'}{q'}\right)^{3/2} \qquad (13)$$

6. THE REVERSE FIELD PINCH

Similar results can be obtained for turbulent energy loss due to resistive g-modes in a Reverse Field Pinch[5]. The convective diffusion coefficient is

$$D_0^{RFP} = c\eta \frac{\delta}{\sigma^2} \qquad (14)$$

and the stochastic field diffusion coefficient is

$$D_s^{RFP} = c\eta\left(\frac{M\beta}{m}\right)^{1/2}\left(\frac{\delta}{\sigma^2}\right)^{3/2} \qquad (15)$$

where $\delta = \frac{rp'}{B_\theta^2} \cdot \frac{r}{B^2}\left(p + B^2\right)'$, $\sigma = \frac{B_\theta}{B}\left(\frac{rB_z}{B_\theta}\right)'$

The differences between these results and the corresponding ones for tokamak arise because in the large aspect ratio tokamak limit only the geodesic curvature of the lines of force is important, whereas in RFP the geodesic curvature is negligible and normal curvature is the dominant influence.

7. CONCLUSIONS

The invariance of the underlying equations under scale tranformations provides valuable information about plasma transport. By applying this argument to specific models in which the physical mechanism of transport and the configuration of the magnetic field are identified, sufficient information may be obtained to determine fully the local transport coefficient (apart from a numerical factor of order unity).

Using this method we have derived the diffusion coefficients for transport due to resistive-fluid turbulence in tokamak and reverse field pinch configurations. We emphasise that the assumptions made in obtaining these results are also made in calculations of renormalised turbulence theory, eg Ref. 4, and our result for the tokamak, [Eq.(13)], is equivalent to that calculation. The fact that we obtain the diffusion coefficient from invariance alone shows that it is a consequence of the basic assumptions of the model and does not depend on renormalisation theory, etc.

For high temperature plasmas the relevant results are those for collisionless transport in stochastic fields [Eq. (13) for tokamak and Eq.(15) for RFP]. These have interesting implications for the relative performance of similar-sized tokamaks and pinches. At a similar value of <u>poloidal</u> β confinement is much better in the tokamak, but at a similar value of total β the RFP has better confinement than the tokamak. This is because in both cases the losses increase rapidly with β, but in tokamak they depend on the ratio of β to its maximum ideal mhd limit, ie on $\beta q^2/\varepsilon$, whereas in RFP they depend on β itself.

Another consequence of Eq.(15) is that it predicts that all ohmically heated RFPs should achieve a similar β $(\sim (m/M)^{1/6})$. Correspondingly their temperature should depend only on I^2/N (where N is the line density). These predictions are in accord with the general trends observed in RFP experiments. On the other hand, the predictions of Eq.(13) are not in good accord with the confinement time scaling suggested for present tokamaks[6]. This implies that other mechanisms are important.

An alternative explanation for the anomalous loss in tokamaks is drift wave turbulence driven by the dissipative trapped-electron instability. In the simplest model of such drift-wave turbulence[7,8,9], ions are described by the collisionless gyro-kinetic equation and electrons by the drift-kinetic Fokker-Planck equation; trapped electrons are included via a bounce-averaged equation but curvature-drifts are ignored. For this model an application of the invariance argument, similar to that described here, leads to a diffusion coefficient

$$D = \frac{T}{eB} \frac{a_i}{r_n} F(u,v) \qquad (16)$$

where

$$u = \frac{\varepsilon^{3/2} \nu_e}{\nu_e L_s} \quad \text{and} \quad v = \frac{r_n}{L_s}$$

As one might expect, since drift-wave turbulence contains many more parameters than resistive mhd, invariance alone does not completely specify the diffusion coefficient. Nevertheless (16) is a useful result; it shows that losses due to these turbulent drift-waves are a function only of the two parameters indicated. The first contains the plasma properties and is $\sim T^2/n$, while the second is purely geometrical. Eq.(16) also specifies completely the dependence on the magnetic field.

We have also investigated plasma models in which collisional resistivity is replaced by collisionless electron damping, electron inertia, or electron parallel pressure. In

these models the invariance argument leads, for $\beta \ll \epsilon/q^2$, to diffusion coefficients of the form

$$D = \left(\frac{mc^2}{e^2}\right) \frac{v_e}{nqR} F\left(\frac{v_e}{v_A}\right)$$

where $v_A = B/\rho^{1/2}$. A diffusion coefficient of the form with F = 1 would be in good agreement with confinement time data for Ohmically heated tokamaks, both in magnitude and scaling. However, the instability responsible for turbulence in this model has not been identified.

REFERENCES

[1] CONNOR, J.W., TAYLOR, J.B., Nucl. Fusion **17** (1977) 1047.
[2] STRAUSS, H.R., Nucl. Fusion **23** (1983) 649.
[3] RECHESTER, A.B., ROSENBLUTH, M.N., Phys. Rev. Lett. **40** (1978) 38.
[4] CARRERAS, B.A., et al., Phys. Rev. Lett. **50** (1983) 503.
[5] CONNOR, J.W., TAYLOR, J.B., to be published in Phys. Fluids.
[6] GOLDSTON, R., Plasma Phys. Contr. Fusion **26** (1984) 87 (Invited Papers of 11th Europ. Conf. Aachen, 1983).
[7] HASSELBERG, G., ROGISTER, A., Nucl. Fusion **23** (1983) 1351.
[8] CHEN, L., et al., Phys. Rev. Lett. **39** (1977) 754.
[9] KADOMTSEV, B.B., POGUTSE, O.P., Pis'ma Zh. Ehksp. Teor. Fiz. **39** (1983) 225.

DISCUSSION

F.W. PERKINS: Which is the larger diffusion coefficient, the magnetic flutter or the convection?

J.B. TAYLOR: It appears that the loss along the stochastic field exceeds the convective loss whenever

$$\beta > \left(\frac{m}{M} \beta_{\max}^{MHD}\right)^{1/2}$$

TOKAMAK DISRUPTIONS

J.A. WESSON
JET Joint Undertaking,
Abingdon, Oxfordshire

A. SYKES, M.F. TURNER
Culham Laboratory,
(Euratom/UKAEA Fusion Association),
Abingdon, Oxfordshire

United Kingdom

Abstract

TOKAMAK DISRUPTIONS.

An explanation is given for the occurrence of tokamak disruptions. Under normal conditions the tearing instability is self-stabilizing through its reduction of the destabilizing current gradient, and a saturated state can then exist. Under certain conditions, however, further growth of the instability is itself destabilizing, and a disruption results. The transition to disruption has the form of a catastrophe.

INTRODUCTION

There are four basic stages, illustrated in Fig. 1, in the development of a typical tokamak disruption [1]:

(i) There is a change in the plasma conditions; for example, the total current, impurity content, or the plasma density. On the time-scale of the disruption this change is usually slow.
(ii) There is a spontaneous growth of MHD activity, principally the m = 2 tearing mode. This growth often occurs after a long period of steady, low-level m = 2 oscillations.
(iii) After a period of growth of the m = 2 mode there is a sudden fall of central plasma temperature and a flattening of the current profile.
(iv) The discharge is brought to an end by a current quench.

None of these stages is properly understood. Because of the role of the m = 2 mode, it seems likely that the initial change in conditions is such as to move the current gradient and the q = 2 surface closer together. This can be the result either of an increase in the current, which moves the q = 2 surface outward, or of a narrowing of the current profile, which moves the region of steep current gradient inward.

For the second stage, an explanation is required of how a small tearing mode island is induced to grow on a time-scale shorter than that of the change in plasma

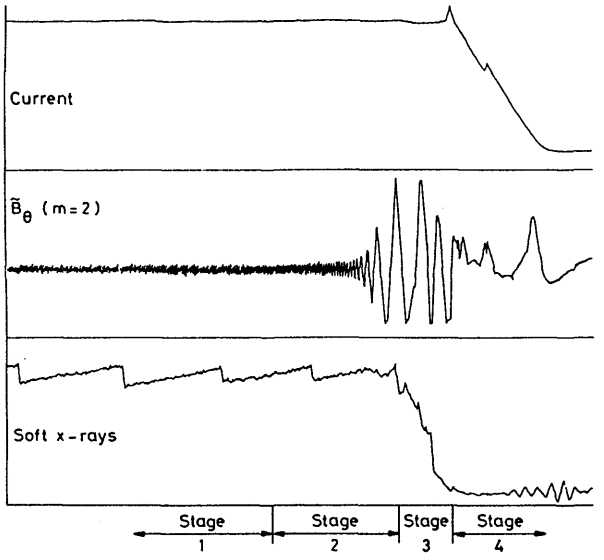

FIG.1. Results from the Frascati Tokamak (FT) experiment showing total current, magnetic oscillations and soft X-ray emission prior to and during a disruption. The traces shown occupy 30 ms.

conditions. This occurs at a stage when the islands are saturated and too small for their interaction to be significant. An explanation of this phenomenon is described here. It rests on calculations which show that although at low amplitude island growth is stabilizing and leads to saturation, at larger island size the island growth can itself be destabilizing.

The explosive growth of the m = 2 mode resulting from this effect leads to transference of energy to other modes and to island overlap. This is presumably the cause of the loss of confinement observed in stage (iii).

The fourth stage seems to be associated with the introduction of impurities into the plasma, causing rapid cooling and leading to a highly resistive plasma.

CATASTROPHE MODEL

We turn now to a description of the theoretical model proposed for the second stage. This starts with a saturated m = 2 island at the q = 2 surface. This state may be regarded as one in which the free energy arising from the destabilizing current gradient has been relaxed by the formation of the island. To explain the disruption we must examine the factors governing the size of the island. We shall find that, whereas under non-disruptive conditions island growth is a stabilizing

effect, beyond a critical condition island growth is destabilizing and disruption occurs. Slightly to one side of this condition, a steady saturated island exists but an arbitrarily small change leads to disruptive growth.

The destabilizing force for the tearing modes arises from the negative current gradient at radii inside that of the resonant surface ($r = r_s$). In linear theory the measure of instability is obtained by solving the equation [2]:

$$\frac{1}{r}\frac{d}{dr}\left(r\frac{d\psi}{dr}\right) - \frac{m^2}{r^2}\psi - \frac{dj_0/dr}{B_{\theta 0}(1 - ng/m)}\psi = 0 \qquad (1)$$

where ψ is the perturbed flux function ($\propto rB_r$) for a mode with poloidal and toroidal mode numbers m and n; j_0 and $B_{\theta 0}$ are the equilibrium axial current density and poloidal magnetic field, and q is the safety factor. Solutions of the equation in the regions $r < r_s$ and $r > r_s$ are then used to calculate

$$\Delta' = \left.\frac{\psi'}{\psi}\right|_{r_s - \epsilon}^{r_s + \epsilon} \qquad \epsilon \to 0$$

If $\Delta' > 0$, an island forms. For small islands an estimate of the island saturation width w_s is given by

$$\Delta'(w_s) = 0 \qquad \text{where} \qquad \Delta'(w) = \left.\frac{\psi'}{\psi}\right|_{r_s - w/2}^{r_s + w/2} \qquad (2)$$

A more complete calculation leads to a correction [3] $\Delta'(w) = \alpha w$, but this is not essential for understanding the basic behaviour. A typical graph of $\Delta'(w)$, showing how it determines w_s, is shown in Fig. 2(a).

For larger islands the non-linear effect of the island on the equilibrium becomes important. This is included in the analysis by writing Eq.(1) in the form:

$$\frac{1}{r}\frac{d}{dr}\left(r\frac{d\psi}{dr}\right) - \frac{m^2}{r^2}\psi = J(w)\,\psi \qquad \text{where} \qquad J(w) = \frac{dj/dr}{B_\theta\,(1 - nq/m)}$$

the variables on the right-hand side now being the equilibrium quantities consistent with the presence of the island. The island size is still given by $\Delta'(w_s) = 0$ but there are now two coupled effects of varying w. One is the effect of varying the position ($r = r_s \pm w/2$) at which ψ'/ψ is calculated; the other is the change in the function J(w). For clarity we designate the Δ' calculated including both effects by the symbol Δ^*. Under conditions of interest in the present context $\Delta^*(w)$ takes the form shown in Fig. 2(b). There are then two

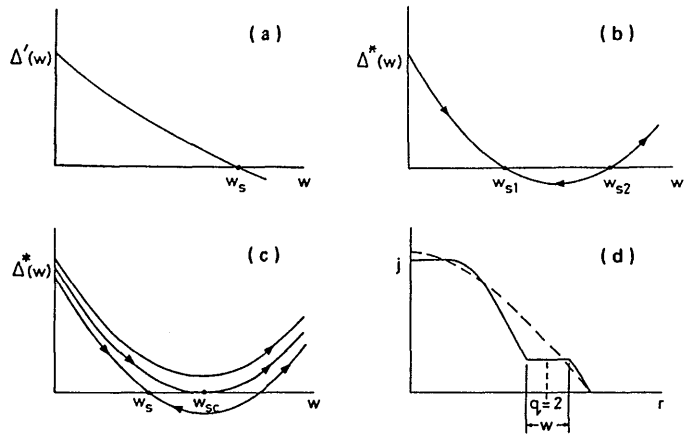

FIG.2. (a) Graph of $\Delta'(w)$ showing how the saturation island width w_s is determined. The island grows until $\Delta'(w) = 0$. (b) Graph of $\Delta^*(w)$ showing how inclusion of the self-consistent modification of the configuration changes the calculation of w_s. There are now two solutions: the stable w_{s1} and unstable w_{s2}. (c) Graphs of $\Delta^*(w)$ showing how the saturated island width w_s adjusts until the catastrophe point w_{sc} is reached. No steady solutions then exist and w grows disruptively. (d) Graph of j(r) showing how a limitation of j round the axis together with the removal of current from the region of the cooled island leads to a non-linearly destabilizing current gradient.

possible non-linear equilibria, with island widths w_{s1} and w_{s2}; their stability is indicated by the arrows. If the imposed conditions are varied by, say, an increase in the total current or amount of plasma impurity there is a set of such curves as illustrated in Fig. 2(c).

If the conditions are slowly changed to produce a larger island, the point w_s moves across adiabatically. If, however, the critical width w_{sc} is reached, the island grows spontaneously and a disruption occurs.

Two basic factors lead to this situation; they are illustrated in Fig. 2(d). The dashed line shows the radial profile of the current density which would occur in the absence of instability and impurities. The first factor leading to disruption is the effect of the cooling of the island region through contact of the island with the limiter or cold plasma in the outer region. As seen from the figure, this displaces current from the island region to enhance the destabilizing current gradient at inner radii. The second factor is the restriction of the current density round the axis either by MHD instability [4] or by increased resistivity due to impurities. This prevents the current from concentrating round the axis and again enhances the destabilizing current gradient, as seen from the figure.

This theory supports and clarifies the calculations of self-consistent 'torn' equilibria carried out by Sykes and Wesson [5] in which it was observed that under conditions associated with disruptions no equilibria could be found.

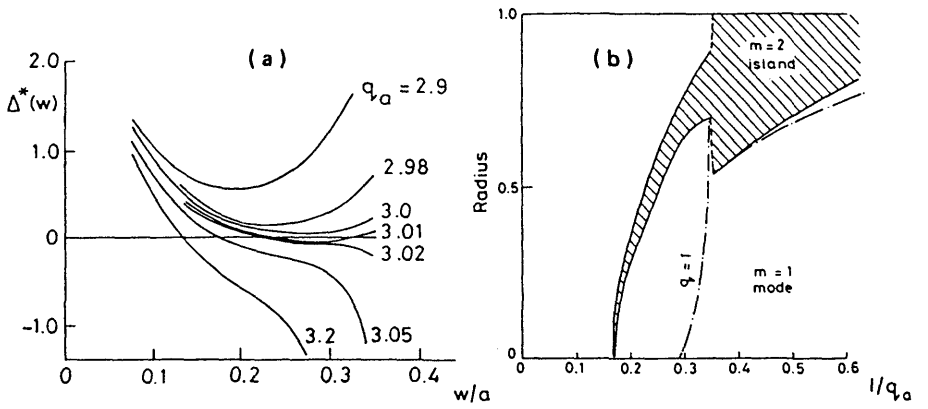

FIG.3. (a) Computed graphs of $\Delta^*(w)$ for a number of values of q_a. (b) The resulting saturated island sizes as a function of $1/q_a$ ($\propto$ total current), showing the sudden change in w at the critical value of q_a.

As an example of the theory, calculations of $\Delta^*(w)$ and w_s have been carried out for disruptions induced by low q_a (q_a being the surface value of q). The model includes limitation of the value of q at the axis by MHD instability and determination of the resistivity profile by a simple transport model (for details see Ref. [6]). Plots of $\Delta^*(w)$ are given in Fig. 3(a), and the resulting island widths are plotted against q_a^{-1} in Fig. 3(b). While the theory is not accurate for the large island widths obtained under conditions of disruption, the catastrophe nature of the disruption is made apparent.

The process of disruption has been studied in a number of calculations. In a simulation by Sykes et al. [7, 8] the m = 2 mode was followed through to a disruption and the resulting loss of confinement was demonstrated. A calculation including many modes was carried out by Carreras et al. [9]. It was found that the m = 2 mode grew less strongly, but the combined effect of all the modes covered a somewhat larger part of the plasma than when the m = 2 mode alone was allowed. It seems likely that the details of the process are not important. The essential point is that, under disruptive conditions, the relaxation of the free energy associated with the current gradient leads to a *more* unstable configuration.

In summary, we can say that certain experimental conditions are found to lead to disruption which can appear without a perceptible change in the pre-existing conditions. Under non-disruptive conditions a saturated island exists. As the conditions are made more severe the island size increases adiabatically. At a critical point a catastrophe occurs and further island growth is destabilizing. This is proposed as the basic cause of disruptions.

ACKNOWLEDGEMENT

We thank the FT Group for permission to use Fig. 1.

REFERENCES

[1] Current Disruption in Toroidal Devices (Proc. IAEA Symp. Garching, 1979), Max-Planck-Inst. Plasmaphysik, Garching, Rep. IPP 3/51 (1979).
[2] WESSON, J.A., Nucl. Fusion **18** (1978) 87.
[3] WHITE, R.B., MONTICELLO, D.A., ROSENBLUTH, M.N., WADDELL, B.V., Phys. Fluids **20** (1977) 800.
[4] SYKES, A., WESSON, J.A., Phys. Rev. Lett. **37** (1976) 140.
[5] SYKES, A., WESSON, J.A., "Saturated kink and tearing instabilities in tokamaks", Plasma Physics and Controlled Nuclear Fusion Research 1980 (Proc. 8th Int. Conf. Brussels, 1980), Vol. 1, IAEA, Vienna (1981) 237.
[6] TURNER, M.F., WESSON, J.A., Nucl. Fusion **22** (1982) 1069.
[7] SYKES, A., WESSON, J.A., in Current Disruption in Toroidal Devices (Proc. IAEA Symp. Garching, 1979), Max-Planck-Inst. Plasmaphysik, Garching, Rep. IPP 3/51 (1979).
[8] SYKES, A., WESSON, J.A., Phys. Rev. Lett. **44** (1980) 1215.
[9] WADDELL, B.V., CARRERAS, B., HICKS, H.R., HOLMES, J.A., Phys. Fluids **22** (1979) 896.

DISCUSSION

K. LACKNER: As I understand your theory, the distinguishing feature of your catastrophe-type curves of $\Delta'(w)$ is that you assume that current profiles adjust continuously so as to keep $q > 1$ at the centre. This adjustment, however, requires current density displacement from the vicinity of $q \sim 2$ to $r = 0$ which, unless you bring in an additional anomalous mechanism, requires resistive diffusion over a relatively large distance, and therefore a long time-scale limiting the dynamics of your disruption model.

J.A. WESSON: For the theory to be consistent with experiment, it must predict a sufficiently short time-scale for the growth of the island and for the adjustment of the equilibrium. Regarding the growth time-scale, we can use the approximate form:

$$\Delta^* = \alpha t + \frac{1}{2}\frac{d^2\Delta^*}{dw^2}(w - w_0)^2$$

and solve the Rutherford equation:

$$\frac{dw}{dt} = \eta\Delta^*(w)$$

to obtain the solution shown in Fig.A. The rapid growth is characterized by a time:

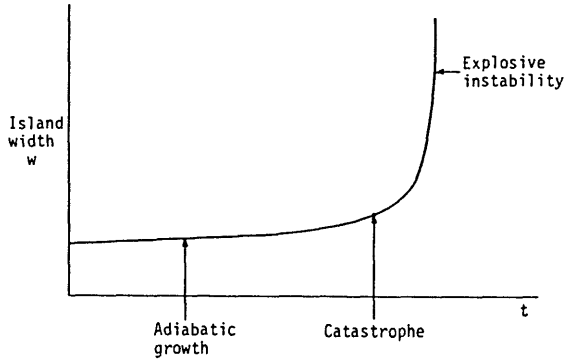

FIG.A. Island width versus time.

$$\tau \sim \left(\eta w \frac{d^2\Delta^*}{dw^2}\right)^{-1}$$

and, typically, $\tau \sim 10^{-2}(a^2/\eta)$, which is consistent with experiment. Turning to the equilibrium change, the length scale over which the equilibrium must adjust is that between the q = 1 surface and the edge of the m = 2 island. In our calculations (see Fig.4 of Ref.[4]) this length is ~0.1 a. The corresponding resistive time-scale is $\tau \sim 10^{-2}(a^2/\eta)$, which is again consistent with experiment. I should also mention that, using the present model, our time-dependent simulations of impurity-driven disruptions gave an island growth time of a few ms for a plasma of 26 cm radius.

H.L. BERK: Do you believe you now understand the reasons why disruptions usually do not occur?

J.A. WESSON: It is clear from the theory that, if the current gradient close to the m = 2 island is not too steep, the plasma is safe from disruptions. In the calculations I have described, this requires only that the value of q_a be sufficiently large. However, we have not made a quantitative study of the dependence of the critical q_a on the plasma parameters, nor have we made a detailed study of the density limit.

Y.-K.M. PENG: Have you also looked at the evolution of $\Delta^*(w)$ for plasmas at constant total plasma current, which may correspond to many of the experimental situations of disruption?

J.A. WESSON: For a constant total current, disruptions are induced by increasing the density. These disruptions are widely believed to be due to cooling of the outer part of the plasma (usually by impurities). We have reproduced such disruptions in our simulations (see Ref.[4]). It is possible, therefore, that the catastrophe model may have a general applicability. However, I do not believe that we properly understand the density limit.

MHD EQUILIBRIUM AND STABILITY FOR STELLARATOR/TORSATRON CONFIGURATIONS*

B.A. CARRERAS, J.L. CANTRELL,
L.A. CHARLTON, L. GARCIA, J.H. HARRIS,
T.C. HENDER, H.R. HICKS, J.A. HOLMES,
J.A. ROME, V.E. LYNCH
Oak Ridge National Laboratory,
Oak Ridge, Tennessee,
United States of America

Abstract

MHD EQUILIBRIUM AND STABILITY FOR STELLARATOR/TORSATRON CONFIGURATIONS.

The stellarator equilibrium and stability studies presented in this paper are concentrated in two areas: the improvement of the understanding of high-beta torsatrons through the concept of flux control and the study of helical-axis configurations.

1. FREE BOUNDARY EQUILIBRIUM AND STABILITY STUDIES FOR ATF

1.1 INTRODUCTION

ATF is a medium aspect ratio (plasma aspect ratio $A_p = 7$) $\ell = 2$ continuous torsatron with twelve field periods ($M = 12$). This configuration has been demonstrated, using the stellarator expansion [1], to have good high beta MHD equilibrium and stability properties [2].

Present studies are directed toward improving the flexibility of the ATF design by determining means of controlling important plasma parameters, such as the magnetic well and the rotational transform profile. We concentrate here on the use of the ATF vertical-field (VF) coil system in providing this control.

The stellarator expansion equilibrium and stability calculations carried out for the ATF device in Ref. [2] feature a fixed-boundary approach [3-4]. This method provides convenient control of the equilibrium shaping and is useful for rapidly producing and considering a wide range of cases. However, with the demonstrated desirability of the ATF configuration from an MHD equilibrium and stability standpoint and with the capability of the

* Research sponsored by the Office of Fusion Energy, US Department of Energy, under Contract No. DE-AC05-84OR21400 with Martin Marietta Energy Systems, Inc.

VF coil system for controlling plasma parameters, the need to study the free-boundary equilibrium and stability of ATF becomes important. To carry out this work, we have used the Princeton Plasma Physics Laboratory free-boundary stellarator expansion equilibrium and stability codes [5-8].

The stellarator expansion was originally derived by Greene and Johnson [1] using an ordering scheme with the ratio of the helical and toroidal magnetic-field strengths as the expansion parameter. In this scheme, toroidal effects are assumed to enter in second order. The crucial feature of the stellarator expansion is the reduction of the equilibrium calculation from three to two dimensions through toroidal averaging over a field period. This feature makes the systematic computational treatment of a large number of cases possible. With this reduction, one solves an equilibrium equation for the averaged poloidal flux function

$$\Delta^*(\psi - \psi_v^*) = -R^2 \frac{dP}{d\psi} - (F + F^*) \frac{dF}{d\psi} \qquad (1)$$

which closely resembles the Grad-Shafranov equation for tokamaks. In Eq. (1), $\psi(R,Z)$ is the averaged poloidal flux function, $\psi_v^*(R,Z)$ is the averaged poloidal flux function of the vacuum, R is the major radius coordinate, Z is the vertical position, $P(\psi)$ is the pressure, $F^*(R,Z)$ is the helical-curvature term, and the averaged toroidal flux function $F(\psi)$ is adjusted to give either strict flux conservation ($\iota = \iota_v$) or zero net toroidal current within each flux surface ($\langle J_\phi \rangle_\psi = 0$). The quantities ψ_v^* and F^* depend only upon the vacuum magnetic field. While the details are discussed in Refs. 1 and 2, it suffices for present purposes to state that F^* depends only upon the helical magnetic field and that $\psi_v^* = \psi_0 + \psi^*$, where ψ^* depends only on the helical field and ψ_0 contains only axisymmetric contributions. In particular, ψ_0 is obtained by solving $\Delta^*\psi_0 = 0$ with the boundary condition $\vec{B}_{0_\perp} = \frac{1}{R} \vec{\nabla}\psi_0 \times \hat{\zeta}$, where $\vec{B}_{0_\perp}$ is the poloidal vacuum field averaged over a field period. Hence, the effect of the axisymmetric VF coil system in these calculations enters entirely through the quantity ψ_0. Although the stellarator expansion is not an exact model for three-dimensional equilibrium and stability (having been derived in the limit of small helical-field variations, large aspect ratio, and low β), comparison of these calculations to the full three-dimensional equilibrium calculations have shown good agreement [2].

The free-boundary code for low-n stability, described in Refs [7] and [8], uses a δW approach, with an optional conducting wall that can be placed at any distance from the plasma. This free-boundary system of codes is a version of the tokamak MHD equilibrium and stability PEST code [5,6] modified to use the stellarator expansion.

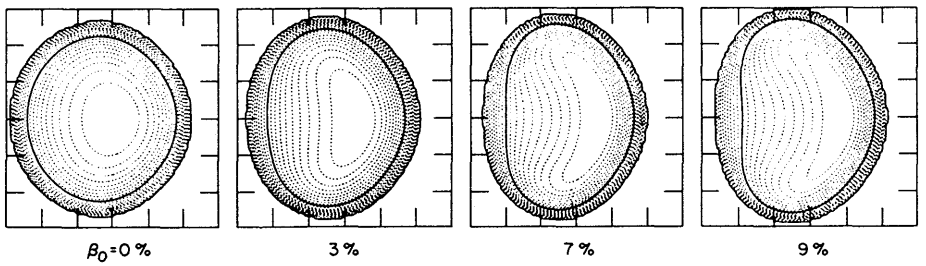

FIG.1. Constant-ι zero-current free-boundary equilibrium sequence as described in the text.

1.2 ROTATIONAL TRANSFORM CONTROL USING THE ATF VF COIL SYSTEM

The ATF VF coil system consists of three pairs of axisymmetric coils. Each pair is up-down symmetric about the toroidal midplane. In Ref. [2] we have shown that by changing the relative currents in the inner and outer VF coils, it is possible to shift the magnetic surfaces in or out in major radius, thereby changing the magnetic well, and hence the stability of the resulting equilibria.

The VF coil system can also be programmed to control the rotational transform profile at high beta by modifying the plasma shape while keeping the magnetic axis fixed [9]. This technique is potentially very useful because if the external fields are not changed as beta is increased, zero net current equilibrium sequences show significant deformation of the rotational transform profile. The rotational transform increases on the magnetic axis, decreases at the (fixed) plasma boundary, and forms intermediate minima. Such major variations of the rotational transform could lead to resistive instabilities and degradation of confinement.

We have found that the flux-controlled equilibrium sequence, in which the VF coils are programmed to maintain constant ι_0, is particularly attractive. Figure 1 shows such a sequence of free boundary average method equilibria. Throughout this sequence, the vacuum-averaged flux surface chosen for the boundary is taken such that $\iota_a = 1$, which is consistent with the principle of a natural limiter. The progressive elongation of the flux surfaces with increasing beta is required to maintain constant ι_0. The flux-controlled equilibrium path also has the favorable property of reduced finite-beta axis shift relative to that of the fixed-configuration equilibrium sequence. This decrease can be understood as a consequence of a reduction in the Pfirsch-Schlüter currents with increasing elongation of the magnetic surfaces [9]. Although one might expect a decrease in the magnetic well in conjunction with the reduced axis shifts and Pfirsch-Schlüter currents, the shaping of the magnetic surfaces accompanying these reductions prevents such a decrease.

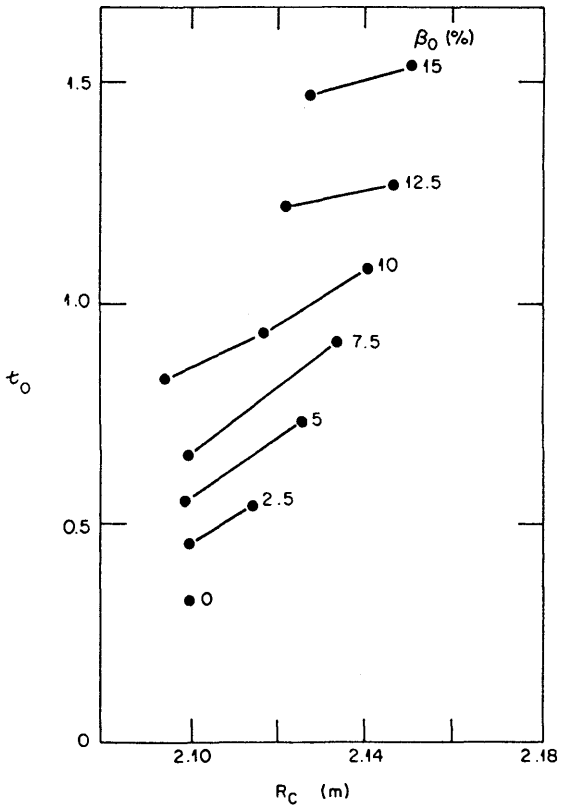

FIG.2. Free-boundary stable equilibrium sequences for standard ATF configuration. R_c is the radial position of the centroid of the last flux surface.

1.3 FREE-BOUNDARY STABILITY CALCULATIONS

The stability of several zero-current equilibrium sequences has been studied. At present we are limited in our studies by the convergence of the equilibrium code at high β. The highest value of β for which we have obtained converged free-boundary equilibria is $\langle\beta\rangle = 4.6\%$. Figure 2 shows several of the equilibrium sequences studied for the standard ATF configuration without shaping of the vertical field. We have not observed any free boundary instability for these sequences, when the plasma is centered. To destabilize the $n = 1$ free-boundary mode, it is necessary to shift the magnetic axis inward, as was the case for internal modes [2]. The stability to global $n = 1$ free boundary modes depends upon the relationship between the rotational transform and magnetic well. As the plasma is shifted inward in major radius, the $\iota = 1/2$ surface shifts outward in minor radius because of profile deformation of the

$\langle J_\phi \rangle_\psi = 0$ equilibria. Simultaneously, the destabilizing region of $V'' > 0$ shifts inward in minor radius. The $n = 1$ kink mode arises with a strong $m = 2$ component as the $\iota = 1/2$ surface moves into the proximity of $V'' > 0$. These modes are observed with the conducting wall at infinity.

2. HELICAL AXIS CONFIGURATIONS

2.1 INTRODUCTION

In this section, the properties of two distinct classes of helical axis stellarators will be studied. First the equilibrium properties of the helical axis ATF [10], which is formed by imbalancing the helical coil currents, will be examined. To study this device, the 3-D NEAR [11] code and an average method [12] have been used. Both of these methods are based on a set of vacuum flux coordinates. The average method is a generalization of the stellarator expansion [2] to helical axis configurations. To leading order, the averaged equilibrium equations yield a Grad-Shafranov equation:

$$\nabla_\perp^2(\psi - \psi_{vac}) = -\frac{F_v}{B_0}\frac{1}{D_v}\frac{\partial P}{\partial \psi} - F\frac{\partial F}{\partial \psi} \qquad (2)$$

Also to leading order, the toroidally varying part of the equilibrium equations reduces to a Poisson-type equation. Numerical methods have been implemented to solve both this Poisson equation and Eq. (2). Full details of this average method are given in Ref. [12].

The other class of helical axis stellarators which have been studied are heliacs [13]. Previous stability studies for these devices show the expectation of high β stability limits in the infinite aspect ratio limit. For the equilibria, it will be shown that finite aspect ratio effects are vital. In particular, the interplay between toroidal and helical curvatures leads to resonant or nearly resonant harmonics which can cause large distortion to the flux surfaces. Unfortunately, the average method is not applicable to heliacs which have comparable helical and toroidal shift and so the fully 3-D NEAR code is used. The NEAR code uses a set of vacuum flux coordinates as an Eulerian basis and solves the equilibrium in a manner similar to the Chodura-Schlüter code [14], but with much better numerical resolution. A detailed description of this method is given in Ref. [11].

2.2 EQUILIBRIUM RESULTS FOR ATF HELICAL AXIS CONFIGURATION

The low rotational transform per field period ($\iota/M \sim 0.1$) and relatively low aspect ratio, result in the equilibrium shift being toroidally dominated for the helical axis ATF. The average method described in the previous section is thus applicable. The flux

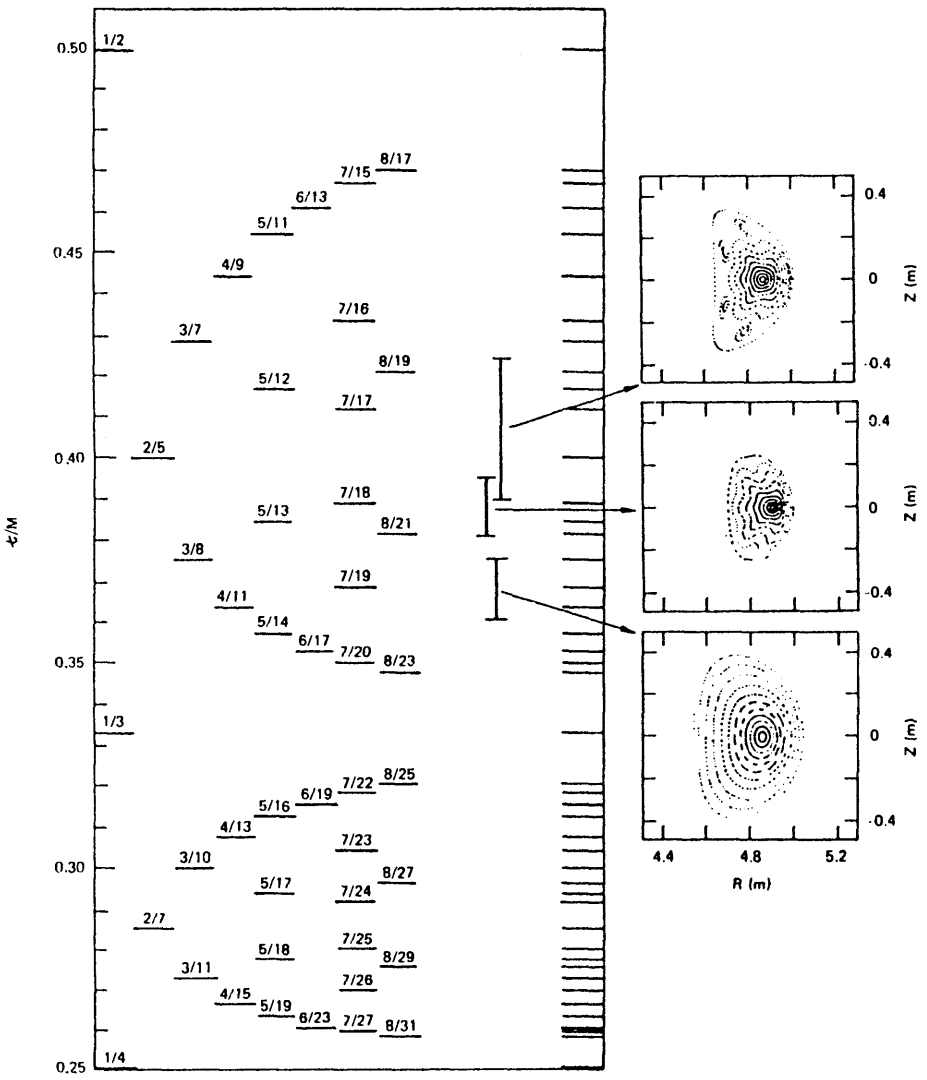

FIG.3. Locations of dominant resonances (per field period) and typical equilibrium flux surfaces associated with ι ranges ($\beta_0 = 5\%$, $A_c = 4$).

surfaces, for the helical axis ATF, computed with 3-D NEAR code and with the average method agree very well [12]. To make this comparison more quantitative, the equilibrium shifts (Δ_p) computed with NEAR (3-D) and the average method have been compared - they agree reasonably well. Good equilibria have been found for the helical axis ATF for central beta up to 10%. However, the

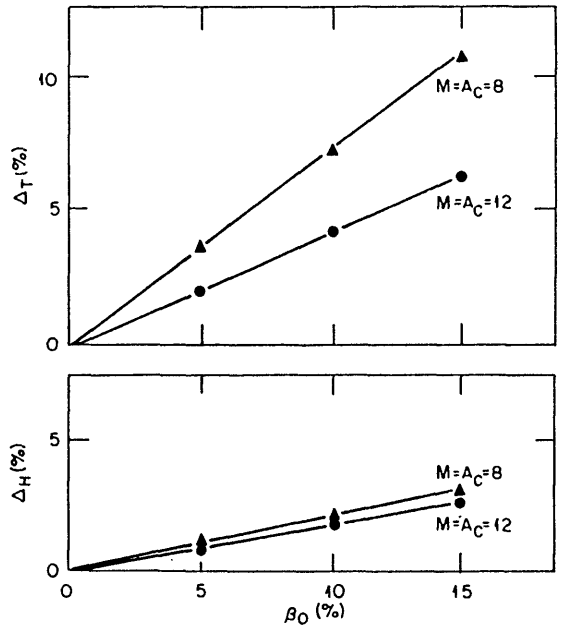

FIG.4. Toroidal equilibrium shift (Δ_T) and helical shift (Δ_H) as functions of β_0 for configurations studied in the $M = A_c$ scan.

importance of resonant harmonics (whose importance is accentuated by the low shear) has not been examined in detail.

2.3 HELIAC CONFIGURATIONS

A wide range of heliac configurations has been studied. These configurations have been selected such that the lowest order resonances within a field period are avoided. These resonances are 1/4, 1/3, 1/2 (Fig. 3). All the configurations considered have a vacuum well. However, these conditions are not sufficient to guarantee good equilibria. Higher resonances, whose effect on the vacuum can be minimized, play an important role. To illustrate this, the particular case of the 2/5 resonance will be considered. In Fig. 3, the ι ranges for three different heliacs are indicated. All three of these heliacs have four field periods (M = 4) and a coil aspect ratio of 4 (A_c = 4). The ι ranges are chosen to include the 2/5 resonance, to have it very close to the plasma boundary and to have it far away from the plasma. The equilibrium flux surfaces for these three cases (β_0 = 5%) are shown in Fig. 4. It is clear that having the 2/5 resonance in the plasma or in close proximity leads to serious distortion of the magnetic surfaces. At higher beta these distortions cause the equilibrium calculations to

fail. The origin of these distortions is the beating of helical and toroidal shifts, which leads to a broadening of the spectrum. This effect has been examined in first order by Reiman and Boozer [15]. It is, therefore, important to select a configuration whose ι range is as far from low order resonances as possible. This requires careful control of ι and shear. It is also important to minimize toroidal effects - without which the nonlinear beatings and distortions cannot occur. Toroidal effects may be reduced directly either by raising the total ι or by raising the aspect ratio at a given pitch. The introduction of a toroidal modulation of the coil currents has little effect at low aspect ratios (plasma aspect ratio $\lesssim$ 10). The results of a fixed pitch scan with $M/A_c = 1$ are summarized in Fig. 4, where the toroidal shift (Δ_T) and helical shift (Δ_H) as functions of β_0 are plotted for the configurations studied. The helical shifts remain practically invariant for all configurations in the pitch scan, while the toroidal shifts decline as the inverse aspect ratio. This is because in a fixed pitch scan the helical curvature remains constant as the toroidal curvature varies. For larger aspect ratio heliacs, such as the $M = A_c = 12$ case, higher beta ($\beta_0 \gtrsim 10\%$) equilibria have been found.

ACKNOWLEDGMENTS

We thank J. L. Johnson and G. Rewoldt for providing us with the PPPL free-boundary stellarator expansion equilibrium and stability codes. We also would like to thank J. L. Johnson, A. H. Boozer, and A. Reiman for several useful discussions.

REFERENCES

[1] J. M. Greene and J. L. Johnson, Phys. Fluids 4, 875 (1961).
[2] B. A. Carreras, H. R. Hicks, J. A. Holmes, V. E. Lynch, L. Garcia, J. H. Harris, T. C. Hender, and B. F. Masden, Phys. Fluids 26, 3569 (1983).
[3] V. E. Lynch, B. A. Carreras, H. R. Hicks, J. A. Holmes, and L. Garcia, Comput. Phys. Commun. 24, 465 (1981).
[4] J. A. Holmes, Y-K. M. Peng, and S. J. Lynch, J. Comput. Phys. 36, 35 (1980).
[5] J. L. Johnson et al., J. Comput. Phys. 32, 212 (1979).
[6] R. C. Grimm, J. M. Greene, and J. L. Johnson, p. 253 in Methods in Computational Physics, Vol. 16, ed. J. Killeen, Academic Press, New York, 1976.
[7] G. Anania, J. L. Johnson, and K. E. Weimer, Phys. Fluids 26, 2210 (1983).
[8] G. Anania and J. L. Johnson, Phys. Fluids 26, 3070 (1983).
[9] B. A. Carreras, H. R. Hicks, J. A. Holmes, V. E. Lynch, and G. H. Neilson, ORNL Report ORNL/TM-9182 (1984).

[10] J. F. Lyon et al., Oak Ridge National Laboratory Report No. ORNL/TM-8496 (1983).
[11] T. C. Hender, B. A. Carreras, L. Garcia, J. Rome, and V. E. Lynch, Oak Ridge National Laboratory Report ORNL/TM-9239 (1984).
[12] T. C. Hender and B. A. Carreras, Oak Ridge National Laboratory Report ORNL/TM-9147 (1984).
[13] A. H. Boozer et al., Plasma Physics and Controlled Nuclear Fusion Research (IAEA, Vienna, 1983), Vol. 3, p. 129.
[14] R. Chodura and A. Schlüter, J. Comput. Phys. 41, 68 (1981).
[15] A. H. Reiman, A. H. Boozer, Princeton Plasma Physics Laboratory Report PPPL-2062 (1983).

STUDY OF STELLARATOR DEVICES BY EXPANSION TECHNIQUES*

J.L. JOHNSON**, A.H. BOOZER, A.E. KONIGES,
G. KUO-PETRAVIC, J. MANICKAM, D.A. MONTICELLO,
H. MYNICK, W. PARK, A. REIMAN, G. REWOLDT
Plasma Physics Laboratory,
Princeton University,
Princeton, New Jersey,
United States of America

Abstract

STUDY OF STELLARATOR DEVICES BY EXPANSION TECHNIQUES.

Expansion techniques have led to new tools for designing stellarators and interpreting experimental results. The stellarator expansion is coupled with Hamiltonian techniques to investigate the effect of plasma pressure on magnetic surface structure. An expansion for non-planar axis systems is described. A reduced-equation initial-value formalism is used to create three-dimensional heliac equilibria. A low-β expansion with an auxiliary expansion about the magnetic axis makes possible the determination of island widths in heliacs and allows analytic determination of the effect of equilibrium modifications associated with plasma pressure on radial transport.

1. THE STANDARD STELLARATOR EXPANSION

Modeling of the Heliotron E device with the stellarator expansion [1] leads to good agreement between the theoretical predictions of instability if $\beta(0)$ is greater than 2.4%, and the value $\beta(0) \approx 2.5\%$ where instabilities are observed experimentally. Modification of the externally imposed field as β is increased, for example by introducing an axisymmetric pusher coil on the outside of the plasma and adjusting the vertical field to distort the lowest-order magnetic surfaces into a backward D, can modify the equilibrium properties and partially stabilize the instabilities.

Application of the code to the Wendelstein VII-A stellarator parameters shows that the fields associated with secondary currents change the shapes of the magnetic surfaces

* Work supported by US Department of Energy Contract No. DE-AC02-76-CHO-3073 with Princeton University.

** On loan from Westinghouse Research and Development Center, Pittsburgh, PA, USA.

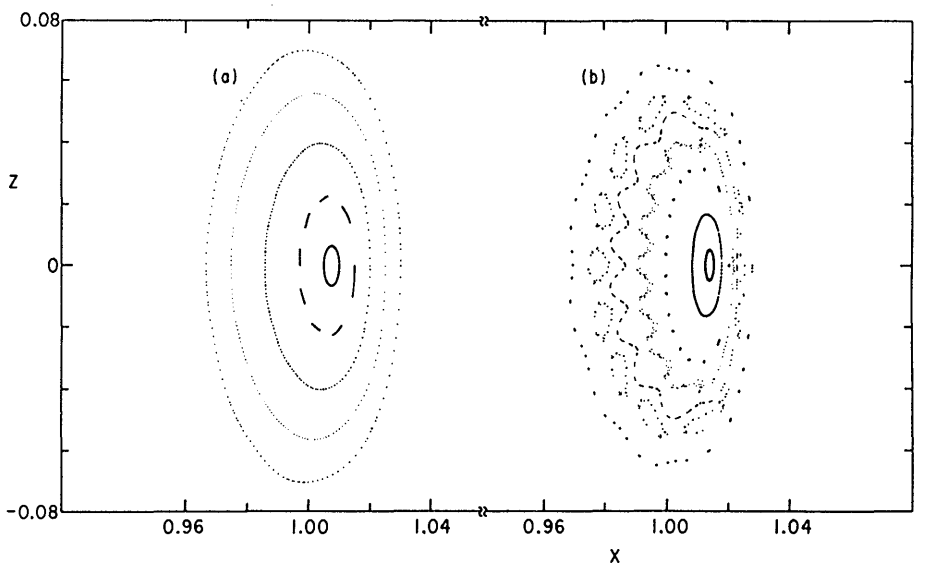

FIG.1. Magnetic surfaces of Wendelstein VII-A constructed with puncture plots for (a) $\beta(0) = 1\%$ and (b) $(\beta)(0) = 2\%$.

and modify the equilibrium properties. Poincaré plots of the magnetic surfaces for cases with $\beta(0) = 1\%$ and $\beta(0) = 2\%$ are shown in Fig. 1. The Shafranov shift is large even at these low values of β, and at $\beta(0) = 2\%$ bad island structure can be observed. In the $\beta(0) = 1\%$ case, Fourier decomposition of $\vec{B} \cdot \nabla\psi$, where ψ is an averaged axisymmetric magnetic surface label, shows an exponential decrease with the poloidal mode number m before numerical scatter causes a leveling off (Fig. 2). Interpolation between the different surfaces indicates island structure with $\Delta/a \approx 0.002$ [2,3].

2. HELICAL AXIS STELLARATOR EXPANSION

An expansion, applicable to systems with nonplanar magnetic axes, is being developed [4]. We consider a vacuum field

$$\vec{B} = a\nabla[\zeta + \gamma\Delta(1 + \gamma^2\rho^2/8)\sin(\theta-\gamma\zeta) + \alpha\theta + (\gamma\varepsilon\Delta/4)\rho^2\sin\gamma\zeta+\ldots]$$

in a quasi-toroidal coordinate system with the ordering $\gamma \approx \alpha^{1/2} \approx \varepsilon^{1/2} << 1$, $\beta \approx \varepsilon^2$, $\Delta \approx 1$. Here $\gamma \equiv ha$ measures the wavelength of an $\ell = 1$ helical field that is responsible for the nonplanarity of the magnetic axis, Δ the helical radius of the

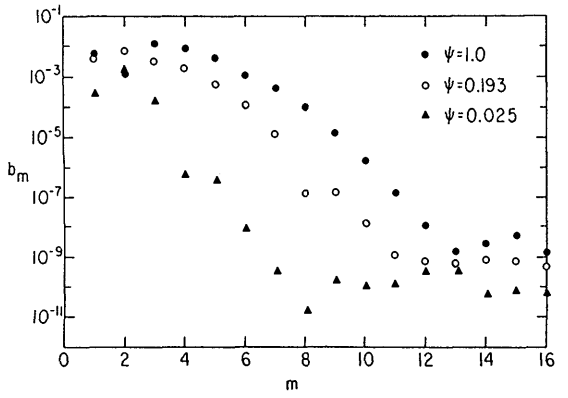

FIG.2. Fourier decomposition of the field normal to an averaged flux surface for the $\beta(0) = 1\%$ case in Wendelstein VII-A as a function of poloidal mode number.

magnetic axis due to that field, α the field associated with a current in the central core, and ε the inverse aspect ratio; $\zeta = z/a$, $\rho = r/a$, and θ are normalized coordinates centered on the core of the helical system. By transforming to characteristic coordinates

$$C_1 \equiv \rho \cos\theta - \Delta \cos t;\ C_2 \equiv \rho \sin\theta - \Delta \sin t;\ t \equiv \gamma\zeta$$

we can reduce the equilibrium problem to the simple formulation

$$\psi^{(0)} = \left(C_1 + \frac{5\varepsilon}{2\gamma^2}\right)^2 + C_2^2 + \int_0^{2\pi} dt\left[\frac{\partial \Xi(C_1, C_2, t)}{\partial C_1} \int_0^t dt' \frac{\partial \Xi(C_1, C_2, t')}{\partial C_2}\right] + \frac{4A^\sigma}{\gamma^3 \Delta^2}$$

$$\partial^2 A^\sigma / \partial C_1^2 + \partial^2 A^\sigma / \partial C_2^2 = -2\varepsilon\, p'\left(\psi^{(0)}\right) C_1/\gamma$$

$$\Xi(C_1, C_2, t) \equiv (\alpha/\gamma^2\Delta) \ln\left[C_1^2 + C_2^2 + 2\Delta(C_1 \cos t + C_2 \sin t)\right]$$

The boundary conditions are the same as in the ordinary stellarator expansion model [1]. A typical result is given in Fig. 3. The magnetic surfaces in an Asperator NP-4 model with $\gamma = 0.5$, $\Delta = 2.0$, $\varepsilon = 0.06$, $\alpha = 0$, and $\langle\beta\rangle = 33\%$ show a Shafranov shift and modification of surface shape due to plasma pressure. This affects the equilibrium properties.

3. INITIAL-VALUE PROGRAM FOR HELIAC EQUILIBRIA

Three-dimensional equilibrium configurations have been studied using a modified version of the HIB code [5]. This code is based on a large-aspect-ratio expansion which annihilates the fast waves. Because higher-order terms are retained, it can

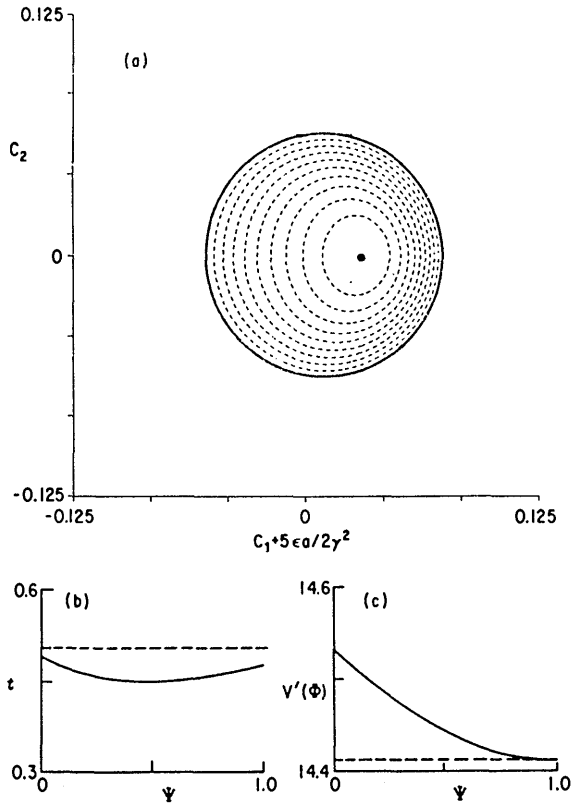

FIG.3. Equilibrium properties of an Asperator NP-4 model with $\langle\beta\rangle = 33\%$. (a) Magnetic surfaces; (b) rotational transform; (c) $V'(\Phi)$. Dashed curves are the vacuum-field properties.

find exact equilibria. It is not limited to the assumption that magnetic surfaces exist or that the transform is frozen into the plasma. Solutions with no net current are determined by introducing resistivity and viscosity into the ideal MHD equations and by continuously averaging the pressure along field lines to ensure that $\vec{B} \cdot \nabla p = 0$. This pressure constraint also supplies energy to balance resistive losses. A model equilibrium for a reference-design heliac with R = 1.5 m, a = 0.5 m, N = 3 and $\langle\beta\rangle$ = 2% is shown in Fig. 4. The pressure and current profiles are typical of zero-net-current symmetric systems that have recently been reported [6]. The rotational transform varies from 0.20 to 0.24. As can be seen in the puncture plots, magnetic islands exist only in the vacuum region. Other configurations with islands inside the plasma were no more difficult to produce.

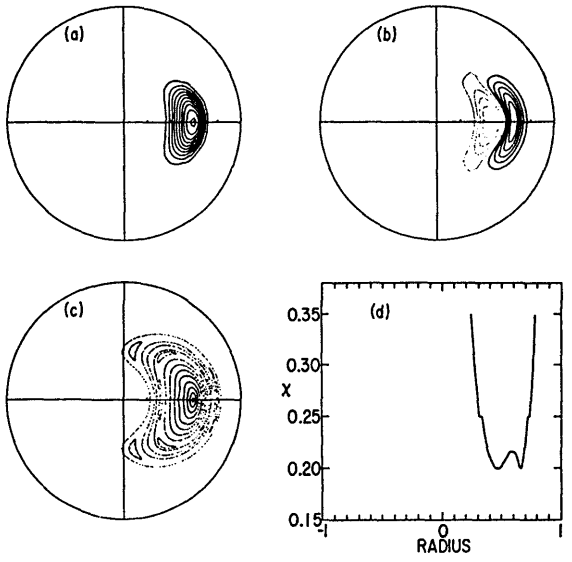

FIG.4. Equilibrium profiles of a heliac with $\langle\beta\rangle = 2\%$. (a) Pressure contours; (b) toroidal current contours; (c) magnetic field puncture plots; (d) rotational transform.

4. ISLAND STRUCTURE STUDY USING EXPANSIONS IN β AND ρ/a

Magnetic island formation is driven by resonant pressure-driven current even if the vacuum field has good flux surfaces [7]. This current is associated with the variation of $\int d\ell/B$ on the rational surfaces, which is nonzero at finite β even if it vanishes for vacuum fields. This decreases the useful aperture of the plasma and provides an equilibrium limit.

The secondary currents can be determined by an expansion in β about the vacuum fields. For a three-period heliac with an aspect ratio of 5 and a rotational transform $\iota = 1.5$ at the axis and $\iota = 1.7$ at the edge, we calculate an equilibrium β-limit of roughly 2%. The conventional limit where the axis shifts half way to the outer flux surface would be 15% for this case.

5. EFFECT ON TRANSPORT OF PRESSURE-INDUCED EQUILIBRIUM MODIFICATIONS

The precise harmonic decomposition of the magnetic field strength B is sensitive to the plasma β. Numerical [8] and analytic [9,10] work has shown that stellarator transport is strongly affected by this decomposition. This can be investigated by using an expansion to determine the harmonic content.

For a stellarator with parameters characteristic of planar-axis devices (m = 2, N = 8, ι = 0.3, and $\varepsilon_T = \varepsilon_H = 0.1$ at r/a = 0.5), combining the analytic equilibrium and transport theories shows a factor of 5 increase in transport as β is changed from 0 to 1% (near the equilibrium β-limit of this configuration). For a similar device, but with the vacuum-field optimized by localizing the ripple towards the inboard side [8-10], the increase is twice as large.

The principal reason for this degradation in confinement is that the outward Shafranov shift redistributes the ripple strength toward the outboard side of the stellarator. Thus, helical axis devices, which have large transform per period, have smaller shifts and so have transport less affected by this mechanism. An external field applied to cancel the shift can eliminate this degradation on a single surface and largely remove the effect on the neighboring surfaces.

REFERENCES

[1] GREENE, J. M., JOHNSON, J. L., Phys. Fluids 4 7 (1961) 875.
[2] BOOZER, A. H., Phys. Fluids 26 5 (1983) 1288.
[3] BOOZER, A. H., Phys. Fluids 27 8 (1984) (in press).
[4] KONIGES, A. E., et al., Bull Am. Phys. Soc. 28 8 (1983) 1183.
[5] PARK, W., et al., Bull. Am. Phys. Soc. 23 7 (1978) 779.
[6] MONTICELLO, D. A., et al., Phys. Fluids 27 5 (1984) 1248.
[7] REIMAN, A. H., BOOZER, A. H., Phys. Fluids 27 9 (1984) (in press).
[8] MYNICK, H. E., et al., Phys. Rev. Lett. 48 5 (1982) 322.
[9] MYNICK, H. E., Bull. Am. Phys. Soc. 26 8 (1981) 856.
[10] SHAING, K. C., HOKIN, S. A., Phys. Fluids 26 8 (1983) 2136.

NEOCLASSICAL ENERGY BALANCE IN STELLARATORS

K.S. DYABILIN, L.M. KOVRIZHNYKH
General Physics Institute,
USSR Academy of Sciences,
Moscow, Union of Soviet Socialist Republics

Abstract

NEOCLASSICAL ENERGY BALANCE IN STELLARATORS.

Numerical calculations of plasma energy balance in terms of neoclassical theory are carried out for different stellarators. Experimental results with Heliotron-E and L-2 are used. Sufficiently good agreement between theory and experiments is demonstrated.

1. The present status of neoclassical transport theory [1] allows its results to be compared with experiments. Preliminary calculations [2, 3] have shown that the theoretical estimates of the plasma energy lifetime are of the order of the experimental values.

In this paper, the results of more accurate calculations for currentless regimes are given and the values obtained, such as temperature profiles, their dependence on input power and time, the ambipolar electric field distribution, etc., are compared with experiments.

2. The basic equations used for the numerical calculations will be the ordinary energy balance equations (see Eq. (9) below), where the expressions for the fluxes of particles, S_j, and energy, Π_j, are taken from Ref. [2].

Remembering, however, that the expressions given in Ref. [2] only hold for a two-component plasma with effective charge $Z^* = 1$, we generalize these expressions to the case of arbitrary Z^*. This is easy to do by using the same approximation as in Ref. [2] and the coefficients given in Ref. [1] (Tables I to VII of Ref. [1]). Thus, we take the expressions for the electron fluxes of particles, S_e and energy, Π_e, in the following form:

$$S_e = S_e^s + S_e^{as}, \qquad \Pi_e = \Pi_e^s + \Pi_e^{as} \tag{1}$$

$$S_e^s = -\frac{2.06\,(0.53 + Z^*)\,a_e\,A_e}{1 + 1.65\,(0.53 + Z^*)\,\alpha_e} - \frac{2.06\,(0.707 + Z^*)\,a_e\,B_e}{1 + 0.55\,(0.707 + Z^*)\,\alpha_e}$$

$$\Pi_e^s = -\frac{2.06\,(0.707 + Z^*)\,a_e\,A_e\,T_e}{1 + 0.55\,(0.707 + Z^*)\,\alpha_e} - \frac{2.06\,(1.59 + 2\,Z^*)\,a_e\,B_e\,T_e}{1 + 0.14\,(1.59 + 2\,Z^*)\,\alpha_e} \tag{2}$$

where

$$A_e = (\ln N_e)' + e_e \Phi'/T_e - \frac{3}{2}(\ln T_e)'; \quad B_e = (\ln T_e)'$$

$$a_e = \nu_e^* N_e q^2 \Delta \left(\frac{R v_e}{r \omega_e}\right)^2; \quad \alpha_e = \frac{\nu_e^* q R^3 \Delta}{r^2 v_e} \tag{3}$$

$$\Delta = (\epsilon + \delta)^{1/2} - \epsilon^{1/2}; \quad \delta = r/R$$

$$\omega_e = \left|\frac{e_e B_0}{m_e c}\right|; \quad v_e = \left(\frac{T_e}{m_e}\right)^{1/2}; \quad \nu_e^* = \frac{4\sqrt{\pi}}{3} \frac{e_e^4 N_e \Lambda}{m_e^{1/2} T_e^{3/2}}$$

N_e, T_e, e_e, m_e are the electron density, temperature, charge and mass respectively; B_0 is the magnetic field strength, $q = \iota^{-1}$ the safety factor, ι the rotational transform, Φ the ambipolar potential, r the mean radius of the magnetic surface, and R the major radius. The prime designates a derivative with respect to r, ν_e^* is the electron collision frequency, Λ the Coulomb logarithm, $Z^* = \sum_k Z_k^2 N_{ik}/N_e$ is the effective charge (Z_k is the charge, and N_{ik} is the ion density of species k), and, finally, $B_0 \epsilon$ is the maximum amplitude of the helical magnetic field ripple along a line of force. For an ideal $\ell = n$ stellarator with one helical harmonic where

$$B_\varphi = B_0 [1 - \delta \cos\theta - \hat{\epsilon}(r) \cos(n\theta - M\varphi)] \tag{4}$$

the quantity ϵ (neglecting the weak dependence on the poloidal azimuth θ) may be written in the form

$$\epsilon(r) \cong [\hat{\epsilon}^2 + (R\hat{\epsilon}')^2/(MM_1)^2]^{1/2}, \quad M_1 = M - n\iota \tag{5}$$

The qualities S_e^s and Π_e^s in expressions (1) describe the fluxes associated with slow untrapped and toroidally trapped particles. The fluxes S_e^{as} and Π_e^{as}, associated with locally trapped particles and including stellarator effects, are given by

$$S_e^{as} = -\frac{0.67 (1 + 1.2 Z^*)^{1/2} b_e^{(s)} A_e}{1 + 1.02 (1 + 1.2 Z^*)^{3/2} \beta_e^{(s)}} - \frac{1.90 (1 + 1.2 Z^*)^{1/2} b_e^{(s)} B_e}{1 + 0.59 (1 + 1.2 Z^*)^{3/2} \beta_e^{(s)}}$$

$$\Pi_e^{as} = -\frac{1.90 (1 + 1.2 Z^*)^{1/2} b_e^{(\pi)} A_e T_e}{1 + 0.59 (1 + 1.2 Z^*)^{3/2} \beta^{(\pi)}} - \frac{7.19 (1 + 1.2 Z^*)^{1/2} b_e^{(\pi)} B_e T_e}{1 + 0.37 (1 + 1.2 Z^*)^{3/2} \beta_e^{(\pi)}} \tag{6}$$

where

$$b_e = N_e \left(\frac{\nu_e^*}{\omega_e}\right)^{1/2} \frac{r^3 v_e}{R^2} \left(\frac{T_e}{r|e_e|E_e^{(s,\pi)}}\right)^{3/2}; \quad \beta_e^{(s,\pi)} = 0.1 \left(\frac{\nu_e^* m_e \omega_e r}{\epsilon e_e E_e^{(s,\pi)}}\right)^{3/2} I^{-1}(\alpha)$$

$$E_e^{(s,\pi)} = |E_a| + \frac{T_e}{|e_e|} \left(\frac{r^3 v_e^2}{\nu_e^* |\omega_e| R^4}\right)^{1/3} (\bar{a}_e^{(s,\pi)})^{2/3}; \quad \alpha = \frac{r\iota}{RM\epsilon}$$

$$\bar{a}_e^{(s)} = \left[\left(\frac{0.25\,(1 + 1.2\,Z^*)^{1/2}}{1.23 + Z^*\,\lambda_e}\right)\left(1 + 1.34\,\frac{\partial \ln T_e}{\partial \ln N_e}\right)\left(\frac{r\,N_e\,T_e^{-3/2}\,|N_e'|}{\int_0^r r\,dr\,N_e^2\,T_e^{-3/2}}\right)\right] \quad (7)$$

$$\bar{a}_e^{(\pi)} = \left[\left(\frac{1.58\,(1 + 1.2\,Z^*)^{1/2}}{0.53 + Z^*}\right)\left(1 + 0.44\,\frac{\partial \ln N_e}{\partial \ln T_e}\right)\left(\frac{r\,N_e^2\,T_e^{-3/2}\,|T_e'|}{\int_0^r r\,dr\,N_e^2\,T_e^{-1/2}}\right)\right]$$

$$I(\alpha) \approx 0.97 \exp\left[-3\,\alpha\,(1 + 0.5\,\alpha^3)\right] + \frac{0.03}{1 + \alpha^3}$$

$$\lambda_e = \sum_k \left(Z_k^2\,N_{ik} \ln \frac{m_{ik}\,T_e}{m_e\,T_{ik}}\right) / Z^*\,N_e \cong \ln \frac{m_i\,T_e}{m_e\,T_i}$$

Here, $E_a = -\partial\Phi/\partial r$ is the ambipolar electric field, m_i and T_i are the mass and the temperature of the main ion component; all other quantities have been defined before denoted above (see expressions (3)). These formulae hold for $\alpha < 1$, which holds true in all stellarators existing and being designed (the condition $\alpha < 1$ may only be violated in the central region of an n = 3 stellarator). Similar formulae can easily be derived for ions. If, however, the mass of the impurity ions, m_{ik}, is large compared to that of the main ions, m_i, the expressions for the bulk ion fluxes can be obtained from the expressions given above by replacing the subscript e by i, $Z^*\,\lambda_e$ by $\lambda_i = \sum_k (Z_k^2\,N_{ik} \ln (m_{ik}/m_i)/N_i$, and the effective charge Z^* by $(Z^*\,N_e/N_i - 1)$. The fluxes of impurities of species k may be derived from formulae (1) to (7) by assuming that the main contribution to the collision frequency of these ions comes from collisions between ions of the same species,

i.e. for the impurity charge so large that $Z_k^2 N_{ik} > N_i$. For this purpose, Z^* in formulae (1) to (7) should be put equal to zero and the subscript e should be changed to i. Taking these remarks into account, we shall not, for the sake of brevity, give here explicit expressions for the ion fluxes. We only note that, in general, to the fluxes given above those due to fast passing particles, with values close to those found in the hydrodynamic approximation, should be added. But since these fluxes are small in the parameter range of interest (low density, high temperature), they can be neglected, while only the ion heat flux equal to

$$\Pi_i^{HD} \approx -2\,(1 + 1.6\,q^2)\,\nu_i^*\,\frac{v_i^2}{\omega_i^2}\,N_i\,T_i' \tag{8}$$

is retained.

3. Hence, our calculations are based on the one-dimensional energy balance equations, where r is the radius of a magnetic surface:

$$\begin{aligned}
\frac{3}{2}\frac{\partial}{\partial t} N_e\,T_e &= -\frac{1}{r}\frac{\partial}{\partial r} r\Pi_e - P_{ei} - P_r + e_e\,E_a\,S_e + P_e \\
\frac{3}{2}\frac{\partial}{\partial t} N_i\,T_i &= -\frac{1}{r}\frac{\partial}{\partial r} r\Pi_i + P_{ei} + e_i\,E_a S_i + P_i
\end{aligned} \tag{9}$$

Here, $P_{e,i}$ denote external heating sources of electrons and ions, respectively (e.g. HF heating), P_{ei} is the heat transfer from electrons to ions via collisions, and P_r is the radiative loss power[1]. The field strength is determined from the ambipolarity condition, $e_e S_e = -e_i S_i$, on the assumption that the impurities are of no importance in the particle balance and that $Z^* \approx 1$. (The effect of impurities on the heat transport will be discussed below).

Before considering the results, we note that the particle balance was not calculated, and hence experimental particle density profiles were included into the calculations. This simplification seems to be reasonable since the particle confinement time is, as a rule, substantially longer than the energy lifetime.

4. HELIOTRON-E. The most detailed comparison of calculations and experimental results was carried out for the Heliotron-E (H-E) device. In this machine, the central electron temperature was raised up to $T_e(0) \approx 1$ keV by ECR plasma heating [4, 5]. In this case, the particle density is low ($N_e(0) \approx (8-10) \times 10^{12}$ cm^{-3}),

[1] Experimental information on the radiative losses cannot always be obtained. So, cases where P_r are taken into account are mentioned especially.

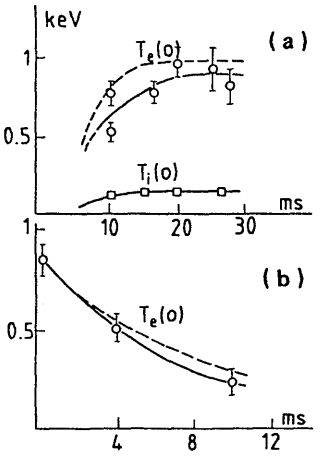

FIG.1. Central-electron temperature dependence during heating and afterglow in Heliotron-E (P_e = 100 kW, $N_e(0) = 10^{13}$ cm^{-3}).

the regime is collisionless and hence the stellarator characteristics of a collisionless regime become extremely pronounced. The distribution of the heating sources was taken to be homogeneous in the plasma volume of a plasma radius of $r \leqslant 0.5$ (a_{pl}). The total input power was P_e = 100 kW.

Figures 1a and b show calculated (dashed) and experimental (full) curves describing the time evolution of the central electron temperature during plasma heating and decay. The somewhat faster approach to stationarity in the calculations (Fig.1a) may be both due to the fact that no additional loss sources (radiation, ionization) were included in the balance equations and to the fact that, in experimental conditions, the power P_e absorbed in the plasma could vary in time, i.e. for example, increase with the electron temperature. The order of magnitude of the ion temperature coincides with the calculated values (for greater detail, see below).

The decrease in $T_e(0)$ during the afterglow also agrees well with the experiments (Fig.1b).

Figure 2 shows the $T_e(r)$ profile in the stationary stage ($t > 15$ ms). The calculated curve coincides with experimental one. Figure 2 also shows the calculated ambipolar electric field E_a.

The ion energy balance is also rather correctly reproduced in the calculations (with an accuracy of up to charge-exchange losses). Figure 3 shows experimental and calculated (dashed) $T_i(r)$ profiles. The calculated curves correspond to two different levels of particle density, $N_i(0)$ (density at the centre) = 10^{13} cm^{-3} and $N_i(0) = 8 \times 10^{12}$ cm^{-3}. The difference between the $N_i(0)$ values agrees approximately with the experimental spread. The temperature profiles are very flat, and it is of interest to note that a slight increase in the ion temperature at the

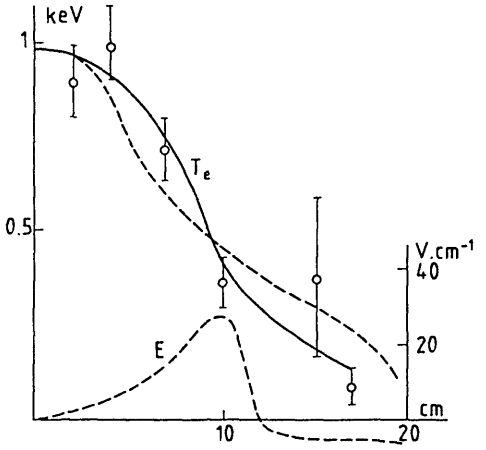

FIG.2. Radial profiles of electron temperature and ambipolar electric field in Heliotron-E (P_e = 100 kW, $N_e(0) = 10^{13}$ cm^{-3}).

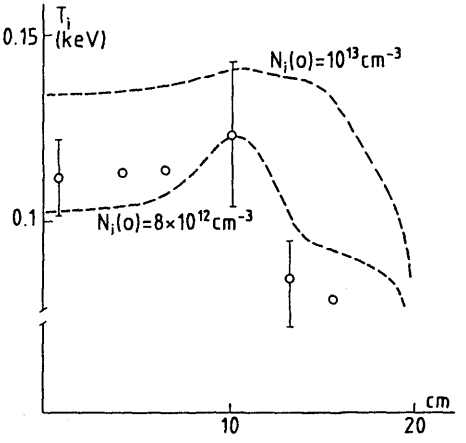

FIG.3. Radial profiles of ion temperature in Heliotron-E (P_e = 100 kW, $t > 15$ ms).

periphery (see the case where $N_i(0) = 8 \times 10^{12}$ cm^{-3}) may be quasi-stationary since heat fluxes proportional to the gradient T_i are not dominant and convective losses due to density gradient, electron temperature and electric field remove energy from the central region and lead to thermal balance. The calculated temperature values seem to be a bit higher than the experimental ones. This discrepancy is, however, insignificant and allows ion confinement in the currentless case to be described in terms of a neoclassical model. Thus, this comparison

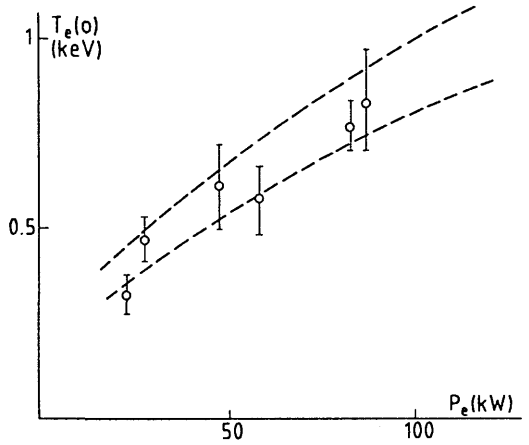

FIG.4. Central electron temperature versus input power in Heliotron-E.

shows rather good agreement between experiments and theory. The calculated electron temperature during heating and decay and the temperature profiles correspond well to the experimentally measured values. The ion energy balance agrees with the experimental data on ion temperature and represents the peculiarities in the temperature profile.

To conclude the results on H-E, we compare the calculated and experimental dependences of the central electron temperature on the power introduced into the plasma [4, 5]. Figure 4 shows two dashed (calculated) curves which correspond to an experimental particle density spread of the order of 20%.

5. L-2 STELLARATOR. First experimental results on plasma heating by an extraordinary polarization wave introduced from the high-field side (f = 30 GHz) were obtained in early 1984 [6]. In the case of ECR, the particle density increases monotonically in time, up to a line-averaged density of $\bar{N}_e = (6-7) \times 10^{12}$ cm^{-3}. The radiative losses also increase in time.

Measurements of the radial parameter distribution show that the particle density profile can be approximated satisfactorily by a parabola; the main fraction of radiation comes from the periphery of the plasma column while in the inner plasma region ($r < 7$ cm) the heat flux is due to thermal conductivity. Estimates inferred from diamagnetic measurements show the energy lifetime to be $\tau_E = 2$ ms and the microwave power absorbed in the plasma reaches values of the order of $P_e \approx 30-40$ kW. Estimates in terms of neoclassical theory give energy lifetime values close to the experimentally measured values. Calculations taking into account experimental data on the spatial and temporal behaviour of the particle density and on the radiative loss profile show neoclassical heat transport

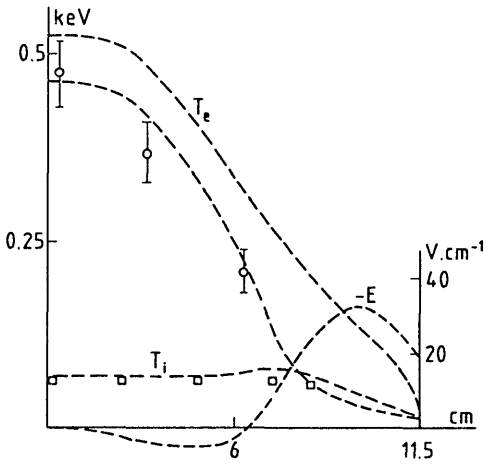

FIG.5. Radial profiles for electron and ion temperatures and ambipolar electric field in L-2 (t = 6.5 ms, P_e = 30 kW).

to be the dominant process in the main plasma volume. The experimental temperature profile is, however, more peaked than the calculated one, which implies that anomalous thermal transport through the electron channel may be possible. To provide agreement with experiments, an anomalous heat flux is added to neoclassical flux:

$$\Pi_e^{an} = -\chi T_e' \ [W \cdot cm^{-2}], \quad \chi = 3 \times 10^{18}/\iota T_e \ [eV]$$

where the quantity χ and its functional dependence on the plasma parameters is obtained by modelling of the electron energy balance in Ohmic-heating regimes. The inclusion of anomalous heat transport allowed good agreement between calculations and experimental data to be achieved. Figure 5 shows a comparison of calculated and experimental temperature profiles for electrons and ions. The calculation is carried out on the assumption that the power absorbed in the plasma is P_e = 30 kW and is homogeneously distributed in the volume of $r \leqslant 0.5\ a_{pl}$. The calculated profiles for the moment of t = 6.5 ms are given. In this figure the upper dashed curve corresponds to the neoclassical mechanism alone. The lower curve is obtained by adding anomalous losses. The calculated T_e agrees well with the measured one (experimental points are obtained by laser scattering). The calculated T_e profile varies only slightly in time. The experimental T_i profile (experimental points in Fig.5 are denoted by squares) is flat and also agrees well with the calculated profile. Figure 5 also shows the ambipolar-field distribution. The order of magnitude of E_a at the periphery is 30 V·cm^{-1}.

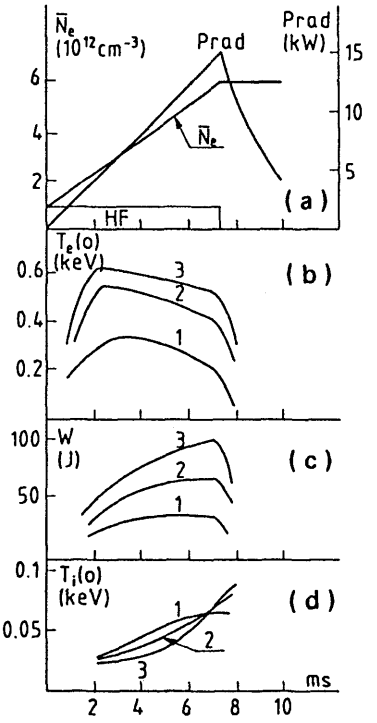

FIG.6. Calculated time dependence of plasma parameters for different levels of input power in L-2.

To conclude the discussion of the energy balance during heating in L-2, we give the calculated dependences of the plasma parameters on the input power. In the calculations, the experimental time and radial dependences of the particle density and the radiative losses as shown in Fig.6a are used. The input power is supposed to be constant during the HF pulse and concentrated in the volume $r \leqslant 0.5\ a_{pl}$. Figure 6b shows the time dependence of the central electron temperature for P_e = 20, 30 and 40 kW. The central temperature is seen to vary noticeably with the input power. The time behaviour of $T_e(0)$ is non-monotonic, the temperature decreases with increasing particle density and radiative losses. Figure 6c shows the time variation in the plasma energy, $W = W_e + W_i$. The calculated value of W increases in time (because of the density increase) and reaches, e.g. at P_e = 30 kW, a value of W = 75 J. Hence, the calculated energy lifetime estimated as $T_E = W/P_e$ varies slightly with P_e and is of the order of 2–2.5 ms. The temperature $T_i(0)$ varies only slightly when the input power is changed (see Fig.6d).

7. DISCUSSION

A nearly complete coincidence of experimental and theoretical results has been achieved for the Heliotron-E device. Neoclassical transport leads to a T_e profile that is very close to experimental one in L-2. For conclusions to be drawn on the anomalous transport in the edge region, data are necessary on the electron temperature at the periphery (which has not been obtained experimentally).

Finally, we should outline the influence of effective charge on heat transfer. The presence of a small impurity component in a plasma with high electron temperature and a particle density of $\leqslant 10^{13}$ cm^{-3} may lead to an increase in the charge up to $Z^* = 2-3$.

The calculations show that during Ohmic heating in H-E and L-2 the increase in charge up to $Z^* = 3$ leads to an increase in temperature at the centre. This is, however, insignificant since its value is 100 eV, which may well lie within the experimental scatter.

ACKNOWLEDGEMENT

The authors would like to express their gratitude to I.S. Danilkin for helpful discussions.

REFERENCES

[1] KOVRIZHNYKH, L.M., Nucl. Fusion **24** (1984) 851.
[2] KOVRIZHNYKH, L.M., Nucl. Fusion **24** (1984) 435.
[3] KOVRIZHNYKH, L.M., Plasma Phys. Contr. Fusion **26** 1A (1984) 195 (invited papers of 11 Europ. Conf. Controlled Fusion and Plasma Physics, Aachen 1983).
[4] UO, K., in Controlled Fusion and Plasma Physics (Proc. 11th Europ. Conf. Aachen, 1983), Vol. 1 (1983) O 19.
[5] SATO, M., et al., Nucl. Fusion **23** (1983) 1333.
[6] ANDRYUKHINA, E.D., et al., this volume, paper D-I-4.

DISCUSSION

A. SAMAIN: If you were to introduce the anomalous losses usually assumed for tokamaks (following the Alcator law), would you not find the balance impossible?

L.M. KOVRIZHNYKH: As I mentioned, the introduction of anomalous losses would make the temperature profile somewhat narrower but would have little effect on the temperature in the centre (for Heliotron-E and L-2). To be able

to provide a more specific answer to the question whether anomalous losses need to be introduced, more detailed and accurate data on the electron temperature at the plasma periphery would be required.

Ker-Chung SHAING: How do you determine the radial electric field profile in the Heliotron-E calculation?

L.M. KOVRIZHNYKH: In the usual way, using the condition of ambipolarity of diffusion.

THEORY AND SIMULATION OF FISHBONE-TYPE INSTABILITIES IN BEAM-HEATED TOKAMAKS

L. CHEN, R.B. WHITE, C.Z. CHENG, F. ROMANELLI*,
J. WEILAND**, R. HAY
Plasma Physics Laboratory,
Princeton University, Princeton, New Jersey

J.W. VAN DAM, M.N. ROSENBLUTH, S.T. TSAI+,
D.C. BARNES++
Institute for Fusion Studies,
University of Texas at Austin, Austin, Texas

United States of America

Abstract

THEORY AND SIMULATION OF FISHBONE-TYPE INSTABILITIES IN BEAM-HEATED TOKAMAKS.

Energetic trapped particles are shown to introduce a new unstable solution to the internal kink and ballooning modes in tokamaks. Both the real frequencies and growth rates of the instabilities are comparable to the trapped particle precession frequency. Simulations including the excitation and particle-loss mechanisms of the internal kink mode are found to reproduce essential features of the 'fishbones'. Furthermore, the energetic trapped-particle-induced ballooning modes are shown to be consistent with the associated high-frequency oscillations observed experimentally. Several possible stabilizing schemes are considered.

1. INTRODUCTION

The role of energetic trapped particles in tokamaks has recently been dramatized by their significant effect on MHD stability properties such as the maximum achievable β ($= 8\pi nT/B^2$) values. In particular, 'fishbone' instabilities ($\sim$20 kHz) observed in tokamaks during high-power, nearly perpendicular neutral beam injection [1] are theoretically explained as the internal kink mode excited by trapped beam ions [2]. The instability mechanism is due to a resonance between the MHD mode and hot trapped particle precessional drifts. This resonance has also been found to cause rapid ejection of the trapped particles [3]. Combining

* Centro Ricerche Energia Frascati, Rome, Italy.
** Institute for Electromagnetic Field Theory and Plasma Physics, Chalmers University of Technology, Göteborg, Sweden.
+ Institute of Physics, Chinese Academy of Sciences, Beijing, China.
++ Science Applications Inc., Austin, TX, USA.

the instability and ejection processes, we can then simulate the complete 'fishbone' event. Since this destabilizing mechanism is rather general, we then apply it to the ideal MHD ballooning mode [4, 5] in order to interpret the high-frequency (~100 kHz) oscillations also observed experimentally [6]. In addition to neutral beam injection, other sources of energetic trapped particles can be considered, such as cyclotron resonant heating and fusion α-particles [7]. Finally, highly energetic trapped particles whose precession frequency exceeds the ideal MHD growth rate can enhance stabilization and possibly provide access to second stability in tokamaks [8].

2. INTERNAL KINK ('FISHBONE') INSTABILITIES

2.1. Stability analysis

Consider a large aspect ratio ($\epsilon \equiv a/R \ll 1$) tokamak plasma consisting of core (c) and hot (h) components. Consistent with the experimental identification [1] of the predominantly m = 1, n = 1 internal kink perturbations (m and n are, respectively, the poloidal and toroidal mode numbers), we adopt the following formal orderings: $\beta_{pc} \sim 1$, $\beta_{ph} \sim \epsilon$, $T_c/T_h \sim \epsilon^2$ and $|\omega/\omega_A| \sim |\bar{\omega}_{dh}/\omega_A| \sim \epsilon^2$. Here $\bar{\omega}_{dh}$ is the hot trapped particle precession frequency, and $\omega_A = V_A/qR$, with q the safety factor and V_A the Alfvén velocity. The core plasma is treated as an ideal MHD fluid, while the hot component is described by the gyrokinetic equation.

Summing the collisionless equations of motion for each species, we obtain:

$$-\omega^2 \rho_m \vec{\xi} = (\delta\vec{J} \times \vec{B} + \vec{J} \times \delta\vec{B})/c - \nabla\delta P_c - \nabla\cdot\delta\vec{\vec{P}}_h \qquad (1)$$

where $\vec{\xi}$ is the fluid displacement, $\rho_m = N_{0i}M_i$, $\delta\vec{B} = \nabla\times(\vec{\xi}\times\vec{B})$, $\delta\vec{J} = c\nabla\times\delta\vec{B}/4\pi$, and $\delta P_c = -[\vec{\xi}\cdot\nabla P_c + \gamma P_c(\nabla\cdot\vec{\xi})]$. Assuming that ω is much less than the hot particle transit and bounce frequencies, the hot particle pressure tensor $\delta\vec{\vec{P}}_h$ is given by

$$\delta\vec{\vec{P}}_h = -\vec{\xi}_\perp\cdot\nabla[P_\perp\vec{\vec{I}} + (P_\parallel - P_\perp)\vec{e}_\parallel\vec{e}_\parallel]_h + \delta\hat{P}_\perp\vec{\vec{I}} + (\delta\hat{P}_\parallel - \delta\hat{P}_\perp)\vec{e}_\parallel\vec{e}_\parallel$$

where

$$\begin{Bmatrix}\delta\hat{P}_\perp\\ \delta\hat{P}_\parallel\end{Bmatrix} = 2^{7/2}\pi M_h B\int_{B^{-1}_{max}}^{B^{-1}} d\alpha(1-\alpha B)^{1/2}\int_0^\infty dE\,\frac{E^{5/2}Q}{\omega-\bar{\omega}_{dh}}\,\bar{J}\begin{Bmatrix}\alpha B/2(1-\alpha B\\ 1\end{Bmatrix} \qquad (2)$$

$\vec{e}_\parallel = \vec{B}/B$; $\alpha B = v_\perp^2/v^2$; $E = v^2/2$; $\bar{A} \equiv (\oint A d\ell/|v_\parallel|)/\oint d\ell/|v_\parallel|$ denotes bounce-averaging; $Q = (\omega\partial/\partial E + \omega_{*h})F_{0h}$; $\omega_{*h} = -(i/\omega_c)(\vec{e}_\parallel\times\nabla\ell n F_{0h})$; F_{0h} is the

hot particle distribution function; $J = (\alpha B/2)\nabla\cdot\vec{\xi}_\perp - (1 - 3\alpha B/2)\,\vec{\xi}_\perp\cdot\vec{\kappa}$; and $\vec{\kappa} = \vec{e}_\parallel\cdot\nabla\vec{e}_\parallel$. Equations (1) and (2) constitute a complete normal mode description in terms of $\vec{\xi}$.

Assuming a fixed conducting boundary, we can derive a dispersion relation variationally. The dispersion functional (quadratic form) is $D[\vec{\xi}] = \delta W_{MHD} + \delta W_k + \delta I$. Here δW_{MHD} is the usual ideal MHD δW involving the total fluid pressure $P = P_c + (P_\parallel + P_\perp)_h/2$; $\delta I = -(\omega^2/2)\int d^3\vec{x}\ \rho_m |\vec{\xi}|^2$ is the inertial energy;

$$\delta W_k = -2^{9/2}\pi^3 M_h \int RB\, rdr \int_{B_{max}^{-1}}^{B_{min}^{-1}} d\alpha \int_0^\infty dE E^{5/2} K_b \bar{J}^* \frac{Q}{\omega - \bar{\omega}_{dh}} \bar{J} \tag{3}$$

with $K_b = \oint (d\theta/2\pi)\,(1 - \alpha B)^{-1/2}$. Note that $\delta W_k^{(2)} \sim \epsilon^2 (B^2 |\vec{\xi}/R|^2 V) \sim \delta I^{(2)}$, where V is the volume and superscripts denote orderings. The variational scheme is then to find a $\vec{\xi}_t$ which minimizes D to $O(\epsilon^3)$. This minimizing procedure is facilitated by separating the regions outside and inside the singular surface located at $q_s = q(r_s) = 1$. For circular cross-sections, we obtain the following dispersion relation [2]:

$$\frac{-i\omega}{\hat{\omega}_A} + \delta\hat{W}_{fc} + \delta\hat{W}_k = 0 \tag{4}$$

where

$$\hat{\omega}_A = \frac{V_A}{(1 + 2q_s^2)^{1/2} R_0 \hat{s}}$$

$$\hat{s} = \frac{r_s q_s'(r_s)}{q_s}$$

$$\delta\hat{W}_{fc} = \pi (r_s/R_0)^2\, \delta\tilde{W}_{TC}$$

In addition, δW_{TC} has been given previously [9] and contains only the core-plasma contribution, and

$$\delta\hat{W}_k = \frac{2^{3/2} M_h \pi^2}{B_0^2} \left\langle \int_{1-r/R}^{1+r/R} d(\alpha B) \int_0^\infty dE E^{5/2} \frac{K_2^2}{K_b} \frac{\omega}{\bar{\omega}_{dh} - \omega} \left(\frac{\partial}{\partial E} + \frac{\hat{\omega}_{*h}}{\bar{\omega}_{dh}}\right) F_{0h} \right\rangle \tag{5}$$

Here $\langle y\rangle \equiv (2/r_s^2)\int_0^{r_s} y\, rdr$ is the average of y within q = 1 surface;
$K_2 = \oint (d\theta/2\pi)\cos\theta\,(1 - \alpha B)^{-1/2}$; and (m = 1, n = 1) perturbations are assumed.

The stability properties are modified qualitatively by the fact that $\delta\hat{W}_k$ contains the mode-precessional drift resonance. A Nyquist analysis reveals the following general characteristics which are relatively insensitive to the F_{0h} one assumes:

(a) There exist two branches of the solution. One is the usual MHD branch driven by $\delta\hat{W}_{fc}$, and the other is a new branch induced by the energetic trapped particle.

(b) Even when the MHD branch is stable ($\delta\hat{W}_{fc} \geqslant 0$), the trapped particle branch can become unstable if $\langle\beta_{h,t}\hat{I}\rangle$ exceeds $\langle\beta_{h,t}\hat{I}\rangle_{crit}$, where

$$\langle\beta_{h,t}\hat{I}\rangle_{crit} \approx \begin{cases} \bar{\omega}_{dh}/\hat{\omega}_A & \text{for } \delta\hat{W}_{fc} < \bar{\omega}_{dh}/\hat{\omega}_A \\ \delta\hat{W}_{fc} & \text{for } \delta\hat{W}_{fc} > \bar{\omega}_{dh}/\hat{\omega}_A \end{cases} \tag{6}$$

Here $\hat{I} \sim (K_2/\epsilon K_b)$ is a trapped particle geometrical factor typically of $O(1/\epsilon)$, and thus $\langle\beta_{h,t}\rangle_{crit} \sim O(10^{-3} - 10^{-2})$.

(c) Both the real frequencies and growth rates of this trapped-particle-induced branch are typically comparable to $\bar{\omega}_{dh}$.

These features are consistent with experimental observations. Specific calculations for slowing down and Maxwellian F_{0h} have been performed [2, 7].

2.2. Simulation of the fishbone cycle

MHD perturbations with ω in resonance with $\bar{\omega}_{dh}$ can cause secular radial drift of energetic trapped particles. To see this, consider a perturbation δB_r rotating toroidally with $\vec{V} = \omega R\vec{e}_\phi$. In the frame moving with the perturbation there is an electric field $\delta\vec{E} = \vec{V} \times \delta\vec{B}$, producing a δE_θ. This in turn produces a $\delta\vec{E}_\theta \times \vec{B}$ radial drift of particles. If the trapped particles and the perturbation remain in phase ($\omega = \bar{\omega}_{dh}$), this motion is secular. A Monte Carlo code based on a Hamiltonian guiding centre drift orbit formalism [3] has been used to study the resonant loss process and to simulate the full fishbone cycle. The mode structure was obtained from a non-linear MHD initial value code which reproduced the two principal diagnostic signals, due to soft X-ray detectors and Mirnov coils. The dispersion relation was calculated numerically using the instantaneous particle distribution. The inital particle distributions were given by beam injection and evolution codes.

The results of a typical simulation using PDX parameters are shown in Fig. 1. As soon as $\langle\beta_{h,t}\rangle$ exceeds $\langle\beta_{h,t}\rangle_{crit}$ the mode begins to grow. At some point the mode reaches a significant amplitude ($\delta B/B \approx 10^{-4}$) and begins to affect particle motion, ejecting particles in a beacon rotating toroidally with frequency $\omega \approx \langle\bar{\omega}_{dh}\rangle$. This loss process is rapid, and $\langle\beta_{h,t}\rangle$ drops to $\langle\beta_{h,t}\rangle_{crit}$ typically in hundreds of μs. The loss begins with particles of highest energy and, since $\bar{\omega}_{dh} \sim E$, this produces a whistling downward of the fishbone frequency ($\sim$20 kHz for PDX) during the

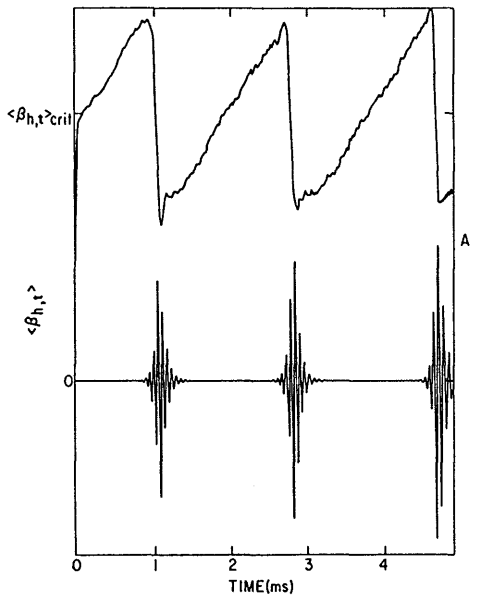

FIG. 1. Results of a 'fishbone' simulation for typical PDX parameters and $\langle\beta_{h,t}\rangle_{crit} \approx 2 \times 10^{-3}$. *Shown here are* $\langle\beta_{h,t}\rangle$ *and the Mirnov signal* $A = \delta B/B$ *with maximum amplitude* 5×10^{-4}.

loss process, which is also observed experimentally. The maximum mode amplitude is reached when $\langle\beta_{h,t}\rangle$ has dropped to $\langle\beta_{h,t}\rangle_{crit}$ (Im $\omega = 0$), and the mode continues to eject particles, driving $\langle\beta_{h,t}\rangle$ well below $\langle\beta_{h,t}\rangle_{crit}$. The mode then decays to a point where it no longer affects particle motion and the cycle begins again. The beam deposition rate is typically much lower than the loss rate, so the time between bursts of MHD activity is longer than the bursts themselves.

Growth rates, frequencies, and other properties of the fishbone cycle depend on the beam injection parameters and the nature of the equilibrium. In particular, high shear can make the particle precession rate a strong function of position, limiting resonance with the mode as a particle moves outwards.

3. TRAPPED-PARTICLE-INDUCED MHD BALLOONING INSTABILITY

By analogy with the theory of 'fishbones', one may expect that energetic trapped particles can also destabilize ideal MHD ballooning modes by introducing a new unstable branch at $|\omega| \cong \bar{\omega}_{dh}$. The major difference is that whereas the m = 1 = n internal kink 'fishbones' involve radially global quantities, the high mode number ballooning instabilities will be localized near a flux surface.

As before, adopt an MHD fluid description for the warm core plasma but use the gyrokinetic equation for the hot component where $\omega \sim \bar{\omega}_{dh}$. With the orderings $\epsilon\beta_{pc} \sim 1$, $\beta_{ph} \sim 1$, and $T_c/T_h \sim \epsilon^2$, the ballooning eigenmode equation can be derived [4] as

$$\frac{d}{d\chi}(1+\hat{s}^2\chi^2)\frac{d\phi}{d\chi} + \Omega^2(1+\hat{s}^2\chi^2)\phi + g(\chi)[\epsilon\beta_{pc}\phi + \widetilde{\epsilon\beta_{ph}\phi}] = 0 \qquad (7)$$

where $\hat{s} = (r/q)dq/dr$; $\Omega = \omega/\hat{\omega}_A$; ϕ is the perturbed electrostatic potential; χ is the extended poloidal angle; and $g(\chi) = \cos\chi + (\hat{s}\chi - \epsilon\beta_{pc}\sin\chi)\sin\chi - \epsilon(1-q^{-2})$. The trapped particle term is

$$\widetilde{\epsilon\beta_{ph}\phi} = \frac{2^{3/2}\pi^2 q^2 M_h}{B^2}\int_{B_{max}^{-1}}^{B^{-1}} \frac{Bd\alpha}{(1-\alpha B)^{1/2}}\int_0^\infty \frac{dE\,E^{5/2}}{(\omega-\bar{\omega}_{dh})}\,Q\overline{g(\chi)\phi} \qquad (8)$$

with notation the same as in Section 2. If small shear, $\hat{s} < 1$, is assumed, Eq.(8) can be analysed in terms of the short and long spatial scales, χ and $z = \hat{s}\chi$. Introducing the subsidiary ordering $\Omega^2 \sim (\epsilon\beta_{pc})^4 \sim \epsilon\beta_{ph} \sim \epsilon(1-q^{-2}) \sim \hat{s}^2$ and then expanding and solving for $\phi = \phi_0(z) + \phi_1(\chi, z) + \ldots$ up to fourth order in powers of $\hat{s}^{1/2}$, one obtains an averaged ballooning equation for the function $\psi(z) = \phi_0(z)(1+z^2)^{1/2}$. Now match the asymptotic solution $\psi \propto \exp[i(\Omega/\hat{s})|z|]$ for $|z| \gg 1$ with the logarithmic derivative of the inner solution for $|z| \sim 1$, assuming $|\Omega/\hat{s}| < 1$ and constant-ψ in the inner region. This yields a dispersion relation of the same form as that for the internal kink mode, Eq.(4), with appropriate replacements of $\delta\hat{W}_{fc}$ and $\langle\beta_{h,t}\hat{I}\rangle$ in terms of surface quantities. The stability properties are thus formally similar to those discussed in Section 2. The $\hat{s} < 1$ limitation on the preceding analysis can be somewhat relaxed if the constant-ψ approximation is replaced by a weakly varying trial function which provides better estimates of $\delta\hat{W}_{fc}$ and $\langle\beta_{h,t}\hat{I}\rangle$ for $\hat{s} \lesssim 1$. Otherwise the stability properties remain unchanged.

The restrictions on $\hat{s}$ and β can be further relaxed in the following way [5]. Assume that the energetic particles are deeply trapped so that the $\widetilde{\epsilon\beta_{ph}\phi}$ term in Eq.(7) is localized near $\chi = 0$, where it couples the zero frequency even and odd solutions ϕ_e and ϕ_0. For $\hat{s}\chi > 1$ each has the asymptotic form $\phi_{e,0} \sim M_{e,0}\chi^\nu + N_{e,0}\chi^{-\nu}$, where the four Mercier coefficients $M_{e,0}$ and $N_{e,0}$ and the exponent ν can be computed numerically for a given equilibrium. With this information, the total inner, MHD, solution $\phi_{in} = \phi_e(\chi) - \phi_0(\chi)\int d\chi\,\widetilde{\epsilon\beta_{ph}}g(\chi)$ can be matched to the small argument form of the Hankel function solution $\phi_{out} = \chi^{1/2}H_\nu^{(1)}(\Omega\chi)$ in the outer, inertial, region where $\Omega\chi \sim 1$. This procedure yields a complex dispersion relation, which can be analysed by the Nyquist technique.

This procedure yields the following results. If M_e, calculated including the diamagnetic stabilization induced by the energetic particles [8], is negative, then the system is unstable to a zero frequency mode. Note that $M_e = 1$ for $\beta_{pc} = 0$ and that the curves for $M_e = 0$, as a function of β_{ph}, are given in Ref.[8]. If $\beta_{ph} = 0$, then $M_e = 0$ at the usual MHD ballooning limit for β_{pc}. If $M_e > 0$, the zero frequency mode is stable, but necessary (and usually sufficient) conditions for an instability near $\bar{\omega}_{dh,max}$ are that both $\epsilon\beta_{ph} > (2\hat{s}/\pi)M_e$ and $\epsilon\beta_{ph} > (8/\pi^3) \times (\bar{\omega}_{dh,max}/\hat{\omega}_A)$. For present experiments, with $\bar{\omega}_{dh}/\hat{\omega}_A \ll 1$, this would indicate an instability threshold well below the MHD threshold at small $\hat{s}$ values, and slightly below it for $\hat{s} \gtrsim 1$. Although the analysis is not strictly valid for $\bar{\omega}_{dh}/\hat{\omega}_A > 1$, it indicates that in the $\bar{\omega}_{dh} \to \infty$ limit a necessary and sufficient condition for stability is $M_e > 0$. For energetic particles, trapped on the inside of the torus, i.e. $\bar{\omega}_{dh} < 0$, stability is more favourable. For this case, necessary and sufficient conditions for stability if $\bar{\omega}_{dh}/\hat{\omega}_A \lesssim 1$ are that both $M_e > 0$ and $\epsilon\beta_{ph} < 4\hat{s}/\pi$.

This trapped-particle-induced ballooning instability appears to be a likely candidate to explain the high-frequency (50 to about 150 kHz) MHD-type oscillations observed in the PDX tokamak during high-power perpendicular injection [6], often as a 'precursor' to the 'fishbone' oscillations.

(a) The ratio of the precursor frequency to the frequency of the n = 1 fishbones is close to the measured toroidal mode number $n \simeq 2-6$ of the precursor. Theory predicts $\omega_r \lesssim \hat{\omega}_{dm}$, in agreement with experiment.

(b) While the high-frequency oscillations tend to occur at high values of beam power and $\epsilon\beta_p$, the fishbones can occur at lower values. Likewise, theory finds a higher $\langle\beta_{h,t}\rangle$ instability threshold than that for the fishbones.

(c) Experimentally, the high-frequency oscillations are localized near the q = 1 surface. Since the q profile flattens there, shear $\hat{s}$ is reduced along with the threshold β value, consistent with theory.

(d) When the high-frequency oscillations are present along with fishbones, they occur in the beginning stage of the fishbones. Since q on axis drops during heating, ballooning modes, which require $q(0) \gtrsim 1$, would occur before the internal kink instability sets in at $q(0) < 1$.

(e) In cases where only the high-frequency oscillations are observed, sawtoothing is generally either absent or has small amplitude, which is consistent with the idea that ballooning modes occur with $q(0) \gtrsim 1$.

4. STABILIZATION SCHEMES

We have demonstrated that 'fishbones' and their high-frequency 'precursors' are excited via the resonant coupling between the curvature drift precessional motion of energetic trapped particles and ideal MHD modes (internal kink and

ballooning, respectively) of the core plasma. To suppress instabilities of this type and the associated loss of hot ions, we propose the following stabilization schemes:

(a) Apply either tangential or not directly perpendicular neutral beam heating in order to reduce the trapped hot ion beta value below its threshold value;
(b) Employ shaping of the plasma cross-section, e.g. bean shape [10], to make $\delta\hat{W}_{fc}$ more positive (i.e. raise the $\langle\beta_{h,t}\rangle$ threshold) and thus make the MHD branch even more stable;
(c) Introduce highly energetic (~MeV) beams [8], in order to raise the threshold trapped particle beta value, which is proportional to the injection energy through the ratio $\bar{\omega}_{dh}/\omega_A$.

ACKNOWLEDGEMENTS

This work was supported by the US Department of Energy under Contract No. DE-ACO2–76–CHO-3073 with Princeton University and Contract No. DE-FG05-80ET-53088 with the University of Texas.

REFERENCES

[1] McGUIRE, K., et al., Phys. Rev. Lett. **50** (1983) 891.
[2] CHEN, L., WHITE, R.B., ROSENBLUTH, M.N., Phys. Rev. Lett. **52** (1984) 1122.
[3] WHITE, R.B., et al., Phys. Fluids **26** (1983) 2958.
[4] WEILAND, J., CHEN, L., in Proc. Annual Controlled Fusion Theory Conf., Incline Village (Sherwood), Nevada, 1984, Lawrence Livermore Natl Lab., Paper No. 2P23.
[5] VAN DAM, J.W., ROSENBLUTH, M.N., LIU, C.S., ANTONSEN, T.M., ibid., Paper No. 2P11.
[6] McGUIRE, K., et al., Bull. Am. Phys. Soc. **28** (1983) 1173.
[7] WHITE, R.B., CHEN, L., ROMANELLI, F., HAY, R., Princeton Plasma Phys. Lab. Rep. PPPL-2115 (1984).
[8] ROSENBLUTH, M.N., TSAI, S.T., VAN DAM, J.W., ENGQUIST, M.G., Phys. Rev. Lett. **51** (1983) 1967.
[9] BUSSAC, M.N., PELLAT, R., EDERY, D., SOULE, J.L., Phys. Rev. Lett. **35** (1975) 638.
[10] CHANCE, M.S., JARDIN, S.C., STIX, T.H., Phys. Rev. Lett. **51** (1983) 1963.

DISCUSSION

S.-I. ITOH: You said that in your analyses the results are not sensitive to the distribution function of the hot component, even when wave-particle interaction is a key process. Is this assumption confirmed by calculations?

L. CHEN: What I said – and I should like to emphasize this – is that many interesting qualitative features of the stability properties are relatively insensitive

to the detailed F_{OH} one assumes. This observation is not an assumption but the result of simple Nyquist analyses, and is indeed borne out by detailed numerical calculations of the dispersion relation.

S.-I. ITOH: As far as global response is concerned, did you find any difference between the anisotropic pressure plasmas?

L. CHEN: This type of instability is due to hot particles trapped on the bad curvature region. Pressure anisotropy is hence not a necessary condition for the instability. I_e will, however, enhance the instability strength, typically by a factor of O(1).

R.D. STAMBAUGH: Which parameter is most important in the fishbone – the poloidal β of the trapped fast ions or their toroidal β?

L. CHEN: Since the fishbone proper and its high-frequency analogues are MHD modes driven unstable by the pressure of the energetic trapped particles, the more relevant parameter is the poloidal β of the trapped particles.

SELF-CONSISTENT TRANSPORT THEORY IN TOKAMAK PLASMAS

B.B. KADOMTSEV, O.P. POGUTSE
I.V. Kurchatov Institute of Atomic Energy,
Moscow,
Union of Soviet Socialist Republics

Abstract

SELF-CONSISTENT TRANSPORT THEORY IN TOKAMAK PLASMAS.

A new set of simplified equations is proposed for the description of microturbulence and enhanced transport in tokamak plasmas. These equations are similar to the reduced MHD equations in that the strong-longitudinal-magnetic-field approximation is used. The equations are obtained by reducing the collisionless drift kinetic equation for electrons and the kinetic equation for ions, together with the charge neutrality condition. They are suited to describe non-linear plasma motion on a scale much larger than the electron cyclotron radius and on arbitrary scale as compared with the ion cyclotron radius. – The consistency of these equations implies that they simultaneously describe the destruction of magnetic-field surfaces and enhanced thermal and particle transport.

1. INTRODUCTION

It is well known that there exists a complex activity of a collective nature in tokamak plasmas confined and stabilized by strong magnetic fields. This activity becomes manifest in MHD-oscillations of finite amplitude and in anomalously high diffusion and electron heat conduction. The view is widely held, at present, that small scale oscillations, together with the 'island' structure of the magnetic surfaces due to large-scale MHD perturbations, are responsible for anomalous heat and particle transport.

So far, no consistent theory has existed of these processes in which the magnetic-surface perturbations would be sufficiently correctly matched with the plasma oscillations and the motion of electrons and ions.

It seems to be convenient to use the simplified equations, in which a strong, longitudinal, magnetic field is taken into account from the very beginning, to see how the motion of particles and the magnetic field lines are correlated.

We have shown previously [1, 2] that large-scale plasma flows have a 'quasi-2D' nature in conditions when the external magnetic field is much stronger than all fields induced in the plasma by currents passing through it. In this case, the MHD equations are substantially simplified and can be reduced to two scalar equations, one for a function of the current, χ, and another one for the magnetic flux, Ψ (whose precise definition will be given below).

Physically, this corresponds to a neglect of fast magnetosonic oscillations and, in many cases, insignificant sonic oscillations. (Moreover, sets of MHD-equations, set up in the spirit of Refs [1, 2], which include sonic oscillations, have been derived recently [3, 4]).

The set of equations [1] was widely used for simulating MHD-processes in a plasma. The non-linear stages of kink and tearing instabilities [5–7] were studied by this set of equations, a theory of mode reconnection was set up for the m = 1 mode, and thus the mechanism producing sawtooth oscillations in a tokamak was explained. Nowadays, these equations are used to simulate the 3D-non-linear stage in the development of MHD-instabilities [9]; they are basic in the theory of major disruptions in tokamaks.

In spite of all advantages, the region of application of these equations is limited in that they are only valid for perturbations with wavelengths longer than the ion Larmor radius. As will be shown below, for a strong magnetic field, hydrodynamic equations, i.e. equations which depend on $\vec{n}$ and on t only and are true for arbitrary plasma inhomogeneities, including short-scale ones, can be written down. They are a natural generalization of the equation from Ref [1].

These equations will be used to consider the phenomenon of field-line reconnection within a collisionless skin layer, c^2/ω_p^2 (ω_p is the plasma electron frequency) and to explain the short-scale diffusion and heat conduction processes in a plasma.

2. PLASMA EQUATIONS IN A STRONG MAGNETIC FIELD IN TWO-FLUID HYDRODYNAMICS

We consider plasma motion within the framework of magnetic two-fluid hydrodynamics and, for simplicity, assume the ion temperature to be equal to zero.

The toroidal plasma column with minor radius r and major radius R is simulated by a straight cylinder, $L = 2\pi R$ long, with identical ends. The z-axis is directed along the cylinder and the longitudinal field, B_0, is considerably greater than the transverse components of field $B_\perp$. Hence, one can expand the MHD equations in terms of inverse powers of B_0.

In this approximation the magnetic field can be represented as $\vec{B} = B_0\vec{e}_z + [\vec{e}_z \times \nabla\Psi]$; where Ψ is the transverse magnetic flux function, and we may assume that the plasma has a plan-parallel flow within each layer [1]. Let us introduce the current function χ, and the plasma curl density, Γ:

$$\vec{v} \equiv \vec{v}_\perp = [\vec{e}_z \times \nabla\chi]; \quad \Gamma = \mathrm{rot}_z\vec{v} = \Delta_\perp\chi \tag{2.1}$$

Here $\vec{v}$ is the ion velocity.

$$Mn\frac{d\vec{v}}{dt} = en\vec{E} + \frac{e}{c}n[\vec{v} \times \vec{B}] \tag{2.2}$$

$$\nabla P_e = -en\vec{E} - \frac{e}{c}n[\vec{v}_e \times \vec{B}] \tag{2.3}$$

Here, $\vec{v}_e$ is the electron velocity, and P_e is the electron pressure. A small electron inertia term is neglected in Eq. (2.3).

Determining the transverse current component, $j_\perp$, from the sum of Eqs (2.2) and (2.3), and substituting it into the equation of quasi-neutrality, $\mathrm{div}\,\vec{j} = 0$, we derive the equation for Γ:

$$Mn\frac{d\Gamma}{dt} = \frac{(\vec{B}\nabla)}{c} j \tag{2.4}$$

Here, M is the ion mass, n the density, $d/dt = \partial/\partial t + (\vec{v}\cdot\nabla)$, $j \equiv j_\parallel = c/4\pi\,\Delta\Psi$ the parallel current component, and the role of the current function, χ, is played by the quantity $(c/B)\varphi$. The electric field is expressed in the form:

$$\vec{E} = -\nabla\varphi + \frac{\vec{e_z}}{c}\frac{\partial\Psi}{\partial t} \tag{2.5}$$

Then, from Eq. (2.3), we obtain:

$$\frac{\partial\Psi}{\partial t} - \frac{c\vec{B}}{B_0}\cdot\left(\nabla\varphi - \frac{1}{en}\nabla P_e\right) = 0 \tag{2.6}$$

We may assume that $(\vec{B}\cdot\nabla)\,T_e = 0$ for electrons, because of high thermal conduction along the magnetic field. Therefore,

$$\frac{(\vec{B}\cdot\nabla)}{n}P_e = (\vec{B}\cdot\nabla)(T_e \ln n).$$

Introducing

$$\lambda = \frac{c}{B_0}\left(\varphi - \frac{T_e}{e}\ln n\right),$$

we rewrite Eq. (2.6) in the form:

$$\frac{\partial\Psi}{\partial t} + [\vec{e_z} \times \nabla\lambda]\cdot\nabla\Psi = B_0\frac{\partial\lambda}{\partial z} \tag{2.7}$$

If we interpret the quantity $|[\vec{e}_z \times \nabla\lambda]|$ as the magnetic surface transport velocity and remember that the operators d/dt and $(\vec{B}\cdot\nabla)$ commute, the equation for the longitudinal magnetic flux,

$$\frac{\partial\Phi}{\partial t} + [\vec{e}_z \times \nabla\lambda]\nabla\Phi = 0 \tag{2.8}$$

will describe the defromation of the magnetic surfaces without violation of their topology. Note that the addition to λ of any function with C (Φ), such that $(\vec{B}\cdot\nabla)C = 0$, does not change the forms of Eqs (2.7) and (2.8).

We now consider the problem of possible convective particle and heat transport in the approximation under study. For this purpose, we invoke the continuity equation:

$$\frac{\partial n}{\partial t} + \mathrm{div}(n\vec{v}_e) = 0 \tag{2.9}$$

Let us represent the electron velocity as $\vec{v}_e = \vec{v}_{\perp e} + \vec{v}_{\parallel e}$. The transverse component can be expressed from Eq. (2.3), the longitudinal component can be written in terms of the longitudinal current component, $\vec{v}_{\parallel e} = -(j_\parallel/en)/(B/B_0)$. Equation (2.9) can be rewritten in the form:

$$\frac{\partial n}{\partial t} + [\vec{e}_z \times \nabla\chi]\nabla n = \frac{c}{4\pi e}\frac{(\vec{B}\cdot\nabla)}{B_0}\Delta_\perp\Psi \tag{2.10}$$

Evidently, the last term in Eq. (2.10) does not describe particle transport across the magnetic surface, and the transverse component of the particle velocity in (2.10) $[\vec{e}_z, \nabla\chi]$ differs from the field line transport velocity, $[\vec{e}_z, \nabla\lambda]$ by an expression proportional to $[\vec{e}_z, \nabla T_e]$. This difference in the velocities is directed along the surface Φ = const, as $T_e = T_e(\Phi)$ is constant on the magnetic surface.

Thus, within the framework of two-fluid hydrodynamics, there is no plasma and heat transport across the magnetic surfaces.

It is easy to show that, when the plasma column touches the ideally conducting case such that the normal velocity and field components are equal to zero, Eqs (2.4), (2.7) and (2.10) possess the following energy integral:

$$\mathcal{E} = \int \left\{ Mn\frac{(\nabla\chi)^2}{2} + \frac{(\nabla\Psi)^2}{8\pi} + T_e n(\ln n - 1) \right\} dV \tag{2.11}$$

3. EQUATIONS OF PLASMA DYNAMICS IN A STRONG MAGNETIC FIELD

As we have seen above, the problem of describing plasma motion in a strong magnetic field is divided into two parts: the description of plane-parallel ion flows and that of magnetic-surface behaviour. For large-scale flows, the motion occurs under conservation of the topology of the nested magnetic surfaces; it is not accompanied by particle or heat transport across the surfaces. One should use the smallest transverse scale in order to make dissipative effects play a role and to find these fluxes.

Assuming finite electric conductivity along the magnetic field, we obtain

$$\frac{\partial \Psi}{\partial t} - \frac{c\vec{B}}{B_0}\left(\nabla\varphi - \frac{\nabla P_e}{en}\right) = \frac{c^2\eta}{4\pi}\,\Delta_\perp \Psi \tag{3.1}$$

Here $\eta = 1/\sigma$ is the resistivity, and σ the electric conductivity of the plasma.

Strictly speaking, Eq. (3.1) is only true for perturbations that are so widely stretched along the magnetic field that the perturbation wavelength is much longer than the mean free path of the electrons. This is not the case in a high-temperature plasma where the condition of non-collisionality is more likely to be satisfied. Therefore, using a drift kinetic equation should be more adequate for electrons:

$$\frac{\partial f}{\partial t} + v_\parallel (\vec{B}\cdot\nabla) f + \frac{c}{B_0}\,[\vec{e}_z \times \nabla\varphi]\cdot\nabla f + \frac{e}{m}\left(\vec{B}\cdot\nabla\varphi - \frac{1}{c}\frac{\partial \Psi}{\partial t}\right)\frac{\partial f}{\partial \nabla_\parallel} = 0 \tag{3.2}$$

Here, f is the electron distribution function with respect to the longitudinal velocity, $v_\parallel = \vec{v}\cdot\vec{b}$, $\vec{b} = \vec{B}/B_0$.

Integrating (3.2) with respect to the longitudinal velocity, $v_\parallel$, we obtain the familiar continuity equation (2.10), where $\chi = (c/B_0)\varphi$ (the contribution of the ions to the longitudinal current vanishes in the approximation that we have adopted).

The Ohm's law also follows from the drift kinetic equation:

$$\frac{\partial \Psi}{\partial t} + [\vec{e_z} \times \nabla\lambda]\cdot\nabla\Psi - B_0\frac{\partial \lambda}{\partial z} = \frac{c^2\hat{\eta}}{4\pi}\,\Delta_\perp \Psi \tag{3.3}$$

where $\hat{\eta}$ is the collisionless plasma resistivity, which is found, in its Fourier representation, from the relationship:

$$\hat{\eta}^{-1}_{\vec{k},\omega} = \sigma_{\vec{k},\omega} = -i\,\frac{e^2\omega n}{T_e k_\parallel}\left\{1 + \frac{\omega}{|k_\parallel| v_e}\,Z\left(\frac{\omega}{|k_\parallel| v_e}\right)\right\} \tag{3.4}$$

Here $v_e = \sqrt{2T_e/m}$, where m is the electron mass, and Z is the dispersion function.

From physical considerations, it is evident that only the real (in the Fourier representation) part of the operator $\hat{\eta}$ makes a contribution to the transport processes.

Remembering the properties of the function Z(x), it is not difficult to show that in the range of high phase velocities, $\omega \gg k_\parallel v_e$ the right-hand side of Eq. (3.4) takes the form $(c^2/\omega_{pe}^2)\,\Delta_\perp\,\partial\Psi/\partial t$ where $\omega_{pe}^2 = 4\pi e^2 n_0/m$, which corresponds to a reversible displacement of electrons along the field lines. For $\omega \lesssim k_\parallel v_e$, the real part of $\hat{\eta}_{\vec{k},\omega}$ is approximately equal to:

$$\mathrm{Re}\,\eta_{\vec{k},\omega} \approx \frac{\sqrt{\pi}}{2}\,\frac{m}{e^2 n}\,|k_\parallel|\,v_e \exp\left(-\frac{\omega^2}{k_\parallel^2 v_e^2}\right) \approx \frac{m|k_\parallel|\,v_e}{e^2 n_0} \tag{3.5}$$

It is sufficient to consider the planeparallel displacement of ions in the potential electric field, $\vec{E}_\perp = -\nabla_\perp \varphi$. The experiment shows that low-scale plasma density fluctuations in tokamaks are practically isotropic. Therefore, we may more or less safely assure that the ion oscillations occur before a uniform background, $n_0 = \mathrm{const}$. In this case, however, the relationship between the density oscillations, $\tilde{n}$, and the potential φ is well known. It can be written symbolically:

$$\tilde{n} = -\frac{e}{T_i}\,n_0\left\{1 - e^{\rho_i^2 \Delta_\perp}\,I_0\,(\rho_i^2 \Delta_\perp)\right\}\varphi \tag{3.6}$$

Here, I_0 is a Bessel function of imaginary argument, $\rho_i^2 = T_i/(M\omega_B^2)$ is the square of the ion Larmor radius, and $\omega_B = eB/(mc)$.

We now substitute $n = n_0 + \tilde{n}$ into the continuity equation (2.10). Then, assuming $n_0 = \mathrm{const}$ (for ions), we obtain an equation for the potential φ which is similar to (2.4) but has another Γ:

$$\Gamma = -\rho_i^{-2}\left\{1 - \exp\,(\rho^2 \Delta_\perp) I_0(-\rho^2 \Delta_\perp)\right\}\frac{c\varphi}{B_0} \tag{3.7}$$

This equation generalizes the expression for a curl of the plasma velocity at the arbitrary ion Larmor radius. For the large-scale motions, when $\rho_i^2 \Delta_\perp \to 0$, we obtain the previous expression for Γ, i.e. $\Gamma = (c/B_0)\Delta_\perp \varphi$.

Equations (2.10), (3.3) and (2.4), together with (3.7), constitute the appropriate set of equations describing slow plasma oscillations in a strong magnetic field for an arbitrary transverse scale of oscillations that is, however, greater than the electron Larmor radius.

The law of energy conservation can be expressed as follows:

$$\frac{\partial}{\partial t}\int dV\left\{Mn\,\frac{(\nabla\chi)^2}{2} + \frac{(\nabla\Psi)^2}{8\pi} + \frac{Mc_s^2 n^2}{2n_0}\right\} = \int dV \hat{\eta} j^2 \tag{3.8}$$

where

$$\chi = \left[\frac{1 - \exp(\rho_i^2 \Delta_\perp) I_0 (-\rho_i^2 \Delta_\perp)}{\rho_i^2 \Delta_\perp} \right]^{1/2} \frac{c\varphi}{B_0}$$

and $c_s^2 = T_e/M$.

If we are interested in the processes of heat conduction through the electron channel, we should add an equation for T_e. This can easily be done, by using the kinetic equation (3.2):

$$\frac{1}{2} \left(\frac{\partial}{\partial t} nT_e + \frac{c}{B_0} [\vec{e}_z \times \nabla\varphi] \nabla (nT_e) \right) = \frac{(\vec{B}\cdot\nabla)}{B_0} q_\parallel + E_\parallel j_\parallel \qquad (3.9)$$

Here, $q_\parallel = -\int \frac{mv_\parallel^2}{2} v_\parallel f \, dv_\parallel$.

The longitudinal energy flux, $q_\parallel$, in the linear approximation may be expressed in terms of $E_\parallel$ by the relationship $q_\parallel = \hat{\mu} E_\parallel$, which is similar to $j_\parallel = \sigma E_\parallel$. The operator $\hat{\mu}$ is easy to calculate by using the kinetic equation (3.2).

4. ANOMALOUS DIFFUSION AND HEAT CONDUCTION IN A STRONG MAGNETIC FIELD

We introduce a function Φ, which satisfies Eq. (2.8) and assume that it coincides with the function of magnetic flux, $\vec{B}\cdot\nabla\Phi = 0$ $(t = 0)$, at the initial instant of time. Calculating the commutator

$$\frac{d}{dt} (\vec{B}\cdot\nabla\Phi) - (\vec{B}\cdot\nabla) \frac{d\Phi}{dt}$$

we find (with due account for (2.8)):

$$\frac{d}{dt} (\vec{B}\cdot\nabla)\Phi = \left[\nabla \frac{c^2\hat{\eta}}{4\pi} \Delta_\perp \Psi \times \nabla\Phi \right]_z \qquad (4.1)$$

i.e.

$$\frac{d}{dt} (\vec{B}\cdot\nabla)\Phi \neq 0$$

and, consequently, the magnetic field lines start to 'pierce' the Φ = const surface.

For low dissipation ($\hat{\eta} \to 0$), the surface Φ = const can be used as an averaged magnetic surface, which becomes a precise magnetic surface when $\hat{\eta} = 0$.

We now calculate the density change inside the surface Φ = const (moving with time):

$$\frac{\partial}{\partial t}\int_{\Phi} n dV = \int_{\Phi} \frac{\partial n}{\partial t} dV + \oint_{\Phi} n\vec{V}_{\Phi} d\vec{S} \tag{4.2}$$

where $\vec{V}_{\Phi} = [\vec{e}_z \times \nabla\lambda]$.

Using (2.10), we obtain:

$$\frac{\partial}{\partial t}\int_{\Phi} n dV \equiv -\oint_{\Phi} \Gamma_n dS = \frac{1}{e}\oint_{\Phi} j \frac{\vec{B}\cdot d\vec{S}}{B_0} = \frac{1}{eB_0}\oint_{\Phi} j \frac{(\vec{B}\cdot\nabla)\Phi}{|\nabla\Phi|} dS \tag{4.3}$$

where Γ_n is the particle flux.

The density change within Φ = const is entirely due to the outflow of electrons along the field lines intersecting (according to (4.1)) the Φ = const surface.

The change in thermal energy per unit volume can be calculated similarly. From (3.1), we easily obtain

$$\frac{1}{2}\frac{\partial}{\partial t}\int_{\Phi} nT_e dV = -\oint_{\Phi} Q_{\parallel e} dS \tag{4.4}$$

where

$$Q_{\parallel e} = -\frac{1}{B_0} q_{\parallel} \frac{(\vec{B}\cdot\nabla)\Phi}{|\nabla\Phi|} \tag{4.5}$$

We first consider the calculation of the diffusion coefficient (assuming T_e = const). The combination $(\vec{B}\cdot\nabla\Phi)$ can be found from Eq. (4.1):

$$(\vec{B}\cdot\nabla)\Phi = \int_{-\infty}^{t} [\nabla c\hat{\eta} j \times \nabla\Phi]_z dt' \tag{4.6}$$

where the integration is carried out along the trajectory $d\vec{r}/dt = [\vec{e}_z \times \nabla\lambda]$.

Substituting expression (4.6) into (4.3), we obtain:

$$\oint_{\Phi} j \frac{(\vec{B}\cdot\nabla)\Phi}{|\nabla\Phi|} dS = c \int_{\Phi} d\vec{S} \int_{-\infty}^{t} dt' \, [\vec{e_z}\, j(t) \times \nabla\hat{\eta}\, j(t')] \tag{4.7}$$

We can now use a quasi-linear approximation to calculate (4.7). We assume that the currents $j'_{\parallel}$ are perturbed and the surface $d\vec{S}$ coincides with the initial cylindrical surface. Then the particle flux has a radial component only:

$$\Gamma_n = \frac{c}{eB_0} \int_{-\infty}^{t} j'(t) \frac{\partial}{r\partial\vartheta} \hat{\eta} j(t') dt' = \frac{c}{eB_0} \int_{-\infty}^{t} j \frac{\partial}{r\partial\vartheta} E'_{\parallel} dt' \tag{4.8}$$

It is now convenient to introduce a local rectangular system of co-ordinates with the x-axis along r, the y-axis along ϑ and the z-axis remaining the same. Then, $(1/r)\,\partial/\partial\vartheta = ik_y$.

Expression (4.8) can be written in the Fourier representation as:

$$\Gamma_n = \frac{c^3}{eB_0(4\pi)^2} \sum_{k,\omega} \frac{k_y}{\omega} k_{\perp}^4 |\Psi'_{\vec{k},\omega}|^2 \eta_{\vec{k},\omega} \tag{4.9}$$

Using the Eqs (2.10) and (3.3) in linearized form, we represent $|\Psi'_{\vec{k},\omega}|$ in terms of the displacement $\xi = -(ck_y/\omega B_0)\varphi$:

$$|\Psi'_{\vec{k},\omega}|^2 = \frac{B_0 k_{\parallel}^2}{k_y^2} \frac{(\omega-\omega_*)^2 |\xi_{\vec{k},\omega}|^2}{\left(\omega - \omega_* - \frac{k_{\parallel}^2 T_e c^2 k_{\perp}^2}{4\pi e^2 n_0 \omega}\right)^2 + \left(\frac{c^2 k_{\perp}^2 \eta_{\vec{k},\omega}}{4\pi}\right)^2} \tag{4.10}$$

where

$$\omega_* = -\frac{c\,T_e k_y}{eB_0} \frac{d\ln n_0}{dr}$$

Substituting (4.10) into (4.9), we obtain for the particle flux:

$$\Gamma_n = -D \frac{dn_0}{dr} \tag{4.11}$$

where the diffusion coefficient, D, is expressed as

$$D = \frac{c^4 T_e}{(4\pi)^2 e^2 n_0} \sum_{\vec{k},\omega} \frac{\omega}{\omega_*} \eta_{\vec{k},\omega} \frac{k_\perp^4 k_\parallel^2 |\xi_{\vec{k},\omega}|^2 \left(1 - \frac{\omega_*}{\omega}\right)^2}{\left(\omega - \omega_* - \frac{k_\parallel^2 T_e c^2 k_\perp^2}{4\pi e^2 n_0 \omega}\right)^2 + \left(\frac{c^2 k_\perp^2 \eta_{\vec{k},\omega}}{4\pi}\right)^2} \tag{4.12}$$

The ratio ω/ω_* is positive for a typical microturbulence which propagates in the direction of the electron diamagnetic drift.

The advantage of introducing ξ is that we have an estimate for ξ. In any case, $\xi \leqslant 1/k_\perp$, equality is reached for strong turbulence. This allows to the upper limit of the diffusion coefficient to be estimated.

Substituting (3.5) into (4.12) and assuming ξ to be equal to $1/k_\perp$, we say that $D \lesssim D_0$, where

$$D_0 \approx c_1 \frac{c^2}{\omega_{pe}^2} |k_\parallel| v_e = c_1 \frac{c^2}{\omega_{pe}^2} \frac{v_e}{qR} \tag{4.13}$$

This expression provides an assessment of the dimensionality of the problem; the constant c_1 depends on the shape of the spectrum.

We have assumed $|k_\parallel| \sim 1/(qR)$ in estimating expression (4.13). This quantity may be considerably smaller for a cylinder under real conditions (for strong localization of the perturbations near the singularities $k_\parallel(r_s) = 0$). $k_\parallel$ has an additional satellite term $\pm 1/(qR)$, whose amplitude is $\epsilon = r/R$ – times less than the fundamental harmonic, in a tokamak because of its toroidicity. It is exactly this term that will make the main contribution to Re $\hat{\eta}$ if $qR < v_e/\omega$. Therefore, the more correct estimation for toroidal systems is as follows:

$$\chi \sim D \sim \frac{c^2}{\omega_{pe}^2} \frac{v_e}{qR} \epsilon^\alpha, \quad (1 \leqslant \alpha \leqslant 2) \tag{4.14}$$

If the electron temperature gradient $dT_{e0}/dr \neq 0$ were taken into account, the expressions for the particle and heat fluxes would be as follows:

$$\Gamma_n = -D\left(\frac{dn_0}{dr} - \frac{1}{2}\frac{n_0}{T_{e0}}\frac{dT_{e0}}{dr}\right); \quad Q_{\parallel e} = -\kappa\left(\frac{dT_{e0}}{dr} + \frac{T_{e0}}{n_0}\frac{dn_0}{dr}\right) \tag{4.15}$$

where D is given the relation (4.12), and the heat conduction coefficient is found to be:

$$\kappa = \frac{c^4}{e(4\pi)^2} \sum_{\vec{k},\omega} \frac{\omega}{\omega_{**}} \mu_{\vec{k},\omega} |\eta_{\vec{k},\omega}|^2 \frac{k_\perp^4 k_\parallel^2 |\xi_{\vec{k},\omega}|^2 \left(1 + \frac{\omega_{**}}{\omega}\right)}{\left(\omega - \omega_* + \frac{\omega_{**}}{2}\right)^2 + \left(\frac{c^2 k_\perp^2 \eta_{\vec{k},\omega}}{4\pi}\right)^2}$$

$$\omega_{**} = -\frac{eT_e k_y}{eB_0}\frac{d\ln T_{e0}}{dr} \tag{4.16}$$

$$\mu_{\vec{k},\omega} = -\frac{ien_0\omega}{k_\parallel^2}\left[\frac{1}{2} + \left(\frac{\omega}{k_\parallel v_e}\right)^2\left(1 + \frac{\omega}{|k_\parallel| v_e} Z\left(\frac{\omega}{|k_\parallel| v_e}\right)\right)\right]$$

A more precise calculation of the diffusion coefficient, D (and the diffusivity χ) can be carried out on the assumption of an oscillation spectrum that is more realistic than $\xi \lesssim 1/k_\perp$.

REFERENCES

[1] KADOMTSEV, B.B., POGUTSE, O.P., Zh. Ehksp. Teor. Fiz. **65** (1973) 575.
[2] KADOMTSEV, B.B., POGUTSE, O.P., Voprosy teorii plasmy, Vol. 5, Moscow, Atomizdat (1967) 209.
[3] KADOMTSEV, B.B., POGUTSE, O.P., YURCHENKO, E.I., in Plasma Physics and Controlled Nuclear Fusion Research (Proc. 10th Int. Conf. Baltimore, 1982), Vol. 3, IAEA, Vienna (1983) 67.
[4] IZZO, R., et al., Princeton PPPL-2007 (1973).
[5] WHITE, R.B., MONTICELLO, D.A., ROSENBLUTH, M.N., STRAUSS, H.R., KADOMTSEV, B.B., in Plasma Physics and Controlled Nuclear Fusion Research (Proc. 5th Int. Conf. Tokyo, 1974), Vol. 1, IAEA, Vienna (1975) 485.
[6] DNESTROVSKIJ, Yu.N., ZAKHAROV, L.E., KUKUSHKIN, A.S., KOSTOMAROV, D.P., SUZDALEVA, A.F., Pis'ma Zh. Ehksp. Teor. Fiz. 1 (1975) 45.
[7] WADDELL, B.V., ROSENBLUTH, M.N., MONTICELLO, D.A., WHITE, R.B., Nucl. Fusion **16** (1976) 528.
[8] KADOMTSEV, B.B., Fiz. Plazmy, 1 (1975) 710.
[9] CARRERAS, B.A., WADDELL, B.V., HICKS, H.R., Nucl. Fusion **19** (1979) 1423.
[10] PARAIL, V.V., POGUTSE, O.P., Pis'ma Zh. Ehksp. Teor. Fiz. 32 (1980) 408.
[11] KADOMTSEV, B.B., MOROZOV, D.Kh., POGUTSE, O.P., Pis'ma Zh. Ehksp. Teor. Fiz. **40** (1984) 80.

ADDENDUM

The anomalous momentum transport is found from equations given in Ref. [11].

DISCUSSION

B. COPPI: Your reduced equations do not contain any 'active' term representing excitation of the instabilities that feed the microturbulent state, and I would be

interested to know how you account for this. Also, the type of diffusion coefficient that you propose:

$$\frac{c^2}{\omega_{pe}^2}\,\frac{V_e}{qR}$$

does not reproduce the desired temperature profiles when used in an appropriate transport code over the entire plasma column.

B.B. KADOMTSEV: I believe that the microturbulence is pumped at the edge of the plasma, where additional enhancement of transport may produce reasonable profiles.

R.J. GOLDSTON: The $\sqrt{T_e}$ scaling in your χ_e could fit with the degradation in confinement generally seen during auxiliary heating in tokamaks. Is there any aspect of this theory which could correlate with the improvement of τ_E with plasma current seen in NBI experiments?

B.B. KADOMTSEV: Dimensional analysis shows that the τ_E current dependence is linked with plasma resistivity, so that resistive enhancement of electron transport should be added and taken into account in the proposed equations.

R.N. SUDAN: While the actual anomalous diffusion may be determined by short-wave turbulence, is it not true that the intensity of the spectrum in this wavelength region will be determined by the cascade of wave energy from long wavelengths? In this way, the anomalous diffusion could be indirectly affected by long-wavelength turbulence.

B.B. KADOMTSEV: I agree that the short-wave turbulence may be, and probably is, produced by the cascade of wave energy from the longer wavelengths. However, the transports are produced by small-scale perturbations.

T. OHKAWA: How much more can your new formalism do than my earlier derivation of the formula which kept the kinetic effects in the parallel direction?

B.B. KADOMTSEV: The new formalism can be used for quantitative treatment of the microturbulence and for calculation of the transport coefficients.

K. BURRELL: We have seen in the work from T-10 which Dr. Mukhovatov presented in Paper A-III-4[1] that inward convection as well as diffusion was required to explain the particle transport results. A similar conclusion was reached several years ago by W. Engelhardt and co-workers from ASDEX data. It is not obvious to me that the equations you have presented contain a term that would give this inward convection.

B.B. KADOMTSEV: This kind of convection may be produced either by the temperature gradient or with the help of toroidal corrections.

---

[1] These Proceedings, Vol.1.

STUDIES OF MAJOR DISRUPTIONS AND TEARING AND BALLOONING MODES

T.M. ANTONSEN Jr., J.F. DRAKE, J.M. FINN,
A.B. HASSAM, R.G. KLEVA, B.D. SCOTT
Laboratory for Plasma and Fusion Energy Studies,
University of Maryland,
College Park, Maryland,
United States of America

Abstract

STUDIES OF MAJOR DISRUPTIONS AND TEARING AND BALLOONING MODES.

Analytical and numerical studies of the linear and non-linear behaviour of resistive tearing and ballooning modes have been completed and applied to two important tokamak physics issues: major disruptions and transport.

1. VACUUM BUBBLES AS A CAUSE OF MAJOR DISRUPTIONS

Major disruptions in tokamak discharges are characterized by a rapid decrease in the toroidal current, leading to the termination of the discharge [1-2]. Kadomtsev and Pogutse first proposed that these disruptions were a consequence of the nonlinear development of ideal kink modes in a current-carrying plasma column; the highly convoluted final states have vacuum bubbles [3]. In later numerical studies it was shown that while such bubbles can develop in the case of a uniform current profile (no magnetic shear), rounded current profiles (with magnetic shear) strongly inhibit their formation [4]. In 2-D the m/n = 2/1 tearing mode saturates benignly, the largest islands having widths w of the order of 0.4a, where a is the minor radius [5]. In full 3-D simulations of resistive tearing modes, the 2/1 mode can sometimes destabilize the 3/2, 5/3 and other modes, culminating in a broad spectrum of magnetic turbulence which destroys the flux surfaces, and therefore confinement [6]. On the other hand, while the 2/1 mode is almost universally observed prior to or during the disruption, it is less clear that the 3/2 and other modes are as ubiquitous. In JIPP T-II the 3/2 modes are only detected during minor disruptions [7]. We show that when the central current profile is fairly flat and $1.8 \gtrsim q(0) \gtrsim 1.5$, where $q(r) = rB_z/RB_\theta(r)$, the $q = 2$ magnetic islands grow to very large amplitude, encompassing essentially the entire plasma cross-section. The formation of these large islands is related to the formation

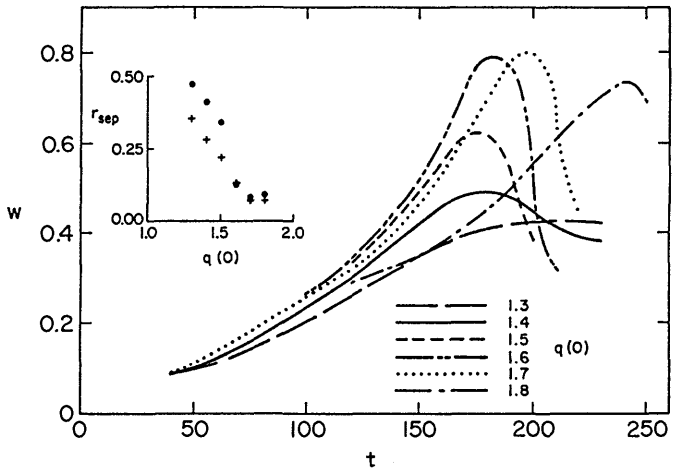

FIG.1. Island width w versus time for q(0) = 1.3 to 1.8 with q(1) = 3.4 and λ = 4. The inset shows the radius of the inner separatrix r_{sep} at maximum island size versus q(0).

of vacuum bubbles during the nonlinear evolution of the ideal 2/1 kink mode. The rapid loss of energy which would result from the growth of these islands is proposed as a mechanism for major disruptions.

The reduced MHD equations for helical perturbations are given by[4]

$$d\nabla_\perp^2\phi/dt - \mu\nabla_\perp^4\phi = \nabla_\parallel J \; ; \; \nabla_\perp\psi^2 = J-2n/m \qquad (1)$$

$$\partial\psi/\partial t = \nabla_\parallel\phi + \eta J \qquad (2)$$

where $d/dt = \partial/\partial t + \hat{z}x\nabla\phi\cdot\nabla$; $\nabla_\parallel = \hat{z}x\nabla\psi\cdot\nabla$ and ϕ and ψ are the stream and helical flux functions; and η and μ are resistivity and viscosity. Times are normalized to the Alfvén time, $\tau_A = R/\tau_A$, and perpendicular gradients to a^{-1}. We consider an equilibrium based on the standard q profile, $q(r) = q(0)[1 + (r/r_0)^{2\lambda}]^{1/\lambda}$ where $r_0^{-2\lambda} = [q(1)/q(0)]^\lambda - 1$, and $\eta \sim J^{-1}$. We treat both the case where the resistivity η is constant in time and where η convects with the fluid and diffuses parallel and perpendicular to $\vec{B}$. We first consider constant η. In Fig. 1 we show the time dependence of the island width w for several values of q(0) between 1.3 and 1.8 for q(1) = 3.4, λ = 4, and $\eta = 5\times10^{-5}$. For q(0) = 1.3 the island grows and saturates at moderate amplitude, $w \approx 0.4$, with essentially no overshoot, consistent with previous analytic models[8]. As q(0) is increased further, the maximum

island size increases dramatically and strongly overshoots. This can be seen most dramatically in the inset of Fig. 1, where we plot the radius of the inner separatrix of the island (at the maximum w), r_{sep}, as a function of q(0) (dots). For $1.6 \lesssim q(0) \lesssim 1.8$ the island essentially extends to the center of the plasma! In Fig. 2(a) we show the contours of the helical flux at maximum island size (t = 351) for q(0) = 1.7 and $\eta = 5\times10^{-6}$ with other parameters as in Fig. 1.

Our interpretation of the numerical results shown in Figs 1 and 2(a) is that, as q(0) increases, the difference in the pitch of the 2/1 tearing mode and the magnetic field lines near the center of the column decreases so that as the island grows inward the magnetic tension is not sufficient to stop the instability. In a peaked current distribution, or when q(0) is smaller, the magnetic tension rises rapidly as the island grows and stops the growth of the island. The results in Figs 1 and 2(a) are not strongly altered when η evolves in time self-consistently. In Fig. 2(b) we show the contours of η^{-1} at late time for a run with the same parameters as in Fig. 1. The entire high temperature region has been expelled to the wall.

It is informative to compare the growth of large magnetic islands in the present calculation with previous investigations of bubble formation by the ideal kink mode. For a flat current profile of radius r_0 ($\lambda \to \infty$), the ideal 2/1 kink is unstable over a range of q(0). For the same parameters as in Fig. 1 but with $\lambda \to \infty$, the ideally unstable region is given by $2 \gtrsim q(0) \gtrsim 1.2$ with the maximum growth rate at q(0) = 1.5. We can compare the size of the "vacuum bubble" produced by such an ideal mode with the islands formed in Figs 1 and 2(a) by integrating the helical equations with λ large. In Fig. 2(c) the ψ contours are shown for q(0) = 1.7 at maximum island size (t = 50) with $\eta = 5\times10^{-5}$ and $\lambda = 20$. For this large value of λ the mode is ideally unstable. The "vacuum bubbles" in Fig. 2(c) are virtually identical to the magnetic islands of Fig. 1.

The scaling of the minimum radius r_{sep} of the vacuum bubbles with q(0) is shown in the inset in Fig. 1 (the daggers). The values of r_{sep} for the resistive and ideal cases approach each other as q(0) increases. Our conclusion from this comparison of the saturation of resistive and ideal modes is that when the magnetic island of the tearing mode is very large, the energetics of the saturation differs very little from that of the ideally unstable flat current profile. The time scale of the growth and saturation of the instability, however, does depend on the profile. The ideal

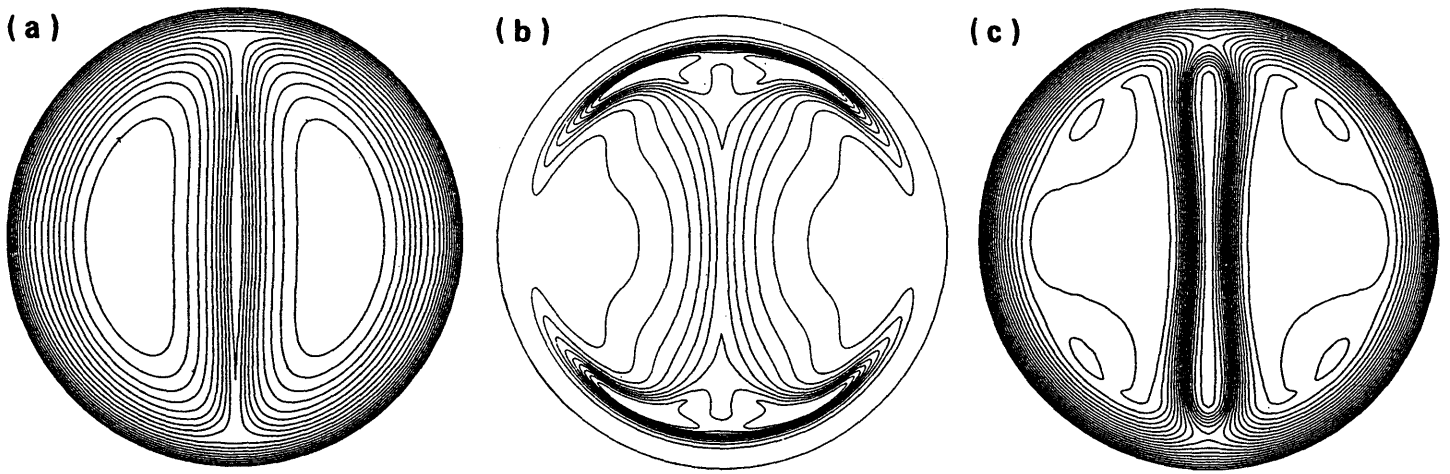

FIG.2. (a) Contours of ψ at maximum island size for $q(0) = 1.7$. (b) Contours of η^{-1} at late time. (c) Contours of ψ at maximum amplitude of ideal mode with $\lambda = 20$.

modes grow and saturate on a time scale of order 50 Alfvén times compared to 200-300 Alfvén times for the tearing mode.

The strongest experimental evidence linking $q(0) \gtrsim 1.5$ with major disruptions comes from Mirnov and Semenov's detailed study of 20 disruptions on the T-4 tokamak [2]. In the time preceding the disruptions, the current channel contracts as a result of the cooling of the edge plasma. The disruptions occur in two stages: a predisruption first causes a radial expansion of the temperature and current profiles, raising q(0) from 1 to greater than 1.5; the major disruption itself results from the rapid growth of an m = 2 perturbation in this flattened current distribution which causes a second expansion of the column to the limiter. The observation that the disruption itself is caused by an m = 2 mode growing in a flattened current profile strongly supports our contention that the large islands formed in such profiles cause major disruptions. Moreover, two-stage disruptions are a rather common occurrence on other tokamaks, including TFR [9], PLT, PDX and TFTR [10].

2. NONLINEAR DRIFT-TEARING MODES

Time-varying magnetic and temperature fluctuations observed in tokamak discharges are often attributed to the propagation of drift-tearing modes at the diamagnetic frequency ω_* [11]. The propagation of these modes results when the magnetic field lines around the islands connect regions of differing electron pressure. The resulting parallel pressure gradient drives a large parallel current which forces the magnetic perturbation to propagate at the diamagnetic frequency. The nonlinear behavior of these drift-tearing modes is not well understood. Biskamp argued that nonlinear mixing of the pressure profile within the magnetic island would cause the diamagnetic propagation to halt at small island widths [12]. However, in detailed numerical simulations, the propagation of the mode continued even for very large magnetic islands [13]. We have completed a detailed numerical investigation of the nonlinear evolution of drift-tearing modes including parallel compression, the sound wave. The sound wave enables the plasma pressure to equilibrate along the magnetic field lines, flattens the local pressure profile across the magnetic islands and causes the diamagnetic propagation of the mode to stop. The island width w_s, where diamagnetic rotation ceases, occurs when the propagation time of the sound wave around the magnetic island, $[k_\parallel(w_s)c_s]^{-1}$, is comparable to the propagation period, ω_*^{-1}, or

$$w_s \sim \rho_s L_s / L_n \qquad (3)$$

where c_s is the sound speed; $\rho_s = c_s/\Omega_i$ is the Larmor radius; $k_\parallel(w_s) = k_\theta w_s/L_s$ is the parallel wavenumber; L_s is the magnetic shear length; and L_n is the density scale length.

The equations describing the drift-tearing mode are similar to the helical equations presented in (1) and (2) with an additional pressure term added to Ohm's Law,

$$\partial\psi/\partial t = \nabla_\parallel \phi + \eta J - (\rho_s c_s \tau_A/a^2)\, \nabla_\parallel n \qquad (4)$$

and the continuity and parallel momentum equations,

$$dn/dt = (\Omega_i \tau_A)^{-1} \nabla_\parallel J_\parallel - \nabla_\parallel v_\parallel \; ; \; dv_\parallel/dt = -(\beta/2)\nabla_\parallel n \qquad (5)$$

The equations are solved in the vicinity of the magnetic island and matched to the ideal solutions in the outer region. In Fig. 3 we show the time evolution of the growth rate, mode frequency and island width. The mode frequency rapidly decreases to a small fraction of its initial value. The behavior of γ and w, on the other hand, is just that obtained by Rutherford, unmodified by drift effects, a conclusion reached previously [12,13]. At late time the density and flux contours are nearly identical, indicating that $n = n(\psi)$. To confirm our assertion that the sound wave is responsible for the rapid decrease of the mode frequency, we plot in Fig. 4 the island width w_s (defined by the point where ω has decreased by 20%) for several values of $\rho_s L_s/L_n$. Figure 4 confirms the scaling in Eq. (3).

For tokamaks such as PLT, $\rho_s \approx 0.1$ cm while $L_s/L_n \approx 10$ so that $w_s \approx 1$ cm. For magnetic islands larger than 1 cm there should be no diamagnetic propagation. The observed rotation of islands larger than this must result from a combination of the radial electric field and toroidal flow.

3. MAGNETIC CURVATURE-DRIFT INSTABILITY

We have found that in the presence of electron temperature gradient and either curvature or crossfield transport, a new fluid instability exists with growth rate $\gamma \sim \omega_*$. When driven by curvature, the instability results from the temperature gradient-induced coupling of a tearing mode with $\omega \sim \omega_*$ and another mode with $\omega \sim \omega_c$, the curvature drift frequency. When driven by cross field transport of particles or heat, the mode is essentially a semicollisional tearing mode which is unstable even for negative Δ'.

We have completed a detailed numerical-analytic study of this instability using the linearized Braginskii fluid

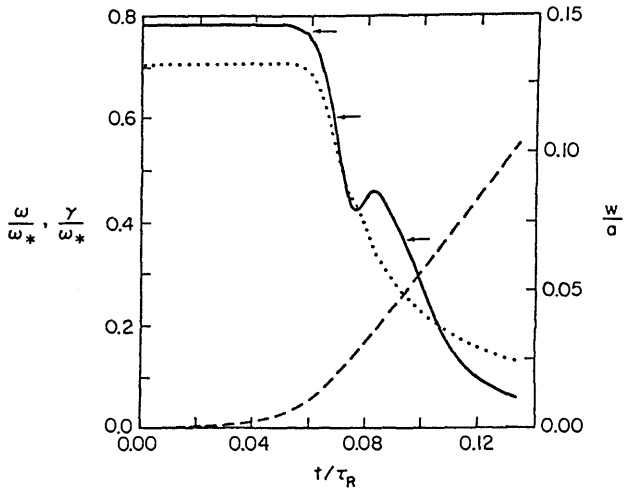

FIG.3. Growth rate γ, frequency ω, and island width w versus time for the non-linear drift-tearing mode.

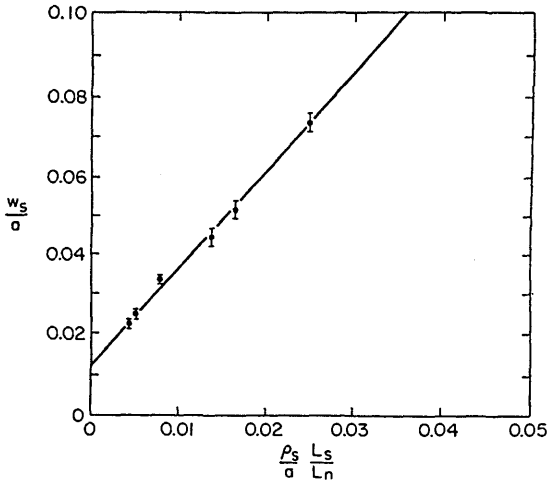

FIG.4. Critical island width w_s where diamagnetic rotation ceases.

equations, including diamagnetic effects, curvature drifts (in a cylindrical model), parallel and perpendicular transport of particles and heat, but with $T_i = 0$. The linearized equations can be solved analytically in the semi-collisional limit if the constant-ϕ approximation is used. We obtain the

dispersion relation

$$i\eta_{\parallel}\Delta' = \frac{\sqrt{2}\,\pi\,\Delta}{a_+ - a_-}\left\{\left[\omega - \omega_* - \omega_{*T}\left(a_- - \frac{5}{2}\frac{\bar{\omega}}{\omega}\right)\right]\left(a_+ - \frac{5}{2}\frac{\bar{\omega}}{\omega}\right)\right.$$
$$\left. \times \frac{\Gamma(3/4 + a_+\,\zeta/2)}{\Gamma(1/4 + a_+\zeta/2)} - [a_+ \leftrightarrow a_-]\right\} \qquad (6)$$

where $a_\pm = 7\bar{\omega}/4\omega \pm (1 + 9\,\bar{\omega}^2/16\omega^2)^{1/2}$; ω_{*T} is the diamagnetic frequency associated with temperature gradient; $\Delta = (4D_\perp/k_\parallel^2 D_\parallel)^{1/4}$ is the scale length obtained by balancing parallel and perpendicular transport; $\bar{\omega} = \omega - \omega_c$; and $\zeta = -i\omega\Delta^2/4D_\perp$. In the limit of no cross field transport ($D_\perp \to 0$ or $\zeta \to \infty$), this dispersion relation simplifies greatly, and the mode is unstable over a range of ω_c given by

$$0.37(1 - 1.6f) < \omega_c/\omega_* < 1.6(1 + 1.6f) \qquad (7)$$

when the coupling between the ω_* mode and the ω_c mode is strong. Note that there is an upper as well as a lower threshold in curvature and we have defined $f \equiv \omega_{*T}/\omega_*$. For large $D_\perp$ (ζ small) the dispersion relation reduces to

$$\omega = \omega_* + i[\pi\zeta_*\omega_{*T}/2 + \Gamma(1/4)\eta_\parallel\Delta'/\sqrt{2}\pi\Gamma(3/4)\Delta] \qquad (8)$$

where $\zeta_* = -i\omega_*\Delta^2/4D_\perp$, so that the growth rate is proportional to the temperature gradient and to $D_\perp^{-1/2}$. Numerical solutions of the dispersion relation (6) as a function of ζ_* are shown in Fig. 5 for $\omega_c = 0$ and $\omega_c = \omega_*/2$. The growth rate γ reaches a maximum for $\zeta_* = 0.4$ without curvature and for $\zeta_* \to \infty$ with curvature.

We have integrated the full set of equations including thermal forces and found that this temperature gradient-driven mode is unstable and dominates the resistive interchange tearing mode for $\omega_* \gtrsim \gamma_t$ (where γ_t is the nominal resistive interchange growth rate) and for $\omega_{*T}/\omega_* \gtrsim 0.05$. For $\omega_{*T}/\omega_* < 0.05$, the previously calculated stabilization of the interchange mode is recovered [14].

For reversed field pinches, ζ and ω_c/ω_* are both of order unity and therefore a broad spectrum of these modes is expected to be strongly unstable. Since the instability is driven by the temperature gradient, it is reasonable to expect that these modes are responsible for the energy confinement scaling in RFPs. The role of instability in tokamak discharges is less clear. The ratio of ω_c/ω_* is small even for strongly ballooning modes where the toroidal curvature dominates. For tokamaks with classical transport

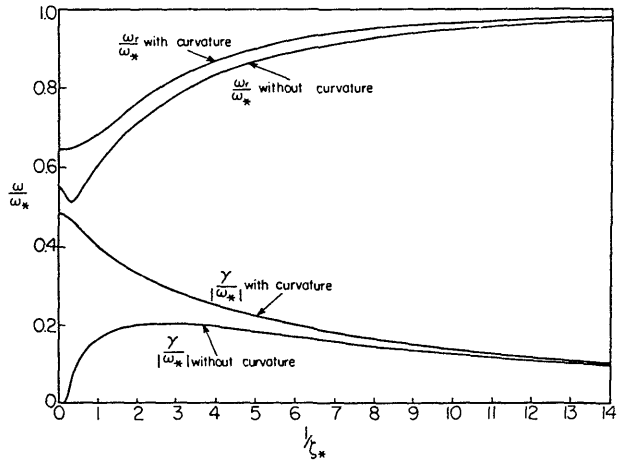

FIG.5. Solution of the dispersion relation in Eq.(6) for magnetic curvature drift instability.

$\zeta_* \sim L_s/L_n \gg 1$, so that from Fig. 5 we see that the growth rate is extremely small (other effects stabilize the mode). Namely, the classical value of $D_\perp$ too small to produce instability. In toroidal geometry the Pfirsch-Schlüter factors increase $D_\perp$ and are therefore destabilizing. Moreover, an anomalous value of $D_\perp$ produces a very strong instability as long as $\beta L_s^2/L_n^2 < 1$ so the non-constant ψ stabilizing effects are not important[15]. The implications of this mode for tokamak transport are currently being investigated.

4. RESISTIVE BALLOONING MODES

A completely analytic dispersion relation for resistive ballooning modes has been derived for values of β below the threshold for ideal ballooning modes. The dispersion relation,

$$\Delta' = 2\frac{\Gamma(1/4)}{\Gamma(3/4)}\frac{c_+ - c_-}{\hat{\gamma}^{1/4}}\left[\frac{\Gamma(1/4 + c_-/2)}{\Gamma(3/4 + c_-/2)} - (c_- \to c_+)\right]^{-1} \qquad (9)$$

depends on only two parameters: the normalized driving energy

$$\Delta' = \frac{\pi}{8}\frac{\Gamma(1/4)}{\Gamma(3/4)}\frac{\gamma_r \tau_A}{\beta_t^{3/2}}\frac{s+2}{s}\left[1 - \frac{s+2}{s}\exp(-2/s)\right] R^2 q^4 \beta'^2 \qquad (10)$$

which represents the energy released as the mode weakly balloons in the ideal region of unfavorable curvature; and the normalized average curvature D_r from the resistive layer,

$$D_r = \frac{2p' rq^2}{\gamma_s s^2 p(1+2q^2)} \left[1 - q^{-2} + s\frac{q^2}{r^4}\int_0^r dr\left(\frac{r^3}{q^2} - R^2 r^2 \beta'\right)\right] \qquad (11)$$

which is unfavorable for $D_r > 0$. The eigenvalue is $\hat{\gamma} \equiv \gamma/\gamma_r$ with $(\gamma_r \tau_A)^3 \equiv n^2 q'^2 a^2 \beta_t^2 \tau_A/\tau_r$; $\beta_t \equiv 4\pi\gamma_s p(1 + 2q^2)/B^2$;

$\tau_A^2 \equiv q^2 R^2 (1 + 2q^2)/c_A^2$; $s = q' r/q$; $\tau_r = 4\pi a^2/\eta c^2$ and

$4c_{\pm} = \hat{\gamma}^{3/2} \pm (\hat{\gamma}^3 + 4D_r)^{1/2}$. This dispersion relation, which is similar to that of Ref. 16, is valid for intermediate toroidal mode numbers $1 \ll n^2 \ll s\beta_t \tau_r/\tau_A$. At larger values of n the spatial scale of the equilibrium and the resistive region become comparable and the two-space scale analysis used to derive Eq. (9) breaks down. The ballooning driving energy in the resistive region must then be included in the calculation [17]. For $D_r < 1$, the finite compressibility of the plasma has a significant stabilizing influence[16] on the resistive ballooning mode which requires $\Delta' \gtrsim 1$ for instability. For $s \sim 1$ and $\beta' \sim \beta/a$ this requires

$$n^2 > \beta^{5/2}(\tau_r/\tau_A)/(\beta q^2 R/a)^3 \qquad (12)$$

Thus, only very high mode numbers are unstable unless the plasma is close to the ideal threshold ($\beta q^2 R/a \sim 1$) or is very cold (τ_r/τ_A is not too large). For typical hot tokamak discharges, resistive ballooning modes may soften the onset of ideal ballooning modes but will not cause poor confinement well below the ideal threshold.

REFERENCES

[1] HOSEA, J.C., BOBELDIJK, C., GROVE, D.J., "Stability experiments on the ST tokamak", Plasma Physics and Controlled Nuclear Fusion Research 1971 (Proc. 4th Int. Conf. Madison, 1971), Vol. 2, IAEA, Vienna (1971) 425;
MIRNOV, S.V., SEMENOV, I.B., "Investigation of macroscopic instabilities of a plasma column in tokamak devices" (in Russian), ibid., p. 401 [Engl. transl. Nucl. Fusion Suppl. 1972, p. 189];
MIRNOV, S.V., SEMENOV, I.B., Sov. Phys.-JETP 33 (1971) 1134.

[2] MIRNOV, S.V., SEMENOV, I.B., "Observation of disruptive-instability fine structure in a tokamak", Plasma Physics and Controlled Nuclear Fusion Research 1976 (Proc. 6th Int. Conf. Berchtesgaden, 1976), Vol. 1, IAEA, Vienna (1977) 291.

[3] KADOMTSEV, B.B., POGUTSE, O.P., Sov. Phys.-JETP **38** (1974) 283.
[4] ROSENBLUTH, M.N., MONTICELLO, D.A., STRAUSS, H.R., WHITE, R.B., Phys. Fluids **19** (1976) 1987.
[5] WHITE, R.B., MONTICELLO, D.A., ROSENBLUTH, M.N., Phys. Rev. Lett. **39** (1977) 1618; Phys. Rev. **A18** (1978) 2735; CARRERAS, B., WADDELL, B.V., HICKS, H.R., LYNCH, S.J., Phys. Rev. **A18** (1978) 2732.
[6] WADDELL, B.V., CARRERAS, B., HICKS, H.R., HOLMES, J.A., Phys. Fluids **22** (1979) 896.
[7] TSUJI, S., PhD Dissertation, Tokyo Univ., 1983.
[8] WHITE, R.B., MONTICELLO, D.A., ROSENBLUTH, M.N., WADDELL, B.V., Phys. Fluids **20** (1977) 800.
[9] LAURENT, L., PhD dissertation, Univ. Paris-Sud,Centre d'Orsay, 1983.
[10] BOYD, D.A., private communication.
[11] COPPI, B., Phys. Fluids 7 (1964) 1501.
[12] BISKAMP, D., Nucl. Fusion **19** (1979) 777.
[13] MONTICELLO, D.A., WHITE, R.B., Phys. Fluids **23** (1980) 366.
[14] FINN, J.M., MANHEIMER, W.M., ANTONSEN, T.M., Jr., Phys. Fluids **26** (1983) 962.
[15] DRAKE, J.F., ANTONSEN, T.M., Jr., HASSAM, A.B., GLADD, N.T., Phys. Fluids **26** (1983) 2509.
[16] CONNOR, J.W., HASTIE, R.J., MARTIN, T.J., SYKES, A., TURNER, M.F., "Beta limitation in tokamaks and the effect of viscosity on resistive ballooning modes", Plasma Physics and Controlled Nuclear Fusion Research 1982 (Proc. 9th Int. Conf. Baltimore, 1982), Vol. 3, IAEA, Vienna (1983) 403.
[17] HENDER, T.C., et al., Inst. for Fusion Studies, Austin, TX Rep. No. 108 (1983).

PHYSICS OF PLASMAS CLOSE TO THE LAWSON LIMIT AND UNDER BURN CONDITIONS‡

B. COPPI* + §, S. COWLEY §, P. DETRAGIACHE*,
R. KULSRUD §, F. PEGORARO*, W. TANG §

* Scuola Normale Superiore,
Pisa, Italy

+ Massachusetts Institute of Technology,
Cambridge, Massachusetts,
United States of America

§ Plasma Physics Laboratory,
Princeton University,
Princeton, New Jersey,
United States of America

Abstract

PHYSICS OF PLASMAS CLOSE TO THE LAWSON LIMIT AND UNDER BURN CONDITIONS.

The main features of the transport analysis of recent high density plasma experiments with values of the confinement parameter $n_0\tau_E$ close to 10^{14} s/cm^3 are described. Included are the arguments which have led to the previous suggestion that production of peaked density profiles was the means of avoiding the onset of enhanced anomalous ion thermal conductivity and the 'degraded' energy confinement in high plasma density experiments performed on the Alcator C machine. Also pointed out is the supporting evidence for the anomalous electron thermal conductivity model which is based on the 'principle of profile consistency'. This has provided rather accurate simulations of Ohmically heated experiments, and its extension to regimes where Ohmic heating is no longer prevalent has been proposed. The anomalous thermal conductivity resulting from the excitation of ion mixing modes in the main body of the plasma column that is suitable for the numerical simulation of existing experiments is formulated and its relationship with the anomalous particle inflow process discussed. In the light of the very favourable confinement characteristics of high density plasma experiments, the reference design parameters are given of an experiment of this class which is potentially capable of producing currents up to the 10 MA range and achieve effective DT burning conditions. Finally, an analysis is reported on the collective modes that can be excited in fusion burning plasmas where an anisotropic distribution of energetic particles in velocity space exists. Special consideration is given to the case where the fuel nuclei are spin-polarized and these modes can produce a significant depolarization rate.

---

‡ Sponsored in part by the US Department of Energy, the Electric Power Research Institute, USA, and by the Ministero della Pubblica Istruzione and the Consiglio Nazionale delle Ricerche, Italy.

I. INTRODUCTION

Recent experiments carried out within the Alcator programme have produced plasmas with values of the confinement parameter $n_0 \tau_E$ nearing that of the Lawson criterion ($n_0 \tau_E \sim 10^{14}$ s/cm^3) with a moderate degree of collisionality ($\nu_* \approx 1$). These conditions are relatively close to those needed to demonstrate the scientific feasibility of a fusion reactor and have been achieved following an induced rapid transient of the main plasma parameters due to the injection of a 'heavy' pellet [1]. The study of this transient is then used to obtain salient information on the nature of the relevant particle and energy transport. We find the experimental results to be consistent with the conclusions of our previous studies, which indicated the presence of an anomalous (i.e. higher than collisional) ion thermal conductivity and with our consequent suggestion that, in order to suppress this, appropriate peaked density profiles had to be produced [2, 3]. In fact, for the plasma discharges with deteriorated confinement properties relative to those expected by extrapolation of previous experiments performed for similar physical regimes, the maximum value of the profile parameter $\eta_i = (d \ln T_i/dr)/(d \ln n/dr)$ was found to be about 4. This is near the threshold for the onset of long-wavelength ion mixing modes that are expected to produce a significant ion thermal conductivity [4]. Another expected observation, resulting from the suggested change of η_i, was that of a redistribution of impurity ions. This has also been confirmed by the experiments.

As indicated in Section VI, these circumstances strongly support the development of high plasma current and density experiments in order to study the physics of fusion burning regimes.

II. ELECTRON THERMAL TRANSPORT

We relate the nature of the observed electron thermal transport to the 'principle of profile consistency' [5]. This implies that the current density profile 'relaxes' toward a nearly Gaussian ('canonical') form as a result of the combined effects of macroscopic stability conditions and of microinstabilities that tend to redistribute the electron pressure. Consequently it was argued that in experiments with relatively flat density profiles but with 'canonical' electron temperature profiles, an enhanced anomalous electron thermal conductivity was not the primary cause of the observed degradation of confinement relative to previous experiments in which η_i was smaller. In support of the suggested forced relaxation of the current density profile, we note that the electron temperature profile has been observed to recover its canonical profile, following a pellet injection, within a time of the order of 1/100th of the electron energy confinement time [1]. At the relatively low temperature values where this occurs it is safe to assume that the resistivity is classical and the current density profile follows the electron temperature closely.

A rather accurate simulation of Alcator C discharges at very high densities with relatively peaked density profiles has been carried out assuming the ion thermal conductivity to be collisional and the effective electron thermal diffusion coefficient:

$$D^e_{th} \cong 4.15 \times 10^{13} \frac{a}{r} B_\theta(r) \left(\frac{Z_i}{A_i}\right)^{2/5} \frac{1}{n^{4/5} T_e} \ (cm^2/s) \qquad (1)$$

where T_e is expressed in eV, n in cm^{-3}, and $B_\theta(r)$, the local value of the poloidal field, in gauss.

In order to apply our analysis [6] to different regimes (e.g. where auxiliary heating and the trapped electron correction to the classical resistivity are important), we write, referring for simplicity to a large aspect ratio toroidal geometry with circular magnetic surfaces $q_e = -\kappa dJ_\parallel/dr$. Here $J_\parallel \cong J_0^0 \exp(-r^2/a_I^2)$ represents the current density profile in the region where no macroscopic oscillations are present [6]:

$$\kappa = \frac{2}{3} \frac{nT_e}{J_\parallel} \times D^e_{th} \times G_w(r)[1 + \gamma_0 \beta_p] \qquad (2)$$

$I(r) = 2\pi \int r\, dr\, J_\parallel(r)$, $L_\parallel$ is the total plasma current,

$$G_w(r) = \left\{ \int_0^r dr\, r\, S^e_T(r)/[S^e_T(r=0)\, a_I^2/2] \right\} I_\parallel/I(r)$$

S^e_T is the total power density deposited on the electron population;
$\beta_p = 8\pi \langle n(T_e + T_i) \rangle / B_p^2$ is the well-known β-poloidal parameter with $B_p \propto L_\parallel/a$, a being the plasma minor radius, and γ_0 is a finite numerical coefficient to be evaluated from a fit with the results of a consistent set of experiments where auxiliary heating is prevalent and finite values of β_p are obtained. This formulation implies that the electron thermal confinement does not deteriorate necessarily as Ohmic heating is replaced by other forms of heating, provided the energy deposition profile is not excessively distorted relative to that typical of Ohmic heating. In particular, in the limit where $\gamma_d \beta_p \gg 1$, Eq. (1) yields $D^e_{eff} \propto 1/B_p$, which corresponds to the scaling $\tau_e \propto a L_\parallel$.

III. ANOMALOUS ION THERMAL ENERGY TRANSPORT

We relate the onset of an effective ion thermal conductivity to the excitation of 'ion mixing modes' [2, 3] within the main body of the plasma column.

Physical arguments as well as quasilinear analysis of these modes indicate that they can contribute effectively to transport when their characteristic wavelengths are considerably greater than the ion gyroradius. We note that the threshold η_c for the onset of these modes [4] can be approximated (as a function of the transverse wavelength) by $\eta_c \cong 6/5 + (7/10)(\log b_i)^2$ for $10^{-2} \leqslant b_i \leqslant 1$ and $T_e \cong T_i$. Here $b_i = k_\perp^2 T_i/(m_i \Omega_i^2)$. In particular, for $b_i \cong 10^{-2}$, $\eta_c \cong 4$. Thus we may argue that when the density and temperature profiles at the edge of the plasma column are set up in such a way that plasma is not allowed to 'filter' toward the centre at a sufficiently high rate, then a relatively flat density profile, such as one represented by $n \cong n_0 (1 - r^2/a^2)^{1/2}$, is formed [1]. In this case the ion temperature profile would not be allowed to peak beyond values of $\eta_i \cong 4$ without exciting macroscopic fluctuations that would redistribute the temperature. To simulate this situation we introduce a diffusion coefficient that is derived from the quasilinear theory of the ion mixing mode but takes into account that the normalized mode amplitude T depends strongly on the radial co-ordinate. Thus we write:

$$D^i_{an} \cong D^i_{QL} F_M(r) \quad \text{and} \quad T = |e\tilde{\phi}/T_i| \, |k_\perp r_{Ti}| = 0(1)$$

where $D^i_{QL} = T^2 (\rho_i/r_{Ti})(qR/r_{Ti}) D^i_B$; $D^i_B \equiv cT_i/eB$; ρ_i is the ion gyroradius; $2\pi qR$ is the relevant connection length; and $r_{Ti} = -(d \ln T_i/dr)^{-1}$. The function $F_M(r)$ is based on considering that the mode amplitude is maximum around the surface $r = r_M$ where a properly chosen instability parameter U is maximum. In particular we take $F_M \cong \exp[-(r - r_M)^2/\lambda_M^2]$ where $\lambda_M^2 = \lambda_\theta \lambda_U$; $\lambda_U^2 = |U/(d^2U/dr^2)|r = r_M$; $\lambda_\theta = 2\pi/k_\theta$; $k_\theta^2 \rho_{iM}^2/2 \equiv b_M$; and b_M is the value of b_i given by the marginal stability condition for $\eta_c = \eta_i (r = r_M)$. As a relevant representative instability parameter we choose

$$U = \eta_i \frac{\rho_i}{r_{Ti}}$$

If we assume a parabolic density profile $[n \cong n_0 (1 - r^2/a^2)]$ and a temperature profile of the form $T/T_0 \approx (J_\parallel/J_0^0)^{2/3}$, we find $r_M \cong a/2$ for realistic values of a_I^2/a^2. With these prescriptions we avoid the problem of having to deal with the simple quasilinear diffusion coefficient that, generally, is too large to fit the experimental observations (an anomaly factor no higher than 5 is sufficient), as

$$D_{QL} \approx T^2 \times 1.4 \times 10^5 \, \mathrm{cm}^2/\mathrm{s} \times \hat{D}$$

where $\hat{D} = (\hat{T}_i^{3/2}/\hat{B}_{100}^2)[qR/(25 r_{Ti})](5 \text{ cm}/r_{Ti})$, $\hat{T}_i = T_i/(1 \text{ keV})$, and $\hat{B}_{100} \equiv \hat{B}/(100 \text{ kG})$. In addition, we take into account, in the form of D^i_{an}, the plausible expectation that the modes with smaller values of λ_θ will produce less diffusion.

Plasma discharges produced by the Alcator C device with values of $\eta_i (r \cong 0) \cong 4$ and $\eta_i (r \cong 0) \cong 5/3$ have in fact been well simulated numerically, as indicated earlier, for the following set of parameters: $R_0 = 64$ cm, $a \cong 16.5$ cm, $B_T \cong 112.5$ kG, $I_{\|} \cong 0.79$ MA, $\bar{n} \gtrsim 0.6 \times 10^{15}$ cm^{-3}, $V_{\|} \cong 2$ volts.

IV. ANOMALOUS PARTICLE TRANSPORT

The anomalous particle transport problem is concerned with both the main ion and the impurity (minority) populations. With regard to the latter population we notice that the strong increase of soft X-ray emission following a pellet injection indicates that at this stage impurities tend to build up at the centre of the plasma column [7]. This observation is consistent with the expected influence of impurity-driven modes when η_i is decreased [8]. However, the impurity redistribution, which is observed to occur in coincidence with the first 'sawtooth' drop, cannot as yet be identified with a specific process.

With regard to the main ion population, we argued in the past that the relevant anomalous transport can be effectively represented by the combination of a diffusion term and an inflow term [9]. Here we note that the associated particle flux can be roughly described by $\Gamma \cong D_p^{out}\, dn/dr - D_p^{in}\,(2r/a^2)n$ where D_p^{out} is taken to be a finite fraction (1/5 to 1/4) of D_{th}^{e} (anomalous electron thermal transport coefficient).

In order to prescribe a form for D_p^{in} that allows for different classes of profiles, we consider it to be dependent on the presence of ion mixing modes [3], which can also produce significant density fluctuations at the edge of the plasma column. In particular, we may write $D_p^{in} = D_{edge}\, D_p^{out}/(D_{edge} + D_p^{out})$, with D_{edge} evaluated by the theory given in Ref.[4]. Notice that if $D_{edge} \gg D_p^{out}$, then $D_p^{in} \cong D_p^{out}$. This leads to well-confined peaked density profiles. On the other hand, if $D_{edge} \ll D_p^{out}$, then $D_p^{in} \cong D_{edge}$. Taking Γ to vanish near the centre of the plasma column leads to 'flat' density profiles which correspond to a degraded state of confinement [3, 4].

V. ADVANCED BURNING CORE EXPERIMENT

The purpose of the machine concept (called Ignitor (BCX)^2), which is based on our present understanding of transport, is to produce plasma currents around 10 MA in a rather compact configuration [10] which employs the high field technologies and solutions developed for the Alcator programme and for the subsequent designs of the Frascati Tokamak and the Ignitor device. Recent developments which have motivated our undertaking of the present study are:

(a) The excellent confinement results for ohmically heated plasmas obtained with currents exceeding 1 MA in such diverse machines as TFTR and JET.

TABLE I. REFERENCE PARAMETERS FOR IGNITOR (BCX)[2]

$I_{\|} \leqslant 11.5$ MA (plasma current)
$a \cong 40$ cm (horizontal minor radius)
$b \cong 64$ cm (vertical minor radius)
$\bar{a} = \sqrt{ab} \leqslant 50.6$ cm (mean radius)
$B_p \cong I_{\|}/(5\bar{a}) \cong 45$ kG (mean poloidal field)
$R_c^i = 38.5$ cm (inner radius of toroidal magnet)
$R_t^i \cong 25.5$ cm (inner radius of transformer)
$q_c = (ab/R^2)(I_c/I_{\|}) \cong \sqrt{2}$ (engineering safety factor)
$R = 100$ cm (major radius)
$I_c \leqslant 63.6$ MA turn (toroidal magnet current)
$B_T \cong 127.2$ kG (toroidal field on axis)

(b) The recognized validity of the structural analysis and of the components [11] designed for the Ignitor device that can be adopted for machines capable of producing considerably higher currents, and the successful test by the JET machine of a low aspect ratio, compact structure in which the toroidal magnet is mechanically coupled to the transformer central element [11];

(c) The extensive evidence that the performance of Ohmic heating experiments is related to the maximum value of the poloidal magnetic field that can be produced.

On this basis it appears that the ignition conditions of deuterium-tritium plasmas can be approached by Ohmic heating alone when the maximum values of the poloidal magnetic field, over the plasma column, are in the range 40 to 50 kG, while the peak current density is around 2.5 kA/cm^2 (as in the case of the reference design considered here). A general discussion of the machine characteristics are given in Ref.[10]. Here we only give a list of the main reference design parameters (Table I). It should also be noted that a comprehensive numerical analysis of the expected plasma heating cycles up to ignition has recently been carried out [12]. This study shows, in particular, that the conditions where substantial D-T burning occurs can be reached within a relatively short time ($\sim$ 0.5 s) after the plasma current has attained its maximum level while the peak optimal plasma density is in the range $0.5 < n_0/(10^{15}\ \text{cm}^{-3}) < 1$.

VI. COLLECTIVE MODES IN SPIN POLARIZED PLASMAS

Referring to fusion plasmas with spin polarized fuel nuclei, we recall that quantitative estimates of the depolarization rate due to single-particle processes, such as binary collisions and field irregularities, give rather long relaxation times [13]. The same conclusion holds in the presence of magnetic fluctuations not significantly above thermal level. However, higher fluctuation levels can be expected due to instabilities driven by the anisotropy in velocity space of the fusion reaction products caused by the coherent polarization of the fusing nuclei [14]. Thus, in an infinite homogeneous plasma, magnetosonic (compressional Alfvén) modes, modified by the so-called two-ion hybrid resonance, and propagating almost perpendicularly to the equilibrium magnetic field, have been shown [14] to be driven unstable by this anisotropy and to be capable of producing a considerable rate of spin depolarization.

However, this conclusion is not necessarily valid in plasmas with finite inhomogeneities [15]. We recall that the relevant dispersion relation is $K(\omega)=1+iR_\alpha/\omega$ where $K(\omega)=(\omega^2/k^2\bar{v}_A^2)(\omega^2-\bar{\bar{\Omega}}^2)/(\omega^2-\Omega_b^2)$ arises from the cold plasma response of the electrons and fuel ions while R_α gives the resonant response of the fusion-produced α-particles. The frequencies $\bar{\bar{\Omega}}=\alpha_D\Omega_T+\alpha_T\Omega_D$ and $\Omega_h=(\Omega_D\Omega_T\bar{\Omega}/\Omega)^{1/2}$ are the cutoff and hybrid resonance frequencies, respectively, with $\bar{\Omega}=\alpha_D\Omega_D+\alpha_T\Omega_T$, $\Omega_{D,T}$ the cyclotron frequencies; and $\alpha_{D,T}=n_{D,T}/n$. In addition $v_A=(\Omega_e\bar{\Omega})^{1/2}d_e$ with $d_e=c/\omega_{pe}$ and

$$R_\alpha=\omega^2\frac{n_\alpha}{n}A\int d^3v\,\delta(\omega-k_\parallel v_\parallel-p\Omega_\alpha)\times H_p\left(\frac{2\epsilon_\alpha}{n_\alpha}\right)\left(\frac{\partial f_\alpha}{\partial\epsilon}+\frac{1}{B}\frac{\partial f_\alpha}{\partial\mu}\right) \quad (3)$$

where

$$A=(2\pi\bar{\Omega}\Omega_\alpha/k^2\bar{v}_A^2)(p\Omega_\alpha/k_\perp v_\alpha)^2;\quad H_p=\left[\lambda J_p\left(\frac{k_\perp v_\perp}{\Omega_\alpha}\right)-\frac{k_\perp v_\perp}{p\Omega_\alpha}J_p'\left(\frac{k_\perp v_\perp}{\Omega_\alpha}\right)\right]^2$$

p labels the harmonic of the α-particle cyclotron frequency Ω_α entering the resonance condition in the δ function; $\lambda=\sum_i[\alpha_i\omega/(\Omega_i^2-\omega^2)]/[\sum_i\alpha_i\Omega_i/(\Omega_i^2-\omega^2)]$ is the polarization factor in the perpendicular plane ($\lambda=-1$ for left circularly polarized waves), J_p and $J_p'(x)=dJ_p(x)/dx$ are Bessel functions; $\epsilon=m_\alpha v^2/2$ and $\mu=m_\alpha v_\perp^2/(2B)$. The α-particle distribution can be written as $f_\alpha=n_\alpha(\mu B/\epsilon)f_\alpha^0(\epsilon)$ where f_α^0 is isotropic and has the characteristic dependence $f_\alpha^0\propto(\epsilon^{3/2}+\epsilon_c^{3/2})^{-1}$ for 0.6 MeV $\cong\epsilon_c\leqslant\epsilon\leqslant\epsilon_\alpha=3.5$ MeV and vanishes for $\epsilon\cong\epsilon_\alpha$. The mode growth rate is given by $\gamma=R_\alpha(\omega\partial K/\partial\omega)^{-1}$. Since $\omega\partial K/\partial\omega>0$, $\partial f_\alpha/\partial\mu$ gives a positive contribution to γ. Positive values of $\gamma/|\omega|$ are obtained characteristically of order 10^{-1} to 10^{-2} n_α/n_e.

Since fusion burning plasmas are expected to have finite values of $\beta_e = 8\pi p_e/B^2$, the effect of the electron transit time damping must be considered. Then the dispersion relation becomes $K(\omega) = 1 + iR_\alpha/\omega - i\sqrt{\pi}\beta_e\xi_e \exp(-\xi_e^2)$, where $\xi_e = \omega/k_\parallel|v_{the}$ and $\beta_e = 8\pi n T_e/B^2 \cong 1.3 \times 10^{-2}[T_e/(8\text{ keV})] \times [n/(10^{14}\text{ cm}^{-3})]/[B/(50\text{ kG})]^2$ and the instability condition requires ξ_e to be larger than unity. To assess the importance of both the plasma and the magnetic field inhomogeneities, we have started from a model toroidal plasma with large aspect ratio, and circular concentric magnetic surfaces[1]. In particular we consider modes represented by $\tilde{B}_\parallel = \hat{B}(r,\theta)\exp(-i\omega t + in\phi)$, where θ and ϕ are the poloidal and toroidal angles and n is an integer, that propagate in θ. Then $\hat{B}(r,\theta) = \hat{\hat{B}}(r)\exp(im\theta)$ where m is an integer such that $m = q(r)\,n$, $q(r) = 2\pi/\iota(r)$ and $\iota(r)$ is the rotational transform. Thus $k_\parallel$ can be made small if we have a mode localized round a surface $r = r_0$.

We have found two classes of (well-confined) normal mode solutions. One involves 'low frequency' modes, which can resonate with the precession frequency of the deuteron $\Omega_D^p \cong 0.87\,\Omega_\alpha$. The relevant homogeneous dispersion equation $K(\omega) = 1$ shows that the resonance-cutoff surfaces fall inside the plasma column. We notice that these modes are localized on the outer part of a 'preferred magnetic surface' and are characterized by a reflected component with toroidal number n and poloidal number $-m$ for which $k_\parallel$ is large. On this basis we conclude that the electron transit time damping becomes important and the growth rate of the modes that can depolarize the deuterium spins can be made negative at sufficiently high values of β_e. There remains an open equation regarding the effects of well-defined normal modes with a very weak damping rate which could conceivably be driven to a sufficient amplitude to cause deuteron depolarization by some form of coupling (e.g. non-linear) to other excited modes.

The other class of modes can depolarize the tritium and, since $\Omega_T^p \cong 5.96\,\Omega_\alpha$, it is characterized by the absence of resonant cutoff surfaces. These modes, like the low frequency modes, are localized in r but propagate along θ. Thus we can increase the value of ξ_e to the point of making the transit time damping smaller than the α-particle resonant contribution. The relevant normal modes have large poloidal wave numbers $m \sim (a/d_i)$, where a is the minor radius of the plasma column and d_i is the ion inertial skin depth. They are confined radially within an annulus of width of the order of $(ad_i)^{1/2}$ which is centred round a magnetic surface whose position is mostly determined by the plasma density profile. Since the value of the magnetic field, and consequently of Ω_α, changes substantially over the plasma column enclosed by this annulus, the mode can resonate with different harmonics of Ω_α at the same time. In addition, the form of the resonant term R_α is modified by the inhomogeneity of the α-particle density that leads to replacement of $\partial f_\alpha/\partial\epsilon$ by $(1 - \omega_{*\alpha}/\omega)\,\partial f_\alpha/\partial\epsilon$ where $\omega_{*\alpha}$ is the α-particle diamagnetic drift frequency. The sign of $\omega_{*\alpha}$, which depends on the direction of propagation

---

[1] Thus the mode-particle resonance condition (see Eq.(3)) is modified by the contribution of the magnetic curvature drift frequency $\omega_{D\alpha}$ and is $\omega - \omega_{D\alpha} - k_\parallel v_\parallel - p\Omega_\alpha = 0$.

of the mode in the poloidal plane, can be chosen so as to reduce significantly the stabilizing influence of $\partial f_\alpha/\partial\epsilon$. The resulting growth rate, which we have computed numerically, can be shown to be positive for a variety of characteristic reactor parameters and of order $\gamma/|\omega| \sim 10^{-1}\, n_\alpha/n_0$.

An important requirement for instability is that the waves be trapped; otherwise they propagate out of the plasma at such a rate that they would not be amplified. If density fluctuations are present, they may scatter the waves onto trapped wave orbits and thus damp them. Similarly, asymmetries in the axisymmetric field could also lead to wave detrapping and damping.

To estimate the rate of depolarization of tritons produced by the considered modes, we note that the precession resonance occurs at $R + r_0\cos\theta = \text{const}$. The relative phase between precession and the wave is proportional to

$$\tfrac{1}{2}\,(d\Omega_T^p/dt)\,t^2 = (t^2/2)(r_0/R)(\sin\theta)v_\parallel\,\Omega_T^p/(qR)$$

The incoherent change in polarization per passage through resonance is $\Omega_T^p\,[(2\pi qR^2)/(\Omega_T^p v_\parallel r_0 \sin\theta)]^{1/2}\,|\tilde{B}_\perp/B|$, where $\tilde{B}_\perp = \tilde{B}_\parallel\, k_\parallel/k_\perp$. The rate of passage through resonance is $2v_\parallel/qR$. If the wave is centred so that $\omega = 6\Omega_\alpha$ at $R + r_0$ then $1/\sin\theta \cong [r_0/(2\Delta)]^{1/2}$ where $\Delta \cong (R/6)(6 - 5.96)$. Averaging $\tilde{B}_\parallel^2$ over the torus and considering the width of the depolarizing region $\sim (r_0\, d_i)^{1/2}$:

$$\nu_{dep} \cong \frac{2\Omega_T^p R}{r_0}\,\frac{\tilde{B}_\parallel^2}{B^2}\,\frac{k_\parallel^2}{k_\perp^2}\left(\frac{d_i}{\Delta\sqrt{2}}\right)^{1/2}$$

We estimate $\tilde{B}_\parallel/B \cong \gamma/\omega \cong 0.1\, n_\alpha/n_0$ since this is when wave breaking occurs. We estimate n_α/n by setting $n_\alpha\,\bar{\epsilon}_\alpha/\tau_s \approx 3nT/\tau_E$ where $\bar{\epsilon}_\alpha$ is the effective α-particle energy, τ_s the slowing-down rate, and τ_E the energy replacement time. Making use of these results and $k_\parallel/k_\perp \lesssim v_A/v_{the}$:

$$\nu_{dep}\,\tau_E \approx 2\times 10^{-2}\,\frac{R}{r_0}\left(\frac{Tm_\alpha}{\bar{\epsilon}_\alpha m_e}\right)^2\frac{\Omega_T^p\, n}{\nu_{ei}^2(n\tau_E)}\left(\frac{v_A}{v_{the}}\right)^2\left(\frac{d_i}{\Delta}\right)^{1/2}$$

where ν_{ei} is the electron-ion collision rate. For reactor parameters and employment of the Lawson criterion, we obtain $\nu_{dep}\,\tau_D \cong 5 - 50$ for $\tau_D \sim 5\tau_E$, τ_D being the particle diffusion time. Since, in practice, we consider many recycling times, depolarization is significant.

ACKNOWLEDGEMENTS

It is a pleasure to thank C. Gomez, D. Düchs, R. Englade, L. Sugiyama, A. Taroni and M. Watkins for fruitful exchanges of ideas and for their contributions.

REFERENCES

[1] GREENWALD, M., et al., Massachusetts Inst. of Technology, Cambridge, MA, Rep. PFC/JA-84-3 (1984).
[2] COPPI, B., ROSENBLUTH, M.N., SAGDEEV, R.Z., Phys. Fluids **10** (1967) 582.
[3] COPPI, B., SPIGHT, C., Phys. Rev. Lett. **41** (1978) 551.
[4] ANTONSEN, T., COPPI, B., ENGLADE, R., Nucl. Fusion **19** (1979) 641.
[5] COPPI, B., Comments Plasma Phys. Controll. Fus. **7** (1982) 1.
[6] COPPI, B., Massachusetts Inst. of Technology, Cambridge, MA (RLE) Rep. PTP-84/4 (1984), to be published in Fiz. Plazmy.
[7] HAMZA, A.M., COPPI, B., PETRASSO, R., Bull. Am. Phys. Soc. **28** (1983) 1083.
[8] COPPI, B., REWOLDT, G., SCHEP, T., Phys. Fluids **19** (1976) 1144.
[9] COPPI, B., SHARKY, N., Nucl. Fusion **21** (1981) 1363.
[10] COPPI, B., Massachusetts Inst. of Technology, Cambridge, MA, (RLE) Rep. PTP-84/8 (1984).
[11] BONIZZONI, G., et al., Massachusetts Inst. of Technology, Cambridge, MA (RLE) Rep. PTP-84/1 (1984).
[12] SUGIYAMA, L., Massachusetts Inst. of Technology, Cambridge, MA (RLE) Rep. PTP-84/1 (1984).
[13] KULSRUD, R.M., FURTH, H.P., VALEO, E.J., GOLDHABER, M., Phys. Rev. Lett. **49** (1982) 1248.
[14] COPPI, B., PEGORARO, F., RAMOS, J.J., Phys. Rev. Lett. **51** (1983) 892.
[15] COPPI, B., COWLEY, S., DETRAGIACHE, P., KULSRUD, R., PEGORARO, F., Massachusetts Inst. of Technology, Cambridge, MA (RLE), Rep. PTB-84/6 (1984), to be published in Comments Plasma Phys. Controll. Fus.

MODELLING ANALYSES OF TOKAMAKS WITH DIVERTORS AND PUMPED LIMITERS

M. PETRAVIC, D. HEIFETZ, D. POST
Plasma Physics Laboratory,
Princeton University,
Princeton, New Jersey,
United States of America

Abstract

MODELLING ANALYSES OF TOKAMAKS WITH DIVERTORS AND PUMPED LIMITERS.

The next generation of tokamak experiments (TFCX, NET, FER and INTOR) will require a system that provides adequate impurity control, helium exhaust and component lifetimes. Both the poloidal divertors and pumped limiters are still in contention for the basic component of such a system. The authors have calibrated their computational models of plasma and neutral transport against the data for divertors and pumped limiters on PDX, D-III and ISX-B, and applied these models to the design of TFCX. The main aim has been to compare the relative merits of limiters and divertors under the design conditions of TFCX, rather than provide the absolute values for the plasma parameters and the neutral exhaust rates. The geometries used therefore contain the essential features of the design but omit a number of details. It was found that a large toroidally symmetric limiter is likely to operate in much the same way as a divertor, i.e. in a high recycling mode, but with less control, a higher erosion rate, and with a considerable perturbation on the main plasma edge, the consequences of which are hard to predict.

1. INTRODUCTION

While the main purpose of divertors and limiters is to provide efficient (H_e) ash removal and good impurity control, they also have to be designed to absorb between 10 and 25% of the generated power without sustaining significant damage over long periods of time. Moreover, their presence must not adversely affect the plasma confinement, either through hydrogen recycling or impurity generation. Traditionally, divertors were thought to provide better impurity control, while limiters were regarded as cheaper to make and easier to replace. More recently, improved confinement (H-mode) was achieved on the ASDEX [1], PDX [2], and DOUBLET-III tokamaks, using poloidal divertors, but there are indications that the H-mode can also exist in the presence of limiters [3]. In another development, the poloidal divertor design has become much simpler, as a

result of the success of the D-III open divertor configuration, with consequent reduction in the cost. With the initial cost of large toroidally symmetric limiters, and the short open poloidal divertors becoming comparable, the choice has to be made on other grounds. We have recently tried to examine and compare the theoretical performance of poloidal divertors, and limiters as regards power handling, ash removal, durability and the possible effect on the main plasma. The theoretical models of the poloidal divertors have been very successful in both explaining and predicting the divertor plasma properties, and in particular in pointing out the way to reduce the sputtering problem [4,5]. We have checked our model against a number of poloidal limiter experiments on D-III and PDX, and found a very satisfactory agreement which gives confidence in its predictions for reactor-like conditions with high densities and recycling rates. In this paper we briefly describe our theoretical model and summarize the modeling of the PDX experiment. We then apply the model to a toroidally symmetric limiter and compare the results with the prediction of the same model for an equivalent poloidal divertor.

2. THE MATHEMETICAL MODEL

The mathematical model for the scrapeoff plasma has been described elsewhere [6,7] and will be described only briefly here. The plasma equations are based on those of Braginskii [8], and they, in the Cartesian geometry and in the steady state limit, take the form:

$$\frac{\partial}{\partial x}(nv_{\parallel}) = S_n + \frac{\partial}{\partial y}\left(D_{\perp}\frac{\partial n}{\partial y}\right) \tag{1}$$

$$\frac{\partial}{\partial x}\left[n\left(mv_{\parallel}^2 + T_i + T_e\right)\right] = S_p + \frac{\partial}{\partial y}\left(D_{\perp}\frac{\partial}{\partial y} nmv_{\parallel}\right) \tag{2}$$

$$\frac{\partial}{\partial x}\left[\frac{5}{2} nv_{\parallel}T_i + \frac{1}{2} nmv_{\parallel}^2 - \chi_{\parallel}^i \frac{\partial T_i}{\partial x}\right] = -v_{\parallel}\frac{\partial(nT_e)}{\partial x}$$

$$+ S_E^i + \frac{\partial}{\partial y}\left[D_{\perp}\left(\frac{5}{2}T_i + \frac{mv_{\parallel}^2}{2}\right)\frac{\partial n}{\partial y} + \chi_{\perp}^i \frac{\partial T_i}{\partial y}\right] + Q_{ei} \tag{3}$$

$$\chi \frac{\partial}{\partial x}\left[\frac{5}{2} nv_{\parallel} T_e - \chi^e_{\parallel} \frac{\partial T_e}{\partial x}\right] = v_{\parallel} \frac{\partial (nT_e)}{\partial x} + S^e_E + \frac{\partial}{\partial y}$$

$$\left(D_{\perp} \frac{5}{2} T_e \frac{\partial n}{\partial y} + \chi^e_{\perp} \frac{\partial T_e}{\partial y}\right) - Q_{ei} \qquad (4)$$

Here $n = n_e = n_i$, T_i, T_e and v are the electron density, ion and electron temperatures, and the ion parallel velocity; m is the ion (deuterium) mass. $D_{\perp}$ is the particle diffusion coefficient and $\chi_{\perp}$ and $\chi_{\parallel}$ are the perpendicular and parallel thermal conductivities. Q_{ei} is the electron-ion Coulomb energy transfer term, and S_n, S_p, S^i_E, S^e_E are the ionization (particle) source, momentum source and the ion and electron energy sources arising from the plasma interaction with neutrals. Classical [8] parallel electron conductivity was used, but no detailed models were used for the diffusion coefficients. We also use the following abbreviations for the various fluxes:

$$\Gamma = (nv_{\parallel}) \qquad (5)$$

$$G = n(mv^2_{\parallel} + T_i + T_e) \qquad (6)$$

$$Q_i = \frac{5}{2} nv_{\parallel} T_i + \frac{1}{2} nmv^2_{\parallel} - \chi^i_{\parallel} \frac{\partial T_i}{\partial x} \qquad (7)$$

$$Q_e = \frac{5}{2} nv_{\parallel} T_e - \chi^e_{\parallel} \frac{\partial T_e}{\partial x} \qquad (8)$$

3. BOUNDARY CONDITIONS

The equations (1) to (4) can be used with a variety of boundary conditions. We regularly specify $\Gamma = \Gamma^o$, $Q_i = Q^o_i$, and $Q_e = Q^o_e$ on the upstream boundary (x=0); along the stagnation line all the three fluxes are zero. The downstream boundary is taken at the sheath ($x = x_{sh}$) where the sheath potential limits the electron heat flux to

$$Q^{sh}_e = \gamma T^{sh}_e \Gamma^{sh} \qquad (9)$$

The matching of the collisional (fluid) region to the collisionless sheath has not been solved exactly but the various kinetic models of the sheath [9] indicate a sonic $v_{\parallel}$ at the sheath boundary. We therefore use

$$v_{\parallel}^{sh} = v_s = [(T_i + T_e)/m)]^{1/2} \qquad (10)$$

There is also a weak boundary condition on $\partial T_i/\partial x$ at the sheath, which is discussed elsewhere [7]. Radially, there are two more boundaries, at least one of which is a solid wall or vacuum, and the other is the contact line with the main plasma, usually the separatrix between the stagnation point and the x-point. The density and the temperatures are set to a low value on the vacuum or outer boundary, while on the inner boundary we have specified the energy and the particle fluxes.

All the source terms in the equations are computed in a separate neutral transport calculation using a Monte-Carlo code DEGAS [10]. The solution of the equations [1-4] is obtained by iteration between the plasma and neutral solutions.

4. TESTS FOR THE MODEL

The model has been applied to a number of experiments on the D-III [11] and PDX [7]. The comparison with the PDX divertor experimental results has provided a particularly stringent test for the model, because the experimental geometry was modeled accurately, and the only free parameter was the incoming particle flux. The overall agreement with all the essential plasma parameters was within ±30% but the predicted neutral pressure was low by a factor of two [7]. We still do not know, however, how significant it is that the attempts to explain the observed H_α emission from the PDX divertor region have so far been unsuccessful.

5. LIMITER MODELING

While numerous calculations have been performed using neutral transport codes to predict the pumping with pumped limiters [12], no fully self-consistent calculation in a realistic geometry has been reported so far. We here consider a simple but realistic pumped limiter geometry of

Fig. 1 , with dimensions roughly corresponding to the TFCX conceptual design[13,14], i.e. a major plasma radius of 3.5 m, minor radius of 1.5 m, and a power flux into the half of the scrapeoff indicated, of 10 MW. (All the fluxes and exhaust rates will be quoted for the half of the limiter shown in Fig. 1). In order to keep the number of unknowns to a minimum we have deliberately not made any assumptions about the main plasma except that the radial particle and energy outflow from it is uniform in the poloidal angle. Also, to reduce computing time, $T_i=T_e$ was assumed throughout. We have kept the energy outflow constant at 10 MW but have varied the particle flux from 1.1×10^{22} to 4.4×10^{22} ions/s. We have deliberately used rather large values for the diffusion coefficient $D_\perp = 10^4$ cm^2/s and the total perpendicular thermal conduction coefficient $\chi_t = 4 \times 10^4$ cm^2/s in order to make a more direct comparison with the already obtained solutions for poloidal divertors. The radial density and temperature profiles along a line passing through the limiter tip are shown in Fig. 2 , for the outflow particle flux of 4.4×10^{22} ions/s. It is seen that the density is still below 10^{14} cm^{-3}, while the maximum scrapeoff temperature is below 100 eV. The problem with modeling limiters is that the recycling rate is dependent on the radial transport coefficients, which is not the case with divertors. This makes predictions for limiters much less definite. Note, however, that for a given heat flux, the electron temperature, density, and the parallel particle flux are related through the boundary conditions (9) and (10), so we can at least partly eliminate the dependence on the particle flux by considering only T_e and n_e. We therefore plot in Fig. 3 the temperature on the main plasma boundary as a function of the electron density. We tentatively conclude that if the electron density reaches 10^{14} cm^{-3} on the main plasma boundary, conditions for a cool, dense scrapeoff will be satisfied and the erosion problems considerably reduced. This conclusion is obviously dependent on the power input into the scrapeoff. With 10 MW onto one half of the divertor there are no cooling problems, the maximum power flux per cm^2 of the limiter surface being 160 W/cm^2 (Fig. 4). There should be no problems at the tip in an actual design, since there the power flux onto a surface normal to the poloidal field is only 50 W/cm^2.

The ash removal efficiency of pumped limiters has been of some concern, the problem being that keeping the power onto the tip within reasonable limits leaves little power to drive the pumping behind the limiter. In our model we

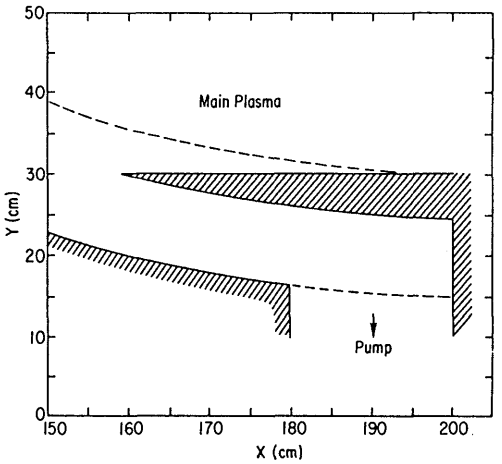

FIG. 1. Sketch of the pumped limiter geometry. The computational region extends over a semicircular region which begins at the stagnation point and ends at the right-hand corner of this figure. The main plasma boundary is drawn as a dashed line, while the solid lines represent a solid wall.

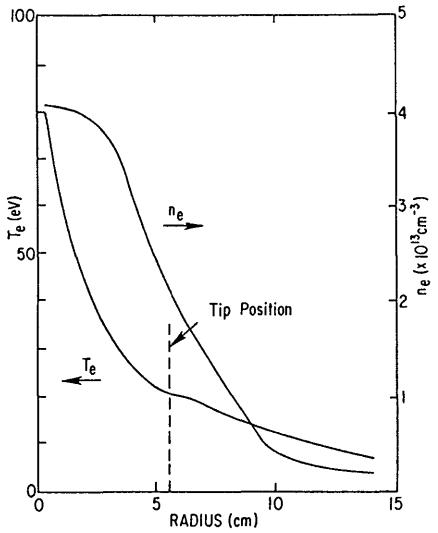

FIG. 2. Radial electron density and temperature profiles taken along a ray going through the limiter tip. The particle flux across the main plasma boundary is 4.4 X 10^{22} ions/s, and the power is 10 MW. There is little variation along the field lines in front of the limiter, but the temperature drops further, and the density rises behind the limiter and towards the stem.

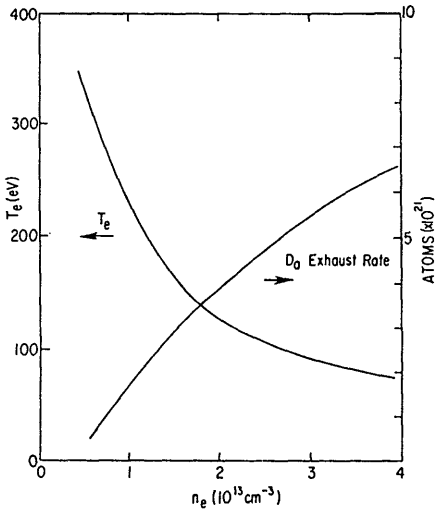

FIG.3. Maximum electron temperature on the limiter face as a function of electron density on the main plasma boundary. The temperature decreases rapidly with density and is estimated to fall below 40 eV at $n_e = 1 \times 10^{14}\,cm^{-3}$.

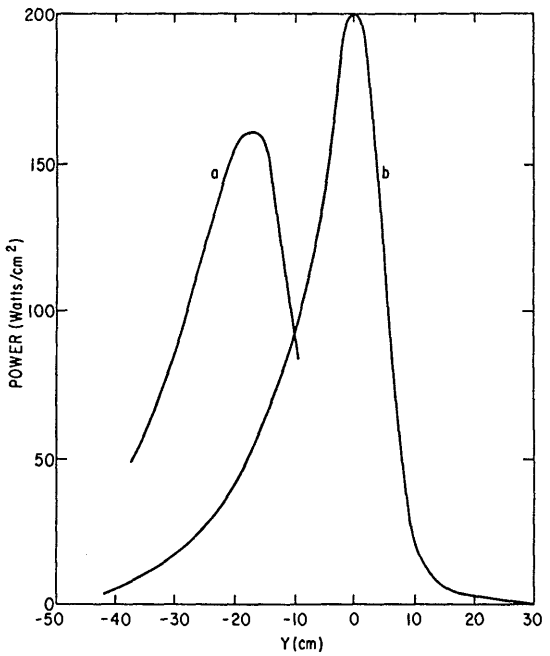

FIG.4. Comparison of the power flux density on the TFCX limiter face: (a) With the corresponding flux onto an equivalent neutralizer plate. (b) The origin (Y = 0) corresponds to the separatrix in the case of the divertor, and to the point of contact of the limiter with the main plasma boundary. The profile for the limiter stops at the origin; the other half of the profile corresponds to the second divertor branch. It is seen that the peak power densities are quite comparable, despite the different ways of spreading the power load.

assumed a pump located in the bottom wall capable of 200 000 L/s. The hydrogen throughput through the pump as a function of the maximum scrapeoff density has been plotted in Fig. 3. The required hydrogen throughput at 5% He concentration is 1.3×10^{21} atoms/s. It is seen that this figure is considerably exceeded for the main plasma boundary densities above 1×10^{13} cm^{-3}. As we pointed out earlier this conclusion is dependent on the diffusion coefficient but there does appear to be enough of a safety margin, and also there may be a better location for the pump opening.

6. DIVERTOR MODELING

Our models employing realistic geometry have so far covered only the region extending from the X-point to the neutralizer plate [7,15]. To compare with the limiter modeling we have modeled a poloidal divertor of comparable dimensions using straight field-line geometry and then correcting for field line spreading to get at the heat load on the plate. Field line spreading from midplane to the plate by a factor of 3 has been assumed, together with a 45° angle between the poloidal field direction and the plate. The peak power load is ~ $200 W/cm^2$ (Fig. 4) for the same input power and transport coefficients or for the limiter. As is by now well known, the scrapeoff plasma temperature can be controlled almost at will with divertors [5] so no particular attention will be payed to it here. Also, ash removal presents no problem with divertors unless the pump opening is far away from the plasma column.

7. SUMMARY

Though a more thorough study is still required, a fairly good comparison of pumped limiters, and poloidal divertors can already be attempted. As shown in Fig. 4, the peak heat loads on the neutralizer are very comparable. However, erosion due to sputtering can be controlled much better with divertors, though it is very interesting to see that the low temperature regime should be possible, unless clamping the main plasma boundary to a very low temperature causes other problems. (With divertors, temperature drops of over 100 eV can be achieved along the field line.)

In ash removal the divertors are again superior but limiters appear adequate. A more thorough study of the open divertor with a single pump on one side (INTOR) is still

needed. Such a study must include the whole of the scrapeoff in order to permit flows from the inner to the outer divertor branch.

The question of impurity control has yet to be addressed properly. For this purpose the flows right next to the first wall in a genuine steady state have to be accurately known. Too little has been done so far in this area so far to permit a meaningful discussion.

The most difficult question concerns the effect of the two devices on the overall energy confinement. So far the divertors have proven superior in this respect but, since the reason for it is not fully understood, final conclusions cannot be drawn.

Overall, the divertors appear superior in providing more flexibility and control. The limiters, on the other hand, are somewhat cheaper, and easier to replace.

ACKNOWLEDGMENT

This work was supported by U S Department of Energy Contract DE-AC02-CH03073.

REFERENCES

[1] WAGNER, F., et al., Phys. Rev. Lett. **49** (1982) 1408.
[2] KAYE, S.M., PDX GROUP, Energy removal and particle control in fusion devices, J. Nucl. Mater. **121** (1984) 115.
[3] BUDNY, R., private communication.
[4] MORGAN, J.G., HARBOUR, P.J., Fusion Technology, Vol. 2, Pergamon Press, Oxford, (1980) 1187.
[5] PETRAVIC, M., et al., Phys. Rev. Lett. **48** (1982) 326.
[6] PETRAVIC, M., et al., J. Nucl. Mater. **111&112** (1982) 234.
[7] PETRAVIC, M., et al., to appear in 6th Int. Conf. Plasma Surface Interactions in Controlled Fusion Devices, Nagoya, 1984, to be published in J. Nucl. Mater.
[8] BRAGINSKII, S.I., Rev. Plasma Phys. **1** (1965) 205.
[9] CHODURA, R., et al., "Self-consistent description of the plasma-wall interaction in tokamak plasmas", Plasma Physics and Controlled Nuclear Fusion Research 1982 (Proc. 9th Int. Conf. Baltimore, 1982), Vol. 1, IAEA, Vienna (1983) 313.
[10] HEIFETZ, D., et al., J. Comput. Phys. **46** (1982) 309.
[11] PETRAVIC, M., et al., "A model for the performance of poloidal divertors", Plasma Physics and Controlled Nuclear Fusion Research 1982 (Proc. 9th Int. Conf. Baltimore, 1982), Vol. 1, IAEA, Vienna (1983) 323.

[12] EVANS, K., et al., to appear in Proc. 6th Int. Conf. Plasma Surface Interactions in Controlled Fusion Devices, Nagoya, 1984, to be published in J. Nucl. Mater.
[13] BOLEY, C.D., ibid.
[14] TFCX PRECONCEPTUAL DESIGN TEAM, The TFCX Preconceptual Design Report, Princeton Plasma Phys. Lab. (1984).
[15] PETRAVIC, M., et al., to appear in Proc. 6th Inf. Conf. Plasma Surface Interactions in Controlled Fusion Devices, Nagoya, 1984, to be published in J. Nucl. Mater.

ADVANCED TWO-DIMENSIONAL SIMULATION OF EDGE PLASMA IN A POLOIDAL DIVERTOR

Yu.L. IGITKHANOV, A.S. KUKUSHKIN,
A.Yu. PIGAROV, V.I. PISTUNOVICH,
V.A. POZHAROV
I.V. Kurchatov Institute of Atomic Energy,
Moscow, Union of Soviet Socialist Republics

Abstract

ADVANCED TWO-DIMENSIONAL SIMULATION OF EDGE PLASMA IN A POLOIDAL DIVERTOR.

The 2-D simulation of the plasma in a poloidal divertor is performed in terms of a more realistic (than previously) Monte-Carlo model for the neutral gas. Calculations are carried out for plasma parameters close to those of ASDEX. The dependence of the divertor plasma parameters on input plasma flow and neutral-gas density in the divertor is obtained. These parameters are shown to be rather insensitive to the plasma flow across the separatrix, thus justifying separate treatment of the edge plasma. All the computed cases exhibit narrow transverse profiles of the edge plasma parameters. A self-consistent 1-D model is developed for the impurity behaviour in the divertor, where charge exchange with hydrogen atoms is taken into account. The carbon impurity distribution along the magnetic field in the divertor is found to provide strong impurity localization near the collector plate. The test particle model is shown to be valid at high recycling levels, the impurity radiation losses being 10 to 20% of the total input power.

1. INTRODUCTION

The first results on 2-D simulation of edge plasma in ASDEX were reported in Ref.[1], where 2D hydrodynamical equations for the plasma and a simple diffusion model for the neutral gas were used. Treatment of the scrape-off layer together with the divertor volume (Fig.1) provided the natural boundary condition of the given particle and heat flows across the separatrix.

The present paper deals with a further development of the model using a more realistic Monte-Carlo description of the neutral gas. The boundary conditions for the neutral gas in the divertor also differ from those used in Ref.[1], where the neutral flow from the divertor plates has been fixed to provide the given level of recycling. In the present paper, the plasma within the divertor is considered to be surrounded by neutral gas with constant density that is independent of the plasma parameters. This approach seems to be more adequate to ASDEX with gas puffing into the divertor chamber [2, 3].

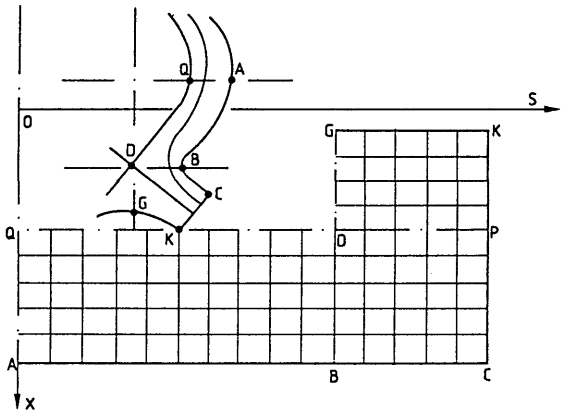

FIG. 1. Computational model of scrape-off layer (AQDB) together with divertor volume (BCPKGD). L = AC = 15 m, AB = 12 m, KC = 0.08 m, Δ = AQ = DB = 0.04.

Another important issue of the edge plasma simulation is the self-consistent description of the impurity dynamics. The hydrodynamical non-coronal model developed in the paper allows the charge state distribution of the impurity ions within the divertor, their role in the energy balance and the possibility of their being retained within the divertor volume to be described. The computations have been carried out for carbon stemming from the plates due to sputtering by the plasma flow, the dependence of the sputtering coefficient on the energy of the particles and their incidence angle being taken into account.

2. MAIN EQUATIONS AND BOUNDARY CONDITIONS

The set of hydrodynamical equations for the plasma has the form:

$$\frac{\partial n}{\partial t} + \operatorname{div} n\vec{v} = S_0 \tag{1}$$

$$m_i \frac{\partial n\vec{v}}{\partial t} + \operatorname{div} \vec{\Pi} = P_0 \tag{2}$$

$$\frac{3}{2}\frac{\partial nT_e}{\partial t} + \operatorname{div}\left(\vec{q}_e + \frac{5}{2} n\vec{v} T_e\right) = \vec{v} \cdot \nabla nT_e - Q_{ei} + Q_{0e} \tag{3}$$

$$\frac{\partial}{\partial t}\left(\frac{m_i n v^2}{2} + \frac{3}{2} nT_i\right) + \operatorname{div}\left\{\vec{q}_i + \left(\frac{m_i v^2}{2} + \frac{5}{2} T_i\right) n\vec{v}\right\} = -\vec{v}\,\nabla nT_e + Q_{ei} + Q_{0i} \tag{4}$$

The continuity equation (1) includes the source of cold ions, S_0 (x,s), due to the ionization of neutral hydrogen. The s-co-ordinate is directed along the field line, and the X-co-ordinate is normal to it in the poloidal direction (Fig.1). The momentum loss in the collisions with neutrals, P_0(x,s), is included in the equation for the momentum transport (2). The components of the total momentum flux can be represented as $\Pi_s = m_i n v_s^2 + nT_i + nT_e - \eta_i \partial v/\partial s$, $\Pi_x = m_i n v_s v_x$.

The longitudinal ion viscosity is taken into account here, while the longitudinal-transverse viscosity term is omitted because of the rather strong magnetization of the ions. The equations for energy transport via the ion and electron components, (3) and (4), include the terms describing the work of the electric forces and the energy losses related to neutrals (Q_{0e}, Q_{0i}), besides convection, thermal conduction, q_i, q_e, and the Coulomb exchange, Q_{ei}. The rest of the symbols are identical with those used in Ref.[1].

Classical values are chosen for the longitudinal heat conduction coefficients, $\chi_{\parallel}^{i,e}$, and for the longitudinal viscosity coefficient, η_i. The transverse flux along the X-axis is chosen to be the diffusive one, $nv_x = -D_\perp \partial n/\partial x$. Different values and functional dependences have been taken for the transverse transport coefficients, $D_\perp$ and $\chi_\perp^{i,e}$. The excitation cross-section for neutral hydrogen is taken from Ref.[4].

The geometry chosen, in contrast to Refs [5, 6], provides natural boundary conditions. The particle fluxes, Φ_s, and the heat fluxes in ions, W_s^i, and in electrons, W_s^e, are pre-set at the separatrix (QD):

$$nv_x = \Phi_s/S \tag{5}$$

$$\left(\frac{5}{2}T_i + \frac{m_i v_s^2}{2}\right) nv_x + q_x^i = W_s^i/S \tag{6}$$

$$\frac{5}{2}T_e + q_x^e = W_s^e/S \tag{7}$$

$$m_i n v_s v_x = 0 \tag{8}$$

Here, S is the separatrix surface area. Condition (8) corresponds to zero plasma velocity along the magnetic field inside the separatrix. Symmetry conditions are assumed to be valid along the lines AQ and DG:

$$v_s = \frac{\partial T_i}{\partial s} = \frac{\partial T_e}{\partial s} = 0$$

and the temperature and the density at the chamber wall (GK and AC) are set to be equal to zero.

The neutral gas is simulated by a Monte-Carlo method which allows a proper interpretation of its interaction with the plasma and with the real surfaces as

well, on the condition that the problem is substantially non-one-dimensional. The neutral flow value, together with the complete absorption of incident particles, forms the boundary conditions along the lines (AB) and (KG). Each particle impinging on the AB or KC surface is reflected as a neutral. The partial return of neutrals entering the bulk plasma is also taken into account.

3. SHEATH BOUNDARY CONDITION AT THE PLATE

The boundary conditions at the collector plate (KC) are obtained from the requirement that the hydrodynamical fluxes of particles, momentum and energy leaving the plasma be transferred to the plate as kinetic fluxes. In fact, these conditions are set at a distance from the plate where the diffusive distribution functions are marginally distorted because of the non-equilibrium conditions near the wall:

$$\frac{5}{2} n v_s T_e + q_s^e = f_e T_e \, n v_s \tag{9}$$

$$\left(\frac{5}{2} T_i + \frac{m_i v_s^2}{2} \right) n v_s + q_s^i = f_i T_i n v_s \tag{10}$$

$$m_i n v_s^2 + n T_i + n T_e - \eta_i \frac{\partial v_s}{\partial s} = f_{p_i} n T_i + f_{p_e} n T_e \tag{11}$$

The kinetic fluxes on the right-hand side of Eqs (9) to (11) are based on the following assumptions: the transition layer where the relaxation of the distribution functions occurs is much shorter than the characteristic longitudinal dimensions but, at the same time, much wider than the Debye layer. The whole transition layer is contracted into a point whose distance from the plate is a relaxation length. A one-sided Maxwellian function that is shifted by the value of some velocity to be determined below is assumed to be the boundary distribution function for the ions, F_i. (Ions and electrons are assumed to be absorbed on the plate.) For electrons, F_e is simulated by a two-sided Maxwellian function truncated due to a cut-off by the Debye constant potential. The density and the fluid velocity may jump at the transition between the hydrodynamical and kinetic regions. The temperature remains unchanged because the heating of the ions in the transition layer due to viscosity is practically compensated for by their being cooled through ion heat conduction and ion acceleration under the influence of the pre-sheath field. Note that the fluid velocity of the plasma at the lower boundary cannot

be of the order of the sound speed, c_s, or higher (as postulated in Refs [5–7] as the boundary condition), because acceleration should only take place within the transition layer where the hydrodynamical equations are not applicable.

The coefficients in conditions (9) to (11) are determined by the distribution functions for the ion and electron components at their escape from the plasma:

$$f_e = 2 + \epsilon \tag{12}$$

$$f_i = \left\{ (2 + M_1^2) e^{-M_1^2} + \sqrt{\pi}\, M_1 \left(M_1 + \frac{5}{2} \right) \mathrm{erf}(-M_1) \right\} G^{-1}(M_1) \tag{13}$$

$$f_{p_i} = 2\sqrt{\pi}\, M \left\{ \frac{M_1}{\sqrt{\pi}}\, e^{-M_1^2} + \left(M_1^2 + \frac{1}{2} \right) \mathrm{erf}(-M_1) \right\} G^{-1}(M_1) \tag{14}$$

$$f_{p_e} = 2\sqrt{\pi}\, M \left\{ -\sqrt{\frac{\epsilon}{\pi}}\, e^{-\epsilon} + \frac{1}{2}\, \mathrm{erf}(-\sqrt{\epsilon}) \right\} G^{-1}(M_1) \tag{15}$$

Here $M = v_s/v_{T_i}$, where v_s is the hydrodynamical plasma fluid velocity, $v_{T_i} = \sqrt{2T_i/m_i}$ is the thermal ion velocity,

$$\mathrm{erf}(-x) = \frac{2}{\sqrt{\pi}} \int_{-\infty}^{x} e^{-t^2}\, dt$$

M_1 is the parameter equal to M at $v_s \geqslant c_s$ and is found from the condition

$\int_0^\infty F_i(M_1)\, v dv = c_s \int_0^\infty F_i(M_1) dv$ at $v_s \geqslant c_s$. A dimensionless sheath potential, $\epsilon = e\varphi_0/T_e$ is found from the condition of quasi-neutrality in the transition zone:

$$\epsilon = \ln \sqrt{\frac{m_i}{m_e} \frac{T_e}{T_i}}\, \frac{\mathrm{erf}(-M_1)}{\mathrm{erf}(-\sqrt{\epsilon})}\, G^{-1}(M_1) \tag{16}$$

where $G(M_1) = e^{-M_1^2} + \sqrt{\pi}\, M_1\, \mathrm{erf}(-M_1)$.

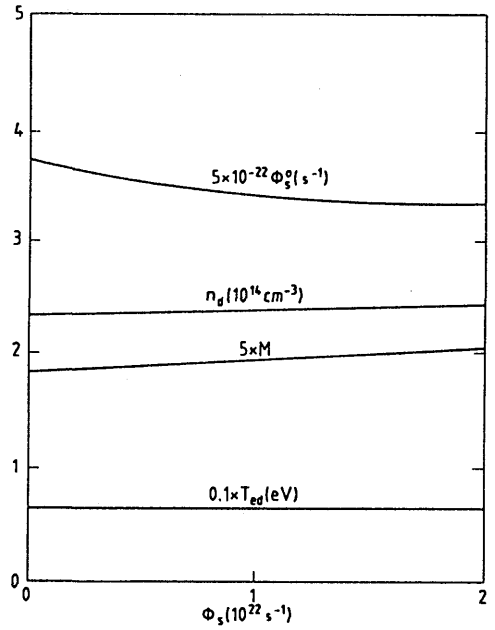

FIG.2. Neutral flow into main plasma, Φ_s^0; plasma density near plate, n_d; electron temperature, T_{ed}; and Mach number, $M = v/c_s$ for plasma flux near the plate versus input plasma flow, Φ_s. All parameters are taken at the separatrix. The power flow enters the layer from the main plasma, $Q_s = 2.5$ MW. Neutral gas density in divertor, outside plasma layer: $N_0 = 3.2 \times 10^{12}$ cm^{-3}.

4. ASDEX MODELLING

The results of simulating the ASDEX divertor experiment are described below. The computations have been carried out for the following parameters:

length of field line from median plane	
to divertor throat	ℓ = 12 m
to divertor plate	L = 15 m
divertor layer width	Δ = 4 cm
pitch angle of magnetic field	$B_\theta/B_\varphi = 0.08$
longitudinal magnetic field	$B_\varphi = 2.8$T

The regime of a power of 2.5 MW entering the layer ($W_s^i + W_s^e = 2.5$ MW) is chosen. The ratio of the input heat flows, W_s^e/W_s^i, is assumed to be equal to 2:1.

The dependence of the plasma parameters, within the divertor layer, on the input plasma flow across the separatrix is given in Fig.2. This dependence is seen to be weak. In particular, a solution with no input flow of particles, corresponding to a recycling level in the divertor of R_s = 100%, has been obtained. The

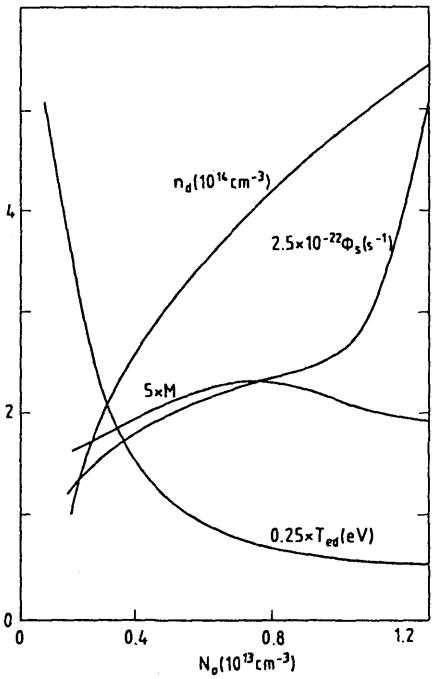

FIG.3. The same as Fig.2 versus neutral-gas density within divertor, N_0. $\Phi_s = 10^{22}\,s^{-1}$, $Q_s = 2.5\,MW$.

existence of such a solution shows that our model is, in principle, consistent with the bulk plasma and can provide particle balance in ASDEX without any additional sources. In reality, the steady-state plasma flow across the separatrix is determined by the particles stemming from the neutral beam, together with the neutral flow entering the main plasma. Therefore, it should differ from zero.

The dependence of the same parameters on the neutral-gas density within the divertor is shown in Fig.3. We see that the plasma temperature in the divertor drops abruptly, and the density rises with an increase in the amount of gas. The rate of gas puffing into the divertor is limited by the disruptive instability in the experiment [2]. Out model does not deal with the main plasma, but we see that the neutral flow across the separatrix rises sharply, which could lead to a disruption.

The power balance versus the neutral-gas density in the divertor is shown in Fig.4. The power deposited by the charged particles on the divertor plate drops with rising neutral density and may be less than 20% of the total discharge power. In this case, the average energy of an ion incident upon the plate drops down to about 10 eV.

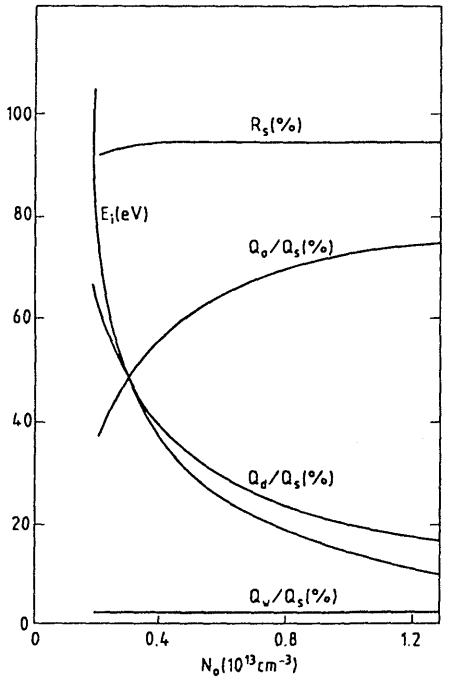

FIG. 4. Power balance in divertor versus density of neutral gas. R_s is recycling in the layer, E_i the energy of ions impinging on the plate, Q_0 the power unloaded by neutrals, Q_d the power deposited on the plate by charged particles, Q_w the power deposited on the walls.

All the cases computed show peaked transverse profiles, with the maximum near the separatrix along the whole length of the layer. This means that cooling by neutrals is not sufficiently effective. The cooling is not provided by the secondary charge-exchange atoms with ranges greater than or equal to the layer width, but by the primary neutrals, which exist only in a narrow layer close to the surface. Thus, the energy exchange has not a volumetric, but a surface nature. In such conditions, the efficiency of energy exhaust can be improved by increasing the interface area between the plasma and the gas. Computations have shown that the transverse distributions are only slightly sensitive to variations in the transverse transport coefficients. Probably, this is due to a relatively weak, square-root dependence of the half-widths on these coefficient values, and also to the fact that the transverse profiles are mainly determined by the classical longitudinal transport coefficients.

Thus, the model allows an interpretation of ASDEX operation with high gas recycling within the divertor chamber. The plasma densities and temperatures observed experimentally near the divertor plates can be obtained at a low feeding

rate of the main plasma during NBI ($\Phi_0 \approx 10^{20}\ s^{-1}$) with a high particle flow recirculating across the separatrix, $\Phi_s \approx 10^{22}\ s^{-1}$, as a background.

5. CARBON IMPURITY BEHAVIOUR

So far, the behaviour of impurity ions in the divertor has been considered with a fixed plasma background, and the effect of the impurities on the plasma parameters has not been taken into account (see, e.g. Ref.[9]). The steady-state distributions of edge plasma parameters, in the presence of an impurity atom flux due to ion sputtering of the plate material, are found within the framework of the 1D equations for the longitudinal transport.

The objectives are:

- to clarify the role of impurities in reaching dense-plasma regimes with high longitudinal gradients;
- to study the distribution of impurity ions within the layer and the divertor for different ionization states;
- to determine the amount and the charge state of impurities originating from a divertor plate, in conditions far from corona equilibrium;
- to study the effect of charge-exchange collisions with neutral hydrogen atoms of the impurity ions on the charge state distribution.

The particle approximation is used ($\Sigma Z^2 n_Z \ll n_e \approx n_i$, where n_e and n_i are the electron and the ion density, respectively, n_Z is the density of a Z-times ionized impurity). The impurity ions at such concentrations do not affect the ambipolar longitudinal electric field, and the change in the momentum of a plasma component due to interaction with an impurity is negligibly small. The only effect of impurities on the plasma parameters consists in radiational losses.

The plasma influx across the separatrix is simulated by pre-setting the volumetric sources of particles and those of the energy along the magnetic field lines. The sources are assumed to be constant within the layer and to vanish in the divertor. The recycling coefficient, $R = 1 - \Phi_S/\Phi_D$ (where Φ_S is the plasma flow across the separatrix, and Φ_D is the plasma flow to the divertor plate) plays the role of a parameter determining the divertor pumping rate.

The density and the velocity of the impurity ions are described by a set of 2Z equations:

$$\frac{\partial n_Z}{\partial t} + \frac{\partial}{\partial s} n_Z v_Z = S_{Z-1} n_{Z-1} - (S_Z + \alpha_Z) n_Z + \alpha_{Z+1} n_{Z+1}$$

$$- R_Z n_Z N + R_{Z+1} n_Z N \qquad (17)$$

$$\frac{\partial}{\partial t}\rho_Z v_Z + \frac{\partial}{\partial s}\left(\rho_Z v_Z^2 + p_Z - \eta_Z \frac{\partial v_Z}{\partial Z}\right) = -eZn_Z E_S - \rho_Z \frac{v_S - v_Z}{\tau_Z} - R_{T_S} \quad (18)$$

$(1 \leqslant Z \leqslant Z_{max})$

Here $\rho_Z = n_Z m_Z$, m_Z is the ion mass, $p_Z = n_Z T_Z$, S_Z/n_e, α_Z/n_e, R_Z are the rates of ionization, recombination and those of charge exchange of the impurity ions with the hydrogen atoms, respectively; τ_Z is the time of longitudinal deceleration of an impurity ion by the ions of the plasma; η_Z is the viscosity coefficient for the impurity ions [8]. In the test particle approximation, the electric field is completely determined by the plasma parameters: $en_e E_s = -\partial p_e/\partial s - 0.71\, n_e\, \partial T_e/\partial s$. The temperature of the impurity ions is assumed to be equal to that of the plasma ions. A thermal force, $R_{T_s} = a_Z\, \partial T_e/\partial s + b_Z\, \partial T_i/\partial_s$, is included in Eq.(18), in addition to the friction and the electric-field terms. The coefficients a_Z and b_Z usually depend weakly on Z [8], but in the $\Sigma Z^2 n_Z \ll n_i$ limit, a_Z and b_Z are proportional to Z^2 [9]. Vanishing of all impurity ion velocities is the boundary condition on the symmetry plane. The fact that the hydrodynamical flows of heat, particles and momentum are equal to the kinetic flows, with account for the Debye layer and the plasma fluid velocity, provides the boundary conditions on the divertor plate. The influx of carbon from the divertor plate is determined by averaging the ion sputtering coefficient, $S(\epsilon, \theta)$ [10] (ϵ is the incident-ion energy, and θ is the angle of incidence), over ϵ and θ. The distribution function of the incident ions is assumed to be a one-sided Maxwellian due to the ion acceleration under the action of the Debye field in the layer.

6. RESULTS OF COMPUTATIONS AND DISCUSSION

The computations have shown that the impurity level is not high in regimes of a dense, cold plasma with recycling no less than 86%, and the test particle approximation is found to be valid. In these regimes, carbon is localized within the divertor volume, because of friction with the ions of the background plasma (Fig.5). The concentration of the impurity ions is negligibly low at the outlet of the divertor. The impurity radiation losses reach 10 to 20% of the input power, depending on the recycling coefficient, and they drop with decreasing temperature when recycling rises.

The charge state distribution of the impurity ions is far from a corona equilibrium. The characteristic longitudinal confinement time is a few milliseconds. This time is comparable with the ionization times and that of the charge exchange with the neutral atoms. The ionization state for carbon is not high ($Z \approx 1-3$) in these regimes, because of a low plasma temperature near the divertor plate ($T_{ed} \approx 10$ eV). The impurity ion distribution is determined by the friction forces and the thermal force. The thermal force counteracts the

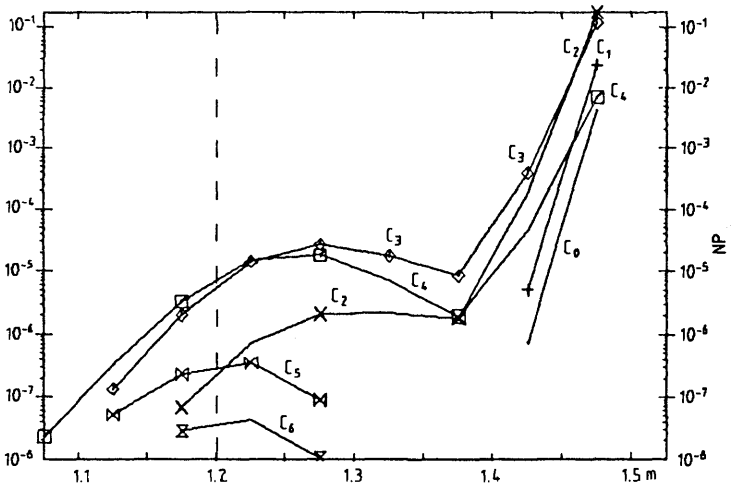

FIG.5. Distribution of carbon ion density in divertor (density in units of 10^{13} cm^{-3}).

friction force and causes a moderation in the motion of the impurities towards the plate. The density has a maximum, with a position that depends on the ion temperature gradient, in the region of moderation. Charge exchange between carbon ions and neutral hydrogen atoms leads to a redistribution of the impurities towards lower charge states, increasing the radiation losses.

Thus, the results of solving the self-consistent problem show that it is possible to localize the light impurities within the divertor volume.

REFERENCES

[1] IGITKHANOV, Yu.L., et al., in Controlled Fusion and Plasma Physics (Proc. 11th Europ. Conf. Aachen, 1983), Vol.2 (1983) 377.
[2] SHIMOMURA, Y., et al., Preprint IPP III/80 (1980).
[3] KEILHACKER, M., Fiz. Plazmy 9 (1983) 90.
[4] VANSTAIN, L.A., et al., Excitation of Atoms and Broadening of Spectral Lines, Moscow, Nauka, 1979 (in Russian).
[5] PETRAVIC, M., et al., in Plasma Physics and Controlled Nuclear Fusion Research 1982 (Proc. 9th Int. Conf. Baltimore, 1982), Vol.1, IAEA, Vienna (1983) 323.
[6] IGITKHANOV, Yu.L., USSR Contributions to Session Four of Phase Two A of INTOR Workshop (March 1982), Group B, VI-72.
[7] HARBOUR, P.J.H., MORGAN, J., NET Report, Part I (December 1982).
[8] ZHDANOV, V.M., YUSHMANOV, P.N., Applied Mathematics and Technical Physics, Vol.4 (1980) 24 (in Russian).
[9] NEUHAUSER, J., et al., Preprint IPP I/216 (1983).
[10] BOHDANSKY, J., J. Nucl. Mater. **93/94** (1980) 44.

APPLICATION OF TWO-DIMENSIONAL MODELLING TO SCRAPE-OFF AND SINGLE-NULL POLOIDAL DIVERTOR PLASMA OF INTOR

B.J. BRAAMS*, M.F.A. HARRISON,
E.S. HOTSTON, J.G. MORGAN
Culham Laboratory,
(Euratom/UKAEA Fusion Association),
Abingdon, Oxfordshire,
United Kingdom

Abstract

APPLICATION OF TWO-DIMENSIONAL MODELLING TO SCRAPE-OFF AND SINGLE-NULL POLOIDAL DIVERTOR PLASMA OF INTOR.

The outer divertor plasma of INTOR and its associated scrape-off plasma have been modelled using a two-dimensional code for transport of plasma energy and particles. It is envisaged that the single-null divertor will operate in a high recycling mode, and in this condition the predicted peak plasma temperatures at the target are $T_e \approx 30$ eV and $T_i \approx 25$ eV. These low values imply that target sputtering will be slight provided that a refractory metal such as tungsten is used. The predicted power loading of the target is ~ 22 MW/m^2 (in the direction normal to the magnetic surfaces), so that the loading could be reduced to an acceptable level (of about 5 MW/m^2) by inclination of the target. The exhaust pumping requirements for helium gas are predicted to be modest.

1. INTRODUCTION

Operation of the single-null divertor in a high recycling mode offers the potential advantages that the sputtering rate of target material is low and the exhaust of helium ash relatively easy [1]. Initial analyses, which were based on simple quasi-two-dimensional concepts of the boundary plasma, aroused concern that the thickness of the energy scrape-off layer would be so small that the divertor target power load would be excessive. In order to clarify these issues the present paper presents results derived from numerical two-dimensional modelling [2,3] of the boundary plasma for the specific case of the outer scrape-off and divertor regions of INTOR.

---

* FOM-Instituut voor Plasmafysica, Nieuwegein, Netherlands.

2. DESCRIPTION OF THE MODEL

A two-fluid description of the plasma electrons and ions is used as a basis for determining transport of energy and particles within the scrape-off and divertor regions. The two-dimensional description employs a pseudo-rectangular geometry with the x-axis along the magnetic field and the y-axis in the radial direction. The following system of equations governs the ion density n_i, the parallel flow velocity u, the radial diffusion velocity v, and the temperatures T_e and T_i.

Continuity:

$$\frac{1}{\sqrt{g}}\frac{\partial}{\partial x}\left(\frac{\sqrt{g}}{h_x}n_i u\right)+\frac{1}{\sqrt{g}}\frac{\partial}{\partial y}\left(\frac{\sqrt{g}}{h_y}n_i v\right)=S_n \tag{1}$$

Momentum balance:

$$\frac{1}{\sqrt{g}}\frac{\partial}{\partial x}\left(\frac{\sqrt{g}}{h_x}\rho u^2-\frac{\sqrt{g}}{h_x^2}\eta_x^i\frac{\partial u}{\partial x}\right)+\frac{1}{\sqrt{g}}\frac{\partial}{\partial y}\left(\frac{\sqrt{g}}{h_y}\rho v u-\frac{\sqrt{g}}{h_y^2}\eta_y^i\frac{\partial u}{\partial y}\right)$$
$$=S_{mu}-\frac{1}{h_x}\frac{\partial p}{\partial x} \tag{2}$$

Radial diffusion:

$$v=-\frac{D}{h_y}\frac{\partial}{\partial y}(\ln n_i) \tag{3}$$

Electron energy balance:

$$\frac{1}{\sqrt{g}}\frac{\partial}{\partial x}\left(\frac{\sqrt{g}}{h_x}\frac{5}{2}n_e u T_e-\frac{\sqrt{g}}{h_x^2}\kappa_x^e\frac{\partial T_e}{\partial x}\right)$$
$$+\frac{1}{\sqrt{g}}\frac{\partial}{\partial y}\left(\frac{\sqrt{g}}{h_y}\frac{5}{2}n_e v T_e-\frac{\sqrt{g}}{h_y^2}\kappa_y^e\frac{\partial T_e}{\partial y}\right)$$
$$=S_E^e-k(T_e-T_i)+\frac{u}{h_x}\frac{\partial}{\partial x}(n_e T_e)+\frac{v}{h_y}\frac{\partial}{\partial y}(n_e T_e) \tag{4}$$

Ion energy balance:

$$\frac{1}{\sqrt{g}}\frac{\partial}{\partial x}\left[\frac{\sqrt{g}}{h_x}\left(\frac{5}{2}n_i u T_i+\frac{1}{2}\rho u^3\right)-\frac{\sqrt{g}}{h_x^2}\left(\kappa_x^i\frac{\partial T_i}{\partial x}+u\eta_x^i\frac{\partial u}{\partial x}\right)\right]$$
$$+\frac{1}{\sqrt{g}}\frac{\partial}{\partial y}\left[\frac{\sqrt{g}}{h_y}\left(\frac{5}{2}n_i v T_i+\frac{1}{2}\rho v u^2\right)-\frac{\sqrt{g}}{h_y^2}\left(\kappa_y^i\frac{\partial T_i}{\partial y}+u\eta_y^i\frac{\partial u}{\partial y}\right)\right]$$
$$=S_E^i+k(T_e-T_i)-\frac{u}{h_x}\frac{\partial}{\partial x}(n_e T_e)-\frac{v}{h_y}\frac{\partial}{\partial y}(n_e T_e) \tag{5}$$

The parameters $\sqrt{g}$, h_x and h_y are metric coefficients. If $\sqrt{g}$ and h_x are constant but h_y is a function of x, then the width of the scape-off layer varies with x but the flow experiences no change in area. The coordinate system may be curvilinear although it must be orthogonal. S_n, S_{mu} and S_E^e and S_E^i are volume sources of ions, momentum and electron and ion energy; also $\rho = m_i n_i$, $n_e = Z_i n_i$ and $p = n_e T_e + n_i T_i$. For a deuterium-tritium plasma $m_i = 2.5 \times m_p$ and $Z_i = 1$.

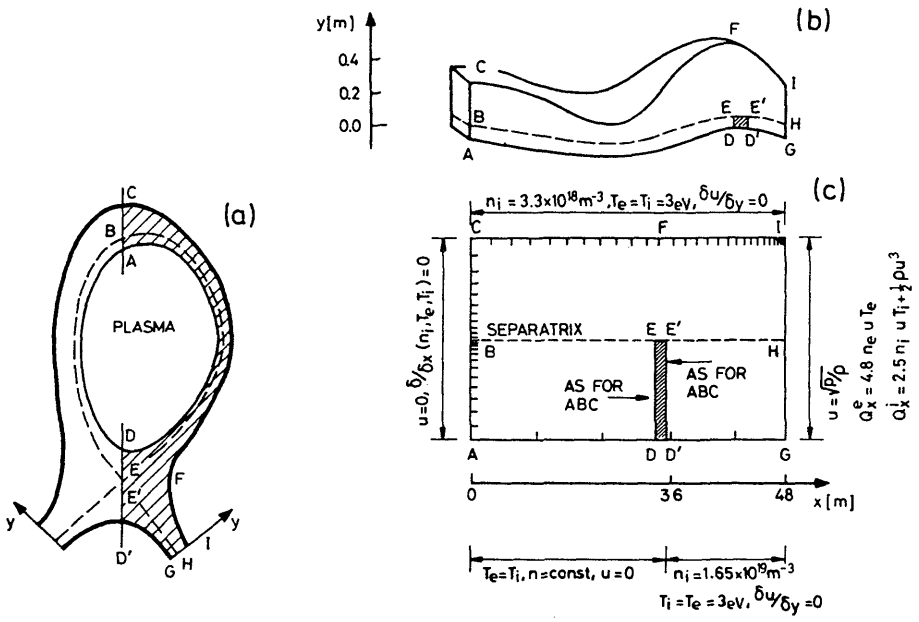

FIG.1. The two-dimensional geometry and boundary conditions used to model the outer divertor and scrape-off plasma of INTOR. (a) is a view in the poloidal plane; the symbols are explained in the text. (b) illustrates the variation of the cross-section of the flow channel as a function of distance x along the magnetic field, and (c) illustrates the pseudo-rectangular geometry used in the computation.

Classical values are assumed for the parallel transport coefficients, η_x^i, κ_x^e and κ_x^i, and also for the equipartition coefficient k. The coefficients for radial transport, η_y^i, D, κ_y^e and κ_y^i, are in the present paper assumed to be anomalous; their values are $\eta_y^i/\rho = 0.2\,\mathrm{m^2 s^{-1}}$, $D = 1.0\,\mathrm{m^2 s^{-1}}$, $\kappa_y^e/n_e = 2.0\,\mathrm{m^2 s^{-1}}$ and $\kappa_y^i/n_i = 0.2\,\mathrm{m^2 s^{-1}}$.

3. APPLICATION TO INTOR

Figure 1(a) illustrates the regions of the outer scrape-off and divertor plasma which are considered in the present study, and Figure 1(c) illustrates the geometry, mesh and boundary conditions employed. The modelled boundary region lies outboard of AG, the magnetic separatrix is represented by B(E/E')H; the null point is at (E/E'); the divertor target lies along GHI and the upstream stagnation region for fluid flow is ABC. The region of main plasma inboard of the separatrix is isolated from the corresponding region within the divertor chamber by a barrier of insulating cells DEE'D'. The outer extremity of the

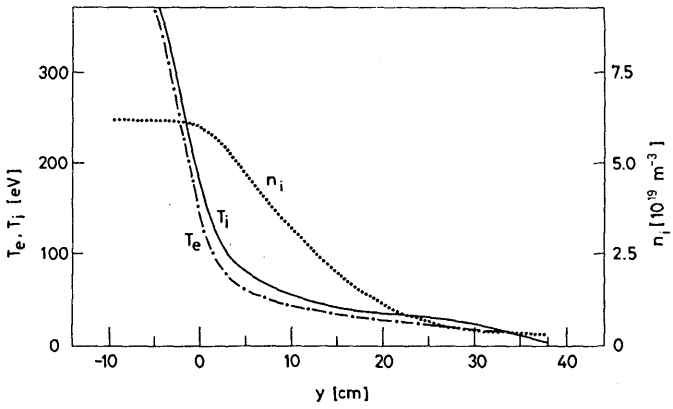

FIG.2. Radial profiles of T_e, T_i and n_i at the flow stagnation region ABC.

plasma (i.e. the first wall) lies along CFI, and variation in separatrix-wall spacing is allowed for in the manner illustrated in Figure 1(b).

The model requires prescribed boundary values of input power flux and plasma density. It is assumed that half of the non-radiated power losses from the main INTOR plasma (i.e. 40 MW) are transported uniformly across the interface AD; electron transport is 37 MW and ion transport is 3 MW. Recycling of plasma at the divertor target is modelled in a simple but reasonable manner. The total ion flux to the target $\Sigma\Gamma(y)$ is distributed as atoms amongst the mesh cells within the divertor (i.e. within the volume defined by DEFIHG) according to a weighting determined by $[n_e S_{CR}(T_e)]$, where n_e and T_e are determined by the plasma parameters within each cell and $S_{CR}(T_e)$ is the collisional radiative ionisation rate coefficient. Allowance is made for the energy reflection of the plasma ions incident upon the tungsten target. A recycling coefficient R is chosen so that the rate of particle loss at the target (which is equal to the input of particles across the separatrix) corresponds to 20 to 50 times the α-particle production rate in INTOR, i.e. $R\Sigma\Gamma(y) \sim$ (0.4 to 1) x 10^{22} DT atoms/s. Plasma density at the interface (AD) is selected so that the density at the separatrix (BE) lies in the range (0.5 to 1) x $10^{20}/m^3$.

4. RESULTS

Radial profiles of the plasma parameters at the stagnation region ABC are shown in Figure 2. At the separatrix $T_e \approx 130$ eV, $T_i \approx 170$ eV and $n \approx 6 \times 10^{19}/m^3$. These values can be regarded as typical for INTOR when the divertor operates in a high recycling regime. The plasma temperature close to the

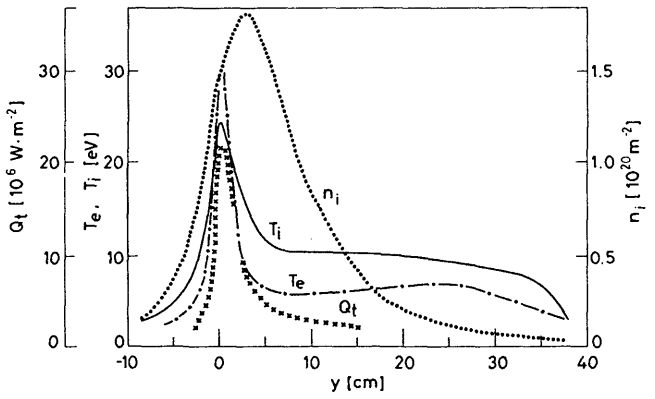

FIG.3. Radial profiles of T_e, T_i, n_i and deposited power Q_t at the target GHI.

divertor target is substantially less than that within the scrape-off region. The radial profiles at the target are shown in Figure 3; the peak temperatures are $T_e \approx 30$ eV, and $T_i \approx 25$ eV. The peak plasma density is about $1.8 \times 10^{20}/m^3$ and is displaced about 3 cm radially outboard of the temperature peaks. At such low temperatures, sputtering of tungsten by DT ions is small if not negligible. The peak of the power density deposited upon the target is about 22 MW/m^2 when the target lies normal to the magnetic surfaces, i.e. in the direction y in Figure 1(a). Power density is strongly peaked; the full width at the half height of the profile is about 3 cm. Even though the energy scrape-off is thin, the peak power load could be reduced to an acceptable level (< 5 MW/m^2) by inclining the target to the magnetic surfaces. The recycling coefficient at the target required for the prescribed throughput of plasma particles is R = 0.995, which implies that only 5×10^{-3} of the incident ions need be pumped, and so the pumping speed required to exhaust helium is not excessive.

REFERENCES

[1] HARRISON, M.F.A., HOTSTON, E.S., Culham Lab. Rep. CLM-R 226 (1982).

[2] BRAAMS, B.J., in Controlled Fusion and Plasma Physics (Proc. 11th Europ. Conf. Aachen,1983), Vol.2 (1983) 431.

[3] BRAAMS, B.J., HARBOUR, P.J., HARRISON, M.F.A., HOTSTON, E.S., MORGAN, J.G., J. Nucl. Mater. **121** (1984) 75.

PERFORMANCE ANALYSIS OF JT-60 PLASMA WITH POLOIDAL DIVERTOR

M. AZUMI, K. SHIMIZU, T. HIRAYAMA, T. TAKIZUKA,
M. SUGIHARA, S. SAITO, H. SHIRAI, K. TANI,
M. NAKANISHI, H. KIMURA, T. IMAI, Y. SHIMOMURA
Japan Atomic Energy Research Institute,
Ibaraki-ken, Japan

Abstract

PERFORMANCE ANALYSIS OF JT-60 PLASMA WITH POLOIDAL DIVERTOR.

Characteristics of JT-60 plasma with poloidal divertor are studied by means of a tokamak transport code combined with a two-point divertor code. An ideal divertor-tokamak plasma is shown to be obtained at relatively high density operation with $\bar{n}_e > 10^{20}\,m^{-3}$ in JT-60.

1. INTRODUCTION

JT-60 is a hydrogen tokamak device completed in summer 1984 with the objectives of producing reactor-grade plasmas and investigating their physical and technological aspects relevant to fusion reactor development [1]. Targets of plasma parameters are set in the range $\bar{T} = 5-10$ keV and $\bar{n}\tau_E = (2-6) \times 10^{19}\,m^{-3}\cdot s$ with a long duration of 5–10 s. To obtain these parameters, JT-60 has a large heating power. The maximum input energy is about 500 MJ and the total number of particles injected by the neutral beam is about 2×10^{22} atoms during a 10 s discharge. Control of impurity, heat and particles is therefore very important.

In a conventional limiter discharge, a large part of the heating power has to be radiated by impurities in a steady state. Self-consistent transport studies of the metal limiter discharge show that the main plasma is heavily contaminated by metal impurities and no reactor-grade plasma will be obtained [2]. Control of heat and particles is also very difficult in conventional limiter discharge, and a compact poloidal divertor has therefore been installed in JT-60.

The poloidal divertor is a promising method for impurity control and is capable of controlling the heat and the particles in the divertor chamber. The characteristics of divertor plasmas were numerically investigated by means of a fluid model [3], and it was suggested that an ideal divertor plasma, i.e. a cold, dense plasma, would be expected with high particle flux in JT-60. However, the relation between the divertor plasma and the main plasma is not clear. In this paper, we study numerically and consistently both the divertor plasma and the

main plasma and investigate the possibility of an ideal divertor-tokamak plasma, i.e. a hot, clean main plasma connected with a cold, dense divertor plasma.

2. SIMULATIONS

To study the interaction between the main plasma and the divertor plasma, transport in the scrape-off layer plasma was included in a one-dimensional transport code. In the scrape-off layer, the Bohm-type diffusion $D = \alpha T_e/16B$ was employed as the radial diffusion, where the MKS-eV unit system was used. The coefficient α is changed from 0.1 to 0.5 and a small change was observed in plasma parameters in the scrape-off layer so that α is fixed at a value of 0.2 in the following calculations. The heat flux along the field line, or the heat flux into the divertor chamber, was evaluated by using collisional heat conduction parallel to the magnetic field, i.e. $q_{\parallel} = k_{\parallel 0}(T^{3.5} - T_D^{3.5})/L_D$, where T_D and L_D are the electron temperature in front of the divertor plate and the length of the magnetic field line in the divertor chamber, respectively, and $k_{\parallel 0} = 6 \times 10^2$ W · $m^{-1} \cdot eV^{-3.5}$. The particle flux along the field line is expressed by $f_{\parallel} = v_{\parallel} n_e$, where $v_{\parallel}$ is the parallel flow velocity at the divertor throat. This flow velocity $v_{\parallel}$ has to be given consistently with the divertor plasma. For this purpose, a two-point divertor code was combined with the transport code. In this code, the plasma parameters at both throat and divertor plate are calculated by

$$v_{\parallel} = C_D \left[R - \sqrt{R^2 - T_{th}/T_D}\right]$$

$$T_{th} = \left[T_D^{7/2} + L_{Dq\parallel}/k_{\parallel 0}\right]^{2/7}$$

$$T_D = 1/\gamma \left[q_{\parallel}/Rf_{\parallel} - E_{rad}(R-1)/R\right]$$

where T_{th}, T_D, C_D and E_{rad} are electron temperatures at the divertor throat and in front of the divertor plate, the sound velocity ($C_D = \sqrt{2T_D/M_i}$) and the radiation energy, respectively, and $\gamma = 7.8$. R is the particle flux multiplication factor, which is evaluated by the ionization mean free path λ_{ion} of the neutral particle in front of the divertor plate. Dependence of R on λ_{ion} changes by the geometry of the divertor and the recycling condition of neutrals in the divertor chamber, and we used the results of detailed analysis by a two-fluid divertor code [4]. This scheme is very efficient and shows good agreement with results of the divertor code in the wide range of particle and heat flux into the divertor.

Figure 1 shows typical time evolution of the main plasma and the divertor plasma. Average density in the main plasma is raised from 5×10^{19} m^{-3} in the Ohmic heating phase to 1.0×10^{20} m^{-3} or 1.4×10^{20} m^{-3} by gas-puffing and neutral beam injection and is then controlled at a constant value. The relatively low density operation with average density 10^{20} m^{-3} gives a rather high temperature

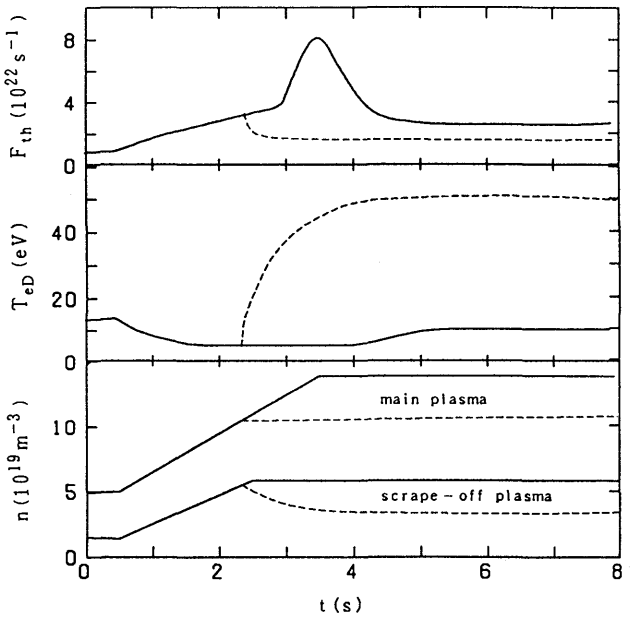

FIG. 1. Time evolution of total particle flux into the divertor F_{th}, electron temperature in front of the divertor plate T_{eD}, and average density in main plasma $\bar{n}$ and scrape-off plasma $\bar{n}_s$, for $\bar{n} = 1.4 \times 10^{20}\,m^{-3}$ (solid lines) and $\bar{n} = 1.0 \times 10^{20}\,m^{-3}$ (dashed lines). Additional heating starts at $t = 0.5$ s and the following transport coefficients are assumed: $\chi_e = 7.5 \times 10^{19}/n_e$ [m^2/s], $\chi_i = 3\chi_{NEO}$ and $D = \chi_e/6$.

of 50 eV in front of the divertor plate in the steady state, as shown by dashed lines in Fig. 1. The average ion temperature $\bar{T}$ is 6 keV, with $\bar{n}\tau_E = 5 \times 10^{19}\,m^{-3}\cdot s$. To achieve an ideal divertor plasma, a high plasma density is required, as shown by the solid line in Fig. 1. In this case, the density in the scrape-off layer or at the divertor throat increases monotonically with the main plasma density, while the particle flux into the divertor remains at a low level. After the cold and dense plasma in front of the divertor plasma has been established, the density in the scrape-off layer saturates, while the particle flux into the divertor increases rapidly. This high particle flux is supplied mainly from the ionization of recycled and gas-puffed neutral particles in the scrape-off plasma. In the phase of constant density, gas-puffing in the main chamber is reduced and the particle flux into the divertor decreases to $2.5 \times 10^{22}\,s^{-1}$ from the maximum value of $8 \times 10^{22}\,s^{-1}$. The density in the scrape-off layer, however, changes little and cold, dense plasma is still observed in the steady phase. Figure 2 shows radial profiles of electron and ion temperature and electron density at the steady state with $\bar{n}_e = 1.4 \times 10^{20}\,m^{-3}$. The heat flux to the divertor is localized in the thin layer with half-width of about 0.2 cm, while the particle flux density has a broad profile.

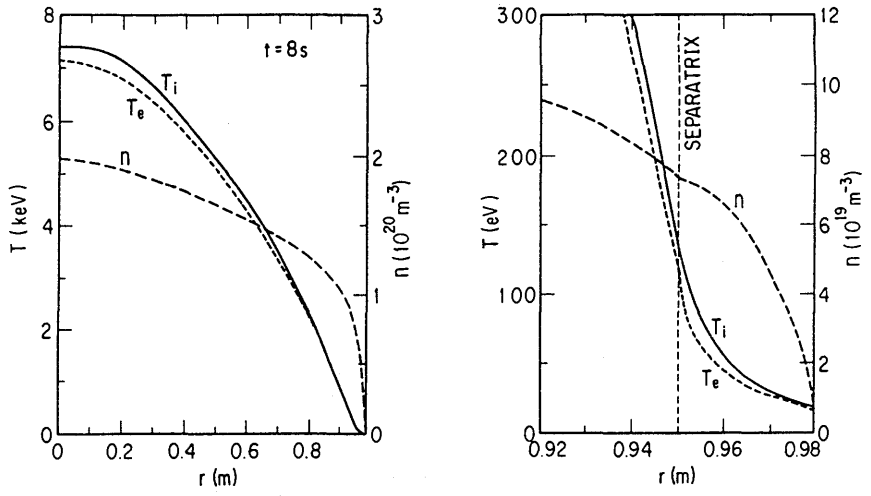

FIG.2. Radial profiles of ion temperature (solid lines), electron temperature (short dashed lines) and electron density (long dashed lines) in main plasma and scrape-off layer for $\bar{n} = 1.4 \times 10^{20}\, m^{-3}$.

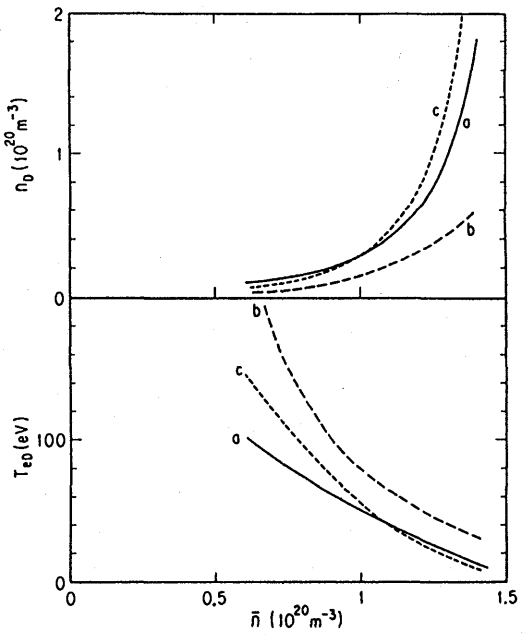

FIG.3. Dependence of electron temperature T_{eD} *and electron density* n_D *in front of the divertor plate on average density in the main plasma* $\bar{n}$ *for different diffusion coefficients in the main plasma. Curve (a)* $D = 1.25 \times 10^{19}/n_e\ [m^2/s]$; *curve (b)* $D = 8.0 \times 10^{18}/n_e\ [m^2/s]$; *and curve (c)* $D = 4.8 \times 10^{20}/n_e \sqrt{T_e}\ [m^2/s]$.

In this study, a rather conservative transport is employed, as shown in Fig.1. A cold, dense divertor plasma is also obtained with different transport, e.g. $D \geqslant 3 \times 10^{20}/n_e\sqrt{T_e}$ [m^2/s] and $D \geqslant 8 \times 10^{18}/n_e$ [m^2/s]. The dependence of electron temperature and density in front of the divertor plate on the average density in the main plasma is summarized in Fig.3. Improved particle confinement in the main plasma requires higher average density in the main plasma for the cold, dense divertor plasma. Threshold density can, however, be reduced by control of the divertor configuration and by gas-puffing directly into the divertor chamber. The effects of divertor conditions on the main plasma were also investigated. The temperature of the main plasma is not affected directly by the divertor plasma owing to the good thermal conduction along the field line, while the divertor condition changes the scrape-off plasma density and affects overall particle confinement in the main plasma.

3. CONCLUSIONS

The main plasma and the divertor plasma were investigated consistently and it has been shown that an ideal divertor-tokamak plasma can be achieved with relatively high density operation in JT-60. This high density operation is reasonable in JT-60 because of the high quality of its neutral beams with an accelerated voltage of 100 keV [5]. Other operating regions with high temperature and low density in the divertor plasma are also interesting, but careful study is needed of the effects of impurity production from the divertor plate and deformed distribution functions of electrons and ions [6].

REFERENCES

[1] OGATA, A., ANDO, T., Nucl. Fusion **20** (1980) 1471.
[2] SHIMOMURA, Y., SHIMIZU, K., HIRAYAMA, T., AZUMI, M., NINOMIYA, H., JT-60 Program, to be published in J. Nucl. Mater.
[3] SEKI, S., et al., J. Nucl. Mater. **121** (1984) 422.
[4] SAITO, S., SUGIHARA, M., FUJISAWA, N., J. Nucl. Mater. **121** (1984) 199.
[5] OKUMURA, Y., et al., Paper No.IAEA-CN-44/H-I-5-2, these Proceedings, Vol.3.
[6] TAKIZUKA, T., TANI, K., AZUMI, M., SHIMIZU, K., Particle simulation of divertor plasma, to be published in J. Nucl. Mater.

DISCUSSION

ON PAPERS IAEA-CN-44/E-II-5-1 TO E-II-5-4

F.W. PERKINS: Did the ASDEX divertor simulation deal with the extraordinarily rapid change in divertor states which is observed experimentally?

M.F.A. HARRISON: No, this work did not consider the fluctuating divertor condition observed in the H-mode in ASDEX.

R.W. CONN: Is there any evidence that the distribution function underlying the fluid equations might be anisotropic? We have heard one presentation which purports to explain the H-mode and which relies heavily on trapping and so on, but if the distribution function is anisotropic, problems will arise with the equations you are using.

M.F.A. HARRISON: That is a very valid point. Since, in fact, one of the most dominant parameters is electron parallel conduction, anisotropy in the electron energy distribution, in particular, will have a powerful effect. All I can say at the moment is that this question is being looked into.

M. SHIMADA: Do any of the papers you have presented consider radiation loss (as a result either of hydrogen or of impurities) in a manner consistent with plasma parameters?

M.F.A. HARRISON: Yes, hydrogen radiation and charge-exchange are taken into account, as are the effects of molecular hydrogen. Impurity radiation is not considered in these papers, but it has been included in comparable studies of impurity transport using 1-D fluid models.

Y.-K.M. PENG: Would you comment on the extent of impurity modelling in the studies you have presented?

M.F.A. HARRISON: The charge state history of carbon sputtered from the divertor plate is modelled and related to the entrainment of the impurity ions within the background hydrogen plasma which drifts towards the target. Friction forces drive the ions back to the target but are opposed by thermal forces in the direction of regions of higher ion temperature. The results of Igitkhanov, in particular, favour the dominance of friction, whereby impurities would tend to be retained within the divertor.

DRIFT WAVE TRANSPORT, SAWTOOTH RELAXATIONS, HEAT PULSE PROPAGATION AND DENSITY LIMIT

A. ROGISTER, G. HASSELBERG,
A. KALECK, F. WAELBROECK
Institut für Plasmaphysik,
Kernforschungsanlage Jülich,
Association Euratom-KFA, Jülich,
Federal Republic of Germany

Abstract

DRIFT WAVE TRANSPORT, SAWTOOTH RELAXATIONS, HEAT PULSE PROPAGATION AND DENSITY LIMIT.

It is proposed that a single hypothesis coherently explains the tokamak temperature profiles, the origin of sawtooth relaxations, the rapid propagation of the heat pulse generated by these sawteeth, and the density limit. A theoretical model of drift wave turbulence which suggested this hypothesis is reviewed. Finally, the reality of toroidicity-induced modes is commented upon.

1. INTRODUCTION

1.1. Purpose of the work

We intend to show that a single hypothesis leads to a coherent interpretation of:

(a) Tokamak temperature profiles (given the density profiles);
(b) The origin and, partly, the mechanism of sawtooth relaxations;
(c) The rapid propagation of the heat pulses generated by these sawteeth; and
(d) The high density limit.

This hypothesis is as follows:

The anomalous electron heat conductivity χ_e increases rapidly with respect to the linear growth rate γ of the instability which is held responsible for the anomaly (more precisely, with respect to the electron destabilizing contribution γ_e to γ).

This can be mathematically formulated as follows:

$$\frac{\Delta \ln \chi_e}{\Delta \ln \gamma_e} \gg 1 \qquad (1)$$

The nature of the instability – the slab branch of the dissipative trapped electron mode – is inferred from the measured profiles.

1.2. A theoretical model

A theoretical model of the non-linear saturation of drift instabilities developed by two of us [1] predicts such a rapid increase of the anomalous electron heat conductivity [2] and, moreover, explains well some characteristics of the observed turbulence spectra and the reduced confinement time of impurities [3] (see Section 3). The idea that the phenomena (a)–(d) have a common denominator arose here, but we want to emphasize that they logically follow from the hypothesis (1) independently of the details of the saturation and transport mechanisms (electrostatic or electromagnetic, across or along the lines of force).

1.3. Toroidicity-induced modes

The hypothesis (1) would not be consistent with the occurrence of thresholdless instabilities (see Section 4) such as the toroidicity-induced branch of the drift mode. We argue that the plasma profiles we have examined are not favourable to the occurrence of these waves, and, more important, that the toroidicity-induced modes are eigenfunctions of the linear theory only [4]. Non-linear mode interaction should thus to some extent restore the shear-induced threshold.

2. CONSEQUENCES OF A RAPIDLY INCREASING χ_e (γ_e)

Starting from the hypothesis that the anomalous electron heat conductivity χ_e increases rapidly in comparison to γ_e, we back up and discuss at greater length the four consequences briefly mentioned in Section 1.1.

2.1. Relaxation of the temperature profiles

The postulated rapid increase of χ_e with γ_e implies that even a moderate instability will lead to large energy transport. Theory shows that the latter will usually react on the profile and tend to reduce the linear growth rate. This scheme is consistent with the results of an analysis we have performed of the

plasma observed in various discharges from the Frascati Tokamak (FT) and the Tokamak Fontenay-aux-Roses (TFR), showing that the profiles are close to marginal instability with respect to the dissipative trapped electron mode over a broad annular region excluding the central core and the plasma periphery (Manheimer and Antonsen had previously arrived at a similar conclusion [5]).

The observed quasi-relaxation of the profiles in turn implies:

(a) The slab branch of the dissipative trapped electron mode plays an unquestionable role in the transport of the plasma.
(b) The commonly used modelling in numerical codes of the anomalous heat conduction coefficient by a smooth function of plasma parameters is inadequate since χ_e undergoes an almost sudden jump as the instability threshold is crossed.
(c) The scaling of the electron energy confinement time $\tau_{E,e}$ should not be sought in relation to the local χ_e, which is poorly defined in terms of the plasma parameters, but rather should be obtained globally from the marginal stability profile.

2.2. Origin of the sawtooth oscillations

The trapped electron mode is stable in the centre of the discharge. Thus, if energy balance cannot be achieved by neoclassical ion transport, the core will heat up until ineluctably another instability, capable of expelling the energy, is excited. This other instability appears experimentally as an $m = \ell = 1$ tearing mode which is driven in the system as the safety factor on axis q_0 falls below unity. The tearing mode gives birth in its non-linear stage to a growing magnetic island which short-circuits the transport across the nested unperturbed magnetic surfaces, thus, according to Kadomtsev [6], triggering the sawtooth relaxation.

We think this model is only partly correct. To explain the sudden burst of energy out of the core and its rapid propagation to the plasma edge, it should further be necessary that the expanding magnetic island reaches the layer where the trapped electron transport is capable of convecting away the released energy. Our point of view is clearly consistent with the observation [7] that the amplitude and period of the sawteeth increase with increasing plasma density. The latter, indeed, by reducing the destabilizing rate of the trapped electrons, enlarges the stable central layer and improves the thermal insulation of the core.

2.3. Propagation of the heat pulse

The front of the heat pulse expelled from the core destabilizes further the trapped electron mode by increasing the local temperature and temperature gradient along its path. The hypothesis of Section 1.1 then suggests that the pulse is able to adjust its propagation through the plasma according to the

relation which links the anomalous heat conductivity and the linear growth rate, much as a collisionless shock wave fixes its own dissipation rate. To verify these ideas quantitatively, we have performed numerical simulations of sawtooth relaxations whereby the electron heat conduction coefficient within the q = 1 surface was suddenly raised to $(0.5-1) \times 10^5$ cm^2/s as q_0, the safety factor on axis, reached 0.8. In these calculations the density profile was frozen, the ion neoclassical heat conductivity was taken from Hinton and Hazeltine [8], and the anomalous electron heat conductivity was assumed to be of the form [2]:

$$\chi_e \propto \left(\frac{m_e}{m_i}\right)^{1/2} \nu_e^{*-1}\, b(\nu_e^{*1/2})\, \frac{a_s^2\, c_s}{|L_s|}\, G_1 \tag{2}$$

(L is the shear length; c_s is the sound speed; $a_s = c_s/\Omega_i$; Ω_i is the ion gyrofrequency; ν_e^* is the electron collisionality parameter; b characterizes the number of electrons which are able to bounce between the mirrors without experiencing a collision), where the function

$$G_1 = \exp(\lambda\gamma) - 1 \text{ if } \gamma \geqslant 0;\ G_1 = 0 \text{ if } \gamma \leqslant 0 \tag{3}$$

simulates the fast increase of the anomalous transport with the linear growth rate.

Figures 1 and 2 demonstrate well the propagation of the temperature pulse and the locally enhanced heat conduction and heat flux. Although the temperature increase is only about 5% at the normalized radius $\rho = r/a = 0.5$, the heat conductivity and the heat flux jumps are more than twice their 'background' values. This result cannot be explained by the $T^{7/2}$ dependence of the coefficient of G_1 in Eq.(2) but only by the rapid increase with temperature, similar to Eq.(1), of the chosen function $G_1(\gamma)$.

Consider the one-dimensional heat equation:

$$\frac{3}{2}\frac{\partial T_e}{\partial t} = \frac{\partial \chi_e}{\partial r}\frac{\partial T_e}{\partial r} + \chi_e \frac{\partial^2 T_e}{\partial r^2} \tag{4}$$

The second term in the right-hand side describes the spreading of the temperature pulse in the moving frame. The first term yields the outward propagation velocity:

$$v = -\frac{2}{3}\frac{\partial \chi_e}{\partial r} \tag{5}$$

At the normalized radius $\rho = 0.65$, we estimate the heat conductivity jump $\Delta\chi_e = 9 \times 10^3$ cm^2/s and the thickness of the wave front $\Delta r = v\Delta t$ where $\Delta t \lesssim 10^{-4}$ s (see Fig.2(a)). Hence $v \gtrsim 0.8 \times 10^4$ cm/s; this propagation velocity is consistent with the value directly estimated from Fig.2 ($v_p \cong 2 \times 10^4$ cm/s).

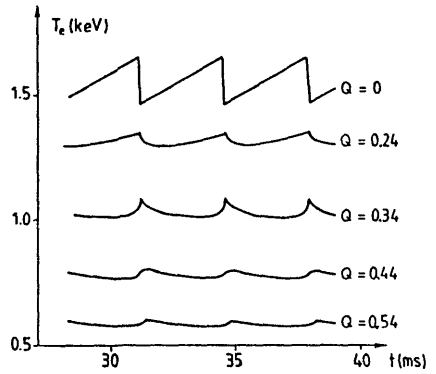

FIG.1. Temperature pulse following sawtooth (excited as $q_0 = 0.8$). Discharge parameters $N_0 = 0.75 \times 10^{14}$ cm^{-3}, $B = 40$ kG, $I_p = 0.2$ MA, $Z_{eff} = 2.5$.

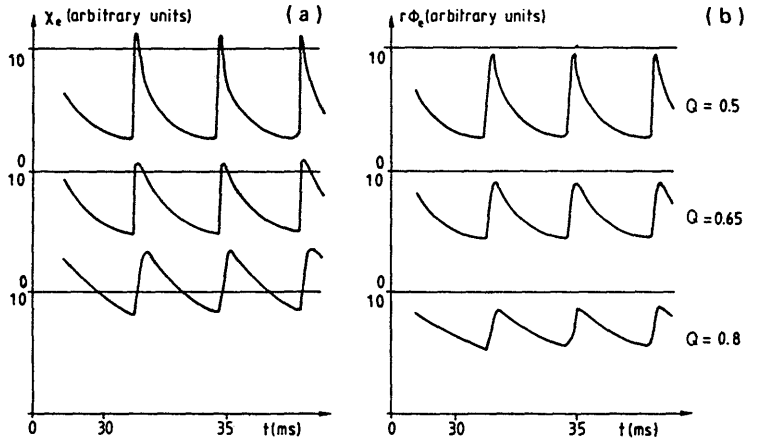

FIG.2. Heat conductivity χ_e and heat flux $r\phi_e$ following sawtooth (same discharge as in Fig.1).

The foregoing suggests that it would be difficult to explain large convection velocities if the heat conductivity χ_e were not a rapidly increasing function of the linear growth rate (we have checked this by freezing χ to its pre-relaxation value and also by decreasing the value of the parameter λ entering G_1 by a factor 2).

It is interesting to note that the calculation leading to Figs 1 and 2 were made with the value of λ derived from the theory presented in Section 3 and Ref.[1]. The corresponding propagation time of the pulse to the plasma edge is of the order of 1.5 ms, which is in good agreement with the experimental data from TFR [9] and FT [10].

2.4. The high density limit

As the mean plasma density increases and the trapped electron mode becomes more stable, it becomes more difficult for the heat pulse generated in the core to make its way to the plasma edge. The quenching of the drift instability and the related clamping of the heat outflow should then lead to overheating of the core, cooling of the periphery, contraction of the current channel and a steepening in the radial gradient of current density, all events which appear to be correlated with the onset of disruptions. Whichever of these phenomena is the *channel* through which the latter is triggered, the ultimate *cause* appears to be the quenching of the trapped electron mode instability. If this is indeed the case, then the high density limit should be obtainable, in particular, from drift stability considerations. It has been shown in Ref.[2] that these yield the following expression for $(N_0)_{max}$ (the subscript 0 refers to the magnetic axis):

$$(N_0)_{max} = 4.2 \times 10^{10} \frac{a^{1/2}}{R^{1/6} A_i^{1/2}} \left(\frac{BZ_{eff}}{q_0 RV} \right)^{4/3} \frac{\mu F(a/q_a R)}{1 + Z_{eff}} \qquad (6)$$

Theoretical evaluations yield the value $\mu \cong 1$. The functional $F \cong 1$ depends on the assumed density and temperature profiles in the predisrupted plasma. A_i is the base ion atomic mass and the units are [V] = V, [B] = G, [L] = cm. Numerically we find $(N_0)_{max} = 2.1 \times 10^{14}$ cm^{-3} if $Z_{eff} = V = 2$, $A_i = 1$, $q_a = 3$, $B_t/q_0 = 5 \times 10^4$, $a = 20$, $R = 10^2$.

This result is very satisfactory in view of TFR performances. Note also that $(N_0)_{max}$ is proportional to the 4/3 power of the current density on axis, which experimentally is likely not to be distinguishable from the Murakami empirical scaling [11].

3. A THEORETICAL MODEL FOR DRIFT WAVE SATURATION AND TRANSPORT

We have proposed [1] that Compton scattering and ion-induced scattering are the dominant non-linear stabilization mechanism of drift instabilities. Both local and non-local energy transfer in k-space have to be considered, given the form of the dispersion relation. Non-local transfer, which we found to deplete the long wavelength spectrum and to fill the short wavelengths, explains well the position of the maximum of the observed spectra [12]; local transfer, or energy cascade, provides the correct spectral index at high mode numbers for the low ion temperature plasma of Macrotor [13]. On the whole, however, agreement with the observed spectra is not very satisfactory; we feel that the discrepancy may arise from a mathematical simplification made in the theory which consists in assuming $T_i \ll T_e$.

As mentioned earlier, the electrostatic transport calculated on the basis of these theoretical spectra is indeed a rapidly increasing function of the linear growth rate; the results obtained with this theoretical model have led us to formulate the hypothesis (1) independently of the details of the saturation and transport theories.

Finally, it is interesting to note that the anomalous impurity transport calculated from the theoretical spectra [3] agrees well with the conclusions from impurity injection experiments [14, 15] in that the self-diffusing part of the impurity flux, which is proportional to the impurity density gradient, increases roughly ten times with respect to its neoclassical value. In contrast, the frictional part of the flux ($\propto n_I \partial n_i/\partial r$) is hardly of the order of the neoclassical one. During the abrupt decay of the sawteeth (according to our calculations) the anomalous impurity diffusion coefficients should increase even more dramatically than the electron heat transport coefficient, which is consistent with the observed, but not understood, cleaning action of these sawteeth.

4. TOROIDICITY-INDUCED MODES

We have developed the idea that the plasma remains in the vicinity of the marginally unstable state corresponding to the threshold of the slab branch of the dissipative trapped electron mode. As this mode also has a toroidicity-induced branch with no threshold (actually its threshold corresponds to much weaker plasma performances), some additional comments are necessary in order to justify various aspects of this work.

First, we have verified [2] on three experimental profiles that the conditions to be satisfied for the toroidicity-induced branch to exist in the strong coupling limit were far from being met. These conditions may be described by the inequality:

$$\frac{(1+y)^2}{y^2} \ll \frac{q^2 \hat{\sigma}^2}{\epsilon_N^2} \left(\frac{|\epsilon_N|\,|1-2\,\hat{\sigma}|}{\hat{\sigma}^2} \frac{1+y}{y} - 1 \right) \qquad (7)$$

where $\epsilon_N = L_N/R$; L_N is the density length-scale; $y = k_\theta\, a_s$; k_θ is the poloidal mode number and $\hat{\sigma}$ is the shear parameter.

Secondly, we argue that the concept of toroidicity-induced eigenmodes is purely linear since it relies on the equal spacing $\Delta\ell$ between the rational surfaces corresponding to a given toroidal mode number ℓ. Since $\Delta\ell \propto 1/\ell$, the concept necessarily breaks down in non-linear theory. This simple argument suggests that these potentially most dangerous modes will disintegrate and their ballooning character will weaken as the amplitude increases. The non-linear interaction could in this way partly restore the shear damping, justifying here also the marginal instability picture [4].

REFERENCES

[1] ROGISTER, A., HASSELBERG, G., Phys. Rev. Lett. **48** (1982) 249; Phys. Fluids **26** (1983) 1467.
[2] HASSELBERG, G., ROGISTER, A., Nucl. Fusion **23** (1983) 1351.
[3] ROGISTER, A., HASSELBERG, G., Nucl. Fusion **23** (1983) 1455.
[4] ROGISTER, A., HASSELBERG, G., submitted to Plasma Phys. Controll. Fus.
[5] MANHEIMER, W.M., ANTONSEN, T.M., Phys. Fluids **22** (1979) 957.
[6] KADOMTSEV, B.B., Fiz. Plazmy **1** (1975) 710.
[7] EQUIPE TFR, Nucl. Fusion **20** (1980) 1227.
[8] HINTON, F.L., HAZELTINE, R.D., Rev. Mod. Phys. **48** (1976) 239.
[9] EQUIPE TFR, "A turbulent mechanism to explain sawtooth activity and disruptions in TFR 600", Plasma Physics and Controlled Nuclear Fusion Research 1982 (Proc. 9th Int. Conf. Baltimore, 1982), Vol.3, IAEA, Vienna (1983) 383.
[10] ALLADIO, F., private communication, 1983.
[11] MURAKAMI, M., CALLEN, J.D., BERRY, L.A., Nucl. Fusion **16** (1976) 347.
[12] MAZZUCATO, E., Phys. Rev. Lett. **48** (1982) 1828.
[13] SEMET, A., et al., Phys. Rev. Lett. **45** (1980) 445.
[14] MARMAR, E.S., et al., Phys. Rev. Lett. **45** (1980) 2025.
[15] EQUIPE TFR, Phys. Lett. **87A** (1982) 169.

ON LIMITING PLASMA PRESSURES AND MHD STABILITY IN TOKAMAKS

L.M. DEGTYAREV, V.V. DROZDOV,
A.A. MARTYNOV, S.Yu. MEDVEDEV
M.V. Keldysh Institute of Applied Mathematics,
USSR Academy of Sciences,
Moscow

A.G. KIROV, M.A. STOTLAND
I.N. Vekua Institute of Physics and Technology,
Sukhumi

Union of Soviet Socialist Republics

Presented by B.B. Kadomtsev

Abstract

ON LIMITING PLASMA PRESSURES AND MHD STABILITY IN TOKAMAKS.

PART A. A technique for determining the pressure distributions over magnetic surfaces limited by ideal-MHD stability is proposed. The limiting tokamak plasma β-values are calculated for different plasma geometries and safety factors at the boundary.

PART B. The results of numerical studies on the stability of ballooning helical and tearing modes in a tokamak plasma with hollow current profile are given.

PART A. ON LIMITING PLASMA PRESSURES IN TOKAMAKS (L.M. Degtyarev, V.V. Drozdov, A.A. Martynov, S.Yu. Medvedev)

1. A number of computational codes [1–3] have been developed by now to calculate the MHD stability of plasma in tokamaks. The limiting β-values and their dependence on the plasma parameters were investigated in Refs [4–7]. The pressure profile was chosen there as a rather simple parametric expression. By changing the pressure in this expression, β-values limited by stability against all internal and external ideal modes were found. The limiting equilibria thus obtained are insufficiently optimized. In this connection, the question arises as to a more complete optimization of the plasma equilibrium in order to achieve larger β. A possible algorithm for such an optimization as well as the results of its application are given in this paper.

2. Full optimization of the pressure profile by the ballooning modes yields much larger β [8, 9] in comparison with the parametric optimization by both the ballooning and external modes with finite values of $n = 1, 2, \ldots$. Following this

it is natural for the given distribution of the safety factor q (ψ) over magnetic surfaces to carry out the two-step optimization of the pressure profile. At the first stage, full optimization by ballooning modes is performed and the equilibria obtained are tested for the stability of the kink modes with finite n. In case the latter are unstable, the pressure profile is changed at the second stage for achieving complete stability.

For the given safety factor q (ψ), there is a rather simple technique for determining the marginal pressure profile p (ψ) stable against ballooning modes for all magnetic surfaces [8]. Such an optimization yields a current density distribution over the plasma cross-section that does not vanish at the boundary. Hence, the equilibria thus obtained may generally be unstable against kink modes. However, by an appropriate choice of the safety factor q (ψ), even a slight additional change of p (ψ) is sufficient to provide stability with respect to kink modes without violating the stability with respect to ballooning modes.

The desired function q(ψ) can be obtained from the force-free (p(ψ) = 0) equilibrium configuration for a given density of the longitudinal current,

$$rj_\varphi = \left[1 - \left(1 - \frac{\psi}{\psi_{max}}\right)^\kappa\right]^\lambda$$

The two parameters κ and λ presented here are quite sufficient to select the force-free equilibrium with given shear inside the plasma and the q-values on the magnetic axis, q_0, and at the plasma boundary, q_s. Then full optimization (over all magnetic surfaces) of the pressure gradient $(dp/d\psi)^\infty$ is carried out for the q(ψ) value obtained in the force-free equilibrium. In this way, the marginal equilibrium stable in the ballooning modes is determined for $\beta = \beta^\infty$. Under such an equilibrium it is usually $(dp/d\psi)_s^\infty \neq 0$ and, hence, the current density does not vanish either. At the second optimization stage, we replace $(dp/d\psi)^\infty$ by

$$\frac{dp}{d\psi} = S(\psi)\left(\frac{dp}{d\psi}\right)^\infty$$

It is sufficient to choose $S(\psi)$ in the form of a bell-like function vanishing at the boundary in order to obtain a current density that vanishes virtually at the boundary, without violating the stability with respect to ballooning modes. Below the results are given for

$$S(\psi) = \exp(-B)\,\frac{\sinh(A - B)}{\sinh A}$$

$$A = 0.45\left(\frac{1}{1-\delta}\right)^{10}, \qquad B = A\left(1 - \frac{\psi}{\psi_{max}}\right)^{10}$$

where the parameter δ controls the 'fullness' of the $S(\psi)$ function profile: $0 \leqslant S(\psi) \leqslant 1$. Increasing δ results in compressing $S(\psi)$ and, hence, in sharper $p(\psi)$ and j_φ, without violating the stability with respect to ballooning modes. At the same time, β decreases as compared with β^∞. Testing the obtained equilibria for stability with respect to kink modes allows the critical δ^c and the corresponding β^c limited by all modes to be obtained.

3. A variational formulation of the spectral problem is the initial point for determining the instability growth rates of the ideal-MHD modes with finite n.

A finite-element method is used in all available codes for numerical solution of this variational problem in flux co-ordinates. Using the hybrid finite elements [3] and their modifications appears to be most effective in computing the MHD spectrum. However, the numerical destabilization typical of this method as well as the continuous spectrum spreading up to $\omega^2 = 0$ make it difficult to determine the marginally stable equilibria and force one to employ the σ-stability criterion: the equilibrium is considered to be stable for $-\omega^2 < \sigma$ [6].

To establish only the fact of stability, it is convenient to use the so-called δW-code so as to determine the sign of the potential energy functional W minimum in the model normalization [2]. A certain analytical transformation of the functional W and a change in the structure of the spectrum allow common finite elements to be used and the marginally stable equilibria to be determined effectively.

In this report, the instability growth rates were computed by using the hybrid finite elements in the flux co-ordinate and a finite Fourier series in the poloidal angle. Usual piecewise linear basis functions in the flux co-ordinate were chosen for the δW-code. The pseudo-displacement method was used to approximate the vacuum part of the potential energy [10]. The computations of the kink modes were performed for an absolutely conducting wall, similar to the boundary of a plasma with the centre on the magnetic axis, and a similarity coefficient of $\Lambda = 5$.

The equilibrium configurations were computed by an algorithm based on the inverse-variable technique [11] on the grid with $N_\psi = 61$, $N_\theta = 64$, where N_ψ and N_θ are the number of points in the flux co-ordinate and the poloidal angle, respectively. To ensure sufficient accuracy of the stability calculations, grid clustering in the flux co-ordinate near the boundary proved to be essential. A characteristic number of harmonics in the finite Fourier series equal to $L = 13$ was used on a half-plasma with respect to $z = 0$.

The accuracy of the computations of the limiting β^c values is an important factor. In this connection the codes for the equilibrium and stability computations have been carefully developed and thoroughly tested. For the test analytical equilibria proposed in Ref. [12], good agreement of growth rates and eigenfunction structures has been obtained.

4. We now consider the computational results. First, we discuss the dependence of β^c on the aspect ratio, $A = R/a$, for a circular-cross-section plasma.

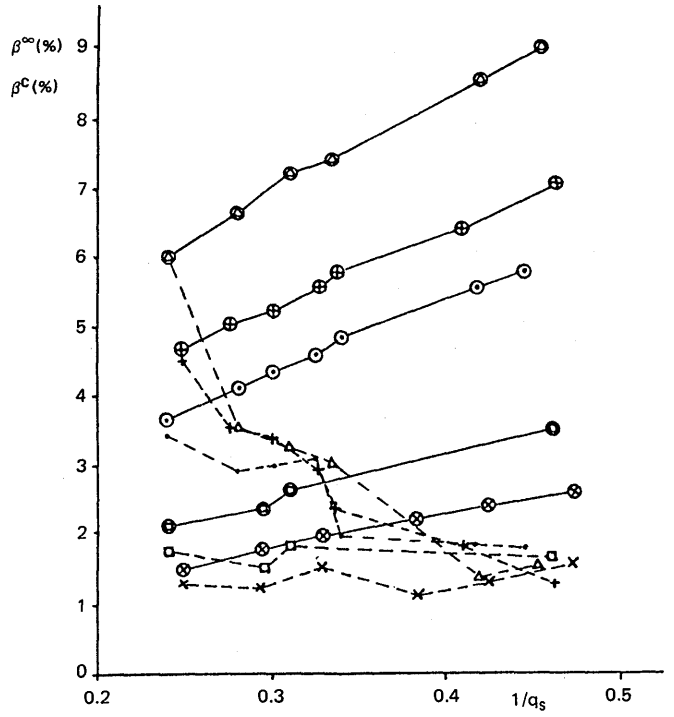

FIG. A1. β^{∞} (solid lines) and β^{c} (dotted lines) versus q_s: ⊙, △: A = 1.5; ⊕, + : A = 1.75; ⊙, • : A = 2; ⊡, □ : A = 3; ⊗, × : A = 4.0. Plasma has circular cross-section, in current density distribution λ = 2.

Then the effects of elongation and triangularity on β^{c} will be shown. The plasma cross-section boundary is given by

$$r = R + a(\cos\theta - \gamma \sin^2\theta)$$

$$z = ka \sin\theta$$

For a fixed geometry, the equilibrium is determined by three parameters: κ, λ, q_0. In all computations given below, we have $q_0 = 1.1$. Increasing κ for fixed λ results in a flattening of the current density distribution near the axis and in a decrease of q_s; increasing λ for fixed κ results in a flattening of the current density near the boundary and an increase in q_s. The functions $\beta^{\infty}(1/q_s)$ and $\beta^{c}(1/q_s)$ are shown in Fig.A1. Here,

$$\beta = 2 \int_v p dv \Big/ \int_v B_T^2 \, dv$$

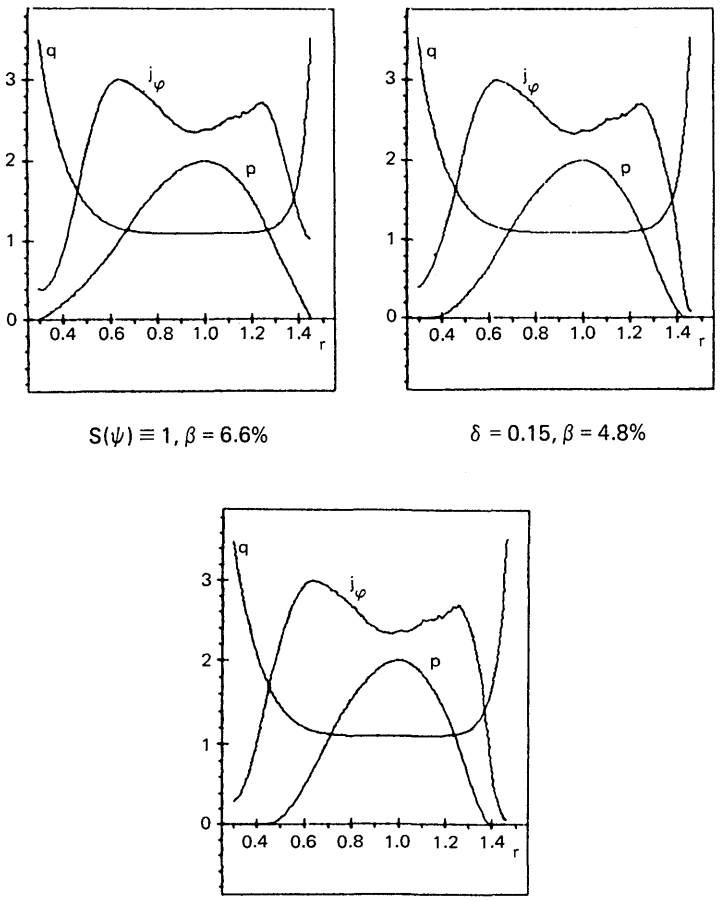

FIG. A2. Profiles of q(r), p(r), $j_\varphi(r)$ at z = 0, A = 1.5, κ = 2.7, λ = 2. Here, the plasma cross-section is circular, j_φ and p are normalized so that max j_φ = 3, max p = 2. Radius r is normalized by value on magnetic axis.

The solid lines connecting circles with different symbols show $\beta^\infty(1/q_s)$ for different aspect ratios. The corresponding $\beta^c(1/q_s)$ are shown by dotted lines. Decreasing q_s (increasing the plasma current) as well as decreasing the aspect ratio A results in a growth of β^∞ (see, e.g. Ref. [8]). However, for steep tori with $A < 2$, strong destabilization of kink modes takes place so that β^c is much less than the corresponding β^∞. Increasing q_s results in a nearly monotonic growth of β^c so that, for $q_s > 4$, $\beta^c = \beta^\infty$ is practically reached. For $A > 3$, toroidal destabilization of the kink modes is less pronounced.

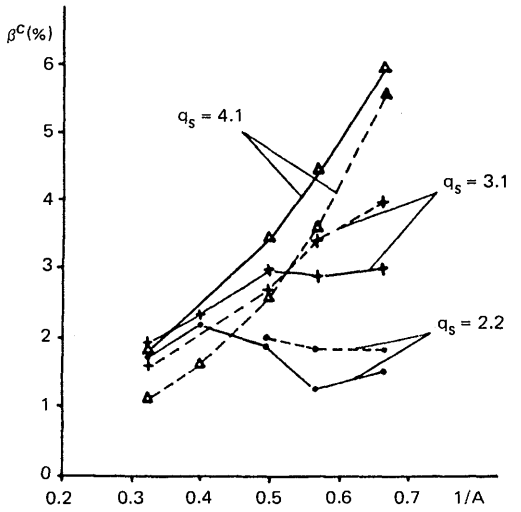

FIG. A3. β^c *versus aspect ratio A. Plasma cross-section is circular, solid lines refer to* $\lambda = 2$, *dotted lines to* $\lambda = 1$.

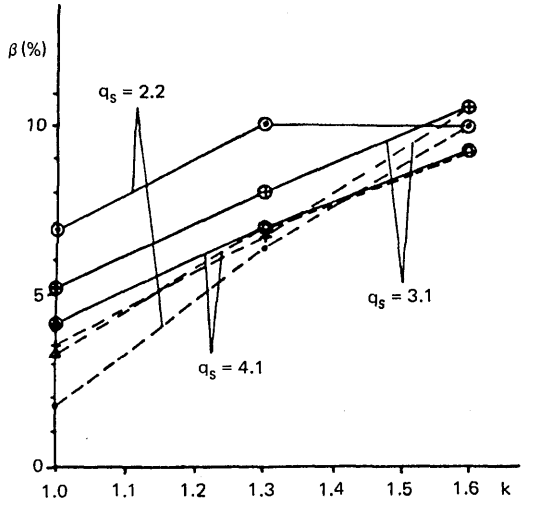

FIG. A4. β^∞ *(solid lines) and* β^c *(dotted lines) versus plasma elongation k :* $\lambda = 1$, $A = 1.75$, $\gamma = 0.3$, *for* $k \neq 1$; $\gamma = 0$ *for* $k = 1$.

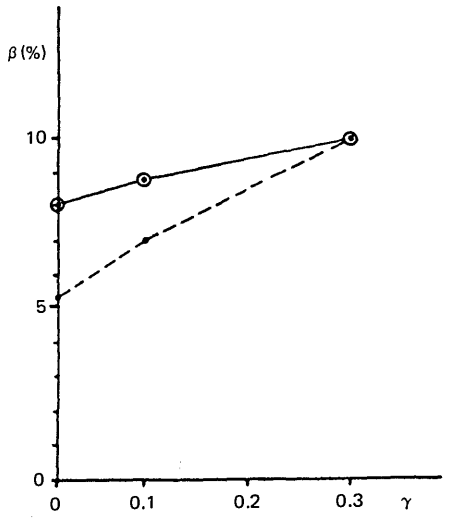

FIG. A5. β^{∞} (solid line) and β^{c} (dotted line) versus triangularity γ : $\lambda = 1$, $A = 1.75$, $k = 1.6$, $q_s = 2.2$.

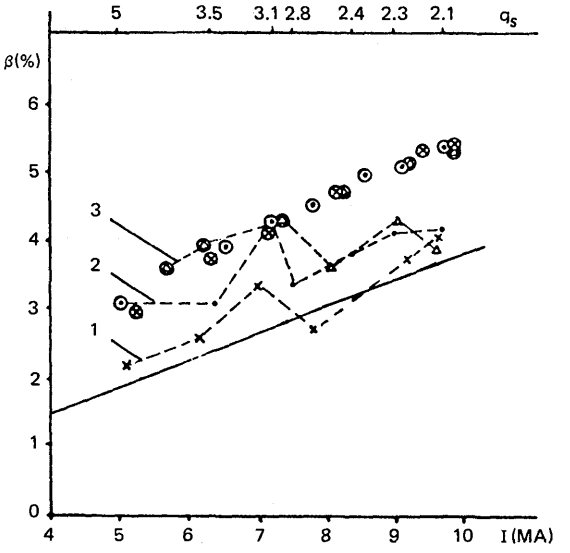

FIG. A6. Behaviour of $\beta^{\infty}(I)$, $\beta^{c}(I)$ for INTOR-like plasma: ⊗ , × : $\lambda = 1$, ⊙ , • : $\lambda = 2$, ◬ , △ : $\lambda = 3$.

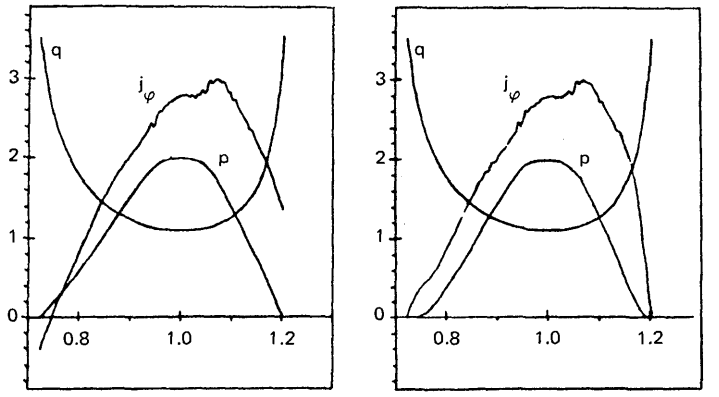

$S(\psi) \equiv 1, \beta = 3.7\%$ $\delta = 0.15, \beta = 2.6\%$

FIG. A7. Profiles of q(r), p(r), $j_\varphi(r)$ for z = 0, κ = 1, λ = 1, A = 4, k = 1.6, γ = 0.3.

Figure A2 shows the functions q(r), p(r) and $j_\varphi(r)$ for various δ at A = 1.5, where $S(\psi) \equiv 1$ corresponds to an equilibrium optimized by the ballooning modes, for which the current does not vanish at the boundary; δ = 0.3 corresponds to an equilibrium stable against all modes.

The functions $\beta^c(A)$ are given in Fig. A3. Here three pairs of curves marked by different symbols correspond to various q_s. The dotted lines refer to the case λ = 1, and the solid lines to a more flattened current distribution near the boundary with λ = 2. For $q_s > 4$, the β^c value grows faster than a linear function of A^{-1}, and a slower drop of the current towards the boundary results in a rise of β^c. Note that here, with decreasing aspect ratio, the effect of the current density distribution over the plasma cross-section on β^c becomes weaker. In contrast, for $q_s \lesssim 3$, the value of β^c is sensitive to the current distribution over the plasma cross-section (to λ), because of toroidal destabilization. Since $q_s \lesssim 3$ and $A < 2$, the effect of current flattening near the plasma boundary is quite opposite to that of $q_s > 4$: the β^c value is larger when the current drops abruptly near the boundary than when it decreases slowly.

An example of the elongation effect (k-effect) on β^c is shown in Fig. A4. Here, for A = 1.75, γ = 0.3, λ = 1, the behaviour of $\beta^\infty(k)$ (solid lines) and $\beta^c(k)$ (dotted lines) is shown for q_s = 2.2; 3.1; 4.1. The considerable growth of β^c with k for steep tori, $A < 2$, for $q_s \lesssim 3$ can be explained by a toroidal destabilization of the kink modes in the circular plasma. As is, however, shown in Fig. A5, the toroidal destabilization is not suppressed for purely elliptic cross-sections. The β^c value grows with k only in a triangular plasma, $\gamma \neq 0$.

5. Consider the computational results for an INTOR-like plasma [13]: A = R/a = 4.0, k = 1.6, γ = 0.3. The dimensional parameters of the equilibrium

are determined by R = 5.2 m and the toroidal field on the magnetic axis, B_0 = 5.5 T. The functions $\beta^\infty(I)$ and $\beta^c(I)$ are shown in Fig. A6, where I is the total longitudinal current in the plasma. Separate points designate the β^∞ values for different values of κ, λ. The dotted lines show the function $\beta^c(I)$: (1) $\lambda = 1$; (2) $\lambda = 2$; (3) $\lambda = 3$. The solid line corresponds to β^c from Ref. [6].

The β^∞ values for different κ and λ very accurately fall on the straight line; for a fixed total current, $\beta^\infty(I)$ only weakly depends on the $q(\psi)$ profile (parameter λ). The second stage of optimization for $\lambda = 1$ yields the smallest values of β^c (curve 1). Flattening of the current density near the boundary ($\lambda = 2,3$) results in a rise of $\beta^c(I)$ (curves 2,3) so that, for $\lambda = 3$ and $q_s > 3$, the β^c value practically coincides with β^∞. A typical feature of $\beta^c(I)$ is that the values of the local maxima are close to one another when q_s is near 2 and 3, which corresponds to the stability gaps for the peaked current in the cylindrical case. We emphasize that $\beta^c(I) \approx 0.8\beta^\infty(I)$ for $q_s \gtrsim 2.2$ and depends only weakly on the current density distribution over the plasma cross-section. The distributions p(r), q(r) and $j_\varphi(r)$ are shown in Fig. A7 for z = 0. Increasing δ results in a compression of the current density and a decrease in β. So, when $\delta = 0.15$, we have $\omega^2/\omega_A^2 = 8.6 \times 10^{-5}$, $\omega_A^2 = B_0^2/(\rho R^2)$, which allows this equilibrium to be considered stable. The computations by the δW-code confirm this result.

6. The results of the above computations allow the following conclusions to be drawn:

(a) The two-stage optimization proposed for equilibrium configurations with a given distribution of q over the magnetic surfaces leads to larger values of β^c than the parametric optimization of $p(\psi)$ and $q(\psi)$.

(b) For the tori with circular cross-sections, β^c is determined by the ballooning modes only for $q_s > 4$. For $q_s < 4$, destabilization of the kink modes takes place, resulting in a decrease of β^c.

(c) Elongation ($k \approx 1.5$) and triangularity ($\gamma \approx 0.3$) of the plasma cross-sections suppress toroidal destabilization of kink modes.

(d) For an INTOR-like plasma, the β^c value is virtually determined by the ballooning modes.

ACKNOWLEDGEMENT

The authors would like to thank V.D. Shafranov for numerous fruitful discussions.

REFERENCES

[1] GRIMM, R.C., GREENE, J.M., JOHNSON, J.L., Methods Comput. Phys. **16** (1976) 253.
[2] GRIMM, R.C., DEWAR, R.L., MANICKAM, J., J. Comput. Phys. **49** (1983) 94.

[3] GRUBER, R., TROYON, F., BERGER, D., BERNARD, L.C., ROUSSET, S., SCHREIBER, R., KERNER, W., SCHNEIDER, W., ROBERTS, K.V., Comput. Phys. Commun. **21** (1981) 323.
[4] TODD, A.M.M., MANICKAM, J., OKABAYASHI, M., CHANCE, M.S., GRIMM, R.C., GREENE, J.M., JOHNSON, J.L., Nucl. Fusion **19** (1979) 743.
[5] BERNARD, L.C., DOBROTT, D., HELTON, F.J., MOORE, R.W., Nucl. Fusion **20** (1980) 1199.
[6] TROYON, F., GRUBER, R., SAURENMANN, H., NET Report, EURXII-324/14 (1983).
[7] BERNARD, L.C., HELTON, F.J., MOORE, R.W., TODD, T.N., Nucl. Fusion **23** (1983) 1475.
[8] VABISHCHEVICH, P.N., DEGTYAREV, L.M., MEDVEDEV, S.Yu., Fiz. Plazmy **9** (1983) 100.
[9] SYKES, A., TURNER, M.F., PATEL, S., in Controlled Fusion and Plasma Physics (Proc. 11th Europ. Conf. Aachen, 1983), Part 2, Aachen (1983) 363.
[10] GRUBER, R., et al., Comput. Phys. Commun. **24** (1981) 363.
[11] VABISHCHEVICH, P.N., DEGTYAREV, L.M., DROZDOV, V.V., Dokl. Akad. Nauk SSSR **25** (1982) 1.
[12] CHANCE, M.S., et al., J. Comput. Phys. **28** (1978) 1.
[13] INTOR, PHASE ONE, International Atomic Energy Agency, Vienna (1982).

PART B. MHD STABILITY OF A STEADY-STATE TOKAMAK WITH A HOLLOW CURRENT (L.M. Degtyarev, A.A. Martynov, S.Yu. Medvedev, A.G. Kirov, M.A. Stotland)

The results of numerical studies on the stability of ballooning, helical and tearing modes in a tokamak plasma with a hollow current are given. Such current density profiles may be formed by a current driven by Alfvén and lower-hybrid waves in a steady-state tokamak reactor [1–3].

It is shown that the hollow-current configuration is highly stable against small-scale ideal ballooning modes ($\beta_c \approx 7\%$ and $\beta \approx 20\%$ for circular and elongated plasma cross-sections with K = 1.6, respectively). Stability against ideal helical modes with $m \geqslant 2$ can be ensured by sharpening the current density profile for $r/a < 1/\sqrt{3}$ or by a small inverse boundary current. For the latter case, in addition to the left-hand stability slit, there arises a right-hand alit for $nq_1 < m$, and the $m \geqslant 2$ helical modes can be stabilized when the safety factor at the boundary has the values $q_1 < 2$ and $q_{min} > 1$.

Regions in the plane $(q_1, q_1/q_{min})$ are found where dangerous double tearing modes are absent, the solitary tearing modes being stabilized or developed in a region close to the axial resonant surface only.

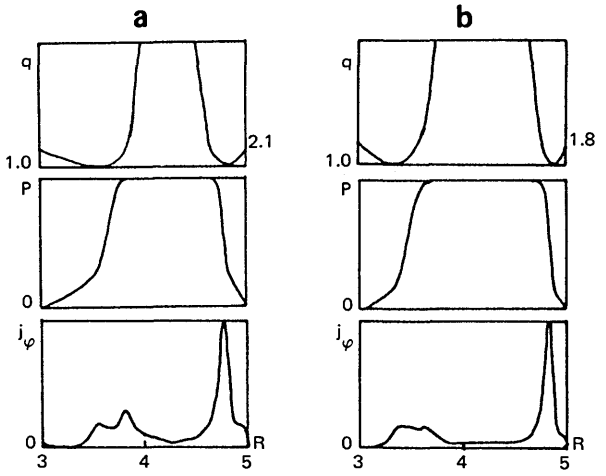

FIG. B1. q(R), p(R), $j_\varphi(R)$ profiles for optimized equilibria: (a) circular cross-section, $r_* = 0.5, \kappa = 8$, $q_1 = 2.1$; $\beta = 7.1\%$; (b) elongated cross-section, $K = 1.6$, $r_* = 0.7$, $\kappa = 8$, $q_1 = 1.8$, $\beta = 21\%$.

1. The stability of ideal small-scale ballooning modes is considered within the region of high wavenumbers, n. Primarily, small-scale ballooning modes are considered since low-n instabilities can be stabilized by various means used to suppress helical modes.

The calculation results show that the hollow current profile regimes in tokamaks have high equilibrium β values and better stability against small-scale ideal ballooning modes. Plasma pressure profile optimizations according to the methods described in Refs [4, 5] allow us to obtain equilibria with critical values of $\beta_c = 7-10\%$ in a circular-cross-section tokamak with a hollow current, the equilibria being stable with respect to the ballooning modes. The calculations have been carried out for an aspect ratio of A = 4; with $q_1 \approx 2$ at the boundary and a minimum value of $q_{min} \approx 1$. When the plasma has an elongated cross-section, K = 1.6, β_c increases up to about 20%. Figure B1 shows the radial distributions of the plasma pressure, p, the q-factor and the toroidal component of the current density, j_φ. In regimes with non-optimized pressure distributions at $\beta > \beta_c$, typically, a narrow annular zone of instability is present which lies in the region of $q' > 0$ close to $q = q_{min}$ (Fig. B2). This zone is, probably, not dangerous since it is so narrow. For the sake of comparison, Fig. B2d shows the instability zone for a parabolic profile of j. The quantity $a = 1 - \psi/\psi_{max}$ is chosen as a radial co-ordinate, ψ being a poloidal flux, and a = 1 at the plasma boundary.

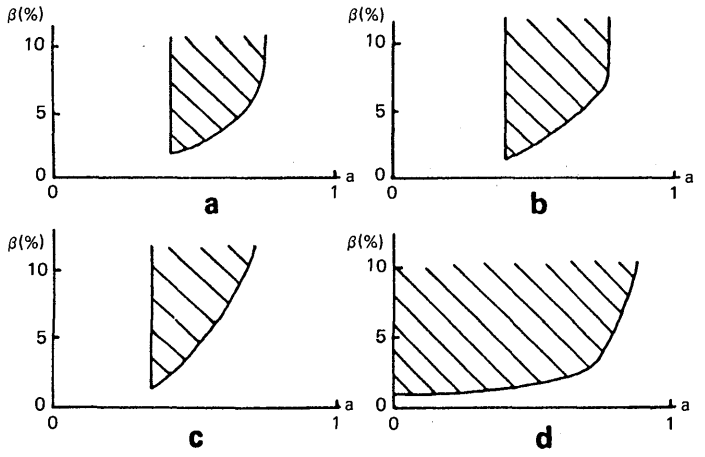

FIG. B2. Instability zones for equilibria with $p' = p_0(1-a)$, $r_* = 0.5$, $q_1 = 2.0$. *(a)* $\kappa = 4$; *(b)* $\kappa = 8$; *(c)* $\kappa = 16$; *(d)* $j_z(r) = 1 - r^2$. *Instability zones are shadowed.*

2. The stability of helical modes is considered by using the energy principle [6] for a cylindrical plasma column with a hollow current profile and also with a current which is inverse with respect to the main current and flows through the plasma periphery region. Analytical studies have been carried out on the stability of distributions simulating hollow and inverse currents, the distributions being piecewise continuous. By a variational method, the stability of smooth hollow-current profiles is studied numerically. It is shown that sharpening of the hollow current density profile, with the maximum r_* fixed, has a stabilizing effect leading to a widening of the stability left-hand slit in the $(q_1/q_{min}, nq_1)$ plane and to a sharp drop in the growth rates. For $r_* < 1/\sqrt{3}$, with the current density profile rather sharp, complete stability is possible against $m \geqslant 2$ helical modes. Numerical studies have been carried out in order to explore the stability and the influence of the inverse current on this stability for the following type of the hollow distribution:

$$j_z(r) = j_0(1 - r/r_1)^{\kappa} r^{\eta} \quad 0 \leqslant r \leqslant r_1 < 1 \qquad (1)$$

The current density has its maximum at the point $r_* = r_1\eta/(\eta + \kappa)$. With r_* being fixed, the increase in the parameter κ corresponds to an increase in the j_z profile sharpening. The inverse current is distributed over the boundary zone $j_z(r) = -j_1(r - r_1)(1 - r)$. Modes with $m = 2,3$, $n = 1,2$ have been considered. For

the sake of comparison, a monotonic current profile has been also studied numerically:

$$j_z(r) = j_0(1 - (r/r_1)^2)^\nu \qquad (2)$$

Figure B3 shows the stability plot for monotonic and hollow profiles of j. We see that, for $r_* \leqslant 0.5$, the q_1/q_{min} values for the stable hollow current are smaller than the q_1/q_0 values for the monotonic current. A small inverse peripheral current (a few per cent of the main current) results in the formation of a right-hand stability slit in the Shafranov diagram for $nq_1 \lesssim m$, as well as in a decrease in the helical instability growth rates and in the usual widening of the left-hand stability slit. As a result, the stability region for helical modes increases substantially, and less sharpened current profiles are allowed (see Fig. B3). This fact, as distinct from stabilizing by means of current profile sharpening, enables us to match $q_1 < 2$ with $q_{min} > 1$, both for hollow and peaked current profiles. The inverse current can be driven by means of a low-power travelling electromagnetic field within the Alfvén frequency range. The ratio of HF powers released in the regions of the main and inverse currents is estimated [7] to be $\lesssim 0.05$ for inverse-to-main current ratios of $I^-/I^+ \lesssim 0.03$.

3. Tearing-mode instabilities in a tokamak with a hollow current density profile (I), and with a non-monotonic profile of $q(r)_0$, respectively, have been estimated for a cylindrical plasma model using the energy principle [8, 9]. In calculating the growth rates, we have used the following density and conductivity profiles: $n \propto (1 - 0.9\, r^2)$, $\sigma \propto (1 - 0.9\, r^2)^{3/2}$.

The configurations considered are distinguished by the fact that interconnected double tearing modes can arise, which are developed close to each of the surfaces with the same m and r values. Our attention has been mainly drawn to determining the conditions which forbid such modes, i.e. when the plasma is stable or can develop a solitary tearing mode only.

Figure B4a shows stability diagrams for m/n = 2/1, 3/2, 4/3 modes when $r_* = 0.4$. The growth rates γ of these tearing modes when j has two profiles with various values of κ are given in Figs B4b and c with increasing ratio of q_1/q_{min}, the ideal helical instability becomes stabilized and, for $m \geqslant 3$, some regions of stability against the tearing modes (both double and solitary ones) appear. When the sharpening grows further a solitary tearing instability arises near the resonant surface adjacent to the axis. The solitary tearing instability zone joins on the right with the instability region where double tearing modes can develop and the stability slit disappears.

For the m = 2 mode, the situation is of another type. The m = 2, n = 1 mode is always unstable: if $q_1 < 2$, the solitary tearing mode developed at the near-axial resonant surface is unstable, and if $q_1 > 2$, a single or two branches of the growth rate exist. For the latter case, one of the branches shows $\gamma \to \infty$ when the resonant surfaces get closer while the second branch shows $\gamma \to 0$ (see Figs B4b

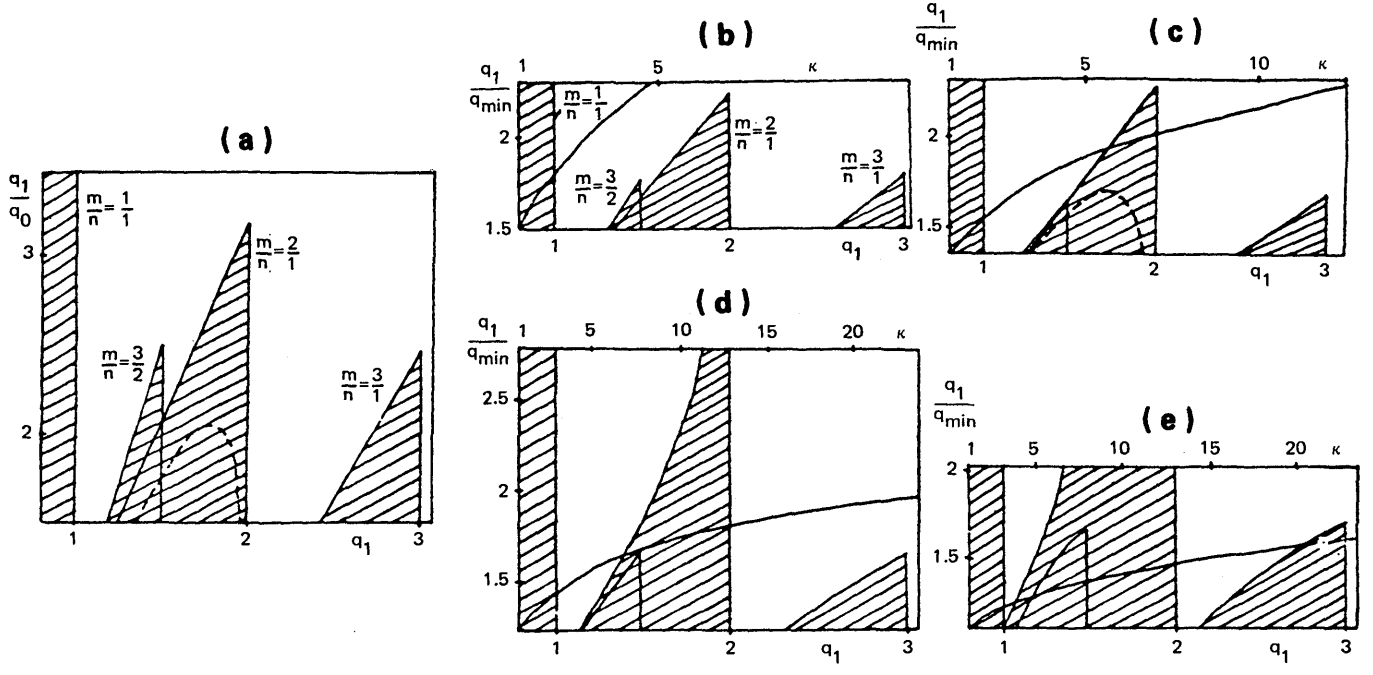

FIG. B3. Stability diagrams (instability regions shadowed). (a) Monotonic distribution $j_z(r) = (1-r^2)^\nu$, $q_1/q_0 = 1+\nu$. *Dotted line corresponds to surface current* $I^- = -0.03\, I^+$. *Hollow current (I) for* $r_1 = 1$ *and various* r_*: *(b)* $r_* = 0.4$, *(c)* $r_* = 0.5$, *(d)* $r_* = 0.6$, *(e)* $r_* = 0.7$. $q_1/q_{\min}$ *is shown versus* κ. *Dotted line in c corresponds to* $I^- = -0.03\, I^+$.

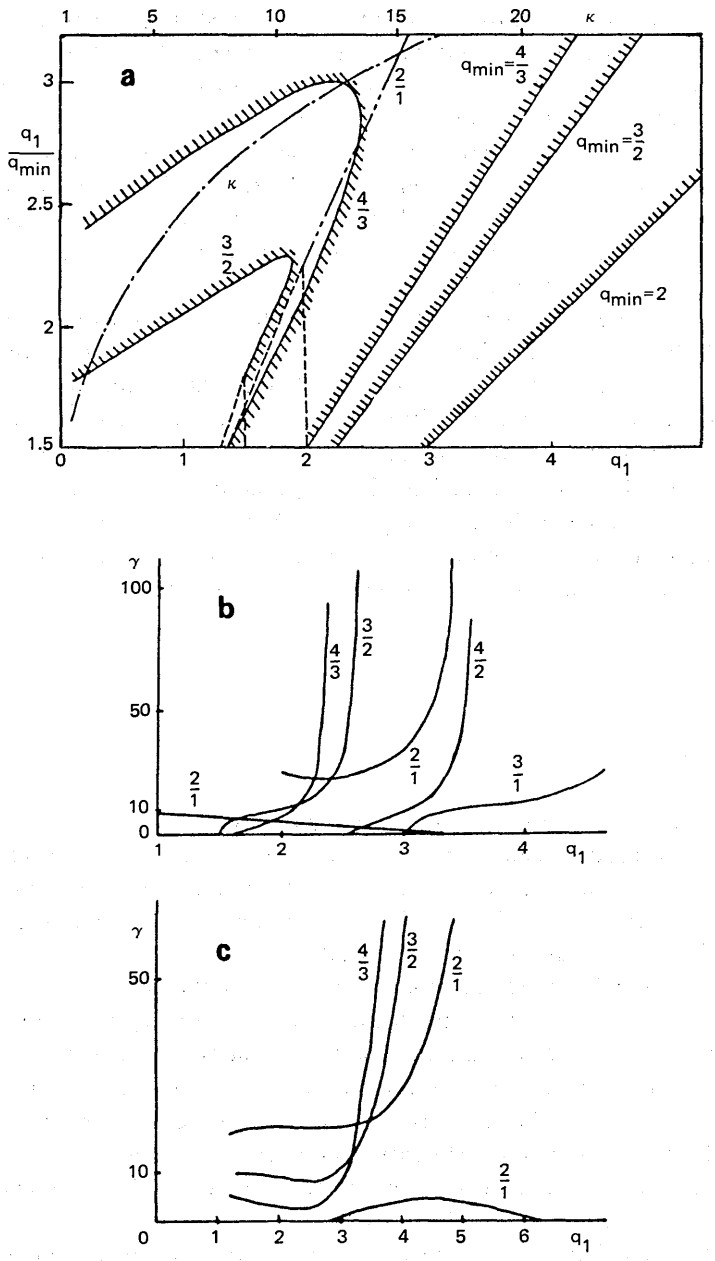

FIG.B4. (a) Tearing-mode stability diagram for $r_* = 0.4$. Zones of instability for ideal helical modes are dotted. For $m = 3,4$ modes, instability region boundaries are shadowed; for $m = 2$, boundary of existence of two unstable modes is indicated. Dot-dashed line is q_1/q_{min} versus κ; (b) growth rates of unstable mode development with $m/n = 2/1, 3/2, 4/3$ for $r_* = 0.4$ at $\kappa = 2$; γ is dimensionless growth rate; (c) the same for $\kappa = 16$.

and c). It should be emphasized that, for sufficiently sharp profiles, a range of q_1 exists which has a single growth rate branch only (Fig. B4c). Note that for $r_* \geqslant 0.5$ the second growth rate branch may appear even at $m > 2$. Besides, the zone of complete stability begins to appear already for $r_* = 0.5$, starting from $m = 4$.

In Ref. [10], for monotonic current profiles ($q' > 0$), the authors show the stabilizing effect of local profile generation by 'breaking' the current density $[j'] < 0$ close to the resonant surface lying in the region $q' < 0$. Note that the HF methods for heating and driving the current, being local, may be used to create a profile for the current density.

Alternative applications of stabilizing breaks near the resonant surfaces appeared to be useful in identifying the surfaces where vicinities are actually characterized by instability development. Such 'diagnostics' with stabilizing breaks in combination with the analysis of $\gamma(q_1)$ plots and stability diagrams lead us to the conclusion that there are regions of stability against the double tearing modes with $m \geqslant 2$ for sufficiently sharpened profiles of hollow currents over the range of practical interest $q_1 (q_1 < 3)$. Only solitary tearing modes with $m = 2$ exist, while modes with $m \geqslant 3$ are entirely stable or appear as solitary ones. All solitary modes arise in the deep-lying near-axis resonant surfaces.

CONCLUSIONS

Tokamaks with hollow current profiles have high values of equilibrium β and higher stability against small-scale ideal ballooning modes. An optimization of the plasma pressure profile allowed us to obtain equilibria that are stable against ballooning modes with $\beta_c = 7-10\%$. When the plasma cross-section is elongated up to $K = 1.6$, β_c increases towards about 20%.

As to ideal helical modes, it is shown that the sharpening of the current density profile, when its maximum position is fixed, has a highly stabilizing influence; besides, when the current density maximum is sufficiently far away from the plasma boundary the helical modes with $m \geqslant 2$ can be completely stabilized. When a small inverse periphery current (of the order of a few per cent of the main current) exists, the stability region for helical modes increases substantially, and less sharpened current profiles may exist. In particular, stable regimes with $q_1 < 2$ and $q_{min} > 1$ are possible.

Regions of stability with respect to double tearing modes with $m \geqslant 2$ are determined within the range of practical importance: $q_1 \leq 3$. Within these ranges of parameters, only solitary $m = 2$ tearing modes exist, while $m \geqslant 3$ modes are either entirely stable or solitary, the solitary $m \geqslant 2$ modes being developed on the near-axis resonant magnetic surfaces and, apparently, without any particular effect on plasma confinement.

REFERENCES

[1] KOLESNICHENKO, Ya.I., et al., in Plasma Physics and Controlled Nuclear Fusion Research 1982 (Proc. 9th Int. Conf. Baltimore, 1982), Vol. 3, IAEA, Vienna (1983) 349.
[2] DEMIRKHANOV, R.A., et al., in Controlled Fusion and Plasma Physics (Proc. 10th Europ. Conf. Moscow, 1981), Vol. 1, paper E-7.
[3] EHST, D.A., et al., Fusion Energy **2** (1982) 83.
[4] VABISHCHEVICH, P.N., et al., Fiz. Plazmy **9** (1983) 163.
[5] DEGTYAREV, L.M., et al., Prepr. Inst. Applied Mathematics, USSR Academy of Sciences, No. 33 (1983).
[6] NEWCOMB, W.A., Ann. Phys. **10** (1960) 232.
[7] DEGTYAREV, L.M., et al., Prepr. Inst. Applied Mathematics, USSR Academy of Sciences, No. 28 (1983).
[8] KERNER, W., TASSO, H., Plasma Physics **24** (1982) 97.
[9] DEGTYAREV, L.M., et al., Prepr. Inst. Applied Mathematics, USSR Academy of Sciences (1984) (to appear).
[10] BLEKHER, P.M., et al., Prepr. Inst. Applied Mathematics, USSR Academy of Sciences, No. 121 (1984).

INVESTIGATION OF HIGH-BETA TOKAMAK STABILITY WITH THE PROGRAM HBT

J.P. GOEDBLOED, G.M.D. HOGEWEIJ,
R. KLEIBERGEN, J. REM
Association Euratom-FOM,
FOM-Institut voor Plasmafysica, Rijnhuizen,
Nieuwegein, Netherlands

R.M.O. GALVÃO
Laboratorio de Estudos Avançados,
Centro Técnico Aerospacial,
São José dos Campos, São Paulo, Brazil

P.H. SAKANAKA
Instituto de Física "Gleb Wataghin",
Universidade Estadual de Campinas,
Campinas, São Paulo, Brazil

Abstract

INVESTIGATION OF HIGH-BETA TOKAMAK STABILITY WITH THE PROGRAM HBT.

The numerical program HBT has been employed to study global and local stability of high-beta axisymmetric toroidal plasmas with various cross-sections. The stability results of different classes of equilibria for a circular plasma show that high stable betas ($\langle\beta\rangle/\epsilon = 0.082$) can be found when negative toroidal current densities are admitted in a small region on the inside of the torus. Shaping the cross-section makes further improvements possible. The optimum betas found are in qualitative agreement with Troyon's scaling law.

1. INTRODUCTION

The numerical program HBT has been developed to study MHD equilibrium, global stability and local stability of high-beta toroidal axisymmetric plasmas. This code has the special feature that the actual equilibrium and stability computation is not carried out in the physical z-plane of the poloidal cross-section but in a w-plane obtained through a conformal mapping z(w). This transformation maps the arbitrary, but prescribed, cross-section onto a circular region of unit radius ($w = se^{it}$, $s < 1$), while the image of the magnetic axis is mapped onto the centre of this circle. The coordinate system thus arrived at is an excellent first approximation to the equilibrium flux surfaces, so that an accurate representation of the poloidal flux, by means of a few harmonics in the angle t, is obtained after a small number of iterations [1,2].

A high-beta tokamak equilibrium is characterized by the shape of the cross-section $r = f(\vartheta)$, the physical parameters: $\varepsilon\beta_p$ (where ε is the inverse aspect ratio and β_p is the poloidal beta) and q^* (the safety factor based on the toroidal plasma current I_p), and unit profile functions $\Pi(\psi)$ and $\Gamma(\psi)$ for the pressure gradient and the current at $\varepsilon\beta_p = 0$, respectively. These profile functions satisfy the conditions: $\Gamma(0) = \Pi(0) = 1$ on the magnetic axis ($\psi=0$) and $\Gamma(1) = \Pi(1) = 0$ at the plasma boundary ($\psi=1$). The latter implies that surface currents are excluded. The parameters $\langle\beta\rangle$, β_p and q^* are defined as follows:

$$\langle\beta\rangle \equiv 2\mu_0\langle p\rangle/B_0^2 , \qquad \beta_p \equiv 8\pi S\ \langle p\rangle/\mu_0 I_p^2$$
$$q^* \equiv 2\pi a^2 e B_0/\mu_0 R_0 I_p \tag{1}$$

Here $\langle\ \rangle$ refers to averaging over the area S of the plasma cross-section, p is the pressure, B_0 is the toroidal vacuum field at the major radius R_0, 2a is the width of the plasma cross-section in the equatorial plane and e is the elongation of the cross-section as compared to a circle: $e = \oint d\ell/2\pi a$. These quantities are related in a simple way:

$$\varepsilon\beta_p = \eta\ \langle\beta\rangle/\varepsilon\ q^{*2} \tag{2}$$

where $\eta \equiv S/\pi a^2 e^2$ is a purely geometric factor.

In the high-beta tokamak ordering ($\beta\sim\varepsilon$, $\varepsilon\to 0$), the equilibrium becomes independent of ε and q^* in the sense that the scaling of the physical quantities $p(\psi)$, $q(\psi)$, etc., is a simple algebraic one, i.e. the pressure profile $p(\psi)$ and the profile of the safety factor $q(\psi)$ vary with q^* only through a simple multiplicative factor. Hence, for given functional dependencies $\Gamma(\psi)$ and $\Pi(\psi)$, the equilibrium is determined by $\varepsilon\beta_p$ only. In HBT this fact is exploited by prescribing the shift of the magnetic axis Δ, from which $\varepsilon\beta_p$ is then computed.

The stability - determined by minimizing the potential energy of the perturbations - depends not only on $\varepsilon\beta_p$ but also on the toroidal current through the quantity nq^*, where n is the toroidal mode number of the perturbations. Therefore, stability results are best presented in an $\varepsilon\beta_p$ versus nq^* diagram where lines of marginal stability separate the stable and unstable regions. In such a diagram the $\beta/\varepsilon n^2 = \text{const}$ lines are parabolas starting at the origin according to Eq. (2), whereas the curves $nq_0 = \text{const}$ and $nq_a = \text{const}$ start from points at the nq^* axis that determine the value of these constants and bend over to the right or the left, respectively, when $\varepsilon\beta_p$ is increased (see Fig. 1). This being understood, we shall suppress the dependence on n in the following.

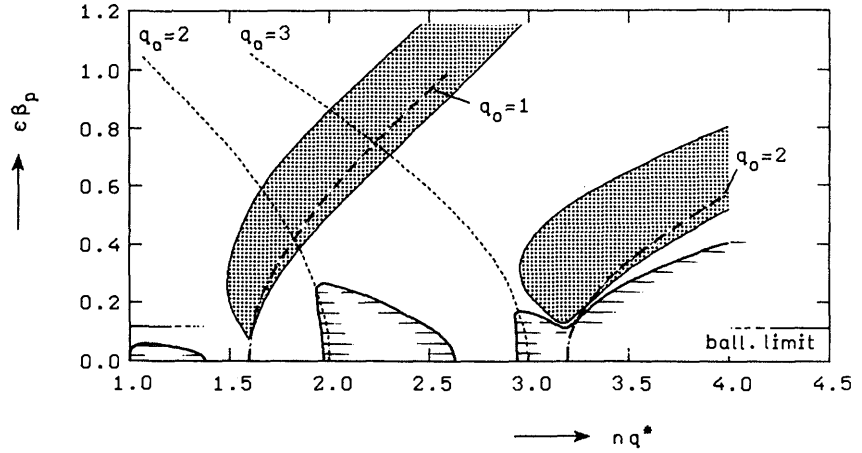

FIG.1. Stability boundaries for the equilibrium $\Gamma = \Pi = 1 - \psi^2$. *The two shaded regions are unstable to the internal m = 1 and m = 2 kink modes (wall on the plasma). The stable regions in the absence of a wall are situated on the shaded side of the thick lines. The dotted lines indicate the loci where q at the plasma surface is given by* $nq_a = 2$ *and 3; the dashed lines are the loci where q on the magnetic axis is given by* $nq_0 = 1$ *and 2.*

2. STABILITY RESULTS FOR A CIRCULAR CROSS-SECTION

The stability studies of a circular plasma with simple profile functions $\Gamma(\psi) = (1-\psi)^{\nu_\Gamma}$, $\Pi(\psi) = (1-\psi)^{\nu_\pi}$ [2], confirmed the fact, known at low beta [3], that a plasma with a peaked current is more stable with respect to external modes than a plasma with a broad current. However, in the range of currents of interest: $q^* \sim 2$ to 3, these profiles always lead to values of q_0 much below unity. Since this feature may be undesirable, we have now considered profile functions that, for the same range of q^*, lead to equilibria with $q_0 > 1$:

$$\Gamma(\psi) = (1-\psi)(1+f_\Gamma\psi), \quad \Pi(\psi) = (1-\psi)(1+f_\pi\psi) \qquad (3)$$

For f_Γ in the range 1 to 0.4, this leads to values for q_a/q_0 between 1.6 and 2. Of course, f_Γ not only affects q_a/q_0 but also the current profile near the plasma surface. Thus f_Γ is the parameter by which external kink modes may be influenced.

In Ref. [4] stability diagrams were shown, in which the position of the external wall was varied in order to exhibit the structure of the stability regions most clearly. The figures of the present paper are similar plots, but we should point out that they have been obtained with a corrected version of the code giving the same qualitative results as previously, but leading to

lower numerical values of $\varepsilon\beta_p$. Figure 1 shows the stability regions for the profile $f_\gamma=f_\pi=1$ with the wall far away (s = 100) and on the plasma surface (s = 1).

With the wall on the plasma, almost the entire $\varepsilon\beta_p$ - nq* plane is stable except for two regions adjacent to the lines $q = 1$ and $q_0 = 2$, associated with the internal m=1 and m=2 kinks. When the wall is removed, the plasma may become unstable to external kinks as well. As is well known [3,5], at $\varepsilon\beta_p = 0$ these modes occur when a mode rational surface lies just outside the plasma, i.e. when $q^* = q_a$ is smaller than 1, 2 or 3 for m=1, 2 or 3, respectively. Removal of the stabilizing wall thus leads to enlargement of the regions where internal kink modes are unstable and to the appearance of new unstable regions due to the external kink modes. These two kinds of region coalesce at higher $\varepsilon\beta_p$'s, leaving only a limited part of the $\varepsilon\beta_p$ - nq* plane for stable operation.

With no stabilizing influence of a nearby wall, the profile $f_\gamma=f_\pi=1$ shows three stable regions: a small region above nq* = 1 (with $q_0 < 1$), one above nq* = 2, and a stable region above nq* = 3. These regions are separated by the unstable regions due to the external m=1, 2, and 3 kink modes and the internal m=1, 2 modes.

The maximum value of $\langle\beta\rangle/\varepsilon$ is reached in the stable region above nq* = 2: $\langle\beta\rangle/\varepsilon = 0.066$ at nq* = 1.94 (where $nq_0 = 1.15$ and $nq_a = 2.00$) and $\varepsilon\beta_p = 0.25$. This optimum is determined by the external m=2 and 3 modes and the internal m=1 mode. Further improvement of this optimum was obtained by changing the current gradient near the plasma surface.

A simple analysis of the equilibrium at $\varepsilon\beta_p = 0$ shows that a decrease of f_γ leads to a decrease in the current gradient at the surface but also to an increase of q_a/q_0. Figure 2 (dashed lines) shows the curves of marginal stability for $f_\gamma = 0.6$. Both effects of the decrease in f_γ are clearly seen.

At $\varepsilon\beta_p = 0$ the unstable regions due to the m=2 and 3 external kinks have shrunk, where the effect on the m=3 mode is much larger, as expected [3]. The shift of the $q_0 = 1$ curve to larger nq*'s exhibits the other effect. The change in f_γ is also accompanied by a shrinkage of the unstable regions associated with the internal m=1 and 2 modes. It was found to be advantageous to let the decrease in f_γ be accompanied by an increase in f_π; the values listed in the caption of Fig. 2 all led to optimum values of $\langle\beta\rangle/\varepsilon$ at that particular f_γ. At $f_\gamma = 0.6$, the result is $\langle\beta\rangle/\varepsilon = 0.074$. A further decrease in f_γ does not improve this optimum because the curve $q_0 = 1$ then moves so much to higher values of nq* that the internal m=1 mode becomes unstable.

The above analysis of the equilibrium belonging to Eq. (3) indicates that a further improvement of the stability can only be arrived at by a change in the profile functions. The fact that the m=1 mode was found to be the limiting factor points out what sort of change must be sought: the current profile should be

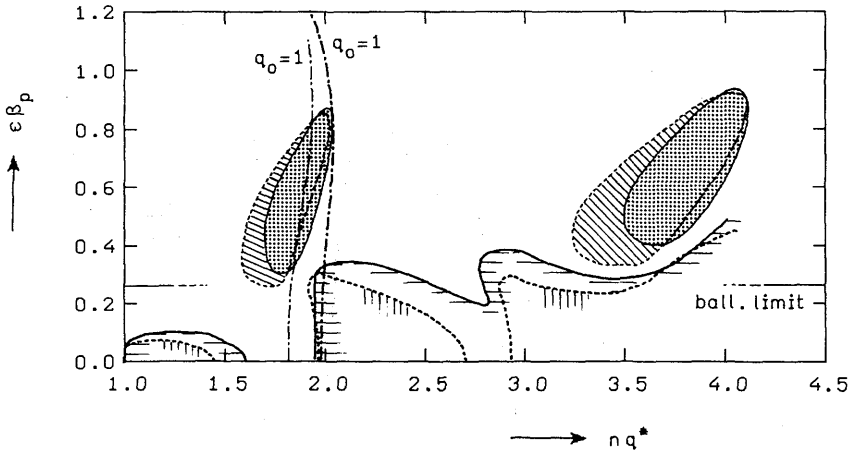

FIG.2. Stability boundaries for the equilibria: dashed lines $\Gamma = (1-\psi)(1+0.6\psi)$, $\Pi = (1-\psi)(1+10\psi)$; *solid lines* $\Gamma = (1-\psi^2)(1-\psi)+4.5\psi^2(1-\psi)^2$, $\Pi = (1-\psi^2)(1+40\psi)$. *Internally unstable and externally stable regions are indicated as in Fig.1.*

broader without increasing the current gradient near the surface. This is accomplished by the profile functions:

$$\Gamma(\psi) = (1-\psi^2)(1+f_\gamma\psi) + g_\gamma\psi^2(1-\psi)^2$$
$$\Pi(\psi) = (1-\psi^2)(1+f_\pi\psi) + g_\pi\psi^2(1-\psi)^2 \qquad (4)$$

The first term in $\Gamma(\psi)$ determines the shear near $q_0 = 1$, while the second makes the profile broad and affects only the current gradient at the surface. Figure 2 shows the marginally stable boundaries for the equilibrium $f_\gamma = -1$, $g_\gamma = 4.5$, $f_\pi = 40$ and $g_\pi = 0$ for two wall positions. With the wall on the plasma, only the internal m=1 and 2 modes are unstable. A comparison of the m=1 region with the corresponding ones for the equilibria shown in Figs 1 and 2 brings out a number of points. Because $q_0 = 1$ has become almost independent of nq*, the region has straightened up. The minimum that was first on the $q_0 = 1$ line has moved to a larger value of $\varepsilon\beta_p$ and to a lower value of q_0 [6,7]. At low $\varepsilon\beta_p$, the character of the mode is more that of an internal kink, while at high values it shows more ballooning features. This was already observed in Ref. [2] and has been extensively investigated in Ref. [8].

Without a wall this equilibrium has now two stable regions, a small one above nq* = 1, where $\langle\beta\rangle/\varepsilon$ reaches a reasonable value: $\langle\beta\rangle/\varepsilon = 0.068$, but $q_0 < 1$ ($q_0 = 0.58$, and $q_a = 1.15$) and one stable region above nq* = 2. The reduction in the current

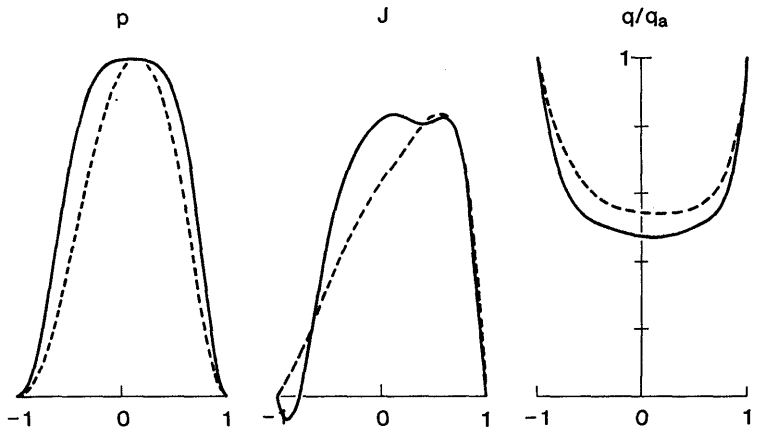

FIG.3. Pressure, current and q-profile in the equatorial plane of the cross-section at nq = 2 and $\epsilon\beta_p = 0.33$ for the equilibria of Fig.1 (dashed lines) and the optimized profile of Fig.2 (solid lines).*

gradient at the plasma surface has led to a complete disappearance of the external m=3 mode. As in the case of the other equilibria, the optimum beta is reached in the second region, namely $\langle\beta\rangle/\epsilon = 0.082$ ($q_0 = 1.01$, $q_a = 2.13$, $nq^* = 2.01$).

The difference between this equilibrium and the first one of the previous class $f_\gamma = f_\pi = 1$ at $\epsilon\beta_p = 0.33$ is portrayed in Fig. 3. The shape of the q-profiles are almost the same; only q_a/q_0 differs. The pressure is now broader and the toroidal current shows a small region with negative currents on the inside of the torus.

The stability of the various equilibria with a circular cross-section has shown that it depends sensitively on essentially the q-profile. Therefore many experimental tokamak plasmas will not reach such values of beta and in particular will encounter unstable regions near $nq^* = 3$ unless special care is taken [9]. Whether it is possible to adjust the q-profile so that the stable region above $nq^* = 1$ can be reached without crossing an unstable region we do not know. No such equilibrium was found.

3. FINAL RESULTS

The stability results obtained for a circular cross-section are in approximate qualitative agreement with Troyon's scaling law [10], which in terms of our parameters should give a linear relationship between $\epsilon\beta_p$ and q^*. However, already for circular cross-sections, higher values are found for the coefficient in the scaling law: $\epsilon\beta_p = 0.16\ q^*$ or $\langle\beta\rangle/\epsilon = 0.16/q^*$ as compared to $\epsilon\beta_p = 0.14\ q^*$ found by Troyon. To obtain this

improvement, a small but negative toroidal current density had to be permitted on the inside of the torus. Further improvement is obtained by subsequently elongating the obtained high-β equilibrium configuration to a D-shaped (JET) or racetrack (SPICA II) cross-section. For these shapes the marginal stability curves of $\varepsilon\beta_p(q^*)$ rise with the elongation. Here, the combination of the conformal mapping technique and the choice of the parameter q^* (with the geometric factor η defined above) permits the construction of a simple picture of high-β stability in terms of optimized parameters.

Optimization with respect to global external and internal kink modes alone gives a value of $\varepsilon\beta_p/q^*$ above the one given by Troyon. However, if we consider stability with respect to ballooning modes as well, the optimum β degrades. This is understood because the equilibria were optimized taking account of the global modes only. We feel that this is the proper approach to the study of tokamak stability since these modes are best described by the ideal MHD model. On the other hand, the additional consideration of the ballooning modes takes a particularly simple form at high β. In the high-β tokamak ordering, the ballooning equation does not depend on nq^* so that one just obtains a threshold in the parameter $\varepsilon\beta_p$ above which the equilibrium becomes ballooning unstable. Thus, the marginal stability curves for the global modes depicted in Figs 1 and 2 are intersected by horizontal lines corresponding to marginal stability with respect to local modes. If the optimum configuration with respect to global modes alone lies above the ballooning threshold, the optimum configuration with respect to both ballooning and kink modes is found at the intersection point in the $\varepsilon\beta_p$-nq^* plane.

For the profiles considered in Figs 1 and 2, the ballooning thresholds are given by $\varepsilon\beta_p = 0.12$ for $\Gamma = \Pi = 1-\psi^2$ (Fig. 1), and $\varepsilon\beta_p = 0.262$ for the optimized profile corresponding to the drawn lines in Fig. 2. We conclude that the optimum configuration in the isolated low-q region at $q^* \sim 1$ (with $q_o < 1$) is ballooning stable as well, whereas the optimum configurations at $q^* \sim 2$ degrade to $\langle\beta\rangle/\varepsilon = 0.031$ for the first case and $\langle\beta\rangle/\varepsilon = 0.069$ for the optimized profile. The latter value corresponds to $\langle\beta\rangle/\varepsilon \cdot q^* = 0.13$.

Thus, consideration of both global kink and local ballooning modes in circular cross-section tokamaks leads to values of $\langle\beta\rangle/\varepsilon \cdot q^*$ that are in agreement with Troyon's scaling law.

ACKNOWLEDGEMENT

This work was performed under the Euratom-FOM Association agreement. It was supported financially by the Stichting voor Fundamenteel Onderzoek der Materie (FOM), the Nederlandse Organisatie voor Zuiver-Wetenschappelijk Onderzoek (ZWO),

EURATOM, the Fundação de Amparo à Pesquisa do Estado de São Paulo, the Conselho Nacional de Desenvolvimento Cientifico e Technológico, and the Comissão Nacional de Energia Nuclear (Brazil).

REFERENCES

[1] GOEBLOED, J.P., Comput. Phys. Commun. **24** (1981) 311; **31** (1984) 123.
[2] GALVÃO, R.M.O., et al., "Global kink and ballooning modes in high-beta systems and stability of toroidal drift modes", Plasma Physics and Controlled Nuclear Fusion Research 1982 (Proc. 9th Int. Conf. Baltimore, 1982), Vol.3, IAEA, Vienna (1983) 3.
[3] SHAFRANOV, V.D., Sov. Phys.-Tech. Phys. **15** (1970) 175.
[4] REM. J., GALVÃO, R.M.O., GOEDBLOED, J.P., SAKANAKA, P.H., in Controlled Fusion and Plasma Physics (Proc. 11th Europ. Conf. Aachen, 1983), Vol.2 (1983) 151; GOEDBLOED, J.P., HOGEWEIJ, G.M.D., KLEIBERGEN, R., REM, J., in Proc. Int. Conf. Plasma Physics, Lausanne, 1984, Vol. 1 (1984) 197.
[5] WESSON, J.A., Nucl. Fusion **18** (1978) 87.
[6] BUSSAC, M.N., PELLAT, R., EDERY, D., SOULE, J.L., Phys. Rev. Lett. **35** (1975) 1638.
[7] KERNER, W., GRUBER, R., TROYON, F., Phys. Rev. Lett. **44** (1980) 536.
[8] MANICKAM, J., Nucl. Fusion **24** (1984) 595.
[9] KADOMTSEV, B.B., Plasma Phys. Contr. Fusion **26** 1A (1984) 217 (Invited Papers of 11th Europ. Conf. Aachen, 1983).
[10] TROYON, F., GRUBER, R., SAURENMANN, H., SEMENZATO, S., SUCCI, S., Plasma Phys. Contr. Fusion **26** 1A (1984) 209 (Invited Papers of 11th Europ. Conf. Aachen, 1983).

ACCESSIBLE BETA VALUE OF TOKAMAKS

T. TUDA, M. AZUMI, K. ITOH, G. KURITA, T. TAKEDA,
T. TAKIZUKA, S. TOKUDA, T. TSUNEMATSU,
M. ADACHI*, Y. TANAKA*, M. WATANABE**,
S.-I. ITOH***
Japan Atomic Energy Research Institute,
Tokai, Naka, Japan

Abstract

ACCESSIBLE BETA VALUE OF TOKAMAKS.

The critical beta of tokamaks is studied by means of a linear analysis of MHD instabilities. The infinite-n ballooning mode and the n = 1 external kink mode are similar in the dependence of their critical beta on the plasma parameters. Elongation and triangular deformation of the plasma co-operatively increase the critical beta value. The saturation mechanism of electrostatic ballooning instability is analysed by simple non-linear model equations. Laminar convective flow appears rather than turbulence.

1. INTRODUCTION

To estimate the performance of a fusion reactor and to design a future large tokamak, a reliable scaling law for the maximum beta limit must be established. Scaling laws of the beta limit have been studied by several authors. However, their investigations were restricted either to the infinite-n (n is the toroidal mode number) ballooning mode [1–3] or the n = 1 kink mode [4, 5]. In this paper, we study the scaling laws of the beta limit in which finite-n free-boundary modes as well as the infinite-n ballooning mode are taken into consideration. First, we optimize the pressure profile against the infinite-n ballooning mode and get a scaling law for the beta limit. Next, we analyse the linear stability of finite-n free-boundary modes for equilibria with optimized pressure profile. From these studies, we obtain the scaling laws yielding the accessible beta limits for the tokamaks.

In an MHD-unstable equilibrium, violent anomalous transport or plasma disruption results in the limitation of beta, whereas a weaker residual instability below the critical beta causes only moderate anomalous transport. Resistive and electrostatic ballooning modes [6] are important for transport of tokamak plasmas, and the saturation process of the electrostatic ballooning modes is studied by using simple non-linear model equations.

---

* On leave from Fujitsu Ltd, Ohta, Tokyo 144, Japan.
** On leave from Nuclear Data Co., Meguro, Tokyo 153, Japan.
*** Institute for Fusion Theory, Hiroshima Univ., Hiroshima 730, Japan.

2. INFINITE-n BALLOONING MODE

The infinite-n ballooning mode is considered to play a crucial role in the limitation of the beta value,

$$\beta = 2\mu_0 \int pdV/B_{t0}^2 \int dV$$

(μ_0 is the vacuum permeability, p the plasma pressure, and B_{t0}, the toroidal magnetic field at the plasma centre). Since the stability of the ballooning mode is sensitive to the plasma shape (A is the aspect ratio, κ the ellipticity, and δ the triangularity), the pressure profile, $p(\Psi)$, and the safety factor profile, $q(\Psi)$, optimization with respect to these parameters is required to realize a high-beta stable equilibrium. We optimize the pressure profile for an equilibrium with given shape of the plasma surface and given q-profile [3]. We compute the marginal pressure gradient by solving the infinite-n ballooning equation with zero growth rate for a given equilibrium. We next solve the Grad-Shafranov equation for the obtained pressure profile and the fixed q-profile (FCT process) and again evaluate the marginal pressure gradient. The final equilibrium is marginally stable against the infinite-n ballooning mode in the whole plasma region. In these analyses, the q-profile is given by a force-free equilibrium with toroidal current profile, $j_\varphi = C(1-\Psi)^\alpha/R$, ($\Psi$ is the normalized poloidal flux function). The values of C and α are adjusted such that the safety factor at the magnetic axis, q_{ax}, and that at the plasma surface, q_s, take the prescribed values.

By fits with the numerical results, we obtain the following scaling law for the critical value of beta for $q_{ax} = 1$:

$$\beta_c(\%) = \frac{30\kappa^{1.5}}{Aq_s}\left\{1 + 0.9(\kappa-1)\delta - 0.6\frac{\kappa^{0.75}}{q_s} + 14(\kappa-1)(1.85-\kappa)\frac{\delta^{1.5}}{q_s^4}\right\} \qquad (1)$$

Figure 1 shows that the numerically obtained critical beta values, β, are well represented by the above formula. Elongation and triangular deformation co-operatively increase the critical beta value. The safety factor q_s for finite beta deviates considerably from that for a cylindrical plasma with non-circular cross-section. For optimized equilibria, the relation between q_s and the total plasma current, I_p, is approximately given by

$$\frac{1}{q_s} = A\sqrt{(1-1/A^2)}\left(\frac{2}{1+\kappa^2} - 0.08\delta\right)\frac{\mu_0 I_p}{2\pi a B_{t0}} - 0.07\{1+(\kappa-1)\delta\} \qquad (2)$$

where a is the plasma minor radius and MKS units are used.

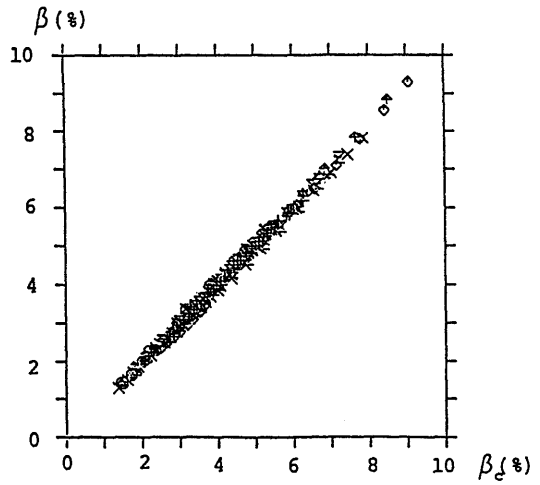

FIG.1. Critical beta value for infinite-n ballooning mode. The numerically obtained beta is well represented by β_c.

3. FINITE-n FREE-BOUNDARY MODES

Free-boundary modes remain unstable for the optimized equilibria against the infinite-n ballooning mode. In this section we study the stability of free-boundary modes for the same equilibria as in Section 2 by using the ERATO code [7]. Figure 2 shows the dependence of the critical beta on the mode number n for the case of no conducting wall. The n = 1 kink mode is the most unstable one, and the beta limit for $n > 1$ is almost the same as that for the infinite-n ballooning mode. Therefore, we study the beta limit of the n = 1 kink mode. The dependence of β_c, for the n = 1 kink mode, on κ, δ and q_s is shown in Fig.3 for A = 3.38 and $q_{ax} = 1$. The points along the dashed and the solid lines correspond to the cases of high shear ($3 < q_s < 4$) and low shear ($2 < q_s < 3$), respectively. The scaling law for the n = 1 kink mode is expressed as

$$\beta_c(\%) = \frac{C\kappa^{1.65}}{Aq_s}\{1 + (\kappa - 1)\delta\}, \quad C = 14\ (2 < q_s < 3) \text{ and } C = 20\ (3 < q_s < 4),$$

$$\beta_c \approx 0 \qquad \text{for } q_s < 2, \tag{3}$$

where inverse proportionality with the aspect ratio is assumed. This formula has a form similar to the dominant terms in Eq.(1) for $q_s > 2$, and Eq.(2) is approximately true in this case.

The scaling laws, Eqs (1) and (3) in the range $q_s > 2$, are roughly expressed in terms of the total current as

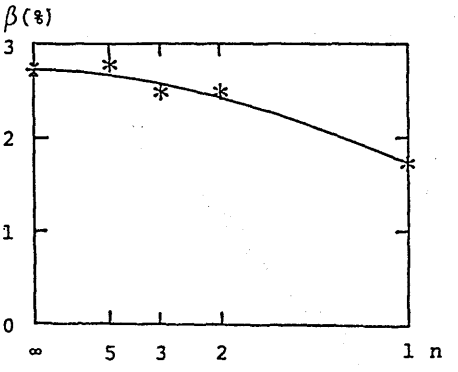

FIG.2. Dependence of critical beta value on n for A = 3.38, κ = 1, δ = 0, q_{ax} = 1, and q_s = 2.6.

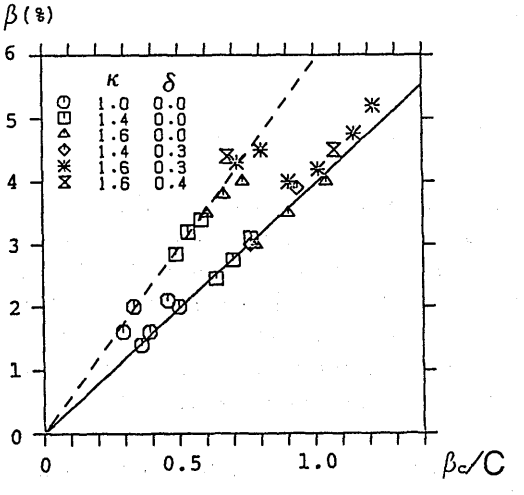

FIG.3. Critical beta value for n = 1 kink mode (A = 3.38, q_{ax} = 1). Points along dashed and solid lines correspond to cases of 3 < q_s < 4 and 2 < q_s < 3, respectively.

$$\beta_B(\%) = (20 \pm 2.5)\mu_0 I_p/(2\pi a B_{t0}) \qquad \text{for the ballooning mode,}$$

$$\beta_K(\%) = (16 \pm 2.0)\mu_0 I_p/(2\pi a B_{t0}) \qquad \text{for the n = 1 kink mode.} \qquad (4)$$

The coefficients in Eq.(4) are almost the same as those obtained by other calculations [1, 4]. The n = 1 kink mode tends to be unstable because j_φ remains finite at the plasma surface, because of the optimization procedure of the pressure profile. If we choose the q-profile with a sufficiently decreasing current profile

near the plasma surface, β_K increases with decreasing β_B and the two beta limits will become closer to one another. The wall stabilization is a recipe for increasing β_K without beta limit degradation due to the ballooning mode if a first wall plays the role of a conducting wall [2, 8]. In our cases, β_K coincides almost with β_B when the conducting wall is placed at $q_w/a = 1.5$ (a_w is the minor radius of the wall).

4. NON-LINEAR MODEL EQUATION FOR BALLOONING INSTABILITY

As a first step in estimating the transport coefficient due to the ballooning instability, we study the saturation mechanism of electrostatic ballooning mode [6] by a two-dimensional model. We use a two-fluids equation system with resistivity, in Cartesian co-ordinates. The strong magnetic field is in the z-direction. The plasma density n_0 and magnetic field strength B vary in the x-direction. In the case of long-wavelength ballooning modes ($\kappa_\perp^2 \rho_s^2 \ll 1$), the dominant non-linear effect is the convective term, and the typical localization length along the field line is given as qR for $\omega \approx \omega_* > c_s/qR$ (q is the safety factor, R the major radius, c_s the sound velocity, ω_* the drift frequency, and ρ_s the ion gyroradius at the electron temperature). Using these assumptions, we derive a two-dimensional model equation for the electrostatic ballooning mode as

$$\frac{\partial N}{\partial t} + v_* \frac{\partial N}{\partial y} + \frac{v_* v_d}{\omega_s} \frac{\partial^2 N}{\partial y^2} + \nu \Delta_\perp^2 N = \frac{v_d}{\omega_s} \frac{T_e}{eB} \left\{ \frac{\partial N}{\partial x} \frac{\partial^2 N}{\partial y^2} - \frac{\partial N}{\partial y} \frac{\partial^2 N}{\partial x \partial y} \right\} \tag{5}$$

where $N = \tilde{n}/n_0$, $v_* = T_e/eBL_n$, $v_d = (T_e + T_i)/eBR$, $\omega_s = \tau_e T_e / 0.51 m_e q^2 R^2$, $1/L_n = -\nabla n_0/n_0$, τ_e is the electron collision time and ν the ion perpendicular viscosity. This model equation is solved numerically with the boundary condition that $N = 0$ at $x = 0$ and $x = L_x$.

Single-mode saturation is realized for a wide range of plasma parameters. In this simulation, the maximum number of linearly unstable modes is about 20. Laminar convective flow rather than turbulence occurs. Figure 4 shows the viscosity dependence of the saturation amplitudes. The mode with maximum linear growth rate remains in the final state and the saturated amplitude is of the order of $N = L_x/L_n$. Non-linear saturation originates from the convective term; background modification is produced by mode-mode coupling.

5. DISCUSSION AND CONCLUSIONS

We obtained scaling laws which give the accessible beta value of tokamaks by the optimization of the pressure profile against the infinite-n ballooning mode and by stability analyses of finite-n free-boundary modes for the optimized

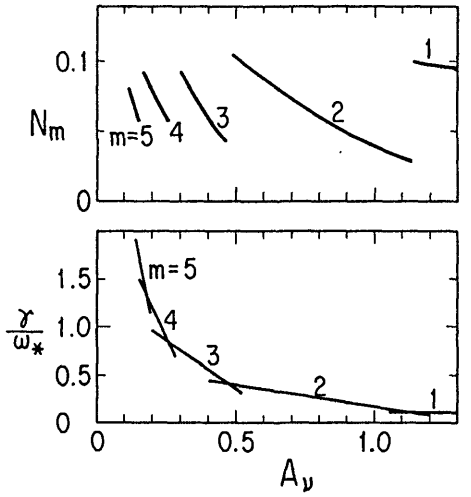

FIG.4. Dependence of saturated amplitude on normalized viscosity $A_\nu \equiv \nu\omega_s/v_* v_d \rho_s^2$ *(upper diagram) and linear growth rate (lower diagram) on* A_ν *for* $L_x/\rho_s = 14$, $L_y/\rho_s = 16$, $L_n/\rho_s = 50$, *where m is mode number in y-direction.*

equilibria. The scaling laws are expressed by Eqs (1) and (3) for the infinite-n ballooning mode and the n = 1 kink mode, respectively. These scaling laws are roughly expressed as $\beta_c \propto I_p$ for $q_s > 2$. It was shown that the elongation and the triangular deformation of the plasma surface can co-operatively increase the critical beta value. We studied the non-linear behaviour of the electrostatic ballooning mode. The mode is saturated by the convective term (background modification by mode coupling) and the saturated amplitude is of the order of $\tilde{n}/n_0 = L_x/L_n$.

REFERENCES

[1] SYKES, A., TURNER, M.F., PATEL, S., in Controlled Fusion and Plasma Physics (Proc. 11th Europ. Conf. Aachen, 1983), Part II B23 (1983) 363.
[2] BERNARD, L.C., HELTON, F.J., MOORE, R.W., TODD, T.N., Nucl. Fusion 23 (1983) 1475.
[3] AZUMI, M., et al., in Plasma Physics (Proc. Int. Conf. Lausanne, 1984), Vol.1 (1984) 200.
[4] TROYON, F., GRUBER, R., SAURENMANN, H., SEMENZATO, S., SUCCI, S., Plasma Phys. 26 (1984) 209.
[5] GOEDBLOED, J.P., HOGEWEIJ, G.M.D., KLEIBERGEN, R., REM, J., in Plasma Physics (Proc. Int. Conf. Lausanne, 1984), Vol.1 (1984) 196.
[6] TUDA, T., ITOH, K., TOKUDA, S., ITOH, S.-I., Phys. Fluids 25 (1982) 1583.
[7] TOKUDA, S., et al., MHD Stability Analysis by Revised Version of ERATO-J, Rep. JAERI-M 9899 (1982).
[8] AZUMI, M., et al., in Plasma Physics and Controlled Nuclear Fusion Research 1980 (Proc. 8th. Int. Conf. Brussels, 1980), Vol.1, IAEA, Vienna (1981) 293.

INFLUENCE OF MAGNETIC FIELD RIPPLE ON PLASMA ROTATION IN TOKAMAKS

V.Ya. GOLOBOROD'KO, Ya.I. KOLESNICHENKO,
V.A. YAVORSKIJ
Nuclear Research Institute of the Ukrainian SSR,
Academy of Sciences, Kiev,
Union of Soviet Socialist Republics

Abstract

INFLUENCE OF MAGNETIC FIELD RIPPLE ON PLASMA ROTATION IN TOKAMAKS.

The problem of plasma rotation in tokamaks with injection is considered. It is shown that the experimental results obtained in the PLT and ISX-B tokamaks can be explained by the presence of the magnetic-field ripple, provided that localized particles exist. The analysis carried out is based on the general expression for the magnetic-field ripple. This expression, which is derived in the present paper, describes the ripple distribution over the plasma cross-section for both the ordinary case and the case of shunted or damaged coils.

1. INTRODUCTION

In recent years, the problem of steady-state current drive in tokamaks has attracted a good deal of attention. It should be noted that the authors of theoretical work in this field usually neglect plasma rotation, assuming that the toroidal momentum transferred to the electrons from the RF-field or the injected ions is dissipated by the background ions. It is, however, clear that the toroidal velocity is not zero and depends on the dissipation of toroidal momentum, but it was not measured in the current drive experiments. If the increase in tokamak size will lead to an attenuation of the dissipative processes, the plasma rotation in a reactor-tokamak may result in an unacceptably small efficiency of the driving current.

In addition, the toroidal rotation may affect the impurity behaviour, and there are some ideas to use it for ash removal. Thus, the study of plasma rotation is of considerable interest.

Experimental research into the toroidal rotation caused by neutral-beam injection was carried out on a number of devices, in particular on the PLT [1–3] and ISX-B [4] tokamaks. It was not, however, clear which process is responsible for the dissipation of toroidal plasma momentum. The authors of Refs [1–3], proceeding from the fact that the strong increase in field ripple does not affect the results, concluded that the ripples do not essentially influence the dissipative process; in Ref.[3], to simulate the process, the concept of anomalous viscosity

was introduced. In Ref.[4], it was concluded that the inapplicability of neoclassical theory to the case of large toroidal velocities is the reason for the disagreement between experiment and theory.

In this paper, plasma rotation in tokamaks is studied theoretically. A classical dissipative mechanism connected with the presence of localized particles is considered (Sections 3 and 4). In particular, results of the PLT and ISX-B experiments are analysed and explained (Section 4). A study of plasma rotation follows the derivation of a general expression determining the field ripple in various tokamaks (Section 2). This expression is also of independent interest.

2. FIELD RIPPLE

For a theoretical description of the processes connected with toroidal field ripple it is important to have an expression that determines the spatial distribution of ripple. Probably the most correct expression of this kind is that to be found in Ref.[5]. It contains, however, two independent parameters so as to specify which of these two should carry out the calculations based on a knowledge of the real spatial ripple distribution. In this section, we derive an expression which gives the ripple distribution, depending on the coil parameters or on the field ripple value in a single point. In addition, a general expression including the case of damaged or shunted coils is obtained.

We introduce toroidal co-ordinates u, θ, φ ($0 \leqslant u < \infty$, $-\pi \leqslant \theta \leqslant \pi$, $0 \leqslant \varphi \leqslant 2\pi$) which are connected with the cylindrical co-ordinates via

$$r = \frac{R \operatorname{sh} u}{\operatorname{ch} u - \cos\theta}, \quad \varphi' = \varphi, \qquad z = \frac{R \sin\theta}{\operatorname{ch} u - \cos\theta} \tag{1}$$

where $R = r(u = \infty)$. Non-zero components of the metric tensor are

$$g_{11} = g_{22} = \frac{g_{33}}{\operatorname{sh}^2 u} = \frac{R^2}{(\operatorname{ch} u - \cos\theta)^2} \tag{2}$$

Assuming periodicity (over φ) of the toroidal field coil arrangement, we approximate the coil current density as follows:

$$j_\theta = J \frac{\delta(u-u')}{2\pi\sqrt{g_{11} g_{33}}} \sum_{m=-\infty}^{\infty} F_m \cos m\varphi \tag{3}$$

Here, J is the current in a single coil; $u = u'$ is a toroidal surface where N coils are arranged; the angle $\varphi = 0$ is chosen in such a manner that $j_\theta(\varphi) = j_\theta(-\varphi)$; F_m is a Fourier component given by the expression

$$F_m = \left[\frac{\sin m\pi}{\sin \frac{m\pi}{N}} \cos \frac{N-1}{N} m\pi - \kappa \right] \frac{\sin \frac{m\alpha}{2}}{\frac{m\alpha}{2}} \tag{4}$$

where α is the angular width of the coil; $\kappa = 0$ for the case of equal coil currents, otherwise $\kappa \neq 0$. In particular, if one coil is damaged (as in the PLT experiment [1–3], then $\kappa = n_1/n$, n and n_1 being the numbers of the total and the shunted coil turns, respectively.

The current given by expression (3) produces a magnetic field with a scalar potential Φ, which in the inner region of the coils ($u' \leqslant u < \infty$) has the form (using the equation $\Delta\Phi = 0$):

$$\Phi = R B_0 \left[\varphi + \sum_{m=1}^{\infty} \frac{1}{m} \delta_m \sin m\varphi \right] \tag{5}$$

where

$$\delta_m = \frac{R^{1/2}}{g_{33}^{1/4}} \sum_{\ell=-\infty}^{\infty} C_{\ell m}(\operatorname{cth} u') P^{-\ell}_{m-\frac{1}{2}}(\operatorname{cth} u) \cos \ell\theta \tag{6}$$

$$C_{\ell m}(t) = (-1)^{\ell} \frac{4J}{cRB_0} F_m (t^2-1) \frac{\Gamma(\frac{1}{2}-\ell)}{\Gamma(\frac{1}{2})} \times \left[P^{\ell}_{-\frac{1}{2}}(t) \frac{d}{dt} Q^{\ell}_{m-\frac{1}{2}}(t) - Q^{\ell}_{m-\frac{1}{2}}(t) \frac{d}{dt} P^{\ell}_{-\frac{1}{2}}(t) \right] \tag{7}$$

Here, $P^{\mu}_{\nu}(t)$ and $Q^{\mu}_{\nu}(t)$ are the associated Legendre functions of the first and second kind, respectively, $\Gamma(x)$ is the gamma function, and $B_0 = 2JN/(cR)$. We note that Eqs (5) to (7) can be derived (by means of some cumbersome calculations) from the general expression for Φ obtained in Ref.[6].

To simplify Eq.(6), we remember that $\operatorname{cth} u - 1 \ll 1$ in the plasma region and $\nu \gg 1$ for $\kappa = 0$ [4]. Then, with a good accuracy for $\kappa = 0$ and a somewhat lower one for $\kappa \neq 0$, the associated Legendre functions can be expressed in terms of the modified Bessel functions of the first and second kind ($I_\mu(x)$ and $K_\mu(x)$):

$$P_\nu^\mu(t) \cong \left(\nu + \frac{1}{2}\right)^\mu I_{-\mu}(\zeta)$$
$$Q_\nu^\mu(t) \cong e^{-i\mu\pi}\left(\nu + \frac{1}{2}\right)^\mu K_\mu(\zeta) \tag{8}$$

where $\zeta = (2\nu + 1)\sqrt{(t-1)/2}$. Using relation (8) and neglecting the terms with $\ell \neq 0$ in Eq.(6), we obtain:

$$\delta_m \cong 2F_m \frac{m}{A_c} K_1(m\eta')I_0(m\eta) \tag{9}$$

where $\eta = \sqrt{2(\text{cth}\, u - 1)}$, $\eta' = \eta(u = u')$. The variable η can be represented in terms of cylindrical co-ordinates as follows:

$$\eta^2 = \frac{(R-r)^2 + z^2}{R\,r}, \quad \eta'^2 = 2\left(\frac{R_0}{R} - 1\right) \tag{10}$$

where $R_0 = R/\sqrt{1 - A_c^{-2}}$, $A_c = R_0/a_c$, R_0 is the value of r for the geometrical centre of the coil, and a_c is the coil radius.

To generalize expression (9) for the finite coil thickness, we should average it over u'. However, for $\kappa = 0$, we obtain from Eq.(9) the aspect ratio of the equivalent coil with zero thickness, provided that the value of δ is known at least at one point. Equation (9) with such an aspect ratio will describe the spatial distribution of ripple for coils of finite thickness.

If the currents in all coils are equal or one coil is partially or completely shunted, then the expression for the magnetic field takes the form:

$$B = B_0 \frac{R}{r}[1 + \delta_N \cos N\varphi - \delta^1(\varphi)] \tag{11}$$

where δ_N is given by Eq.(9) with m = N,

$$\delta^1(\varphi) = \sum_{m<N} \delta_m \cos m\varphi \approx \hat{\delta}(\cos 3\varphi + 1)\eta\left(\frac{\pi}{3} - |\varphi|\right) - \bar{\delta}$$

for the case of a shunted coil, otherwise $\delta^1 = 0$ (where $\hat{\delta}$ and $\bar{\delta}$ are the values determined by n and n_1, $\eta(x) = \int_0^x dx\delta(x)$, and the middle of the shunted coil corresponds to $\varphi = 0$).

3. TOROIDAL PLASMA ROTATION IN THE PRESENCE OF LOCALIZED PARTICLES. ISX-B EXPERIMENTS

We assume that there is a group of localized particles in a tokamak, i.e. we consider the following condition to be fulfilled:

$$\nu_{ii} < \frac{N v_{T_i} \delta_N^{3/2}}{2\pi R_0} \tag{12}$$

where v_{T_i} is the thermal ion velocity, and ν_{ii} is the ion-ion collision frequency. Then, on the basis of qualitative considerations, we may write an equation for the toroidal momentum of the plasma in tokamaks with injection:

$$1.46\, m_i n_i \langle \Delta^{1/2} \rangle \nu_{ii}\, u = M \tag{13}$$

Here, u is the toroidal velocity, M is the momentum input per unit time and unit plasma volume, m_i and n_i are the ion mass and the ion density, respectively, and $\langle \Delta^{1/2} \rangle$ is the flux-surface-averaged fraction of localized particles given by the expression:

$$\langle \Delta^{1/2} \rangle = \frac{\int_S \Delta^{1/2}\, dS}{\int_S dS} \tag{14}$$

Δ is the local magnetic well depth. In particular, for the equal current coils, the expression for Δ is well known:

$$\Delta = 2\delta_N \left(\sqrt{1-\gamma^2} - \gamma \cos^{-1}\gamma\right) \tag{15}$$

where

$$\gamma = \left| \frac{\epsilon \sin\theta}{N q \delta_N} \right| \tag{16}$$

$\epsilon = \rho/R_0$, ρ is the distance from the torus magnetic axis, and q is the tokamak safety factor. The numerical factor 1.46 in Eq.(13) follows from geometrical considerations [7]. Note that an equation similar to Eq.(13) is presented in Ref.[7]; it contains, however, $\delta_N^{1/2}$ instead of $\langle \Delta^{1/2} \rangle$.

Let us study whether Eq.(13) can be applied for a description of the plasma rotation in ISX-B. This device was operated with 18 and 9 coils and the toroidal velocity was measured for both regimes [4]. When ISX-B operated with 9 coils,

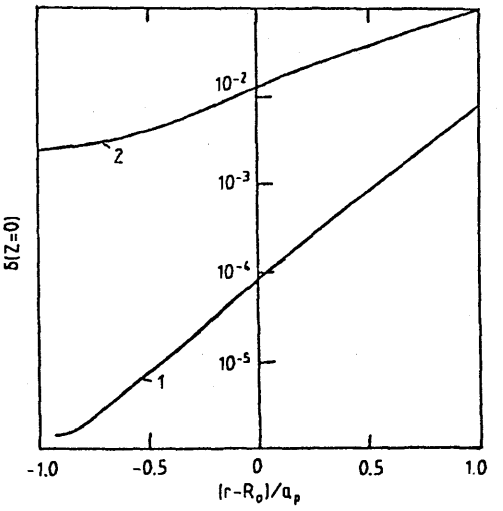

FIG.1. Equatorial distribution of ISX-B magnetic field ripple following from Eq.(9): (1) 18 coils energized; (2) 9 coils energized. a_p is the plasma radius.

the ripple depth strongly increased; this is seen from Fig.1, which was obtained by means of Eqs (9) and (11). Using the tokamak parameters of the experiment [4], we conclude that Eq.(12) is invalid for all coils operating. Therefore, in this case there are no localized particles and the velocity as measured is related to different factors; in the regime with nine coils, however, Eq.(12) is valid, and Eq.(13) yields:

$$\begin{aligned} u(0.37) &= 1.6 \times 10^6\ \mathrm{cm\cdot s^{-1}},\ \left.\frac{u}{u_{exp}}\right|_{x=0.37} \approx 1.1 \\ u(0.81) &= 4.3 \times 10^5\ \mathrm{cm\cdot s^{-1}},\ \left.\frac{u}{u_{exp}}\right|_{x=0.81} \approx 1.3 \end{aligned} \qquad (17)$$

where $u = u(x)$, $x = \rho/a$, a is the plasma radius, u_{exp} is the measured value of u. To calculate (17), we used the radial dependence of $\langle \Delta^{1/2} \rangle$, which was found from Eqs (9), (14) and (15) and which is presented in Fig.2. The radial distributions of the plasma parameters and the momentum input were assumed to be parabolic.

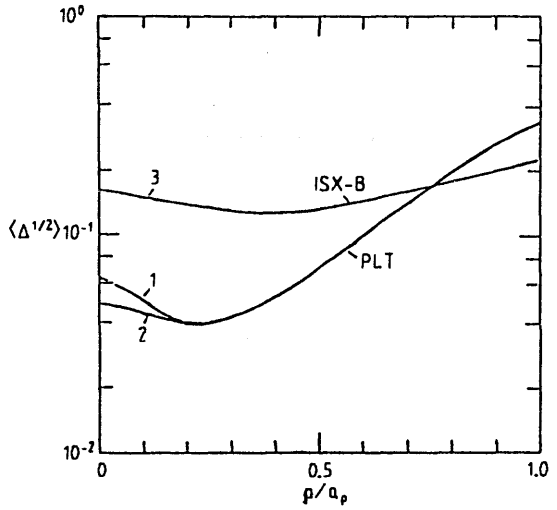

FIG.2. Fraction of localized particles averaged over flux surface for PLT and ISX-B devices. Curves 1 and 2 correspond to usual and 'accidental' regimes of PLT operation, respectively. Curve 3 corresponds to 9-coil case of ISX-B.

4. ROLE OF LOCALIZED PARTICLES IN PLT EXPERIMENTS

Plasma rotation caused by neutral-beam injection was studied in the PLT device for two regimes which were the usual regime and the 'accidental' one (one coil of the magnetic field partially shunted). Despite the large difference in the value and the distribution of the ripple, the toroidal velocity was the same in both regimes. Therefore, the dissipation of the toroidal plasma momentum would be expected to be independent of the magnetic field ripple. However, we show here that, actually, the toroidal velocity is determined by Eq.(13), and we explain why coil shunting does not affect the rotation.

We start with the usual regime ($\delta_N(0) \approx 0.2\%$). Using the measured plasma parameters [3] and assuming the electron and ion temperature profiles to be similar, we conclude that Eq.(13) is well applicable to the region far from the magnetic axis and is marginally applicable near the axis. Solution of Eq.(13) yields (it is assumed that $M(\rho) \approx 1-\rho^2$):

$$u(0.25) = 2.9 \times 10^7 \text{ cm}\cdot\text{s}^{-1}, \left.\frac{u}{u_{exp}}\right|_{x=0.25} = 2.2$$

$$u(0.75) = 3.1 \times 10^6 \text{ cm}\cdot\text{s}^{-1}, \left.\frac{u}{u_{exp}}\right|_{x=0.75} = 1.1 \qquad (18)$$

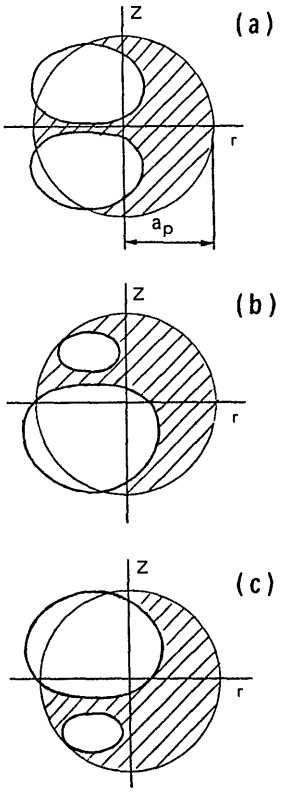

FIG. 3. Qualitative picture of regions where local ripple wells exist (shaded regions) over PLT plasma cross-section in the case of 'accidental' operation for different values of φ: (a) $\varphi = 0$; (b) $-\pi/6 < \varphi < 0$; (c) $0 < \varphi < \pi/6$. Poloidal dimension of flux surface sections where ripple wells exist weakly depends on φ (except for narrow near-axis region). This is the reason why coil shunting virtually does not affect quantity of localized particles.

In the 'accidental' regime, the magnetic field is determined by Eq.(11) with $\delta^1(\hat{\delta}, \overline{\delta}) \neq 0$. Using the results of Ref.[2] and remembering that the dependence of $\hat{\delta}$ on ρ and θ is weak, we take $\hat{\delta} = 1.3\%$, $\overline{\delta} = 0$. The appearance of δ^1 affects the magnetic field in two ways. First, it produces a single deep magnetic well in the region $|\varphi| < \pi/3$; second, it changes the region of existence of wells with the usual modulation period ($\Delta\varphi \lesssim 2\pi/N$). The question arises of whether the deep magnetic well leads to a trapping of a large fraction of particles. For an answer, we use the PLT parameters [3] and conclude that the condition for particle trapping in the single well is not satisfied:

$$\nu_{ii} > \frac{3\, v_{T_i}\, \hat{\delta}^{3/2}}{2\pi R_0} \tag{19}$$

Therefore, we conclude that in the 'accidental' as well as in the usual regime the non-uniform toroidal field leads to particle trapping in regions with $\Delta\varphi \lesssim 2\pi/N$. However, the regions where local magnetic wells exist are determined by a condition that is more complicated than in the case of $\delta^1 = 0$:

$$\tilde{\gamma} = \left| \frac{\epsilon \sin\theta}{N q \delta_N} + \frac{3\hat{\delta} \sin 3\varphi}{N \delta_N} \eta\left(\frac{\pi}{3} - |\varphi|\right) \right| < 1 \qquad (20)$$

The qualitative picture following from Eq.(20) is shown in Fig.3. The depth of the magnetic wells in the 'accidental' regime is determined by Eq.(15), where γ should be replaced by $\tilde{\gamma}$. The radial profiles of $\langle\Delta^{1/2}\rangle$ for the PLT parameters in both regimes are presented in Fig.2. We see that in the regions where the measurements were made the coil shunting does not change $\langle\Delta^{1/2}\rangle$. For this reason, the shunting should not affect the plasma rotation, which was observed in the experiments.

5. CONCLUSIONS

We have shown that plasma rotation in the injection experiments on PLT [1–3] and ISX-B [4] tokamaks can be explained in terms of a classical mechanism of toroidal momentum dissipation. Such a mechanism is, specifically, the friction between the rotating plasma and the ions trapped by the field ripple. The calculated toroidal velocities are in good agreement with the measured values (Eqs (17) and (18)). One should, however, remember the following facts: first, the radial profile of the momentum input was assumed to be parabolic, without any calculations. Second, because of the lack of experimental data, we used a parabolic distribution for the plasma parameters in ISX-B. Third, Eq.(13) for the momentum should be justified more firmly.

REFERENCES

[1] EUBANK, H.P., et al., in Heating in Toroidal Plasmas (Proc. 2nd Joint Varenna-Grenoble Int. Symp. Como, 1980), Vol.2, CEC, Brussels (1980) 701.
[2] GOLDSTON, R., et al., ibid., 711.
[3] SUCKEWER, S., et al., Nucl. Fusion **21** (1981) 1301.
[4] ISLER, R.C., et al., Nucl. Fusion **23** (1983) 1017.
[5] GRIBOV, Yu.V., TSAUN, S.V., YUSHMANOV, P.N., I.V. Kurchatov Institute of Atomic Energy Prepr. 3681/7, Moscow (1982).
[6] KOVRIZHNYKH, L.M., Zh. Tekh. Fiz. **33** (1963) 377.
[7] CONNOR, J.W., CORDEY, J.G., Nucl. Fusion **14** (1974) 185.

THE RADIAL ELECTRIC FIELD IN A NON-AXISYMMETRIC TORUS*

K.C. SHAING, R.H. FOWLER, D.E. HASTINGS,
W.A. HOULBERG, E.F. JAEGER, J.F. LYON,
J.A. ROME, J.S. TOLLIVER
Oak Ridge National Laboratory,
Oak Ridge, Tennessee

J.D. CALLEN
University of Wisconsin,
Madison, Wisconsin

United States of America

Abstract

THE RADIAL ELECTRIC FIELD IN A NON-AXISYMMETRIC TORUS.

The radial electric field E_r in a non-axisymmetric torus has been studied using two models. One is radially local, the other includes a radial coupling term due to the finite orbit size. The analytic expressions for the particle fluxes employed in these models compare favourably with Monte Carlo simulations. The stability of E_r is studied from the thermodynamic point of view. Stable E_r occurs at the minimum of a potential, generalized heat production rate. These two models are coupled with the density and energy transport equations to simulate the plasma behaviour. For Advanced Toroidal Facility (ATF)-like parameters, both models predict reasonable confinement time and plasma beta.

1. INTRODUCTION

In a non-axisymmetric torus (e.g. stellarator, ELMO Bumpy Torus (EBT)), the particle fluxes are not intrinsically ambipolar, and a radial electric field E_r develops to ensure quasi-neutrality. The value of E_r needs to be determined self-consistently from the transport equations. We develop the evolution equations for E_r from neoclassical transport theory. Two models for E_r have been considered. One is a radially local model obtained by balancing the electron and ion particle fluxes. In the radially non-local model, besides the usual particle fluxes, a higher-order particle flux due to the finite size of the particle drift orbits is included. The stability of E_r is studied by defining a thermodynamic-like potential. To be specific, analytic models for the particle and heat fluxes for a stellarator and EBT

* Research sponsored by the Office of Fusion Energy, US Department of Energy, under Contract No. DE-AC05-840R21400 with Martin Marietta Energy Systems Inc.

are developed. These models for the fluxes compare favourably with the Monte Carlo simulations. Although the theory for determining E_r will be discussed with a stellarator and, to a lesser degree, an EBT as examples, it is general enough to be applied to any other non-axisymmetric device.

2. TRANSPORT FLUXES AND MONTE CARLO SIMULATIONS

The asymptotic expressions of the particle and heat fluxes for a stellarator in the low-collisionality regimes ($\nu_{eff} < \omega_b$, where ν_{eff} and ω_b are the effective collision and bounce frequencies, respectively, for the helically trapped particles) have been calculated [1]. We connect these formulas phenomenologically to obtain a model that is valid in all the collisionality regimes. The models for particle (Γ_a) and heat (Q_a) fluxes are

$$\begin{Bmatrix}\Gamma_a \\ Q_a\end{Bmatrix} = -\epsilon_t^2 \sqrt{\epsilon_h}\, V_{da}^2 n_a \begin{Bmatrix}1 \\ T_a\end{Bmatrix} \int_b^\infty dx\, x^d e^{-x} \frac{\nu_a(x)}{\epsilon_h \omega^2} \frac{\partial \ln f_{Ma}}{\partial r} \qquad (1)$$

where $d = 2.5(3.5)$ for $\Gamma_a(Q_a)$; $\omega^2 = \omega_d^2 + \omega_s^2 + \omega_p^2 + \omega_\nu^2$; $\omega_d^2 = 1.67\,(\epsilon_t/\epsilon_h)\,(\omega_E + \omega_{\nabla Ba})^2$; $\omega_s^2 = 0.25\,(\epsilon_t/\epsilon_h)^{3/2}\omega_{\nabla Ba}^2$; $\omega_p^2 = 0.6\,|\omega_{\nabla Ba}|\nu_a(x)/\epsilon_h$; and $\omega_\nu^2 = 3\nu_a^2(x)/\epsilon_h^2$. In these expressions the subscript a denotes the particle species (a = i for ions, a = e for electrons); n_a, T_a, ν_a, e_a are the density, temperature, collision frequency and electric charge; $\omega_E = c\Phi'/Br$ and $\omega_{\nabla Ba} = -cxT_a\epsilon_h'/e_aBr$, with c the speed of light; B is the magnetic field strength; r is the minor radius, and $V_{da} = cT_a/e_aBr$. Since only those particles with energy $x \equiv E/T_a > b \equiv (\nu_{at} R/v_{ta} m\epsilon_h^{3/2})^{1/2}$ [with $\nu_{at} = \nu_a(x = 1)$, R the major radius, and v_{ta} the thermal speed] can satisfy $\nu_{eff} < \omega_b$, the energy integral in Eq.(1) is carried out for $b \leqslant x \leqslant \infty$. Equation (1) is valid for a model stellarator with $B = B_0[1 - \epsilon_t \cos\theta - \epsilon_h \cos(\ell\theta - m\phi)]$, where ϵ_t and ϵ_h are toroidal and helical modulations of the magnetic field, and ℓ and m are numbers of helicity and toroidal field periods. The dominant frequency in ω^2 determines the collisionality regime of a particle with energy x. For example, if ω_ν^2 is the largest term in ω^2, the particle is in the $1/\nu$ regime. However, if $\omega_E \gg \omega_{\nabla Ba}$ and $\nu_a(x) \ll \omega_E$, the particle is in the collisionless detrapping regime. In case of resonance with $\omega_d^2 = 0$, Eq.(1) gives rise to the superbanana and superbanana plateau fluxes. Since the resonant transport has not been accurately calculated, Eq.(1) is valid to within an order of unity in this case.

The transport coefficients given in Eq.(1) have been compared with Monte Carlo simulations [2]. The guiding-centre particle orbit is calculated numerically in the flux co-ordinates (ψ, θ, ϕ) [3]. The particles are initially

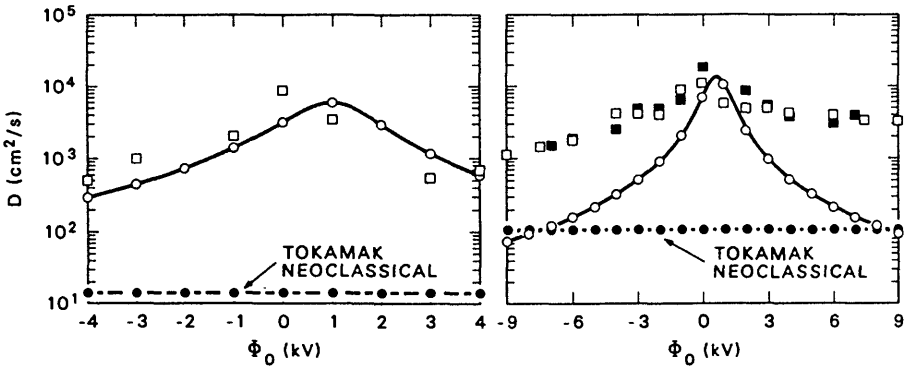

FIG.1. Monte Carlo results (squares) and analytic prediction (solid curve) of the diffusion coefficient versus radial electric field for a stellarator (left) and ATF (right). For the ATF case, both vacuum field (squares) and $\langle\beta\rangle = 2\%$ (solid squares) are shown.

on the same flux surface ψ_0 but have a uniform random distribution in θ, ϕ and pitch angle. The energy distribution is a Maxwellian. The collisionless motion of particles is first followed for several orbit times to obtain a quiet start. Particles that are lost during this phase are replaced. Once a satisfactory group of particles is obtained, collisions are introduced. The group of particles is followed for several 90° scattering times. The diffusion coefficient D is calculated from the expression $D = (\langle\psi^2\rangle - \langle\psi\rangle^2)/2t$, where the brackets imply ensemble average at time t. The results obtained for D versus E_r for a model stellarator with $\ell = 1$, $m = 12$, $\epsilon_t = 0.05$, $\epsilon_h = 0.15$, $n = 3 \times 10^{13}$, $B = 5$ T, and for ATF, are shown in Fig.1, along with the values of D predicted by Eq.(1). There is good agreement between analytic and Monte Carlo results at small E_r. At large E_r, the Monte Carlo results tend to saturate, but the analytic value of D keeps decreasing. The discrepancy is due to the lack of momentum conservation in the Monte Carlo calculation, which enhances the tokamak diffusion coefficient by a factor of $\sqrt{M_i/M_e}$ where M_i (M_e) is ion (electron) mass. By subtracting this fictitious saturation there is again agreement between these two results at large E_r.

A bounce-averaged Monte Carlo code in a Clebsch co-ordinate system ($\nabla\alpha \times \nabla\beta = B$) is employed to simulate the transport process in an EBT. The results for the resonant transport have been reported in Ref.[4]. The non-resonant transport Monte Carlo results and the analytic calculations of Kovrizhnykh [5] and Hastings [6], which have included the effects of the shift of the plasma centre relative to the geometric centre and the poloidal electric field, are shown in Fig.2. At small radius ($\alpha_N = 0.02$, $\alpha_N \equiv \alpha/\alpha_a$, and $\alpha_a = \alpha$ at the edge), the simulation results agree with the Hastings calculations. At large radius ($\alpha_N = 0.5$), the simulation results fall between those two analytic results; this may be due to the inadequacy of the magnetic field model employed in the analytic calculations.

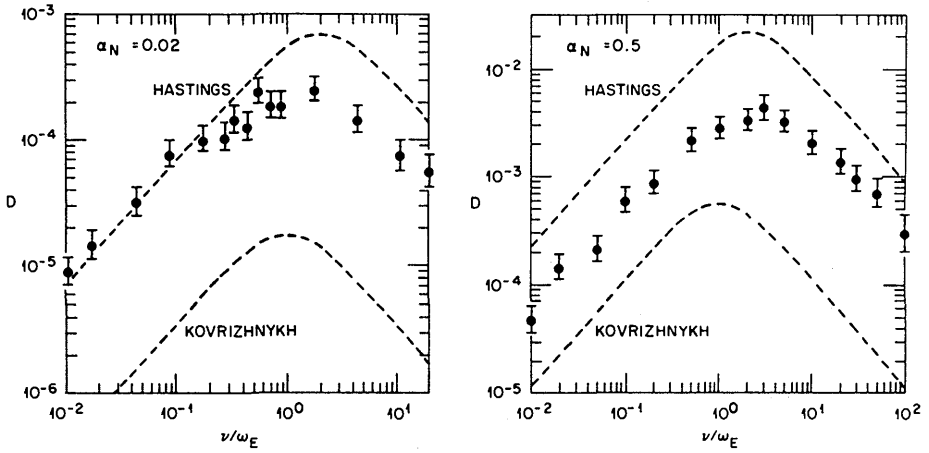

FIG.2. Monte Carlo results and theoretical predictions of D versus ν/ω_E at $\alpha_N = 0.02$ (left) and $\alpha_N = 0.5$ (right).

3. STABILITY OF RADIAL ELECTRIC FIELD AND TRANSPORT SIMULATIONS

We derive the equation for E_r by taking the radial component of Ampère's law and performing the flux surface average to obtain

$$\frac{\partial \Phi'}{\partial t} = [4\pi/(1 + c^2/V_A^2)] \sum_a e_a \Gamma_a = - \partial \dot{S}_\ell / \partial \Phi' \qquad (2)$$

where $$V_A^2 = \sum_a B^2/4\pi n_a M_a c^2$$

and $\dot{S}_\ell$ is the generalized heat production rate [7]. The definition of V_A^2 is valid for EBT. For a tokamak, B^2 should be replaced by B_p^2, the poloidal magnetic field strength, in the definition of V_A^2. For a stellarator, the dependence of V_A^2 on the magnetic field needs to be investigated. At steady state, $Q = e(\Gamma_e - \Gamma_i) = 0$ or $\dot{S}_\ell$ is extremal (i.e. $\partial \dot{S}_\ell / \partial \Phi' = 0$ determines the value of E_r that ensures quasi-neutrality). Since the particle flux is a non-linear function of E_r, $Q = \partial \dot{S}_\ell / \partial \Phi' = 0$ can have multiple solutions of E_r [8]. The functions Q and $\dot{S}_g = \dot{S}_\ell (1 + c^2/V_A^2)$ versus $ea\Phi'/T_e$ for a stellarator are shown in Fig.3. In this specific case, there are three solutions of E_r for $Q = \partial \dot{S}_\ell / \partial \Phi' = 0$. Some of them are unstable. The stability of E_r can be determined by examining the extreme of $\dot{S}_\ell$ [7]. If $\dot{S}_\ell$ is

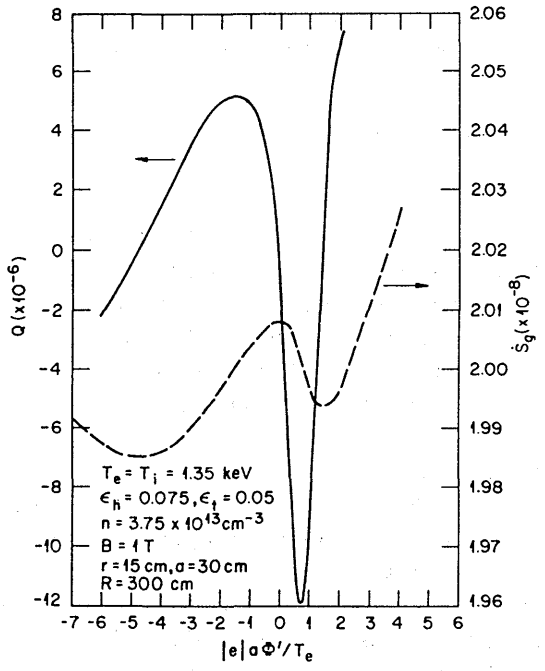

FIG.3. The functions Q and $\dot{S}_g$ versus $ea\Phi'/T_e$. The profiles for density, temperature and ϵ_h are parabolic.

a local maximum (minimum), E_r is unstable (stable). In cases where $\dot{S}_\ell$ has multiple local minima, the value of E_r is determined by the initial conditions if the fluctuations of E_r are neglected. If the fluctuations are included, Eq.(2) can be converted to a stochastic differential equation [9], which can be solved for a steady-state probability distribution (P_s) of E_r that has a maximum at the smallest minimum of $\dot{S}_\ell$. Thus, if the time-scale for the plasma parameter to change is slower than that to establish P_s, E_r is determined by the smallest minimum of $\dot{S}_\ell$ instead of the initial conditions.

The model given by Eq.(1) is radially local since the value of E_r depends only on the local value of the plasma parameters. The resultant E_r profile can have discontinuities due to the sudden disappearance of one stable value of E_r. To smooth out the discontinuities we use a radially non-local model [7]:

$$\frac{\partial \Phi'}{\partial t} = [4\pi/(1 + c^2/V_A^2)] \sum_a e_a \Gamma_a + \frac{1}{r} \frac{\partial}{\partial r} \left(r D_E \frac{\partial \Phi'}{\partial r} \right) \qquad (3)$$

where D_E is the diffusion coefficient for E_r and has been calculated for both stellarators and EBTs [10]. The diffusion term in Eq.(3) represents the coupling

of neighbouring flux surfaces due to the finite orbit size. A stable profile for E_r obtained from Eq.(3) is again at the minimum of the potential defined as

$$\dot{S}_n = \int dr\, r[\dot{S}_\ell + (D_E/2)\,(\partial\Phi'/\partial r)^2]$$

Both models for E_r have been coupled to the density and energy transport equations to study the plasma transport behaviour in a stellarator. Besides the fluxes given in Eq.(1) due to the helically trapped particles, twice neoclassical tokamak and Alcator-like anomalous transport fluxes are also employed in the transport equations to account for the transport associated with the banana and circulating particles and edge turbulence. ATF parameters are employed in the simulations with R = 210 cm, a = 30 cm, $\ell = 2$, m = 12, $\epsilon_h = 0.22(r/a)^2$, and $\epsilon = 0.3 + 0.6(r/a)^2$. The boundary conditions are $\partial n_a/\partial r = \partial T_a/\partial r = 0$ at r = 0, and $(\partial \ln n_a/\partial r)^{-1} = 0.5(\partial \ln T_a/\partial r)^{-1} = 2$ cm at r = a. For the radially non-local model, the boundary conditions for E_r are $\Phi' = 0$ at r = 0 and $\partial \ln \Phi'/\partial r = 0$ at r = a. The results of a deuterium plasma heated by 3 MW of hydrogen neutral beams with low-density (1×10^{13} cm^{-3}) and high-density (4×10^{13} cm^{-3}) startup scenarios are shown in Fig.4. The ion density and electric field profiles for the high-density startup with both models are shown in Fig.4(a) and (b). Note that the ion density profiles are similar and are inverted for both models. E_r is positive around r = 0 and negative on the outside for the local model. For the non-local model, E_r is everywhere negative. The electron energy confinement time is about 20 ms, and the plasma beta (β) is about 2% for the high-density startup. The ion density and electric field profiles for the low-density startup with both models are shown in Fig.4(c) and (d). The profiles for both models in this case are similar except that E_r vanishes sharply at the origin for the non-local model but goes to zero smoothly at the origin for the local model. The electron energy confinement time for the low-density startup is about 30 ms and $\beta \cong 6\%$.

4. CONCLUSIONS

We have studied the evolution of the radial electric field E_r required for quasi-neutrality in non-axisymmetric toroids from both a radially local analysis ($\Gamma_i = \Gamma_e$), where multiple roots for E_r appear, and a radially non-local one, which adds a higher-order diffusion term (D_E) to smooth out possible discontinuities in E_r. The stability of the various E_r roots has been elucidated in terms of thermodynamic-like potentials for both radially local ($\dot{S}_\ell$) and non-local ($\dot{S}_n$) models. When fluctuations in E_r are present, the self-consistent E_r can be that at the absolute (or global) minimum of the potential ($\dot{S}_\ell$ or $\dot{S}_n$) instead of being determined by the initial

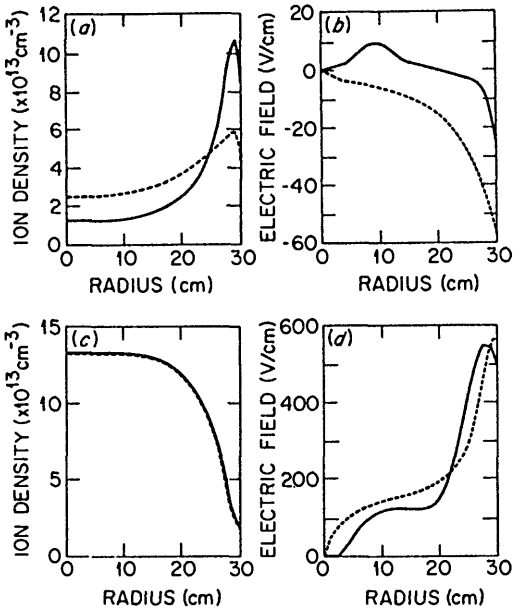

FIG.4. Ion density and electric field profiles for high-density (a, b) and low-density (c, d) startup scenarios from both radially local (solid curve) and non-local (dashed curve) models.

conditions. The analytically obtained transport fluxes for both EBT and stellarator configurations have been compared with Monte Carlo simulations. Transport simulation of the radial structure of E_r for low- and high-density startup scenarios for the ATF torsatron have shown that the best confinement can be expected for a low-density startup, which facilitates obtaining $E_r > 0$ throughout the plasma.

REFERENCES

[1] GALEEV, A.A., SAGDEEV, R.Z., "Neoclassical theory of diffusion", Advances in Plasma Physics (SIMON, A., THOMPSON, W., Eds), Vol.6, Wiley, New York (1976) 311.
[2] FOWLER, R.H., ROME, J.A., LYON, J.F., Monte Carlo Studies of Transport in Stellarators, Oak Ridge Natl Lab. Rep. ORNL/TM-9193 (1984).
[3] BOOZER, A.H., Phys. Fluids **25** (1982) 520.
[4] TOLLIVER, J.S., et al., Phys. Fluids **26** (1983) 1391.
[5] KOVRIZHNYKH, L.M., Sov. Phys.-JETP **29** (1969) 475.
[6] HASTINGS, D.E., Phys. Fluids **27** (1984) 939.
[7] SHAING, K.C., Phys. Fluids **27** (1984) 1567.
[8] JAEGER, F.F., et al., Phys. Rev. Lett. **40** (1978) 866;
MYNICK, H.E., HITCHON, W.N.G., Nucl. Fusion **23** (1983) 1053;
KOVRIZHNYKH, L.M., Nucl. Fusion **24** (1984) 435.
[9] SHAING, K.C., to be published in Phys. Fluids.
[10] HASTINGS, D.E., to be published in Phys. Fluids.

THERMAL INSTABILITY AND DISRUPTIONS IN A TOKAMAK

P.H. REBUT, M. HUGON
JET Joint Undertaking,
Abingdon, Oxfordshire,
United Kingdom

Abstract

THERMAL INSTABILITY AND DISRUPTIONS IN A TOKAMAK.

A theoretical model is developed in which it is predicted that a major cause of anomalous confinement and disruptions in tokamaks is thermal instability. Owing to the large thermal conductivity along magnetic field lines, confinement is assumed to be poor in regions where the lines of force have an ergodic behaviour in contrast to the regions where the magnetic surfaces are nested (laminar case or islands). The ergodic region results from the interaction between chains of islands. It is shown that thermal islands can grow, when $\mathscr{P}_v/q'$ is negative, where $\mathscr{P}_v$ is the net power input to the electrons in the island (excluding thermal conduction) and q' is the radial gradient of the safety factor q. Conclusions are drawn on the occurrence of disruptions (critical electron density) and on confinement in the outer region of the plasma. Finally, suggestions are made to increase the critical density at which disruptions occur.

1. INTRODUCTION

Anomalous confinement and the limitations imposed by disruptions in tokamaks are not well understood. However, various theories (tearing modes [1,2], global power balance [3], drift modes, trapped electrons [4], ...) have been proposed, but do not provide a coherent explanation of experimental results.

In this paper, the loss of confinement in tokamaks is explained by a change in the magnetic field line topology from the normal nested magnetic surfaces. Three magnetic configuration states can be distinguished:

(i) a "laminar state", composed of one set of nested magnetic surfaces;
(ii) an "intermediate state", made up of individual islands, forming different sets of nested surfaces;
(iii) an "ergodic state", where the mutual interaction of neighbouring islands has destroyed the magnetic surfaces.

We propose a model in which thermal instabilities induce such a complex topology. In the laminar case or inside the islands we assume classical behaviour of the perpendicular thermal conductivity or, less explicitly, good plasma confinement properties compared to the

ergodisation state. Although other phenomena could be considered, thermal instabilities seem to be a good candidate for such a change of topology, since an increase in the plasma thermal conductivity results.

For these magnetic configurations, the various equilibrium states are studied, the conditions of existence evaluated and the stability is analysed. The consequences for plasma confinement are then deduced.

2. THE MODEL

The mathematical treatment of the model follows the equilibrium bifurcation theory used, for the first time, to show the existence of tearing modes [1, 5].

The basic idea of this model is that the thermal insulation of an island, resulting from its intrinsic magnetic field, leads to its growth through the thermal dependence of the resistivity [6]. Before analysing the island's magnetic structure (Section 2.3) and calculating the thermal balance of an island (Section 2.4), the M.H.D. equations in helical geometry (Section 2.1) and their solution outside the islands (Section 2.2) are briefly recalled. These equations are solved inside the islands (Section 2.5) and both external and internal solutions are matched at the boundaries (Section 2.6).

2.1. M.H.D. Equations in Helical Geometry

The basic M.H.D. equations in helical geometry are used as follows. Let r, θ and z be the cylindrical coordinates, and r and $s = \frac{z}{p} - \theta$ be the helical coordinates, where p is the helix pitch. It is assumed that the magnetic field **B** and current density **J** are invariant under helical transformation. **B** and **J** are defined by:

$$\begin{cases} \mathbf{B} = B_h \mathbf{e}_h + \nabla \mathscr{A} \times \mathbf{e}_h & (1) \\ \mathbf{J} = J_h \mathbf{e}_h + \nabla \mathscr{H} \times \mathbf{e}_h & (2) \end{cases}$$

with:

$$\mathbf{e}_h = \frac{p}{p^2 + r^2} (r \mathbf{e}_\theta + p \mathbf{e}_z) \qquad (3)$$

Ampère's law in helical geometry is:

$$\begin{cases} \Delta_h \mathscr{A} = \dfrac{2p}{p^2 + r^2} B_h - 4\pi J_h & (4) \\ B_h = 4\pi \mathscr{H} & (5) \end{cases}$$

with:

$$\Delta_h = \frac{p^2 + r^2}{pr} \frac{\partial}{\partial r} \left(\frac{rp}{p^2 + r^2} \frac{\partial}{\partial r} \right) + \frac{p^2 + r^2}{p^2 r^2} \frac{\partial^2}{\partial s^2} \qquad (6)$$

The plasma balance equation $\nabla P = J \times B$ is:

$$4\pi J_h = 4\pi \left(\frac{p^2 + r^2}{p^2}\right) \frac{dP}{d\mathscr{A}} + \frac{1}{2} \frac{dB_h^2}{d\mathscr{A}} \tag{7}$$

If the helical flux $\mathscr{A}$ is a function of r only: $\mathscr{A} = \mathscr{A}_o(r)$, Eq. (1) yields:

$$\nabla \mathscr{A}_o(r) = B_\theta \left(\frac{q}{q_o} - 1\right) e_r \tag{8}$$

with:

$$p = q_o R \quad \text{and} \quad q = \frac{r B_z}{R B_\theta} \tag{9}$$

If q_o corresponds to the value of q at $r = r_o$, $q_o = q(r_o)$, the expression for $\mathscr{A}_o(r)$ in the vicinity of r_o is:

$$\mathscr{A}_o(r) = \frac{1}{2} B_\theta \frac{q'}{q_o} (r - r_o)^2 \tag{10}$$

2.2. Perturbation theory - external solution

In the regions where the plasma pressure is small, $\frac{dP}{d\mathscr{A}}$ can be neglected in Eq. (7). Let $\mathscr{A}(r,s)$ be:

$$\mathscr{A}(r,s) = \mathscr{A}_o(r) + \tilde{\tilde{\mathscr{A}}}(r,s) \tag{11}$$

where $\mathscr{A}_o(r)$, defined by Eq. (10), is a solution of Eq. (4) and $\tilde{\tilde{\mathscr{A}}}(r,s) < \mathscr{A}_o(r)$.

$$\text{If} \quad \begin{cases} \delta B_h = B_h(\mathscr{A}(r,s)) - B_h(\mathscr{A}_o(r)) \ll B_h \\ \delta J_h = J_h(\mathscr{A}(r,s)) - J_h(\mathscr{A}_o(r)) \ll J_h \end{cases} \tag{12}$$

and after combining Eqs. (4), (7) and (8), we find that $\tilde{\tilde{\mathscr{A}}}(r,s)$ is a solution of:

$$\Delta_h \tilde{\tilde{\mathscr{A}}}(r,s) = \left[\frac{8\pi p}{p^2 + r^2} \frac{J_h(\mathscr{A}_o)}{B_h(\mathscr{A}_o)} - 4\pi \frac{\frac{dJ_h(\mathscr{A}_o)}{dr}}{B_\theta \left(\frac{q}{q_o} - 1\right)} \right] \tilde{\tilde{\mathscr{A}}}(r,s) \tag{13}$$

Consider $\tilde{\tilde{\mathscr{A}}}(r,s)$ of the form:

$$\tilde{\tilde{\mathscr{A}}}(r,s) = \frac{\tilde{B} \cdot r_o}{m} \sum_{n=0}^{\infty} a_n(r) \cos n\Theta \tag{14}$$

with: $\Theta = -ms$ (15)

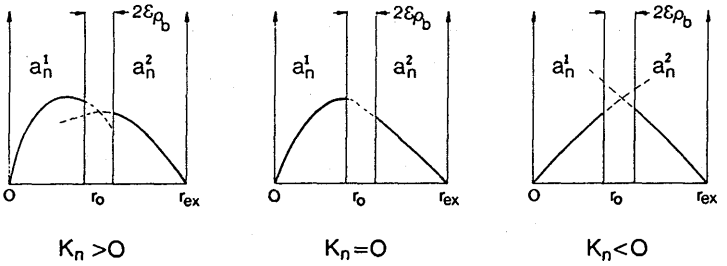

FIG.1. Solutions of Eq.(16) with the boundary conditions (17) giving $a_n(r)$ versus r for the three cases: $K_n > 0$, $K_n = 0$, $K_n < 0$. The value of K_n is related to the difference between the $a_n(r)$ gradients each side of r_0.

Using Eqs (6), (14) and (13), it can be shown that $a_n(r)$ satisfies the following equation:

$$\frac{p^2+r^2}{pr}\frac{d}{dr}\left(\frac{pr}{p^2+r^2}\frac{d}{dr}a_n(r)\right) = \left[\frac{p^2+r^2}{p^2}\frac{m^2n^2}{r^2} + \frac{8\pi p}{p^2+r^2}\frac{J_h(\mathscr{A}_o)}{B_h(\mathscr{A}_o)} - 4\pi\frac{\frac{dJ_h(\mathscr{A}_o)}{dr}}{B_\theta\left(\frac{q}{q_o}-1\right)}\right]a_n(r) \tag{16}$$

If $n \neq 0$, the boundary conditions for $a_n(r)$ are: $a_n(0) = 0$ and $a_n(r_{ex}) = 0$ (17), where r_{ex} is the radius at the plasma edge. In general, Eq. (16) has no solution for $a_n(r)$ that fulfils conditions (17). If the perturbation is in resonance with the field line, it creates islands at $r = r_o(q = q_o)$. Eq. (16) can be solved in two regions, which exclude the region close to the radius r_o. Let $a_n^1(r)$ be the solution for $0 \leqslant r \leqslant r_o - \epsilon\rho_b$ and $a_n^2(r)$ be the solution for $r_o + \epsilon\rho_b \leqslant r \leqslant r_{ex}$.

Define K_n by:

$$K_n = \frac{r_o}{a_n^2(r_o+\epsilon\rho_b)}\frac{da_n^2(r_o+\epsilon\rho_b)}{dr} - \frac{r_o}{a_n^1(r_o-\epsilon\rho_b)}\frac{da_n^1(r_o-\epsilon\rho_b)}{dr} \tag{18}$$

In the first approximation, K_n does not depend on the value of $\epsilon\rho_b$. The value of K_n is related to the difference between the slopes of $a_n(r)$ each side of r_o. This is indicated in Fig. 1. $K_n = 0$ corresponds to marginal stability for tearing modes [1,2,5] (bifurcation point). In the case of neutral islands (i.e. islands not contributing to the perturbation), when K_n is negative, the plasma is stable with respect to tearing modes. However, it can be shown that islands do not remain neutral when size and thermal balance are taken into account.

In vacuum or if mn is not too small, terms depending on J_h can be neglected with respect to $(\frac{p^2+r^2}{p^2 r^2}) m^2 n^2$ in Eq. (16) provided that $r \neq r_o$. In a region close to r_o, but excluding r_o, it can be shown that

$$K_n = -2mn\frac{\sqrt{p^2+r_o^2}}{p} \tag{19}$$

2.3. Magnetic structure of the islands - ergodisation

In the vicinity of r_o, for which $q_o = q(r_o)$ and $\mathscr{A}_o(r_o) = 0$, the equation of a magnetic surface $\mathscr{A} = ct$ is given by:

$$\mathscr{A} = \frac{1}{2}\frac{r_o}{R} B_z \frac{q'}{q_o^2} (r-r_o)^2 + \tilde{\mathscr{A}}(r,s) \tag{20}$$

Let $\tilde{\mathscr{A}}(r,s)$ be: $\tilde{\mathscr{A}}(r,s) = \frac{\tilde{B}\cdot r_o}{m} A(\rho,\Theta)$ (21)

with:

$$\begin{cases} \rho = \dfrac{r-r_o}{\epsilon} & \epsilon > 0 \\ \Theta = -ms \end{cases} \tag{22}$$

It is assumed that $A(\rho,\Theta)$ is an even function of Θ with a period 2π. $A(\rho,\Theta)$ also satisfies the normalisation conditions:

$$\begin{cases} A(1,0) = 2 & \dfrac{\partial A}{\partial \rho}(0,\pi) = 0 \\ A(0,\pi) = 0 \end{cases} \tag{23}$$

If the supplementary condition ($\rho = 1$ for $\Theta = 0$ and $\mathscr{A} = 0$) is imposed, a definition of ϵ is obtained:

$$\epsilon^2 = -4\frac{R}{m}\frac{\tilde{B}}{B_z}\frac{q_o^2}{q'} \qquad \text{with } \frac{\tilde{B}}{q'} < 0 \tag{24}$$

and Eq. (20) becomes: $2\rho^2 - A(\rho,\Theta) = -A_o$ (25)

with: $A_o = \frac{m\mathscr{A}}{\tilde{B} r_o}$ (26)

The singular points of Eq. (25) are defined by:

$$\begin{cases} 4\rho - \dfrac{\partial A}{\partial \rho}(\rho,\Theta) = 0 \\ \dfrac{\partial A}{\partial \Theta}(\rho,\Theta) = 0 \end{cases} \tag{27}$$

As $A(\rho,\Theta)$ is an even function of Θ, satisfying conditions (23), the point $\rho = 0$, $\Theta = \pi$ is always singular. For $\Theta = \pi$, we can

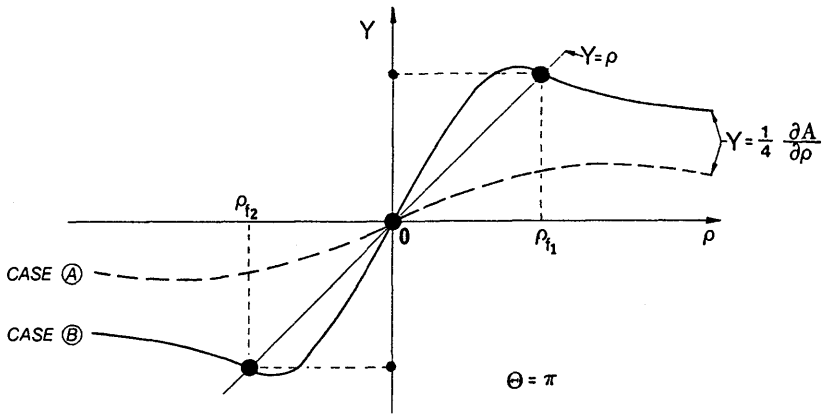

FIG. 2. Singular points of Eq. (25) at $\Theta = \pi$.
Case A: $\frac{1}{4}\frac{\partial^2 A}{\partial \rho^2}(0,\pi) < 1$; *case B:* $\frac{1}{4}\frac{\partial^2 A}{\partial \rho^2}(0,\pi) > 1$.

distinguish two cases according to the relative magnitude of 1 and $\frac{1}{4}\frac{\partial^2 A}{\partial \rho^2}(0,\pi)$, as shown in Fig. 2.

(i) Case Ⓐ

If $\frac{1}{4}\frac{\partial^2 A}{\partial \rho^2}(0,\pi) < 1$, only one singular point exists for $\Theta = \pi$ at $\rho = 0$, and it can be shown that this point is nodal. This situation occurs when q' is not too small. Then, Eq. (25) represents continuous periodic curves for $A_0 < 0$, the separatrix for $A_0 = 0$ and islands which turn in the same direction for $0 < A_0 \leqslant A(0,0)$, as shown in Fig. 3 in the r, Θ coordinate system. ϵ represents the half width of the separatrix.

(ii) Case Ⓑ

If $\frac{1}{4}\frac{\partial^2 A}{\partial \rho^2}(0,\pi) > 1$, Fig. 2 indicates that there are three singular points for $\Theta = \pi$ corresponding to $\rho = 0$, ρ_{f_1} and ρ_{f_2}. This case takes place, when q' is small (at the plasma centre or near the current maximum in a hollow profile). Fig. 3 shows the corresponding solutions of Eq. (25), in which case the islands can turn in both directions.

This paper deals only with case Ⓐ.

The nodal points are sensitive even to weak perturbations. For instance, the interaction between two chains of islands can destroy the

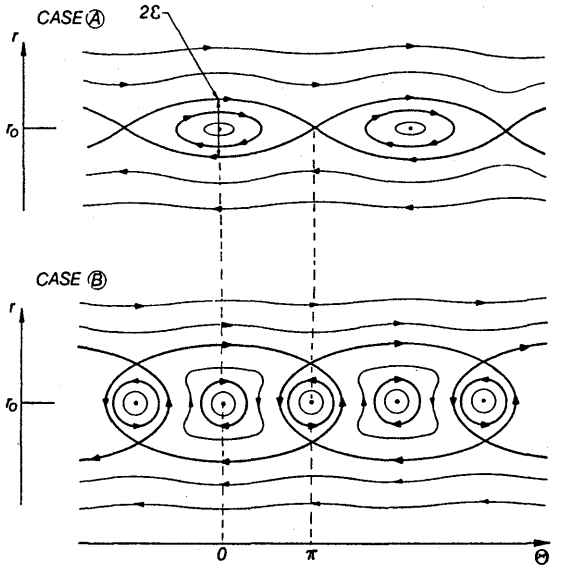

FIG.3. Solutions of Eq.(25) in cases A and B (see Fig.2) showing the two island configurations.

nodal points and give rise to ergodic field lines. This is shown in Fig. 4, where Δ represents the distance between both chains of islands, $\alpha = \sqrt{1 - \frac{A_{oc}}{2}}$ and A_{oc} defines the last undestroyed magnetic surface of an island. If $\Delta > \epsilon_1 + \epsilon_2$, the size of the ergodic zones is small and $A_{oc} \simeq 0\ (\alpha \simeq 1)$. If $\Delta < \epsilon_1 + \epsilon_2$, the interaction is strong enough to destroy the last nested surface, resulting in the ergodic zones joining and creating secondary islands. The size of the primary islands decreases as $\frac{\Delta}{\epsilon_1 + \epsilon_2} \to 0$ (in the first approximation, $\alpha \simeq \frac{\Delta}{\epsilon_1 + \epsilon_2}$).

If m is limited to a maximum value m_ℓ and if the lower value for m is taken on each magnetic surface, the distance Δ is given by $\Delta = \frac{3q^2}{m\ell^2 |q'|}$. The equality $\Delta = \epsilon_1 + \epsilon_2$ can be written with $\epsilon_1 = \epsilon_2 = \epsilon$:

$$\frac{\epsilon}{r_o} = \frac{3q^2}{2m\ell^2 |q'| r_o} \tag{28}$$

Eq. (28) represents the limiting value of ϵ, for which all field lines between chains of islands become ergodic.

Due to the large thermal conductivity along the magnetic field lines, we assume that the confinement is poor inside the ergodic zone and relatively good in the laminar zone or inside the islands.

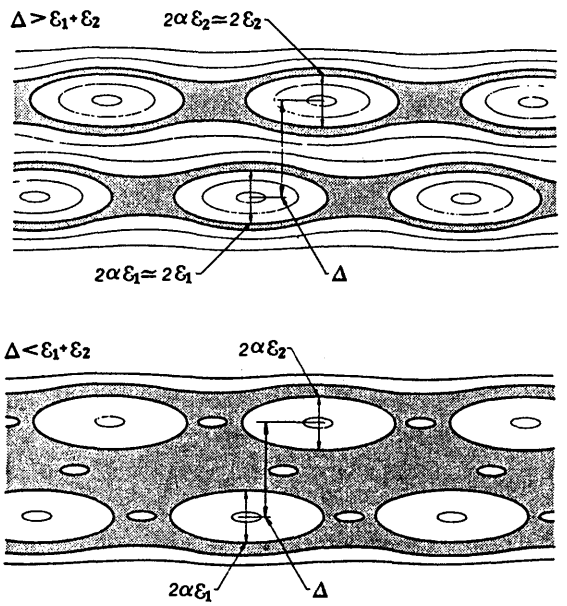

FIG. 4. Creation of ergodic regions (shaded area) by interaction between two chains of islands. When $\Delta < \epsilon_1 + \epsilon_2$ the ergodic zones are joined and secondary islands appear.

2.4. Thermal balance of an island

In this calculation, each island is treated individually. As the exchange of thermal energy is fast along the magnetic field lines, there is a common electron temperature, T_e, for each magnetic surface: T_e is a function of the magnetic surface only, which can be expressed as $T_e = T_e(A_o)$, with A_o given by Eq. (25).

For each island, the electron temperature satisfies the following thermal balance equation:

$$- \iint_{(s)} \chi_{\perp e} \cdot \nabla T_e \cdot ds = \iiint_{(v)} \mathscr{P}_v \, dV \tag{29}$$

where $\chi_{\perp e} \cdot \nabla T_e$ represents the electron conduction term and $\mathscr{P}_v$ is the net power input to the electrons in the island excluding the conduction term.

$$\left[\text{Generally, } \mathscr{P}_v = \eta J^2 + \mathscr{P}_{e(\text{add.heat.})} - \mathscr{P}_{\text{rad.}} - \frac{n(T_e - T_i)}{\tau_{eq}} \right]^1$$

[1] Other terms such as the electron cooling resulting from ionisation may need to be taken into account.

Assuming that the islands are thin ($\frac{m\epsilon}{r_o} \ll 1$), Eq. (29) gives:

$$\frac{dT_e}{dA_o} = \frac{\epsilon^2 \mathscr{P}_v}{4\chi_{\perp e}} + \frac{\epsilon^2}{4\chi_{\perp e}} \frac{d\mathscr{P}_v}{dT_e} (T_e(A_o) - T_e(A_{oc})) \tag{30}$$

If $\delta T_e = T_e(A_o) - T_e(A_{oc})$ is small compared to $T_e(A_{oc}) = T_o$, (where A_o and A_{oc} ($A_{oc} < A_o$) define a magnetic surface inside the island and its last undestroyed surface, respectively), Eq. (30) can be integrated to give:

$$\delta T_e = \frac{\epsilon^2 \mathscr{P}_v}{4\chi_{\perp e}} (A_o - A_{oc}) \tag{31}$$

provided that $\frac{d\mathscr{P}_v}{dT_e} \delta T_e < \frac{\mathscr{P}_v}{2}$

Assuming that the current density (Eq. (2)) depends on the temperature through the resistivity: $\frac{\delta J_h}{J_{ho}} = \frac{3}{2} \frac{\delta T_e}{T_o}$, it can be shown by using Eq. (31) that:

$$\delta J_h = \left(\frac{3}{8} \frac{J_{ho}}{T_o} \frac{\mathscr{P}_v r_o^2}{\chi_{\perp e}} \right) \frac{\epsilon^2}{r_o^2} (A_o - A_{oc}) \tag{32}$$

δJ_h represents the difference between the current densities circulating inside and outside the island.

2.5. Field produced by the island - internal solution

If $\mathscr{A}(r,s)$ is expressed as $\mathscr{A}(r,s) = \mathscr{A}_o(r) + \tilde{\mathscr{A}}(r,s)$, the combination of Eqs (4) and (7), in the case where $\frac{dP}{d\mathscr{A}}$ can be neglected, leads to the following equation satisfied by $\tilde{\mathscr{A}}(r,s)$:

$$\Delta_h \tilde{\mathscr{A}}(r,s) = \left(\frac{8\pi p}{p^2 + r^2} \right) \frac{J_{ho}}{B_{ho}} \tilde{\mathscr{A}}(r,s) - 4\pi \delta J_h(\tilde{\mathscr{A}}(r,s)) \tag{33}$$

From the expressions for δJ_h (Eq. (32)) and A_o (Eq. (25)) and taking into account Eqs (21), (22) and (24), we obtain:

$$4\pi \delta J_h(\tilde{\mathscr{A}}(r,s)) = \left(\frac{3\pi}{2} \frac{J_{ho}}{T_o} \frac{\mathscr{P}_v r_o^2}{\chi_{\perp e}} \right) \frac{\epsilon^2}{r_o^2} (A(\rho,\Theta) - A_{oc}) \tag{34}$$

Taking into account the definition of Δ_h (Eq. (6)) and changing $\tilde{\mathscr{A}}(r,s)$ to $A(\rho,\Theta)$ (Eqs (21), (22)), we derive from Eqs (33) and (34)

an equation satisfied by $A(\rho,\Theta)$. This can be simplified in the case of thin islands $(\frac{m\epsilon}{r_o} \ll 1)$:

$$\frac{\partial^2 A}{\partial \rho^2}(\rho,\Theta) = -N\frac{\epsilon^2}{r_o^2}(A(\rho,\Theta) - A_{oc}) \tag{35}$$

where

$$N = -6\pi \frac{J_{ho}\cdot r_o}{B_z}\frac{\mathscr{P}_v}{\chi_{\perp e} T_o}\frac{R q_o^2}{q'} \tag{36}$$

For thin islands, $A(\rho,\Theta)$ is insensitive to ρ across the island $(-\rho_b \leqslant \rho \leqslant \rho_b ; \rho_b < 1)$, and can be approximated by $a(\Theta)$. Eq. (35) can be integrated from $-\rho_b$ to $+\rho_b$, where ρ_b is the value of ρ at the boundary of the island at $\Theta = ct$, ρ_b being defined by $2\rho_b^2 - a(\Theta) = -A_{oc}$:

$$\frac{\partial A}{\partial \rho}(\rho_b,\Theta) - \frac{\partial A}{\partial \rho}(-\rho_b,\Theta) = \begin{cases} -N\frac{\epsilon^2}{r_o^2}\sqrt{2}\,(a(\Theta) - a(\Theta_o))^{3/2} & -\Theta_o \leqslant \Theta \leqslant \Theta_o \\ 0 & -\pi \leqslant \Theta \leqslant -\Theta_o \text{ and } \pi \geqslant \Theta \geqslant \Theta_o \end{cases} \tag{37}$$

In this equation, $a(\Theta_o) = A_{oc} = -2\alpha^2 + 2$ for $0 \leqslant \Theta_o \leqslant \pi$, α being the value of ρ at $\Theta = 0$ for the last undestroyed surface of the island. The separatrix corresponds to $A_{oc} = a(\pi) = 0$.

In the case of thick islands, N must be multiplied by a "shape factor" not too different from 1.

2.6. Complete solution for thermal islands

The internal and external solutions of $\mathscr{A}(r,s)$ are now matched at the boundaries of the last undestroyed surface of the island ($r = r_o \pm \epsilon\rho_b$), by considering the continuity of $\mathscr{A}(r,s)$ and $\frac{\partial \mathscr{A}}{\partial r}(r,s)$.

Let $a(\Theta)$ be $$a(\Theta) = \sum_{n=0}^{\infty} a_n \cos n\Theta \tag{38}$$

From the definitions of $\tilde{\tilde{\mathscr{A}}}(r,s)$ (Eq. (14)) and $\tilde{\mathscr{A}}(r,s)$ (Eq. (21)) with the assumption $A(\rho,\Theta) = a(\Theta)$, the continuity of $\mathscr{A}(r,s)$ at the boundaries implies that:

$$a_n = a_n^1(r_o - \epsilon\rho_b) = a_n^2(r_o + \epsilon\rho_b) \tag{39}$$

If we consider Eqs. (14), (18) and (21), it follows from the continuity of $\mathscr{A}(r,s)$ (Eq. (39)) and $\frac{\partial \mathscr{A}}{\partial r}(r,s)$ at the boundaries

that:

$$\sum_{n=0}^{\infty} a_n K_n \cos n\Theta = \frac{r_o}{\epsilon}\left(\frac{\partial A}{\partial \rho}(\rho_b, \Theta) - \frac{\partial A}{\partial \rho}(-\rho_b, \Theta)\right) \tag{40}$$

Combination of Eqs (40) and (37) gives:

$$\sum_{n=0}^{\infty} a_n K_n \cos n\Theta = \begin{cases} -N\frac{\epsilon}{r_o}\sqrt{2}\,(a(\Theta) - a(\Theta_o))^{3/2} & -\Theta_o \leqslant \Theta \leqslant \Theta_o \\ 0 & -\pi \leqslant \Theta \leqslant -\Theta_o \text{ and } \pi \geqslant \Theta \geqslant \Theta_o \end{cases} \tag{41}$$

with the normalisation conditions $A(1,0) = 2$, $A(0,\pi) = 0$, $A(\alpha, 0) = 2\alpha^2 + A_{oc}$ and $A(0,\Theta_o) = A_{oc}$.

Eq. (41) defines the thermal islands at equilibrium, ϵ being the half width of the separatrix, which is real if the islands are not destroyed and imaginary if the islands are partly destroyed and surrounded by an ergodic zone.

Eq. (41) is equivalent to a non-linear eigenfunction equation, whose solution has been computed for different values of Θ_o (by taking $K_n = -2mn\frac{\sqrt{p^2 + r_o^2}}{p}$ for $n > 1$ (Eq. (19))).

If $\Theta_o = \pi$, the first harmonic dominates and it can be shown that:

$$\frac{\epsilon}{r_o} = -\frac{K_1}{2N} \quad \text{if} \quad |K_1| \lesssim 2m\frac{\sqrt{p^2 + r_o^2}}{p} \tag{42}$$

When m is not too small, Eq. (42) becomes:

$$\frac{\epsilon}{r_o} = \frac{m}{N}\frac{\sqrt{p^2 + r_o^2}}{p} \tag{43}$$

(Note that $\epsilon > 0$ (see Eq. (22)).)

If $\Theta_o \neq \pi$, the harmonics $n > 1$ play a major role and must be considered in the calculation. However, the result is not sensitive to the precise value of K_1 which has been equated with

$$-2m\frac{\sqrt{p^2 + r_o^2}}{p}$$

Table I shows that ϵ increases sharply with a slight decrease of α.

TABLE I. ALPHA AND ϵ AS FUNCTIONS OF Θ_0

Θ_0	π	$\pi/2$	$\pi/4$	$\pi/8$	$\pi/16$
α	1	0.88	0.77	0.66	0.61
$r_0/N\epsilon$	0.98	0.58	0.26	0.1	0.05

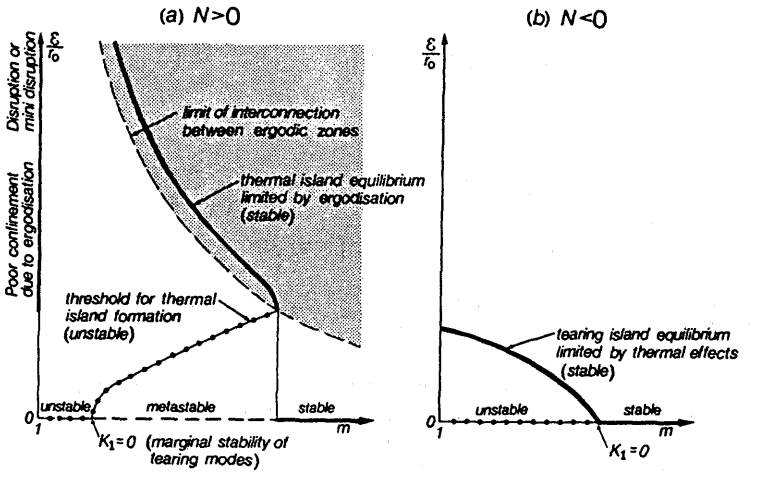

FIG.5. Equilibria diagrams for the islands for (a) $N > 0$ and (b) $N < 0$. In (a) the shaded area corresponds to a state dominated by ergodic behaviour of magnetic field lines with $\Delta < \epsilon_1 + \epsilon_2$ (see Fig.4); the clear area corresponds to the case where the magnetic field lines show mainly laminar behaviour with $\Delta > \epsilon_1 + \epsilon_2$ (see Fig.4).

3. DISCUSSION

Magnetic shear and thermal exchanges play a crucial role in the behaviour of islands, as discussed below:

(1) General case (q' not too small; case (A) in Section 2.3)

According to its stability, the island equilibrium (defined by Eq. (42)) corresponds to the threshold for the formation of thermal islands (when unstable) or to the saturation level of tearing islands (when stable). From Eq. (42), islands in equilibrium can only exist if $K_1/N < 0$. The plasma is stable with respect to thermal instabilities (or tearing modes, respectively), when N (or K_1, respectively) is negative. Two cases are distinguished according to the sign of N, and Fig. 5 shows the island equilibria diagram for (a) $N > 0$ and (b) $N < 0$.

(a) $N > 0$:

When N is positive, thermal instabilities can exist (i.e. $\mathcal{P}_V/q'$ is negative, c.f. Eq. (36)). Two different situations are considered:

(i) In normal tokomak discharges, q' is positive. Then, N can be positive only when the net power input to the electrons in the island (excluding thermal conduction), $\mathcal{P}_V$, is negative (see Section 2.4). Typical tokomak examples are the radial profiles

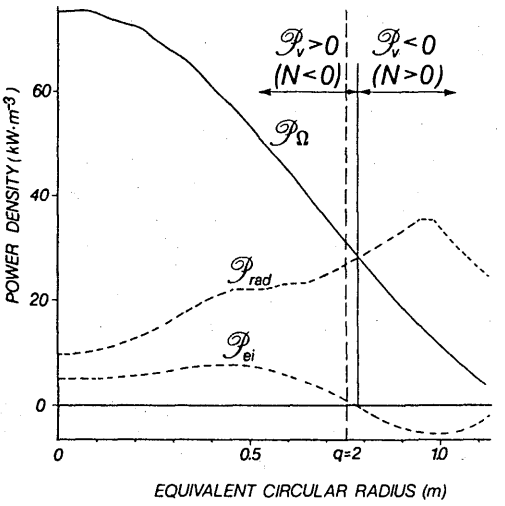

FIG. 6. Radial profiles on JET for Ohmic input power density, $\mathscr{P}_\Omega$; radiated power density, $\mathscr{P}_{rad}$; and electron-ion transfer, $\mathscr{P}_{ei}$. The vertical dashed line indicates the position of the $q = 2$ surface. The vertical full line corresponds to $\mathscr{P}_v = 0$.

obtained on JET, which are shown in Fig. 6 for ohmic input power density, $\mathscr{P}_\Omega$, radiated power density, $\mathscr{P}_{rad}$, and electron-ion transfer, $\mathscr{P}_{ei}$. $\mathscr{P}_v$ is negative (corresponding to an underheating of the plasma) for $q \gtrsim 2$, indicating that thermal islands should exist in this region. These islands correspond to a deficiency in current density (see Eq. (32)). (This result contrasts with the plasma slab case, in which islands are created by an excess of current density (overheating) [6,7], in which case, shear results from the current profile only).

Fig. 5(a) shows ϵ/r_0 plotted as a function of m. The lower curve, Eq. (42), varies linearly with m except at the lowest values of m, when K_1 becomes significantly different from $-2m\sqrt{p^2+r_0^2}/p$ (for these low m values, the conditions to initiate a tearing mode are approached). This curve determines the threshold for the formation of thermal islands, but the corresponding equilibria are unstable. If ϵ is larger than the threshold value, the islands grow (ϵ increases). When many chains of islands interact together, this growth is accompanied by the development of ergodic regions. The dashed curve (Eq. (28)) represents the limit at which these ergodic zones are interconnected. The upper full curve corresponds to stable equilibria, for which the islands tendency to grow due to thermal effects (underheating when $q' > 0$) is counterbalanced by their destruction by ergodisation. These different equilibria are represented by an S curve (Fig. 5(a)). This S curve defines the change of the magnetic configuration from a laminar state ($\epsilon = 0$)

to a state dominated by the ergodic behaviour of magnetic field lines (as described in Fig. 4; $\Delta < \epsilon_1 + \epsilon_2$).

When the surface q = 2 is in the domain where $\mathscr{P}_V$ is negative, large thermal islands (m = 2) may grow and bridge the q = 1 and q = 2 regions, resulting in ergodisation throughout the plasma (disruption). The condition for a disruption to occur can be written: $\mathscr{P}_V < 0$ at q = 2. From the definition of $\mathscr{P}_V$ in the ohmic case (Section 2.4) and using that $\mathscr{P}_{rad} + n(T_e - T_i)/\tau_{eq}$ is proportional to n^2, it can be deduced that the critical electron density for disruptions increases linearly with the current density, as long as other plasma parameters are maintained constant.

If $\mathscr{P}_V$ is negative for $q \gtrsim 2$, smaller islands (m = 3 to 10) can grow and their interaction creates a large ergodic zone where the confinement is poor. These islands could be the Mirnov modes [8, 9].

(ii) When $q' < 0$ and $\mathscr{P}_V > 0$ (which corresponds to an overheating of the plasma), thermal islands may also grow. This case is also described in Fig. 5(a). This could occur in the radial region inside the maximum of a hollow current profile (created by a skin effect or by a peaked Z profile). The growth of this instability leads to mini-disruptions by ergodisation of a large part of the plasma.

(b) $N < 0$:

When N is negative (i.e. $\mathscr{P}_V/q'$ is positive), K_1 is positive, since $K_1/N < 0$. There are no thermal instabilities, but the plasma is unstable with respect to tearing modes. Fig. 5(b) shows the corresponding equilibria curve. In the region where q' is positive, $\mathscr{P}_V$ is positive and the tearing mode is limited by overheating. Correspondingly, in the region where q' is negative, $\mathscr{P}_V$ is negative and the tearing mode is limited by underheating.

(2) Weak shear case (q' small; case (B) in Section 2.3)

Whatever the sign of q', thermal islands above a critical size (calculated from Eq. (27)) grow independent of the sign of $\mathscr{P}_V$ (corresponding to an underheating (if $\mathscr{P}_V < 0$) or an overheating (if $\mathscr{P}_V > 0$) of the plasma). For example, this situation could occur near the plasma centre in a normal tokomak discharge or near the maximum of a hollow current profile. Moreover, in these cases, the plasma could already be strongly unstable to tearing modes if the q value near the current maximum permits small m number modes to develop. The previous limitation on tearing modes by thermal effects disappears.

4. CONCLUSION

We have shown that thermal islands can grow, when $\mathcal{P}_V/q'$ is negative, $\mathcal{P}_V$ being the net power input to the electrons in the island excluding the conduction term. The size of these islands is limited by ergodisation due to their mutual interaction. In a tokamak, ergodisation leads to disruption for small m numbers (m = 2 at q = 2) or to poor confinement in the outer plasma region, where the power losses are large compared to the input power (underheating). The region located between the q = 1 and $q \simeq 2$ surfaces is generally free from these thermal instabilities ($q' > 0; \mathcal{P}_V > 0$). It has been shown that, in an ohmic discharge, the condition for a disruption ($\mathcal{P}_V < 0$ at q = 2) implies that the critical electron density increases linearly with current density, if all other parameters are kept constant.

We suggest four possibilities to increase the critical density at which disruptions occur:

- increase the input power at the surface q=2 (additional heating).
- decrease the power losses in the q = 2 region by using low Z materials for the walls (e.g. carbon or beryllium).
- refuel the plasma centre ($q \simeq 1$ zone) by pellet injection and if necessary pump the edge to limit the density at q = 2.
- suppress thermal effects by decoupling the current density from the electron temperature (e.g. slide-away discharges, current drive).

ACKNOWLEDGEMENTS

The authors are very indebted to Dr B.E. Keen for a careful reading of the manuscript. They gratefully acknowledge Dr A. Samain for the interest he has taken in the subject. They also thank Mr M. Rebut for his assistance in programming the equations.

REFERENCES

[1] REBUT, P.H., Plasma Phys. **4** (1962) 159.
[2] FURTH, H., KILLEEN, J., ROSENBLUTH, M.N., Phys. Fluids **6** (1963) 459.
[3] REBUT, P.H., GREEN, B.J., "Effect of impurity radiation on tokamak equilibrium", Plasma Physics and Controlled Nuclear Fusion Research 1976 (Proc. 6th Int. Conf. Berchtesgaden, 1976), Vol.2, IAEA, Vienna (1977) 3.
[4] PERKINS, F.W., in Heating in Toroidal Plasmas (Proc. 4th Int. Symp. Rome, 1984), 977.
[5] LAVAL, G., PELLAT, R., REBUT, P.H., Nucl. Fusion **3** (1963) 99.
[6] REBUT, P.H., SAMAIN, A., in Controlled Fusion and Plasma Physics (Proc. 5th Europ. Conf. Grenoble, 1972), Vol.1 (1972) 29.
[7] STEINOLFSON, R.S., Phys. Fluids **26** (1983) 2590.
[8] THOMAS, P.R., et al., Paper No.IAEA-CN-44/A-V-5-4, these Proceedings, Vol.1.
[9] MORRIS, A.W., ROBINSON, D.C., private communication, 1984.

ANOMALOUS TRANSPORT AND CONFINEMENT SCALING STUDIES IN TOKAMAKS

W.M. TANG, C.Z. CHENG, J.A. KROMMES, W.W. LEE,
C.R. OBERMAN, F.W. PERKINS, G. REWOLDT, R. SMITH
Plasma Physics Laboratory,
Princeton University,
Princeton, New Jersey

P. BONOLI, B. COPPI, R. ENGLADE, J. MARTINELL,
L. SUGIYAMA
Massachusetts Institute of Technology,
Cambridge, Massachusetts

United States of America

Abstract

ANOMALOUS TRANSPORT AND CONFINEMENT SCALING STUDIES IN TOKAMAKS.

In addressing the general issue of anomalous energy transport, results of theoretical studies are reported concerning: (1) the characteristics and relative strength of the dominant kinetic instabilities likely to be present under realistic tokamak operating conditions; (2) specific non-linear processes relevant to the saturation and transport properties of drift-type instabilities; (3) the construction of semi-empirical models for electron thermal transport and the scaling trends inferred from them; and (4) the application of specific anomalous transport models to simulate recent large-scale confinement experiments (TFTR and JET) and current drive experiments.

KINETIC STABILITY PROPERTIES IN TOKAMAKS

In order to identify physical processes most likely to affect anomalous electron thermal transport, attention is focused on: (a) the relative strength of high-n MHD ballooning modes compared to other short-wavelength instabilities; and (b) the basic characteristics of instabilities which should persist in the "H-mode" tokamak discharges. Concerning the first topic, a comprehensive stability code [1] has been developed to analyse the appropriate kinetically generalized form of the ballooning modes together with the usual electrostatic microinstabilities (such as trapped-particle drift modes). The calculations here are fully electromagnetic and include the relevant dynamics associated with compressional ion acoustic waves. Trapped-particle effects together with all forms of collisionless dissipation (bounce, transit, and drift resonances) are taken into account without approximations. The influence of

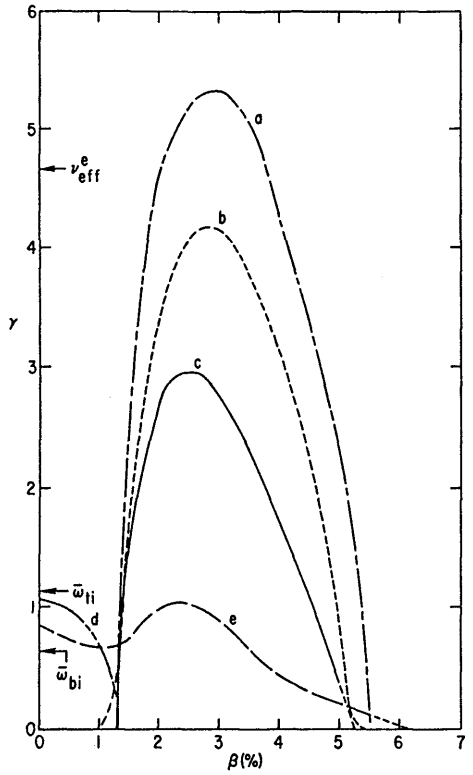

FIG.1. Typical linear growth rates for short-wavelength instabilities as a function of β for a model tokamak equilibrium. The curves represent: (a) the usual ideal MHD estimate for ballooning modes without coupling to compressional ion acoustic waves; (b) kinetic collisionless estimate in the same limit; (c) and (d) full kinetic collisionless results for, respectively, the ballooning mode and the trapped-electron drift modes; and (e) a 'hybrid' of (c) and (d) when collisional dissipation is modelled with a Krook operator. All fequencies are normalized to ω_{*e}.

collisional dissipation is estimated by employing a model Krook operator. A detailed description of the resultant system of integral equations and the numerical procedure used to solve them are given in Ref.[1]. Application of these calculations to both model and numerical MHD equilibria for parameters appropriate to existing tokamaks lead to the typical results given on Fig. 1. The general indication is that unstable short-wavelength modes with significant growth rates can extend from $\beta = 0$ to values above the upper ideal MHD critical beta (β_c) associated with the "second stability" regime. Although the strength of the dominant modes increases above the first β_c and begins to drop as the second β_c is approached, the transitions in magnitude are relatively gradual. Hence, the results here

support a "soft" beta limit picture involving a continuous (rather than abrupt or "hard") modification of anomalous transport already present in low beta tokamaks. However, the increasing dominance of the electromagnetic component of the perturbations at higher beta could lead to significantly different transport scaling properties. With regard to the "H-mode" confinement characteristics, analytic estimates show that for the relatively flat density profiles common to these discharges, electrostatic microinstabilities driven by temperature gradients and unfavorable magnetic curvature effects can persist. As noted earlier, for moderate values of beta, the kinetic ballooning modes could also be significant. Since the strength of these instabilities scales with the total pressure gradient, they too should persist in "H-mode" cases. These trends are consistent with experimental observations in that the electron thermal transport, while reduced, clearly remains strongly anomalous. In addition, detailed numerical calculations for "H-mode" conditions in the PDX tokamak yield kinetic instability growth rates which are typically about 50% smaller than corresponding cases for "L-mode" conditions. This is again consistent with the observed improvement in the energy confinement time in that the strength of the relevant instabilities is significantly reduced here.

NONLINEAR PROPERTIES OF DRIFT INSTABILITIES

For the moderate to low-beta conditions typical of most present generation tokamaks, the drift-type electrostatic modes (including trapped-particle instabilities) appear to be the most important. In order to gain some insight into the nonlinear processes likely to influence their saturation and transport properties, gyrokinetic particle simulations as well as analytic and numerical methods have been applied to the model problem of collisionless and collisional drift instabilities in a shearless slab system. In particular, it is found that the dominant saturation process need not always follow the conventional "source and sink" picture involving a coupling of energy from linearly unstable modes to those which are damped. Instead, it appears that in many cases saturation occurs when the nonlinear $\underline{E} \times \underline{B}$ advection of the electrons (rather than the ions) acts to directly eliminate the flow of energy from the electrons to the waves. In the collisionless limit, the saturation amplitude for the most unstable modes ($k_\perp \rho_s \lesssim 1$) is found to be $e\phi/T_e = (\gamma_\ell/\Omega_i)/(k_\perp \rho_s)^2$, where γ_ℓ is the linear growth rate; $\Omega_i \equiv eB/M_i c$; $\rho_s \equiv v_s/\Omega_i$; and $v_s \equiv (T_e/m_i)^{1/2}$. Generally, these modes dominate the initial phase of the instability. In the second stage of development, the effect of the nonlinear $\underline{E} \times \underline{B}$ advection for the ions becomes important and is responsible for the energy cascade from modes with $k_\perp \rho_s \lesssim 1$ to modes with smaller $k_\perp \rho_s$. Finally, the fully nonlinear stage (steady state)

is characterized by the energy exchange between these competing modes due to the nonlinear parallel acceleration of the electrons. It results in a broad and rather flat wavenumber spectrum and broad frequency spectra with $\Delta\omega_k \sim \omega_k$. Here, the maximum amplitude for each individual $\underline{k}$ mode does not deviate appreciably from the saturation amplitude for the most unstable modes. The diffusion in the simulation resembles more of a random walk process and is smaller than the quasilinear estimate of $D_{q\ell} \simeq (\gamma_\ell/\omega_*)^2(\gamma_\ell/k_\perp^2)$ with γ_ℓ being the growth rate of the fastest growing linear mode in the system. Note here that the usual ambient gradient argument gives $e\phi/T_e \simeq (\omega_*/\Omega_i)/(k_\perp\rho_s)^2$ and $D_{q\ell} \simeq \gamma_\ell/k_\perp^2$. In the collision-dominated regime ($\nu_{ei} > |\omega|$), the saturation amplitude becomes $e\phi/T_e \simeq (\omega_*/\Omega_i)/k_\perp\rho_s$ for the most unstable modes. Nonetheless, the nonlinear development of the instability appears to be qualitatively similar to those of the collisionless cases. Although the diffusion in the simulation is significantly enhanced, its measured coefficient is still smaller than the quasilinear estimate of $D_{q\ell} \simeq \nu_{ei}\rho_s^2$. It is particularly interesting to note that even when collisions are quite weak ($\nu_{ei} \ll |\omega|$), the nonlinear behavior of the steady state fluctuations follows closely that of the collision-dominated cases. On the other hand, the linear evolution for such cases remains unaltered from the collisionless limit. These observations serve to illustrate that general conclusions about the nonlinear properties of drift waves based on collisionless models could in fact be quite limited.

SEMI-EMPIRICAL MODELS FOR ANOMALOUS TRANSPORT

Since usable anomalous transport models based on self-consistent theoretical calculations still remain to be developed, it is necessary to turn to "semi-empirical" approaches which use experimentally observed trends to help select the dominant "first principles" physics features modeled. To deal with the anomalous energy confinement properties of low-beta ohmically heated plasmas, a microinstability-based model for the electron thermal transport coefficient (χ_e) is proposed in which its radial dependence is determined by a "profile consistent" constraint [2]. In particular, this involves assuming that anomalous processes in the plasma tend to maintain current profiles consistent with MHD stability to long-wavelength modes (e.g. low-n tearing modes near the q = 2 surface). Also incorporated in this model are the following experimentally observed features of ohmic discharges: (a) the region of effective thermal confinement lies between the q = 1 and q = 2 surfaces [3]; (b) the electron temperature profiles are well approximated by Gaussian shapes [4]; (c) the location of the q = 1 surface is well represented by $r_1/a = 1/q_a$ with a denoting the plasma edge [5]; and (d) the density profiles are roughly parabolic, $n_e(r) = n_{eo}(1 - r^2/a^2)^{\alpha_n}$

[4]. The current profile is related to the electron temperature profile by a form of Ohm's law, and the steady-state energy balance equation (without radiation) is solved to give the basic constraint condition which determines the radial profile of χ_e. Its magnitude and scaling characteristics are governed by the properties of the dominant anomalous mechanism. The fact that trapped-electron drift type microinstabilities are predicted to be strongly unstable in low-β ohmic cases [6] then motivates the choice of the simple γ/k^2 strong turbulence estimate[1] for the magnitude of χ_e. Using this with the constraint condition from the aforementioned solution to the energy balance equation leads to:
$\chi_e(r) = 2 \times 10^4 n_{eo}^{-1} aR^{-1.9} q_a^{-1.6} B_T^{0.3} Z_{eff}^{0.2} F(r)$ with
$F(r) = \exp[(2\alpha_q/3)(r^2/a^2)] - \exp[-(\alpha_q/3)(r^2/a^2)] \; /(r^2/a^2)[1 - (r^2/a^2)]^{\alpha_n}$ where $n_{eo}(10^{14}cm^{-3})$, B_T(Tesla), a(m), R(m), and, typically, $\alpha_q \simeq q_a + 0.5$ and $\alpha_n \simeq 1$. Application of this model to a representative set of ohmic cases from the PDX experiment yields good agreement with the empirically estimated values for χ_e. This model also leads to the following scaling for central electron temperature and volume-averaged electron temperature: $T_{eo} \propto B_T^{0.7} a^{0.4} R^{0.1} q_a^{-0.2} Z_{eff}^{0.3}$ and $\langle T_e \rangle \propto B_T^{0.7} a^{0.4} R^{-0.1} q_a^{-0.9} Z_{eff}^{0.3}$. With regard to the energy confinement time, if $\tau_E \propto \tau_{E,e}$, then the model yields $\tau_E \propto n_{eo} aR^{1.9} q_a^{0.6} B_T^{-0.3} Z_{eff}^{-0.2}$ or $n_{eo} a^{2.2} \times R^{1.3} B_T^{0.3} I_p^{-0.6} Z_{eff}^{-0.2}$. These results are in good agreement with the empirically determined scaling trends for $\langle T_e \rangle$ [8] and for τ_E [5] obtained from the general experimental data base for ohmic discharges.

To estimate the confinement scaling trends in auxiliary heated discharges, a low-β electrostatic drift wave turbulence model [9] applied in the collisionless regime ($\omega_{*e} > \nu_{ei} R/r$) gives $\chi_e = A(T_e^{3/2} M_i^{1/2} c^2/e^2 B_T^2)(2r\alpha_n/a^2)(1-r^2/a^2)^{-1}(r/R)^{1/2}$ with A = constant. Taking ignition conditions into account, this model leads to an electron heat balance equation of the form: $(A/r)(d/dr)[(T_{eo}^{2.5} r^{2.5} \alpha_n n_{eo})/B_T^2 R^{0.5} a^2 (1-r^2/a^2)^{(1-\alpha_n)}](d\tau/dr) = n^2 \times \langle \sigma v \rangle E_\alpha/4 + P/4\pi^2 Rar$. The neutral beam heating profile used here models recent PDX results [10]. Note that the temperature dependence of the loss term on the left side of this equation is almost the same as that of the thermonuclear cross-section in the range $5 < T(keV) < 20$. This result implies that the ignition condition for tokamaks becomes independent of the temperature at which ignition occurs and takes the form [9]: B_T^2

[1] In estimates of this type the linear growth rate characterizes the strength of the instability and its use does not imply that the linear properties persist in the non-linear state. See e.g. Ref. [7].

$\times n_{eo}R^{0.5}a^{2.5}\alpha_n^{-1} > 10^3$. Dimensional analysis of the energy balance equation here yields the scalings: $T_{eo} \propto B_T^{0.8}(P/n)^{0.4} \times (a/R)^{0.2}q_a^{0.1}\alpha_n^{-0.4}$ and $\tau_{E,e} \propto I_p^{0.9}R^{1.7}n^{0.6}P^{-0.6}a^{0.4}B_T^{-0.1}\alpha_n^{-0.4}$. The central electron temperature scaling is in good agreement with the empirical trend deduced from experimental data for neutral-beam-heated tokamaks [11]. With regard to confinement scaling, the observed improvement from L- to H-mode confinement can be interpreted in terms of the flattening of the density profile (i.e. a reduction from $\alpha_n \simeq 1$ to $\alpha_n \simeq 0.3$).

ANOMALOUS TRANSPORT IN THE PRESENCE OF IMPURITIES

Up to the present, the plasma produced and confined in large scale experiments (TFTR and JET) have been characterized by values of $Z_{eff} > 1$ and radiation losses in the current-carrying part of the plasma column which are significant in the overall energy balance. Another characteristic of these discharges is that the $q = 1$ surface extends out to a significant fraction of the plasma radius. In order to simulate these operating conditions, a specific 1D radial transport code, which was successful in simulating smaller scale experiments, has been employed. In this code both the impurity radiation and the MHD sawtooth oscillations inside the $q = 1$ surface are taken into account. The anomalous transport properties are governed by a model based on the "profile consistent" constraint [2] described earlier together with a modified form of the Coppi-Mazzucato prescription for the loop voltage [12]. Specifically, the electron heat flow can be expressed as $Q_e = -K_e dJ_\parallel/dr$ where $J_\parallel \simeq J_o\exp(-r^2/a_I^2)$ represents the current density and $K_e = (\varepsilon_s/24\pi)(I_p/8\pi e)(a_I T_e/r^2)W_N(r)C_s^{2/5}$ with $a_I \equiv$ radius of the current carrying channel; $C_s \equiv (v_s/v_{Te})(\nu_{ee}/v_{Te}^2)\omega_{pi}d_e^2$; and $W_N(r) \equiv \int_o^r drr(J_\parallel E_\parallel - L_R)/[(E_\parallel I_p/2\pi) - L_R(r = 0)a_I^2/2]$. Here L_R is the impurity radiation energy loss, ω_{pi} is the ion plasma frequency, $d_e \equiv c/\omega_{pe}$ is the electron inertial skin depth, and the free parameter ε_s is about 1.3 (as suggested by a fit of the results from previous small scale experiments). The factor C_s was constructed to reflect the presence of current-driven magnetic reconnecting modes. An alternative choice [13], which would introduce a stronger scaling with R, is to replace C_s with $C_N = (v_s/L_pR)(a_I/R)^{3/2}(\nu_{ee}d_e^2/v_{Te}^2)$ with L_p being the pressure gradient scale length associated with the presence of instabilities driven by the combined effects of the pressure gradient and unfavorable magnetic field curvature. Proceeding with the calculations using C_s, it is found that the presence of impurities can influence transport in two ways: (a) the presence of heavy impurities in the current-carrying part of the plasma column may increase the loop voltage above that associated with a clean plasma; and (b) the presence of light

impurities can cause T_e to be raised above the values that would be predicted by assuming a clean plasma. In the latter case, increasing Z_{eff} does not appreciably affect the loop voltage but does increase the electrical resistivity. Consequently, $T_{eo} \propto Z_{eff}^{2/3}$ and $\tau_{E,e} \propto Z_{eff}^{2/3}$. This tends to indicate that at equal densities, cleaner discharges will tend to be cooler. The code described here has been applied to a TFTR discharge exhibiting strong radiation from light ion (primarily carbon) impurities. For this case the total radiated power was roughly 60-90% of the ohmic power, while the impurity radiation during the current flat-top was characterized by a fairly flat emissivity profile. Typical parameters were I_p = 1.4MA, B_T = 2.7T, n = 2.3 × $10^{13}cm^{-3}$, R = 2.55m, a = 0.82m, V_{loop}(meas.) = 1.2V, and Z_{eff}(meas.) = 4.5 ± 0.9. During a sawtooth oscillation, experimental values of the maximum/minimum central temperatures(keV) were T_{eo} = 1.9/1.6 and T_{io} = 1.6/1.5. Results of the simulation using the modified transport coefficient with Z_{eff} = 3 and neoclassical resistivity [14] indicate good agreement with the observed values of the relevant parameters when the impurity radiation profile was assumed to be flat and to constitute 60-75% of the ohmic power.

THEORETICAL INTERPRETATION OF CURRENT DRIVE EXPERIMENTS

The interpretation of results from current drive experiments [15,16] in the lower hybrid frequency range at relatively low density has been undertaken with attention focused on the upshift of the parallel wave number (i.e. reduction of phase velocity) caused by toroidal effects on the waves launched at the plasma edge. If multiple reflections of wave energy at low density cutoffs are included, this mechanism enables waves with small initial $k_\parallel$ to interact with a large number of electrons and thus generate substantial current. In addition, the anomalous electron energy transport here is associated with the thermal electrons (with little contribution from the current carrying superthermal electrons). These processes are taken into account in a combined analytic and numerical model comprised of a 1D radial transport code, a toroidal ray tracing code, and a relativistic quasilinear calculation of the longitudinal electron distribution function. The distribution of launched wave energy as a function of $k_\parallel$ for a lower hybrid wave grill is obtained with a linear Brambilla code. In the transport code block of this numerical model, conservation equations for the time evolution of the bulk electron and ion temperatures and the magnetic stream function $\psi(B_\theta \equiv \partial\psi/\partial r)$ are solved for a particular choice of transport coefficients. In addition, diffusion equations for the RF-generated current densities parallel and anti-parallel to the toroidal magnetic field are also solved [17]. The ray tracing code uses the ray equations of geometric

optics to follow the propagation of individual lower hybrid waves for a dispersion relation that includes electromagnetic and warm plasma effects and a Shafranov equilibrium. The assumed absorption mechanisms are electron and (unmagnetized) ion Landau damping and nonresonant collisional damping. A quasilinear diffusion coefficient D_{ql} is found by summing ray amplitudes for multiple passes through a magnetic surface. The quasilinear calculation of the longitudinal electron distribution function consists of the numerical solution of a relation obtained by integrating a relativistically correct, 2D steady-state Fokker-Planck equation over perpendicular momentum with appropriate simplifying assumptions. Included here are the effects of the waves (via D_{ql}), a DC electric field, a large effective perpendicular temperature, and a particle loss time that increases monotonically with energy. The model described is found to adequately reproduce many of the results of the PLT and Alcator-C steady-state current drive experiments. At "optimal" waveguide phasing (60° for PLT, 67.5 for Alcator-C) and "maximum" B_T (3.1T for PLT, 10T for Alcator-C), the simulations can be summarized by a figure of merit of the form $C \equiv n(10^{19}m^{-3})\ I_{RF}(kA)R(m)/P_{RF}(kW) \simeq 1$, in reasonable agreement with observations. The code does not predict a sharp drop in efficiency above the density limits of $\bar{n} \simeq 7 \times 10^{18}m^{-3}$ and $\bar{n} \simeq 2 \times 10^{20}m^{-3}$ for PLT and Alcator-C respectively. Increasing the waveguide phasing angle and thereby decreasing the energy launched in high phase velocity waves brings about a decrease in the calculated value of C. Lowering B_T also reduces the calculated C due to poorer accessibility of high phase velocity waves to the center of the plasma. The experimental observations mirror both of these trends. It should also be noted that the present model effectively reproduces the time-dependent behavior observed at the beginning of otherwise "steady-state" experiments and throughout runs where the plasma is overdriven and the current ramps up at a rate which is a fraction of the pre-RF inverse L/R time. In the former case, the rapid drop in the loop voltage to the value near zero ($\lesssim$ 50 ms for PLT, $\lesssim$ 15 ms for Alcator-C) is a consequence of the spatial diffusion of the RF current density mentioned above. In the latter case, a slow current rise results from the restraining influence of a negative DC electric field on the magnitude of the RF current.

Acknowledgment

This work was supported by U S DoE Contract # DE-AC02-76-CHO-3073 and DE-AC02-78-ET-51013.

REFERENCES

[1] REWOLDT, G., et al., Phys. Fluids **25** (1982) 480.
[2] COPPI, B., Comments Plasma Phys. Controll. Fusion **5** (1980) 261.
[3] MIRNOV, S.V., "Scaling law for the plasma energy life-time in tokamaks", Plasma Physics and Controlled Nuclear Fusion Research 1978 (Proc. 7th Int. Conf. Innsbruck, 1978), Vol. 1, IAEA, Vienna (1979) 433.
[4] FAIRFAX, S., et al., "Energy and particle confinement in the Alcator tokamaks", Plasma Physics and Controlled Nuclear Fusion Research 1980 (Proc. 8th Int. Conf. Brussels, 1980), Vol. 1, IAEA, Vienna (1981) 439.
[5] GOLDSTON, R., Plasma Phys. Contr. Fusion **26** 1A (1984) 87 (Invited Papers of 11th Europ. Conf. Aachen, 1983).
[6] REWOLDT, G., et al., Phys. Fluids **21** (1978) 1513.
[7] DUPREE T.H., Phys. Fluids **10** (1967) 1049.
[8] PFEIFFER, W., WALTZ, R.E., Nucl. Fusion **19** (1979) 51.
[9] PERKINS, F.W., in Heating in Toroidal Plasmas (Proc. 3rd Int. Symp. Rome, 1984).
[10] KAYE, S.M., et al., Princeton Plasma Physics Lab. Rep. PPPL-2109 (1984).
[11] STRACHAN, J.D., SOLTWICH, H., in Controlled Fusion and Plasma Physics (Proc. 11th Europ. Conf. Aachen, 1983), Vol. 1 (1983) 65; NEILSON, G.H., et al., Nucl. Fusion **23** (1983) 285.
[12] COPPI, B., Massachusetts Inst. Technol. Rep. PTP-84/4 (1984).
[13] COPPI, B., TANG, W.M., Massachusetts Inst. Technol. Rep. PTP-84/7 (1984).
[14] HAWRYLUK, R., et al., Princeton Plasma Phys. Lab. Rep. PPPL-2106 (1984).
[15] BERNABEI, S., et al., Phys. Rev. Lett. **49** (1982) 1255.
[16] PORKOLAB, M., et al., "Lower-hybrid heating and current drive experiments on the Alcator C and Versator II tokamaks", Plasma Physics and Controlled Nuclear Fusion Research 1982 (Proc. 9th Int. Conf. Baltimore, 1982), Vol. 1, IAEA, Vienna (1983) 227.
[17] ENGLADE, R., et al., Bull. Am. Phys. Soc. **28** (1983) 1163.

MAGNETIC ISLANDS IN TOROIDALLY CONFINED PLASMA

M. KOTSCHENREUTHER, A.Y. AYDEMIR,
D.C. BARNES, J.R. CARY, J.D. HANSON,
R.D. HAZELTINE, P.J. MORRISON
Institute for Fusion Studies,
University of Texas at Austin,
Austin, Texas,
United States of America

Abstract

MAGNETIC ISLANDS IN TOROIDALLY CONFINED PLASMA.

The production of magnetic islands in toroidal confinement systems is examined analytically and numerically in several contexts: (1) The resistive dynamics of magnetic islands is examined analytically, including curvature and pressure. A Grad-Shafranov equation is derived to describe the MHD equilibria of thin islands. The resistive evolution is then obtained. Interchange effects are very important for small islands and progressively less so for larger ones. (2) A numerical method for eliminating stochasticity in vacuum magnetic fields is introduced. Application of this method shows that stochasticity can be made negligible by proper choice of the coil configuration. It is possible to increase the equilibrium β-limit by factors of two or more over that of a simple, 'straight' coil winding law. (3) The production of magnetic islands by the introduction of plasma pressure into non-axisymmetric confinement configurations is analysed, assuming scalar pressure. Far from the rational surfaces a procedure based on linearization in β applies. Singularities at the resonant surfaces are resolved with a non-linear analysis. Scaling is found by using the approximation of nearly circular flux surfaces. Island size depends dramatically on whether or not a magnetic well is present. If a magnetic hill is present, islands overlap for arbitrarily low pressure.

1. RESISTIVE DYNAMICS OF MAGNETIC ISLANDS

Here we analytically derive the resistive nonlinear dynamics of thin magnetic islands including the effects of pressure and curvature. This combines and extends the nonlinear island calculation of Rutherford[1] and the linear stability results of Glasser, Greene and Johnson [2].

A principal result is that there is a critical island width Δx_c. Islands wider than Δx_c are dominated by Δ', measuring the magnetic free energy, while narrower islands are dominated by pressure and curvature in the island vicinity. Δx_c is given by

$$\Delta x_c^s \Delta'_* \sim k_2(E+F) \qquad (1)$$

where E, F, H and D_I = E+F+H are standard measures of magnetic curvature[2], $s = \sqrt{1-4D_I}$, and Δ'_* is the finite-β generalization[2] of Δ'. k_2 is roughly 6.3.

To obtain this result, a Grad-Shafranov equation is derived for thin islands which describes the resonant magnetic field in the island vicinity. Interestingly, the curvature enters this nonlinear equation through an expression proportional to the Mercier ideal interchange criterion.

The resistive evolution is then obtained. H is relatively unimportant in the resistive dynamics, similarly to the linear theory [2].

An expansion in the tokamak inverse aspect ratio ε is used for simplicity, using either $\beta \sim \varepsilon^2$ or $\beta \sim \varepsilon$. We believe the essential physics for general geometries is similar.

For tokamaks with stabilizing curvature and destabilizing Δ', Equation (1) gives the minimum island width for growth. This matches linear theory in the following sense. An island just barely into the Rutherford regime, whose width equals the linear layer width, requires a Δ' to overcome curvature stabilization, which scales as the critical Δ' of linear theory. Only for high β, $\beta \sim \varepsilon$, can Δx_c be a significant fraction of the minor radius. For destabilizing curvature and stabilizing Δ', Equation (1) gives the saturated island width for a single resistive interchange.

Nonlinear islands grow relatively slowly, so following Rutherford we neglect inertia. Therefore, our starting equations are

$$\underset{\sim}{j}\times\underset{\sim}{B} = \nabla p \tag{2}$$

$$\nabla\cdot\underset{\sim}{j}_{\parallel} = \underset{\sim}{B}\cdot\nabla p\times\nabla(-1/B^2) \tag{3}$$

and Ohm's law $E_{\parallel} = \eta j_{\parallel}$. The right-hand side of Equation (3) was neglected in Rutherford's treatment.

The island grows on an equilibrium field $\underset{\sim}{B}_0 = \nabla\chi\times\nabla(q(\chi)\vartheta - \zeta)$, with safety factor $q(\zeta)$ and toroidal angle ζ. We focus attention on the region near a rational surface with $\ell = m/n = q_0$. We define a periodic angle coordinate $\alpha = \vartheta - \zeta/q_0$. All quantities f have resonant and nonresonant parts. Since these parts generally behave differently, we define an averaging operator to select out the resonant part, $\bar{f}(\chi,\alpha) = \oint d\zeta\ f(\chi,\alpha,\zeta)/\oint d\zeta$; the nonresonant part is $\tilde{f} = f-\bar{f}$. We also define

$$[A,\bar{B}] = \nabla\zeta\cdot(\nabla A\times\nabla B) \tag{4}$$

Equations (2) and (3) are now ordered for the case of islands which are thin compared to the minor radius. Also, an

aspect ratio expansion is used. However, we keep terms one additional order higher[3] than usual in ε, but not in β. This is accurate enough to give the lowest-order average curvature for $\beta \sim \varepsilon$ or $\beta \sim \varepsilon^2$.

The total average magnetic flux, ψ_h, through a helical ribbon α = const, plays the role of a flux function for the island. In the island region, the perturbed flux ψ_1 is given by the covariant ζ component of the vector potential.

ψ_1 is obtained from Ampère's law, which for thin islands is

$$|\nabla\chi|^2 \frac{\partial^2\psi_1}{\partial\chi^2} = I \tag{5}$$

where I is the covariant ζ current. $\bar{\psi}_1$ is found by multiplying Equation (5) by $|\nabla\chi|^{-2}$ and averaging. I is found by considering the average and nonresonant parts of Equations (2) and (3). To requisite order $\bar{p}$ is a function of ψ_h. $\bar{I}$ is given by

$$[\psi_h, \bar{I}] = [\bar{p}, \bar{h}] + \overline{[\tilde{p}, \tilde{h}]} - \overline{[\tilde{\psi}, \tilde{I}]} \tag{6}$$

where h gives the effect of curvature, $h = -1/B_0^2 + 2P_0/B_0^4$. Without pressure and curvature, $\bar{I}$ is a function of ψ_h; $\bar{h}$ gives the effect of average normal curvature, and the last two terms give the effect of geodesic curvature and Pfirsch–Schlüter currents.

Explicit expressions for the last two terms are obtained using the nonresonant parts of Equations (2), (3) and (5). The calculation is lengthy but similar to linear theory, since the magnetic nonlinearity is negligible for the nonresonant component. The sum of these terms can be written in the form $[\bar{p}, h_g]$, with h_g depending on the geodesic curvature.

With this form, Equation (7) is easily solved:

$$\bar{I} = J(\psi_h) + p'(\psi_h)(h+h_g) \tag{7}$$

where J is an arbitrary function.

The results for I are substituted into Equation (5), and equilibrium quantities are Taylor–expanded about the rational surface $\chi = \chi_0$. We thus obtain a Grad–Shafranov equation describing the flux function ψ_h in the island region:

$$\frac{\partial^2\psi_h}{\partial\chi^2} = J_*(\psi_h) + (\chi-\chi_0)(G_1+G_2)\frac{\partial p(\psi_h)}{\partial\psi_h} \tag{8}$$

where J_* is an arbitrary function, where G_1 and G_2 are (to relevant order in ε) E+F and H divided by $(\partial p/\partial \chi_0)\{q_0/(\partial q/\partial \chi_0)\}^2$. The Mercier instability criterion is E+F+H > 1/4.

It remains to determine $J_*(\psi_h)$ and the dynamics. The average of Ohm's law and Faraday's law give to lowest order

$$\frac{\partial \bar{\psi}_1}{\partial t} + \frac{1}{q_0}[\psi_h, \bar{\varphi}] = \eta \bar{I} \tag{9}$$

where φ is the electrostatic potential, and η is the resistivity. As in Rutherford's[1] analysis, Equation (9) is flux-averaged (denoted by < >) at constant ψ_h, thus determining $<\bar{I}>$ and eliminating $\bar{\varphi}$. J_* is determined from $<\bar{I}>$. Matching to the exterior region far from the island introduces Δ'_*.

To solve Equation (8) analytically we assume that: (1) a single harmonic m dominates in $\bar{\psi}_h$ (e.g. the most unstable one), so that $\bar{\psi}_h \cong q_0^1(\chi-\chi_0)^2/q_0^2 + A(\chi,t)\cos m\alpha$; (2) $A(\chi,t)$ is nearly constant in χ near the island. This requires a subsidiary expansion in which G_1 and G_2 are small.

The pressure profile $p(\psi_h)$ near the island is assumed to be dominated by diffusion. The pressure gradient is maintained by sources deep in the plasma interior and is determined for slowly growing islands by the condition that the flux of pressure is constant. In view of the large anomalous transport inferred from experiments, we simply assume a large constant diffusion coefficient in the island region.

The resulting evolution equation for A(0,t) is best expressed in terms of the island width $\Delta\chi = 4\sqrt{q_0^2 A/(\partial q_0/\partial \chi)}$.

$$\frac{k_1}{\eta}\frac{\partial \Delta\chi}{\partial t} = \Delta'_* \Delta\chi^{s'} + k_2 \frac{(E+F)}{\Delta\chi} \tag{10}$$

where $s' = -1 + \sqrt{1-4D_I}$, $k_1 \simeq 3$, $k_2 \simeq 6.3$. For β=0, this agrees with Rutherford's result (the island width grows linearly with time). The driving term from pressure dominates for $\Delta\chi < \Delta\chi_c$ given by Equation (1).

2. ELIMINATION OF STOCHASTICITY IN STELLARATOR VACUUM FIELDS

We describe here a numerical method of optimizing the coil winding law in stellarators to greatly reduce magnetic stochasticity in the vacuum magnetic field. For numerous

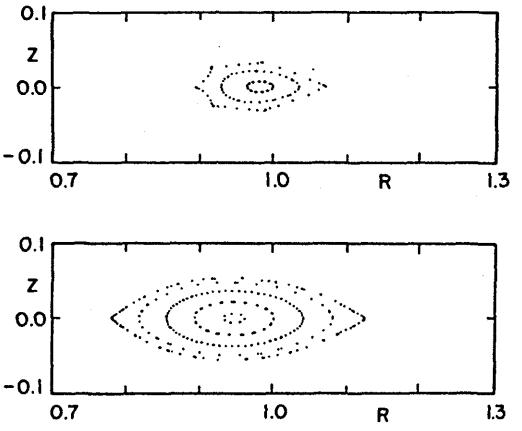

FIG.1. Surfaces of section of unoptimized and optimized stellarators.

examples it has led to much higher usable plasma volume, rotation number ι and inverse aspect ratio.

The crucial ingredient of this method is a measure of the nonintegrability (i.e. size of island or amount of stochasticity), called the residue. First, the coil winding law is given as a function of several parameters. Those parameters are then varied to minimize the stochasticity.

Consider a field line through the points (R_0, z_0, ζ) and $(R, z, \zeta+2\pi/m)$, where R, z and ζ are cylindrical coordinates, and m is the field periodicity. The qth iterated return map is $N^q(R_0, z_0) = (R, z)$. The residue[4] of a fixed point of N^q is related to the eigenvalues of the linearization of N^q. For an integrable system without island structure, the eigenvalues are unity and r=0. We thus expect, and have found in practice, that reducing the residue decreases the stochasticity near the corresponding rational surface.

In the following example, the coils are wound on a torus with major radius $R_0 = 1$ and minor radius $r = 0.3$. The coils are wound on a function $\eta(\zeta)$, where η is the ordinary poloidal angle about $R_0 = 1$, z=0. The parameters we vary are the Fourier coefficients of η.

The top of Figure 1 shows the surface of section for an unoptimized stellarator with $\ell_0 = 2$, $m_0 = 5$, $B_0 = 1$, two helical coils, and $\iota_{axis} = 0.72$.

The bottom of Figure 1 shows the results of minimizing the residues of the fixed points with rotation numbers 1/3, 1/4, 1/5. The usable area is clearly substantially larger. ε was increased by 80%, $\langle\iota\rangle$ by 15%. A rough estimate[5] of the equilibrium β limit for a stellarator is $\beta_{eq} \sim \langle\iota^2\rangle\varepsilon$. Here, β_{eq} was increased by a factor of 2.4.

3. PRESSURE-INDUCED EQUILIBRIUM ISLANDS IN 3-DIMENSIONAL PLASMAS

Here, we consider the plasma equilibrium resulting from the introduction of a small amount of plasma pressure into a nonaxisymmetric vacuum magnetic field with good flux surfaces, free of islands. We examine the pressure-induced islands within the MHD model. As in the resistive island dynamics section, local interchange effects are analysed (but without an aspect ratio expansion) and found to be important.

Newcomb[6] noted that there is a singularity at each rational surface in the equilibrium MHD equations which leads to the requirement that $\int d\ell/B$ must be constant on each surface. This is not generally true for vacuum magnetic fields. The islands at the rational surface resolve the singularity and relax this constraint.

An analytic formula for the induced island width is derived under the approximation of nearly circular flux surfaces. Magnetic perturbations arise both from currents far from the resonant surface and from those in the island region. Once β exceeds a threshold value β_t, island size depends strongly on whether there is a magnetic well. β_t is typically quite small. Island widths in regions of good average curvature do not increase for $\beta > \beta_t$. This occurs because the external magnetic perturbation is attempting to drive the island against stabilizing interchange forces.

In the case of bad curvature, the island width scales linearly with β for $\beta > \beta_t$. The island in this case is a saturated resistive interchange (as in the previous section), and the exterior currents play the role of an initiating perturbation. It is significant that then the island scales with mode number ℓ' as $1/\ell'$. Since the mean spacing of rational surfaces with rotation number $\iota = m/\ell$ (for both m, $\ell < \ell'$) scales as $1/\ell'^2$, island overlap always occurs for sufficiently high ℓ.

We choose flux coordinates χ, ϑ, ζ of the vacuum magnetic field, $\underset{\sim}{B}_0 = \nabla\chi\times\nabla\vartheta + \iota(\chi)\nabla\zeta\times\nabla\chi$. ζ is chosen to be a constant times the scalar potential[7] of $\underset{\sim}{B}_0$, and the Jacobian $J = \gamma/B_0^2$.

The currents in the exterior region are computed by linearization in the plasma pressure, $\underset{\sim}{j}_1 \times \underset{\sim}{B}_0 = \nabla p_1$.

The perpendicular current is obtained directly. $\nabla\cdot j = 0$ gives the parallel current $j_\parallel$. Define $j_\parallel = Q\underset{\sim}{B}$. After Fourier-transforming in ϑ and ζ, $Q = \sum_{\ell m} Q_{\ell m}\, e^{i(\ell\vartheta - m\zeta)}$, we obtain

$$Q_{\ell m} = \frac{-\ell P_1'(\chi) J_{\ell m}(\chi)}{\ell\iota(\chi) - m} + \hat{Q}\zeta(\chi - \chi_{\ell m}) \qquad (11)$$

where $\iota(\chi_{\ell m}) = m/\ell$. Note that $J_{\ell m}$ is proportional to the variation of $\int d\ell/B$ on a flux surface. The singularity in the linearized equations is resolved by islands, thus determining $\hat{Q}$.

Since the singularities are integrable, the vector potential $\underset{\sim}{A}_1$ of the perturbed magnetic field can be found by a Green's function integration. This gives a formal solution:

$$\underset{\sim}{A}_1(\chi,\ell,m) = \underset{\sim}{C}_1(\chi,\ell,m) + \sum_{\ell',m'} \underset{\sim}{D}(\chi,\ell,m,\ell',m')\hat{Q}_{\ell',m'} \qquad (12)$$

To make further analytical progress, we introduce the approximation of nearly circular flux surfaces. This decouples the harmonics. Expressions can then be obtained in terms of the equilibrium profiles. For large ℓ, these depend only on local quantities at the resonant surface, and the covariant ζ components of Equation (12) (which produce the islands) are

$$C_\zeta = \frac{-R_0}{\partial \ell^2}\left(\frac{dP}{dr} J_{\ell m}\right)^{-1} \frac{d}{dr}\left[r\left(\frac{dp}{dr} J_{\ell m}\right)^2 / \frac{d\tau}{dr}\right]$$

$$D_\zeta = \frac{R_0}{\partial \ell}\left[1 + \left(\frac{mr}{\ell R_0}\right)^2\right]^{1/2} \qquad (13)$$

where R_0 is the mean major radius of the magnetic axis, and r is the minor radius of the magnetic surface.

The solution for the interior region is formally almost identical to that in the case of resistive islands, except that ζ is now proportional to the magnetic potential. Since we are considering here low β, h is taken as $1/B^2$, and the last two terms of Equation (6) can be neglected. Again for low-β, the constant ψ approximation[1] is made. The arbitrary function $J(\psi)$ is determined from the condition that the average toroidal current must vanish (corresponding to a resistive steady state).

Boozer[7] has pointed out that resistive diffusion near a resonant surface becomes singular for nonvanishing $J_{\ell m}$ and tends to flatten the pressure profile. This diffusion has been computed for the present case with an island at the resonant surface. Again, the island resolves the singularity. For sufficiently large islands (corresponding to $\beta > \ell^2 J_{\ell m}/J_{00}$, which is extremely low-β) this diffusion is smaller than the nonresonant diffusion and causes little flattening. There is some island-induced resonant diffusion, but this virtually never reduces the space-integrated current from the interior region by more than a factor $U \sim 1 - 1/2$.

We again assume a single harmonic dominates in $\bar{\psi}_1$ with coefficient $A_{\ell m}$. Having obtained $\hat{Q}$ as a nonlinear function of the island width, Equation (12) becomes, for circular flux surfaces:

$$0 = C_\zeta(\chi_0, \ell, m) - A_{\ell m} - \frac{\partial p}{\partial r}\frac{\partial J_{00}}{\partial r} UD_\zeta(\chi_0, \ell, m)|A_{\ell m}|^{1/2}$$

$$\times \text{sign}(A_{\ell m})/|\tau_r'| \qquad (14)$$

where $\partial J_{00}/\partial r$ gives the magnetic well. For low-β, $A_{\ell m} \sim \beta$ the island width $\sim \beta^{1/2}$, and the island current term $\sim \beta^{3/2}$ is negligible. All terms are comparable at $\beta \sim \beta_t$. For $\beta >> \beta_t$ the third term becomes large.

For the good curvature case, the second and third have the same sign. Thus, the third balances the first, resulting in slower island growth with β. For the bad curvature case, the second and third nearly cancel, leading to a larger island, almost independent of C_ζ. This is the saturated state of a resistive interchange.

ACKNOWLEDGMENT

This work was supported by the U S Department of Energy, under contract #DE-FG05-80ET-53088.

REFERENCES

[1] RUTHERFORD, P.H., Nonlinear growth of the tearing mode, Phys. Fluids 16 (1973) 1903.

[2] GLASSER, A.H., GREENE, J.M., JOHNSON, J.L., Resistive instabilities in general toroidal plasma configurations, Phys. Fluids 18 (1975) 875.

[3] STRAUSS, H.R., Finite aspect ratio MHD equations for tokamaks, Nucl. Fusion 23 (1983) 649.

[4] GREENE, J.M., A method for determining a stochastic transition, J. Math. Phys. 20 (1979) 1183.

[5] SHAFRANOV, V.D., Magnetohydrodynamic theory of plasma equilibrium and stability in stellarators: survey of results, Phys. Fluids 26 (1983) 357.

[6] NEWCOMB, W.A., Magnetic differential equations, Phys. Fluids 2 (1959) 362.

[7] BOOZER, A.H., Plasma equilibrium with rational magnetic surfaces, Phys. Fluids 24 (1981) 1999.

ROLE OF MULTIPLE HELICITY NON-LINEAR INTERACTION OF TEARING MODES IN DYNAMO AND ANOMALOUS THERMAL TRANSPORT IN REVERSED-FIELD PINCH

Z.G. AN*, P.H. DIAMOND, R.D. HAZELTINE, J.N. LEBOEUF, M.N. ROSENBLUTH, R.D. SYDORA, T. TAJIMA
Institute for Fusion Studies,
University of Texas at Austin, Austin, Texas

B.A. CARRERAS, L. GARCIA, T.C. HENDER, H.R. HICKS, J.A. HOLMES, V.E. LYNCH
Oak Ridge National Laboratory,
Oak Ridge, Tennessee

H.R. STRAUSS,
Courant Institute of Mathematical Sciences,
New York University, New York, N.Y.

United States of America

Abstract

ROLE OF MULTIPLE HELICITY NON-LINEAR INTERACTION OF TEARING MODES IN DYNAMO AND ANOMALOUS THERMAL TRANSPORT IN REVERSED-FIELD PINCH.

A theory of magnetic fluctuation dynamics, the dynamo mechanism, and anomalous thermal transport in the reversed-field pinch is presented. Non-linear generation of and coupling to $m \geq 2$ modes is advanced as an $m = 1$ tearing mode saturation mechanism. The processes by which $m = 1$ tearing modes sustain the magnetic configuration and stabilize themselves by lowering the safety factor on axis ($q(0)$) are elucidated. The non-linear dynamics of resistive interchange modes is discussed. Stochastic magnetic field transport arguments are used to estimate anomalous thermal conductivity and confinement scaling.

1. INTRODUCTION

Recently, results from several Reversed-Field Pinch (RFP) experiments have shed light on the structure of the observed magnetic fluctuations[1,2,3], their role in dynamo activity[4], and, in at least one case[1], their relation to anomalous thermal transport. It is widely believed that resistive tearing and interchange instabilities drive the

---

* Permanent address: The Southwestern Institute of Physics, Leshan, Sichuan, China.

magnetic fluctuations. Thus, a theory of the nonlinear evolution of interacting tearing modes is required for an understanding of RFP operation. In this paper, the results of several theoretical and computational investigations of the multiple helicity nonlinear interaction of tearing and resistive interchange modes are summarized. The implications of these results for models of dynamo activity and anomalous thermal transport are discussed.

2. PLASMA MODEL - REDUCED MHD FOR RFP

The parameters of current RFP discharges indicate that resistive MHD is an adequate plasma model. Recently, a new set of reduced resistive MHD equations for RFP plasmas has been derived [5]. These equations,

$$\frac{\partial \psi}{\partial t} = \underline{B} \cdot \nabla \phi + \eta C \tag{1}$$

$$\frac{D}{Dt} \nabla \cdot \frac{\rho}{B^2} \nabla \phi = \underline{B} \cdot \nabla (C - \langle \underline{J} \rangle \cdot \langle \underline{B} \rangle / \langle \underline{B} \rangle^2) \tag{2}$$

$$(\nabla_\theta^2 + \nabla_z^2) \chi = \langle \underline{B} \rangle \cdot \nabla (\partial \psi / \partial r) \tag{3}$$

for the fluid stream function ϕ, the parallel vector potential component ψ, and χ, determined from the condition of radial force balance, describe the basic dynamics of RFP plasmas. Here $C = (1/\langle \underline{B} \rangle^2) \nabla \cdot (\langle \underline{B} \rangle^2 \nabla \psi - \langle \underline{B} \rangle \langle \underline{B} \rangle \cdot \nabla \psi - \langle \underline{B} \rangle \cdot \nabla \chi \nabla r)$ is the perturbed parallel current $(J)_\parallel$, $\langle \underline{B} \rangle$ and $\underline{B}$ are the average and total magnetic field, ρ is the density and η is the resistivity. Throughout this paper, times and lengths are normalized to τ_A and a, respectively, so that $S^{-1} = \tau_A / \tau_R$, where $\tau_A^{-1} = |\langle \underline{B} \rangle| / (4\pi\rho)^{1/2} a$ and $\tau_R^{-1} = \eta / a^2$. A cylindrical model with coordinates r, θ, z is used, and all fluctuations are expanded in toroidal (n) and poloidal (m) harmonics, so that $\underline{k} \cdot \langle \underline{B} \rangle = k_\parallel = (\langle B_\theta \rangle / r)(m - nq(r)) \cong -(\langle B_\theta \rangle / r)(nq' x)$. Computational solutions of these equations manifest the basic properties of RFP dynamics.

3. DYNAMICS OF M=1 TEARING MODES

3.1. Theory of multiple helicity nonlinear interaction

In the RFP, where the safety factor q(r) decreases monotonically in radius, a spectrum of m=1 tearing modes, with $10 < n < 20$ and resonant surfaces within the reversal surface (see

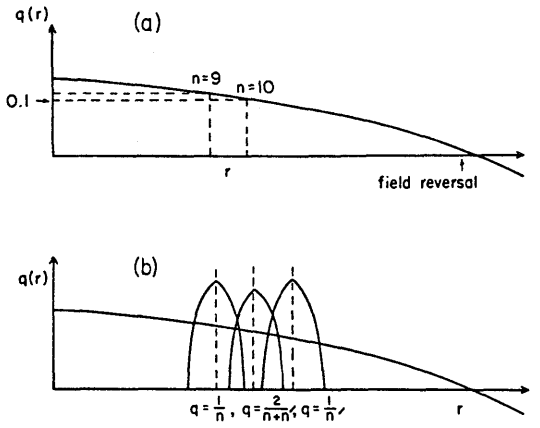

FIG.1. (a) RFP q(r) profile with location of resonances (not to scale). (b) Location of primary (m = 1) and nonlinearly driven (m = 2) modes (not to scale).

Figure 1a), is destabilized by resistive diffusion of the magnetic configuration[6] away from a Taylor state[7], thus resulting in the formation of magnetic islands. Due to the proximity of neighboring rational surfaces, where $q(r_1)=1/n$ and $q(r_2)=1/n+1$, respectively, the islands overlap for fluctuation levels of $(\delta B_r/B_o)\cong\varepsilon/n^2rq'\sim\varepsilon^2$, where $\varepsilon=a/R$. For $\varepsilon\sim1/4$, island overlap occurs at fluctuation levels less than that which are observed [1]. Indeed, for $S\leq10^5$, neighboring magnetic islands overlap while the tearing modes are still in the linear growth phase. Thus, strong nonlinear mode interaction, which generates turbulence and magnetic field line stochasticity, occurs throughout the RFP core.

As a consequence of the nonlinear interaction of the islands formed at r_1 and r_2, an m=2, n'=2n+1 current sheet and island are resonantly driven (see Figure 1b). The m=2, n'=2n+1 mode is linearly stable ($\Delta'_{m=2}<0$) and is further stabilized by flattening of the equilibrium current gradient by (global) m=1 modes. Thus, the driven (stable) m=2 modes nonlinearly absorb energy from the primary m=1 modes, which saturate when the rate of coupling of energy to m=2 balances the rate of equilibrium magnetic energy release by m=1's. This progressive current filamentation process (cascade) continues with the generation of $m \gtrsim 3$, and eventually terminates when the driving energy (tapped through m=1 modes) is resistively dissipated at small scales and depleted by quasilinear profile modification.

The natural methods for theoretical analysis of these phenomena are those of renormalized turbulence theory. The derivation of spectral equations and the extraction of

quantitative results[8] were facilitated by observing that the region of resonant tearing mode interaction is located well within the reversal surface, where $B_{oz} > B_{o\theta}$. Hence, conventional[9] reduced resistive MHD is an adequate plasma model. Using standard methods[10], it follows that the equations for kinetic and magnetic energies $E^K_{\underline{k}}$ and $E^M_{\underline{k}}$, where $\underline{k}=(m,n)$, are:

$$\frac{\partial E^K_{\underline{k}}}{\partial t} = i\int dx \phi_{-\underline{k}}\, k_\parallel J_{\underline{k}} - \int dx \langle \phi \nabla_\theta \psi \rangle_{\underline{k}} \langle J \rangle' + \int dx \sum_{\underline{k}'} \left(1 - \frac{n'^2}{n''^2}\right) \Delta'_{\underline{k}''} \frac{\delta(x'')}{\Delta\omega_{\underline{k}''}} I(\underline{k}', \underline{k}) \tag{4}$$

$$\frac{\partial E^M_{\underline{k}}}{\partial t} = i\int dx J_{-\underline{k}} k_\parallel \phi_{\underline{k}} - \int dx \langle \hat{J}^2 \rangle_{\underline{k}} / S + \int dx \left\{ \sum_{\underline{k}'} \frac{n^2}{n''^2} \Delta'_{\underline{k}''} \frac{\delta(x'')}{\Delta\omega_{\underline{k}''}} I(\underline{k}, \underline{k}') - \frac{\Delta'_{\underline{k}}}{\Delta\omega_{\underline{k}}} \delta(x) \sum_{\substack{\underline{p},\underline{q} \\ \underline{p}+\underline{q}=\underline{k}}} I(\underline{p}, \underline{q}) \right\} \tag{5}$$

where $I(\underline{r},\underline{s}) = \left[\langle (\nabla_\theta \psi)^2 \rangle_{\underline{r}} \langle (\nabla_r \phi)^2 \rangle_{\underline{s}} + \langle (\nabla_\theta \phi)^2 \rangle_{\underline{r}} \langle (\nabla_r \psi)^2 \rangle_{\underline{s}}\right]$

and $\Delta\omega$ is the nonlinear decorrelation frequency. Equations (4) and (5) indicate that m=1 mode saturation occurs when

$$-\int dx \sum_n \langle \phi \nabla_\theta \psi \rangle_{1,n} \langle J \rangle' = \int dx \sum_{n,n'} |\Delta'_{2,n''}| \frac{\delta(x'')}{\Delta\omega_{2,n''}} \langle (\nabla_\theta \psi)^2 \rangle_{1,n'} \langle (\nabla_r \phi)^2 \rangle_{1,n} \tag{6}$$

i.e. when coupling (by interaction with neighboring m=1's) to stable m=2 modes ($\Delta'_{2,n''} = -|\Delta'_{2,n''}| < 0$) balances growth due to $\langle J \rangle'$ relaxation. The nonlinear decorrelation frequency $\Delta\omega$ is determined by the m=1 fluctuation level (since m=1 modes are the dominant fluctuations), and is $\Delta\omega \sim (\delta B/B_o)_{rms} / |\Delta'_2 a|^{1/2}$. Here n and n' are the mode numbers for test (n) and background (n') m=1's and $(\delta B/B_o)_{rms}$ is the root mean square m=1 fluctuation level in the RFP core. Energy coupled to m=2 is

then scattered to $m \geq 3$ by similar processes, and ultimately dissipated by resistive diffusion at small scales (large m,n). Analytical results indicate that a power law energy spectrum ($E_m \sim m^{-\alpha}, \alpha \sim 1$) characterizes the nonlinearly generated modes.

A physical interpretation of the saturation mechanism is that the multiple helicity interaction of neighboring m=1's with stable ($\Delta' < 0$), driven m=2's generates a nonlinear $\underline{J} \times \underline{B}$ force which stabilizes the m=1 mode by opposing the growth of m=1 vorticity. Note that this scenario is the opposite of that discussed in Reference [11] where the nonlinearly driven mode has positive Δ', and the resulting nonlinear destabilization triggers the onset of the major disruption in tokamaks.

In order to obtain a quantitative estimate of the saturated m=1 fluctuation level, it is necessary to calculate the left side of Eq. (6). Since m=1 tearing modes do not exhibit a Rutherford phase and because the islands overlap for very modest fluctuation levels ($\delta B/B \sim 10^{-3}$ for $\varepsilon \leq 1/4$), a straightforward recourse is to calculate the driving term using linear eigenfunctions. One finds that $(\delta B/B_o)_{rms} \approx (\gamma_{m=1}\tau_A)/|\Delta'_2 a|^{1/2}$, where $\gamma_{m=1}\tau_A \sim S^{-1/3}$ is the m=1 mode linear growth rate. However, a (more appropriate) nonlinear calculation of $\langle \phi(\nabla_\theta \psi) \rangle_{1,n}$ [12] and the inclusion of the effects of quasilinear flattening of $\langle J \rangle'$ may yield modifications to this result.

Numerical solution of the nonlinear, full incompressible MHD equations can be used to test and clarify aspects of the theory. The reliability of this type of calculation is extensively discussed in Reference [13]. Previous numerical calculations [14] indicated that multiple helicity coupling effects play a significant role in the nonlinear evolution and saturation of m=1 tearing modes in RFP. As an additional test here, in Figure 2, the temporal evolution of the m=1, n=12 mode kinetic energy including coupling to m=2, n=23 (through interaction with m=1, n=11) is compared to the m=1, n=12 kinetic energy evolution when the m=2, n=23 is omitted. It is apparent that multiple helicity coupling to m=2 plays a significant role in the nonlinear saturation of m=1 tearing modes in the RFP. Indeed, since the number of large m,n modes (the ultimate energy sink) retained in the numerical calculation is severely limited, the effects of multiple helicity interaction are probably considerably more significant than indicated by Figure 2. It is useful to note that the apparent discrepancy between these results and those reported by other investigators [15,16] is probably due to the unphysical aspect ratio ($\varepsilon \sim 1$) used in their cylindrical geometry calculations. Noting that $(\delta B_r/B_o) \cong \varepsilon/n^2 r q' \sim \varepsilon^2$ is required for island overlap, it is clear that taking $\varepsilon \sim 1$ implies that an unphysically large fluctuation level is necessary (for overlap). This misrepresents the actual

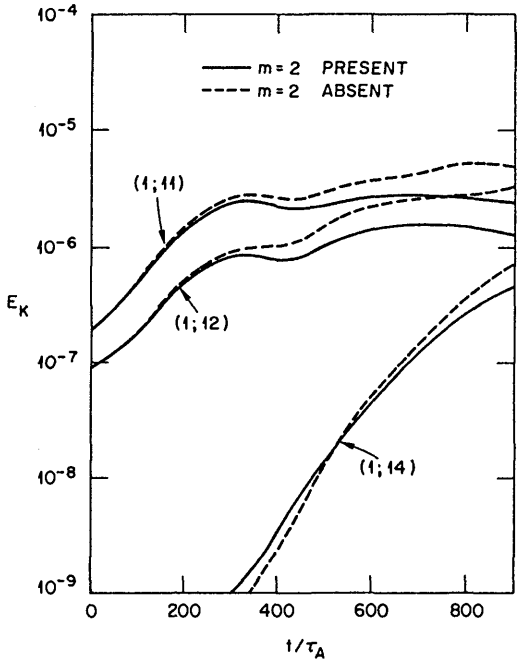

FIG.2. Comparison of kinetic energy evolution with and without m = 2 coupling.

dynamics by diminishing the effects of multiple helicity interaction. An extensive discussion of the numerical calculations, including comparisons with studies of the tokamak disruption, is contained in Reference [13].

The results of the numerical calculations can also be used to reconcile the theoretical prediction of the nonlinear generation of fluctuations with $m \geq 2$ [8], with the experimental observation that nearly all the fluctuation power spectrum has m=0 or m=1 (including harmonics generated by toroidal distortion) [1]. In Figure 3, $\tilde{B}_\theta(r)/B_o$ (obtained from the numerical solution) for m=1, n=11,12, and m=2, n=23 are plotted as a function of radius. Note that the m=2 $\tilde{B}_\theta$ fluctuation is much more localized than the m=1 fluctuation, and that, near the wall, $(\tilde{B}_\theta)_{m=2}/(\tilde{B}_\theta)_{m=1} < 10^{-2}$. Thus, it is not surprising that magnetic coil arrays located outside the liner, or (in the case of internal probes) at the edge of the plasma, detect comparatively little $m \geq 2$ signal.

3.2. Quasilinear dynamics of magnetic fields

Experimental evidence has linked dynamo events (increases in $|\langle B_z \rangle|$ near r_{wall}) to m=1 MHD activity [4]. Due to their

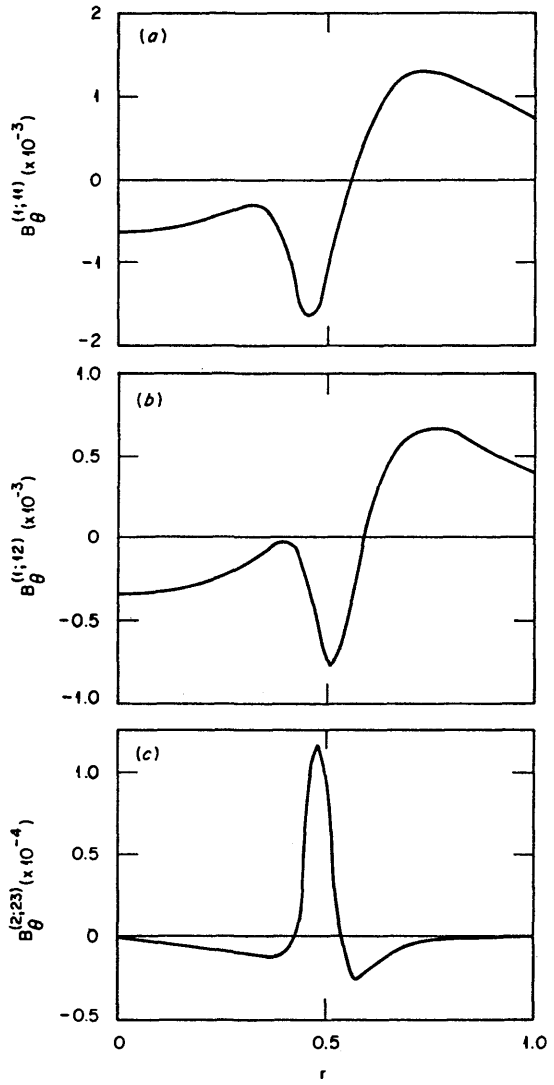

FIG.3. Comparison of radial structure of m = 1 and nonlinearly driven m = 2 modes.

large radial extent and comparatively high fluctuation levels, it is not surprising that m=1 tearing modes can induce significant magnetic field profile modification. Their effects on the evolution of the average toroidal field $\langle B_z(r)\rangle$ at and beyond the reversal surface, and on the safety factor q (on axis) are of particular interest.

An understanding of profile modification effects requires a quantitative estimate of $\langle \hat{\underline{V}} \times \hat{\underline{B}} \rangle$, the average electric field

induced by turbulence (m=1 modes) [8,16]. Since the phenomena of interest occur at radii away from the m=1 resonance surfaces in the core, a (renormalized) quasilinear calculation of $\langle \hat{\underline{V}} \times \hat{\underline{B}} \rangle$, using the exterior region, ideal MHD equation $\hat{\underline{B}} = \nabla \times \hat{\underline{\xi}} \times \langle \underline{B} \rangle$ to relate $\hat{\underline{B}}$ to displacement $\hat{\underline{\xi}}$, is valid. When $\hat{\underline{\xi}}$ has the form of a kink displacement, the average poloidal electric field $\langle E_\theta \rangle$ induced by (m=1) turbulence and resistive diffusion near the reversal surface r_o is given by:

$$\langle E_\theta(r) \rangle = -\{ \sum_n \left[(1-nq(r)) \frac{|\hat{\xi}_{1,n}(r)|^2}{r} \Delta\omega_{1,n} \right] \langle B_\theta(r) \rangle - \frac{1}{S} \langle J_\theta(r) \rangle \} \tag{7a}$$

and near r_{wall} is given by

$$\langle E_\theta(r) \rangle = -\{ \left(\sum_n \left[\frac{\partial}{\partial r} |\hat{\xi}_{1,n}(r)|^2 \right] \Delta\omega_{1,n} \right) \langle B_z(r) \rangle - \frac{1}{S} \langle J_\theta(r) \rangle \} \tag{7b}$$

where $\hat{\xi}(r)$ is the radial displacement and $\hat{\underline{v}} = \Delta\omega \hat{\underline{\xi}}$. It is important to recall that $\Delta\omega$ refers to the decorrelation rate for the saturated, stationary turbulence, and not the linear growth rates of the m=1 modes. Faraday's law ($\partial \langle \underline{B}(r) \rangle / \partial t = -\nabla \times \langle \underline{E}(r) \rangle$) shows that the condition for the local balance of turbulent generation of $\langle B_z(r) \rangle$ with decay by resistive diffusion is simply $\langle E_\theta(r) \rangle = 0$.

Equations (7a,b) indicate that when (i) $\partial \langle B_z(r) \rangle / \partial r < 0$ and $q(r) < 1/n$ ($dq/dr < 0$ in RFP) at the reversal surface, and (ii) $\partial |\hat{\xi}_{1,n}(r)|^2 / \partial r < 0$ and $\langle B_z(r) \rangle$ is reversed at the wall, then $\langle E_\theta(r) \rangle \to 0$ for $(\hat{\xi})_{rms} \sim (S\Delta\omega)^{-1/2}$. Thus, m=1 tearing mode fluctuation levels of $(\hat{\xi})_{rms} \sim (\delta B/B_o)_{rms} \sim S^{-1/3}$ and $\Delta\omega \sim S^{-1/3}$ (which are consistent with the results of Section 3.1) can induce modifications in $\langle B_z(r) \rangle$ which offset resistive diffusion, thus maintaining the magnetic configuration.

Some physical insight into the dynamo mechanism may be obtained by examination of the $\hat{z}$ component of the curl of Eq. (7a), which implies that $\partial \langle B_z \rangle / \partial t - (1/S) \nabla_r^2 \langle B_z \rangle \sim \alpha \langle J_z \rangle$, where $\alpha = \sum (1-nq(r)) |\hat{\xi}_{1,n}(r)|^2 \Delta\omega_{1,n} / r$. Thus, it is apparent that helical m=1 modes "twist" toroidal current into the poloidal direction, thus generating $\langle B_z(r) \rangle$ acording to an α-effect[17] relation. The directional asymmetry necessary for this α-effect is a consequence of the radial dependence of $k_\parallel$ ($dq/dr < 0$) imposed by the magnetic configuration structure. Also, in the RFP, global m=1 modes convert poloidal field magnetic energy density (tapped at the mode resonance surfaces

in the core) into toroidal field energy density. Thus, the RFP dynamo is merely a process of redistribution of magnetic energy and current density, and must be maintained by an external driving agent, such as the toroidal electric field.

A very important feature of the quasilinear dynamics of m=1 tearing modes in RFP is that they cause a decrease in the value of q(0). Near the origin, the evolution of q is given by[16]

$$\frac{\partial q}{\partial t} \approx \frac{dq}{dr} \sum_n \frac{\Delta\omega_{1,n}}{r} |\hat{\xi}_{1,n}(r)|^2 \qquad (8)$$

Thus, the m=1 modes tend to stabilize themselves by lowering q(0), thereby pushing their resonant surfaces into the origin. This process is another possible m=1 mode saturation mechanism. Hence, while resistive diffusion away from a Taylor state destabilizes the m=1 modes, the finite amplitude fluctuations act to oppose this trend and stabilize themselves by lowering q(0) and, in the process, drive $\langle B_z \rangle$ toward reversal. Since the competing effects balance for $(\tilde{\xi})_{rms} \sim (S\Delta\omega)^{-1/2} \sim S^{-1/3}$ for $\Delta\omega \sim S^{-1/3}$, it is not surprising that full nonlinear and quasilinear numerical calculations reveal qualitatively similar temporal evolution of F and θ, while exhibiting grossly different fluctuation dynamics. Finally, it should be emphasized that quasilinear theory alone does not sufficiently characterize the saturated state.

4. NONLINEAR INTERACTION OF RESISTIVE INTERCHANGE MODES

The RFP is characterized by strong shear, average unfavorable curvature, and high β_p, where typically $\beta_p \sim 10\%$. Hence, it is not surprising that the resistive interchange mode has been proposed as a candidate for the explanation of the observed magnetic fluctuations and confinement deterioration in RFP. Previous[18] and contemporary[19] investigations have been primarily computational[18], or are based on simple dimensional analysis [19]. Here, the results of an analytical investigation[20] of resistive pressure-driven turbulence are summarized and compared to the results of particle simulation. The basic approach is similar to that used in the study of resistive ballooning mode turbulence [21].

The nonlinear dynamics of resistive interchange modes are most easily investigated using a simple electrostatic pressure convection model based on reduced MHD. Using Ohm's law to eliminate the current $J_\parallel$, it follows that the basic equations are:

$$\frac{\partial p}{\partial t} + \nabla\phi \times \underline{z} \cdot \nabla p = -\nabla_\theta \phi \partial \langle p \rangle / \partial r \qquad (9)$$

$$\frac{\partial}{\partial t}\nabla_\perp^2\phi + \nabla\phi\times\underline{z}\cdot\nabla\nabla_\perp^2\phi = -S\nabla_\parallel^{(0)2}\phi - \kappa\nabla_\theta p \tag{10}$$

where p is the pressure, $\nabla_\parallel^{(0)} = \langle\underline{b}\rangle\cdot\nabla$, and κ is the curvature parameter ($\kappa>0$). The linear growth rate γ and radial mode width λ are $\gamma=S^{-1/3}(\kappa\langle p\rangle' k_\parallel')^{2/3}$ and $\lambda = S^{-1/3}(\kappa\langle p\rangle')^{1/6}(k_\parallel')^{-1/3}$, where $k_\parallel=k_\parallel' x$.

It is commonly believed that resistive interchange modes saturate when the turbulence level is sufficient to diffuse a parcel of pressure a distance λ in one growth time γ^{-1}, i.e. when $D=\gamma\lambda^2$, where D is the diffusion coefficient for turbulent convection. To examine this mixing length theory, renormalized fluid equations for $p_{\underline{k}}$ and $\nabla_\perp^2\phi_{\underline{k}}$,

$$\frac{\partial p_{\underline{k}}}{\partial t} - \frac{\partial}{\partial x} D \frac{\partial}{\partial x} p_{\underline{k}} = -ik_\theta\langle p\rangle' \phi_{\underline{k}} \tag{11}$$

$$\frac{\partial}{\partial t}\left(\nabla_\perp^2\phi\right)_{\underline{k}} - \frac{\partial}{\partial x} D \frac{\partial}{\partial x}\left(\nabla_\perp^2\phi_{\underline{k}}\right) + k_\theta^2 C_{\underline{k}}\phi_{\underline{k}} = Sk_\parallel'^2x^2\phi_{\underline{k}} - i\kappa k_\theta p_{\underline{k}} \tag{12}$$

have been derived. Here $D = \sum_{\underline{k}'} k_\theta'^2\langle\phi^2\rangle_{\underline{k}'}/\Delta\omega_{\underline{k}}''$ is the fluid turbulence diffusion coefficient, and $C_{\underline{k}} = \sum_{\underline{k}'} \langle(\nabla_\perp^2\hat{\phi})^2\rangle_{\underline{k}'}/\Delta\omega_{\underline{k}}''$, a term which is a consequence of symmetrization, ensures that the energy-conserving property $\int d^3x\phi(\nabla\phi\times\underline{z}\cdot\nabla\nabla_\perp^2\phi)=0$ is preserved in the renormalized theory. Thus, the kinetic energy evolves according to:

$$\frac{\partial E^k}{\partial t} = -\int dx \sum_{\underline{k}} \{k_\parallel'^2x^2S|\phi_{\underline{k}}|^2 - i\kappa k_\theta\phi_{-\underline{k}}p_{\underline{k}}\} \tag{13}$$

where $\partial E^k/\partial t=0$ at saturation. Note that the resistive field line bending term $\sim k_\parallel'^2x^2S$ damps the growth of E^k, and opposes the drive due to $\langle p\rangle'$ relaxation. The saturated state may be characterized by the diffusion coefficient D and a nonlinear mixing length $\Delta_{\underline{k}}$. The asymptotic balance of the anomalous viscosity (voriticity diffusion) and (resistive) field line bending terms of Eq. (12) implies that $\Delta_k=(k_\parallel'^2S/D)^{-1/6}$. Taking $p_{\underline{k}}\simeq -ik_\theta\langle p\rangle'\phi_{\underline{k}}/(D/\Delta_{\underline{k}}^2)$, $k_\parallel'^2x^2S\simeq k_\parallel'^2\,\overline{\Delta^2}_{\underline{k}}S$ and requiring $\partial E^k/\partial t=0$ yields $D=\kappa\langle p\rangle' L_s^2/S$ and thus, by substitution,

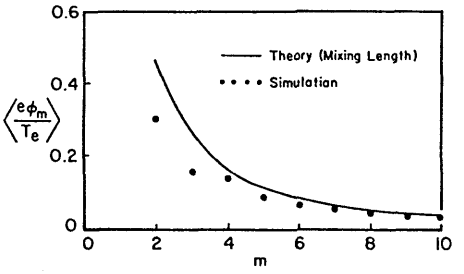

FIG.4. Comparison of fluctuation level from simulation with mixing length theory for resistive interchange mode saturation level.

$\Delta_{\underline{k}}=S^{-1/3}(\kappa\langle p\rangle')^{1/6}(k_{\parallel}')^{-1/3}$. Note that $\Delta_{\underline{k}}=\lambda$ and $D=\gamma\lambda^2$. Thus, the simple mixing length theory is vindicated. Noting that $\Delta\omega_{\underline{k}}\sim D/\Delta_{\underline{k}}^2$, it follows that the electrostatic fluctuation level is $(e\phi/T_e)_{rms}\sim(D/\rho_s c_s k_\theta \Delta_{\underline{k}})_{rms}$ and, using Ohm's law, $(\delta B_r/B_o)_{rms}\sim\beta_p^{4/3}S^{-2/3}$.

A three-dimensional electrostatic particle simulation[22] has been used to investigate the nonlinear, multiple helicity interaction of resistive interchange modes in a sheared slab, where curvature is modeled by a gravity force. In Figure 4, the n-averaged value of $e\phi_m/T_e$ obtained from the simulation results is plotted versus m. Agreement with the prediction of mixing length theory is good. Extensions to the regime of large diamagnetic frequency ($\omega_{*e}>\gamma$) are in progress.

5. ANOMALOUS THERMAL TRANSPORT AND SCALING LAWS

Experimental evidence has linked heat transport along stochastic magnetic field line generated by the overlap of m=1 tearing modes with confinement in the HBTXIA pinch [1]. Using the saturated state magnetic fluctuation level obtained in Section 3, a quasilinear estimate of the (collisionless) thermal conductivity χ_E in the core region is $\chi_E\sim(0.01)v_{Te}aS^{-2/3}$, where v_{Te} is the electron thermal velocity. Balancing heat loss with ohmic heating yields (for plasma density proportional to current I_p) $T_e\sim I_p^{0.7}$. For $S\sim10^5$, $\beta_p\sim10\%$ is predicted. The temperature scaling and β_p value are in reasonable agreement with experiment.

In comparison, following the procedure of Reference [21], the (collisionless) electron thermal conductivity which results from magnetic fluctuations driven by resistive

interchange modes is $\chi_E \sim (\varepsilon/q)^3 \beta_p^{3/2} v_{Te} a/S$. Balancing heat loss with ohmic heating yields (for density proportional to I_p) $T_e \sim I_p$ and $\beta_p \sim (q/\varepsilon)(m_e/m_i)^{1/6} \sim 10\%$. Thus, the thermal loss prediction for resistive interchange modes is qualitatively similar to that for m=1 tearing modes, but smaller in magnitude. Also, electromagnetic resistive interchange modes[18] and, especially near the plasma edge, rippling modes[23,24] may cause significant losses.

ACKNOWLEDGEMENTS

The authors are grateful to Drs I. Hutchinson, C. Gimblett, A. Aydemir, E. Caramana, R. Gerwin, A. Hasegawa, C.S. Liu, R. Nebel and D. Schnack for many useful conversations. This research was supported by the United States Department of Energy, Office of Fusion Energy, under contracts DE-FG05-80ET-53088 with The Institute for Fusion Studies, DEAC05-840R2 1400 with Martin Marietta Energy Systems, Inc., and DE-AC02-76ER03077 with New York University.

REFERENCES

[1] HUTCHINSON, I.H., et al., Nucl. Fusion **24** (1984) 59.
[2] WURDEN, G.A., Phys. Fluids **27** (1984) 554.
[3] LaHAYE, R.A., et al., Nucl. Fusion **21** (1982) 1235.
[4] WATT, R.G., NEBEL, R.A., Phys. Fluids **26** (1983) 1168.
[5] STRAUSS, H.R., Dynamical equations for the reversed field pinch, submitted to Phys. Fluids, 1983.
[6] CARAMANA, E.J., et al., Phys. Fluids **26** (1983) 1305.
[7] TAYLOR, J.B., Phys. Rev. Lett. **33** (1974) 134.
[8] DIAMOND, P.H., et al., Inst. for Fusion Studies, Austin, Texas, Rep. No. 136 (1984).
[9] STRAUSS, H.R., Phys. Fluids **19** (1976) 134.
[10] DIAMOND, P.H., et al., Phys. Fluids **27** (1984) 1449.
[11] CARRERAS, B.A., et al., Phys. Rev. Lett. **46** (1981) 1131.
[12] DIAMOND, P.H., AN, Z.G., in Proc. Annual Controlled Fusion Theory Conf. (Sherwood), Incline Village, Nevada, 1984, Paper No. 2P13.
[13] HICKS, H.R., et al., Oak Ridge Natl Lab. Rep. ORNL TM-9127 (1984).
[14] HOLMES, J.A., et al., Inst. for Fusion Studies, Austin, Texas, Rep. No. 124 (1984), to appear in Phys. Fluids.
[15] AYDEMIR, A., BARNES, D., in Proc. Annual Controlled Fusion Theory Conf. (Sherwood), Incline Village, Nevada, 1984, Paper No. 1D2.
[16] STRAUSS, H.R., The dynamo effect in fusion plasmas, Submitted to Phys. Fluids.
[17] MOFFATT, H.K., Magnetic Field Generation in Electrically Conducting Fluids, Cambridge Univ. Press (1978).

[18] HENDER, T.C., ROBINSON, D.C., "Non-linear modes in the RFP and possible relationships to energy confinement", Plasma Physics and Controlled Nuclear Fusion Research 1982 (Proc. 9th Int. Conf. Baltimore, 1982), Vol.3, IAEA, Vienna (1983) 417.
[19] CONNOR, J.W., TAYLOR, J.B., Paper No. IAEA-CN-44/E-I-2, these Proceedings, Vol.2.
[20] AN, Z.G., DIAMOND, P.H., in Proc. 6th US Symp. on Compact Toroid Research, Princeton Plasma Physics Lab., 1984, to be published.
[21] CARRERAS, B.A., et al., Phys. Rev. Lett. **50** (1983) 503.
[22] SYDORA, R.D., et al., Inst. for Fusion Studies, Austin, Texas, Rep. No. 125 (1984), to appear in Phys. Fluids.
[23] CALLEN, J.D., et al., "Edge turbulence in tokamaks", Plasma Physics and Controlled Nuclear Fusion Research 1982 (Proc. 9th Int. Conf. Baltimore, 1982), Vol.1, IAEA, Vienna (1983) 297.
[24] GARCIA, L., et al., Inst. for Fusion Studies, Austin, Texas, Rep. No. 146 (1984).

RESISTIVE SPECTRUM OF CONFIGURATIONS WITHOUT MAGNETIC SHEAR

D. LORTZ, G. SPIES
Max-Planck-Institut für Plasmaphysik,
Euratom-Association, Garching,
Federal Republic of Germany

Abstract

RESISTIVE SPECTRUM OF CONFIGURATIONS WITHOUT MAGNETIC SHEAR.

A previously given phase-integral description of the normal modes of a slightly resistive incompressible plasma slab with a unidirectional magnetic field and a monotonic pressure profile was restricted to slow magnetosonic modes with $\eta k^2 \ll 1$ and $\eta n^2 = 0(1)$, where k and n are nodal numbers in the ignorable and the non-ignorable directions. This description is now completed by including the Alfvén modes and arbitrary mode numbers. It is found that: (i) the Alfvén spectrum and the slow mode spectrum are identical in the limit $\eta \to 0$; (ii) the eigenvalue locus of the 'ballooning modes' ($\eta k^2 = 0(1)$) is detached from the ideal continuum; (iii) the distance between the Alfvén mode and the slow mode 'boundary layer eigenvalues' ($\eta k^2 \ll 1$ and $\eta n^2 \ll 1$) is $0/(\eta^{1/3}/|\log\eta|)$.

1. INTRODUCTION

Knowledge of the eigenvalues of the motion of a resistive plasma about a static equilibrium is useful in various branches of magnetic fusion theory, such as stability, wave propagation and heating. Numerical investigations [1-5] have indicated that the continuous ideal spectrum for finite resistivity is broken up into discrete eigenvalues whose locus in the complex plane is independent of resistivity. Analytical studies [6-9] have confirmed this behaviour and related it to Stokes' phenomenon in the asymptotic theory of analytic functions [10].

In the present paper we extend the theory to the case of "ballooning modes" ($k^2 = 0(1)$) and of "boundary layer modes" ($\eta k^2 << 1$ and $\eta n^2 << 1$). We present a complete asymptotic description of the entire resistive spectrum, thus filling the gaps in a previous investigation [6].

2. BASIC EQUATIONS

The equations of resistive incompressible magnetohydrodynamics, when linearized about a static equilibrium subject to $\nabla P + \vec{B} \times \text{curl } \vec{B} = 0$ and $\text{div } \vec{B} = 0$, are

$$\rho\, \partial\vec{u}/\partial t + \nabla p + \vec{B} \times \text{curl } \vec{b} + \vec{b} \times \text{curl } \vec{B} = 0$$
$$\partial\vec{b}/\partial t + \eta\, \text{curl curl } \vec{b} - \text{curl } (\vec{u} \times \vec{B}) = 0$$
$$\text{div } \vec{u} = 0\ ,\ \text{div } \vec{b} = 0 \qquad (1)$$

Here, p and $\vec{b}$ are the perturbations of the equilibrium pressure P and magnetic field $\vec{B}$; $\vec{u}$ is the flow velocity; and ρ and η (both assumed to be constants) are the mass density and resistivity. We impose the boundary conditions pertaining to a perfectly conducting rigid wall.

It was shown in [11] that for slab geometry ($\partial/\partial y = \partial/\partial z = 0, B_x = 0$) the system (1) reduces to

$$\sigma \rho\, \Delta u - F\, \Delta b + F'' b = 0$$
$$\sigma b - \eta\, \Delta b + F u = 0$$
$$\sigma^2 \rho\, a - \sigma \eta \rho\, \Delta a + F^2 a + G'(Fb - u) = 0 \qquad (2)$$

where the Fourier decomposition $\exp(\sigma t + i k_y y + i k_z z)$ and the abbreviations $F = k_y B_y + k_z B_z$, $G = k_y B_y - k_z B_z$, $k^2 = k_y^2 + k_z^2$, $\Delta = d^2/dx^2 - k^2$, $u = -i u_x$, $b = b_x$, $a = i(k_z b_y - k_y b_z)$ have been used and primes denote derivatives with respect to x. The boundary conditions are $u = 0$, $b = 0$, $a' = 0$ at $x = 0$ and $x = L$.

In what follows we assume that the magnetic field $\vec{B}$ is unidirectional. Then we may assume $F \neq 0$, which enables us to eliminate the unknown u. Introducing dimensionless variables by writing $x = L\bar{x}$, $k^2 = \bar{k}^2/L^2$, $F = F_o \bar{F}$, $\sigma = F_o \rho^{-1/2}\, \bar{\sigma}$, and $\eta = L^2 F_o \rho^{-1/2}\, \bar{\eta}$ (F_o is a characteristic value of F), and then omitting the bars, we have the fourth-order slow mode equation

$$\left(\eta\, \Delta \frac{1}{F}\, \Delta F + \frac{d}{dx} D \frac{d}{dx} - k^2 D\right) \frac{1}{F}\, b = 0 \qquad (3)$$

with boundary conditions $b = 0$, $b'' = 0$ at $x = 0$ and $x = 1$ and the second-order Alfvén mode equation

$$(\eta\, \Delta + D)\, a = 0 \qquad (4)$$

with boundary conditions $a' = 0$ at $x = 0$ and $x = 1$.
Here $D = -\sigma - F^2/\sigma$.

Equation (3) can be simplified by observing that every solution b(x) varies fast compared to F(x) wherever the first term is

not negligible. Therefore, multiplication by F may be interchanged with differentiation, and Eq. (3) reduces to

$$(\eta \Delta^2 + \frac{d}{dx} D \frac{d}{dx} - k^2 D) \frac{1}{F} b = 0 \qquad (5)$$

3. PROPERTIES OF THE SPECTRUM

Since Eqs (4) and (5) have no singular points for $\eta > 0$, the resistive spectrum is purely discrete. In contrast, the ideal spectrum ($\eta = 0$) is purely continuous (it consists of the ranges of the functions $\sigma = \pm i F(x)$). Obviously, the spectrum is symmetric to the real axis.

To obtain estimates, we multiply Eq. (4) by the complex conjugate of a and integrate with respect to x to obtain

$$\sigma^2 <|a|^2> + \sigma\eta <|\nabla a|^2> + <F^2|a|^2> = 0 \qquad (6)$$

where <...> is the x-average. Analogously, Eq. (5) yields

$$\sigma^2 <|\nabla \frac{b}{F}|^2> + \sigma\eta <|\Delta \frac{b}{F}|^2> + <F^2|\nabla \frac{b}{F}|^2> = 0 \qquad (7)$$

Either of the relations (6) and (7) implies that the spectrum is restricted to the negative real axis and to the intersection of the annulus $F_{min}^2 \leqq |\sigma|^2 \leqq F_{max}^2$ with the half-plane $\mathrm{Re}\,\sigma \leqq -\eta k^2/2$.

We note that this domain shrinks to a line (viz. the negative real axis plus a circular arc) in the homogeneous case $F \equiv 1$. In this case either family of modes is governed by the dispersion relation $\sigma^2 + \sigma\eta (k^2 + n^2 \pi^2) + 1 = 0$ (where n is an arbitrary integer), which shows that the entire line is densely filled with eigenvalues in the limit $\eta \to 0$.

4. STANDARD MODES

The theory [6] of these modes (defined by $\eta k^2 << 1$ and $\mathrm{Re}\,\sigma = 0(1)$ if $\mathrm{Im}\,\sigma \neq 0$ so that D is bounded away from zero) will not be described in detail here (see for instance [11]).

If the pressure profile P(x) is monotonic, F(x) is monotonic too. For definiteness, let $F > 0$, $F' > 0$, and $\mathrm{Im}\,\sigma \geqq 0$. Then the phase integral [12]

$$\alpha(x,\sigma) = \int_{x_o(\sigma)}^{x} d\,x\, D^{1/2} \qquad (8)$$

is introduced, where x is considered as complex, x_o solves the equation $D(x_o,\sigma) = 0$, and the complex α-plane is cut along the ray $\arg \alpha = \pi/2$. For the case considered here the eigenvalues

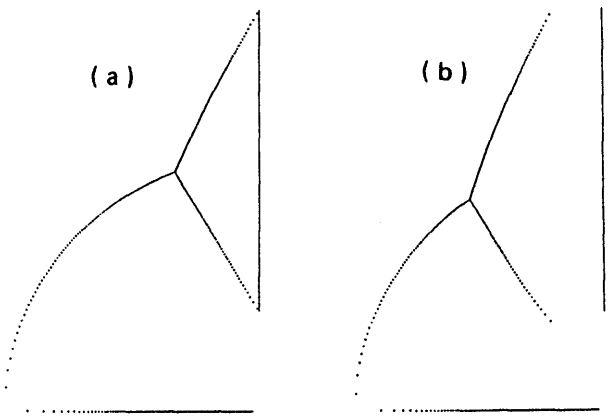

FIG.1. Resistive eigenvalues (points) and ideal continuum (solid line) in the upper left quadrant of the complex σ plane: (a) standard modes; (b) ballooning modes.

for the slow modes and for the Alfvén modes coincide asymptotically and are described by the relations:

$$(1)\quad \alpha_1(\sigma) - \alpha_o(\sigma) = \eta^{1/2}\, n\pi\ ,\ \mathrm{Im}\ \alpha_\nu \leqq 0$$

$$(2)\quad \alpha_o(\sigma) = -\eta^{1/2}\,(n+\tfrac{1}{4})\pi,\ \mathrm{Im}\ \alpha_1 \geqq 0$$

$$(3)\quad \alpha_1(\sigma) = \eta^{1/2}\,(n+\tfrac{1}{4})\pi,\ \mathrm{Im}\ \alpha_o \geqq 0 \qquad (9)$$

where $\alpha_\nu(\sigma) = \alpha(\nu,\sigma)$, $\nu = 0,1$ and n is a positive integer, limited by the side condition on Im α_ν.

Branch (1) corresponds to the spectrum of the homogeneous case (circular arc plus negative real axis). At the "triple point" where both α_o and α_1 are real it splits into branches (2) and (3) which reach the two tips of the ideal continuum as $\eta n^2 \to 0$. Fig. 1(a) shows the standard eigenvalues in the upper left quadrant of the complex plane for the profile $F = 1 + 3x$ and for $\eta = 10^{-5}$.

5. BALLOONING MODES

Again considering monotonic profiles, we now assume that k^2 is so large that $\eta k^2 = O(1)$. Then Re $\sigma = O(1)$, and D(x) is nowhere small. Hence all solutions b(x) of the slow mode equation (5) vary fast everywhere, and multiplication by F or D may be interchanged with differentiation to yield

$$\eta\Delta\, y + D\, y = 0 \qquad (10)$$

where $y = \Delta b$, thus being subject to the boundary conditions $y = 0$ at $x = 0$ and $x = 1$. The Alfvén modes are governed by the same equation with the boundary conditions $y' = 0$.

The method of Section 4 can be used to solve Eq. (10) asymptotically with the only difference that D is replaced by $D - \eta k^2$. It turns out that the dispersion relation is the same for both sets of boundary conditions. Thus the spectrum is given by the three branches of Eq. (9), with

$$\alpha_\nu(\sigma) = \int_{x_o(\sigma)}^{\nu} d x \, (D - \eta k^2)^{1/2} \qquad (11)$$

where x_o now solves the equation $D(x_o,\sigma) = \eta k^2$.

The endpoints of branches (2) and (3), given by $\alpha_0 = 0$ and $\alpha_1 = 0$, are easily seen to satisfy the relations $\sigma^2 + \sigma \eta k^2 + F(m)^2 = 0$ $(m = 0,1)$, thus being the intersections of the circles $|\sigma|^2 = F(m)^2$ with the vertical line $\mathrm{Re}\,\sigma = -\eta k^2/2$. The endpoint of branch (2), together with the triple point, reaches the real axis for $\eta k^2 = 2 F_{min}^2$, while the endpoint of branch (3) becomes real for $\eta k^2 = 2 F_{max}^2$. Hence all eigenvalues are real if $\eta k^2 \geq 2 F_{max}^2$. Fig. 1(b) shows the ballooning eigenvalues for $F = 1 + 3x$, $\eta = 10^{-5}$, and $\eta k^2 = 1$.

6. BOUNDARY LAYER MODES

The dispersion relations (9) are not valid near the ideal continuum (i.e. for $\eta n^2 \to 0$ and $\eta k^2 \to 0$). Considering a boundary layer at $x = 0$ it is found (for details see [11]) that the boundary layer eigenvalues of branch (2) are still on the curve $\alpha_o(\sigma) < 0$, that this curve forms an angle $\pi/6$ with the imaginary axis, and that the spacing of the eigenvalues is $O(\eta^{1/3})$.

The analysis is correct to leading order for both families of boundary layer modes. The relative error, however, while being $O(\eta^\alpha)$, $\alpha > 0$ for the Alfvén modes, is $O(1/|\log \eta|)$ for the slow modes. To compute the logarithmic correction we expand about $x = 0$:

$$\sigma \simeq i F_o + \eta^{1/3} 2^{-1/3} F_o'^{2/3} \lambda, \quad F_o = F(0), \quad F_o' = F'(0)$$

and find that Eq. (5) yields the boundary layer equation

$$\frac{d}{d\xi} \left(\frac{d^2}{d\xi^2} + i \xi - \lambda\right) \frac{d}{d\xi} b = 0 \qquad (12)$$

where ξ is a stretched variable defined by

$$x = \varepsilon \xi, \quad \varepsilon = \left(\frac{\eta}{2F_o'}\right)^{1/3}$$

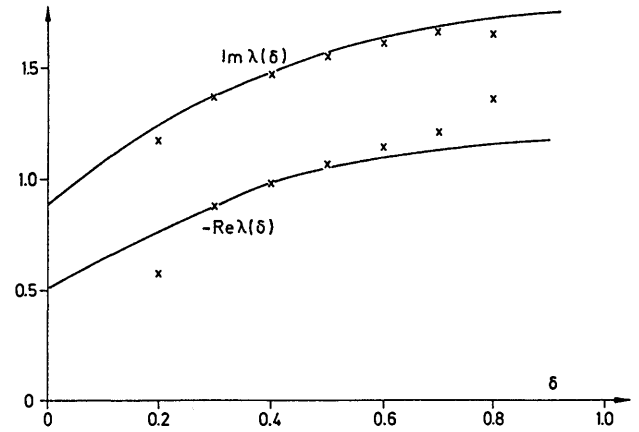

FIG.2. Real and imaginary parts of smallest boundary layer eigenvalue λ as a function of δ.

For large ξ the function b must behave as $b \approx \gamma + \log(\varepsilon\xi)$, where the constant γ is determined by the ideal solution, which vanishes at x = 1. The boundary conditions for Eq. (12) can then be written:

$$\xi = 0 : b = d^2b/d\xi^2 = 0$$

$$\xi \to \infty : b \to 1 - \delta \log \xi , \quad \delta = -1/(\gamma + \log \varepsilon) \qquad (13)$$

Evaluation [11] of the boundary value problem (12), (13) yields the dispersion relation

$$\delta(b_0 d^2b_1/dz^2 - b_1 d^2b_0/dz^2) - d^2b_1/dz^2 = 0, \quad z = -\lambda \qquad (14)$$

where [13]

$$b_0(z) = \log z - i\frac{\pi}{2} + \int_0^\infty dt(2t-t^4)e^{-\frac{1}{3}t^3}\left[-\frac{e^{zt}}{z} - t\,E_1(-zt)\right]$$

$$-E_1(-zt) = \int_{i\infty}^{z} d\,z\,e^{zt}/z, \quad b_1(z) = \int_{i\infty}^{z} dz\,A_+$$

and A_+ is the Airy function which has its "Stokes line" at $\arg z = -\pi/3$.

We have computed the smallest complex root λ(δ) of Eq.(14) for $0 \leq \delta \leq 1$. The result is plotted in Fig. 2 together with the result of a numerical integration of Eq. (3) with F(x) = 1+x and $k^2 \to 0$. The solid line represents the present asymptotic theory, while the points were obtained by applying a matrix eigenvalue solver to 200 Fourier coefficients. The two methods agree

for $0.3 < \delta < 0.5$ (corresponding roughly to $10^{-5} < \eta < 10^{-3}$). For smaller values the asymptotic theory is correct, while the numerical integration fails; for larger values the latter is correct, while the former fails because there is no boundary layer anymore (there are no eigenvalues on branches (2) and (3)).

REFERENCES

[1] RYU, C.M., GRIMM, R.C., in Proc. Annual Controlled Fusion Theory Conference (Sherwood), Incline Village, Nevada, 1984, Lawrence Livermore Natl Lab., Paper No. 3P21.

[2] KERNER, W., LERBINGER, K., in Proc. Int. Conf. Plasma Physics, Lausanne, 1984, Paper No. P 16-18.

[3] FREIDBERG, J.P., HEWETT, D.W., J. Plasma Phys. **26** (1981) 177.

[4] DAVIES, D., Phys. Lett. **100A** (1984) 144.

[5] RYU, C.M., GRIMM, R.C., Princeton Plasma Physics Lab. Rep. PPL-2020 (1983).

[6] LORTZ, D., SPIES, G.O., Phys. Lett. **101A** (1984) 335.

[7] DEWAR, R.L., DAVIES, B., Australian Natl Univ. Rep. TPP 84/01 (1984).

[8] PAO, Y., KERNER, W., to be published in Phys. Fluids.

[9] BORIS, J.P., Dissertation, Princeton Univ., 1968.

[10] HEADING, J., Introduction to Phase-Integral Methods, Methuen/Wiley, London/New York (1962).

[11] LORTZ, D., SPIES, G.O., Max-Planck-Inst. für Plasmaphysik, Garching, Rep. IPP 6/242 (1984).

[12] SIROVICH, L., Techniques of Asymptotic Analysis, Springer, Berlin (1971).

[13] ABRAMOWITZ, M., STEGUN, I., (Eds), Handbook of Mathematical Functions, Natl Bureau of Standards, Washington (1964).

Session C

OPEN CONFINEMENT SYSTEMS

Chairmen of Sessions

Session C-I	D.D. RYUTOV	(USSR)
Session C-II	S. MIYOSHI	(Japan)

THERMAL BARRIER CONFINEMENT EXPERIMENTS IN THE TMX-U TANDEM MIRROR*

T.C. SIMONEN, S.L. ALLEN, D.E. BALDWIN, T.A. CASPER, J.F. CLAUSER, F.H. COENSGEN, R.H. COHEN, D.L. CORRELL, W.F. CUMMINS, C.C. DAMM, J.H. FOOTE, T.K. FOWLER, R.K. GOODMAN, D.P. GRUBB, D.N. HILL, E.B. HOOPER, R.S. HORNADY, A.L. HUNT, R.G. KERR, G.W. LEPPELMEIER, J. MARILLEAU, J.M. MOLLER, A.W. MOLVIK, W.E. NEXSEN, J.E. OSHER, W.L. PICKLES, P. POULSEN, G.D. PORTER, E.H. SILVER, B.W. STALLARD, J. TASKA, W.C. TURNER
Lawrence Livermore National Laboratory,
University of California, Livermore, California

J.D. BARTER, T.W. CHRISTENSEN, G. DIMONTE, T.E. ROMESSER
TRW Corporation, Redondo Beach, California

R.F. ELLIS, R.A. JAMES, C.J. LASNIER
University of Maryland, Baltimore, Maryland

T.L. YU
Johns Hopkins University, Baltimore, Maryland

L.V. BERZINS, M.R. CARTER, C.A. CLOWER, B.H. FAILOR, S. FALABELLA, M. FLAMMER, T. NASH
University of California-Davis, Davis, California

W.L. HSU
Sandia National Laboratory, Livermore, California

United States of America

Abstract

THERMAL BARRIER CONFINEMENT EXPERIMENTS IN THE TMX-U TANDEM MIRROR.

In recent experiments on the TMX-U thermal barrier device, end plugging was achieved of axial ion losses up to a central cell density of $n_c = 6 \times 10^{12}$ cm^{-3}. During lower density experiments the axial potential profile characteristic of a thermal barrier was measured; an ion-confining potential greater than 1.5 kV and a potential depression of 0.45 kV in the barrier region were found. The average β of hot end plug electrons has reached 15% and of hot central cell ions, 6%. In addition, deuterium ions in the central cell were heated with ICRF to an average perpendicular energy of 2 keV. During strong end plugging at low density (7×10^{11} cm^{-3}), the axial ion confinement time $\tau_\parallel$ reached 50 to 100 ms while the non-ambipolar

* Work performed under the auspices of the US Department of Energy by the Lawrence Livermore National Laboratory under contract No. W-7405-ENG-48.

radial ion confinement time $\tau_\perp$ was 14 ms – independent of end plugging. Electrically floating end walls increased the radial ion confinement time by a factor of 1.8. At higher densities and lower potentials $\tau_\parallel$ was 6 to 12 ms and $\tau_\perp$ exceeded 100 ms.

1. INTRODUCTION

The Tandem Mirror Experiment-Upgrade (TMX-U) is the first thermal-barrier tandem mirror to operate. Our recent experimental results demonstrate the formation of microstable sloshing-ion distributions [1,2], end plugging with a density larger in the central cell than the end plug, and formation of thermal barrier axial potential profile [3]. Additional work has shown the following: a continuing increase of hot electron beta up to 15% when we increase electron-cyclotron resonant heating (ECRH) power [4], heating of the central cell ions with ion-cyclotron resonant frequency (ICRF)[5], and decreasing radial ion transport with end wall potential control [6].

The TMX-U magnetic-field configuration consists of a 8-m-long 0.3 T solenoidal central cell, terminated at each end by a 3-m-long 0.5 T quadrupole mirror cell that performs the dual role of providing a thermal barrier potential profile for axial confinement as well as a magnetohydrodynamic (MHD) anchor.

Six 20-kV neutral beams, which are injected in the end plugs at 47° to the magnetic field lines, form sloshing-ion distributions and pump trapped ions out of the thermal barriers. In each end plug, a 200-kW 28-GHz gyrotron heats electrons near the second harmonic resonance at the bottom of the magnetic well to create the thermal barrier; a second gyrotron at the fundamental resonance (ω_{ce}) locally heats electrons between the bottom of the well and the outside mirror to create the ion-confining potential peak. Central cell ions are heated by two 200-kW ICRF antennas and by seven neutral beam injectors. The plasma is fueled by injecting gas in the central cell.

2. MEASUREMENTS OF THERMAL BARRIER POTENTIAL

Using three electrostatic analyzers with grids [7] located at the ends of the TMX-U, we measured the thermal barrier potential profile shown in Fig. 1b. Sloshing beams and ECRH heating were applied in the standard manner to create an end-plugging plasma in the west end cell (Fig. 1a). To make this measurement we used only second harmonic ECRH in the east end cell; therefore, no potential peak or end plugging occurred in the east end cell. To measure the barrier potential ($\phi_e - \phi_b$) shown in Fig. 1b in the west end cell, we injected a diagnostic neutral beam at an 18° angle to the magnetic

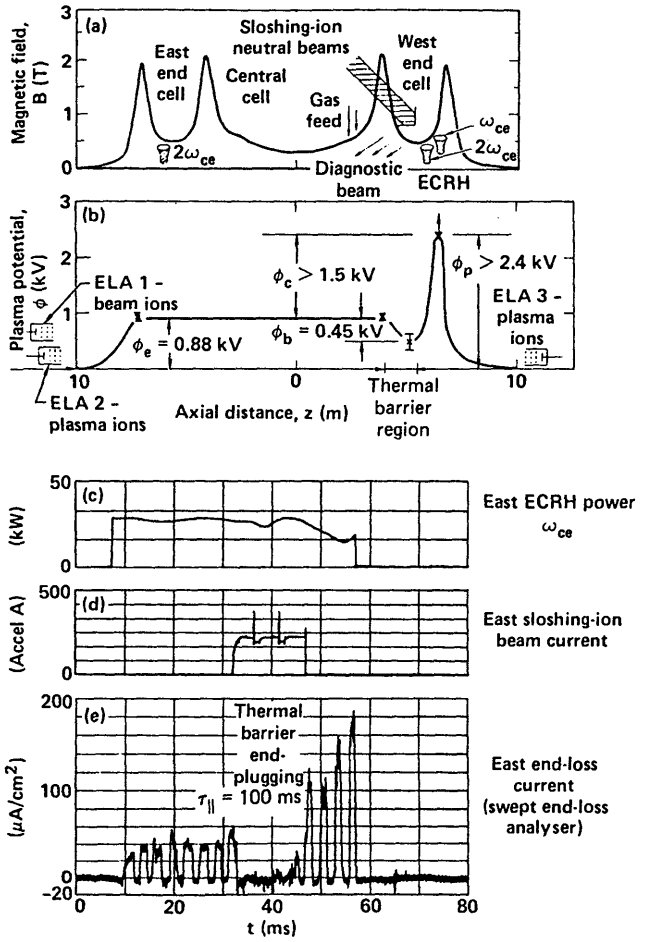

FIG.1. Thermal barrier measurements in TMX-U. (a) Axial profile of the magnetic field with illustration of the heating systems used for single-end plugging operation. (b) Axial measured potential profile. (c) Time history of ECRH power. (d) Time history of sloshing beam current. (e) Time history of resulting end-loss current measured with a swept end-loss analyser showing that both ECRH and sloshing beams are required to reduce end losses.

axis. The ionized diagnostic-beam atoms stream along magnetic field lines out the east end of the machine. Their energy shift, measured by the analyzer ELA1, gives a direct measure of the barrier potential. The analyzers labeled ELA2 and ELA3 were swept through a lower energy range--from ground to 2.4 keV. Ions detected by these analyzers have a minimum energy ϕ_e (ELA2) or ϕ_p (ELA3), as determined by the decrease in ion current when the ion-repeller grid voltage was swept through

these values of potential. The peak potential height ϕ_p was not resolved because ions lost out the west end had energies greater than the maximum grid bias of 2.4 kV. Therefore, the central cell ion-confining potential $\phi_c = \phi_p - \phi_e$ exceeded 1.5 kV.

Several additional facts supporting the existence of a thermal barrier are as follows:

1. Non-Maxwellian plug electrons with bulk "temperature" exceeding central cell temperature;
2. Potential peak was enhanced by ECRH;
3. Rapid rise of end loss when plug ECRH was turned off;
4. End plugging required both sloshing ions and ECRH;
5. Axial confinement was improved;
6. End plugging was observed with $n_c > n_p$;
7. Plugging required hot electrons;
8. No plugging occurred unless central cell ions were sufficiently hot.

A remarkable feature of these thermal barrier experiments is that both the energetic ions and electrons remain stable to ion- and electron-cyclotron modes. Although weak fluctuations are detected, we have not observed degradation in confinement resulting from either ion or electron modes. In our experiments, impurity concentrations (C,N,O) were also low, $\leq$1%.

3. PLASMA CONFINEMENT

The potential peaks in the end plugs reduce the axial loss of central cell ions when both ECRH (Fig. 1c) and sloshing ions (Fig. 1d) are present. Figure 1e shows end-loss currents out one end when both ends are plugged (the other end is similar). The pulsed nature of the end-loss current seen in Fig. 1e results from sweeping the analyzer ion-repeller voltage to measure the energy distribution. When the ion-repeller voltage exceeds the plasma potential plus a few times the central cell ion temperature, almost no ions reach the collector, and the remaining signal is a negative current of energetic electrons that pass through the -2.0 kV electron-repeller grid. Using a second analyzer to measure the electron current, we determined that the ion axial-confinement time was at least 100 ms.

We determine the nonambipolar radial ion-confinement time $\tau_\perp$ by measuring the net current collected on the end walls. Negative currents, implying that the axial current of electrons exceeds that of ions, are measured. To preserve charge balance, we assume that there is an equal radial current of ions. This radial current value is used to calculate $\tau_\perp$.

The experimental scaling of $\tau_\perp$ with the central cell density (n_c) and the potential of the central cell plasma relative to ground (ϕ_e) are shown in Fig. 2 over a wide range of conditions.

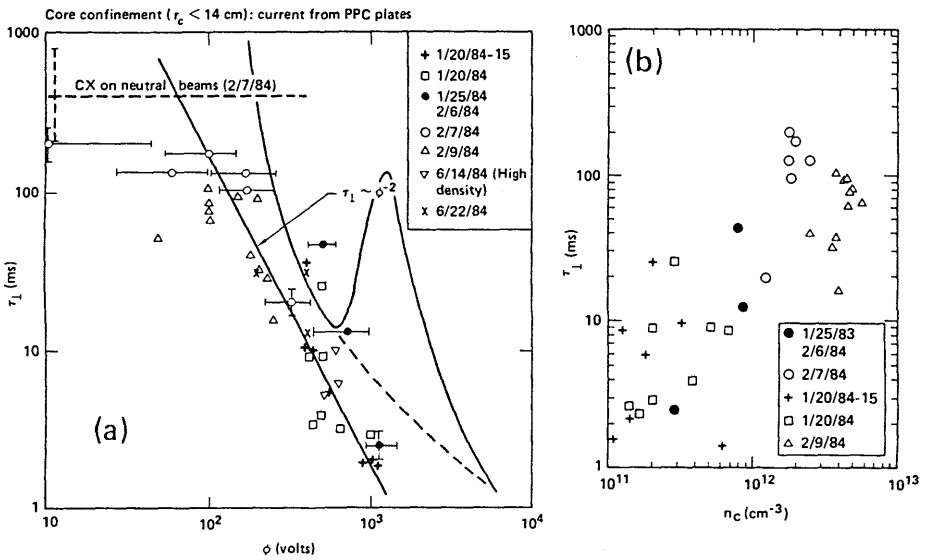

FIG.2. Scaling of non-ambipolar radial ion transport for $r_c \leqslant 12.9$ cm with (a) central cell potential ϕ_e and (b) density n_c. In part (a) the curved theory line was calculated using $T_i = \phi_e/4$ and the dashed line is a sketch of the expected effects of collisional stochasticity.

In Fig. 2a, above ϕ_e = 150 V, $\tau_\perp$ decreases as ϕ_e^{-2}; whereas at lower potentials $\tau_\perp$ is equal to 0.1 to 0.2 s. The region of ϕ_e^{-2} scaling begins near the resonance between the ion axial bounce and azimuthal **E x B** drift motions, where resonant transport theory predicts a general increase in radial transport [8]. The measured $\tau_\perp$ is less than predicted by theory by a factor 1 to 3. Overall, our experiments show the importance of avoiding operation at excessively high values of potential (relative to the ion and electron temperatures, as predicted by theory). Figure 2b shows that $\tau_\perp$ reaches 100 ms at densities above 10^{12} cm^{-3} when the potential is lower. There is less correlation of $\tau_\perp$ with n_c than with ϕ_e.

The average hot electron beta increases with ECRH power to 15% (30% locally on axis). After ECRH turnoff, the diamagnetic hot electron signal initially decays with a 10 to 20 ms decay rate, which later increases to 100 ms. The central cell beta, resulting mainly from the neutral-beam-injected ions, reaches 6% averaged over the radius to the limiter. Because the hot ions are undoubtedly localized in the plasma core, the on-axis beta is several times higher. The hot ions' diamagnetic decay time is usually 3 to 5 ms, which is believed to be limited mainly by charge-exchange on cold gas and electron drag.

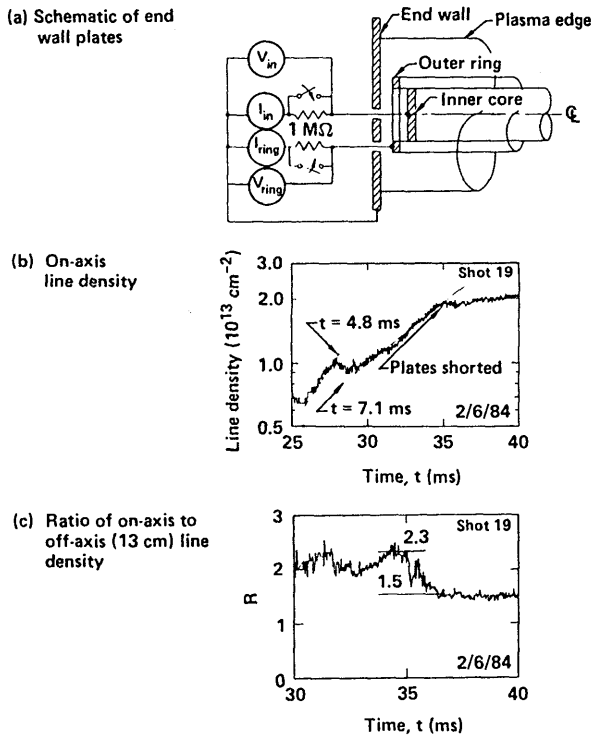

FIG. 3. Plasma behaviour using electrically floating end plates: (a) Schematic of the end plates; (b) central cell line density versus time with the end plates initially floating and then shorted at t = 35 ms; and (c) ratio (R) of line densities measured on radial chords through $r_c = 0$ and $r_c = 13$ cm.

4. POTENTIAL CONTROL

Because of its nonambipolar nature and its relation to central cell potential, radial ion transport is amenable to control by adding conducting plates to the end walls of the machine; these may either be electrically floated or biased.

Results from our first experiments using potential control on TMX-U are shown in Fig. 3. In this arrangement (Fig. 3a), two end wall electrodes at each end of the device may be either electrically floated and the voltage measured, or switched to ground and the current measured. The inner elliptical disc maps to a 9.8-cm radius in the central cell, whereas the outer electrode extends to 12.9 cm. Because the actual plasma extends to 25 cm, these plates only influence the plasma core.

In Fig. 3b, the end plates are floating (-1200 V on the inner plates--similar to the central cell potential) until t = 35 ms when they are grounded. Because the plasma sources are fixed, the fact that the exponential build-up rate decreases as the plates are shorted is clear evidence of superior confinement while the plates are floating. The nonambipolar radial confinement time increased from 5.8 to 12.0 ms with the plates floating, a factor of 2.1. Additional evidence of improved radial confinement is the narrower radial density profile before these plates are shorted (Fig. 3c).

Additional data taken by separately grounding the inner and outer electrodes show that suppressing the negative current corresponds to a decrease in the outward radial ion current rather than an increase in the outward radial electron current.

5. THERMAL BARRIER SCALING

Since the first observation of end plugging in TMX-U in February 1983, the central cell density n_c has been steadily increased with vacuum improvements [9] and with higher levels of ICRF and ECRH heating power from 1.5×10^{11} to 6×10^{12} cm^{-3}. Our goal is 2×10^{13} cm^{-3}. In this section we describe two thermal barrier scaling relations.

The central cell density and temperature must be increased concurrently to avoid excessive collisional trapping of the ions and charge neutralizing of the warm electrons in the thermal barrier region. In TMX-U, trapped ions are removed by charge-exchange pumping, which occurs when we inject approximately 100 atom A of neutral beam current into each end plug. Equilibrium between the collisional filling and charge-exchange pumping determines the lines of constant $n_c/T_{ic}^{3/2}$ shown in Fig. 4a; these lines separate the region where the thermal barrier can be formed from the region where the barrier cannot be formed because of insufficient pumping in TMX-U. Also shown in Fig. 4a are data points indicating where end plugging was or was not achieved.

Figure 4a also schematically depicts regions where end plugging is either routinely observed or not observed in TMX-U. In addition to collisional trapping, cold ions can be trapped in the thermal barrier by ionization of neutral particles penetrating the plasma; this may account for some of the scattering of data points in Fig. 4a. We infer from Fig. 4a that strong microinstabilities do not exist because large departures from Coulomb processes do not occur. Figure 4a indicates that the path to achieving thermal barriers at higher densities lies in increasing the temperature of passing ions. Central cell ions are heated by ICRF using a Faraday-shielded double-loop antenna excited in an m = 1 azimuthal configuration. Each loop subtends a 170° arc around the plasma

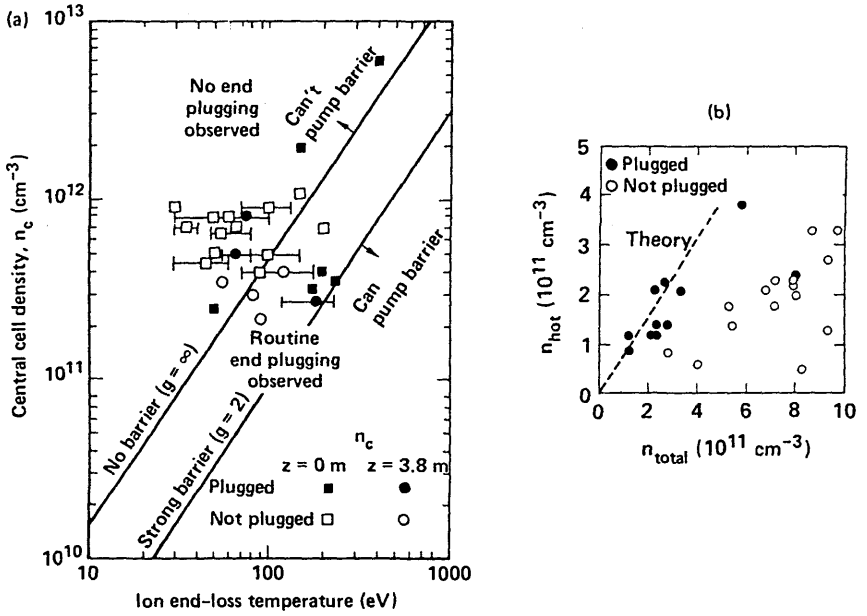

FIG. 4. Thermal barrier scaling curves for: (a) thermal barrier formation versus barrier-filling parameters n_c and T_{ic}, and (b) thermal barrier formation versus hot electron fraction.

circumference. Ions have been heated to 2 keV in the perpendicular direction and to 0.4 keV in the parallel direction. In addition, we are also beginning to operate a slot type ICRF antenna located on the other side of the central cell midplane.

Another critical parameter for thermal barrier formation is the fraction of hot mirror confined electrons. For TMX-U, theory [10, 11, 12] predicts that a ratio of $n_{e\text{-}hot}/n_{total} \simeq 0.8$ is required for a confining potential of $\phi_c > 0$. We measured the hot electron temperature for a series of shots with a radiometer and combined our results with diamagnetism measurements to estimate the hot electron density. We measured the total density with a microwave interferometer. Figure 4b depicts our data: the hot electron density data are plotted vs total density data for shots that did and did not achieve end plugging of central cell ions. With the exception of a single entry, the data show that end plugging requires a large fraction of hot electrons. In addition, the shots with end plugging lie close to the theoretical, minimum-required, hot-electron fraction.

REFERENCES

[1] SIMONEN, T.C., et al., Phys. Rev. Lett. **50** (1983) 1668.
[2] ORZECHOWSKI, T. J., S. L. Allen, J. H. Foote, et al., Phys. Fluids **26** (1983) 2335.
[3] GRUBB, D. P., et al., "Thermal Barrier Production and Identification in a Tandem Mirror", Lawrence Livermore National Laboratory, Livermore, CA, UCRL-90536. Accepted for publication in Physical Review Letters.
[4] STALLARD, B. W., et al., (Proc. of 4th International Symposium on Heating in Toroidal Plasmas, Rome, Italy, March 21-28, 1984).
[5] MOLVIK, A. W., et al., (Proc. of 4th International Symposium on Heating in Toroidal Plasmas, Rome, Italy, March 21-28, 1984).
[6] HOOPER, JR., E. B., et al., "Radial transport reduction in tandem mirrors using end wall boundary conditions," Lawrence Livermore National Laboratory, Livermore, CA, UCRL-90639. Accepted for publication in Physics of Fluids.
[7] MOLVIK, A. W., Rev. Sci. Inst. **52** (1981) 704.
[8] COHEN, R. H., and ROWLANDS, G., Phys. Fluids **24** (1981) 2295; MIRIN, A. A., et al., Nucl. Fusion **23** (1983) 703.
[9] TURNER, W. C., et al., "Gas pressure in the end plug regions of the TMX-U thermal barrier experiment", Lawrence Livermore National Laboratory, Livermore, CA, UCRL-89938, (1983), to be published.
[10] COHEN, R. H., Phys. Fluids **26** (1983) 2774.
[11] MATSUDA, Y. and ROGNLIEN, T. D., Phys. Fluids **26** (1983) 2778.
[12] STALLARD, B. W. et al., Nucl. Fusion **23** (1983) 213.

DISCUSSION

J. KISTEMAKER: What is the function of the floating electrodes at the end of your system? Do they reduce the electric field in the radial direction and, if so, what is the physical influence of such a reduction?

T.C. SIMONEN: The purpose of the floating end electrodes is to reduce the radial electric field which drives resonant neoclassical radial transport.

R.S. PEASE: Did you make measurements of the thermal barrier potential as a function of any of the parameters, for example, ECRH power?

T.C. SIMONEN: We have concentrated our experiments on exploring various operating modes and therefore have only a limited amount of potential measurements and no parametric measurements as a function of ECRH power.

R.S. PEASE: Does the potential agree with estimates?

T.C. SIMONEN: The magnitude of the TMX-U potentials agrees with that predicted by the strong RF theory of Cohen, Rognlien and Matsuda published in 1983 in Physics of Fluids Letters.

E. THOMPSON: What is the impurity content of the plasma in the central cell?

T.C. SIMONEN: Between 0.5 and 1%, and it consists mainly of O, C and N.

H.R. GARNER: In the graph of $\tau_\perp$ versus density (Fig.2) there was a lot of scatter in the data. During this scaling study, were other parameters held constant?

T.C. SIMONEN: No, other parameters were not constant. The scatter in the data may result from the fact that parameters such as central cell ion temperature, ECRH power, antenna configurations and gas puffing rates varied during our studies.

H.R. GARNER: How was $\tau_\perp$ measured?

T.C. SIMONEN: The non-ambipolar radial transport time was determined from measurements of the net electron flow to end plates which extend to 13 cm radius in the central cell (half that of the 25 cm limiter radius).

PLASMA POTENTIAL CONTROL AND MHD STABILITY EXPERIMENTS IN THE PHAEDRUS TANDEM MIRROR

N. HERSHKOWITZ, R.A. BREUN, D.A. BROUCHOUS,
J.D. CALLEN, C. CHAN, J.R. CONRAD, J.R. FERRON,
S.N. GOLOVATO, R. GOULDING, S. HORNE*, S. KIDWELL,
B. NELSON, H. PERSING, J. PEW, S. ROSS, G. SEVERN,
D. SING
Nuclear Engineering Department,
University of Wisconsin-Madison,
Madison, Wisconsin
United States of America

Abstract

PLASMA POTENTIAL CONTROL AND MHD STABILITY EXPERIMENTS IN THE PHAEDRUS TANDEM MIRROR.

The Phaedrus tandem mirror has been operated with min - |B| quadrupole end cells, with axisymmetric end cells and without end cells. ICRF, ECRF and biased (and heated) end rings have been used to achieve plasma potential control and MHD stability. Axial and radial plasma potential control is achieved by modifications to the electron distribution functions using ICRF and ECRF, or by radial end wall bias. Large ion-confining potentials are located near where $\omega = 0.8\ \omega_{ci}$. These are not associated with significant increases in ion density. By varying the bias on sets of concentric end rings it has been possible to adjust the shape of the radial potential profile throughout the device. Radial ponderomotive force from the ICRF with $\omega > \omega_{ci}$ provides MHD stability to the central cell plasma and allows operation without end cells or with axisymmetric end cells. A heated end ring is also found to enhance the MHD stability of a marginally stable plasma. ICRF with $\omega < \omega_{ci}$ is found to be destabilizing but it is found that ECRF can provide some stability to a plasma heated with such ICRF. ECRF is also found to produce electron tails to energies of several keV. Application of too large a radial electric field using the biased end rings also results in unstable plasmas. Azimuthal ponderomotive force from half-turn antennas results in plasma convection across the magnetic field.

1. INTRODUCTION

In tandem mirrors, axial plasma confinement comes from end cell potential barriers while radial confinement depends on the radial plasma potential profile. MHD stability comes from sufficiently high beta in end cell "anchors". In the RF-sustained Phaedrus tandem mirror, both the axial and the radial potential profiles behave quite differently from that usually envisioned for tandem mirrors. ICRF and ECRF have been found to provide a variety of new techniques for improving the MHD

---

* Present address: Plasma Fusion Center, Massachusetts Institute of Technology, Cambridge, MA, USA.

stability. This paper is divided into two parts. In the first we discuss plasma potential control by ICRF and ECRF and by radial end wall bias. In the second part we discuss the use of ICRF, ECRF and end wall bias to enhance MHD stability and to induce instabilities.

2. PLASMA POTENTIAL CONTROL

In Phaedrus the radial potential profile is found to be hollow, even though the radial density profile is approximately gaussian. The west end cell ion-confining potential is $2T_e/e$ even though the end cell density is never more than 2.5 times the central cell density. Thus non-Boltzmann processes must be involved. While central cell beta continues to increase with input power, reaching values as high as 8%, the plasma density saturates at approximately 6×10^{12} cm^{-3} in the present configuration. It has also been difficult to achieve end cell fueling with neutral beams. These results have now been shown to be a consequence of operating Phaedrus with ICRF as the principal power input [1]. Control over the axial and radial potential profiles has been achieved by appropriate choices of ICRF and ECRF and by applying a radial potential profile to the end wall.

2.1. Electron Heating Effects on the Potential

Most of the electron heating is accomplished by application of ICRF (with frequency below ω_{ci}, the ion cyclotron resonance frequency). End cell ion heating can be enhanced by the application of ECH at twice the electron cyclotron frequency ω_{ce}. Best RF sustained operation [1] is achieved when the ICRF frequency is chosen to be approximately $0.8\ \omega_{ci}$. For Phaedrus parameters the z component of the slow wave electric field peaks at this frequency. Optimization of RF-sustained operation is now understood as being a consequence of parallel (to the B field) electron heating by Landau damping. Electron drag on hot ions also makes a contribution. ICRF ion heating is limited by electron drag which scales as $T_e^{3/2}$, so even small changes in electron temperature T_e can result in large changes in T_i for fixed ICRF input power [2].

Parallel electron heating peaks at large radii because E_z decays rapidly with decreasing radius. This heating has been directly identified using end wall energy analyzers which show that $T_{e\parallel}$ increases with increasing radius. It is likely that this heating is responsible for hollow potential profiles that are found in both the Phaedrus central cell and end cell. Radial electric fields as large as T_e/er_i, where r_i is the ion gyroradius, have been found in the end cells. The radial electric fields result in E x B rotation of MHD flute modes.

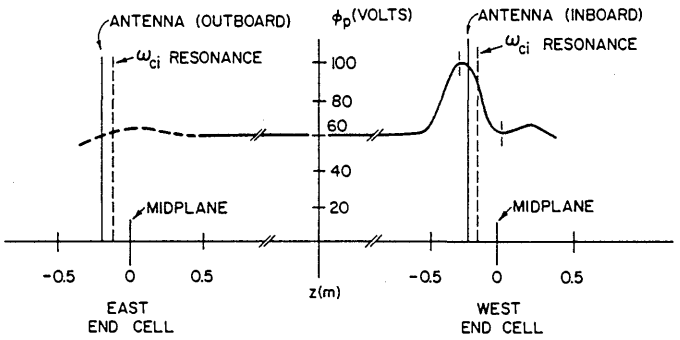

FIG.1. Axial plasma potential profile in Phaedrus.

2.2. Axial Potential Profile

Axial ion confinement by end cell potential barriers is an essential feature of tandem mirrors. In previous experiments (Gamma 6, TMX and TMX-U), ion-confining barriers were created with neutral beams by increasing the plug ion density or by helping to create electron thermal barriers. In Phaedrus an ion-confining potential is produced in the west end cell (but not the east end cell) by using ICRF (see Fig. 1). This results in a substantial reduction of the ion end loss current out of the west end of the machine compared to the east end. Thus a net electron current is lost at the west end while a net ion current is lost at the east end. The asymmetry is due to the end cell antenna locations which are inboard (on the central cell side) in the west end cell and outboard in the east end cell.

The large increases in the axial potential in the west end cell were located where $\omega = 0.8\ \omega_{ci}$ rather than at the end cell midplane where $\omega > \omega_{ci}$. Increases as large as $2\ T_e/e$ and $2\ T_{ic}/e$ have been observed on the inboard side of the ICRF resonance. This increase in potential was not found to be associated with an increase in plasma density. Neutral beam attenuation measurements of the axial density profile show at most an increase in density of 30% (see Fig. 2). The increase in potential appears to be associated with modification of the electron distribution function by parallel electron heating. The most interesting feature of this technique for creating potential barriers is that it favors low ion densities (which can be less than central cell densities). Plasma potential measurements were made directly with emissive probes and indirectly with end loss analyzers. Substantial charge exchange loss in the end cells allowed the energy analyzers to determine the potential maxima on both sides of the end cell.

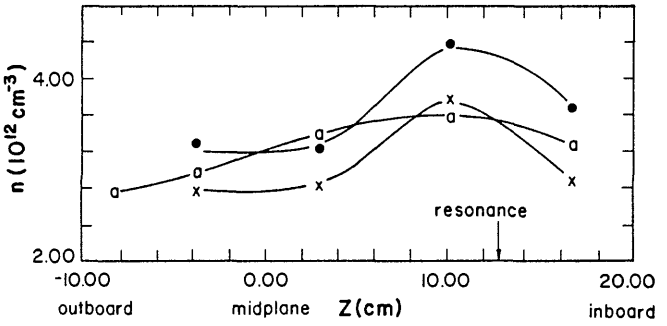

FIG.2. Axial density profile in west end cell obtained from neutral beam attenuation. Three different shots are shown.

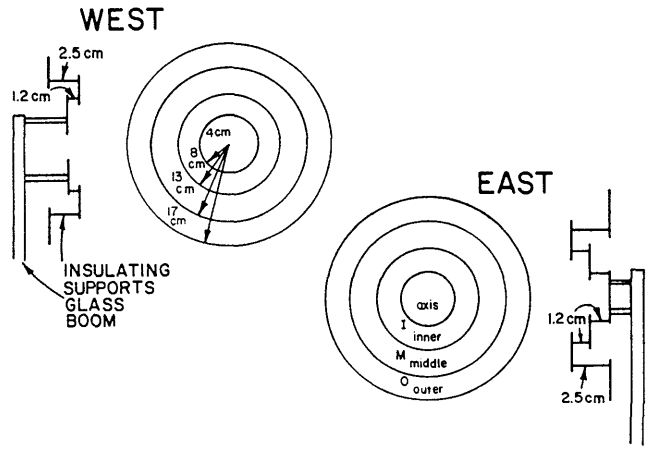

FIG.3. Schematic of copper end rings placed near Phaedrus end walls.

Similar effects have also been observed in the central cell during RF-stabilized axisymmetric operation. Large increases in the total end loss current immediately after the central cell RF is shut off demonstrate end loss current plugging. Plugging factors as high as 7 have been observed in single-cell operation.

2.3. Radial Potential Profile Control

Control of the radial potential profile is of major importance to the tandem mirror program because radial transport can become the dominant loss when axial potential barriers are erected in the end cells. Since mirrors are open systems, the radial electric field can be adjusted by varying

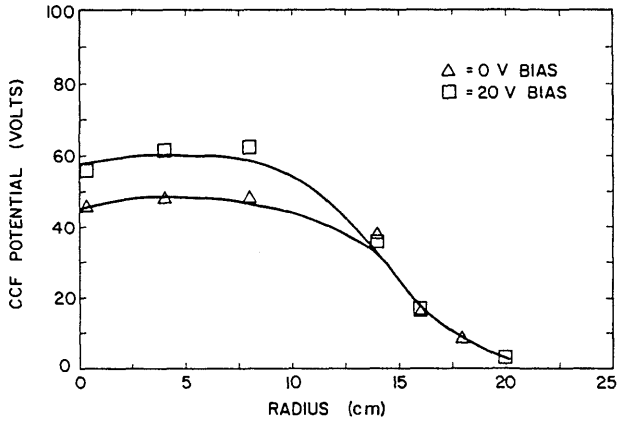

FIG.4. Central cell radial floating (CCF) potential profiles corresponding to 0 and 20 V bias applied to the middle ring.

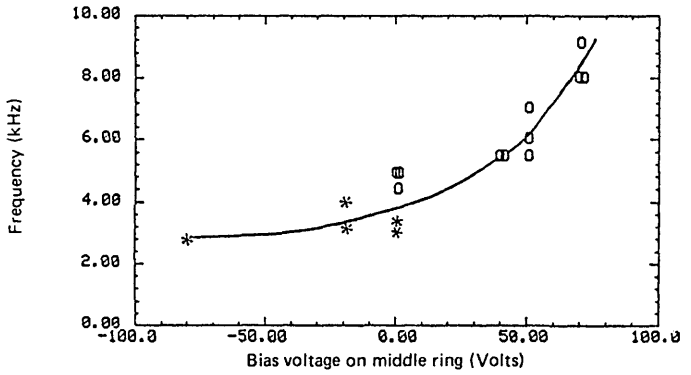

FIG.5. Fluctuation frequency measured by central cell Langmuir probe versus middle ring bias voltage.

the end wall radial potential profile. This has been attempted by placing four concentric rings at each end of Phaedrus (see Fig. 3). Plasma was initiated with ECH breakdown so no stream guns were required. The radial potential profile in the central cell, measured with Langmuir probes, is given in Fig. 4 for several values of potential on the third ring from the center. It is apparent that while the general shape of the profile inside of the flux tube which mapped to the biased ring did not change, the average value of the potential did change and with it the average value of the radial electric field. Sheaths near the end walls absorb the difference between the applied and observed potentials. The ability to change the average radial electric field was confirmed by the observed variation in the rotation velocity of the flute modes which

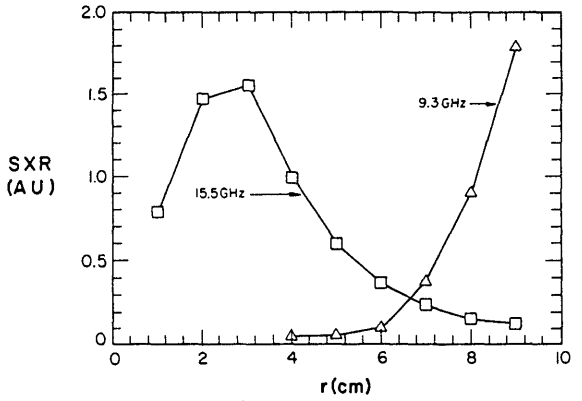

FIG.6. Soft X-ray (SXR) signal versus target probe radius during RF-sustained operation with fundamental electron heating at 9.3 GHz and second harmonic heating at 15.5 GHz.

depends on the $\vec{E} \times \vec{B}$ drift velocity. Representative data showing such frequency control are given in Fig. 5 . By varying the potential on all rings we have been able to achieve considerable control over the shape of the radial potential profile. One issue currently under investigation is the time required for the plasma parameters on axis to respond to changes at large radii. When the potential at r = 10 cm was changed, the central cell potential and end loss current measured on axis changed in less than 50 microseconds. In addition, the electron current drawn by positively biasing the third rings was considerably greater than the current expected from the assumption that electrons are confined to the flux tube on which they were born. We believe that rapid radial transport is associated with the strong azimuthal dependence of the ICRF heating which comes about because of the use of half-turn antennas in the central cell and line antennas in the quadrupole end cells. Achieving more symmetric heating has now become a major goal.

2.4. ECH Effects on Potential

Application of ECH at $2\omega_{ce}$ has been shown to result in increases in end cell plasma potential as high as T_e/e [2]. Soft x-ray profiles (see Fig. 6) show that hot electrons are produced across most of the plasma cross-section. The peak in the x-ray signal at a radius of 3 cm is interpreted as resulting from the right hand (R) cutoff preventing deeper penetration of the X-mode microwaves. Experiments with ω_{ce} heating of low density plasmas (1.0×10^{12} cm^{-3}) have resulted in tail heating to energies of several keV. The hot electrons appear to be concentrated at the plasma surface (see Fig. 6).

Conventional tandem mirror end cell potential increase with neutral beams has not been achieved. Neutral beam fueling with > 50A of 10 keV neutrals into the end cells has been found to be limited by charge-exchange from gas produced by the ICRF from end cell vacuum surfaces.

Results of these experiments have been incorporated in a Phaedrus upgrade design which continues to depend heavily on the use of ICRF but also takes advantage of electron heating at ω_{ce} in the end cells and introduces thermal barriers and choke coils.

3. MHD STABILITY EXPERIMENTS

The conventional technique for providing MHD stability in tandem mirrors is to use high-β end cell "anchors". Previous experiments on the Phaedrus tandem mirror verified β ratio limits for stability from quadrupole end cells[3] and also showed that line-tying to on-axis stream gun plasmas could provide MHD stability. Recent experiments with the Phaedrus tandem mirror with plasma sustained only with RF have found a variety of new techniques for improving MHD stability. Preliminary experiments have demonstrated that central cell ICRF with $\omega > \omega_{ci}$ can provide stability[4] while ICRF at $\omega < \omega_{ci}$ was found to destabilize the plasma but to heat electrons and ions. We are continuing to explore these methods of operation and also have begun to study the operation with ICRF at $\omega \approx 0.75\ \omega_{ci}$ in combination with ICRF at $\omega \geq \omega_{ci}$. Other new experiments have found that the presence of ECH during startup enhances stability when used with ICRF at $\omega = 0.75\ \omega_{ci}$.

3.1. RF Stabilization of Axisymmetric Mirrors

Evidence of stabilization by RF comes from oscillations which appear in a quiet plasma immediately after the RF is shut off. We believe that a radial ponderomotive force due to a radial gradient in the applied RF electric field provides stability by opposing the centrifugal force due to field line curvature. Phaedrus has been operated both as an axisymmetric single cell and as a tandem mirrror consisting of three simple mirror cells with end cells providing electrostatic confinement[4]. In the latter case it appears that excess central cell ponderomotive force acts as an anchor for unstable end cells. Representative data for ponderomotive force-stabilized plasmas are shown in Fig. 7. Note that all plasma parameters increase with coupled power and that only the density saturates at high power levels. Plasma pressure and density are uniform out to r = 12 to 15 cm and fall off sharply at the plasma edge. RF electric field profiles calculated using these density profiles show a steep gradient in the region of the plasma surface. This indicates that the RF

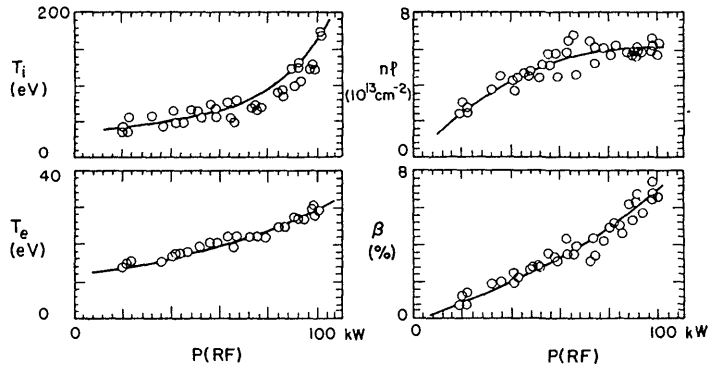

FIG. 7. Electron temperature T_e, T_i line density nℓ and beta versus coupled RF power for ponderomotive force-stabilized plasmas.

provides surface stabilization while the center region maintains a stable pressure profile. We have begun to study the effects of adding ICRF at $\omega = 0.75\ \omega_{ci}$ to enhance electron heating. The lower frequency RF is found to be destabilizing but is effective at heating. Stable plasmas can be maintained when the power applied at $0.75\ \omega_{ci}$ is not too high.

The half-turn antennas used in the Phaedrus central cell produce non-axisymmetric RF electric fields. The corresponding azimuthal ponderomotive force results in plasma drifts that are parallel to surfaces of constant RF field strength and result in radial transport. Ion end loss current profiles show that the highest end loss currents are located where the ions are expected to drift [5]. This provides confirmation of azimuthal ponderomotive force.

3.2. Stability Using ECH and ICRF at $\omega < \omega_{ci}$

Maintaining stable plasmas during startup is an important issue since startup plasmas can have quite different axial density and pressure profiles than steady state plasmas. Most previous experiments have depended on stability provided by end cell anchors. In Phaedrus, reliable central cell startup has been achieved without the use of end cell ICRF by using low power ECH breakdown (as low as 1.5 kW) and ICRF. Using only ECH, peak densities as high as four times cutoff density have been obtained. Satisfactory results have been achieved with either $\omega > \omega_{ci}$ (which provides a stabilizing ponderomotive force) or $\approx 0.75\ \omega_{ci}$ (which destabilizes). The addition of low power ECH to steady state operation has enhanced MHD stability in the core plasma and produced plasmas with fluctuation levels as low as 20% even when only a destabilizing

ponderomotive force was present. It has been found possible to sustain a plasma using only high power (greater than 50 kW coupled power) ICRF at $\omega = 0.75\ \omega_{ci}$, but the fluctuation level observed in this case was a factor of two greater than the case in which both ECH and ICRH were applied.

3.3. End Ring Experiments

Using quadrupole anchors, it was found that when a sufficiently large radial electric field was applied at the end wall rings, the plasma could not be RF-sustained. Since increasing the radial electric field resulted in an increased E x B rotation frequency, it is likely that it was driven rotationally unstable. In other experiments the rings were replaced by a floating hot ring (which mapped to e^{-1} in the radial density profile) at only one end of the device. The central cell to end cell β ratio was adjusted with ICRF so that the β limit was reached in the middle of the plasma shot. It was found that the time for the onset of MHD fluctuations was delayed by $\approx$ 6 ms when the end ring was heated. These results indicate that surface line-tying can enhance stability, as has been suggested[6].

ACKNOWLEDGEMENT

These studies were supported by U S Department of Energy Contract No. DE-AC02-78ET51015.

REFERENCES

[1] BREUN, R.A., et al., Phys. Rev. Lett. 47 (1981) 1833.
[2] SING, D., et al., Phys. Fluids 27 (1984) 16.
[3] MOLVIK, A.W., et al., Phys. Rev. Lett. 48 (1982) 742.
[4] FERRON, J.R., et al., Phys. Rev. Lett. 51 (1983) 1955.
[5] YASAKA, Y., and ITATANI, R., Phys. Rev. Lett. 44 (1980) 1763.
[6] FORNACA, S., et al., Phys. Rev. Lett. 42 (1979) 772.

DISCUSSION

H.L. BERK: Is there a difference in efficiency when ponderomotive forces are applied at frequencies significantly shifted from the cyclotron frequency?

N. HERSHKOWITZ: We find that less power is required for stabilization when ω is selected so that it is significantly shifted from ω_{ci}. In that case, the heating of the antenna is less effective, so a greater portion of the coupled power goes towards stabilization.

T.C. SIMONEN: You observed ICRH MHD stabilization at frequencies of 1.005, 1.3 and 1.6 ω_{ci}. Do you find that stabilization occurs only at these frequencies?

N. HERSHKOWITZ: These are the only frequencies we have tried so far. We believe that any frequency greater than ω_{ci} and less than 1.6 ω_{ci} (the highest we have tried so far) will be stabilizing. Itatani at Kyoto has shown that stability can be achieved at frequencies as high as 2 ω_{ci}.

T. CONSOLI: With ICRH and/or ECRH the ponderomotive force changes sign – and thus also direction – if ω_{ce} or ω_{ci} is greater than or less than ω_{RF}. This could explain the inverse effect of the RF applied on plasma end plugging and also on radial diffusion. The effect, which is strong when $\nu_{collision} < \omega_{RF}$, is damped when ν increases. In France we observed this effect in an earlier experiment in 1963.

N. HERSHKOWITZ: Several recent theoretical studies of RF stabilization now predict that many other terms are present in the expression which gives the effective force. Our results are at present consistent with $F \propto (\omega - \omega_{ci})^{-1}(\partial E_+/\partial r)$, where E_+ is the left circularly polarized field. We are currently investigating whether other terms are important.

A.A. NEWTON: Your β increases with RF power (Fig.7); can you please comment on the limit of β, its definition and the extent of the high-β region?

N. HERSHKOWITZ: We have achieved β-values as high as 10%. So far, β has been limited by our power supplies. The radial β-profile is quite flat, so β is approximately constant out to e^{-1} in the density profile (12 to 15 cm). Beta is also quite uniform axially in the central cell. A zeroth-order effect is that finite β shifts the local ion cyclotron frequency, and hence the stability, through $1/\omega - \omega_{ci}$.

POTENTIAL FORMATION IN AXISYMMETRIZED TANDEM MIRROR GAMMA 10

T. CHO, M. ICHIMURA, M. INUTAKE, K. ISHII,
A. ITAKURA, I. KATANUMA, T. KAWABE,
Y. KIWAMOTO, A. MASE, S. MIYOSHI,
Y. NAKASHIMA, T. SAITO, K. SAWADA,
D. TSUBOUCHI, N. YAMAGUCHI, K. YATSU
Plasma Research Center, University of Tsukuba,
Ibaraki, Japan

Abstract

POTENTIAL FORMATION IN AXISYMMETRIZED TANDEM MIRROR GAMMA 10.

The paper reports experimental results on potential formation and end plugging in the axisymmetrized tandem mirror GAMMA 10. The plugging at both ends has been achieved by a combination of neutral beams and gyrotrons. The presence of a plug potential with a thermal barrier in an axisymmetric mirror has been confirmed by direct measurement of the axial potential profile. Enhancement of axial particle confinement has been observed during the end plugging. Non-ambipolar radial transport has been greatly reduced in the axisymmetrized magnetic configuration. – The potentials measured by beam probes and end loss analysers are 0.7, 0.4 and 1.1 kV in the central, barrier and plug regions, respectively. Strong end plugging is observed when the central-cell density is higher than the densities in the plug and the barrier, and the plug density remains higher than the barrier density. The plug electron temperature is higher than the central temperature. Hot electrons forming a football-shaped profile have been stably produced in the axisymmetric mirror. The beta value and the fraction of the hot electrons reach up to 5% and 0.8, respectively. Central-cell ion-cyclotron resonance heating can sustain a stable plasma with higher density and ion temperature when resonance surfaces exist in both the anchor and the central cells.

1. INTRODUCTION

Significant progress has been made on end loss reduction by potential plugs [1–3] in tandem mirrors [4, 5]. The thermal barrier [6] is one of the critical issues under investigation in TMX-Upgrade [7], GAMMA 10 [8] and TARA [9].

Another improvement is to attain axisymmetric confinement of central-cell ions for reducing radial losses due to a non-axisymmetric configuration [10]. GAMMA 10 is now under operation with an effectively axisymmetric configuration. The one-end plugging experiment was achieved in January, 1984. A both-end plugging experiment is reported in this paper.

2. GAMMA 10 DEVICE

The GAMMA 10 device and its magnetic flux configuration are shown schematically in Fig. 1(a). It consists of a central cell, anchor cells and axisymmetric end mirror cells. The anchor cell is a minimum-B mirror for suppressing MHD instabilities. Plug potential and thermal barrier are produced in the axisymmetric mirror. Ramp coils set at both ends of the central cell throttle the fraction of passing particles flowing into the minimum-B anchors and the plug/barrier cells.

The magnetic field intensity and the normal and geodesic curvatures of the magnetic field lines are shown in Fig. 1(b). The minimum-B mirrors are designed to be symmetric with respect to the midplane so as to cancel the geodesic curvature. This results in zero net drift from a flux surface for particles passing through the non-axisymmetric region [11] and zero parallel current flowing into the central cell if the azimuthal $\vec{E} \times \vec{B}$ drift is small. When the axial potential hill is kept low in the anchor/transition region, the central-cell ions are either reflected by the ramp field or pass through the anchor and are reflected by the axisymmetric plug. This means that GAMMA 10 has an effectively axisymmetrized configuration.

The dimensions of GAMMA 10 are 27 m in total length, 6 m in length and 1 m in diameter of the central-cell vessel, and 40 cm in diameter of the central-cell limiters. The total volume of the vessel is 120 m^3. The base pressure is less than 1×10^{-8} torr.

The heating systems are shown in Fig. 1(a). The magnetoplasma-dynamic (MPD) guns and an electron beam injector (E-beam) produce initial plasmas. Neutral-beam injectors (NBI) with 20 kV, 60 A and 35 kV, 70 A drains are used to produce sloshing ions in the plug/barrier cells and hot ions in the anchor cells. Four 28 GHz/100 kW gyrotrons are used to produce magnetically trapped hot electrons near the midplane (0.5 T, second-harmonic resonance $2\omega_{ce}$), which helps the formation of the barrier potential well, and to produce warm electrons off midplane (1.0 T, fundamental resonance ω_{ce}). Ion-cyclotron-resonance-frequency heating (ICRF) is carried out by Nagoya type-III antennas at both ends of the central cell in order to heat and to sustain the central-cell plasma.

3. EXPERIMENTAL RESULTS

The initial plasma produced by MPD guns is injected along the magnetic field lines from the ends. The line density in the central cell increases up to $(1-3) \times 10^{13}$ cm^{-2}. The line density can increase up to $(2-10) \times 10^{13}$ cm^{-2} by applying central-cell ICRF heating with gas puffing near the antennas. The gas flow rate is about (10–30) torr·s^{-1}. Thereafter, neutral beams are injected into the anchors and plug/barrier cells. The time variation of the line densities in each cell is shown in Fig. 2(a).

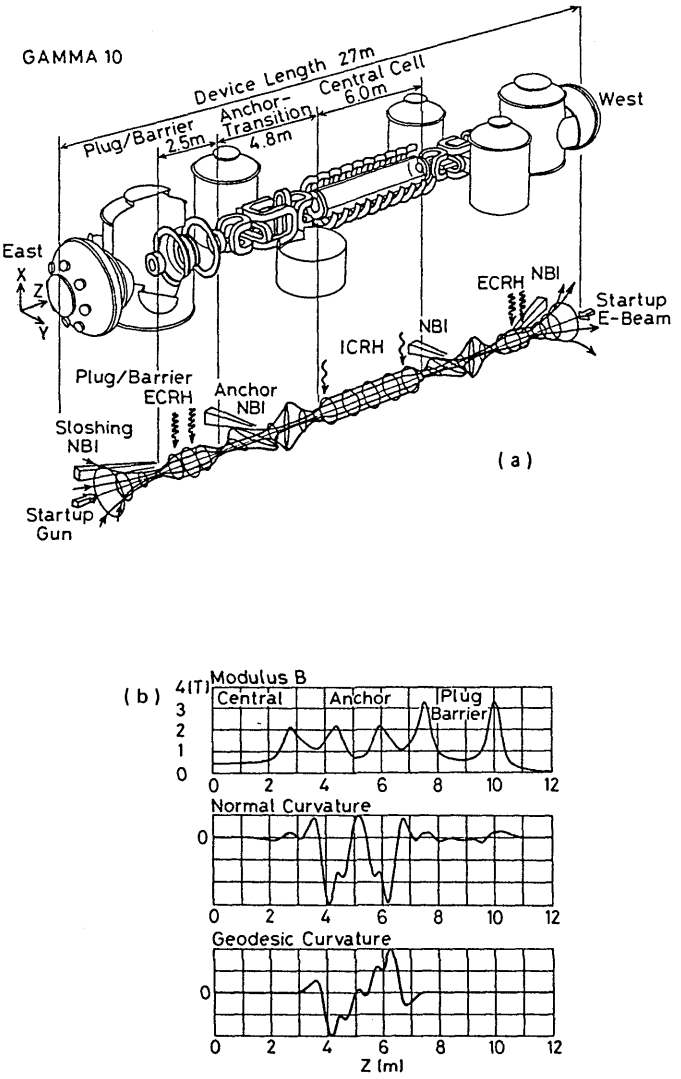

FIG.1. (a) Schematics of GAMMA 10 device and magnetic flux tube, together with heating systems. (b) Axial profiles of magnetic field intensity, normal and geodesic curvatures.

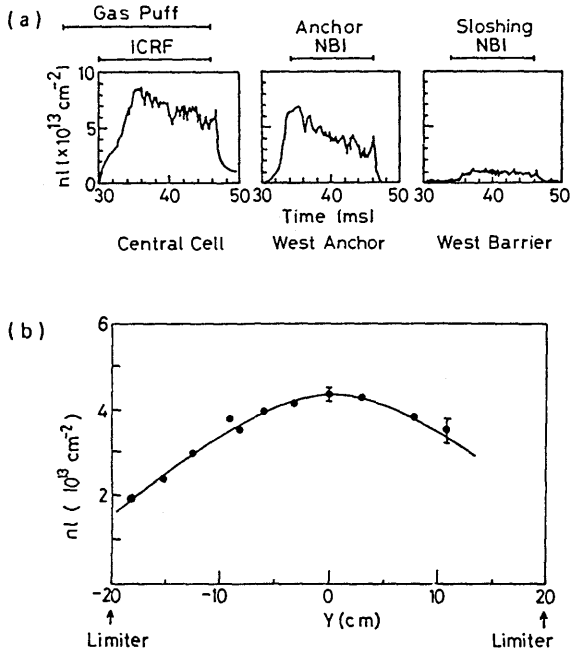

FIG.2. (a) Line densities of ICRF- and NBI-sustained plasma in central cell, west anchor and west plug/barrier. (b) Radial profile of central-cell line density measured by movable microwave interferometer.

The experiments have been carried out under an ambient gas pressure of less than 1×10^{-6} torr.

The ICRF oscillator output power is about 200 kW, and the coupled power is estimated to be 50 to 100 kW for each antenna. The line density profile of RF-produced plasma is parabolic in the central cell as is shown in Fig. 2(b). The ion temperature measured by a time-of-flight charge-exchange analyser and/or a diamagnetic loop is 0.15 to 1.4 keV, depending on the plasma parameters. At the same time, the electron temperature is about 30 eV without ECRH. Plasma production and sustainment have been achieved when an ion-cyclotron resonance surface exists both near the RF antennas and near the midplane of the anchor cells. The central-cell plasma cannot be sustained without anchor resonance, presumably because of the absence of RF trapping in the anchor cell.

Sloshing ions are formed in the plug/barrier cell by skew injection (40°) of NBI with a 20 kV/60 A drain. The angular distribution of the sloshing ions is confirmed by signals of the secondary-emission detector (SED) array [12] placed at the sloshing-ion turning point. The distribution has its peak at 40°, which agrees with the injection angle of NBI.

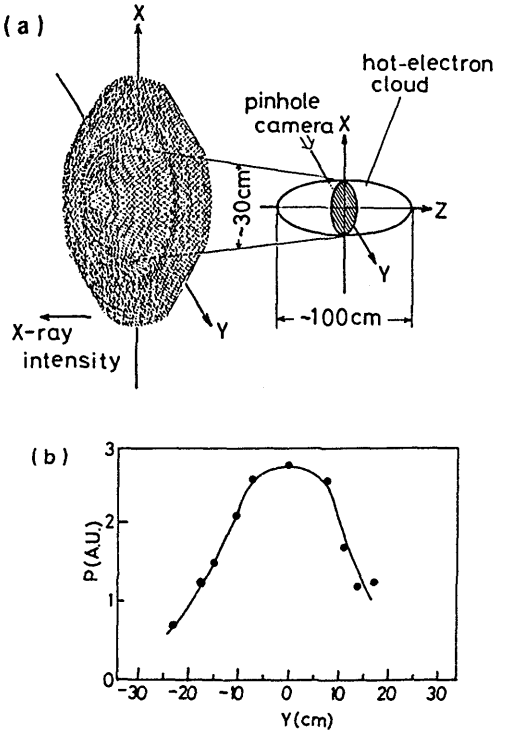

FIG.3. (a) Two-dimensional distribution of X-ray intensity emitted from barrier hot electrons (Abel-transformed from X-ray pinhole camera image). (b) Chord-integrated distribution of $5\omega_{ce}$ (70 GHz) emission from barrier hot electrons.

For an effective formation of the plug potential, the density of hot electrons should be a substantial fraction of the total electron density in the thermal-barrier region. The TE_{02}-mode microwave is converted to a linearly polarized X-mode and is injected in the form of a pencil beam of 15 cm diameter so that a strong second-harmonic resonant ($2\omega_{ce}$) absorption may occur in a limited region without runaway heating. From a pulse height analysis (PHA) of the radiated X-rays, the hot-electron temperature T_{eh} is observed to rise quickly and saturate in 1 to 3 ms. The obtained value of T_{eh} is up to 30 keV, depending on ECRH power, initial plasma parameters and gas puffing rate. The diamagnetism increases stably in time without saturation for at least 50 ms. From the measurements of the X-ray pinhole camera image [13], a cyclotron emission profile as shown in Figs 3(a) and (b) and the diamagnetism, it is confirmed that the hot-electron density is fairly uniform with a diameter of 30 cm and an axial length of about 100 cm. The distribution is football-shaped. The maximum line density and the fraction of hot electrons obtained so far are 1×10^{12} cm^{-2} and 0.8, respectively, with an averaged beta value of 5%.

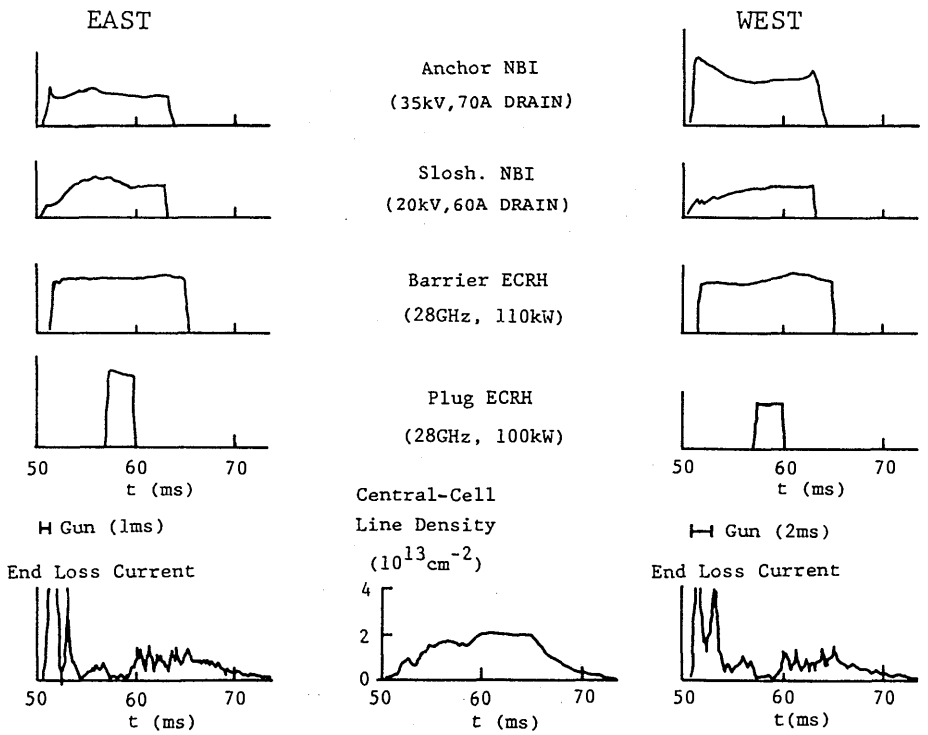

FIG.4. Both-end plugging. Time sequence of plugging experiment; line density of central-cell electrons; end loss flux to each end is stoppered when the plug ECRH pulse is applied.

The end plugging experiment is demonstrated in Fig. 4; it is carried out by combining NBI and ECRH. During the ECRH pulse, the ion loss fluxes to both ends decrease significantly. The plasma potentials in the plug, ϕ_p, in the central cell, ϕ_e, and in the barrier, $\phi_e - \phi_b$, are measured by end loss analysers (ELA) and A_u neutral-beam probes, respectively. Both ϕ_p and ϕ_e increase sharply with the ECRH pulse, while ϕ_b changes gradually.

The axial distributions of plasma density n, electron temperature T_e and potential ϕ under end plugging in the low-density case are shown in Fig. 5. The density ratio n_p/n_b of plug to barrier is enhanced when sloshing beams are injected. The average electron temperature in the plug region is determined to be 300 eV, from a measurement of the $2\omega_{ce}$ emission and from the soft-X-ray absorption method. The electron temperature in the central cell is 50 eV, which is much lower than the plug temperature. The barrier potential rises gradually towards the central-cell potential and the density ratio n_p/n_b decreases owing to collisional filling and charge exchange in the barrier region, resulting in the failure of plugging.

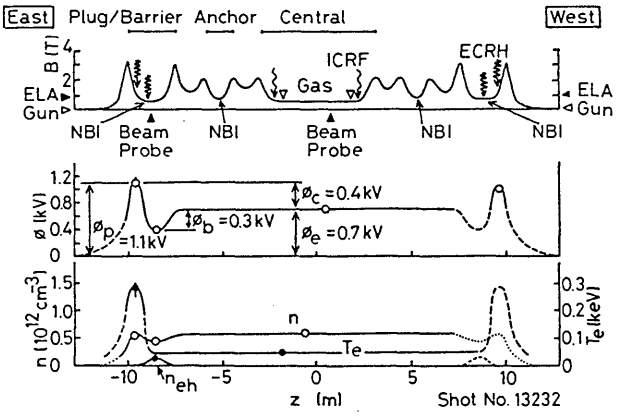

FIG.5. Axial distribution of magnetic field strength and positions of heating and relevant diagnostics (top); potential distribution measured by central-cell and barrier beam probe and end loss analyser (middle); axial distribution of density (open circles) and electron temperature (closed circles) of plasma (bottom).

The radial distributions of the ion end loss flux and of the plug potential are measured by using movable end loss analysers. The radius of the suppressed-end-loss region coincides with that of the region of high plug potential. This radius is found to be mapped along the magnetic field to the radius of the warm electrons at the plug, which is determined by the beam width of the ECRH there. The axial particle confinement time of the end-plugged core plasma is estimated to be 50 ms, ten times as long as that of unplugged plasma.

The heating of the central-cell ions is brought about by ICRH, combined with NBI and ECRH. End plugging is observed at T_{ic} = 250 eV, with central-cell densities of up to 2×10^{12} cm^{-3}.

Segmented end plates are installed at each end. They constitute an array of plates separated into five plates radially and four plates azimuthally. The plates are either grounded or floated. The net currents flowing into the grounded, segmented end plates are measured to be small in the core plasma region. This shows that non-ambipolar radial transport is greatly reduced in the axisymmetrized magnetic field configuration of GAMMA 10. The non-ambipolar radial confinement time is longer than the axial one. When the plates are floated, the positive central-cell potential decreases. The floating potential at the segmented end plates goes down negatively with the parabolic radial distribution. The decrease in the central-cell potential lowers the radial-electric-field strength. This reduction is important in realizing the axisymmetric confinement by cancelling the radial ion drift and the central-cell parallel current due to the quadrupole field.

In conclusion, we may say that the experimental results show the existence of a plug potential with a thermal barrier in the axisymmetric end mirror and significant enhancement of axial particle confinement with reduced non-ambipolar radial transport.

REFERENCES

[1] MIYOSHI, S., et al., Plasma Physics and Controlled Nuclear Fusion Research (Proc. 8th Int. Conf. Brussels, 1980), Vol. 1, IAEA, Vienna (1981) 113.
[2] COENSGEN, F.H., et al., Phys. Rev. Lett. **44** (1980) 1132.
[3] BREUN, R., et al., Phys. Rev. Lett. **47** (1981) 1833.
[4] DIMOV, G.I., ZAKAIDAKOV, V.V., KISHINEVSKI, M.E., Fiz. Plazmy **2** (1976) 597; Sov. J. Plasma Phys. **2** (1976) 326.
[5] FOWLER, T.K., LOGAN, B.G., Comm. Plasma Phys. Contr. Fusion **2** (1977) 167.
[6] BALDWIN, D.E., LOGAN, D.G., Phys. Rev. Lett. **43** (1979) 1318.
[7] SIMONEN, T.C., et al., Phys. Rev. Lett. **50** (1983) 1668.
[8] INUTAKE, M., et al., in Fusion Reactor Design and Technology (Proc. 3rd IAEA TCM and Workshop, Tokyo, 1981), Vol. 1, IAEA, Vienna (1983) 429.
[9] KESNER, J., POST, R.S., McVEY, D.M., SMITH, D.K., Nucl. Fusion **22** (1982) 549.
[10] RYUTOV, D.D., STUPAKOV, G.V., Fiz. Plazmy **4** (1978) 50; Sov. J. Plasma Phys. **4** (1978) 278.
[11] INUTAKE, M., et al., in Plasma Physics and Controlled Nuclear Fusion Research (Proc. 9th Int. Conf. Baltimore, 1982), Vol. 1, IAEA, Vienna (1983) 545.
[12] YATSU, K., et al., Phys. Rev. Lett. **51** (1983) 388.
[13] YAMAGUCHI, N., AOKI, S., et al., in preparation.

DISCUSSION

D.E. BALDWIN: During plugging, do you see a profile in ion end loss current? And do you at the same time see improvements in other parameters, such as central cell density and electron temperature?

M. INUTAKE: Yes, we have measured the ion end loss profile. Before plugging, the ion loss flux has its peak on the axis, while during strong plugging it has a hollow profile with a strongly suppressed loss region about 20 cm in diameter and a moderately plugged annular region of 28 cm outer diameter mapped into the central cell. A slight increase in central cell line density has been observed during plugging.

T. OHKAWA: If $\tau_{\parallel}$ becomes much longer as a result of end plugging, and if $\tau_{\perp}$ is longer than $\tau_{\parallel}$, the plasma density should increase with end plugging. So why was only a small density increase observed?

M. INUTAKE: In the shot I showed, the total end loss current just before strong plugging is 7 A for the core plasma ($d \leqslant 28$ cm). The core plasma volume

is about 800 litres. The line density increase during the 3 ms strong plugging period is estimated as follows:

$$\Delta n \times \ell = \frac{\text{(loss flux)} \times \text{(plugged period)} \times \text{(core plasma diameter)}}{\text{(charge)} \times \text{(core plasma volume)}}$$

$$= \frac{7(\text{A}) \times 3 \times 10^{-3}(\text{s}) \times 28(\text{cm})}{1.6 \times 10^{-19}(\text{c}) \times 8 \times 10^{5}(\text{cm}^3)} = 4.6 \times 10^{12}\ \text{cm}^{-2}$$

This increment is 25% of the central cell line density and agrees reasonably well with the slight increase observed.

R.S. PEASE: What is the energy confinement time of the plasma in the central cell?

M. INUTAKE: The energy loss of the central cell ions is dominated by charge-exchange because the plasma is sustained by gas puffing in the central cell. The charge-exchange time is 1 to 2 ms in the central cell. Investigation of the detailed power balance in GAMMA 10 will be a task for the future.

TARA AND CONSTANCE B MIRROR CONFINEMENT EXPERIMENTS AND THEORY*

R.S. POST, M. GERVER, J. KESNER, J.H. IRBY, B.G. LANE,
M.E. MAUEL, B.D. McVEY, A. RAM, E. SEVILLANO,
D.L. SMATLAK, D.K. SMITH, J.D. SULLIVAN, J. TRULSEN**,
A. BERS, J.W. COLEMAN, M.P.J. GAUDREAU, R.E. KLINKOWSTEIN,
R.P. TORTI, X. CHEN, R.C. GARNER, D.L. GOODMAN,
P. GOODRICH, S.A. HOKIN
Plasma Fusion Center,
Massachusetts Institute of Technology,
Cambridge, Massachusetts,
United States of America

Abstract

TARA AND CONSTANCE B MIRROR CONFINEMENT EXPERIMENTS AND THEORY.

The axisymmetric TARA central cell has been heated using aperture and double half-turn ICRF antennas to produce stable plasmas with $\beta \leqslant 0.2\%$. Parameters suitable for startup of thermal barriers with $n = 3.5 \times 10^{12} \cdot cm^{-3}$ and $Ti_{\perp} \approx 30$ eV have been reached. Hot electron plasmas with $\beta \leqslant 15\%$ are obtained in the TARA and Constance quadrupoles. Electron cyclotron instabilities are analysed. A new scheme for single frequency drift pumping with stochasticity by ICRF is proposed. ICRF modulated at the electron bounce frequency is shown to yield stochastic parallel electron heating for thermal barriers.

TARA [1] is a tandem mirror (Fig.1) in which the central cell is bounded by axisymmetric plug cells which in turn are connected through a transition to quadrupole min-B anchor cells. The TARA design provides for axisymmetric central cell ion confinement with MHD stability to be provided by a low-density, hot electron anchor [2]. The ion axisymmetric central cell is operated at a mid-plane field of 2 kG which gently tapers to 15 kG in the present experiments or to 30 kG for plugging experiments. End plugging will be provided by 120 A of 20 kV neutral beams injected at 40° from the axis for the formation of sloshing ions. Axial confining potentials will be generated by strong ECRH diffusion of the electrons in the outer sloshing-ion peak. ECRH is provided by two 28 Gc gyrotrons and coupled to the plasma with coaxial cavities with a polarizing radiating grill which illuminates the plasma uniformly. Magnetically trapped electrons heated at the bottom of the plug mirror by separate 28 Gc gyrotrons at 2 ω_{ce} will provide the thermal barrier [3] necessary to prevent excessive flow

* Research sponsored by US Department of Energy Contract No.DE-AC02-78ET51013 and in part by NSF Grant ECS 82-13430.

** University of Tromsø, Norway.

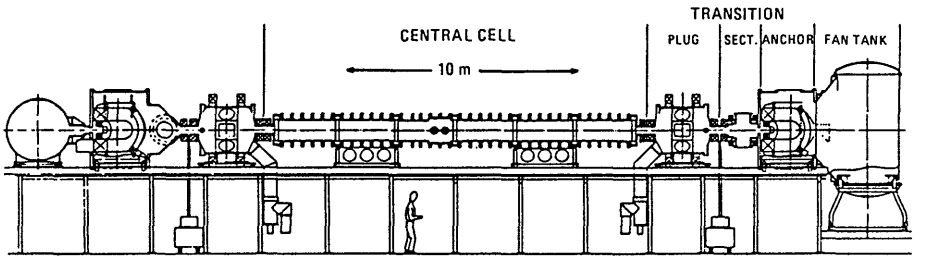

FIG.1. TARA tandem mirror.

of the lower-temperature central cell electrons from penetrating the outer high-potential plugging peak.

The plug is mapped through an 80 cm transition to the 110 cm, R = 2, quadrupole anchor operated at a midplane field of 4.8 kG. The high-β anchor plasma is produced by ECRH heating in a cavity. Coupling of this high-β_H hot electron plasma to low frequency central cell/plug flute-like fluctuation is to be made via a finite-β, ICRF-heated, core ion population. In this way the effective beta is calculated [3] to be $\beta^* = \beta_H/(1 + (\beta_H \Delta/\beta_C R))$. Thus $\beta^* \rightarrow \beta_H$ for $\beta_C \gg \beta_H \Delta/R$, the Van Damm-Lee limit for the EBT problem. The experimental plan of TARA has been divided into two phases. The present phase involves RF heating using ECRH and ICRF to start up the central cell to the necessary parameters to achieve thermal barrier operation. Testing the macroscopic stability of the TARA configuration is also under way. The second phase, to begin in 1985, will involve central cell plugging outlined above. Since the present experiments do not employ axial plugging, the $n\tau$ value cannot exceed those of simple mirrors.

CENTRAL CELL STARTUP

RF heating experiments have been performed in the central cell of TARA. Low power ECH (<5 kW) is used for pre-ionization of a fast gas puff, and high power ICRF heating (100–600 kW) is used to build up the plasma density and energy content. Two ICRF antennas are employed. A rectangular-aperture antenna consists of two rectangular windows located on opposite sides of a long conducting cylindrical tube with an interconnecting slot. This arrangement has low inductance, about 0.5 μH, which results in a low-Q match for variation in plasma density over an order of magnitude. For 500 kW coupled through the antenna, the peak voltages are below 7 kV. The second antenna is a double half-turn loop. Both antennas have adjacent limiters and no Faraday shield. The antennas are located in the uniform magnetic field region of the central cell.

Typical parameters for the aperture antenna at 250 kW are $\beta = 0.1\%$, $\bar{n} = 10^{12}\,cm^{-3}$, $T_\perp$ (ion) ~ 50–100 eV, $T_\parallel$ (ion) ~ 0.1–0.2 keV, and T_e ~ 20–60 eV, filling a central cell volume of 420 litres.

For the aperture antenna at a fixed radiofrequency, a magnetic field scan indicates that build-up of plasma density and energy occurs over the range ($0.75 \leqslant \omega/\omega_{ci} \leqslant 1.05$). The range of operation is skewed to lower ω/ω_{ci}, suggesting that excitation of the ion cyclotron wave may assist the density build-up from less than 10^{11} to 10^{12} cm^{-3}. At $\omega \geqslant \omega_{ci}$ and at higher densities, the antenna plasma coupling is through near-field heating and excitation of an m = 1 fast wave. A gas puff variation shows that for a given power there is an optimal gas flow rate (4–8 torr·L·s^{-1}) to maximize the energy content of the plasma.

The plasmas generated by the aperture antenna have radial density profiles that are flat. The density drops toward zero at the limiter (r = 15 cm) for $n = 10^{12}\,cm^{-3}$. The electron temperature profile as measured by swept Langmuir probes is 15 eV on axis rising to > 60 eV inside the limiter. Radial profiles of the ion saturation current suggest that the ion temperature peaks on axis. The radial potential profiles, as measured by emissive probes, and end loss analysers indicate that the potential profile is flat or slightly hollow. Measurements of energy content from diamagnetic loops and power input to the antenna yield a global energy confinement time of 0.4 ms. Measurements of gas flow, density decay at RF turnoff indicate a corresponding particle confinement time of 1–2 ms. With inverted profiles during ICRH, the net current on axis is positive, corresponding to net transport of ions inward or electron outward with $\tau \cong 10$ ms. At lower density ($n \sim 2 \times 10^{11}\,cm^{-3}$), the current changes sign corresponding to $\tau \sim 4$ ms. Large currents to limiters (on the order of tens of ampères) are observed, being largest on the limiter closest to the antenna. The dominant power loss mechanism is charge-exchange. Surface plasma direct electron heating is evident by detuning from resonance ($\omega = 1.1\ \omega_{ci}$) and observing that high power is coupled to the plasma (> 400 kW) with no significant ion heating. In this case, a large electron current (40 A) to the limiter was observed, indicating surface electron heating.

When the double half-turn antenna is used to further heat the plasma generated by the aperture antenna, the desired startup parameters are achieved: $\beta = 2.5\%$; $n_c \approx 3.5 \times 10^{12}\,cm^{-3}$; $T_{\perp i} \approx 620$ eV. When 400 kW are coupled to the plasma, we have observed a maximum β of 0.2% at $n_e \approx 3 \times 10^{12}\,cm^{-3}$. The time dependence of β, $\overline{n_c \ell}$ and the global energy confinement time are shown in Fig.2 for 170 kW on the slot and 130 kW on the loop antenna and a gas input of 16 and 2 torr·L·s^{-1} into the central cell at R = 4 at the north and south ends, respectively. The particle τ is computed for the plasma core for $r \leqslant 5$ cm in Fig.2(d) from the line density and the end loss measured by Faraday cups. In this shot, the density in the central cell on its north end was twice as high as on the south side. The asymmetry across the slot antenna can be controlled by varying the gas puffing. The north and south net currents from the core are shown in Figs 2(g), (h) as well as the calculated non-ambipolar radial loss times. Note that the sign of the

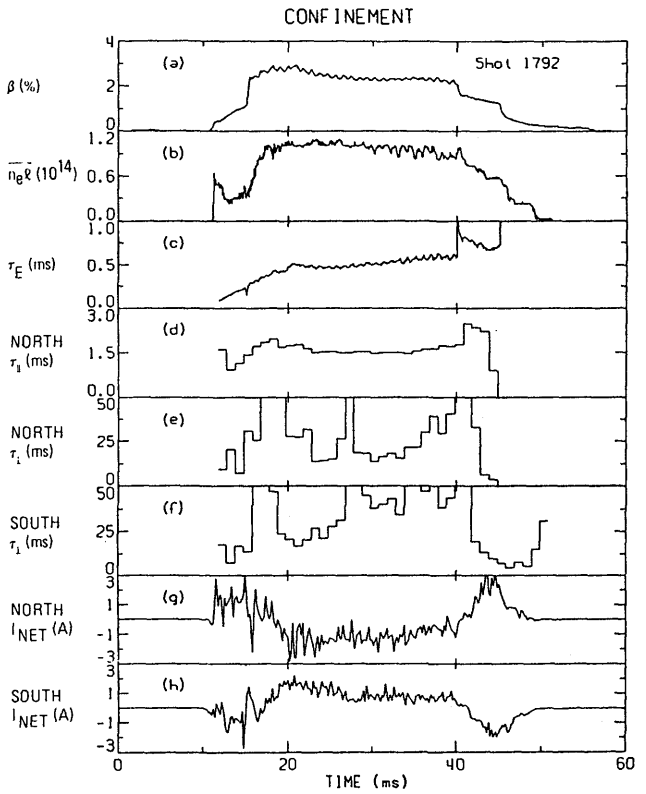

FIG.2. Central cell fundamental ICRF heating results. The aperture antenna is turned on at 10 ms and off at 45 ms; the double half turned on at 15 ms and off at 40 ms.
(a) Central cell β. (b) Central cell midplane line density.
(c) Central cell energy confinement time $\tau_E = nk(T_e + T_i)\,vol/P_{RF}$.
(d) Central cell particle confinement time measured by north end loss:

$$\tau_\parallel = eL_c \int_{R=15\,cm} dA\, n_c \Big/ \left(\frac{2B_{ec}}{B_w} \int_{R=15\,cm} dA\, J_i\right)$$

(e), (f) North and south non-ambipolar perpendicular confinement times measured from net current using the form of the equation in (d) except that the integral is over the core $r < 5$ *cm and* J_i *is replaced by* $|J_{net}|$.
(g), (h) North and south net currents from central cell core.

TABLE I. ANCHOR PLASMA PARAMETERS: SHOT No. 1567

Parameter	ECH only	ICRH 30 ms
Density, n_A	2×10^{11} cm^{-3}	7×10^{11} cm^{-3}
T_e (hot electrons)	200 keV	200 keV
Beta	15%	15%
T_i	$<$100 eV	$>$1 keV

TABLE II. ICRH IN BOTH ANCHORS: FUELLING EFFECTS

Fuelling location	n_A north anchor (cm^{-3})	n_A south anchor (cm^{-3})	n_c central cell (cm^{-3})
North end of central cell	7×10^{11}	1×10^{11}	1.5×10^{12}
South end of central cell	2.4×10^{11}	5×10^{11}	1×10^{12}
North and south	7×10^{11}	5×10^{11}	1.5×10^{12}
No ICRF in central cell	7×10^{10}	5×10^{10}	$<10^{11}$

net currents is opposite. Either there is no radial current and therefore no radial non-ambipolar loss or opposite species are lost radially on opposite sides of the slot antenna.

HOT ELECTRON ANCHOR

In TARA we seek stability against low-m MHD modes and other curvature and rotationally driven modes by a quadrupole minimum-|B| cell located outside the plug cells. This anchor cell is pressure-weighted by a high-β electron component and a low-β ICRF-heated core plasma. The anchor plasma is built up from a low pressure hydrogen gas puff ($P_{H_2} \approx 10^{-6}$ torr) by a 3 s long, 1.6 kW, ECH pulse at 14 GHz. The parameters achieved as measured by microwave interferometers, diamagnetic loops, bremsstrahlung X-rays and end loss analysers are summarized in Table I. The full density is obtained in about 10 ms of breakdown. The hot electron component grows more slowly, corresponding to half the total density. The stored energy rises linearly over 3 to 4 s to the 10–15% β level. After that time, we initiate ICRF startup of the central cell and anchors for a period of about 30 ms.

The response of the anchor plasma to the application of ICRF power ($P \cong 50$ kW at $\omega = \omega_{ci}$) depends on the presence of the loss stream from the central cell as a plasma source. In the presence of sufficient central cell loss flux, the anchor density is increased by the ICRF from $n_e < 5 \times 10^{11}\,cm^{-3}$ to $n_e > 10^{12}\,cm^{-3}$. This is interpreted as heating the streaming particles in the 'loss cone' region of the anchor velocity space, diffusing them into the magnetically trapped region, consistent with the observed limit $n_A \leqslant n_{cc}$. In these experiments the location of the central cell gas fuelling provides a strong end-to-end asymmetry. Build-up of an anchor density using ICRF is only possible when a gas feed is present on the corresponding end of the central cell. This result is summarized in Table II and is consistent with the existence of a potential rise in the vicinity of the ICRF antenna due to either a ponderomotive or ambipolar potential. As noted in Table II, a lack of central cell build-up (no ICRH) results in a decrease in n_A during anchor ICRH. The density drop may reflect weak confinement of the intermediate energy ions needed to fuel the magnetically trapped population.

Ion heating by the anchor ICRH is evidenced by an increase in the average energy of end loss ions from $\langle E_i \rangle < 200$ eV to $\langle E_i \rangle > 1$ keV and by detection of energetic charge-exchange neutrals from the anchor plasma. With these anchor parameters, $\beta_C \approx 0.2\%$.

STABILITY

The central cell with β up to 0.2% is macroscopically stable for the ICRF pulse length but is observed to have fluctuations. The plasma column is limited to a 15 cm radius by four limiters along its length inside a conducting wall of 25 cm radius. The fluctuation level in the central cell is not well correlated with the presence or absence of an anchor plasma with $\beta_H = 15\%$ and $\beta_C = 0.2\%$. Stable equilibria are obtained even if the anchor magnetic field is shut off and the plug volume is used to expand the field lines. Under a range of fuelling and heating conditions and with grounded limiters, the edge (R = 12 cm) fluctuations vary from $\delta n/n \lesssim 5\%$ to 25%. The fluctuation frequency ranges from 5 to 8 kHz with m = 1 and is not flute-like. At higher plasma potential, the mode shifts to a 12 kHz, m = 1 mode and is flute-like. Both modes rotate in the E X B direction. A 1 kHz oscillation m = 0 appears to be a relaxation oscillation which occurs on the τ_p time-scale owing to antenna loading interactions with the equilibrium parameters.

The stability of the central cell does not appear to be related to the sign of $\omega - \omega_{ci}$ and does not show the behaviour of ponderomotive stabilization of Phaedrus. Stability is strongly influenced by the limiter bias. A negative bias (-250 V $\rightarrow$ 50 V) decaying in 5 ms causes the plasma to be unstable (Fig.3(a)) for the plasma duration. A positive bias causes the plasma to be quiescent (Fig.3(b)).

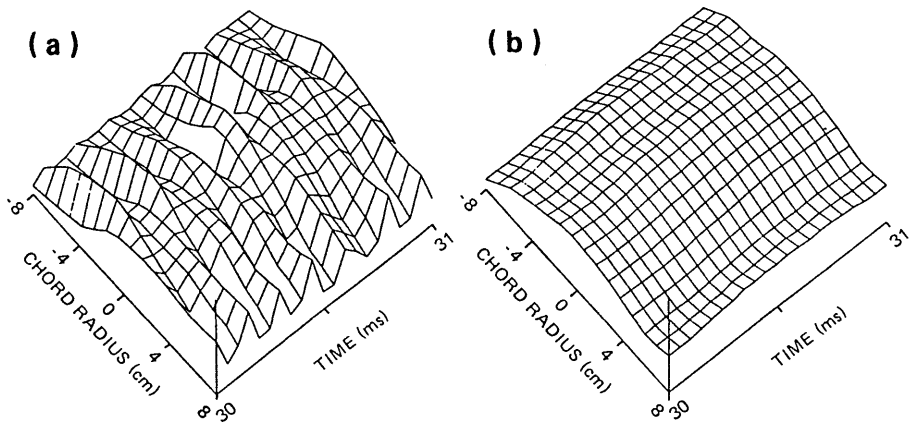

FIG.3. Chord measurements of Cu II radiation in the central cell versus time. (a) An unstable case with initial negative limiter bias. (b) A stable case with positive bias. The 1 kHz oscillation is caused by transmitter loading interaction.

These data were taken under the same conditions as Fig.2. In the unstable case, τ_E and τ_p drop by two.

The ICRF-heated plasmas have $P_\perp/P_\parallel \approx 10$ to 30. Although the axial profile is not well known, estimates of the central cell MHD growth time yield about 10 μs. Thus, we might expect a loss of the stability due to flute modes for both the ICRF-heated phase and the decay, contrary to observations. The effect of finite Larmor radius (FLR) is significant with $\rho/R \approx 6$ to 10. Under conditions of a long low-curvature mirror cell, the FLR term should stabilize all $m > 1$ [4].

CONSTANCE B EXPERIMENT

In the Constance B quadrupole mirror experiment, hot electron plasmas are generated using fundamental ECRH. Constance B is a minimum-B device with a midplane magnetic field 3200 G, mirror ratio 2.1, and a mirror length 80 cm. Using 3 kW of ECRH power, hot electron plasmas with $\beta \lesssim 30\%$ and $T_{eh} \gtrsim 200$ keV are obtained. This plasma makes possible the study of physics issues relevant to thermal barriers of reactors and MFTF-B. In particular, hot electron heating and stability, thermal barrier pumping via stochastic ion bounce resonance and radial potential control can be examined. Positive ambipolar potentials of up to 500 V have been measured when 3 kW of ECRH are applied. Isolation of the plasma from the walls through a 75-fold expansion of the flux area yields low end-wall generation of electrons which would otherwise reduce the potential. Using

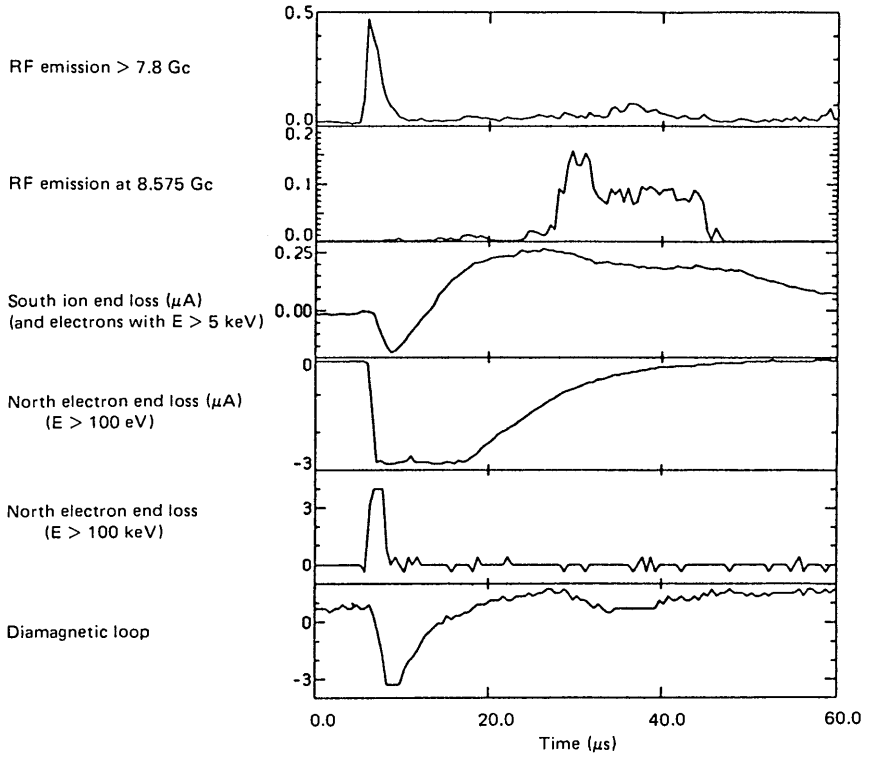

FIG.4. Correlations of signals during RF burst.

600 W of ECRH at 11.0 GHz, the potential is approximately 120 V, the ion temperature is 30 eV, the electron temperature is about 100 V, and densities of (2–3) X 10^{11} cm^{-3} are measured with an interferometer. Hard X-ray measurements indicate a 200 keV hot electron temperature. The shape of the spectra implies that the hot electron distribution function falls off slightly slower with energy than a Maxwellian. The hot electron temperature undergoes a linear growth in time (300 keV/s) while the ECRH is on.

Hot electron microinstability has been observed for frequencies between 7.8 Gc and 9.2 Gc with a midplane cyclotron frequency of 9.0 Gc and an applied heating frequency of 11.0 Gc. Bursts of RF emission occur and correlate with bursts of electron end loss, ion end loss, ion radial loss, diamagnetism fluctuations, and potential fluctuations (Fig.4). These bursts typically last from 1 to 5 μs. They recur at intervals of approximately 1 ms as long as the ECH power is on. The electron end loss current during a burst is typically ten times larger than the current between bursts. For electrons greater than 100 eV this

ratio is as high as 50. The energies of the electrons contained in the end loss bursts have been measured to be as high as 7000 eV; the average energy of electrons in a burst is about 3000 eV. The ion energy measured at the end wall increases from 20–30 eV without bursts to as high as 500 eV during a burst. The total energy loss during a burst, as measured either by the end loss analyser or diamagnetic loop, is 1 mJ. The total plasma energy is 20 J.

THEORY

Ions which collisionally trap in the end plugs of a tandem mirror must be pumped out to maintain the potentials necessary for a thermal barrier. This can be achieved through diffusion of low energy ions driven radially by a perpendicular δB which resonates with their bounce motion. When a single-frequency δB is applied, transport occurs only in a narrow layer where $\omega = \omega_b$. Outside this resonant layer, ion motion is superadiabatic. One method to induce radial transport throughout the plasma is to apply a sufficient number of frequencies so that resonant layers overlap [5]. Recent theoretical work at MIT indicates that a resonant layer may be substantially broadened by the application of ICRH, thus allowing pumping with the use of only a single frequency. The resonant width scales as $E^{2/3}$ where E is the ICRH field amplitude.

The bounce and ICRH frequency fields are generated in the same box-shaped slot antenna. For Constance parameters, 40 kW at the bounce frequency and 3 kW of ICRH are used. As a drift pump application in a tandem mirror, two phased antennas would be needed to eliminate the portion of the $k_\parallel$ spectrum which resonates with passing ions, to avoid ICRH trapping into the thermal barrier.

We have studied the possibility of bounce-resonance electron heating using a frequency modulated (FM) low frequency electrostatic wave (ESW) for plug potential generation in thermal barrier tandems. We consider the one-dimensional motion of electrons trapped in a static well and being perturbed by an FM-ESW:

$$m \frac{d^2z}{dt^2} = -\epsilon \sin(k_0 z) - eE_0 \sin(kz - \omega t - \delta \sin(\omega_m t))$$

where ϵ is the potential, and δ and ω_m are the modulational index and frequency, respectively. The product $\delta\omega_m$ is the bandwidth. It is well known that for an ESW perturbation the electron motion becomes stochastic around the phase-space location of its phase velocity for some critical E_0. However, for an FM-ESW with $\omega/k \gg V_e$ and $eE_0 \ll \epsilon$, with V_e the thermal speed, there exist values of ω and δ for which there is another distinct region of phase-space stochasticity located inside the confining potential and far away from the wave phase velocity. The trapped electron distribution function in the plug can be significantly modified

without affecting the passing electrons. The transition takes place for $\omega_b - \delta\omega_m \leqslant \omega \leqslant \omega_b + \delta\omega_m$ where $\omega_b = (\epsilon k_0/m)^{1/2}$ is the bounce frequency (which is in the ICRF range). The width of the stochastic region is proportional to $\delta\omega_m$. The best results are obtained for the lower value of ω. The value of δ determines the time the distribution function will take to flatten out in the stochastic regime. The approximate conditions for the onset of stochasticity are obtained analytically by using the Čerenkov resonance overlap criterion and agree favourably with the exact numerical solutions of the equation.

For TARA parameters, the electron distribution function in the plug region can be flattened for energies less than twice the thermal velocity on a time-scale small compared to the electron-electron collisional time. This requires an applied RF field of $E_0 \leqslant 0.2$ V/cm, $\omega = 3.7 \times 10^7 s^{-1}$, $\delta = 10$ and $\omega_m = 0.01\ \omega_b$ (corresponding to a bandwidth of 10% which can be achieved experimentally).

Electrons may be heated in the ECRH resonance in the fan and are lost when their perpendicular energy is equal to the potential drop between the ECRH resonance location and the end wall. The density in the well is determined by equating the ionization rate of neutrals by hot electrons to the ion loss rate. An electron which is electrostatically trapped, passing between the fan and the well but not reaching the ECRH resonance in the fan, will pitch-angle scatter until it reaches the resonance in a time τ_c. The electrons will then be rapidly heated by ECRH and lost. The potential drop between the mirror throat and the resonance in the fan is determined by requiring τ_c to be equal to an ion loss time. For Constance parameters this potential drop is comparable to T_i. For strong ECRH and low electron collision frequency, the electron will be lost once it reaches the resonance, in a time short compared to an electron collision time, so the electron distribution function will go almost to zero at this line in $\epsilon - \mu$ phase space. From quasi-neutrality the potential drop between the resonance and the end wall is found; the axial potential profile is a linear function of B. For Maxwellian electrons the axial potential profile is a logarithmic function of B. Both types of behaviour of the axial potential profile have been observed in different runs of Constance.

REFERENCES

[1] KESNER, J., POST, R.S., McVEY, B.D., SMITH, D.K., Nucl. Fusion **22** (1982) 549.
[2] KESNER, J., POST, R.S., SMITH, D.K., BALDWIN, D.E., LEE, Y.C., Nucl. Fusion **22** (1982) 577.
[3] BALDWIN, D.E., LOGAN, B.G., Phys. Rev. Lett. **43** (1979) 131.
[4] FERRON, J.R., HERSHKOWITZ, N., BREUN, R., GOLOVATO, S., GOULDING, R., Phys. Rev. Lett. **51** (1955) 1983.
[5] CHEN, Y.J., BALDWIN, D.E., HUA, T.Q., "Analytic model and simulations of RF drift pumping of thermal barriers", Meeting of Plasma Physics Div. of American Physical Society, Los Angeles, Nov. 1983, Poster 7Q11.

DISCUSSION

N. HERSHKOWITZ: Could you suggest what the mechanism which provides stability might be when ω is much less than ω_{ci}?

R.S. POST: We have no clear answer at present. We find that a finite Larmor radius (FLR) should stabilize all $m > 1$ owing to the great length of the central cell relative to the length of bad curvature. The question that needs to be answered is what causes the stability of $m = 1$. TARA has a closer wall than Phaedrus ($r_\omega = 25$ cm; $r_p = 15$ cm) and there are eight limiters in the central cell, which may affect $m = 1$ stability.

R.J. TAYLOR: How do you explain the apparent similarity between your results, namely good temperatures obtained without plugging, and the other experiments we have heard described, in which plugs are used?

R.S. POST: Although the parameters n and T_i are similar, other conditions are not necessarily the same. Phaedrus, for example, is not operated with plugging, and so similar parameters and $n\tau_E$ can be anticipated. The τ_E of TMX-U is an order of magnitude larger than that of TARA, but perhaps someone from the Lawrence Livermore Laboratory should tell you about plugging in TMX-U.

T.C. SIMONEN: In contrast to experiments in TARA, our TMX-U experiments have required end-plug plasma production for subsequent auxiliary heating of the central cell plasma. We have indications that a minimum amount of ion β is required in the end plugs to maintain central cell MHD stability.

R.S. POST: To return to the question, you have in any case to compare the total energy balance via $n\tau_E$ if your comparison is to be valid.

R.J. TAYLOR: I should just like to point out that, at present densities (mid-$10^{12}/cm^3$), τ_E tends to be dominated by charge-exchange rather than by end loss.

THEORETICAL STUDIES IN TANDEM MIRROR PHYSICS*

R.H. COHEN, S.P. AUERBACH, D.E. BALDWIN, J.A. BYERS, Y.-J. CHEN, B.I. COHEN, R.P. FREIS, J.M. GILMORE, J.H. HAMMER, T.B. KAISER, L.L. LODESTRO, B. McNAMARA, Y. MATSUDA, W.A. NEWCOMB, W.M. NEVINS, L.D. PEARLSTEIN, T.D. ROGNLIEN, J.W. SHEARER, G.R. SMITH, J.J. STEWART
Lawrence Livermore National Laboratory,
University of California,
Livermore, California

I.B. BERNSTEIN
Yale University,
New Haven, Connecticut

M.W. PHILLIPS
Grumman Aerospace Corporation,
Princeton, New Jersey

United States of America

Abstract

THEORETICAL STUDIES IN TANDEM MIRROR PHYSICS.

Recent developments in six areas of tandem mirror theory are explored. Specifically, finite Larmor radius (FLR) terms (including electric field drift) have been added to the authors' 3-D paraxial MHD equilibrium code. Their low-frequency MHD stability analysis with FLR, which previously included only $m_\theta = 1$ rigid perturbations, has been extended to incorporate moderate m_θ, rotational drive, finite-β effects on wall stabilization, and the well-digging effect of energetic electrons by using three computational techniques. In addition, the microstability of relativistic electrons with a loss-cone distribution has been examined, emphasizing the Whistler and cyclotron-maser instabilities. The authors have also studied techniques for controlling radial transport, including the floating of segmented end plates and the tuning of transition-region coils, and have quantified the residual transport in a tandem mirror with axisymmetric throttle coils. Earlier work on the effect of ECRH on potentials in thermal barrier cells has been extended. The transition between the weak and strong heating regimes has been examined using Fokker-Planck and Monte Carlo codes; an analytic model for the potentials relative to the end wall has been developed. Finally, investigation of drift-frequency pumping of thermal barrier ions has demonstrated that pumping is optimized when the magnetic fluctuation is perpendicular to both the unperturbed field and the thin fan, and that an adequate pumping rate is obtainable in future machines.

* Work performed under the auspices of the US Department of Energy by the Lawrence Livermore National Laboratory under contract number W-7405-ENG-48.

1. INTRODUCTION

In this paper we report on the status of recent developments in several areas of tandem mirror theory: magneto-hydrodynamic (MHD) equilibrium and stability, electron microstability, ion radial transport, electron-cyclotron resonant heating (ECRH), and drift pumping.

2. MAGNETOHYDRODYNAMIC EQUILIBRIUM AND STABILITY

2.1. MHD Equilibrium

In quadrupole tandem mirrors, field lines are nearly paraxial and thus MHD equilibrium equations are obtained by keeping leading-order corrections to an axisymmetric magnetic field. Similarly, FLR effects can also be computed as the leading-order correction to the same axisymmetric field. Because both corrections are second-order in their respective smallness parameters, they enter additively. Thus, by combining results from Ref. [1], we can construct the energy:

$$U = 1/2 \int \frac{dz}{B}\, d\psi d\theta \left\{ Q\, \vec{x}_z^{\,2} + Y\, \vec{x}_\theta^{\,2} \right\} \tag{1}$$

where $Q = B^2 + p_\perp - p_{\parallel}$ ($Y = -\rho\omega_M\omega_{GC}$) are the MHD(FLR) stresses, respectively, and $\omega_M(\omega_{GC})$ are the macroscopic and mean guiding-center frequency, respectively. The latter expression takes this simple form for an isothermal Maxwellian plasma. In Eq. (1), $x = (x,y)$ is the position of the field line and the subscripts refer to partials. The first variation of U, subject to the Jacobian constraint $1 - [x,y]B = 0$, produces the current balance equation:

$$B\frac{\partial}{\partial z}\frac{iQ}{B^2} = -\left[\frac{\partial Q}{\partial\psi}(x_\theta x_{zz} + y_\theta y_{zz}) + B\frac{\partial}{\partial\theta}\frac{i_{FLR}Y}{B^2} + \frac{\partial Y}{\partial\psi}(x_\theta x_{\theta\theta} + y_\theta y_{\theta\theta})\right] \tag{2}$$

where the parallel current per unit flux is

$$i \cong B([x_z,x] + [y_z,y]) \equiv B[x_{z\psi}x_\theta - x_{z\theta}x_\psi + (x\leftrightarrow y)] \tag{3a}$$

and, analogously,

$$i_{FLR} = B([x_\theta,x] + [y_\theta,y]) \tag{3b}$$

These equations--in addition to the lowest-order perpendicular pressure balance ($2p_\perp + B^2 = B_V^2$), parallel pressure balance,

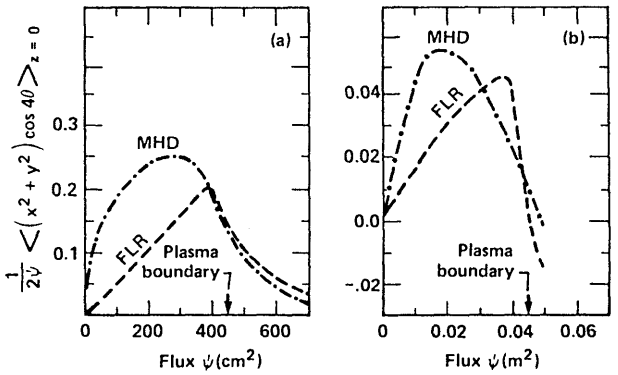

FIG.1. Octupole moment of flux surface versus flux $r^2/2$ at the midplane of the central cell with B normalized to unity. (a) TMX-U: $\beta_c = 0.35$, $\beta_p = 0.35$; (b) MFTF-B: $\beta_c = 0.15$, $\beta_p = 0.35$.

and the boundary conditions--determine the equilibrium. Both Q and Y must be positive for well-posed equilibrium.

The numerical procedure [2][1] is to assume isorrhopic pressure profiles $p(\psi,B)$, determine mod-B from the perpendicular pressure balance, and then analytically solve the Jacobian constraint to obtain an initial choice for the field-line trajectories. Subsequent motion of the field lines is incompressible ($d\vec{x}/dt = \nabla\phi \times \hat{z}$), and so Eq. (2) is linearized and integrated over z to generate an equation for $(B\phi)_z$. We solve, with Fourier transforms to eliminate aliases and resolve θ-derivatives, and obtain:

$$\phi(\psi,\phi,z) = \frac{1}{B}\left[\int_{\Theta}^{z} dz(B\phi)_z + \Lambda(\psi,\theta)\right] \tag{4}$$

The remaining function (Λ) is determined from the constraint that the line integral of the right side of Eq. (2) must vanish, producing an elliptic equation that is singular on the plasma boundary. Note that at intermediate stages of this iterative procedure the parallel current does not vanish at the ends. The field lines are moved and the linearization is repeated until Eq. (2) is satisfied, the constraint vanishes, and the parallel current at the ends is equal to zero. It should be pointed out that only Λ determines the motion of the flux surface at the midplane, which is predominantly an octupole motion.

---

[1] The form most suitable for quadrupole geometry is best obtained from the papers cited in Ref. [1].

For this study we assume that there is no radial electric field, consequently $Y = -\rho\omega_{*i}\langle\omega\nabla_B\rangle$, and because $\omega\nabla_B = 0(\beta)$, the FLR term is peaked on axis away from the plasma boundary. Thus, we find that the octupole distortion of the flux surface is limited more to the plasma surface when the FLR terms are included. This is shown in Fig. 1 where we compare the octupole moment of the flux surfaces for the Tandem Mirror Experiment-Upgrade (TMX-U) and the Mirror Fusion Test Facility (MFTF-B). In this study there are 10 Larmor radii in the radial scale length, and the betas of the figure caption are peak values. The average beta is 44% of the peak. With FLR the overall distortion is smaller, the parallel currents flowing through the central cell are reduced, and the axisymmetry of the central cell is better preserved. Note that the relative octupole distortion in MFTF-B is significantly lower than in TMX-U, which was a design goal.

2.2. MHD Stability

In three significant computational efforts, the low-frequency MHD stability of both quadrupole and axisymmetric tandem mirrors has been examined using standard FLR theory [1], which combines paraxial and FLR expansions. The ballooning, interchange and rotational stability of TMX-U, MFTF-B, the Mirror Advanced Reactor Study (MARS), Phaedrus, TARA, and proposed axisymmetric configurations has been addressed. These studies have defined beta limits and determined the requirements on magnetic curvature, plasma pressure and ambipolar potential profiles for stability.

The MHD stability studies using the TEBASCO code [3] generally are limited to the rigid ($m_\theta = 1$) displacement because it has been shown that, in the absence of $\vec{E} \times \vec{B}$ rotation, FLR terms stabilized all but the lowest mode numbers [4]. Recently the theory of other low-mode numbers including rotation has been added. This theory assumes that the lowest radial mode for a given m_θ dominates--again a consequence of FLR. However, these studies are limited to sharp-boundary pressure profiles, a valid approximation because the modes examined are global. In addition, the ballooning equation for a rigid displacement has been modified to include an improved wall representation and diamagnetic effects; the latter introduces an important stabilizing term pointed out by Berk [5]. These two additions lead to higher central cell beta values on the stability boundary in TMX-U as well as in MFTF-B.

We have also initiated studies of wall stabilization in axisymmetric configurations to verify the stability criterion $\beta L_B^2/L_p^2 > 1$, where the subscripts refer to vacuum mod-B and the plasma scale lengths, respectively [5]. Typical results are shown in Fig. 2 where stability can be achieved for sufficiently high betas. Stability at lower beta requires

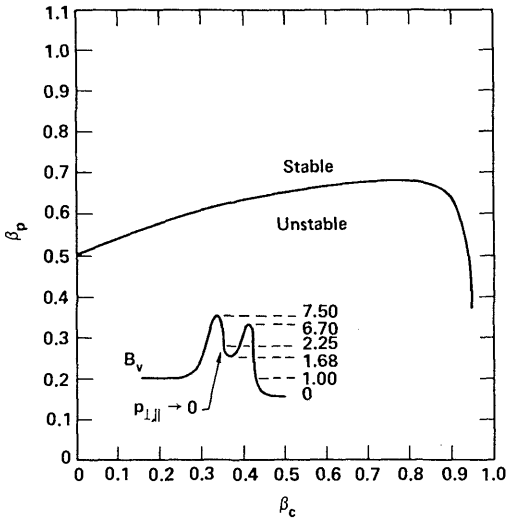

FIG.2. Beta stability diagram for a wall-stabilized, axisymmetric tandem mirror with $s_\beta = (R_w/R_p - 1)/2 = 0.2$ *and* $L_p \ll L_B$.

shorter plasmas. However, we expect that adiabaticity and/or anisotropy-driven modes may severely limit the possible parameter ranges for wall-stabilized axisymmetric mirrors.

The stability analysis of quadrupole tandems with FLR effects has also been addressed with a three-dimensional eigenvalue code. The associated Euler-Lagrange equations are solved using a Galerkin approach to determine the spectrum of complex-valued eigenfrequencies at low and moderate m_θ. However, there is no restriction on the form of the radial trial functions; thus the rigid approximation presumed in TEBASCO can be checked.

Growth rates and stability boundaries for ballooning, interchange and rotational modes in the low-beta TARA and Phaedrus configurations have been calculated. These results verify the strong stabilizing effect of FLR on curvature-driven ballooning modes: FLR indeed forces the mode to be rigid. As the FLR decreases, the mode becomes non-rigid and the coupling of higher angular components induced by the quadrupole coils becomes important. The $m_\theta = 1$ rigid mode is stable for the TARA and Phaedrus parameters, but the $m_\theta = 2$, $n = 0$ rotational mode is predicted to be most unstable. There is some corroborative evidence of this in Phaedrus experimental data (unpublished).

The FLORA MHD/FLR initial-value stability code integrates the Euler-Lagrange equations for the displacement of the

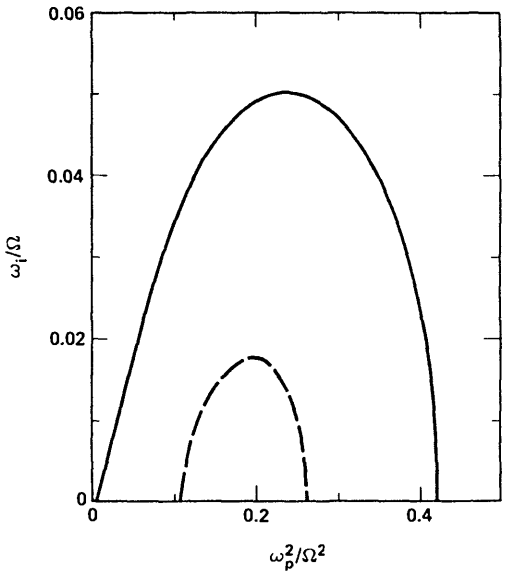

FIG.3. Growth rate of cyclotron-maser instability at $\vec{k} = 0$ as a function of density. The two curves contrast the results obtained with two different energy distributions. Parameters are $E/mc^2 = 0.15$, $\theta = 60^\circ$ and $n_{cold} = 0$.

magnetic field line using finite differences in (ψ,z,t) and Fourier-analyzing in θ. We determine the MHD stability of a finite-beta, paraxial, axisymmetric equilibrium without restriction on the mode structure. In fact, a rigid, energetic electron ring can be located in the anchor cells of the tandem to provide a stabilizing magnetic well [6]. Electron ring-stabilized, generic, axisymmetric, tandem-mirror configurations have yielded a central cell beta as large as 70%. Finally, we employed FLORA to study rotational modes with axial or radial shear in the equilibrium $\vec{E} \times \vec{B}$ rotation profile. For $m\theta = 1$ and large FLR, FLORA verifies the rigid mode behavior postulated in TEBASCO.

3. ELECTRON MICROSTABILITY

We study the linear stability of waves with frequency comparable to the electron-cyclotron frequency. The modes have a zero perpendicular wave number, and the plasmas are described by a loss-cone distribution f of relativistic electrons. In terms of the kinetic energy E and the pitch angle ϕ, we take $f = F(E)G(\phi)$ with $G(\phi) = 1$ for $\theta < \phi < \pi - \theta$ and zero otherwise, to allow analytic evaluation of one of the velocity-space integrals that appear in the dispersion relation for any F(E).

For the whistler instability, we agree with previous authors [7,8] that relativistic effects weaken the instability at mean electron energies $E > 0.1\ mc^2$. Realistic parameter regimes exist for which spatial growth of whistler modes are negligible in TMX-U and MFTF-B.

We find that the cyclotron-maser instability is sensitive to the shape of the energy distribution F(E). We contrast results obtained with $F_1(E)$, which approximates a step function (F_1 = const at low E, zero at high E), to those with the Maxwellian $F_2(E) \propto \exp(-aE)$. Figure 3 shows the temporal growth rate ω_i, normalized to the rest-mass cyclotron frequency Ω, as a function of ω_p^2/Ω^2 for F_1 (solid curve) and F_2 (dashed curve). Note that F_1 yields much higher growth rates, a higher maximum density, and a very low minimum density. Also, we find that the stabilizing effect of cold plasma is much stronger for distribution F_2 than for F_1.

4. ION RADIAL TRANSPORT

We examine two techniques for actively controlling ion radial transport: adjustment of transition-region coils to minimize the radial step and floating segmented end plates to control the electric field. In a tandem mirror with axisymmetric throttle coils separating the axisymmetric solenoid from the quadrupolar transition regions, solenoid ions fall down sizable magnetic and potential hills before entering the transition regions; consequently, these ions have $v_{\|} \approx v \approx$ const. We find the radial step per bounce Δr varies as $\Delta r \propto \sin 2\theta_{tp} \int dz\, \hat{\kappa}(z) \cos 2\delta\theta(z)$, where $\theta(z) = \theta_{tp} +(-)\ \delta\theta(z)$ is the azimuthal angle of an outgoing (incoming) ion, θ_{tp} is θ at the turning point, and $\hat{\kappa} \sin 2\theta$ is the geodesic curvature.

Although MFTF-B was designed to have $\int \hat{\kappa}\, dz \cong 0$ so that Δr is near zero if the azimuthal drift in the transition regions is negligible, azimuthal drifts defeat this cancellation and lead to unacceptably large stochastic (overlapping drift-bounce resonances) radial transport for MFTF-B parameters. The above expression for Δr suggests resetting the transition coils to make $\int dz\, \hat{\kappa} \cos 2\delta\theta = 0$. This retuning will depend on the self-consistent radial electric field E_r.

Another approach to transport control is to electrically insulate the field line ends. This forces end loss, and therefore radial loss, to be ambipolar. In current designs that have small electron diffusion coefficients, radial ion losses are reduced: readjustment of E_r leads to lower mobility, smaller $\int dz\, \hat{\kappa} \cos 2\delta\theta$, and fewer resonant particles experiencing quadrupole fields.

In TMX-U, insulated field-line ends are approximated by segmented floating end plates. We study these plates using

the radial transport code TMT. The effect of field-line errors is modeled as a finite conductance between adjacent plates proportional to the fractional magnetic flux connecting them. We simulate TMX-U with two and four concentric end-plate segments using resonant-plateau ion radial transport coefficients. In the ideal case (no field-line errors) with two segments, the ion particle confinement time in the central-cell core plasma is a factor of 2.0 larger when the plates are floating than when they are grounded. Field-line errors (7% connecting flux) reduce this factor to about 1.1. We note that these factors are comparable to the experimental values [9]. When five segments are used, the factors become 2.0 and 1.3, respectively.

Assuming that these control techniques are sufficiently successful to avoid stochasticity in MFTF-B, the dominant contribution to transport comes from a boundary layer separating particles trapped in the solenoid from those passing to the nonaxisymmetric cells. A drift-kinetic analysis gives the particle diffusion coefficient: $D \simeq 0.39\ a^2\ (\nu_{th} u_s/RL)^{1/2}$, where $a \equiv \Delta r/\sin 2\theta_{tp}$, ν_{th} is the ion pitch-angle scattering rate at speed $v = v_{th} \equiv (2T/m)^{1/2}$, R is the mirror ratio from the solenoid to the peak of the axisymmetric throttle, $u_s \equiv v_{th}(1-R^{-1})^{1/2}$, and L is the solenoid length. The implied radial lifetime for MFTF-B with zero radial electric field in the transition region is about 0.4 s.

5. ELECTRON-CYCLOTRON RESONANT HEATING

Electron-cyclotron resonant heating (ECRH) is used in the thermal barrier region of tandem mirrors to enhance the ion-confining, or plug, electrostatic potential. We have studied this process both analytically and numerically, using both a multi-region Fokker-Planck code and a Monte Carlo code. Recent calculations [10,11] show a more favorable scaling of plug-to-barrier potential Φ_{pb} when ECRH dominates collisional diffusion than in the opposite (weak ECRH) limit. When strong ECRH takes place at both the thermal barrier and the end plug but the diffusion at the barrier is stronger than at the plug, the following relation is obtained:

$$\Phi_{pb} = T_s \left(\frac{3}{4} \sqrt{\pi}\, \frac{R_{pb}^{-1}}{R_{pb}}\, \frac{n_p}{n_m}\, \exp \hat{\epsilon} \right)^{2/3} \tag{5}$$

where T_s is the solenoid electron temperature; R_{pb} is the plug-to-barrier mirror ratio; n_p is the plug density; $n_m = n_s \exp(-e\Phi_{sb}/T_s)$; n_s is the solenoid density; $\Phi_{sb} \equiv \Phi_s - \Phi_b$ (where Φ_s and Φ_b are the potentials of the solenoid and barrier relative to the end wall), $\hat{\epsilon} = e\Phi_{sb}/[T_s/(R_{mb}-1)]$; and R_{mb} is the mirror ratio from the solenoid mirror throat to the barrier.

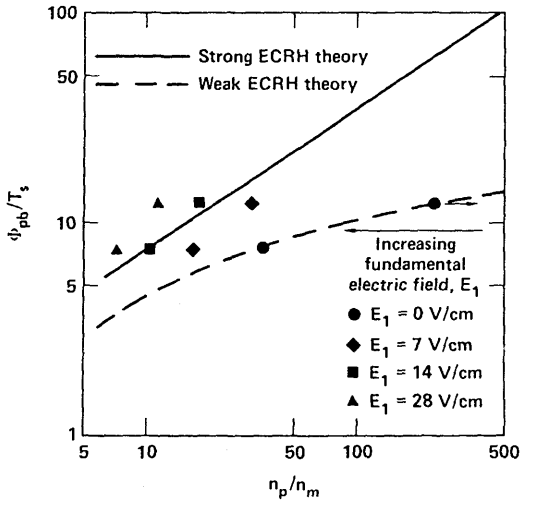

FIG.4. Potential between the thermal barrier and end plug versus plug density. Data points are Fokker-Planck code results showing the transition from weak to strong ECRH regimes.

The power law relation between Φ_{pb} and n_p replaces the logarithmic relation [12] valid for weak ECRH. The numerical solutions to the Fokker-Planck equation show (Fig. 4) the transition between Eq. (5) and the weak ECRH limit as the level of ECRH is varied. The ECRH power found at this transition agrees with an analytic estimate [10]. The strong ECRH limit should be accessible for power levels available in TMX-U.

In early experiments on TMX-U at low end-cell density ($n \sim 5\times10^{11}$ cm^{-3}) and even lower solenoid density, a large plasma potential ($\sim$1 keV) resulted when the plug ECRH was applied. We ascribe this potential rise to the increased loss caused by plug electrons diffusing rapidly along their ECRH characteristics. At higher energy, these characteristics come closer together, and a small-angle scattering places electrons on characteristics intersecting the loss region, causing immediate loss. A model of this phenomenon gives the predicted loss rate $\nu_e = \nu_p(\Phi_s) + \tau_{rf}^{-1}(\Phi_b)$, where ν_p is the Pastukhov [13] loss rate and $\tau_{rf} \simeq \tau_{ee}\,\Phi_b/2E_h$. Here τ_{ee} is the electron angle-scattering rate and E_h is the hot electron energy. When equating ν_e to the ion loss rate, potentials of the order of 1 keV are obtained.

6. DRIFT PUMPING

Drift pumping is the use of RF fields to remove potential trapped ions by transporting them radially to the

plasma halo where they are lost by axial flow and/or by increasing their parallel energy so that they are no longer trapped. Both heating and transport require that the RF field resonate with one of the natural frequencies of ion motion. To preserve the ion magnetic moment, the axial bounce frequency ω_b or the drift frequency ω_d is preferred.

We identify the resonant frequencies as $\omega = k\omega_b \pm m\omega_d$; $k,m = 0,1,2...$ for two RF field configurations--one with the magnetic fluctuations perpendicular ($B_\perp$) and the other parallel ($B_\parallel$) to the unperturbed field. For a simplified B model, we have derived analytically and verified numerically the requirement of resonance overlap for producing stochasticity. In general, stochasticity depends on the frequency spectrum and amplitude of the applied field in combination with properties of ion motion in the equilibrium field. For $m = 1$ and $B_\perp$, the diffusion coefficient is optimum when $\vec{B}_\perp$ is perpendicular to the thin fan, then scaling as $D \approx [\kappa_y B_\perp (2W_\parallel + W_\perp)]^2/\Delta\omega$, where κ_y is the curvature normal to the thin fan and $\Delta\omega$ is the bandwidth of the RF field. The resulting pumping rate is marginal for TMX-U but safe for MFTF-B and MARS.

Unless $B_\parallel$ can excite a parallel electric field, it appears that $B_\parallel$ is less effective than $B_\perp$. There are advantages of applying the RF field at the drift frequency resonance; i.e. $k = 0$: (1) unwanted trapping can be induced by breaking the axial bounce invariant $J = \int ds\, v_\parallel$ by the ω_b resonance, and (2) pumping impurities can be accomplished if the drift is predominantly electric field drift.

REFERENCES

[1] NEWCOMB, W.A., Ann. Phys. **81** (1973) 231; J. Plasma Phys. **26** (1981) 529.

[2] McNAMARA, B., US–Japan Third Workshop on 3-D Simulation, Oak Ridge Natl Lab., 1984, Lawrence Livermore Natl Lab. Rep. UCRL-90437 (1984).

[3] BULMER, R.H., et al., "Gyrokinetic equilibrium and stability in quadrupole tandem mirrors", Plasma Physics and Controlled Nuclear Fusion Research 1982 (Proc. 9th Int. Conf. Baltimore, 1982), Vol. 1, IAEA, Vienna (1982) 531.

[4] NEVINS, W.M., BALDWIN, D.E., KAISER, T.B., PEARLSTEIN, L.D., in Proc. Annual Controlled Fusion Theory Conf. Austin, Texas (Sherwood), 1981, Paper No. 3A1.

[5] BERK, H.L., in Proc. Annual Controlled Fusion Theory Conf. Incline Village, Nevada (Sherwood), 1984, Paper No. 1B1.

[6] D'IPPOLITO, D.A., MYRA, J.R., OGDEN, J.M., Plasma Phys. **24** (1982) 707.

[7] GLADD, N.T., Phys. Fluids **26** (1983) 974.

[8] TSANG, K.T., to be published in Phys. Fluids **27** (1984).

[9] HOOPER, E.B., BALDWIN, D.E., FOWLER, T.K., KANE, R.J., TURNER, W.C., Phys. Fluids **27** (1984) 2264.

[10] COHEN, R.H., Phys. Fluids **26** (1983) 2774.

[11] MATSUDA, Y., ROGNLIEN, T.D., Phys. Fluids **26** (1983) 2778.

[12] COHEN, R.H., BERNSTEIN, I.B., DORNING, J.J., ROWLANDS, G., Nucl. Fusion **20** (1980) 1421.
[13] PASTUKHOV, V.P., Nucl. Fusion **14** (1974) 3;
COHEN, R.H., RENSINK, M.E., CUTLER, T.A., MIRIN, A.A., Nucl. Fusion **18** (1978) 1229;
NAJMABADI, F., CONN, R.W., COHEN, R.H., Nucl. Fusion **24** (1984) 75.

DISCUSSION

R.J. GOLDSTON: It seems to me that, with five segmented rings, it is possible to impose a radial electric field in only four narrow regions with width of the order of the Debye length. How does this affect overall confinement?

R.H. COHEN: The radial electric field is not being imposed anywhere, but it must readjust everywhere so that the net current crossing the flux-surface bounding rings will be zero. The current across intermediate flux surfaces is generally non-zero. The flux across the boundary flux surfaces is thus of the ambipolar form I showed in my presentation, and this in turn has a significant impact on the confinement time for the entire region covered by plates.

NEW RESULTS OF GAS-DYNAMIC TRAP RESEARCH

I.A. KOTEL'NIKOV, V.V. MIRNOV, V.P. NAGORNYJ,
D.D. RYUTOV
Institute of Nuclear Physics,
Novosibirsk,
Union of Soviet Socialist Republics

Abstract

NEW RESULTS OF GAS-DYNAMIC TRAP RESEARCH.

The gas-dynamic trap (GDT) is an axisymmetrical magnetic mirror cell which has a very large mirror ratio and whose length exceeds the effective free path of ions in relation to scattering in the loss cone. The authors describe their findings after analysing two possible applications of the gas-dynamic trap: as a full-scale thermonuclear reactor and as a neutron source for technological testing of materials. – The main disadvantage of using the GDT as a reactor is its great length. The authors suggest a way of reducing the length of the trap by adding some additional magnetic mirror cells of specially chosen length on either side. It is shown that when K magnetic mirror cells are added, the loss rate decreases by K + 1 times. This enables the length of the device to be reduced by the same number of times. Some aspects of the physics of the GDT reactor are also examined. – A compact 14 MeV neutron source based on a GDT could be created for technological research. The source involves using a two-component plasma: a relatively cold main (deuterium) plasma and a plasma with slight fast tritium ion impurity. Oblique injection of fast tritium ions makes it possible to obtain a significant local strengthening of the neutron flux close to the reflection points of the fast ions.

1. INTRODUCTION

The gas-dynamic trap (GDT) described by Mirnov and Ryutov [1, 2] is a magnetic mirror cell with a large mirror ratio $R \gg 1$ and with a length L which satisfies the condition

$$L \gg \lambda_{ii} \ln R/R \qquad (1)$$

where λ_{ii} is the Coulomb mean free path of the ions. Given condition (1), the confinement time of the plasma in the GDT is determined by the simple gas-dynamic estimate (corresponding to the escape time of a gas from a vessel with a small aperture):

$$\tau \approx RL/\sqrt{(T_e + T_i)/M} \qquad (2)$$

where T_e and T_i are the temperatures of the electrons and ions, respectively, and M is the ion mass.

An important advantage of the GDT is the fact that microfluctuations which may develop in the plasma (which constitute a serious danger for many other types of open trap) have no effect on estimate (2).

Another feature of the GDT [1, 2] is that the MHD stability of the plasma in it can be guaranteed within the axisymmetrical plasma configuration. This is possible thanks to the relatively high density of the plasma near the mirror, located in the region of 'favourable' curvature of the field lines and having a stabilizing effect on the system as a whole (more details are given by Nagornyj et al. [3]).

The prospects of a thermonuclear reactor based on a GDT have been discussed by Mirnov, Ryutov and Nagornyj [1, 2, 4, 5]. The key element and also the most complex element of such a reactor is the mirror coil, which has to create a magnetic field with a strength of several hundred kilogauss. One factor which makes it somewhat easier to solve this problem is that such a strong field is needed in a volume with a diameter of only 10 cm and a length of 10–20 cm. There are reasons to believe that in such a volume it would be possible to create a field with a strength of 450 kG [6]. In this case, the GDT reactor parameters where $Q = 3$ are the following: length 5 km, plasma diameter 0.7 m, plasma density $2 \times 10^{14}\,\mathrm{cm}^{-3}$, magnetic field strength at the homogeneous region 15 kG, $\beta = 0.7$, power of the heating systems 5 GW. The length of the system seems somewhat daunting but it should be recalled that it contains a simple axisymmetrical solenoid with a field of only 15 kG. Nevertheless, it would be desirable to reduce it (and the heating power) by three to five times. One possible way of doing this, involving several additional magnetic mirror cells on either side of the device, is discussed in Section 2.

That section also shows the effect of neutral-beam injection on the MHD stability of the plasma which is important for gas-dynamic traps with additional magnetic mirror cells. The levels of accuracy required in producing the magnetic system are also described.

Section 3 examines the possible application of the GDT as a 14 MeV neutron source for technological testing of materials. The source would be based on oblique injection of fast tritons into a relatively cold target deuterium plasma. Such a scheme enables high neutron fluxes to be obtained at a relatively low injection power.

The physics of gas-dynamic traps can be studied without violating the necessary conditions of similitude, on a relatively small experimental device. Section 4 discusses physical experiments which need to be carried out on a model device.

2. THERMONUCLEAR REACTOR BASED ON A GDT

2.1. Reduction of reactor length

The length of the GDT reactor can be reduced if one extra magnetic mirror cell is added to each side with a length which satisfies condition (1) and having very short ('point') mirrors:

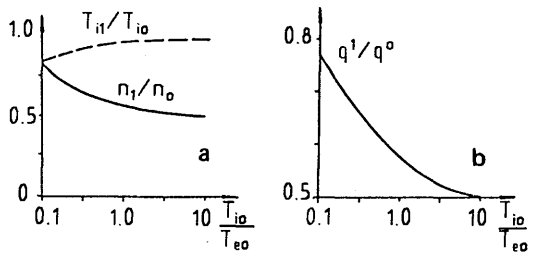

FIG.1. Dependence of parameters of GDT with one additional mirror cell on temperature ratio of ions and electrons, T_{i0}/T_{e0}, in central mirror cell. (a) Graph of the ratio n_1/n_0 (continuous line) and T_{i1}/T_{i0} (broken line). "0" indicates values in central mirror cell and "1" those in additional cell. (b) Particle flux q^1 from GDT with additional mirror cell in relation to flux q^0 from simple GDT.

$$L_M \ll \lambda_{ii} \ln R/R \tag{3}$$

Here, L_m denotes the distance over which the magnetic field grows from minimum to maximum. In the case of such additional mirror cells, the particle balance in each of them has the form:

$$(n-\tilde{n})\, v_{Ti} \approx \tilde{n}\, v_{Ti} \tag{4}$$

where n and $\tilde{n}$ are, respectively, the plasma density in the main trap and in the additional mirror cells. The left-hand side of Eq.(4) determines the influx of plasma from the main magnetic mirror cell to the additional one. The right-hand side of the equation determines the plasma flux from the additional magnetic mirror cell to the expander. The magnetic field strength in all the mirrors is, of course, the same. From Eq.(4) it follows that $\tilde{n} \cong n/2$. Therefore the loss of plasma from the system is reduced by a factor of two. It must be stressed that this conclusion is valid only when the dimensions of the mirror cells are large enough and the length of the mirrors satisfies the inequality (3) (if the mirror cell is too short the particles incident upon it freely drift into the opposite mirror; if the mirrors are too long the plasma behaves like an ideal fluid).

To obtain a quantitative result, we must examine the particle exchange between the main and additional magnetic mirror cells taking into account the ambipolar electrical field occurring close to the mirror 'necks'. The calculations are close to those put forward by Mirnov and Ryutov [2]. The results are given in Fig.1. The figure shows that in the range of ratios of T_i/T_e ($1 < T_i/T_e < 2$) which is of practical interest, the particle fluxes and energies are indeed reduced by a factor of approximately two.

To reduce λ_{ii} and thereby make it easier to comply with condition (1) with a moderate length of the additional mirror cells, it is possible to introduce a certain quantity of impurities into them with $Z \approx 10$, thereby increasing Z_{eff}.

Estimates show that, when $Z_{eff} = 3$, the length of the additional mirror cells can be reduced to 30 m. In such conditions, the bremsstrahlung it still not large.

Reasoning along similar lines shows that the addition on each side of the trap of two mirror cells reduces the losses by approximately three times, three cells by four times and so on [7].

The introduction of additional mirror cells could create particular complications involving reduction of the maximum (in relation to the excitation of ballooning modes) value of β. However, this effect is neutralized by the stabilizing action of neutral-beam injection (see Section 2.2).

2.2. The effect of neutral-beam injection on the MHD stability of plasma

When the plasma absorbs a neutral-atom flux, the atoms transfer their pulse to it. This may affect the MHD stability of the plasma. For the sake of clarity, the estimates of this effect will be given for a GDT without additional mirror cells.

Let us assume that a narrow tube of force with cross-section ΔS moves as a whole in radial direction at a distance ξ_* (ΔS and ξ_* relate to the homogeneous part of the device). In the new position, the tube will be surrounded by a plasma with different density and temperature values. Therefore, absorption of neutrals into it will be distinguishable from absorption into the surrounding plasma and an uncompensated radial force will begin to act on the tube:

$$f_0 \approx \frac{\Delta S L \xi_*}{a^2} M n_0 v_0^2$$

where M, n_0, v_0 are the mass, density and velocity of the neutral atoms (we assume that the length of neutral absorption is of the order of the radius of the plasma a). From the material balance condition in the initial equilibrium state we have:

$$2\pi a L n_0 v_0 \approx \frac{2\pi a^2}{R} n v_{Ti} \tag{5}$$

from which

$$f_0 \sim \frac{\Delta S \xi_*}{aR} m n v_{Ti} v_0 \approx \frac{\Delta S \xi_*}{aR} \frac{v_0}{v_{Ti}} p$$

where p is the plasma pressure.

On the other hand, the force determined by the curvature of the field lines which acts on the tube is

$$f_1 \approx \frac{\Delta S \xi}{a} \frac{a^2}{L_m} p \tag{6}$$

where L_m is the length of the mirror. The force f_1 is a source of flute instability. Comparison of Eqs (5) and (6) reveals that the effect of neutral-beam injection is significant when

$$L_m > aR \frac{v_{Ti}}{v_0} \tag{7}$$

Usually, v_0 exceeds v_{Ti} by a factor of two to three, so that condition (7) is relatively weak.

The symbol f_0 and, accordingly, the symbol of the effect (stabilizing or destabilizing) depends on the size and direction of the density and temperature gradients of the plasma. The stabilization condition has the form

$$\frac{\partial |q_\perp|}{\partial n} \frac{\partial n}{\partial r} + \frac{\partial |q_\perp|}{\partial T} \frac{\partial T}{\partial r} < 0$$

where $|q_\perp|$ is the absolute radial pulse absorbed per unit time per unit volume of plasma. This condition is met provided that the plasma parameter distributions are not too exotic.

This stabilizing effect is particularly significant when additional mirror cells are included and there is the risk of ballooning modes occurring associated with the appearance of additional regions of unfavourable curvature.

2.3. Limitations of indefiniteness in the magnetic field

Non-axisymmetric distortions of the magnetic field may have a marked effect on plasma equilibrium and transverse transport.

Let us begin by looking at the question of equilibrium. Of course, we assume that the magnetic system in the homogeneous part of the device is such that the drift of the field lines associated with the errors is small in comparison with the plasma radius. In this case the main source of plasma equilibrium distortions are non-axisymmetric defects in the magnetic field at the expanders. They result in the emergence of longitudinal currents. These currents flow into the central part of the device and perturb the field there. The longitudinal currents can be estimated by a method similar to that used in the theory of non-axisymmetric tandem traps [8]. The condition which guarantees that the magnetic field of these currents does not lead to noticeable drift of the field line to the homogeneous region has the form

$$\max \frac{1}{a} \left| \frac{\partial \ell}{\partial \varphi} \right| \ll \frac{Ra}{\beta L}$$

where a is the plasma radius at the centre of the trap, ℓ is the length of the field line region from the mirror to the plasma receptor in the expander, φ is the angle of azimuth.

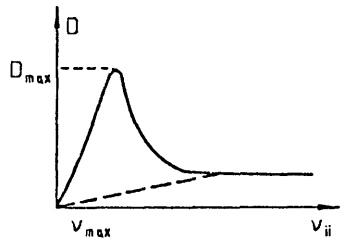

FIG.2. Approximate graph showing dependence of diffusion coefficient on frequency of ion-ion collisions: the continuous line relates to the case where $\beta = 0$ and there is no electrical field, the broken line to $\beta \approx 1$.

The distortion of the field lines caused by the flow of longitudinal current and by the presence of defects in the magnetic system in the central part of the GDT leads to radial wandering of the particles as a result of drift in the non-uniform field. Therefore, the diffusion coefficient may become higher than its 'classical' value,

$$D_{c\ell} \approx r_{ii}\nu_{ii}\,(m/M)^{1/2}$$

At relatively low collision frequency ν_{ii}, the main contribution to diffusion is associated with losses of particles whose longitudinal velocity is so small that they are trapped between the local maxima of the magnetic field module at the field line. Figure 2 shows an approximate graph of the diffusion coefficient D against the collision frequency ν_{ii}. The maximum value of D in the region of low ν_{ii} is governed by the trapped particles. The value of the maximum depends on the perturbation of the field Δb, and its characteristic length ℓ (along the axis of the trap):

$$D_{max} \approx r_{Li}v_{Ti}(\Delta ba/\ell B_{min})^{3/2}$$

The maximum is reached when

$$\nu_{ii} \approx \nu_{max} \approx (\Delta b/B_{min})^2\,\frac{r_{Li}v_{Ti}}{\ell^2}$$

Given the expected parameters of the GDT reactor, the frequency ν_{ii} appears to be significantly greater than ν_{max}. Therefore, the limitations on the size of perturbation are not very severe. The condition that the diffusion coefficient does not exceed $D_{c\ell}$ has the form:

$$\Delta b/B_{min} < \sqrt{\nu_{ii}\ell/v_{Ti}}\;(m/M)^{1/4}$$

3. NEUTRON SOURCE BASED ON A GDT

3.1. Energy characteristics

For small-scale devices – such as neutron sources – a two-component GDT variant with a relatively cold main (deuterium) plasma and plasma with a slight fast tritium ion impurity may be of particular interest. The tritium ions participate in reactions with the deuterium nuclei, thereby generating neutrons, and also serve as an energy source for the main plasma.

A characteristic of the two-component variant is that the injected ions are slowed down by the electrons much more quickly than they are scattered by the plasma ions. Hence, their angular distribution does not differ greatly from the angular distribution of the primary neutrals, which can be made quite narrow. This means that considerable local increase of the neutron flux density can be obtained (see below), which is of interest for fast accumulation of the necessary dose of neutron radiation during technological testing of materials.

The deuterons receive energy from the electrons and their temperature is several times lower than that of the electrons. The particle and energy losses from the trap are therefore determined by the electron temperature T_e (see (2)); in this case the particle flux q and energy flux W in the mirror are equal [2, 9].

$$q \approx 0.61\, n\sqrt{T_e/M_D}, \quad W \approx 3.64\, n\, T_e \sqrt{T_e/M_D} \tag{8}$$

where n is the deuteron density at the centre of the trap, and M_D is their mass. If we define the power injected into the trap as P_{inj}, we can write the following energy balance equation:

$$2W \frac{B_{min}}{B_{max}} \pi a^2 = P_{inj} \tag{9}$$

where a is the plasma radius in the homogeneous magnetic field region. For a given plasma density, Eq.(4) enables us to find the electron temperature.

It is convenient to characterize the state of the plasma in the neutron source by dimensionless parameters

$$\beta = 8\pi n T_e / B_{min}^{(v)^2}, \quad N = a/r_{Li}, \quad R = B_{max}/B_{min}^{(v)} \tag{10}$$

where $B_{min}^{(v)}$ is the vacuum magnetic field at the homogeneous region of the trap and ν_{ii} is the Larmor radius of the deuterons calculated for the magnetic field weakened as a result of diamagnetism of the plasma:

$$r_{Li} = \frac{M_D c}{e B_{min}} \sqrt{\frac{\pi T_e}{2M_D}} \tag{11}$$

$$B_{min} = B_{min}^{(v)} \sqrt{1-\beta} \tag{12}$$

It should be noted that B_{min} occurring in Eq.(9) should also be calculated from Eq.(12).

Since the inequality $T_e \gg T_i$ holds, we shall calculate the Larmor radius of the ions from the electron temperature – the same value ν_{ii} also occurs in formulas determining the excitation conditions of drift turbulence.

Assigning values for the injection power P_{inj} and the magnetic field strength in the mirror B_{max},[1] and with the dimensionless parameters R, β and N, it is possible to find the basic plasma parameters: T_e and a. We will put the corresponding formulas in 'practical' units:

$$T_e = \left(\frac{P_{inj}\, R \sqrt{1-\beta}}{65\, \beta N^2} \right)^{2/3} \tag{13}$$

$$n = 2.5 \times 10^{13} \beta \frac{B_{max}^2}{R^2 T_e} = 4 \times 10^{14} \frac{B_{max}^2 N^{4/3} \beta^{5/3}}{R^{8/3} P_{inj}^{2/3} (1-\beta)^{1/3}} \tag{14}$$

$$a = \frac{5.8\, NR\sqrt{T_e}}{B_{max}\sqrt{1-B}} = 1.45 \frac{N^{1/3} R^{4/3}}{B_{max}[\beta(1-\beta)]^{1/3}} \tag{15}$$

Here, T_e is everywhere in keV, P_{inj} in MW, B_{max} in kG, a in cm and n in cm^{-3}.

At the low temperature of the main plasma which is characteristic of the two-component GDT regime, the fast-triton distribution function is formed as a result of the tritons being slowed down by the electrons. Here the maximum power $\mathscr{P}_N$ released per unit volume of plasma in the thermonuclear 14 MeV neutrons corresponds to an injection energy $W^* = 240$ keV [9]. Since we are interested in maximum production of neutrons, we take it that the injection is carried out at this energy. Taking this into account, we obtain the following formula for $\mathscr{P}_N$ (in which $\mathscr{P}_N$ is expressed in the same units as the power density introduced into the system $\mathscr{P}_{inj} = P_{inj}/\pi a^2 L$):

$$\mathscr{P}_N = 0.16\, T_e^{3/2}(\text{keV})\, \mathscr{P}_{inj} \tag{16}$$

We shall characterize the quality of the system as a neutron source by the magnitude of the neutron energy flux at the plasma surface:

$$Q_N = a\, \mathscr{P}_N/2 \tag{17}$$

---

[1] This value does not have to be adjusted to the plasma pressure since, in the mirror, β is always $\ll 1$.

TABLE I. SOURCE PARAMETERS WITH LIMITATIONS MENTIONED IN THE TEXT

No.	P_{inj} (MW)	B_{max} (kG)	R	Q_N ($MW \cdot m^{-2}$)	$Q_{N\,max}$ ($MW \cdot m^{-2}$)	L (m)	a (cm)	a_m (cm)	I_{0T} (equiv. A)
1	20	250	20	0.75	3.9	4	6.3	1.4	83
2	50	350	20	2.5	10.9	5	6.6	1.5	210

TABLE II. 'PHYSICAL' PARAMETERS FOR SOURCE VARIANTS

No.	β	R	N	$n(\times 10^{-14})$ (cm^{-3})	T_e (eV)	T_i (eV)	S^* (m^2)
1	0.05	20	17	2.7	580	75	0.26
2	0.04	20	25	4.2	760	82	0.28

Q_N can be expressed with the help of Eqs (13, 14) through 'external' parameters of the problem (B_{max}, L, P_{inj}) and the dimensionless 'physical' characteristics of the system (β, N, R)

$$Q_N(MW \cdot m^{-2}) = 3.84 \frac{P_{inj}^{5/3} B_{max} (1-\beta)^{5/6}}{L(m)\, R^{4/3} N^{7/3} \beta^{2/3}} \qquad (18)$$

In selecting the parameters β, N and R, care must be taken to ensure that the pressure of the fast particles is not too high: $\beta^* < 1$ (here and below the values relating to the fast particles are denoted by an asterisk); it should also be remembered that oblique injection is only possible at high values of R; N should not be small, as otherwise drift turbulence may develop in the system and lead to increased transport. The source parameters calculated with allowance for these limitations are given in Table I. For all the variants it is assumed that the injected particles are tritons, that the injection energy is 240 keV, that the angle of injection is $\theta^* = 1/3$ rad, and that the main plasma is deuterium. I_{0T} is the equivalent current of tritium neutrals, and a_m is the radius of the plasma in the mirror. The 'physical' parameters for the corresponding source variants are given in Table II.

The method of injecting neutrals at a small angle to the axis makes it possible to obtain a local increase in the neutron flux density in the region of transport from the homogeneous magnetic field of the central part to the mirrors, accompanied by an increase in the fast-particle density near the point of reflection. Calculations show [9] that the neutron flux density in the region of compression

increases by $\xi = (\theta^* \Delta\theta^*)^{-1/2}$ times, where $\Delta\theta^*$ is the half-width of the angular triton spread at half the injection energy: $\Delta\theta^* = 11\,(T_e/W^*)^{3/4}$. Table I gives the neutron fluxes in the region of increase: $Q_{N\max} = \xi Q_N$, and Table II gives the surface area of the plasma at these regions, S^* (the length of the regions was taken as one metre from each side).

The great advantages of this neutron source system are, first, that the region of neutron emission is separated from the mirrors (the reflection point of hot tritons lies in a field 2.5 times smaller than B_{max}), which simplifies the problem of shielding the strong field coils, and, secondly, that the radius of the plasma in the mirror does not exceed 1.5 cm, and therefore the maximum field can be created in a very small volume.

3.2. Microinstabilities in the plasma

Anisotropy of the distribution function of the injected ions may be a source of various kinetic instabilities in the plasma. The fact that the density of fast particles is small by comparison with the density of the main plasma makes it much easier to analyse these kinetic instabilities. If we consider that the plasma is homogeneous and we ignore the angular distribution of the fast particles, then the system is formally unstable in terms of Alfvén and magneto-acoustic wave excitation at the resonances $\omega - k_\parallel v_\parallel = \pm n\omega_{Hi}$. However, as is shown by calculations, the radial non-uniformity of the plasma leads to a rapid change in $k_\perp$ during propagation of the wave packet across the magnetic field. The packet inevitably spends a significant amount of time in the regions of $k_\perp$ values that correspond to wave damping, and their growth is stopped.

An additional stabilizing effect are ion-ion collisions, the frequency of which is quite high due to the low ion temperature.

It would be possible to show that hot ions should cause excitation of ion-acoustic instability due to the presence of counter ion fluxes moving along the field (oblique injection). It is easy however to show, by directly integrating the distribution function for transverse velocities, that this instability decreases in the longitudinal direction:

$$f(v_\parallel) = 2\pi \int f(v_\parallel, v_\perp)\, v_\perp dv_\perp \sim \frac{1}{|v_\parallel|} \tag{19}$$

In the case of such a distribution function Cherenkov resonances apparently cause wave damping.

4. EXPERIMENTAL MODEL OF A GAS-DYNAMIC TRAP

The gas-dynamic trap, like many other types of open trap, is characterized by a long uniform magnetic field region and not too large a parameter of

$N \equiv a/r_{Li}$. This may be important in terms of the effect on excitation of drift turbulence in the plasma and on anomalous transverse transport. Therefore, it would be useful to conduct a preliminary experimental study of anomalous transport at a facility where the basic dimensionless characteristics of the plasma (β, N, L/a, λ_{ii}/L) are close to those characteristic for a GDT thermonuclear reactor. This could be done at a relatively small experimental facility with a plasma injection power of up to 0.5 MW. The length of such a facility could be 10 m, with a plasma diameter of 30 cm and magnetic field strength in the uniform part of about 2–3 kG and in the mirrors of 200 kG. The anticipated plasma parameters are: $T_i = 0.3$ keV, $T_e = 0.4$ keV, $n = 3 \times 10^{13}\,cm^{-3}$.

At such a facility the possible role of plasma rotation under the influence of a radial electrical field could be studied. This effect is potentially very dangerous for long open traps. The axisymmetry of the device enables the radial profile of the electric field to be controlled by dividing the end plates of the facility into sections.

REFERENCES

[1] MIRNOV, V.V., RYUTOV, D.D., Pis'ma Zh. Tekh. Fiz. **5** (1979) 678.
[2] MIRNOV, V.V., RYUTOV, D.D., in "Voprosy atomnoj nauki i tekhniki", Termoyadernij sintez **1(5)** (1980) 57.
[3] NAGORNYJ, V.P., RYUTOV, D.D., STUPAKOV, G.V., Prepr. Inst. Nucl. Phys. Siberian Branch of the USSR Academy of Sciences (1983) 83.
[4] MIRNOV, V.V., NAGORNYJ, V.P., Prepr. Inst. Nucl. Phys. Siberian Branch of the USSR Academy of Sciences (1982) 83.
[5] RYUTOV, D.D., Proc. Course on Mirror-Based and Field-Reversed Approaches to Magnetic Fusion, Varenna (1983) 72.
[6] MONTGOMERY, D.B., Poluchenie sil'nykh magnitnykh polej s pomoshch'yu solenoidov. Magnitnye i mekhanicheskie svojstva konstruktsij iz obychnykh i sverkhprovodyashchikh materialov. Mir, Moscow (1971) 359.
[7] VASIL'EV, Yu.V., MIRNOV, V.V., Prikl. Mat. Tekh. Fiz. **6** (1974) 14.
[8] STUPAKOV, G.V., Fiz. Plazmy **5** (1979) 871.
[9] MIRNOV, V.V., NAGORNYJ, V.P., RYUTOV, D.D., Prepr. Inst. Nucl. Phys. Siberian Branch of the USSR Academy of Sciences (1984) 84.

DISCUSSION

B.G. LOGAN: Did you consider Alfvén-type microinstabilities driven by the narrow tritium-ion angular distribution?

D.D. RYUTOV: The stability analysis for the homogeneous part of the device is greatly simplified by the fact that the hot ion density there is very low, so that one can use the perturbation technique. Using this technique, we have shown that the radial inhomogeneity of the magnetic field caused by a finite-β and the inhomogeneity in plasma density result in the smearing-out of the resonances with the interaction between the hot ions and Alfvén waves. The conclusion we draw is that the system is stable.

STABILIZATION OF AN AXISYMMETRIC MIRROR CELL AND TRAPPED PARTICLE MODES*

H.L. BERK, C.W. HORTON Jr., M.N. ROSENBLUTH, H.V. WONG
Institute for Fusion Studies,
University of Texas at Austin, Austin, Texas

J. KESNER, B. LANE
Plasma Fusion Center,
Massachusetts Institute of Technology,
Cambridge, Massachusetts

T.M. ANTONSEN Jr.
University of Maryland, College Park, Maryland

K.T. TSANG, X.S. LEE, B. HAFIZI
Science Applications Inc., Boulder, Colorado

J.A. BYERS, R.H. COHEN, J.H. HAMMER, W.M. NEVINS,
T.B. KAISER, L. LODESTRO, L.D. PEARLSTEIN, G.R. SMITH
Lawrence Livermore National Laboratory,
Livermore, California

H. RAMACHANDRAN
Department of Electrical Engineering and Computer Science,
University of California, Berkeley, California

W.M. TANG
Plasma Physics Laboratory, Princeton University,
Princeton, New Jersey

United States of America

Abstract

STABILIZATION OF AN AXISYMMETRIC MIRROR CELL AND TRAPPED PARTICLE MODES.

The criteria for the robust stabilization of axisymmetric tandem mirrors using wall stabilization and hot particle finite Larmor radius (FLR) effects are discussed. It is shown that a stable high-β system can be made compatible with the stability criteria for anisotropy-driven modes. The trapped particle mode formalism is extended to non-eikonal analysis. The effects of radial electric fields and dissipation are studied and it is found that: (1) previously stabilized modes are subject to dissipative instabilities; (2) trapped particle rotational instability is possible even for $m = 1$; (3) there is a new trapped particle mode, driven only by electric fields in the plug; (4) the FLR effect from sharp equilibrium profiles can improve stability.

* Research supported under contracts from the US Department of Energy.

1. GENERAL INTRODUCTION

In this paper we discuss two important stability questions in tandem mirrors. The first is how a symmetric tandem mirror can be stable to MHD modes by using wall stabilization and finite Larmor radius effects. The second topic is a discussion of trapped particle modes, especially in regard to the effect of plasma rotation and the instabilities induced by dissipation.

2. INTRODUCTION TO STABILIZATION OF SYMMETRIC TANDEM MIRRORS

We discuss how a plasma with a hot component and a nearby conducting wall can stabilize a symmetric tandem mirror system. In previous works summarized in ref. 1, it was found that although a hot component can decouple from the usual MHD response if the background core beta was sufficiently low, there exist many mechanisms for the plasma to destabilize due to negative energy perturbations, coupled to either positive energy waves, dissipation, or to their own self-consistent response. Thus, it would appear difficult to operate a hot plasma system stably in a reactor-relevant regime.

To achieve stability in a robust manner it is necessary to eliminate the source of negative energy. This can be achieved by invoking a sufficiently large finite Larmor radius effect coming from the perturbed parallel magnetic field which can stabilize all modes except the rigid m=1 perturbation. The m=1 mode relies on wall stabilization which, in order to be effective, requires a disc shaped hot plasma profile. We find that the stability criterion is identical to that derived for Astron [2,3], a single Larmor radius configuration, when parameters are expressed in terms of currents.

When robust stabilization is achieved, the Lee-Van Dam-Nelson [4] limit, β_{cr}, is no longer a stability limitation. For a core beta $\beta_c >> \beta_{cr}$, the hot component theory becomes identical with MHD. The correct analysis has now been performed for the MHD response of a radially rigid plasma mode enclosed by a conducting wall, and additional stabilizing terms are found when $\beta \sim 1$. Stability can be achieved at relatively low beta, if $P_{\parallel}/P_{\perp} << 1$. However, one still needs to assess anisotropy-driven instabilities, particularly that associated with the Alfvén-ion cyclotron (AIC) mode [5] (or in the case of hot electrons, the whistler-electron cyclotron mode). To stabilize this mode it is necessary to limit the axial scale length to 10-20 Larmor radii. The compatibility of AIC stability and magnetic moment conservation may then become an issue.

We present here a first attempt to assess all these effects, to find configurations compatible with MHD, anisotropy instability and orbit adiabaticity.

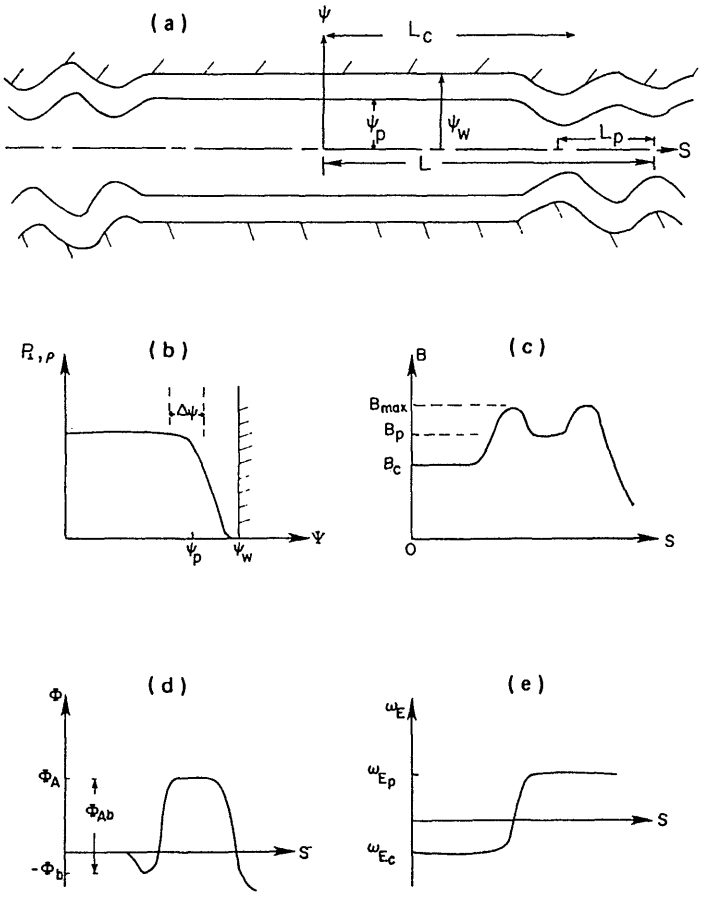

FIG.1. Tandem mirror geometry. (a) Flux tube shape of tandem mirror with conducting walls; (b) radial and pressure profile, (c) axial magnetic field variation; (d) axial ambipolar potential; (e) azimuthal rotational velocity.

3. ANALYSIS

We consider an azimuthally symmetric tandem mirror with a magnetic field $\underset{\sim}{B} = \nabla\psi \times \nabla\vartheta$, with ψ the magnetic flux and ϑ the azimuthal angle in a configuration shown in Figs 1(a) and 1(b). The standard ordering [6,7] that has been developed for treating the hot plasma problem is

$$1 >> \varepsilon \equiv \kappa/\left[\frac{r_p}{B}\frac{\partial P_{\perp h}}{\partial \psi}\right] \approx \frac{\omega}{\omega_{Bh}} \approx \frac{a_h^2}{r_p^2} \approx \frac{P_{\perp c}}{P_{\perp h}} ; \frac{\omega_{Bh}}{\omega_{bh}} \approx \frac{n_h}{n_c} \approx \varepsilon^2 \qquad (1)$$

where κ is the field line curvature, r_p the plasma radius, a_h the hot particle Larmor radius, the subscripts h and c refer to hot particles and background plasma respectively, ω_{Bs} is the grad-B drift of the sth species, ω_{bs} the bounce frequency, $P_{\perp s}$ the perpendicular pressure, and n_s the particle density. The stability analysis is based on the extremizing of a quadratic variational form for the linear amplitudes with the approximations of Eq. (1).

One finds that the perturbed Lagrangian magnetic field is $Q_L = B_{\parallel}+\underset{\sim}{\xi}\cdot\nabla B = C_j(\psi)\exp(im\vartheta)\partial P_{\perp h}/B\partial\psi$, where the subscript j refers to the jth region of the tandem mirror. The variational expression, including $\omega/\omega_{ci}\sim 1$ ($\omega_{ci} \equiv$ ion cyclotron frequency) and hot particle finite Larmor radius effects, then has the following form:

$$\pi \int \frac{d\psi ds}{B} \mathscr{L}(\Phi,C) = 0 \tag{2}$$

$$\mathscr{L}(\Phi,C) = -\omega^2\rho I(\Phi,C)+B(\Phi,C)-\Phi^2 D_c-(\Phi-C)^2 D_h+C^2 G+F\hat{LR}(\Phi,C) \tag{3}$$

$$\text{Inertia} \equiv I(\Phi,C) = \left(1-\frac{\omega^2}{\omega_{ci}^2}\right)^{-1}\left\{\frac{m\Phi}{rB}-\frac{\omega}{\omega_{ci}}\left[r\frac{\partial\Phi}{\partial\psi}-r\frac{(C-\Phi)}{B^2}\frac{\partial P_{\perp}}{\partial\psi}\right]\right\}^2 + \left[r\frac{\partial\Phi}{\partial\psi}+(\Phi-C)\frac{r}{B^2}\frac{\partial P_{\perp}}{\partial\psi}\right]^2$$

$$\text{Line Bending} \equiv B(\Phi,C) = \sigma\left\{\frac{m^2}{r^2}\left(\frac{\partial\Phi}{\partial s}\right)^2 + B^2r^2\left[\frac{\partial}{\partial s}\left(\partial\Phi/\partial\psi+\frac{(\Phi-C)}{B^2}\frac{\partial P_{\perp}}{\partial\psi}\right)\right]^2\right\}$$

$$\text{Hot Plasma Curvature Drive} \equiv D_h = \frac{m^2\kappa}{Br_p}\frac{\partial}{\partial\psi}(P_{\perp h}+P_{\parallel h})$$

$$\text{Background Plasma Curvature Drive} \equiv D_c = \frac{m^2\kappa}{Br_p}\frac{\partial}{\partial\psi}(P_{\perp c}+P_{\parallel c})$$

Lee–Van Dam and Precessional Mode Parameters $\equiv G$

$$= m^2\frac{\partial}{\partial\psi}\left(P_{\perp c}/B^2\right)\frac{\partial P_{\perp h}}{\partial\psi}+m\omega q_h B\frac{\partial}{\partial\psi}\left(n_h/B\right) \equiv D_h\left(\tilde{\beta}_c+\frac{\omega}{\omega_\kappa}\right)$$

Hot Particle FLR $\equiv F\hat{LR}(\Phi,C)$

$$= m^2\frac{\partial P_{\perp h}}{\partial\psi}\frac{\partial}{\partial\psi}\left(\overline{P_{\perp h}a_h^2B^2}\right)\left\{r^4\left[\frac{\partial}{\partial\psi}\left(\frac{C}{Br}\right)-\frac{\partial}{\partial\psi}\left(\frac{\Phi}{Br}\right)\right]^2+\frac{m^2-1}{B^4r_p^2}(C-\Phi)^2\right\}$$

with ρ the background ion mass density, q_h the hot particle's charge and $\overline{P_{\perp h}a_h^2B^2} = \left(M_hB^2/8\right)\int d^3v\, F_h\, v_{\perp}^4/\omega_{ch}^2$ with M_h the hot particle mass and ω_{ch} its cyclotron frequency and $\Phi = \underset{\sim}{\xi}\cdot\nabla\psi$.

If $\omega_B^2/\omega_b^2 \approx O(1/\varepsilon)$ a similar quadratic form can be derived, where now $C=C(\psi,s)$, and one additional term, $\mathscr{L}_1$, needs to be added to $\mathscr{L}$:

$$\mathscr{L}_1 = \frac{2}{m^2}\left(\frac{dC}{ds}\right)^2 \frac{q^2 h}{M_h} B \int d^3v v_\parallel^2 \frac{\partial F_h}{\partial \psi}/(v_\perp^2 \partial B/\partial \psi)$$

Then by taking variations, a fourth-order equation can be derived. However, if $\omega_{bh}^2/\varepsilon\omega_{Bh}^2 >> 1$, we find $dC/ds=0$, and Eq. (2) is recovered.

We now specifically consider the steep pressure profile shown in Fig. 1(b). If the finite Larmor radius term is relatively large, i.e. $\beta_h a_h^2 B^3 r_p^3/[\kappa(\Delta\psi)^3] >> 1$, only relatively long radial wavelength modes can be unstable. For m=1, the only possible unstable mode is a nearly rigid displacement. The equation has been analyzed for arbitrary beta in the MHD limit (i.e. when $C\to 0$ can be justified) and results will be discussed below. If $m\Delta\psi/\psi_p<1$, analysis have been performed in the limits $1>>\beta_h>>\varepsilon$, and $1>>\omega/\omega_{ci}$, L_p/L_c, $P_{\parallel h}/P_{\perp h}$. The dispersion relation, given in refs [8,9], describes a considerable number of effects including the description of hot particle dynamics when the MHD equations are not suitable, hot particle FLR effects, the coupling between plugs and central cell and dissipation due to shear Alfvén resonances in the gradient region.

The critical aspect of the dispersion relation is the sign of

$$\gamma_{MHDh}^2 \propto -|m|\int_0^L \frac{ds}{B^2 r_p} P_{\perp h}\left[\kappa(\psi_p) - \frac{\kappa_s}{|m|}\left(1+\frac{\psi_p^{|m|}}{\psi_W^{|m|}}\right) - \frac{(m^2-1)}{r_p B^3 \Delta\psi}\overline{P_{\perp h} a_h^2 B^2}\right] \quad (4)$$

where κ_s is the self-curvature produced by the plasma currents. If $\gamma_{MHDh}^2 < 0$, a robust stability arises independent of the parameter $\delta = \gamma_{MHDh}/\omega_\kappa + \bar{\beta}_c$. The stability arises from the $|m|=1$ mode as a result of only the external curvature contributing to the instability drive and the overcoming of this destabilizing influence by a conducting wall. The wall stabilization term is proportional to the product of self-curvature, κ_s, and ψ_p/ψ_w. For m>1, the total field line curvature tends to be the destabilizing drive, and the effect of the conducting wall is small. However, stability can arise from the distortion energy produced from finite Larmor radius.

If $\gamma_{MHDh}^2>0$, the conventional MHD instability condition is recovered if $\delta>>1$. For $\delta<<1$, a non-MHD analysis is required, and a "fragile" stability window may be present. However, one finds a negative energy mode at $\omega \simeq \omega_\kappa(1-\bar{\beta}_c)$, which is destabilized by the dissipation found from shear Alfvén resonance or by the interaction with a surface Alfvén wave when frequencies match.

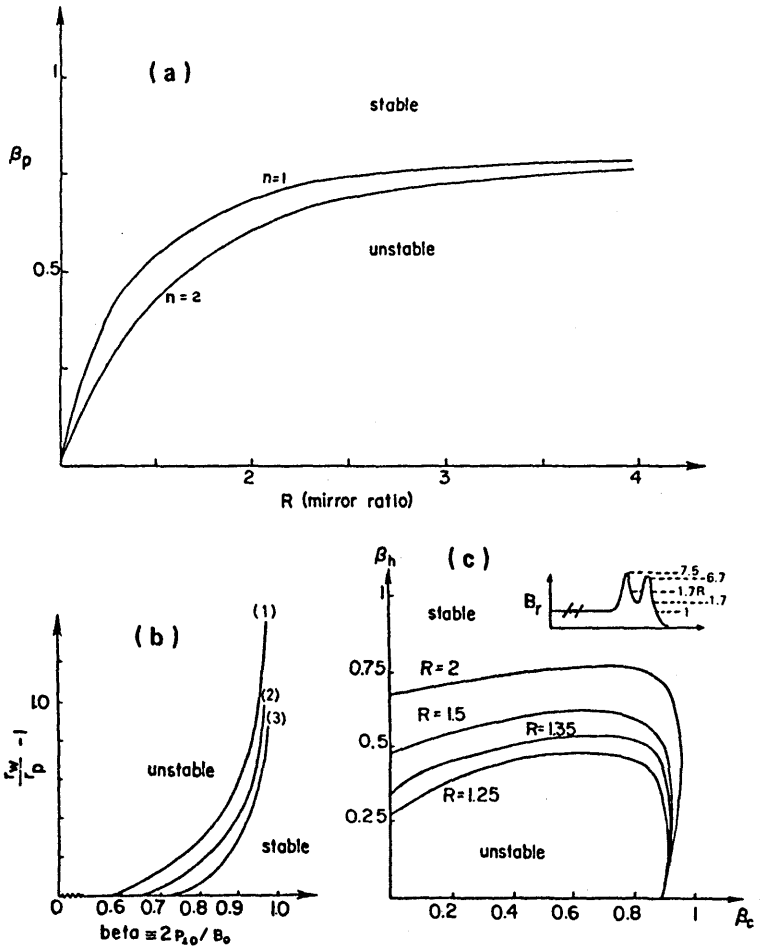

FIG. 2. (a) Marginal stability curves of plug beta versus mirror ratio. Magnetic field varies as $B_v = B_0(1 + s^2/L^2)$, *pressure as* $P_\perp = P_{\perp 0}[(R^2B_0^2 - B^2)/(R^2 - 1)B_0^2 + 2P_{\perp 0})]^n$. *Conductor is on edge of plasma.*

(b) Marginal stability curves as a function of wall conductor position for field variation $B_v = B_0[1 + 2(R-1)s^2/L^2 - (R-1)s^4/L^4]$ *and pressure profile* $P_\perp = P_{\perp 0}[(R^2B_0^2 - B^2)/((R^2 - 1)B_0^2 + P_{\perp 0})]^n$. *For curve (1)* $n = 2$, $R = 2$; *curve (2)* $n = 1$, $R = 2$; *curve (3)* $n = 2$ *(or 1),* $R = 4$.

(c) Marginal stability as a function of plug beta β_p *to central cell beta* β_c, *with conductor at plasma edge.*

Numerical investigations have also been made in the limit $\omega_{bh}^2/\omega_{Bh}^2<1$, with the eikonal approximation when $(m\Phi>Br^2\partial\Phi/\partial\psi)$ but with ω/ω_{ci} finite. If FLR and wall stabilization are not accounted for, the study shows that the shear Alfvén wave in the central cell is altered by ion cyclotron effects but that the system is still unstable to either the Alfvén–precessional mode interaction [10] or to the magnetic compressional instability [1].

For $\delta<<1$, more conventional MHD description with strong FLR describes the system. The energy, δW, for $|m|=1$ is found to be

$$\delta W = \int ds\{(1+\sigma\frac{B^2}{B_v^2})\frac{B_v}{B}[\frac{d}{ds}(\frac{\Phi B^{1/2}}{B_v^{1/2}})]^2+(\Lambda-1)(\frac{d\Phi}{ds})^2+(P_\perp+P_\parallel)\frac{(\kappa-\kappa_s)\Phi^2}{r_pB_v^2}\} \quad (5)$$

with $\Lambda=|\psi_W+\psi_p|/(\psi_W-\psi_p)$ and $B(s) = B_v(s)[1-\beta_\perp(s)]^{1/2}$. When $\psi_W \to \psi_p$

$$\delta W \geq \Phi^2 \int ds\{\frac{(\kappa-\kappa_s)(P_\perp+P_\parallel)}{B_v^2r_p}+\frac{(\frac{d\beta_\perp}{ds})^2[1+\sigma B^2/B_v^2]}{16(1-\beta_\perp)^2}\} \quad (6)$$

This form demonstrates stronger stabilization than Eq. (4) as $\beta_\perp \to 1$. In Figs 2(a)–2(c) numerical stability curves from Eq. (5) are given. These results demonstrate that at sufficiently high beta, the m=1 mode can be wall-stabilized. For $P_\parallel/P_\perp<<1$ the stabilization can even arise at relatively low beta.

The system may still be susceptible to anisotropy modes such as mirror modes or Alfvén–Ion Cyclotron (AIC) (or in the case of hot electrons, whistler–electron cyclotron instability). For some axial pressure profiles, such as $P_\perp \propto (B_{max}-B)^{3/2}$, one can readily show that at small mirror ratios, mirror mode and MHD stability are barely compatible. Other axial profiles, such as $P_\perp \propto (B_{max}-B)$ or $P_\perp \propto (B_{max}^2-B^2)$ will achieve MHD stability at beta values substantially below the mirror mode limit (in fact the latter profile is always mirror-mode stable). The AIC is insensitive to pressure profiles but is sensitive to the pitch angle cut–off of the distribution function. The beta threshold for absolute instability in infinite medium theory is considerably below the beta values needed for MHD–like stabilization. The beta threshold can be increased by considering finite axial geometry. The threshold is calculated using WKB phase-integral methods [5], and typical stability curves are shown in Fig. 3. For pressure profiles similar to $P_\perp \propto (B_{max}^2-B^2)$ one finds that the AIC threshold and MHD stability can be compatible even when a_h/L_B is not too large, where a_h is the hot ion Larmor radius in the interior

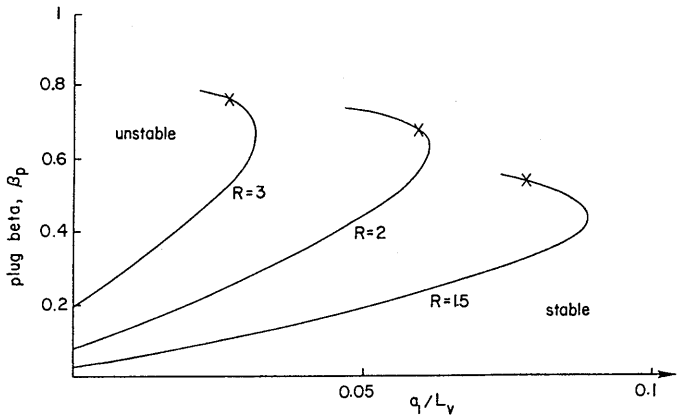

FIG. 3. Stability boundaries for AIC mode for various values of the confining mirror ratio R in a vacuum magnetic field $B = B_0(1 + s^2/L_v^2)$. a_i/L_v *is the ratio of ion Larmor radius to scale length in vacuum field. Roughly,* $a_i/[1-\beta_\perp)L_v]$ *is ion Larmor radius to axial scale length in self-consistent field. Crosses roughly indicate position of MHD stability.*

magnetic field $B=B_v(1-\beta_\perp)^{1/2}$, and $2/L_B^2 = (d^2B(0)/ds^2)/B(0)$. Typically, particle adiabaticity [11] is maintained for $a_h/L \lesssim .1(P_\perp/P_\parallel)^{1/2}$. Specific examples of the adiabaticity parameter at thresholds to MHD and AIC stability are: $R\equiv B_{max}/B_v(0)=3$, $\beta_\perp=0.75$, $a_h/L_B=0.09$; $R=4$, $\beta_\perp=0.78$, $a_h/L_B=0.06$; $R=5$, $\beta_\perp=0.79$, $a_h/L_B=0.045$.

4. DISCUSSION

Achievement of stabilization requires several important factors:

(1) Disc-like Pressure Profiles. A ring-like pressure profile, with particle Larmor radii smaller than the plasma radius, is not effective as the equilibrium plasma current profile becomes dipole in shape, which only allows a weak interaction with a conducting wall.

(2) High Energy Ions. In a reactor regime, the energies need to be in the MeV region if B~5 Tesla. Hot electrons can only supply the needed FLR effect for B~0.5 Tesla, which may be suitable in a present-day experiment that attempts to prove the stabilization principle.

(3) Attainment of High Beta. The "fragile" stability window may be crucial in building up to a high beta. Build-up can occur when $\tilde{\beta}_c$ is insignificant. Such build-up has been demonstrated with hot electron rings [12], and to some extent with disc-shaped plasmas [13]. When conditions for robust stability are achieved, one can then build-up the beta of the background plasma. One may also reach the robust stability regime somewhat more easily by forming the plasma in a time

less than the conductor's skin time. It can then be shown that the wall stabilization, at low beta, is twice as effective.

5. INTRODUCTION TO TRAPPED PARTICLE MODES

In past work it was established that tandem mirrors, particularly those with thermal barriers, are susceptible to trapped particle modes with MHD-like growth rates [14]. Achieving stability relies on a charge-uncovering mechanism arising from the particles transiting both the locally MHD unstable central cell and the locally MHD stable plug region, as the different forces of the axial electric field cause electrons and ions to sample different regions of space. In this paper we discuss additional effects that arise in trapped particle modes of tandem mirrors due to radial electric fields from an equilibrium potential Φ_e [15,16] and dissipative effects.

To simplify the analysis, we use a formalism where the tandem mirror is taken as azimuthally symmetric, although favorable curvature in the tandem plugs, usually arising from quadrupole fields, is assumed. In addition the equilibrium is taken with radial and axial electric fields and all quantities are assumed symmetric about the mid-plane. The configuration is shown in Figs 1(a)-1(e). Past analysis has been generalized so that the properties of the quadratic form: (1) are transparently related to conventional MHD theory, (2) treat long wavelength modes not described by the eikonal approximation, (3) treat arbitrary bounce frequency in the collisionless limit (4) describe collisional effects in the high bounce frequency limit.

6. QUADRATIC FORMS

In a collisionless plasma, with an azimuthally symmetric magnetic field given by $\underset{\sim}{B}=\nabla\psi\times\nabla\vartheta$, in the weak-curvature finite Larmor radius limit, the self-adjoint quadratic form governing the normal mode response of the system for modes proportional to $\exp[-i\omega t+im\vartheta]$ can be written:

$$\delta W = \frac{1}{2}\int\Big[d^3r\sigma\Big[\frac{m^2}{r^2}\Big(\frac{\partial\chi}{\partial s}\Big)\Big]^2 + B^2\sigma r^2\Big[\frac{d}{ds}\Big(\frac{\partial\chi}{\partial\psi}+\frac{B_1}{B}\Big)\Big]^2 + \tau m^2\Big(Q_L-\frac{\sigma}{\tau}\frac{\phi\kappa}{r}\Big)^2$$
$$-\frac{\kappa m^2\phi^2}{Br}\frac{\partial}{\partial\psi}(P_\perp+P_\parallel) - \rho\omega^2\Big\{r^2\Big[\frac{B\partial}{\partial\psi}(\phi/B)+\frac{Q_L}{B}\Big]^2+\frac{m^2\phi^2}{B^2r^2}\Big)$$
$$-\rho A\Big\{r^4B^2\Big[\frac{\partial}{\partial\psi}(\phi/rB)\Big]^2+(m^2-1)\frac{\phi^2}{B^2r^2}\Big)\Big] + D_{kin} \qquad (7)$$

with

$$D_{kin} = i\sum_s \frac{2\pi^2}{M_s^2} \int d\psi d\varepsilon d\mu \left(\omega \frac{\partial F_s}{\partial \varepsilon} + \frac{m}{q_s}\frac{\partial F_s}{\partial \psi}\right) \int_0^T dt' \int_{-\infty}^{\infty} dt \exp[i|\Omega(t,t')|]$$

$$\times\left[-isg(t-t')\, q_s \frac{d}{dt'}\left[\Phi(t') - \chi(t')\right] + m\mu Q_L(t') + q_s\Phi(t')\omega_\kappa\right]$$

$$\times\left[isg(t-t')\, q_s \frac{d}{dt}\left[\Phi(t)-\chi(t)\right] + m\mu Q_L(t) + q_s\Phi(t)\omega_\kappa\right] \qquad (8)$$

$\Phi=\underset{\sim}{\xi}\cdot\nabla\psi$ with $\underset{\sim}{\xi}$ the displacement, $Q_L=\underset{\sim}{B}\cdot(\underset{\sim}{B}_1+\underset{\sim}{\xi}\cdot\nabla B)/|\underset{\sim}{B}|$ is the perturbed Lagrangian magnetic field, $\underset{\sim}{B}_1$ the perturbed magnetic field, $\frac{\partial\chi}{\partial s} \propto \underset{\sim}{A}'\cdot\underset{\sim}{B}/|B|$ with $\underset{\sim}{A}'$ the perturbed vector potential, $\tau=1+(\partial P_\perp/\partial B)/B$, $\varepsilon=M_s v^2/2+q_s\Phi_e$ is the particle energy, $\mu=M_s v_\perp^2/2B$ is the magnetic moment, $\Omega=\omega-\omega_d$ with

$$\omega_d = \omega_E + \omega_B + \omega_\kappa \equiv m\left\{\frac{\partial \Phi_e}{\partial\psi} + \frac{\mu}{q_s}\frac{\partial B}{\partial\psi} + \frac{2\kappa}{q_s rB}\left[\varepsilon-\mu B-q_s\Phi_e\right]\right\}$$

$$T = \int_{-s_T}^{s_T} \frac{ds}{|v_\parallel|}, \text{ with } v_\parallel(\pm s_T) = 0 \ , \ sg(x) = \begin{cases} -1 \ , & x<0 \\ 1 \ , & x>0 \end{cases}$$

$$\rho A = \rho\left[\omega_E^2 - 2\omega_E\omega\right] - (\omega-\omega_E)\frac{mM_i}{q_i B}\frac{\partial}{\partial\psi}\cdot(P_{\perp i}B) - \rho\omega_2^2$$

$$\rho\omega_2^2 = \frac{-M_i^3 m^2}{8q_i^2}\left[\frac{\partial}{\partial\psi}\int d^3v\, F_i v_\perp^4\right]\frac{1}{B}\frac{\partial B}{\partial\psi}$$

For MHD modes $\Phi=\chi$ and typically $Q_L=0$. There is then a large stabilizing bending energy term which is eliminated if we set $\chi=0$. If $L_c/L_p>>1$, it has been shown that $Q_L=0$ for trapped particle modes. For the rest of the paper we consider a piecewise constant test function where $\Phi=\Phi_c$ in the central cell and $\Phi=\Phi_p$ is in the plug and $\Delta\Phi=\Phi_c-\Phi_p$. The response D_{kin}, to $\vartheta(\kappa^2)$ is then found to be

$$D_{kin} = \frac{4\pi^2\Delta\Phi^2}{M_s^2} q_s^2 \sum_s \int d\psi d\varepsilon d\mu \left(\omega\frac{\partial F_s}{\partial\varepsilon} + \frac{m}{q_s}\frac{\partial F_s}{\partial\psi}\right) \times$$

$$\left\{\sin\left(\frac{1}{2}\oint_{plug}\Omega dt\right)\cos\left(\frac{1}{2}\oint_{plug}\Omega dt\right) - \left[\sin\left(\frac{1}{2}\oint_{plug}\Omega dt\right)\right]^2 \cot\int_0^{T/2}\Omega dt\right\} \qquad (9)$$

where $\oint dt\ldots$, denotes a complete transit integral of a passing particle during its transit through the plug. The phase-space integral is only over those particles whose orbits

sample both the central cell and the plug. A dissipative response arises from $\cot \int_0^T \Omega dt \equiv P \cot \frac{1}{2} \int_0^T \Omega dt \times -i\pi \sum \delta(\frac{1}{2} \int_0^T \Omega dt - n\pi)$. If $\lambda \equiv \oint \Omega dt \approx (\omega - \omega_E^2) L_p / v_{th} << 1$, $L_p/L_c << 1$, and if the distribution is Maxwellian we find:

$$D_{kin} = -\Delta\phi^2 \sum_s \int_{plug} \frac{ds}{B} \frac{n_{ps}}{T_s} \frac{q_s^2}{M_s} (\omega - \omega_{Ep}) (\omega - \omega_{Ec} - \omega_{cs}^*) + \delta D_{kin} \qquad (10)$$

with $\omega_{cs}^* = (mT_s B/q_s n_c) \partial(n_c/B)/\partial\psi$, n_{ps} the passing particle density of species s in the plug. Roughly, in all bounce frequency regimes, δD_{kin} is

$$\delta D_{kin} = -i\Delta\phi^2 \sum_s \int \frac{ds}{B} \frac{n_{ps}}{T_s M_s} q_s^2 (\omega - \omega_E)(\omega - \omega_{Ec} - \omega_{sc}^*) g(\omega) \qquad (11)$$

with $g(\omega) \angle sg(\omega) \equiv [\alpha \bar{\lambda}^3 L_c^2/L_p^2$, if $\bar{\lambda} L_c/L_p < 1$; $\alpha_2 \bar{\lambda}$, if $L_p/L_c < \bar{\lambda} < 1$, $\alpha_3/\bar{\lambda}$; if $\bar{\lambda} > 1]$, where $\bar{\lambda}$ is the mean value of λ and the α's are geometrical factors that need detailed evaluation (here we assume $\alpha \approx 1$). In addition if $\bar{\lambda} >> 1$, $\mathrm{Re} D_{kin} \to 0$.

Collisions have been taken into account when $\int \Omega dt << 1$. In this paper we only account for the more important collisional effect of electrons. The only term that is altered is δD_{kin}, and in the case $\omega_E = 0$ and no radial temperature gradient, it is given by

$$\delta D_{kin}\left(\begin{matrix}\text{electron} \\ \text{collisions}\end{matrix}\right) = \frac{-q_e^2 \Delta\phi^2 \omega}{T_e M_s} n_{pe} \int_{plug} \frac{ds}{B} \int h d^3v (\omega - \omega_e^*) \qquad (12)$$

where h satisfies the equation $-i\omega h + C(h) = 0$, with C(h) the Fokker–Planck collision operator in the plug, and h at the separatrix is equal to the lowest order collisionless solution.

The solution for a square well plug model is found to be

$$\int h d^3v = \left|\frac{2q_e \Phi_{Ab}}{T_e}\right|^{1/2}$$

$$\times \quad \{\exp(\frac{i\pi}{4})(\frac{\nu_D}{\omega})^{1/2}[1+(1+Z)^{1/2}(\pi R/16)^{1/2}]sg(\omega)$$

$$+ i \frac{B_{max}}{B_p} (\frac{\pi}{2})^{1/2} \exp(\frac{|q_e \Phi_{Ab}|}{T_e}) \frac{\nu_p}{\omega + i\nu_p}\}$$

with Pastukhov loss rate [17] ν_p given by

$$\nu_p = \frac{2\nu_D(1+Z)\exp(-\frac{q_e \Phi_{Ab}}{T_e})(\frac{2q_e \Phi_{Ab}}{T_e})^{1/2}}{(2\pi)^{1/2} \ell n[2R(1+Z)]}, \quad \nu_D = \frac{4\pi n(plug) \ell n\Lambda \, q_e^4}{M_e^{1/2} |2q_e \Phi_{Ab}|^{3/2}}$$

$$Z = q_i/|q_e|$$

7. ANALYSIS

A. Electric Fields

We consider a model where ω_E is independent of radius and has values ω_{Ec} in the central cell and ω_{Ep} in the plug with $\Delta\omega_E=\omega_{Ep}-\omega_{Ec}$. We consider two models that can be solved analytically. One, the sharp profile model of Fig. 1(b), where we take $\Delta\omega_E=0$, and the second, a diffuse profile with all pressures and densities varying radially as $\exp(-r^2/2r_0^2)$. In the first case a dispersion relation is obtained when $m\Delta\psi/\psi_p \ll 1$, of the form

$$q\Omega^2+\Omega\left[2\omega_E-(m^2-1)\omega_i^*-\omega_i^*\Delta Q\right] + m^2\gamma_{MHDc}^2+\omega_E^2-(m^2-1)\hat{\omega}_2^2 = 0 \qquad (13)$$

where $\Omega=\omega-\omega_E$, $I_m(z) \equiv$ Bessel Function, $z=Q^{1/2}$
$q=zI_m'(z)/I_m(z) \approx |m|+Q^{1/2}$, $\omega_i^* = -P_{\perp i}/2n_c q_i \psi_p$

$$\gamma_{MHDc}^2 \int_0^{L_c}\frac{ds\rho}{B^2} = -\int_0^{L_c} ds\ \frac{\kappa(P_\perp+P_\parallel)}{B^2 r_p}$$

$$\hat{\omega}_2^2 = \overline{\frac{1}{B}\frac{\partial B}{\partial\psi}}\ \frac{M_i^3}{8\rho q_i^2\psi_p}\int d^3v F_i v_\perp^4 \approx \frac{\beta_i r\omega_i^{*2}}{2\Delta m^2}$$

$$Q = \sum_s \frac{n_{ps}L_pB_cr_p^2T_i}{n_cL_cB_pa_i^2T_s}\ ;\ \Delta Q = \sum_s \frac{q_s n_{ps}L_pB_cr_p^2}{q_i n_cL_cB_pa_i^2}$$

With $y_m \equiv (m^2-1+\Delta Q)\omega_i^*/2\omega_E$, the stability condition is

$$y_m > 1+(|m|+Q)^{1/2}\left[\frac{m^2\gamma_{MHDc}^2}{\omega_E^2}+1-\frac{(m^2-1)\hat{\omega}_2^2}{\omega_E^2}\right]^{1/2}, \text{ if } y_m>0$$

$$y_m < 1-(|m|+Q)^{1/2}\left[\frac{m^2\gamma_{MHDc}^2}{\omega_E^2}+1-\frac{(m^2-1)\hat{\omega}_2^2}{\omega_E^2}\right]^{1/2}, \text{ if } y_m<0 \qquad (14)$$

Note that if $y_m<0$, a somewhat smaller magnitude of y_m is needed for stability than if $y_m>0$. However, if $\Delta Q<0$, as has been proposed for the Tara experiment [18], there is a parameter hole at $-\Delta Q \approx m^2-1$, due to cancellation of axial and radial charge-uncovering effects, that is particularly susceptible to instability. However, if $-\Delta Q \lesssim 1$, stability can be achieved with sufficient FLR effects and careful passing particle control. A robust stabilization can arise if the square root term in Eq. (14) is imaginary. Total stability then arises if

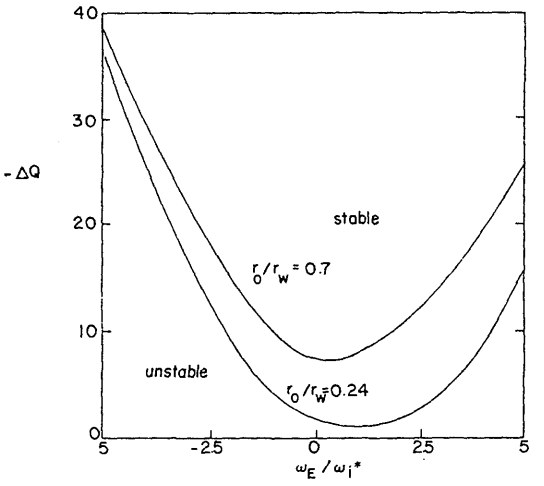

FIG.4. Rotation stability boundaries: marginal stability curves for diffuse profile for m = 1 mode as a function of charge-uncovering parameter, for two wall positions. Other parameters are $T_e/T_i = 1$, $n_{pi} = 0$, $n_{pe} = n_c$, $\Delta\omega_E = 0$, $\gamma^2_{MHDc}/\omega^2_E = 1$.

$$\frac{\beta_i \omega_i^{*2} r}{m^2 \Delta} > \frac{8}{3}\left(\gamma^2_{MHDc} + \frac{\omega_E^2}{m^2}\right)$$

and Eq. (14) is satisfied for m=1.

An alternate model, analyzed to take into account smooth profiles, assumes the density and pressure vary as $\exp(-r^2/2r_0^2)$ in the central cell and $\kappa=\kappa_0 r/r_0$. If one now defines $\omega^*_{ic}=mT_i(\partial n_c/\partial\psi)/q_i n_c$, an analytic dispersion relation at low beta can be found, which with a wall at $r=r_W$, is given by

$$1 - k_\perp^2 r_0^2 = \frac{\omega^2+m^2\gamma^2_{MHDc}}{(\omega-\omega_i^*-\omega_{Ec})(\omega-\omega_{Ec})} + \frac{(\omega-\omega_{Ep})\left[Q(\omega-\omega_{Ec})-\Delta Q\omega^*_{ic}\right]}{(\omega-\omega_{Ec}-\omega_i^*)(\omega-\omega_{Ec}-\delta\Delta\omega_E L_p/L)} \quad (15)$$

where $k_\perp^2 r_0^2$ is parameter that depends on the placement of a conducting wall, and $k_\perp^2 r_0^2 = |m|+2|n|$ if $r_0/r_W \ll 1$ and $\delta\approx 1$. If $\Delta\omega_E=0$, the stability criterion, with y_k defined as $y_k = (k_\perp^2 r_0^2 - 1 + \Delta Q)\omega_i^*/2\omega_E$,

$$y_k > 1 + (k_\perp^2 r_0^2 + Q)^{1/2}\left(1+m^2\gamma^2_{MHDc}/\omega_E^2\right)^{1/2}, \quad y_k > 0$$

$$y_k < 1 - (k_\perp^2 r_0^2 + Q)^{1/2}\left(1+m^2\gamma^2_{MHDc}/\omega_E^2\right)^{1/2}, \quad y_k < 0 \quad (16)$$

This result is qualitatively similar to Eq. (14), with somewhat different m dependences.

If $\omega_{Ec}=0$, and if $\Delta\omega_E > \gamma_{MHDc}$, we find that instability can occur if $\omega_i^*\Delta\omega_E\Delta Q > 0$ (i.e. if $\Delta Q>0$, with outward electric fields in the plug, if $\Delta Q<0$, with inward electric fields). If further we assume $\Delta\omega_E >> \omega_e^*$, ω_i^* (this can happen if the electric potential scales as the plug temperature, which is usually much bigger than the central cell temperature) and $\Delta Q = -QT_e/T_i$ (this occurs if $n_{pi} << n_{pe}$ or $\bar{\lambda}_i >> 1$, which is likely for large $|m|$), the instability condition is $\delta\Delta\omega_E L_p/\omega_e^* L<1$, with the band of unstable $k_\perp$ satisfying

$$-\left(1-\frac{\delta\Delta\omega_E L_p}{\omega_e^* L}\right)^{1/2}\left(1+\frac{T_i}{T_e}\right)^{1/2} < \frac{Q\Delta\omega_E}{2\omega_e^* k_\perp^2 r_0^2} - 1 - \frac{T_i}{2T_e} - \frac{\delta L_p \Delta\omega_E}{2L\omega_e^*}$$
$$< \left(1-\frac{\delta\Delta\omega_E L_p}{\omega_e^* L}\right)^{1/2}\left(1+\frac{T_i}{T_e}\right)^{1/2} \qquad (17)$$

where the growth rate γ is roughly given by $\gamma \approx (\omega_e^* Q\Delta\omega_E)^{1/2}/k_\perp r_0$.

Additional instability effects can arise due to the placement of a conducting wall at $r=r_W$ and then $\min k_\perp^2 r_0^2 > |m|$. Specific rotational stability curves, with $\Delta\omega_E = 0$, $m=1$, are shown in Fig. 4.

B. Dissipative Modes

When dissipative terms are analyzed in the dispersion relation, additional instabilities are possible even when the previous stability criteria are fulfilled. Then in the absence of dissipation there are two real frequency modes. If the dissipation is weak the mode frequencies are

$$\omega^+ \approx \omega_i^* \ (k_\perp^2 r_0^2+\Delta Q)/(k_\perp^2 r_0^2+Q) \ , \ \omega^- \approx m^2\gamma_{MHDc}^2/(k_\perp^2 r_0^2+\Delta Q) \qquad (18)$$

If the charge uncovering mechanism is positive (negative), the ω^+ mode is destabilized (stabilized) by ion dissipation and stabilized by electron dissipation, while the ω^- mode is stabilized (destabilized) by ion dissipation and destabilized (stabilized) by electron dissipation.

As the electron collision frequency increases so that $\gamma_{MHDc}^2/\omega_e^* < \nu_D < \omega_e^*$, the ω^- mode will be predominantly purely growing (damping) if $\Delta Q>0$($\Delta Q<0$) with a growth rate (damping rate) $\sim \nu_D$. When $\nu_D \gtrsim \omega_e^*$, the nature of the modes changes, and the only important wave in all cases has a frequency approaching ω_e^* and is destabilized by electron collisions. If $\nu_D >> \omega_e^*$, the growth rate becomes quite small.

8. CONCLUSION

By carefully controlling the charge-uncovering mechanism and finite Larmor radius effect, it appears possible to find a stable operating window to non-dissipative curvature and rotational trapped particle instabilities. Having a disc-like

pressure profile and a relatively high central cell beta enables one to achieve a robust stabilization for modes with $m \geq 2$ and rely on a negative charge separation mechanism for stability of the m=1 mode.

A new trapped particle mode has been found that is driven by radial electric fields in the plug. Even if the flute mode driven by the axial shear of the rotation velocity [14,16] is stabilized by hot particle effects in the plug, the system still may be susceptible to a mode that isolates in the central cell. This mode may be relevant in interpreting the anomalous radial losses in TMX-U [19]. The dissipative trapped particle modes may also be of some relevance to enhanced losses of present-day and future experiments.

REFERENCES

[1] ABE, H., et al., "Curvature-driven instabilities in the Elmo Bumpy Torus", Plasma Physics and Controlled Nuclear Fusion Research 1982 (Proc. 9th Int. Conf. Baltimore, 1982), Vol. 3, IAEA, Vienna (1983) 427.

[2] CHRISTOFOLIS, N.C., et al., Lawrence Livermore Lab. Rep. UCRL 14282 (1965).

[3] BERK, H.L., SUDAN, R.N., J. Plasma Phys. 6 (1971) 413.

[4] NELSON, D.B., Phys. Fluids **23** (1980) 1850.

[5] SMITH, G., Phys. Fluids **27** (1984) 1499;
SMITH, G., NEVINS, W.M., SHARP, W.M., Phys. Fluids **27** (1984) 2120.

[6] VAN DAM, J.W., ROSENBLUTH, M.N., LEE, Y.C., Phys. Fluids **25** (1982) 1349.

[7] ANTONSEN, T.M., Jr., LEE, Y.C., Phys. Fluids **25** (1982) 132.

[8] BERK, H.L., ROSENBLUTH, M.N., WONG, H.V., ANTONSEN, T.M., Jr., Inst. for Fusion Studies, Austin, Rep. IFS 130 (1984) to be published in Phys. Fluids.

[9] BERK, H.L., KAISER, T.B., Inst. for Fusion Studies, Austin, Rep. IFS 132 (1984), to be published in Phys. Fluids.

[10] BALDWIN, D.E., BERK, H.L., Phys. Fluids **26** (1983) 3595.

[11] COHEN, R.H., ROWLANDS, G., FOOTE, T.H., Phys. Fluids **21** (1978) 627.

[12] DANDL, R.A., EASON, H.D., EDMONDS, P.H., ENGLAND, H.C., Nucl. Fusion **11** (1971) 411.

[13] LAZAR, N.H., et al., TRW, Redondo Beach, CA, Rep. 84.TRW/STM-108 (1983).

[14] BERK, H.L., ROSENBLUTH, M.N., WONG, H.V., ANTONSEN, T.M., Jr., BALDWIN, D.E., Fiz. Plasmy **9** (1983) 176 [Sov. J. Phys. **9** (1983) 108].

[15] ROSENBLUTH, M.N., KRALL, N.A., ROSTOCKER, N., "Finite Larmor radius stabilization of "weakly" unstable confined plasmas", Plasma Physics and Controlled Nuclear Fusion Research (Proc. 1st Int. Conf. Salzburg, 1961), Nuclear Fusion 1962 Supplement, Part 1, IAEA, Vienna (1962) 143.

[16] LEE, X.S., CATTO, P.J., AAMODT, R.E., Phys. Fluids **25** (1982) 1491.

[17] PASTUKHOV, V.P., Nucl. Fusion **14** (1974) 3.

[18] KESNER, J., LANE, B., Massachusetts Inst. of Technology, Cambridge, Rep. PFC/JA-83-21, to be published in Phys. Fluids.

[19] DRAKE, R.P., et al., Phys. Fluids **25** (1982) 2439.

PLASMA HEATING, CONFINEMENT AND STABILIZATION EXPERIMENTS IN AN AXISYMMETRIC MIRROR-CUSP DEVICE*

S. OKAMURA, R. KUMAZAWA, K. ADATI, T. AOKI,
H. FUJITA, K. HATTORI, S. HIDEKUMA, T. KAWAMOTO,
Y. OKUBO, T. SATO, T. HATORI, K. MURAOKA**,
K. UCHINO**, M. MAEDA+, M. HAMAMOTO++,
K. SUNAKO§, K. TAKAYAMA§
Institute of Plasma Physics, Nagoya University,
Chikusa-ku, Nagoya, Japan

D.R. BAKER, H.R. GARNER, H.D. PRICE,
P.B. PARKS, A.M. SLEEPER
GA Technologies Inc.,
San Diego, California,
United States of America

R. ITATANI, Y. YASAKA
Kyoto University, Sakyo-ku, Kyoto, Japan

Abstract

PLASMA HEATING, CONFINEMENT AND STABILIZATION EXPERIMENTS IN AN AXISYMMETRIC MIRROR-CUSP DEVICE.

The paper describes recent experimental data on ICRH plasma production, RF plugging and ambipolar potential plugging in RFC-XX-M (IPP, Nagoya). Results of ICRF heating and RF stabilization in HIEI (Kyoto) are also described.

1. INTRODUCTION

Axisymmetricity is an important means of suppressing the radial transport in linear confinement systems. The RFC-XX-M device has a linear, axisymmetric MHD-stable configuration which is a simple mirror field terminated by spindle cusp fields with radiofrequency (RF) plugging. HIEI is also an axisymmetric mirror machine in which MHD stability is achieved by RF stabilization.

---

* Work supported in part by the United States Department of Energy.

** Kyushu University, Kasuga, Fukuoka, Japan.
+ Kyushu University, Hakozaki, Fukuoka, Japan.
++ Oita University, Oita, Japan.
§ Tokai University, Hiratsuka, Japan.

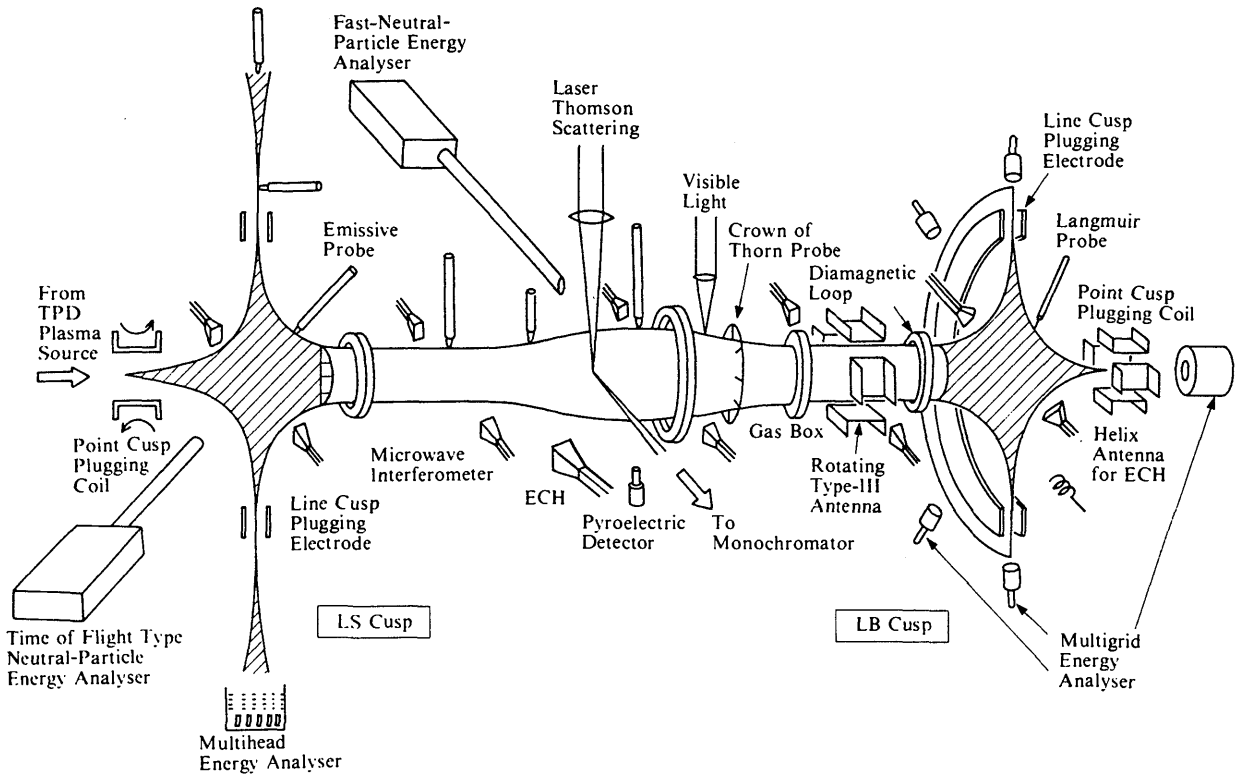

FIG. 1. Schematic drawing and diagnostic system of RFC-XX-M.

In RFC-XX-M, plasma confinement by RF plugging has been greatly improved since the last conference. JAPAN/USA co-operation in investigating ambipolar potential plugging in RFC-XX began in 1982 and, among other results, led to an increase in axial confinement time. In HIEI, ICRF heating for a deuterium-hydrogen plasma was carried out. The mechanism of RF stabilization for the MHD mode was clarified.

2. EXPERIMENTS ON RFC-XX-M

2.1. ICRH-sustained plasma

A schematic diagram of RFC-XX-M is shown in Fig.1. The distance between field-null points is 3 m. The magnetic field strength of the central mirror is 0.35 T at the midplane and 0.96 T at the throat. To produce plasmas, a rotating type-III antenna [1] is installed at the mirror throat and excited by two 0.4-MW RF oscillators. We can excite the $m = -1$ mode (left-handed rotation), the $m = +1$ mode (right-handed rotation), or the $m = \pm 1$ mode (no-rotation).

An initial seed plasma is injected externally or produced by ECRH (2.45 GHz) in the field-null region. After the partial decay of the seed plasma, the rotating type-III antenna is excited simultaneously with hydrogen gas puffing. The frequency is 7 MHz, which corresponds to an ω/ω_{ci} at the antenna of 0.48 to 0.97 when the magnetic field is varied from 100 to 50%. For the $m = -1$ mode, the radial density profile is nearly flat with a value of 10^{13} cm^{-3}, for a net RF input power of 100 kW. The ion (perpendicular) temperature can be varied between 100 and 500 eV by changing the RF power. The electron temperature changes from 10 to 30 eV. The on-axis neutral density is less than 1×10^{10} cm^{-3}, so that charge-exchange energy loss is not the dominant process. For the $m = +1$ mode, the radial profile has a sharp on-axis peak of 7×10^{13} cm^{-3}, and the ion temperature is about 50 eV.

In RFC-XX-M the entire plasma is stabilized by the favourable curvature of the cusp field. We do not observe any unstable activity for the standard operation, except for the case with reduced gas puffing which makes the pressure ratio of the cusp plasma to the central mirror plasma smaller than the threshold value. In this case, plasma stability can be regained by additional gas puffing only in the cusp region so that the cusp plasma pressure is increased.

The confinement of the hotter plasma produced by the $m = -1$ mode has been investigated without RF plugging. The energy confinement time τ_E is determined from the decay time of the midplane diamagnetic loop signal. In Fig.2, τ_E is plotted as a function of the on-axis perpendicular ion temperature $T_{i\perp}$ measured by a diamagnetic loop and a neutral-particle energy analyser. The electron drag time τ_d is evaluated from the spatial distribution of the electron temperature measured by Thomson scattering taking account of the profile of

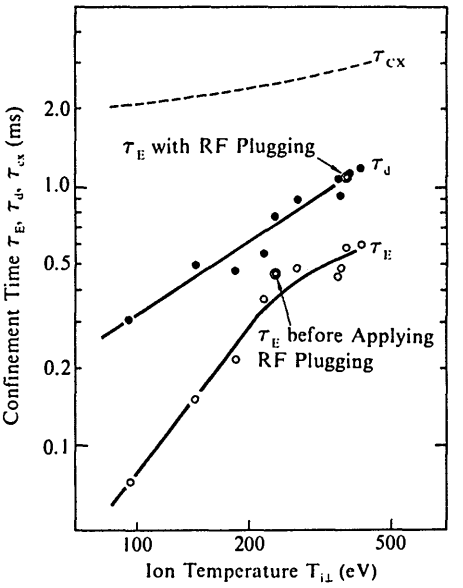

FIG.2. Dependence of τ_E, τ_{cx}, τ_d and τ_E^p on ion temperature.

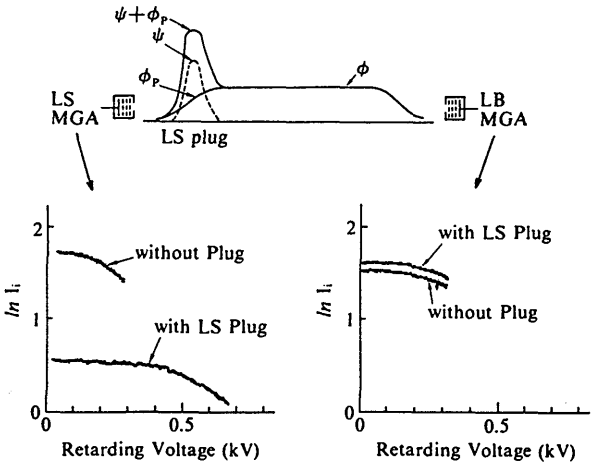

FIG.3. Current-voltage characteristics of MGA measured at LS and LB line cusps when RF plugging is applied only at LS line cusp.

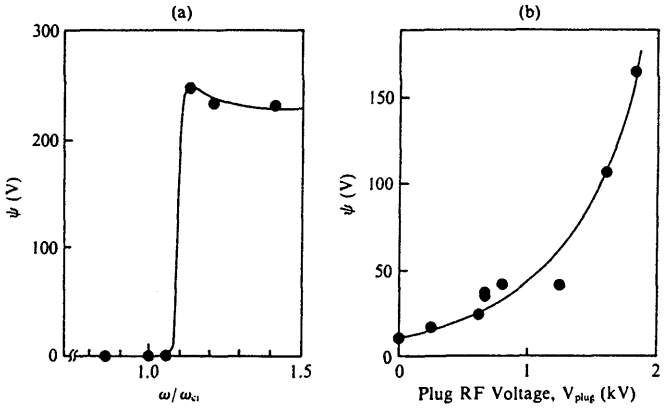

FIG.4. (a) ψ versus ω/ω_{ci}. (b) ψ versus plug RF voltage V_{plug}.

electron density. The charge exchange time τ_{cx} is also estimated on the basis of neutral-hydrogen density measurements by the laser fluorescent method [2]. From the relation $1/\tau_E = 1/\tau_d + 1/\tau_{cx} + 1/\tau_E^p$, where $1/\tau_E^p = 1/\tau_{E_\parallel} + 1/\tau_{E_\perp}$, we estimate the energy confinement time due to the particle loss τ_E^p. The values of τ_E^p are in the range of 0.2 to 2 ms for $T_{i\perp} = 100$–500 eV.

2.2. RF plugging

The entire plasma in the region between two line cusps including the central mirror is confined by RF plugging in both line cusps. The plugging RF is applied to a pair of ring electrodes installed in each line cusp. The frequency is 24.5 MHz which gives $\omega/\omega_{ci} \approx 1.1$. With the RF plug to both line cusps, the total energy confinement is improved to $\tau_E = 1.1$ ms with $n = 6 \times 10^{12}$ cm^{-3}, $T_{i\perp} = 380$ eV, and $T_e = 46$ eV. For this case, we obtain estimations of $\tau_d = 2$ ms and $\tau_{cx} =$ 3–4 ms which give $\tau_E^p \approx 10$ ms (within a factor of two).

To measure the RF plug potential directly, series of experiments have been carried out using multigrid energy analysers (MGA) set up around the line cusp end wall and emissive probes inserted near the RF electrodes. Figure 3 shows the MGA current voltage curve for the case of a single line cusp plugging. The knee of the curve gives the sum of the RF plug potential ψ and the plasma potential ϕ_p in the plug region. When RF plugging is applied at the LS line cusp only, the potential $\psi + \phi_p$ measured by the LS MGA increases remarkably, while the value measured at the LB MGA increases slightly. The RF plug potential is given approximately by the difference in potentials measured by the LS MGA and the LB MGA as depicted in Fig.3. The values of ψ are plotted against ω/ω_{ci} in Fig.4(a). This shows that ψ can be produced for $\omega/\omega_{ci} > 1$. This is consistent with the dispersion relation of the electrostatic-wave eigenmode.

The plasma potential at the plug can be measured directly by an emissive probe in the LS plug section. Typical values of ϕ_p range from 85 to 130 V when the plug RF voltage is varied up to 1.8 kV. Subtracting ϕ_p from the potential measured by the MGA, one obtains ψ. Figure 4(b) shows that ψ is almost proportional to V_{plug}^2 as is expected from the theory.

2.3. Ambipolar plugging

RFC-XX-M has been operated as an ambipolar plugged tandem mirror. This is done by fuelling the cusp end cells by hydrogen gas so as to build up high densities. No RF plugging is used. In this mode, the cusp end cells serve both as anchor and plug. Since no thermal barriers are present, electrons heated either by drag from the ions or directly from the ICRH ionize the injected gas in the cusp. As ICH beaches exist on the inboard and outboard sides of the cusp anchors, the possibility exists that some heating/trapping of ions takes place here.

The time history of a shot with end cell gas puffing is shown in Fig.5. Startup is from 2.5 ms to 6 ms. ICH and central-cell gas puffing sustain the plasma from 6 ms onwards for a period of 12 ms. After turning on the ICH (at 2 ms), end cell gas puffing is started. An equilibrium is reached and maintained with $n_{ec}/n_{cc} \approx 3.3$.

The typical plasma parameters in the ambipolar plugging mode are $n_{cc} \approx 5 \times 10^{12}$ cm^{-3}, $T_{i\perp} \approx 250$ eV, and $T_e \approx 25$ eV. The axial density profile of this mode is shown in Fig.6 before and after end cell gas puffing. Even without end cell puffing, RFC-XX-M is MHD-stable with the end cell pressure considerably lower than the central-cell pressure, because of the strong curvature in the cusp end cell. For $n_{ec}/n_{cc} \approx 2$, the resulting plugging potential is about 50 eV. In general, the plugging potential is higher than that predicted by the Boltzmann relation.

The axial confinement time of the entire plasma (determined as the ratio of the total number of confined particles to the total end loss flux) increases by a factor of three to five over that for the standard operating mode. During ambipolar plugging, the central-cell density increases. The time evolution of the central-cell radial density profile suggests that the ambipolar plugging potential peaks radially on axis.

The confinement of near-axis particles (which otherwise may be non-adiabatic) is improved most distinctly. Thomson scattering electron temperature measurements demonstrate that when end cell puffing starts the on-axis electron temperature is depressed but then recovers its initial value within 3 ms.

During ambipolar plugging, the spectra of density and floating potential fluctuations in the central cell were obtained. Modes tentatively identified as density gradient drift waves propagating in the electron drift direction were observed with $\tilde{n}/n \cong 5\%$, $\tilde{\phi}/T_e \approx 50\%$, and $\omega \approx (1/5)\,\omega_e^* \approx 6 \times 10^4$ s^{-1}. The

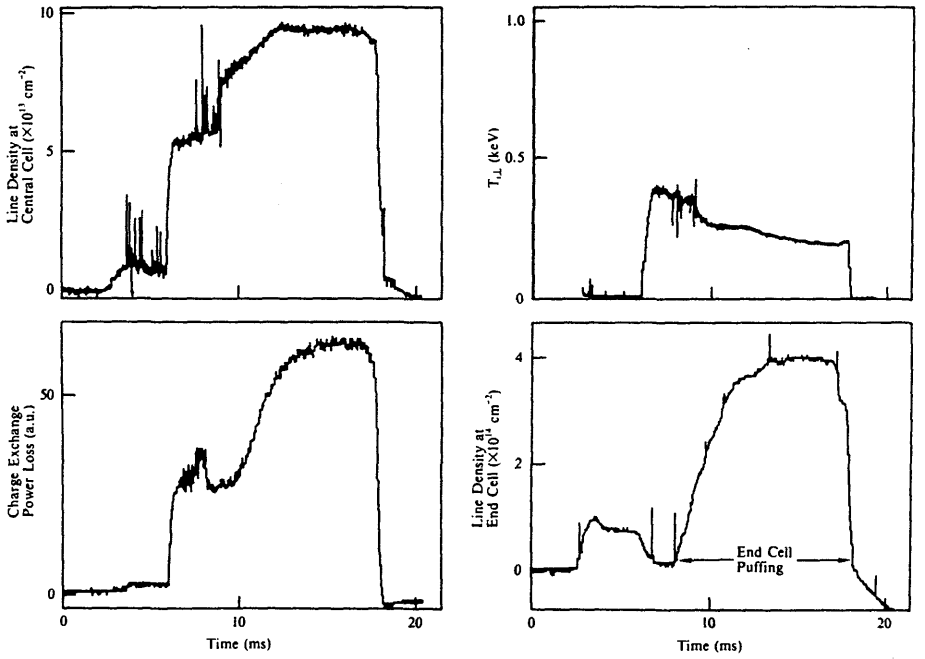

FIG.5. Typical data for a shot with end cell gas puffing.

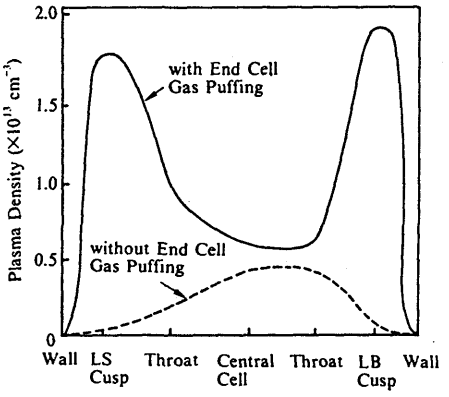

FIG.6. Axial density profiles with and without end cell gas puffing.

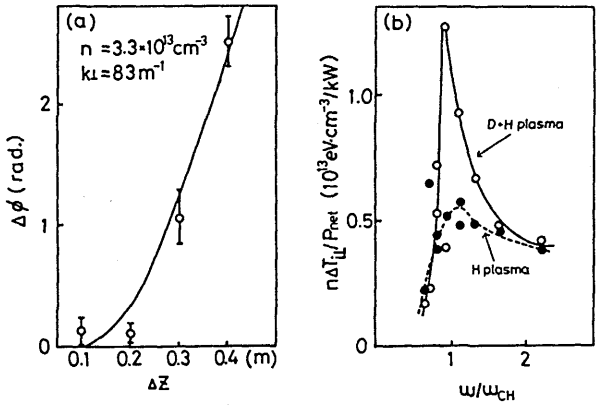

FIG. 7. (a) Phase difference of fast wave along the axis obtained experimentally (circles) and theoretically (solid line); (b) heating rate versus ω/ω_{cH} at the throat.

maxima in $\tilde{n}$ and $\tilde{\phi}$ occur near the maximum density gradient. The calculated upper bound on the radial diffusion coefficient arising from these fluctuations is $D_\perp \approx 1 \times 10^4\ cm^2 \cdot s^{-1}$. The fluctuation levels are decreased by at least 50% in this high-end-cell-density mode as compared to the low-density mode.

3. FAST-WAVE HEATING AND STABILIZATION IN HIEI

In HIEI, a deuterium plasma with 10–30% of hydrogen concentration or a pure hydrogen plasma of density $n = 10^{13}-10^{14}\ cm^{-3}$ is produced in a static magnetic field of up to 1.1 T at the throat. The length between the mirror points is 1.2 m, and the mirror ratio R is variable from 1.4 to 4.

The RF antenna at the throat produces circularly or linearly polarized fields of the $|m| = 1$ mode in a line-tied D + H plasma. Fast waves of $k_\parallel \lesssim 10\ m^{-1}$ were observed to propagate towards the midplane for linearly and right-hand circularly polarized excitation with $\omega/\omega_{cD} > 1$. No wave was found for left-hand polarized excitation. Figure 7(a) shows the phase difference of the wave magnetic field along the axis obtained from experiment and cold-plasma theory with a WKB approximation for R = 1.5 and $\omega/\omega_{cD} = 3$ at the throat.

The increment of $nT_{i\perp}$ is plotted in Fig.7(b) as a function of ω/ω_{cH} at the throat. For H plasma, the heating may be due to collisional effects and a small left-hand polarized component of the partially excited slow wave near the periphery. For the D + H plasma, a large increase in $nT_{i\perp}$ is observed when the ion-ion hybrid resonance zone lies inside the throat. The maximum heating rate was $\approx 1.2 \times 10^{13}\ eV \cdot cm^{-3} \cdot kW^{-1}$ for $\omega/\omega_{cH} = 0.95$.

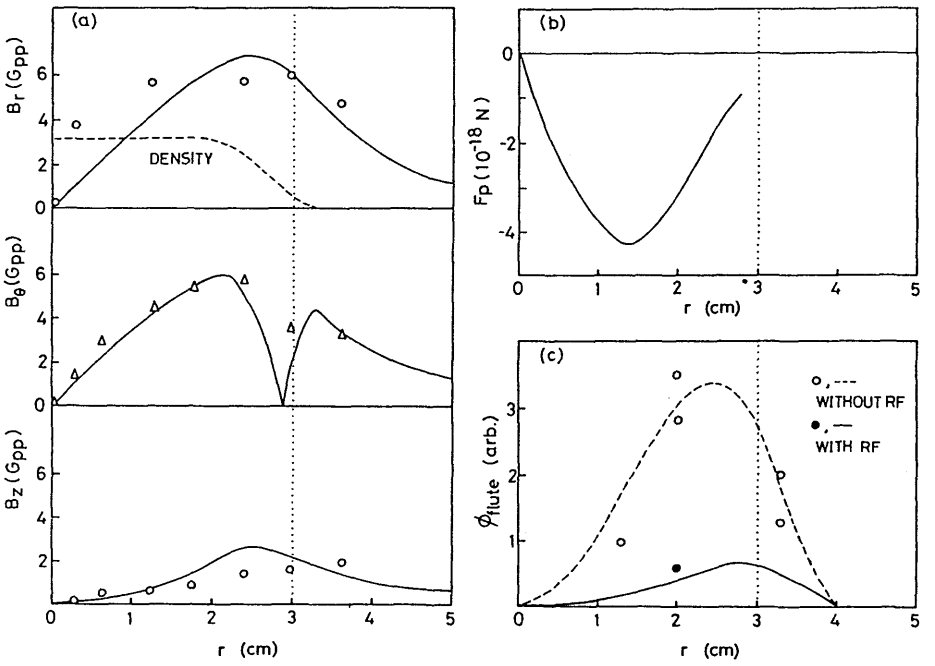

FIG.8. (a) Measured and calculated wave magnetic field versus r for $n = 5 \times 10^{13}$ cm^{-3} and $\omega/\omega_{cH} = 2.4$; (b) radial ponderomotive force for ions for wave field in (a); (c) measured and calculated amplitudes of flute fluctuation.

When line-tying is removed, the plasma becomes flute-unstable, and the RF heating is very inefficient. This shows that the RF field of the |m| = 1 mode cannot produce the ponderomotive force needed to balance the effective gravity. Stability is achieved when the m = ±2 RF field is further applied by the midplane antenna [3]. Figure 8(a) shows the measured radial distribution of the RF magnetic field at the midplane by which the flute instability is stabilized in the H plasma. The solid curves denote the self-consistent RF fields in a diffuse-boundary cold plasma obtained from the Hojo-Hatori RF code. The radial ponderomotive force for ions for this RF field is calculated in Fig.8(b). The measured fluctuation amplitudes of flute mode with and without midplane RF are compared with the result of Hojo's stability code in Fig.8(c). The eigenfunction of the dispersion relation of the flute mode [4] with (solid line) and without (dotted line) the ponderomotive force shown in Fig.8(b) is plotted. The good agreement between experiment and calculation leads to the conclusion that the ponderomotive force is essential for stabilizing the flute mode.

ACKNOWLEDGEMENTS

The authors would like to express their gratitude to Professor H. Kakihana, the former director of the Institute of Plasma Physics, and to Drs T. Ohkawa and R.L. Freeman for their encouragement. They also wish to acknowledge stimulating discussions with Prof. J.H. Malmberg, and collaboration of Dr. H. Hojo using his computer codes.

REFERENCES

[1] WATARI, T., et al., Nucl. Fusion **22** (1983) 1359.
[2] MURAOKA, K., et al., in Plasma Surface Interactions in Controlled Fusion Devices, (Proc. 6th Int. Conf. Nagoya, 1984).
[3] INUTAKE, M., et al., in Plasma Physics and Controlled Nuclear Fusion Research 1982 (Proc. 9th. Int. Conf. Baltimore, 1982), Vol.1, IAEA, Vienna (1983) 545.
[4] ROSENBLUTH, M., SIMON, A., Phys. Fluids **8** (1965) 1300.

DISCUSSION

R.S. PEASE: In all the experiments you have described, the electron temperature is low, and it seems that electron drag is the central cause of energy loss. How will you improve the electron temperature and the electron thermal insulation?

T. SATO (IPP, Nagoya): We are preparing the microwave system for ECRH. In January 1985 we shall reach a level of 64 kW at 35 GHz using ECH for fundamental end-cell heating or second harmonic central cell heating. Power balance calculations indicate that we should get $T_e \approx 80-100$ eV, thereby reducing drag losses by a factor of 3 to 5. By increasing the electron temperature in this way we shall obtain a longer confinement time.

In the RF plugging scheme, electron thermal insulation between the plug section and the central section is not necessary.

N. HERSHKOWITZ: In the HIEI experiment, what was the m of the unstable mode and what was the m that was stabilized in Hojo's calculation?

R. ITATANI: Perhaps I can answer this question. The RF of the $m = \pm 2$ mode can stabilize the MHD instability of both $m = 1$ and $m = 2$ modes, and they follow the same scaling law according to Hojo's code. However, application of an $m = 1$ RF field does not stabilize the MHD instability of any mode.

BEAM HEATING OF PLASMA IN SOLENOIDS

A.V. ARZHANNIKOV, B.N. BREJZMAN, A.V. BURDAKOV,
V.S. BURMASOV, S.G. VOROPAEV, L.N. VYACHESLAVOV,
V.I. EROFEEV, A.M. ISKOL'DSKIJ, B.A. KNYAZEV,
V.S. KOJDAN, V.V. KONYUKHOV, Eh.P. KRUGLYAKOV,
S.V. LEBEDEV, V.N. LUK'YANOV, K.I. MEKLER,
O.I. MESHKOV, A.A. PODYMINOGIN, V.V. POSTUPAEV,
A.I. ROGOZIN, D.D. RYUTOV, S.L. SINITSKIJ,
A.D. KHIL'CHENKO, Yu.A. TSIDULKO, V.V. CHIKUNOV,
M.A. SHCHEGLOV
Nuclear Physics Institute,
Novosibirsk,
Union of Soviet Socialist Republics

Abstract

BEAM HEATING OF PLASMA IN SOLENOIDS.

The results of studies on the interaction between relativistic electron beams (REBs) and plasma performed at the Nuclear Physics Institute, Siberian Branch, USSR Academy of Sciences, are reported. It has been demonstrated on the INAR device that injection into the plasma of a beam with a small angular spread leads to a distribution function of heated electrons which is uneven. In addition to the main group of electrons, which have a temperature of some tens of eV, the plasma contains fast electrons with energies between a few hundred eV and several tens of keV. On the GOL-1 device it has been shown that REBs with a large angular spread transfer their energy to a small group of electrons with energies of a few tens of keV. The density of particles in this group decreases with increasing angular spread of the beam. Theoretical estimates of the density and characteristic energy of the hot electrons have been obtained on the assumption that plasma heating is produced by the excitation of Langmuir turbulence, the level of which is limited as a result of elastic scattering of waves by plasma density perturbations generated by ponderomotive force. A brief description is given of the GOL-3 device, which is being constructed at the Nuclear Physics Institute, and experimental results are provided on the production of powerful microsecond REBs on the U-1 accelerator, which serves as the basic beam source module for this device.

Studies on the interaction between powerful relativistic electron beams (REBs) and plasma at the Nuclear Physics Institute since 1971 have concentrated on the use of such beams for heating a dense ($10^{17}-10^{18}$ cm^{-3}) plasma in long systems with magnetic thermal insulation [1]. It is intended in a thermonuclear reactor of this type to heat the plasma in two stages [2, 3], involving the production, in the central part of the reactor, of a region of low-density plasma (10^{15} cm^{-3}), where the beam transfers most of its energy. The physical phenomena characteristic of this region have been studied in experiments on the INAR [4] and GOL-1 [5] devices.

1. EXPERIMENTS ON THE INAR DEVICE

In earlier experiments on this device it was shown [6] that when a dense ($n_b \cong 10^{12}$ cm^{-3}) REB with a small angular spread ($\sqrt{\overline{\theta^2}} \leqslant 10°$) is injected into a plasma with a density $n = (1-3) \times 10^{15}$ cm^{-3} in a magnetic field of 2.5 T the energy loss of the beam reaches 35% over a length of 2.4 m.

From both the theoretical and the practical points of view, the question of how the energy transferred by the beam is distributed among the plasma particles is very important. Analysis of diamagnetic, corpuscular, laser and X-ray measurements [6–8] shows that this energy is transferred mainly to plasma electrons and that the distribution function of the heated electrons may be extremely uneven.

Recently, systematic studies of the distribution function of heated plasma electrons have been done on the INAR device. The preliminary results of these studies are described in Ref. [9]. An electron beam with an energy of 1 MeV, a current of 25 kA and a duration of approximately 70 ns was injected through a thin foil (9 μm Al or 6 μm Ti) into a hydrogen plasma, the density of which varied between 10^{14} and 10^{16} cm^{-3}. The plasma column had a longitudinal magnetic field in mirror geometry. The magnetic field strength was 2.5 T in the homogeneous part and 4.2 T in the mirrors (in one of which a diode was placed). References [6, 9] contain detailed descriptions of the device and the diagnostics used.

The plasma electron distribution function was studied in a wide energy range (0–100 keV) using a number of methods. In the region of 0–8 keV, it was studied by Thomson scattering of the light of a ruby laser at angles of 90° and 8°. An estimate of the energy content in the range 1–5 keV was also obtained by analysing X-rays from the surface of the anode foil through which the beam is injected into the plasma. The radiation was detected simultaneously by twelve channels in which filters of different thicknesses had been placed. Using semiconductor detectors of low sensitivity to the hard X-rays of the accelerator, the soft bremsstrahlung signal of plasma electrons could be reliably identified. In these experiments the absolute power of soft X-rays was measured. The distribution function of electrons in the range 10–100 keV was studied by using a multi-foil analyser placed in the outlet mirror of the device.

Detection of the spectrum of Thomson scattering at an angle of 90° with strong interaction between the REB and the plasma ($n_b = 0.7 \times 10^{12}$ cm^{-3}, $n = 1.5 \times 10^{15}$ cm^{-3}, injection through 9 μm Al) shows that, when the laser pulse is delayed by 100 ns relative to the beginning of beam injection, most of the experimental points correspond to a Maxwellian distribution of electrons with a temperature of 20 eV (Fig.1(a)). It will also be seen that there are experimental points lying considerably higher than the straight line corresponding to T = 20 eV, i.e. the plasma contains a significant group of fast electrons (E > 100 eV). Further evidence of this is provided by the increased temperature of the main

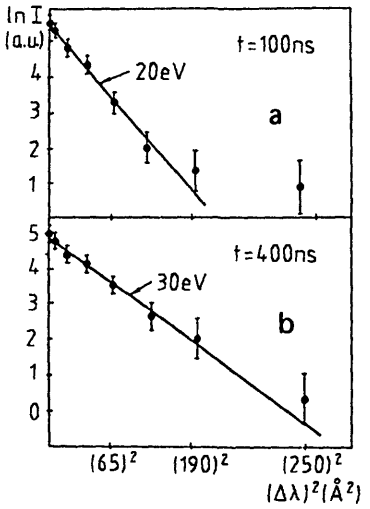

FIG.1. Spectra of Thomson scattering at an angle of 90°.

group of electrons after 300 ns (Fig.1(b)). These electrons are heated by pumping of energy from the high-energy component as a result of Coulomb collisions.

The purpose of the Thomson scattering experiments at an angle of 8° was indirect detection of 'hot' plasma electrons (with an energy of $\gtrsim 1$ keV). The experiments have shown that the parameters of this group of electrons depend on the density of the beam. Thus, where $n_b = 0.7 \times 10^{12}$ cm^{-3}, the electron density in the range 0.3–8 keV is $(4.5 \pm 1.5) \times 10^{13}$ cm^{-3} and their average energy is 650 ± 250 eV. With an increase in n_b up to 2×10^{12} cm^{-3}, the average energy of this group of electrons rises to 3 keV and their density decreases to 1.5×10^{13} cm^{-3}.

The hot plasma electrons were also detected by means of bremsstrahlung X-rays from the anode foil. By analysing this radiation with the filter method the range of electron energies was determined, and the flux density of these electrons to the foil was estimated in absolute terms from the power of the bremsstrahlung. The energy content of the electrons with energies of 1–5 keV is estimated to be 120 ± 70 J from the results of the X-ray measurements. This means that not less than one third of the energy lost by the beam in the plasma is in this energy range. As far as faster electrons are concerned, X-ray measurements show that electrons with energies of 5–50 keV remove less than 20 J – corresponding to approximately 15% of REB energy loss – from the trap through the inlet mirror.

Electrons with energies above 10 keV were detected by a multi-foil analyser. The time dependence of electron density in the flux through the outlet mirror for two energy ranges (10–30 keV and 30–50 keV) is shown in Fig.2. The electrons of the given spectrum are seen in the analyser to have considerable ($\approx$ 20 ns) delay relative to the beginning of the REB. The reason for this delay may be the finite

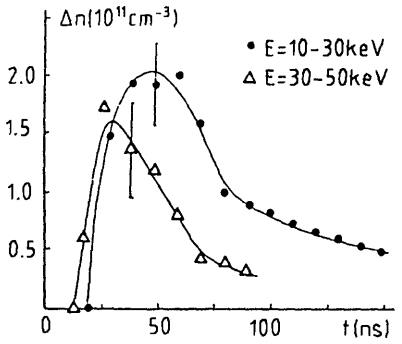

FIG.2. Time behaviour of the density of high-energy electrons in the flux through the magnetic mirror.

gain time of high-energy electrons. In addition, it is very likely that these electrons are formed near the injection point, where energy deposition is at a maximum [6]. On the basis of X-ray measurements and data from the multi-foil analyser, it can be concluded that in the range 5–100 keV the energy content of heated electrons does not exceed 30 J.

Figure 3 compares the contributions of electrons of different energies to the transverse plasma pressures as measured by diamagnetic sensors. High-energy ($E > 10$ keV) electrons, when caught in the trap, distribute themselves evenly over the length in about 50 ns. Electrons of lower energies ($E \lesssim 1$ keV) remain unevenly distributed in accordance with the inhomogeneity of energy deposition even 100 ns after the beginning of beam injection. This explains the inhomogeneity of diamagnetism over the length observed at this moment in time. If the contributions of electrons of different energies are compared for a point 90 cm away from the place of beam injection (the point where the laser diagnostics are located), the total pressure, at this point, of electrons in the range 0–10 keV (from laser measurements) and in the region 10–100 keV (from analyser measurements) is close to that determined by diamagnetism, the energy content in the region $E < 10$ keV amounting to not less than 70% of the energy remaining in the plasma up to the moment $t = 100$ ns.

2. EXPERIMENTS ON THE GOL-1 DEVICE

The distinguishing features of the device are the great length of the magnetic system (7.5 m) and the high beam current (up to 75 kA), which make it possible

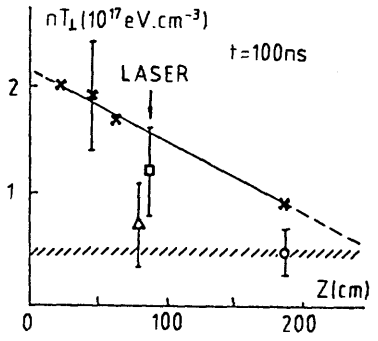

FIG.3. Comparison between laser, foil and diamagnetic measurements.

to perform plasma heating experiments with a large REB cross-section (30 cm^2). The beam was injected into the plasma through a titanium foil 17 μm thick ($\sqrt{\overline{\theta^2}} = 23°$) via a magnetic mirror from a field near to the maximum (B_{max} = 2.4 T), so that as the beam entered the homogeneous field region (B_0 = 1.35 T), the angular spread was reduced to 18°.

The device is long enough for studying the possibility of controlling energy deposition along the axis of the system. Figure 4(a) shows the longitudinal distribution of plasma diamagnetism immediately after the beam has been switched off. It corresponds to an energy content of $(3/2) \int W_\perp (z)\, dz \approx 100$ J or an effectiveness of interaction of 10%. For these conditions (J_b = 1.5 kA·cm^{-2}, plasma density on the axis $n_0 = 3 \times 10^{14}$ cm^{-3}) Ref. [10] gives a considerably higher energy content. The discrepancy can be accounted for by the fact that, in the case corresponding to Fig.4(a), there is a considerable radial inhomogeneity in the plasma: $|dn/dR| \approx 8 \times 10^{13}$ cm^{-4} (the density increases up to 4.5×10^{14} cm^{-3} at the beam edge). According to the theory of Ref. [2], with this inhomogeneity a disruption of beam instability should occur. The incomplete suppression observed in the interaction is presumably explained by the existence of a low-gradient region near the axis. The influence of the radial inhomogeneity on energy deposition is demonstrated by Fig.4(b): over the first three metres experimental conditions are the same here as for Fig.4(a), whereas beyond the separating foil (12 μm of titanium) a more homogeneous plasma is formed ($|dn/dR| \lesssim 1.5 \times 10^{13}$ cm^{-4}) with the same density on the axis. In practice, the effect of the interaction being suppressed by the radial inhomogeneity may be exploited for transporting the REB over long distances without loss and also for controlling the energy deposition.

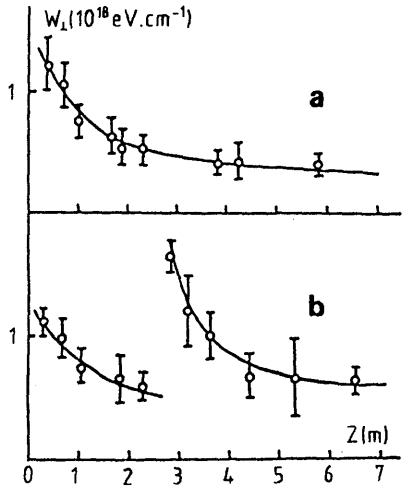

FIG.4. Distribution of plasma diamagnetism immediately after the REB pulse ends: (a) with a plasma density on the axis of 3×10^{14} *cm*$^{-3}$ *and the outer edge of the beam (*$R_b = 3$ *cm) of* 4.5×10^{14} *cm*$^{-3}$*; (b) for* $0 < z < 3$ *m the conditions are the same as for (a); beyond the separating foil there is a homogeneous plasma (*$n = 3 \times 10^{14}$ *cm*$^{-3}$*).*

It has been pointed out earlier [3] that the bulk of the plasma electrons remains cold ($T \cong 10$ eV) in REB/plasma interaction and that the energy transferred to the plasma is absorbed by a group of electrons which is small in terms of density (the non-equilibrium 'tail' of the distribution function). Investigation of the tail parameters is a somewhat complex task owing to the low density of the hot electrons. By comparing the decrease in diamagnetism in two magnetic configurations (with the outlet mirror switched on and switched off) a rough estimate has been made of the energy of the tails [10]. A more precise determination of the parameters of epithermal electrons was obtained by the injected target method [11], which consists basically of the following: using a pulse valve near the outlet end plate of the device, a gas cloud[1] with a density of the order of 10^{15} cm^{-3} and a length of approximately 1 m is injected into the system. The parameters of the tail are determined from the power of the characteristic radiation P_K reaching the detection system: $P_K = E_K n_* n_z \sigma_K v_e \Omega V/4\pi$. Here, E_K is the energy of a photon for the K-layer, n_* is the density of hot electrons, n_z is the target density, V is the radiating volume observed, Ω is the solid angle of the detection system and $\sigma_K(E)$

[1] Targets of Ne, Ar, Kr and Xe were used. In all cases (with the exception of Xe) the K-line radiation was detected. The condition of the transparency of targets to hot electrons was fulfilled.

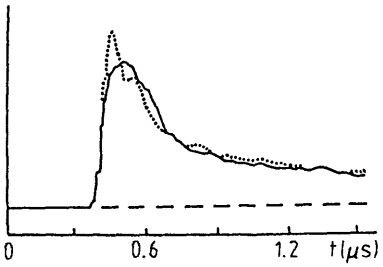

FIG.5. Time behaviour of the power of the characteristic radiation for the xenon target (dotted line) and plasma diamagnetism (solid line).

stands for the cross-section of excitation with K-line emission. For electrons of energies three or four times higher than the excitation threshold, the product $\sigma_K v_e$ is virtually independent of their energy [12, 13]. Thus, by determining the power P_K, it is possible to find the density of these electrons. Using various gases for targets it is in principle possible to reconstruct the electron distribution function. Unfortunately, owing to the bad reproducibility of the pre-plasma parameters, this has not yet succeeded. It has, however, been possible to find the average energy of the hot electrons. Figure 5 shows two oscillograms, one of which (dotted line) corresponds to the time behaviour of the power of the characteristic radiation (Xe, E_L = 4.8 keV), and the other (solid line) to the time behaviour of the diamagnetic signal with a diagnostic loop situated nearby. The good correlation found between the two signals (a similar correlation was observed in the experiments with other targets) shows that a considerable proportion of the plasma diamagnetism is determined by energetic electrons. Target experiments were performed with a plasma density of $(4.5 \pm 1.1) \times 10^{14}$ cm^{-3} and an REB injection current of 60 kA (current density 2 kA·cm^{-2}). For these conditions, the tail parameters take the following values: mean density $n_* = (0.7 \pm 0.2) \times 10^{12}$ cm^{-3}, mean energy $E_* = 45 \pm 20$ keV.

It has been shown on the INAR device that, with increasing angular spread of the beam, the effectiveness of its interaction with the plasma decreases [14]. However, the question of what happens in this case to the electron distribution function remains open. Preliminary results for this problem have been obtained on the GOL-1 device. Figure 6 shows two X-ray signals from a xenon target. The stronger signal corresponds to beam injection through a 17 μm titanium foil ($\sqrt{\overline{\theta^2}} = 18°$) and the weaker signal to injection through 50 μm of titanium ($\sqrt{\overline{\theta^2}} = 31°$). Since the strengths of the signals are proportional to the hot-electron densities, it can be concluded from Fig.6 that the density of the tail decreases as the angular spread of the REB increases (decreasing by a factor of approximately three for a threefold increase in the square of the angular spread).

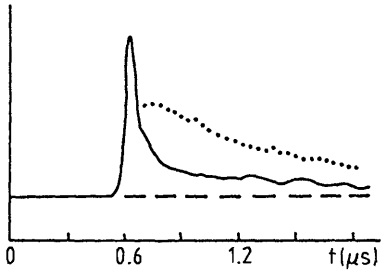

FIG. 6. Influence of the angular spread of the REB on the power of the characteristic radiation for the xenon target (E_L = 4.8 keV); dotted line: $\sqrt{\overline{\theta^2}} = 18°$, solid line: $\sqrt{\overline{\theta^2}} = 31°$.

3. ESTIMATES OF HOT-ELECTRON PARAMETERS

In accordance with the data obtained on the INAR and GOL-1 devices, the plasma heating can be regarded as the result of the development of beam instability, and the heating process can be described in the context of the following assumptions:

The beam excites in the plasma Langmuir waves with phase velocities of the order of the velocity of light;
As a consequence of non-linear processes, the wave spectra change to the region of lower phase velocities;
As the phase velocity decreases, Landau damping sets in and the waves are absorbed by a small group of fast electrons;
Together with Landau damping, collisional absorption of waves occurs (this is responsible for heating the bulk of the plasma electrons).

When there is a magnetic field in the plasma, a non-linear decrease in the phase velocity of Langmuir waves may be due to elastic scattering of these waves by plasma density perturbations generated by the Langmuir turbulence itself [15]. Elastic scattering redistributes the waves along the lines $\omega_{\vec{K}} = \text{const}$, where

$$\omega_{\vec{K}} = \omega_p \left[1 + \frac{1}{2} \frac{k_\perp^2}{k^2} \frac{\omega_H^2}{\omega_p^2} \left(1 - \frac{\omega_p^2}{k^2 c^2} \right) + \frac{3}{2} k^2 r_D^2 \right]$$

Since, for oscillations generated by the beam, the dispersion correction to the plasma frequency is estimated to be equal to $\omega_p (\omega_H/\omega_p)^2$, the condition $\omega_{\vec{K}} = \text{const}$ means that the phase velocity of the waves may decrease during the scattering process down to a value of the order of $v_{T_e} (\omega_p/\omega_H) \ll c$. If the plasma contains a sufficient number of electrons with velocities exceeding $v_{T_e} (\omega_p/\omega_H)$, secondary waves may effectively be absorbed by such electrons. Taking this

dissipation channel to be the main one, we can write the following energy balance condition:

$$\Gamma_b W_b = \Gamma_* W_* \qquad (1)$$

where Γ_b is the growth rate of the beam instability, Γ_* is the wave damping decrement by hot electrons, and W_b and W_* are the energy densities of the excited and damped waves.

Since the balance between pumping and damping is maintained as a result of elastic scattering of waves, the scattering frequency ν_{eff} in each part of the spectrum should be of the order of Γ. Estimates show that, in the case of interest to us, ν_{eff} hardly depends at all on the wavelength of Langmuir oscillations, being given by the expression

$$\nu_{eff} \sim \omega_p (\delta n/n)^2 (\omega_p/\omega_H)^2$$

where $(\delta n/n)^2$ is the mean square of relative fluctuations in plasma density. Thus, from the conditions $\Gamma_b \sim \nu_{eff}$ and $\Gamma_* \sim \nu_{eff}$ there follows the relationship $\Gamma_* \sim \Gamma_b$, which determines the dependence of the hot-electron density n_* on the beam and plasma parameters:

$$n_* \sim n\Gamma_b/\omega_p \qquad (2)$$

The relationship $\Gamma_* \sim \Gamma_b$ also means that the energy densities W_* and W_b are of the same order of magnitude; this is consistent with the conclusion reached earlier in Ref. [16] on the basis of experimental data.

Under the experimental conditions prevailing in the INAR and GOL-1 devices the wave energy W is maintained at a level near the modulation instability threshold:

$$\frac{W}{nT} \sim (\omega_H/\omega_p)^2 \qquad (3)$$

Estimates which explain how this level is reached are given in Ref. [17]. Relationships (1)–(3) can be used for finding the rate of plasma heating and for estimating the characteristic energy of hot electrons

$$E_* \sim \omega_p \tau T (\omega_H/\omega_p)^2 \qquad (4)$$

Here, τ is the duration of beam injection (in the case of the GOL-1 device) and the time of longitudinal loss of hot electrons from the trap (in the case of the INAR device). The temperature of cold electrons T in formulae (3) and (4), as has already been mentioned, is determined by the collisional damping of Langmuir waves. Direct measurements of the temperature from laser scattering are

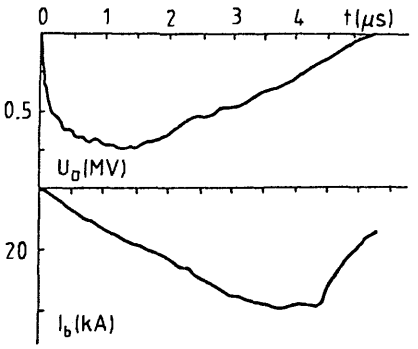

FIG.7. Oscillograms of the voltage on the U-1 accelerator diode (top) and of the beam current (bottom).

in reasonable agreement with this estimate, as is confirmed indirectly by the correctness of relationship (3). Note that, in accordance with formula (3), the increase in temperature T during the heating process leads to a rise in Langmuir wave energy and, consequently, to an increase in the power transferred by the beam to the plasma. This means that an increase in plasma heating effectiveness can be expected when a change is made to beams of longer duration.

4. THE GOL-3 DEVICE

To model the physical processes in a thermonuclear reactor on the basis of a multi-mirror magnetic trap, a device of the next generation, the GOL-3, is being constructed at the Nuclear Physics Institute. The programme of work on this device includes the following:

- Heating of a dense ($n \approx 10^{17}$ cm^{-3}) plasma using REBs;
- Study of the possibility of wall confinement of a plasma with $\beta > 1$;
- Study of the MHD stability of a plasma with simultaneous wall and multi-mirror confinement.

The device will consist of the following components:

- An REB generator for plasma heating (beam current 100 kA with a pulse duration of 10 μs and electron energy of 1 MeV);
- A pulse solenoid 22.5 m long with an average magnetic field of 6 T;
- A solenoid supply system (capacitor bank with an energy reserve of 13.5 MJ).

When an REB of long duration is used, the plasma in the device will be produced as a result of gas ionization by the beam itself in a relatively short

($\sim$ 1 μs) time compared with the total duration of the beam. The plasma is to be longitudinally confined in a magnetic system of 30 mirror cells with a mirror ratio of 2. To achieve two-stage heating, the middle part of the device is to have a section of homogeneous magnetic field. The parameters of the plasma after it has been heated should be as follows: average diameter 6 cm, density 10^{17} cm^{-3}, temperature 1 keV and estimated confinement time 10^{-4} s.

The main components of the device are currently being designed, manufactured and tested. Three solenoid sections (each 2.5 m long) have been constructed. The first section of the capacitor bank, with a capacity of 1.5 MJ, has been tested under load. The REB generator is being built in modules on the basis of the existing U-1 accelerator [18]. On this accelerator, a macroscopically homogeneous beam with a duration of 5 μs and a total energy of 55 $\pm$ 5 kJ has been obtained. Oscillograms of the voltage on the accelerator diode and of the beam current are shown in Fig.7. The beam (cross-section) has been compressed twenty-fold in a longitudinal magnetic field with a mirror configuration (B_{max} = 12 T). As a result, a beam 4 cm in diameter with a current density of 3 kA$\cdot$cm^{-2}, which is sufficient for plasma heating experiments, has been obtained.

REFERENCES

[1] BUDKER, G.I., in Controlled Fusion and Plasma Physics (Proc. 6th Europ. Conf. Moscow, 1973), Vol. 2, Moscow (1974) 136.

[2] BREJZMAN, B.N., RYUTOV, D.D., Nucl. Fusion **14** (1974) 873.

[3] ARZHANNIKOV, A.V., et al., in Plasma Physics and Controlled Nuclear Fusion Research (Proc. 7th Int. Conf. Innsbruck, 1978), Vol. 2, IAEA, Vienna (1979) 623.

[4] ABRASHITOV, Yu.I., KOJDAN, V.S., KONYUKHOV, V.V., LAGUNOV, V.M., LUK'YANOV, V.N., MEKLER, K.I., Pis'ma Zh. Ehksp. Teor. Fiz. **18** (1973) 395.

[5] BUDKER, G.I., et al., in Plasma Physics and Controlled Nuclear Fusion Research (Proc. 5th Int. Conf. Tokyo, 1974), Vol. 2, IAEA, Vienna (1975) 753.

[6] ARZHANNIKOV, A.V., et al., in High Power Electron and Ion Beam Research and Technology (Proc. 3rd Int. Top. Conf. Novosibirsk, 1979), Vol.1, Novosibirsk (1979) 29.

[7] ARZHANNIKOV, A.V., et al., in Plasma Physics and Controlled Nuclear Fusion Research (Proc. 5th Int. Conf. Tokyo, 1974), Vol. 3, IAEA, Vienna (1975).

[8] KOJDAN, V.S., ROGOZIN, A.I., Zh. Ehksp. Teor. Fiz. **71** (1976) 1837.

[9] ARZHANNIKOV, A.V., BURDAKOV, A.V., KOJDAN, V.S., VYACHESLAVOV, L.N., Phys. Scr. **T2**/2 (1982) 303.

[10] BURMASOV, V.S., et al., in Controlled Fusion and Plasma Physics (Proc. 10th Europ. Conf. Moscow, 1981), Vol. 1, Moscow (1981) C-2.

[11] KRUGLYAKOV, Eh.P., LUK'YANOV, V.N., PODYMINOGIN, A.A., in Diagnostics of High-Temperature Plasma (Proc. 3rd All-Union Conf.), Dubna (1983) 151 [in Russian].

[12] DOLGOV-SAVEL'EV, G.G., PANCHENKO, V.E., Opt. Spektrosk. **28** (1970) 1065.

[13] TAWARA, H., HARRISON, K.G., DE HEER, F.J., Physica **63** (1973) 351.

[14] ARZHANNIKOV, A.V., et al., Pis'ma Zh. Ehksp. Teor. Fiz. **27** (1978) 173.

[15] BREIZMAN, B.N., RYUTOV, D.D., in Plasma Physics (Proc. Int. Conf. Nagoya, 1980), Vol. 2, Nagoya (1980) 55.

[16] BREJZMAN, B.N., KRUGLYAKOV, Eh.P., in Phenomena in Ionized Gases (Proc. 15th Int. Conf. Minsk, 1981), Invited Papers, Minsk (1981) 93.
[17] BREJZMAN, B.N., EROFEEV, V.I., Preprint IYaF 84-32, Institute of Nuclear Physics, Siberian Branch of the USSR Academy of Sciences (1984) [in Russian].
[18] VOROPAEV, S.G., et al., Dokl. Akad. Nauk SSSR **276** (1984) 65.

DISCUSSION

J.D. SETHIAN: What is your energy transfer efficiency from the electron beam to the 10^{15}-density plasma?

D.D. RYUTOV: What we have observed experimentally is that the energy deposition efficiency is about 10% per metre. One can expect that for a 7 m interaction length (as it will be in the GOL-3 device) the overall efficiency will be 60–70%.

J.D. SETHIAN: What is the energy transfer efficiency from the 10^{15} plasma to the denser 10^{17} plasma?

D.D. RYUTOV: We have detected no radial losses of hot electrons; all their energy must be transferred to dense plasmas by binary collisions.

D.E. BALDWIN: In a reactor, how would you maintain the low-density section between two high-density regions?

D.D. RYUTOV: The system will be a pulsed one, so that we can use pulsed gas valves to produce any density distribution desired along the system.

PLASMA END LOSS CONFINEMENT STUDIES IN A LINEAR THETA PINCH WITH MAGNETIC MIRRORS

G.G. ZUKAKISHVILI, V.N. RYZHKOV,
R.G. SALUKVADZE, Eh.K. TIKHANOV,
Z.D. CHKUASELI
I.N. Vekua Institute of Physics and Technology,
Sukhumi

P.P. VOLOSEVICH, I.I. GALIGUSOVA,
N.A. DAR'IN, V.Ya. KARPOV, E.I. LEVANOV
M.V. Keldysh Institute of Applied Mathematics,
Academy of Sciences of the USSR, Moscow

Union of Soviet Socialist Republics

Abstract

PLASMA END LOSS CONFINEMENT STUDIES IN A LINEAR THETA PINCH WITH MAGNETIC MIRRORS.

Plasma end losses are investigated when the plasma is confined in a linear theta pinch by a quasi-stationary corrugated magnetic field of a three-mirror configuration. Gas-dynamic ($\lambda_{ii} \ll \ell$) or nearly gas-dynamic ($\lambda_{ii} \lesssim \ell$) modes have been reached for the following plasma parameters: $n = 10^{17}$ cm^{-3}, $T_e + T_i = 150$ eV and $n = 4 \times 10^{16}$ cm^{-3}, $T_e = 150$ eV, $T_i = 300-350$ eV. An analysis of the experimental results and a numerical simulation show that the rate of end losses decreases with growing mirror ratios. This observation is in satisfactory agreement with the plasma axial-confinement theory of gas-dynamic traps.

1. INTRODUCTION

The theory of longitudinal plasma confinement in multi-mirror traps is fairly well developed, by now [1, 2]. The theory has more or less completely been confirmed by experiments carried out in rare, cold alkali [3, 4] and hydrogen [5] plasmas. Recently, gas-dynamic traps (GDTs) have been arousing a good deal of interest because of their simplicity and the possibility of stabilizing MHD plasma instabilities by rather simple means. GDTs appear to be promising in terms of realizing a hybrid reactor and a compact source of 14 MeV neutrons for technical testing of materials [6].

The possibility of performing GDT studies in relatively small devices is also attractive. The present paper gives the results of plasma end loss confine-

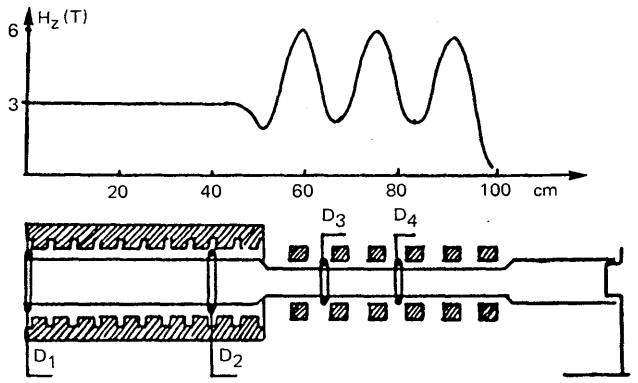

FIG. 1. Device circuitry and field distribution.

ment studies in a linear theta pinch with magnetic mirrors [7] for plasma densities of $n = 10^{16}-10^{17}$ cm^{-3}, temperatures of $T_{ei} \lesssim 300$ eV and $\beta \cong 0.5$. The main topics of the studies were gas-dynamic ($\lambda_{ii} \ll \ell$) and nearly gas-dynamic ($\lambda_{ii} \lesssim \ell$) regimes.

2. EXPERIMENTAL DEVICE

Figure 1 shows the circuitry of half of the KP-1M device and the magnetic field distribution along the system axis at theta pinch field maximum. The central part of the device is a linear theta pinch, 1 m in length. A homogeneous axial theta pinch magnetic field ($H_z = 2-3$ T) is generated by a single-turn solenoid, 11 cm in diameter. The field rise-time is $\tau/4 = 3.5-5$ μs. In crowbarring a unipolar magnetic field pulse is formed with a decay time of $\tau = L/R = 60$ μs. Quasi-stationary mirror fields ($\tau/2 = 10^{-4}$ s) of various configurations at the theta pinch ends are generated by six single-turn coils (each of which is 7 cm in diameter and 4 cm in length), arranged at a distance of 8 cm from each other. Each coil has its own feeding.

The present paper gives the results of experiments for a three-mirror magnetic-field configuration for a range of strengths: $H_n = 3.2$, 4 and 6 T. Each mirror is 16 cm long (length, ℓ), the mirror ratio being $k = H_{n\,max}/H_{n\,min} = 2.7$.

The quartz discharge chamber has different longitudinal sections: under the theta pinch coil, it is 10 cm in diameter while in the mirror region it is 6 cm. At the moment of theta pinch ignition, the temperature of the preliminary plasma created by a combined zeta-theta discharge reaches 2 to 3 eV.

The mirror field is turned on 40 μs before the main discharge and partially penetrates into the region under the theta pinch coil. As is shown by the experiments, the plasma parameters decrease substantially as a result of positive magnetic flux trapped by the theta pinch. Therefore, to compensate for the scattered mirror fields, an inverse quasi-stationary magnetic field is generated in the theta pinch coil by means of a special bank.

The axial distributions of the mirror magnetic fields in all the experiments were controlled by twelve magnetic probes. The plasma energy content, NT_0, was measured by diamagnetic sensors, D_1 to D_4; their arrangement is shown in Fig.1. The plasma electron temperature was determined from the weakening of soft X-rays in aluminium foils of various thickness by means of a three-channel streak camera. The plasma propagation velocities in the region of the stopping coils were estimated from spectroscopic measurements. Photoscanning from the ends was used to elucidate macroscopic plasma behaviour. The experiments were carried out for two initial deuterium concentrations: 1.4×10^{15} cm^{-3} and 4.5×10^{15} cm^{-3}.

3. EXPERIMENTAL RESULTS

Figure 2 shows three typical sets of diamagnetic signals and the corresponding end scanning of the discharges. Figure 2a represents a case with well defined oscillations in the diamagnetic signal at the initial stage of the discharge, the oscillations corresponding to the inertial waves of the plasma column. This regime is realized for small powers of the discharge or at high initial concentrations as well as for arbitrary initial conditions in an untrained discharge chamber (during the first discharges of each of the new series of experiments). The linear density as estimated from the frequency of these oscillations for trained-chamber conditions, $N_0 = \pi R_k^2 n_0 = \omega^2 m_i/q^2 H^2$ (q is a factor close to unity [8]), is in fair agreement with the initial number of particles per unit length of the plasma column. Switching on the inverse magnetic field, lowering the initial pressure or increasing the rate at which the magnetic field rises induce partial (Fig.2b) or entire (Fig.2c) collapses of the oscillations in the diamagnetic signal. However, on the photographic pictures the plasma column oscillations are, as a rule, retained. Apparently, the collapse of the oscillations is due to microinstabilities developing in the current sheet and leading to intensified diffusion of the external magnetic field into the plasma and its anomalously rapid heating.

As a result, the plasma shell compression passes from an inertial regime into the quasi-equilibrium one (for each of the time points $nkT + H_i^2/8\pi = H_e^2/8\pi$). The oscillations observed on the photos may be due to propagation of shock waves tearing off the current sheet.

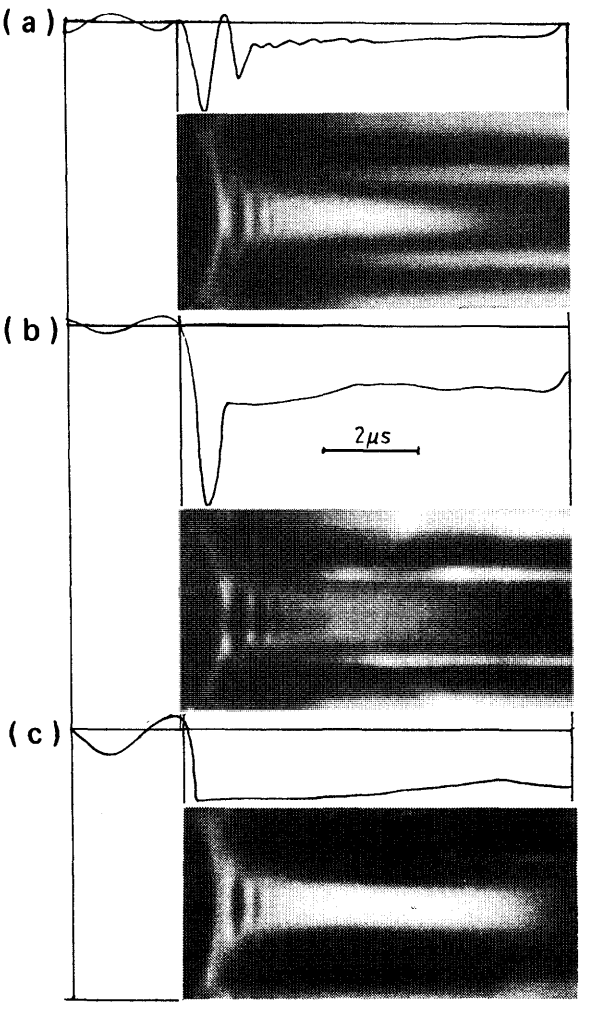

FIG.2. Diamagnetic signal oscillograms, D_1, and plasma photoscanning for $n_0 = 4.5 \times 10^{15}$ cm^{-3}. a) $H_z = 2$ T; b) $H_z = 2$ T; $H_{z0} = -0.3$ T; c) $H_z = 2.5$ T; $H_n = 3.2$ T.

For theta pinch magnetic-field maximum at an initial density of $n_0 = 1.4 \times 10^{15}$ cm^{-3}, the electron temperature becomes 100 to 150 eV, the concentrations reach $(2-4) \times 10^{16}$ cm^{-3}, the ion temperatures are 200 to 300 eV, and the plasma column radius, R_p, is equal to 1 cm. In this case, the mean free path length for ions is $\lambda_{ii} = 3-7$ cm, and it hardly varies during a half-cycle of the discharge current. For an initial density of $n_0 = 4.5 \times 10^{15}$ cm^{-3}, we have

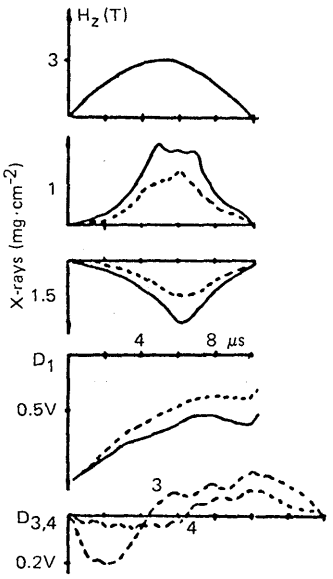

FIG.3. Discharge traces for initial pressure of deuterium filling, $n_0 = 1.4 \times 10^{15}$ cm^{-3}.

$T_e = T_i = 70-100$ eV, $n = 10^{17}$ cm^{-3} and $\lambda_{ii} \leqslant 1$ cm. The ratio of ion Larmour to plasma column radius is $\rho_{ii}/R_p \ll 1$. Thus, for both cases, we have a gas-dynamic regime or a regime close to gas-dynamic.

Figure 3 shows traces of the theta pinch magnetic field (H_z), soft X-rays having passed through aluminium foils, 1 and 1.5 mg·cm^{-2} in thickness, and diamagnetic signals from the central section of the theta pinch (D_1) and from the mirror region (D_3, D_4) for $n_0 = 1.4 \times 10^{15}$ cm^{-3}. Solid lines refer to the regime with the mirrors turned on, while dotted lines are for the mirrorless case.

When the plasma is free to expand beyond the theta pinch limits, the diamagnetic signals change their polarity (see Fig.3, traces D_3 and D_4). This is because the plasma moves in a decaying magnetic field at the theta pinch end and, at the same time, an oppositely directed current is induced in it, whereas the primary current drops rapidly as a result of plasma cooling during its contact with the discharge chamber wall.

Figure 4 shows the time variation of NT_0 corresponding to the traces in Fig.3. We see that, up to the third microsecond, when the rarefaction wave from the theta pinch ends has not yet reached the central section, the plasma parameters are identical for both cases. After the third microsecond, with the mirrors turned on, the diamagnetic signal drop decelerates and NT_0 decreases in the central region of the theta pinch as compared to the mirrorless regime. Nearly at the same time, the mirror region is filled by a hot plasma flowing from the theta pinch.

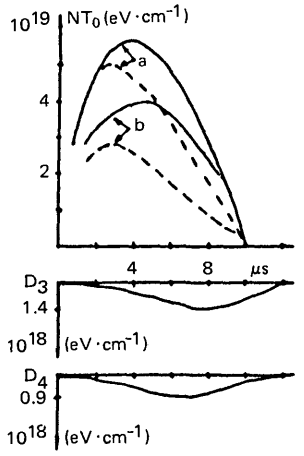

FIG.4. Plasma energy content, NT_0, at central section of theta pinch and in D_3 and D_4 mirrors: (a) experiments; (b) calculations.

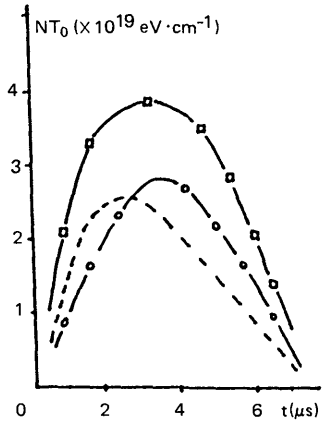

FIG.5. Plasma energy content, NT_0, for various values of mirror magnetic field, $n_0 = 1.4 \times 10^{15}$ cm^{-3}, $H_z = 2.5$ T: (---) without mirrors; (-o-o-) $H_n = 3.2$ T; (-□-□-) $H_n = 4$ T.

For this case, the value of NT_0 in the theta pinch is an order of magnitude higher than in the mirror region. This fact indicates that the plasma trapping observed takes place mainly at the first mirror.

The confinement of the plasma end losses can be assessed indirectly from the increase in the intensities of the soft X-rays (Fig.3) and from the relatively slow shortening of the plasma column radius. For $n = 4.5 \times 10^{15}$ cm^{-3}, this fact is easy to perceive by comparing the photos in Figs 2a and c.

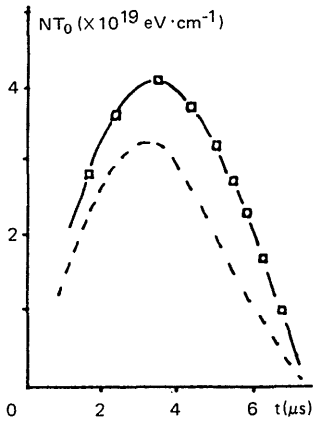

FIG.6. NT_0 versus time for $n_0 = 4.5 \times 10^{15}$ cm^{-3}; $H_z = 2.5$ T. (-□-□-) $H_n = 4$ T.

Figure 5 shows NT_0 versus the mirror magnetic field. As was expected, the plasma energy content increases with growing mirror field.

The trends described above also occur for higher initial concentrations. Figure 6 gives NT_0 versus time for $n = 4.5 \times 10^{15}$ cm^{-3}. Both regimes reveal radial displacement of the plasma column at the end of a half-cycle of the theta pinch discharge current. The displacement rate increases with decreasing initial plasma pressure and growth in the magnetic field strength in the mirror and theta pinch regions. It is not clear, at present, whether the plasma column displacement is associated with the equilibrium destruction due to the radial inhomogeneity of the magnetic field or due to an instability developing as a result of the unfavourable field curvature in the mirror region. It is not excluded that the radial displacements are due to wobble instabilities ($m = 1$ mode), which are observed in several experiments on long theta pinches [9].

The most clearly defined instability was found in experiments with short-circuited theta pinch current. Figure 7 shows the traces of the theta pinch field, D_β lines and NT_0 measured in the theta pinch central section; photo-scanning of the discharge is also shown, taken from the ends of the discharge chamber. The variations in NT_0, with the mirrors turned off, are shown by a dotted line to permit comparisons. At 4.5 μs after the start of the discharge, the plasma column departs from the equilibrium and touches the chamber walls in the magnetic-mirror regions. During the time of plasma contact with the wall (≈5 μs), intense end losses take place. Later on, the plasma column is detached from the walls, and, according to the diamagnetic signal, the losses are decreased substantially; NT_0 is kept at a level of 1×10^{19} eV·cm^{-1}, during several tens of microseconds.

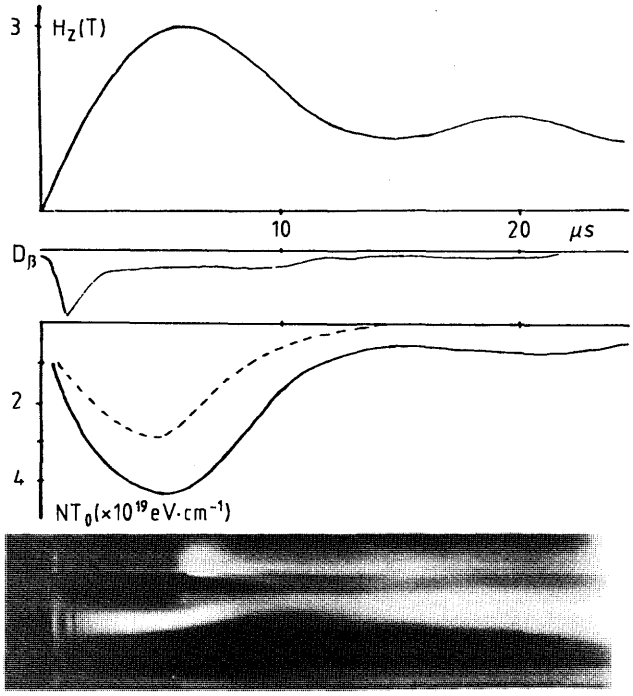

FIG. 7. Magnetic field traces H_z, curves D_β, NT_0 with mirror (solid line) and without mirror (dotted line), and photoscanning of discharge with short-circuited current. $n_0 = 4.5 \times 10^{15}$ cm^{-3}, $H_z = 3$ T, $H_n = 6$ T.

4. NUMERICAL SIMULATION

The process of plasma column contraction and heating by the magnetic field has been studied on the assumption of axial symmetry in a single-fluid, double-temperature, one-dimensional (R, Z) approximation, in terms of electron and ion thermal conductivities, Joule heating, bremsstrahlung and volume losses of mass and energy which simulate 'end' losses [10]. The values of plasma densities and temperatures during the preliminary heating, and the circuit parameters (condenser bank capacity, charging voltage, circuit inductance and resistance) serve as initial data.

Since it has been shown experimentally that end losses become confined mainly at the first mirror, a gas-dynamic approximation with a single mirror has been used in the calculations for the mass drain power:

$$\chi = \frac{2}{K\eta L}\left|\frac{2k(T_e + T_i)}{m_i}\right|^{\frac{1}{2}}$$

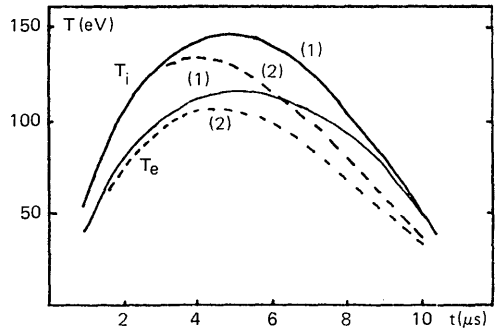

FIG.8. Time variations of plasma column temperature (T_e and T_i) for (1) K = 5 and (2) K = 1.

where K is the mirror ratio, L the theta pinch length and $\eta = 2.7$ is a dimensionless factor measured experimentally in Ref.[9].

Figure 4b shows calculated values for the K = 1 (mirrorless) and K = 5 cases. We see that the experimental results are in qualitative agreement with the numerical calculations. Some quantitative divergence can be accounted for as due to the one-dimensionality of the model. Thus, the calculations show that in the experiments with the mirrors turned on, the rate of plasma end losses is decreased four to five times, which corresponds to the gas-dynamic model since the time-averaged values of K in the first mirror region are equal to four or five as a result of time variations of the theta pinch magnetic field strength.

In the calculations, as well as in the experiments, some increase in the plasma temperature was observed after turning the mirrors on (Fig.8). This is associated with the two facts: 1) each particle leaving the trap carries away an enthalpy of (5/2)kT, and not a thermal energy of (3/2)kT, and 2) there is a magnetic flux frozen into the plasma, which is not affected by the mass drain. Verification calculations show that, at $\beta = 1$, with the thermal energy carried away by particles, the mass drain induces an auxiliary plasma heating. If $\beta = 1$, but the enthalpy is carried away, the mass drain does not affect the plasma parameters. Thus, in practice, when $\beta < 1$, end losses result in plasma cooling. In this case, β decreases with time since the external field work does not only consist in heating the remaining particles but in compressing the internal magnetic flux as well.

Figure 9 shows the radial distributions of the internal magnetic field at the same point in time for K = 1 and K = ∞.

5. CONCLUSIONS

(1) It is shown that, in a collisional plasma, the rate of end losses decreases in inverse proportion towards the mirror ratio; this observation is in agreement with the gas-dynamic model of plasma axial confinement in an open trap.

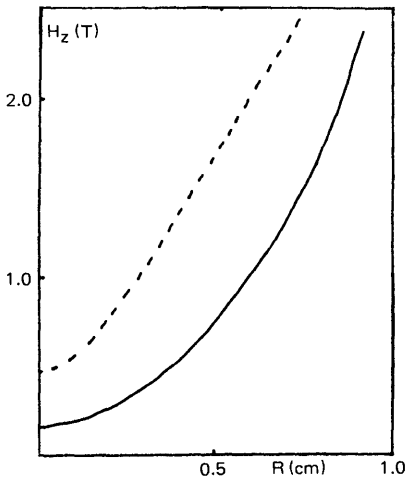

FIG. 9. Magnetic field (H_z) distributed along plasma column radius with mass drain absent (solid line) and present (dotted line) at H_z field peak ($t = 5$ μs).

(2) In the experiments described, the end losses were mainly confined by the first mirror since, because of the short duration of the discharge, the plasma pressure could not be distributed evenly over the whole length of the device.

(3) In the mirror region, an MHD instability was observed whose nature has not yet been clarified.

REFERENCES

[1] MIRNOV, V.V., RYUTOV, D.D., Institute of Nuclear Physics, Novosibirsk, Prepr. 69–71 (1971).

[2] MAKHIJANI, A., LICHTENBERG, A.J., LIEBERMAN, M.A., LOGAN, B.G., Phys. Fluids **17** (1974) 1299.

[3] LOGAN, B.G., BROWN, I.G., LIEBERMAN, M.A., LICHTENBERG, A.J., Phys. Fluids **17** (1974) 1302.

[4] BUDKER, G.I., DANILOV, V.V., KRUGLYAKOV, E.P., RYUTOV, D.D., SHUNKO, E.V., Pis'ma Zh. Ehksp. Teor. Fiz. **17** (1973) 117.

[5] PRICE, H.D., LICHTENBERG, A.J., LIEBERMAN, M.A., TUSZEWSKI, M., Nucl. Fusion **23** (1983) 1043.

[6] MIRNOV, V.V., NAGORNY, V.P., RYUTOV, D.D., Institute of Nuclear Physics, Novosibirsk, Prepr. 84–40 (1984).

[7] ZUKAKISHVILI, G.G., RYZHKOV, V.N., SALUKVADZE, R.G., TIKHANOV, Eh.K., CHKUASELI, Z.D., in Controlled Fusion and Plasma Physics (Proc. 10th Europ. Conf. Moscow, 1981), Vol.1, Moscow (1981) 17.

[8] BODIN, H.A.B., McNAMARA, B., Plasma Phys. **9** (1967) 505.

[9] McKENNA, K.F., BARTSCH, R.R., COMISSO, R.J., EKDAHL, C., QUINN, W.E., SIEMON, R.E., Phys. Fluids **23** 7 (1980) 1443.

[10] BUSURIMA, L.N., VOLOSEVICH, P.P., ZUKAKISHVILI, G.G., LATSABIDZE, G.S., LEVANOV, E.I., POPOV, Yu.P., SKHIRTLADZE, N.M., TIKHANOV, Eh.K., Fiz. Plazmy **8** (1982) 421.

Session D

ALTERNATIVE AND SUPPORTING SYSTEMS

Chairmen of Sessions

Session D-I	L.A. BERRY	(USA)
Session D-II	T. UCHIDA	(Japan)

Papers D-II-4-1 and D-II-4-2 were presented by T. Sato as Rapporteur

Session D-III	R.J. BICKERTON	(CEC/JET)

Papers D-III-2-1 and D-III-2-2 were presented by R.E. Siemon as Rapporteur

Papers D-III-6-1, D-III-6-2, D-III-6-3 and D-III-6-4 were presented by S. Denus as Rapporteur

Session D-IV (Posters)

PLASMA CONFINEMENT AND THE EFFECT OF ROTATIONAL TRANSFORM IN THE WENDELSTEIN VII-A STELLARATOR

W VII-A TEAM:
G. CATTANEI, D. DORST, A. ELSNER, V. ERCKMANN, G. GRIEGER, P. GRIGULL, H. HACKER, H.J. HARTFUSS, M.A. HELLBERG*, H. JÄCKEL, R. JAENICKE, J. JUNKER, M. KICK, H. KROISS, G. KUEHNER, H. MAASSBERG, C. MAHN, S. MARLIER, G. MÜLLER, W. OHLENDORF, F. RAU, H. RENNER, H. RINGLER, F. SARDEI, M. TUTTER, A. WELLER, H. WOBIG, E. WÜRSCHING, M. ZIPPE

NI GROUP:
K. FREUDENBERGER, W. OTT, F.-P. PENNINGSFELD, E. SPETH

PELLET INJECTION GROUP:
H. BÜCHL

Max-Planck-Institut für Plasmaphysik,
Euratom-Association, Garching,
Federal Republic of Germany

Abstract

PLASMA CONFINEMENT AND THE EFFECT OF ROTATIONAL TRANSFORM IN THE WENDELSTEIN VII-A STELLARATOR.

The confinement of NI-heated (B = 3 T) and ECR-heated (B = 1 T) currentless plasmas in W VII-A is strongly influenced by the particular values of the rotational transform. Compared to irrational values of iota, island formation and convective losses may cause confinement to deteriorate for rational values of the transform at the plasma edge: $\iota(a) = m/n$; e.g. 1/2, 1/3, 2/3 . . . . Consequently, a plasma current $I_p < 2$ kA originating from the plasma pressure, $\beta(0) \leqslant 1\%$, or produced by the heating mechanism as well as the external transform, have to be controlled for stationary operation in the shearless ($\Delta\iota_0/\iota_0 < 1\%$) magnetic configuration of W VII-A to maintain optimum confinement. Neutral injection heating in W VII-A leads to build-up of radial electric fields, which increase the heating efficiency η by the reduction of orbit losses and even influence the ion heat transport. Collisional slowing-down is found by neutron measurements for D^0 injection into D^+ plasmas as well as by charge-exchange measurements.

---

* Permanent address: Plasma Physics Research Institute, Department of Physics, University of Natal, Durban, South Africa.

1. INTRODUCTION

By the application of neutral injection (NI) heating, favourable transport and stability properties with $\beta(0) \cong 1\%$ at $B_0 = 3$ T have been achieved for 'currentless' operation of the W VII-A Stellarator at particular values of the rotational transform $\iota(a) = 0.52$ and $\iota(a) = 0.45$ [1–3]. Recent investigations using a 28 GHz VARIAN gyrotron at 1 T succeeded in substituting Ohmic heating for pre-ionization, plasma build-up and heating [4]. In future, a combination of ECRH and NI will be possible at main fields $B_0 = 2.5$ T by means of the 70 GHz VARIAN gyrotron which has already been delivered to IPP Garching.

A combination of different non-Ohmic heating methods: ECRH, NI and ICRH seems mandatory in order to explore in a wide parameter range the stability and transport properties of the plasma as a function of the particular magnetic field configuration. For optimization of the different stellarator configurations, various detailed properties of the particular heating mechanism (mass flow, power deposition profile, current drive) have to be taken into account.

2. PLASMA BEHAVIOUR IN W VII-A

2.1. Parameter range β-limits

In contrast to the Heliotron E [5] magnetic configuration, which has high transform and high shear, the helical winding system ($\ell = 2$, $m = 5$) of W VII-A produces a rotational transform of $\iota_0 \leqslant 0.6$ with low shear ($\Delta\iota_0/\iota_0 < 1\%$) for $B_0 \leqslant 3.5$ T.

'Currentless' plasmas with *NI heating* (4 injectors, 27 kV, typically $H^0 \rightarrow D^+$ with $P_N \cong 1$ MW) have been studied at $B_0 = 2.5$ to 3.5 T. In spite of the moderate size of W VII-A ($R = 2$ m main radius, $a = 0.1$ m plasma radius), high β-values have been obtained at densities $n_e \approx 10^{14}$ cm^{-3} and temperatures $T_e < T_i \cong 1$ keV. Figure 1 shows the central β as a function of heating power for various discharges. The highest values already correspond to about half the equilibrium limit of W VII-A.

For *ECRH* at 1 T (28 GHz, 200 kW, heating efficiency $\eta \cong 0.5$), plasmas could be maintained with $n_{e0} \lesssim n_{cutoff} \approx 10^{13}$ cm^{-3} and $T_i < T_e \lesssim 1.5$ keV. In Fig.2 theoretical predictions [6, 7] for both stability and equilibrium betas are compared with experimental data. Only a significant increase of the heating power would allow an approach to critical β values, owing to the dependence of the transport on B and ι. No MHD instabilities have so far been observed within the accessible β range.

The energy replacement time $\tau_E = W/P_{IN}$ varies from $\tau_E = 10$ to 20 ms for NI at 3 T to $\tau_E = 1$ to 2 ms for ECRH at 1 T for 'currentless' discharges at optimum confinement.

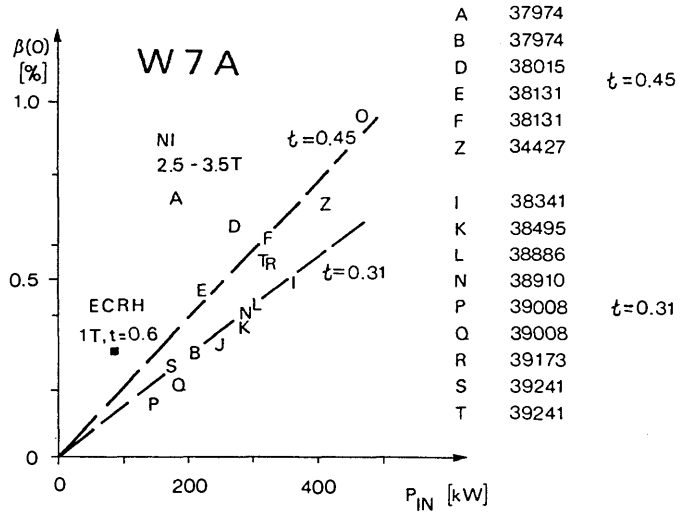

FIG.1. Maximum β(0) values in W VII-A depending on the effective heating power P_{IN}. Data for NI heating (2.5–3.5 T) and ECRH (1 T) are included.

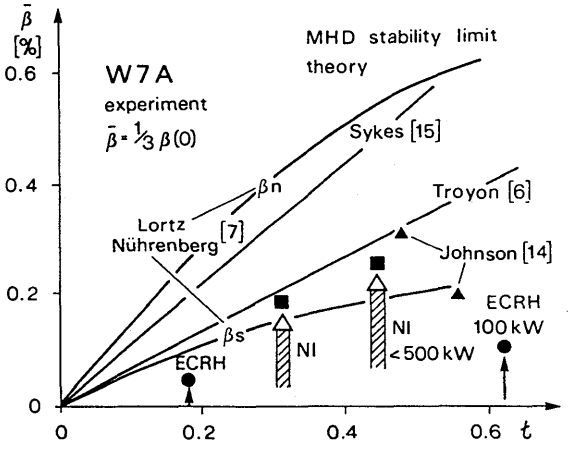

FIG.2. Comparison of β limits as predicted by theory for stability in W VII-A with experimental data.

2.2. NI heating

For NI-heated discharges in W VII-A, a local energy transport analysis has always been difficult. Both power deposition profiles and local transport properties are strongly affected by the radial electric fields built up by the almost perpendicular NI. Both high heating efficiencies and preferential ion heating have been postulated [1–3, 8] to explain the experimental results.

2.2.1. *Heating efficiency*

Measurements of power input agree with code predictions if electric fields deduced from poloidal plasma rotation measurements are included [2, 8]. For the almost perpendicular injection, radial electric fields have strong influence on particle trajectories and thus on lost orbits, which in turn determine the electric field to achieve ambipolarity. By measuring sputtered Fe atom densities ($n_{Fe} \cong 1.5 \times 10^8$ cm^{-3}) via laser-induced fluorescence, the existence of orbit losses has been shown in positions of the vacuum vessel where the calculations predict the orbits to intersect the stainless steel wall.

Experiments have also been performed with all currents and magnetic fields reversed, which leaves the magnetic configuration unchanged. In this case, both ∇B drift and EXB poloidal rotation have to change sign, whereas the radial electric field remains unchanged. The orbit losses are now expected to be deposited on the opposite side of the vacuum vessel. Both effects have been verified experimentally. Reversing currents and fields also corresponds to a change from co- to counter-injection, for which direction the heating efficiency is expected to be smaller [8]. From the experiment, no difference in heating efficiency was found. The higher poloidal velocity, $\cong 30$ km$\cdot$s^{-1} as compared to 20 km$\cdot$s^{-1} for co-injection, is in agreement with this observation.

2.2.2. *Preferential ion heating*

The simultaneous existence of central ion and electron temperatures of 1 keV and 0.6 keV, respectively, and of neoclassical ion heat conduction could only be explained if, in the central plasma region ($r \lesssim a/2$), all the beam power were primarily transferred to the ions [2].

Ion cyclotron emission has been measured: therefore neutral beam (NB)-driven ion modes have been considered as possible candidates for preferential ion heating. Theoretically, the transient slowing-down distribution function has been found unstable to low harmonic ion cyclotron modes after switching on the NB [9]. In the case of stationary slowing down, the distribution function based on Coulomb scattering was found to be stable, except for a very small regime around the injection energies, resulting in strong instability at the plasma resonance with frequencies above the lower hybrid frequency. These instabilities would, however, smooth the distribution function only in the vicinity of the injection energies. Therefore, only a small energy transfer from the beam to the waves would be expected. Thus, for stationary conditions, the slowing down of the beam particles should be determined mainly by Coulomb scattering.

2.2.3. *Slowing down*

Any mechanism leading to preferential ion heating would necessarily be connected with a faster slowing down of the injected fast ions. Considerable

effort has therefore been put into measuring both the stationary ion distribution function and ion slowing-down times by switching off one or more of the injectors [10]. To clarify the energy transfer mechanism, further experiments have been carried out based on the idea that beam/plasma interaction may be localized at the injection port. One injector, operated with deuterium (D) was pulsed for 20 ms into a standard currentless deuterium discharge (B_0 = 3.2 T, $\iota < 0.5$) maintained by three H^0 beams. The neutron flux from the reaction D + D → n + ^{3}He was measured at various positions round the machine by a ^{3}He proportional counter. Except for some enhancement at the injection port, a symmetric distribution round the machine was found. The enhancement at the injection port could be attributed to D + D reactions between shine-through particles and adsorbed deuterium gas at the beam dump.

The total neutron production was calculated and compared with the measurements. A homogeneous plasma cross-section 10 cm in diameter was used, taking $T_e(0)$, $n_e(0)$, Z_{eff}, and the deuteron/proton ratio from measurements. The distribution function of the injected fast deuterons was calculated from the Fokker-Planck equation based on Coulomb collisions; the total number density was taken from both the beam composition and the fraction absorbed by the plasma. It was found that the measured total neutron flux also agrees with these classical calculations within a factor of 2.

To study the dependence of the decay time on plasma density and temperature, the D-beam was switched off at various times during the discharge and the decay of the neutron fluxes recorded. In Fig.3, a comparison of the measured and calculated (dashed line) curves shows remarkable agreement with collisional slowing down. For the same discharge, the slowing down of fast charge-exchange particles was also measured and compared with calculated slowing-down times (Table I). Agreement was found within a factor of 2.

In contrast to earlier hypotheses, the conclusion from all these more detailed experiments is that the energy transfer in W VII-A with almost perpendicular injection (84° with respect to the B-field) is in fact collisional. As a consequence of the collisional slowing down, the assumption of preferential ion heating can no longer be made.

2.2.4. Ion heat conduction

The measured high ion temperatures are compatible with the lower electron temperatures only if the ion heat conduction is smaller than the simple neo-classical prediction. Such a reduction may indeed be expected from proper consideration of the observed high radial electric fields.

Note that hydrogen is injected into a deuterium target plasma almost perpendicular to B, and $T_{i,cx}$ is measured perpendicular to B also, but using the deuterium component. So, if the distribution function were not Maxwellian the bulk temperature would not be obtained from these charge-exchange measurements.

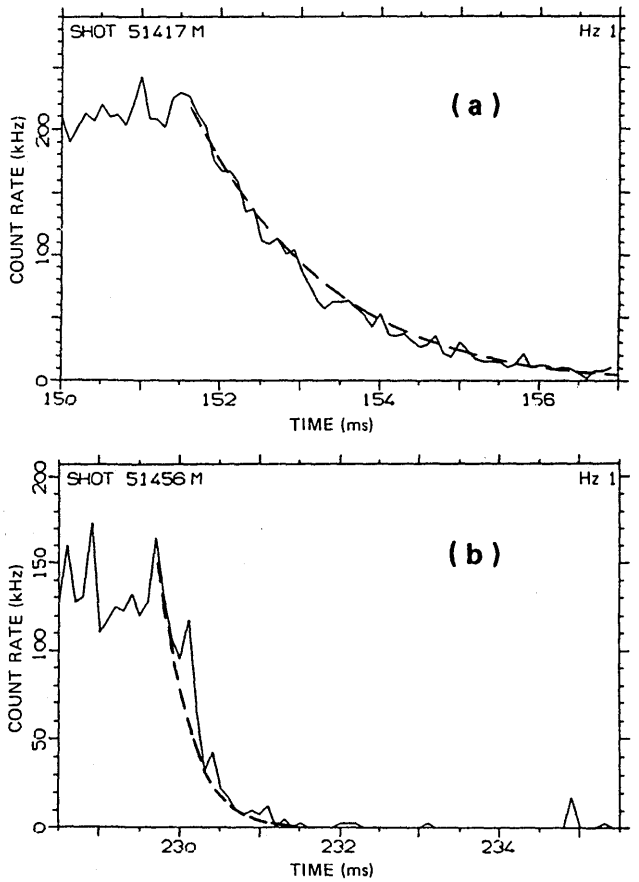

FIG.3. Decay of the neutron flux after switching off the D^0 injector compared with the calculated decay (dashed lines):

(a) $n_{e0} = 3.5 \times 10^{13}$ *cm*$^{-3}$, $T_{e0} = 620$ *eV.*

(b) $n_{e0} = 8.3 \times 10^{13}$ *cm*$^{-3}$, $T_{e0} = 320$ *eV.*

An additional measurement of T_i was performed via Doppler-broadened oxygen lines, both parallel and perpendicular to B. The line used is an O VIII (8–7) line at 2977 Å produced by charge-exchange recombination [11]. Within 10% these Doppler temperatures agree with $T_{i,cx}$, indicating a Maxwellian distribution.

With the usual neoclassical formulas of heat conduction in the plateau regime, the ion energy balance cannot be fulfilled for collisional slowing down. These formulas for thermal transport are derived for thermal plasmas requiring only small electric fields for ambipolarity. However, in W VII-A the ambipolar potential may be dominated by the very energetic ions coming from the almost perpendicular neutral injection. Such strong radial electric fields have been

TABLE I. DECAY TIME (ms)

E (keV)	Measured	Calculated	Measured	Calculated
28.6 ± 3.9	0.4 ± 0.1	1.05 ± 0.25		0.5 ± 0.1
20.5 ± 2.3	2.45 ± 0.45	3.1 ± 0.5	1.3 ± 0.1	1.2 ± 0.3
12.7 ± 1.2	1.3 ± 0.3	1.6 ± 0.5	0.95 ± 0.25	1.25 ± 0.25
8.8 ± 0.7	2.6 ± 0.2	2.75 ± 0.3	1.75 ± 0.25	1.25 ± 0.25
6.3 ± 0.5	4.35 ± 0.75	4.8 ± 0.9	2.15 ± 0.4	2.35 ± 0.5
Plasma parameters	$n_{e0} = 5 \times 10^{13}$ cm^{-3} $T_{e0} = 540$ eV $T_{i0} = 1200$ eV		$n_{e0} = 9 \times 10^{13}$ cm^{-3} $T_{e0} = 360$ eV $T_{i0} = 475$ eV	

Energies of injected particles: $E_0 = 27$ keV; $(1/2)\,E_0 = 13.5$ keV; $(1/3)\,E_0 = 9$ keV.

deduced from poloidal rotation measurements and have been found responsible for the reduction of the fast particle orbit losses and the corresponding increase in heating efficiency.

In the plateau regime, the deviation of the drift surfaces of thermal ions from the magnetic surfaces is strongly reduced by the electric field if the poloidal rotation velocity $v_{E\times B}$ is large compared to the poloidal component of the parallel velocity, $\iota(r/R)v_{th}$. Note the large aspect ratio in W VII-A of $R/a \cong 20$. With increasing E×B drift, the poloidal turning points for more and more toroidally trapped particles vanish depending on particle energy. For the measured E-fields there are practically no banana-type orbits for thermal ions any longer. Consequently, the plateau transport coefficients are believed to be strongly reduced by these electric fields [12].

2.3. Effect of rotational transform ι

Similar to the experiments with low-β Ba plasmas in W II-A [13], the confinement in W VII-A is strongly dependent on the rotational transform ι. Figure 4 shows the energy content W versus rotational transform for stationary ECRH sustained plasmas. In Ref. [3], equivalent measurements have been reported for NI. Generally speaking, the energy content, hence the energy replacement time τ_E, increases with ι. Therefore, in spite of the reduction of the effective plasma radius due to the ellipticity of the magnetic surface, a reduction of electron heat transport with increasing ι is found, as expected from theory. At rational values of the transform $\iota(a) = m/n$, with $m \leqslant 3$, $n < 10$, minima of confinement

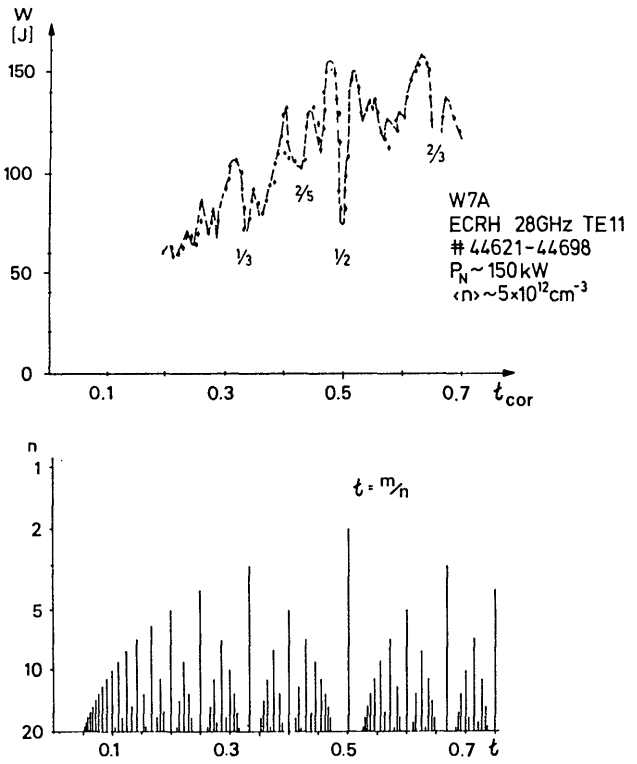

FIG.4. Energy content depending on rotational transform $\iota = \iota_0 + \iota_p$ for ECRH. For correlation, rational numbers $\iota = m/n$ are given and are indicated for low n only.

occur. At values of the transform, where the density of low-order rational numbers is small, optimum confinement is found.

2.3.1. Plasma current for $U_L = 0$

The plasma current I_P observed for $U_L = 0$ modifies the rotational transform corresponding to the current density profile j(r). At the plasma edge the iota profiles are:

$$\iota(a) = \iota_0 + \iota_p \quad \text{with} \quad \iota_p \sim \int_0^a j(r) \frac{r}{B} \, dr$$

Therefore, currents produced by the plasma pressure (positional shift, bootstrap current originating from pressure gradients) or by the heating mechanism influence the confinement. For *NI* into W VII-A, the plasma current I_P is observed to be

almost proportional to the plasma energy content W. The direction of the current agrees with the prediction for the bootstrap current and is such as to increase the rotational transform.

The transition from co- to counter-injection by reversing all magnetic fields also changes the direction of the current. The unaffected dependence of $|I_p|$ on W may exclude NI heating as the source for this current. The magnitude of the observed current, $|I_p|$ up to 2 kA, is larger than the bootstrap current calculated from the measured pressure profiles by a factor of up to 5, but bootstrap theory is not yet well established for non-axisymmetric configurations.

During *ECRH* with a pulse duration of $\Delta t \lesssim 40$ ms, a steady increase of a current with $dI_p/dt \approx 20$ kA/s is observed. The dominant process responsible for this current seems to be the confinement of non-thermal electrons produced by the heating mechanism.

2.3.2. *Control of the edge value of rotational transform*

Variations of the external transform for different values of the plasma current show that it is mainly the edge value of the transform, $\iota(a) = \iota_0 + \iota_p$, which determines the gross plasma behaviour. Details of the confinement depend on the entire iota profile which is influenced by the plasma pressure and residual currents, both of them introducing some shear [3]. By control of either the residual plasma current (ι_p) or the current in the helical windings (ι_0), rational values of iota can be avoided ($\iota_0 + \iota_p \neq m/n$) and stationary conditions at optimum confinement can be maintained. For NI experiments with constant ι_0, a loop voltage of $|U_L| < 0.3$ V has been used so far for controlling preprogrammed plasma currents within a range of $|I_p| < 2$ kA. At 3 T a current of $I_p = 1$ kA modifies the edge values of the transform by $\Delta\iota = 0.015$. During *ECRH* the increasing current I_P has been compensated by a corresponding change of the helical current I_H, controlled by feedback.

In Fig.5 the effects of current density distribution (shear!) on plasma confinement are demonstrated by comparing two discharges with $\iota_0 \approx 0.5$ and small but different plasma currents, $I_p = 0$ and $I_p = 2$ kA respectively. In both cases the signals from the soft X-ray diode array indicate a deterioration of the confinement once the edge value of iota passes through $\iota = 0.5$. The plasma with $I_p = 0$ even vanishes for $\iota = 0.5$ and recovers when iota is above 0.5. In contrast, the discharge with $I_p = 2$ kA (shear!) can be maintained even with $\iota(a) = 0.5$ because of $\iota(0) > 0.5$ resulting from peaked distributions of the plasma current. In this way the perturbations remain localized at the plasma edge. Corresponding shrinking of the density and temperature profiles is observed.

2.3.3. *Control of the ι profile*

$\iota(a) \neq m/n$ is necessary for operation with optimum confinement. The vacuum transform profile, however, is modified by residual currents and effects

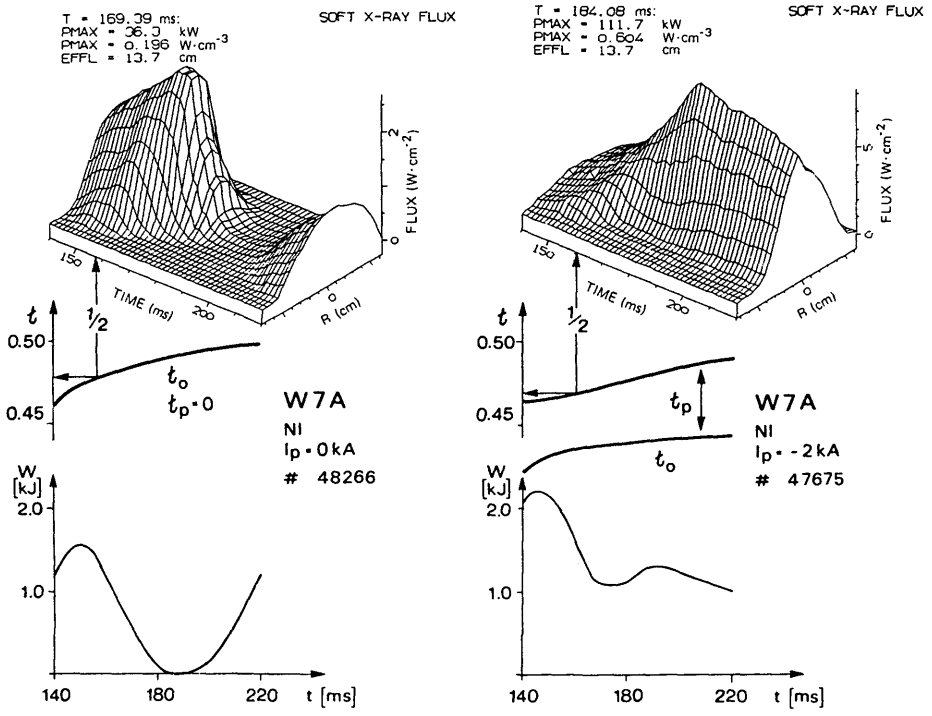

FIG.5. Influence of shear. The time development of the energy content W, the rotational transform ι and soft X-ray profile measurements in the vicinity of $\iota = 1/2$ have been correlated for $I_p = 0$ and -2 kA (NI counter, $B_0 = -3.2$ T).

due to the finite-β plasma. Equilibrium calculations using the Princeton code [14] confirm the effect of the plasma pressure. The ι profiles are *not* directly measurable, and it is therefore difficult to distinguish plasma pressure effects. First experiments slightly modulating the external transform, $\iota_0 + \tilde{\iota}$, indicate localization of the resonant surface by analysis of soft X-ray or electron cyclotron emission measurements with high spatial and time resolution. Fine adjustment of the transform ι_0 may then allow impurity flow and plasma pressure profiles to be modified.

2.4. Magnetic islands convection

In stellarators at rational values of the transform, magnetic islands are caused by small perturbing fields. Such perturbation fields are introduced, for example, by the current leads or the helical bridges. Islands of significant width can be calculated for low-order rational numbers $\iota = m/n$: 1/3, 2/5, 3/7, 1/2, 2/3. The largest islands are formed at $\iota = 1/2$.

Convection can be generated by inhomogeneous sources of particles, energy and momentum. On the basis of a fluid model it can be shown that the perturbation caused by these sources is localized to a very narrow vicinity of rational magnetic surfaces. In the case of anomalous electron heat conductivity such regions can be significantly enlarged. The effect becomes strong if the rational surface is close to the boundary, where the anomalous heat conductivity $\chi_{e\perp} \propto 1/T^{2/3}\, n$ [3] has its maximum and the parallel conductivity $\chi_{e\parallel} \propto T^{5/2}/n$ has its minimum.

The presence of magnetic islands enhances that effect. It is shown that close to the separatrix of the island large, Pfirsch-Schlüter currents, $j_\parallel$, arise, which lead to large electric fields and convective motion across the island.

Therefore a combined effect of magnetic island and convective motion rather than instabilities may be responsible for the increased losses at rational $\iota = m/n$.

3. CONCLUSIONS

Two heating methods, NI and ECRH, have been used to study stability and transport in the shearless $\ell = 2$ magnetic configuration of W VII-A. Good confinement can be maintained for particular values of the rotational transform in the vicinity of, but not at, $\iota = m/n$, e.g. 1/2, 1/3, 2/3. The available heating power seems to determine the maximum achievable β. No limitations by MHD instabilities have yet been found. At resonant magnetic surfaces, island formation and convection perturb the plasma behaviour. By control of the edge value of the rotational transform, ι-effects of a residual plasma current I_p can be compensated. Such currents are generated by plasma pressure (bootstrap current) or by the heating mechanism. Small shear produced by a non-homogeneous current density distribution apparently influences the localization and width of islands. Because of the small plasma radius and steep gradients of W VII-A, islands localized at the edge strongly influence even the global parameters. For higher plasma pressures than are accessible at present in W VII-A, modifications of the vacuum ι-profiles must be considered. Configurations with moderate shear and larger plasma diameter, as foreseen for W VII-AS, may therefore experience smaller effects at resonant magnetic surfaces also.

Heating, magnetic configuration and confinement properties are closely linked together in a stellarator. This has been demonstrated with the help of small plasma currents I_p, which modify the magnetic configuration. In addition, radial electric fields are present as a consequence of the nearly perpendicular injection. The corresponding reduction of the orbit losses increases heating efficiency. Corrections of the model for the ion heat conduction also seem to be necessary. The high ion temperatures have been confirmed by means of various diagnostics, and $T_{i\perp}$ and $T_{i\parallel}$ were found to be equal. Anomalous slowing down and preferential heating of the ions by the injected beam can now be excluded.

Consequently, a significant reduction of the ion heat conduction has to be assumed in order to describe the ion heat balance. If the large radial electric fields, $E \approx 0.1$ kV/cm, are properly introduced into the neoclassical transport model, banana-type orbits disappear and the transport coefficients in the plateau regime are strongly reduced. Certainly, these findings need further investigation, both by theory and experiment.

REFERENCES

[1] W VII-A TEAM and NEUTRAL INJECTION TEAM, "Neutral injection in the Wendelstein VII-A Stellarator with reduced Ohmic current", Plasma Physics and Controlled Nuclear Fusion Research 1980 (Proc. 8th Int. Conf. Brussels, 1980), Vol.1, IAEA, Vienna (1981) 185.

[2] W VII-A TEAM and NEUTRAL INJECTION GROUP, "Neutral-injection heating in the Wendelstein VII-A Stellarator", Plasma Physics and Controlled Nuclear Fusion Research 1982 (Proc. 9th Int. Conf. Baltimore, 1982), Vol.2, IAEA, Vienna (1983) 241.

[3] RENNER, H., et al., Plasma Phys. Contr. Fusion **26** 1A (1984) 183 (Invited Papers of 11th Europ. Conf. Aachen, 1983).

[4] ERCKMANN, V., et al., Paper No. IAEA-CN-44/D-I-5, these Proceedings, Vol.2.

[5] UO, K., et al., in Heating in Toroidal Plasmas (Proc. 4th Int. Symp. Rome, 1984), Vol.2 (1984) 947.

[6] TROYON, F., et al., Plasma Phys. Contr. Fusion **26** 1A (1984) 209 (Invited Papers of 11th Europ. Conf. Aachen, 1983).

[7] LORTZ, D., NÜHRENBERG, J., Nucl. Fusion **17** (1977) 125.

[8] W VII-A TEAM and NEUTRAL INJECTION GROUP, in Heating in Toroidal Plasmas (Proc. 4th Int. Symp. Rome, 1984), Vol.1 (1984) 95.

[9] MAASSBERG, H., HELLBERG, M.A., in Proc. Int. Conf. Plasma Physics, Lausanne, 1984, Vol.1, p. 55.

[10] W VII-A TEAM and NI GROUP, in Proc. 11th Europ. Conf. Controlled Fusion and Plasma Physics, Aachen, 1983, Vol.7D, p. 453.

[11] FONCK, R.J., et al., Princeton Plasma Physics Lab. Rep. PPPL-2067 (1983).

[12] STRINGER, T.E., in Proc. Symp. Int. School on Plasma Physics, Varenna, 1971.

[13] GRIEGER, G., OHLENDORF, W., PACHER, H.D., WOBIG, H., WOLF, G.H., "Particle-confinement minima in the Wendelstein II-a-Stellarator", Plasma Physics and Controlled Nuclear Fusion Research 1971 (Proc. 4th Int. Conf. Madison, 1971), Vol. 3, IAEA, Vienna (1971) 37.

[14] ANANIA, G., JOHNSON, J.L., Phys. Fluids **26** (1983) 3070.

[15] SYKES, A., et al., in Proc. 11th Europ. Conf. Controlled Fusion and Plasma Physics, Aachen, 1983, Vol. 7D, p.363.

NBI HEATING OF CURRENTLESS PLASMA IN HELIOTRON E

K. UO, A. IIYOSHI, T. OBIKI, O. MOTOJIMA, S. MORIMOTO,
M. WAKATANI, A. SASAKI, K. KONDO, M. SATO,
K. HANATANI, T. MUTOH, H. ZUSHI, H. KANEKO,
S. BESSHOU, M. NAKASUGA, F. SANO, T. MIZUUCHI,
S. SUDO, J. HARRIS*, I. OHTAKE, M. IIMA, H. OKADA,
Y. NAKASHIMA
Plasma Physics Laboratory, Kyoto University,
Gokasho, Uji, Kyoto,
Japan

Abstract

NBI HEATING OF CURRENTLESS PLASMA IN HELIOTRON E.

Recent results of the neutral beam heating (NBI) experiment with Heliotron E currentless plasmas are reported. The currentless heliotron plasma is initiated by the microwave power from gyrotrons (ECR, 53.2 GHz, 200 kW/tube) and heated by NBI of maximum 4.0 MW. At a magnetic field of 1.9 T, a maximum ion temperature of 1.0 keV is obtained at a density of 1.9×10^{13} cm^{-3} with NBI. The maximum $\bar{N}_e \tau_E^{NET}$ value is 2.4×10^{12} cm^{-3}·s. By reducing the magnetic field down to 0.94 T and using second-harmonic resonance of microwaves for producing a target plasma, a high-beta plasma is obtained with NBI. The maximum central and volume-averaged beta values obtained are 3.6% and 2%, respectively. A theoretical analysis of the MHD activities is performed, which explains the experimental data satisfactorily. By pellet injection, the line average density is increased up to 1.35×10^{14} cm^{-3}. In the NBI experiment, particles localized (trapped) by the helical ripple play an important role in the slowing-down process of the fast ions. It is observed experimentally that localized particles are well contained by the heliotron helical field using a neutral-particle energy analyser, a phenomenon that has been predicted numerically by a Monte-Carlo beam orbit Fokker-Planck code.

1. INTRODUCTION

This paper describes the results of the NBI heating experiments on the currentless plasma of the Heliotron E device. It is a final objective of Heliotron E experiments to produce a high energy currentless plasma, which will lead to the demonstration of the feasibility of the steady state operation of a helical system [1-8]. We have started an additional heating experiment in 1981 using NBI and 28 GHz gyrotron. In 1984, five 53.2 GHz

---

* Oak Ridge National Laboratory, Oak Ridge, Tennessee, USA.

gyrotrons were installed, which generated a microwave power up to 200 kW/tube at the frequency of 53.2 GHz. The maximum pulse length is 100 msec. Five TE02 circular oversize waveguides, which include flexible bends to avoid a mode conversion to TM mode are used to inject the microwave power to the vacuum chamber. It is possible to produce a target plasma for NBI with the density of $\bar{N}_e$ = 1.0 - 3.0 x 10^{13} cm^{-3} and temperatures of T_e = 100 - 1100 eV. The neutral beam was injected into this target plasma to produce a high energy currentless plasma. The NBI system has three beam lines [9]. The neutral beam power, the beam energy, and the maximum pulse duration are 1.3 - 4 MW, 23 - 30 keV, and 200 msec, respectively. A hydrogen pellet injector has been developed, with a gas gun of the basic type used at ORNL [10]. The form of a pellet is cylindrical and is shot out with a velocity of 600 - 1000 m/sec. A detailed description of the Heliotron E device is written in the references [1] and [6].

In the NBI heated Heliotron E plasma, trapped particles by helical field ripples play an important role in the slowing down process of fast ions and heating efficiency. They are called localized particles and once were theoretically believed to escape rapidly from the plasma. However, the effectiveness of the perpendicular NBI into the Heliotron E device was predicted by a guiding center drift orbit calculation including the classical slowing-down of the fast ions [14]. We performed an experiment to demonstrate this directly using a neutral-particle energy analyzer. The observed relaxation process of the fast ions agreed well with the numerical calculation.

In this paper, recent results of the currentless plasmas produced by ECR and NBI are reported. In Sections 2, 3, and 4, the results of the NBI heating experiment at high field (B = 1.9 Tesla), high-beta experiment, theoretical analysis, and pellet injection experiment to produce a high-density plasma are reported. In Section 5, we discuss about the orbit calculation of the localized fast ions and the experimental observation.

2. NEUTRAL-BEAM HEATING EXPERIMENT

The purpose of this section is to describe the heating efficiency and energy balance of the NBI heated currentless plasma. Figure 1 shows the experimental ion-heating efficiency in the currentless operation. The ion heating efficiency of neutral beam injection is found to be ΔT_i^{ch} = 2.0 x P_{abs} (kW)/$\bar{N}_e$ (10^{13} cm^{-3}) and saturation of T_i^{ch} has not been observed, where T_i^{ch} is the center-chord ion temperature determined by the

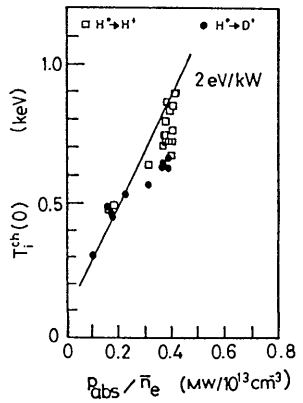

FIG.1. Ion heating efficiency with NBI. $T_i^{ch}(0)$ is central-chord ion temperature measured by neutral-particle energy analyser.

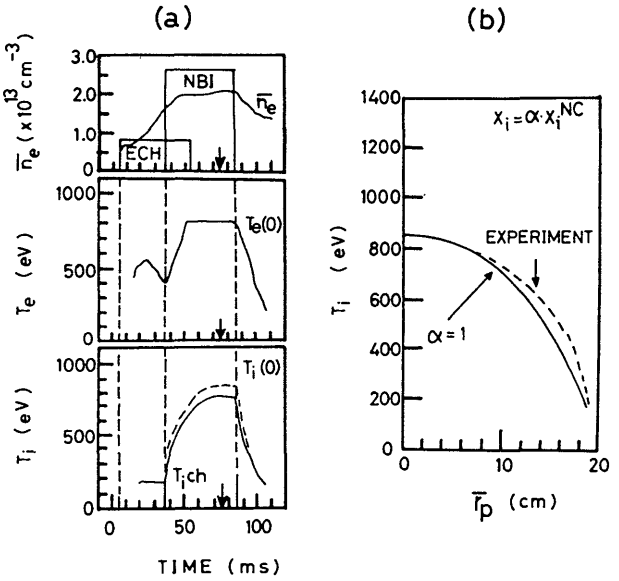

FIG.2. (a) Time traces of plasma parameters.
$B = 1.9$ T, $P_{NBI} = 1.8$ MW.
(b) Result of 1-D transport code calculation of ion thermal conductivity.
Reference is Hazeltine-Hinton ion thermal conductivity, χ_i^{NC}.

neutral particle analyzer. The central ion temperature $T_i(0)$ reaches more than 1.0 keV at $\bar{N}_e = 2 \times 10^{13}$ cm^{-3} for a port through neutral beam power of 1.8 MW. For better understanding of energy confinement properties, a detailed analysis of ion and electron energy balance has been performed on a series of typical

high-temperature NBI plasma. Figure 2 (a) shows the time traces of plasma density, electron temperature and ion temperature. This is the typical plasma with low beta but high temperature (B = 1.9 Tesla). The collisionality is in the localized particle regime for $\bar{r}_p \geq \bar{a}_p/2$, while the central portion lies in the plateau regime. The 1-D transport code could simulate the ion temperature profile in the steady-state phase by using the Hazeltine-Hinton ion thermal conductivity χ_i^{NC}. The result is shown in Fig. 2 (b). The dotted line shows experimental data. The effect of the helical field ripple is not included in the calculation. Within half a radius, the dominant energy loss of the ions is found to be through thermal conduction. The analysis of electrons with the 1-D code shows that the electron thermal conductivity is close to the value of so-called INTOR scaling. These results suggest that the ion heating during NBI can be reasonably explained in terms of classical beam power deposition (calculated using a Monte-Carlo beam-orbit code [14]). The $\bar{N}_e \tau_E^{NET}$ value has reached approximately 2.4×10^{12} cm^{-3}sec. Here τ_E^{NET} is defined as $\tau_E^{NET} = (W_e + W_i)/(P_{abs} - P_{rad})$; W_e and W_i are the electron and ion internal energy; P_{abs} is the initially deposited neutral beam power on the target plasma; P_{rad} is the total bolometric power loss.

The energy balance analysis has also been performed for a high-beta plasma ($\langle\beta\rangle \leq 2\%$). Ion thermal diffusivity is also close to the neoclassical value. However, it is found that an anomalous inward plasma flux is necessary to explain the observed density gradient. It is supposed that a modified transport mechanism exists in the case of the high-beta plasma with strong gas puffing and large neutral beam power. The detailed analysis of particle transport is now in progress with reference to the electron diffusivity.

3. HIGH-BETA EXPERIMENT AND THEORETICAL ANALYSIS

In order to increase the central beta value to more than 1%, it is necessary to reduce the helical magnetic field by a factor of 2. Therefore, the plasma production by the second-harmonic cyclotron wave absorption is used to produce a target plasma. The obtained central beta values are shown as a function of averaged density in Fig. 3. The maximum value is 3.6%. This beta value does not include the high-energy beam component. However, the beam-component is estimated to be relatively small in the high-density case. The obtained average beta value of 2% is high enough to demonstrate the high performance of the heliotron

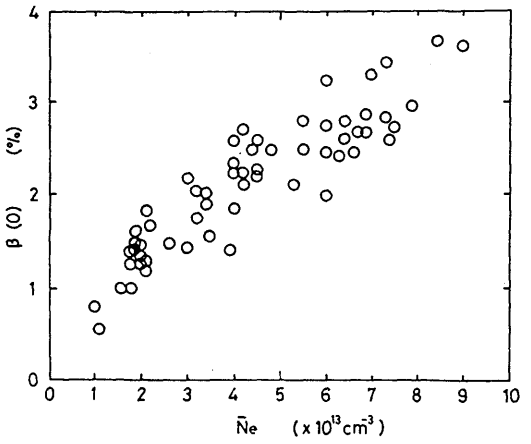

FIG.3. Central beta value obtained as a function of line-averaged density.

magnetic field configuration with high rotational transform and shear.

We have observed sawtooth oscillations on the soft x-ray signals when the central beta value exceeds about 2%. On the signals of the FIR interferometer, the electron cyclotron emission and the bolometer, we have observed in-phase oscillations. These oscillations are observed when the electron and ion temperatures or density profiles are peaked. When the strong gas puffing is applied, the temperature and density profiles become flat and MHD fluctuation diminishes. We have defined stable-quiet mode and MHD-unstable sawtooth mode as Q and S mode, respectively. The primary differences are observed in the parameter profiles and the impurity contents which are attributed to the difference of the amount of gas puffing. The essential difference of the MHD-activity between the Q mode and the S mode is the pressure profile. The former has a flatter profile than the latter.

This tendency is consistent with linear stability analyses to the low-n interchange ballooning modes of the Heliotron E device [11]. From the experimental data, the relaxation oscillation in the S mode has a poloidal mode number, m = 1, dominantly. There is a ι = 1 surface at $\bar{r}_p/\bar{a}_p$ = 0.7 in the vacuum magnetic configuration. The S mode appears for $\beta(0) \geq 2\%$, which is a little bit smaller than the linear stability analyses of the n = 1 mode for the assumed pressure profile, $P(\bar{r}_p/\bar{a}_p) = P(0) \times (1-(\bar{r}_p/\bar{a}_p)^2)^2$, which is close to the experimental profile of the S

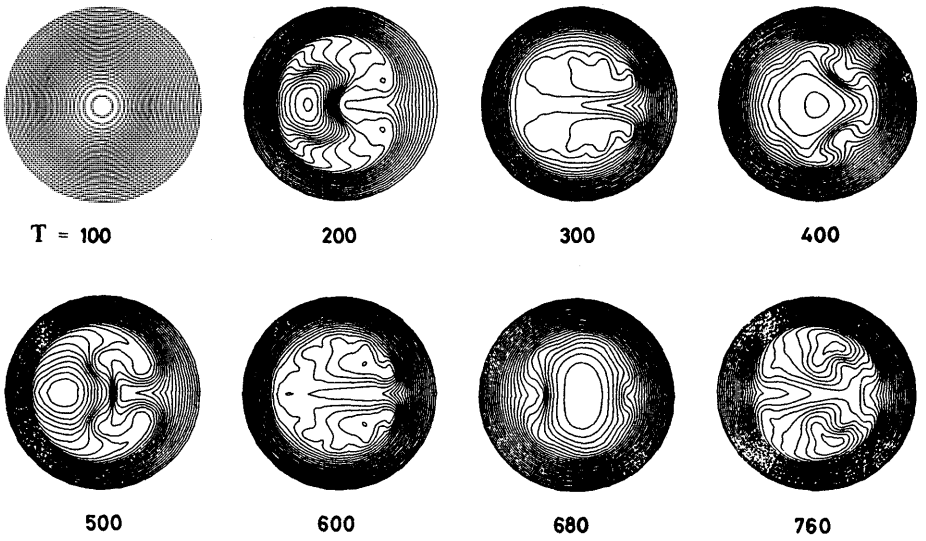

FIG.4. Time evolution of pressure profile. T is time normalized by poloidal Alfvén transit time. Central beta value is 2.3%.

mode. These facts suggest that the m = 1/n = 1 resistive interchange mode at the beta value marginal to the ideal mode brings about the relaxation oscillation. In the high-beta experiments of the Heliotron E device, the magnetic Reynolds number using a poloidal magnetic field S is less than 10^5, which is sufficient for a substantial growth rate of the resistive interchange mode.

In order to study the details of the relaxation instability, we have carried out the non-linear calculation of the m = 1/n = 1 resistive interchange mode. The non-linear MHD-model equations for the vorticity and the magnetic flux are the same as given by Strauss [12] under the straight approximation. For the pressure equation we include the transport term and the heating term,

$$dP/dt = k_\perp \nabla^2 P + \gamma_h P$$

where $k_\perp$ is the thermal diffusion coefficient and γ_h is the heating rate. The degradation of the heating rate is assumed simply $\gamma_h = 0.012\ (1 + (P_T(0)/P_o(0))^2)^{-1}$, which means that γ_h decreases, when $\beta(0)$ increases and the pressure-driven mode grows. Here $P_T(0)$ denotes a central plasma pressure at the timing of T. The numerical method to solve the resistive non-linear MHD equation is the same as used for ref. [13].

The numerical result in Fig. 4 shows a relaxation oscillation of the pressure profile. The parameters used for Fig. 4 are $\beta(0) = 2.3\%$, $k_\perp = 10^{-4}$ and $S = 5 \times 10^3$. Viscosity $\mu = 6 \times 10^{-6}$ is also included in the vorticity equation. The initial profile (T = 0) is given as $P(\bar{r}_p/\bar{a}_p) = P(0) \times (1 - (\bar{r}_p/\bar{a}_p)^2)$. At T = 200 (normalized by the poloidal Alfvén transit time), pressure profile shows an m = 1 deformation, and at T = 300 the central region within the $\iota = 1$ surface shows a flat profile. After the saturation it recovers a peaked profile approximately at T = 400. The m = 1 deformation is seen again T = 500. The peaked profile is also found at T = 680. From the variation of the kinetic energy the oscillation period seems about 250, which corresponds to about 125 μsec in the case of the Heliotron E device. In the S mode, there appear oscillations with period of 200 - 300 μsec at the internal disruption stage. Good agreement between the numerical results and the experiments is seen. It should be noted that both the transport and the heating process play a role in the nonlinear evolution of the pressure-driven mode.

4. PELLET INJECTION EXPERIMENTS

Pellet injection experiments with a pellet (1.6 mm^{ϕ} x 2 mmL, 0.6 - 1.0 km/s) have been carried out in order to increase the density. Target plasmas are current-free NBI heated plasmas. In the typical pellet injection experiments, only one beam line (BL-1) is turned on first at t = 20 ms after the beginning of ECR pulse, and 30 ms later two beam lines (BL-2 and BL-3) are additionally turned on. The latter stage continues for about 95 ms. The powers of BL-1, BL-2 and BL-3 are 580 - 670 kW, 720 - 840 kW and 570 - 670 kW, respectively. The acceleration voltage of neutral beams is 27 kV.

Figure 5 shows the temporal development of line-averaged density measured by FIR interferometer (alcohol laser, wavelength 118 μm). The case (1) (broken line) denotes a plasma without pellet injection. In the case (2), one pellet is injected at t = 22 ms after the beginning of the late stage of NBI, i.e. three beam lines are turned on. In the case (3), one pellet is injected 15 ms after the timing of the case (2). The behavior of the density change is similar to the case (2), but the peak line-average density increases to 1.35×10^{14} cm^{-3}, which is the highest density obtained in Heliotron E experiments. Disruption does not occur. The increase of the line-averaged density is 8.2×10^{13} cm^{-3}, which is roughly equal to the total particle number contained in the pellet ($\sim 10^{20}$ particles). It should be noted that the time scale of the decay of the density is very long.

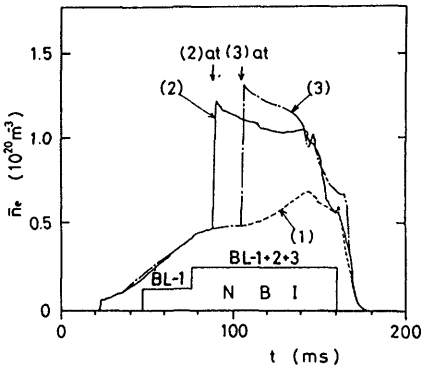

FIG.5. Temporal development of line-averaged density with pellet injection: (1) Without pellet; (2) and (3) with pellet. B = 1.9 T; total particle number is about 10^{20}.

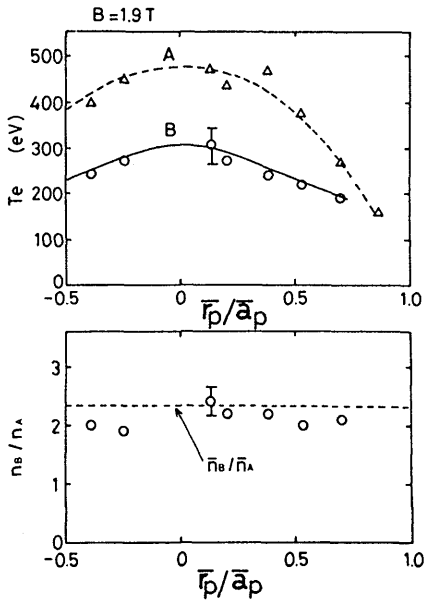

FIG.6. Top: electron temperature profiles with (Case B) and without (Case A) pellet. Bottom: ratio of local densities between Cases A and B.

Profiles of electron temperature and density are measured by a laser Thomson scattering system. Temperature profiles in the cases of (1) and (2) are shown in the upper part of Fig. 6. The profile B in the figure is measured at t = 7 ms after the pellet injection of the case (2). The profile A is measured at the same

timing as B, which is the case without pellet injection. In 7 msec, the electron temperature increases again to the 60% of the original value. The lower part of Fig. 6 shows the ratio of local density of the case B to that of the case A. The broken line denotes the ratio of the line-averaged density between the cases A and B. These two values independently measured are self-consistent within experimental errors. The apparent decay time of density after pellet injection was longer than 50 ms in the conditions of B = 1.9 Tesla and most of B = 0.94 Tesla. However in some experiments of B = 0.94 Tesla we observed that it was less than 10 ms, in which the bolometric loss seems to reach the limit of the energy balance of NBI plasma.

5. CONFINEMENT OF LOCALIZED FAST-ION ORBITS

Helically trapped particles play a key role in non-axisymmetric magnetic traps such as stellarator and heliotron. They are called localized particles and were once believed theoretically to escape out easily from the plasma. In a previous paper [14], however, we predicted an effectiveness of the perpendicular NBI into the Heliotron E device using the guiding-center drift orbit calculation with classical slowing-down process of fast ions. Good ion heating efficiency has been observed in a series of NBI experiments [1][3][5-6][15-16]. The purpose of this section is to show the experimental verification of the numerically predicted containment of the localized-fast-ions orbit calculated by the Monte-Carlo beam orbit Fokker-Planck code. Two beam lines, which have injection angles of perpendicular (BL-3) and 28^{o} (BL-1), are used for the experiment. The direction of BL-1 is that of the co-injection of the equivalent current of helical field. The drift orbit calculation shows that the fast ions created by BL-1 are depositted initially on passing orbits. However, in the case of BL-3 (perp.) injection, the fast ions are deposited on localized orbits, which is shown in Fig. 7 (a).

A passive 10-channel neutral-particle energy analyzer (NPA) is oriented perpendicularly to the magnetic axis to detect those drift orbits of the localized fast ions. Hydrogen-neutral beams (E_{inj} = 26 keV) were injected into a currentless deuterium plasma. A co-beam (700 kW) was turned on for 170 ms. Then a perp. beam (300 kW) was superimposed in the last 70 ms of the co-beam pulse (Fig. 7 (b)). Energy spectra of the fast-hydrogen neutrals were analyzed with NPA. In the highest-energy channel of NPA which almost corresponded to the injection energy (E_{NPA} = 23.9 keV), no neutral-particle flux was detected during the period of co-beam pulse. On the contrary, neutral-particle flux

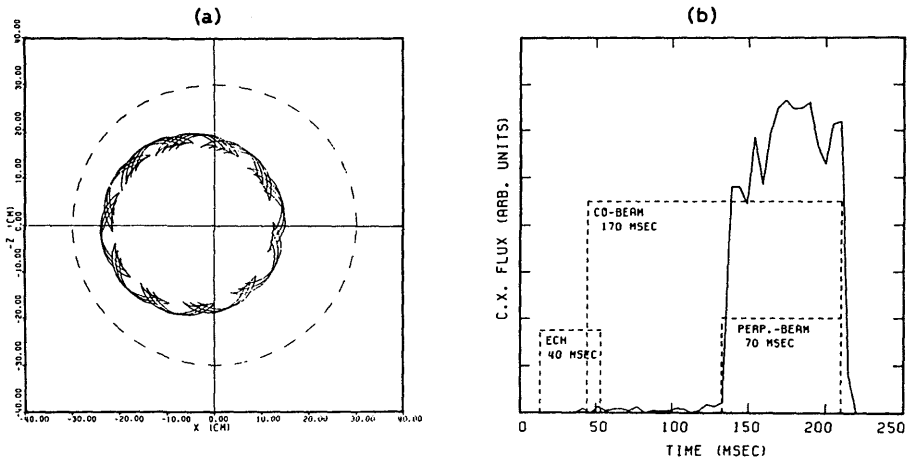

FIG. 7. (a) Poloidal contour of localized orbit of high-energy ion.
(b) time trace of neutral-particle flux with highest-energy channel (E_{NPA} = 23.9 keV).

was detected in the same energy channel which showed a quick response to the onset of the perp.-beam pulse. In the next lower energy channel (E_{NPA} = 15.8 keV), both co- and perp.-beam fluxes were detected; the flux intensity of the perp.-beam was much stronger than that of the co-beam although the input power of the former was less than half of the latter.

These results indicate (1) a strong anisotropy of the distribution of the hydrogen ions which have an energy range of E_{inj} in the velocity space and (2) the presence of the relaxation process of this anisotropy by pitch-angle scattering as they slow down to the lower energy. These results, however, indicate another important experimental fact related to the behavior of the localized particles in the heliotron-type magnetic field with deep helical field ripple. The high distinct neutral-particle flux synchronized with the perp.-injection timing (Fig. 7(b)) demonstrates that the fast ions with very large perpendicular energy can circulate around the major radius of the Heliotron E plasma since the perp.-beam (BL-3) is located at the opposite side of the torus with respect to the neutral-particle-energy analyzer. The high neutral-particle flux observed during the perp.-injection is an experimental result that indicates the confinement of the localized fast ions and their circulation around the torus without gettering into the loss cone in the velocity space.

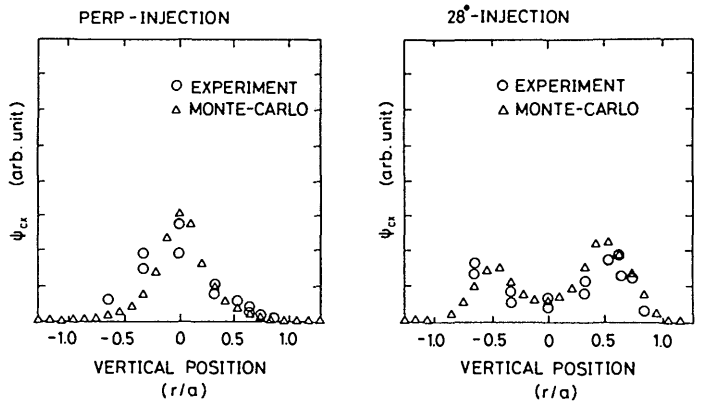

FIG.8. Vertical profiles of fast-neutral fluxes in cases of perpendicular and co(28°)-injections.

There was an interesting observation that the profiles of the fast-neutral flux were different between above perp.- and co-injections. They are shown in Fig. 8. The flux profiles of the co- and perp.-beam were markedly different. The co-beam flux had doubly-peaked profile. The perp.-beam flux was, however, singly-peaked, with a peak at the plasma center. To explain the observed flux profiles, a full Monte-Carlo calculation has been carried out. Because the detected flux depends on (a) geometries of the injector and detector, (b) fast-ion orbit and (c) plasma parameters, the whole experimental condition should be included in the 3D-2V Monte-Carlo techniques. It was found that the doubly-peaked profile of the co-beam flux and the singly-peaked profile of the perp.-beam flux were both reproduced by this calculation. The good agreement suggests that the classical assumptions of the drift orbit and the slowing-down process of the fast ions may be adequate for the description of the present NBI experiment.

6. CONCLUSION

We have analyzed the results of NBI heating experiments on the current less plasma. Fundamental and second-harmonics ECR plasmas are used as target plasmas for NBI. The density is increased by gas puffing during the NBI phase, and the central density exceeds 1 - 10 x 10^{13} cm^{-3}. The maximum ion temperature exceeds 1.0 keV. The maximum $\overline{N}_e \tau_E^{NET}$ value is 2.4 x 10^{12} cm^{-3} sec. By reducing the magnetic field, a high-beta plasma was

obtained. Maximum central and volume-averaged beta values obtained were 3.6% and 2%, respectively. Properties of the observed MHD-activities are explained well by the non-linear calculation of the m = 1/n = 1 interchange mode. The highest density of $\overline{N}_e$ = 1.35 x 10^{14} cm^{-3} was obtained by the pellet injection. The apparent decay time of the density after the pellet injection is longer than 50 msec in the cases of B= 1.9 Tesla. The confinement time is improved after the pellet injection. This satisfies the conditions for the proof-of-principle experiment in the Heliotron E device. We experimentally showed that the localized particles were well contained by the helical heliotron field by using the neutral-particle energy analyzer, which was numerically predicted by the Monte-Carlo beam orbit Fokker-Planck code. This is an encouraging result which motivates us to coninue the confinement experiment in the very rare collisional regime.

ACKNOWLEDGEMENT

We are grateful to the members of the Heliotron E supporting group for their excellent arrangement of the experiments.

REFERENCES

[1] UO, K., Heliotron E group, in Heating in Toroidal Plasmas (Proc. 3rd Joint Grenoble-Varenna Int. Symp. Grenoble, 1982), CEC, Brussels (1982).
[2] W VII-A TEAM (BARTLETT, D.V., et al.), NEUTRAL INJECTION TEAM (COOPER, D., et al.), in Plasma Physics and Controlled Nuclear Fusion Research (Proc. 8th Int. Conf. Brussels, 1980), Vol. 1, IAEA, Vienna (1981) 185.
[3] UO, K., HELIOTRON E GROUP, in Controlled Fusion and Plasma Physics (Proc. 10th Europ. Conf. Moscow, 1981) E-1.
[4] IIYOSHI, A., HELIOTRON E GROUP, Phys. Rev. Lett. **48** (1982) 745.
[5] UO, K., HELIOTRON E GROUP, in Plasma Physics and Controlled Nuclear Fusion Research 1980 (Proc. 8th Int. Conf. Brussels, 1980), Vol.1, IAEA, Vienna (1981) 217.
[6] UO, K., HELIOTRON E GROUP, in Plasma Physics and Controlled Nuclear Fusion Research 1982 (Proc. 9th Int. Conf. Baltimore, 1982), Vol.2, IAEA, Vienna (1983) 209.
[7] W VII-A TEAM (CATTANEI, G.,et al.), NI GROUP (FREUDENBERGER, K., et al.), ibid., 241.
[8] SATO, M., HELIOTRON E GROUP, Nucl. Fusion **23** (1983) 1333.
[9] OBIKI, T., SASAKI, A., SANO, F., UO, K., Rev. Sci. Instrum. **62** (1981) 1445.
[10] MILORA, L.L., FOSTER, C.A., Rev. Sci. Instrum. **50** (1979) 482.
[11] WAKATANI, M., IEEE Trans. Plasma Sci. **PS-q** (1981) 243.
[12] STRAUSS, H.R., Plasma Phys. **22** (1980) 733.
[13] WAKATANI, M., et al., Nucl. Fusion **23** (1983) 1669.

[14] HANATANI, K., WAKATANI, M., UO, K., Nucl. Fusion **21** (1981) 1067.
[15] UO, K., et al., Nucl. Instrum. Methods **207** (1983) 151.
[16] SANO, F., HELIOTRON E GROUP, in Controlled Fusion and Plasma Physics (Proc. 11th Europ. Conf. Aachen, 1983) 331.

DISCUSSION

H.R. GARNER: Your data show that fast (24 keV) ions injected perpendicularly were observed on a charge-exchange diagnostic around the torus. I would be interested to know how long these ions are confined and whether this confinement time can be measured from the decay of the charge-exchange signal after shut-off of the perpendicular beam. Also, what is the decay time of this signal?

K. UO: I have not yet checked this point in detail. However, it will be seen from the figure I showed that the decay time of the 24 keV ions appears to be about 3 ms, while their slowing-down time is about 10 ms. The detector observes only ions with an energy of 24 keV which, from the point of view of the observer (neutral particle analyser), are exactly perpendicular to the minor axis of the torus. It is therefore difficult to find the actual decay time at present, and this point requires further examination.

H.P. FURTH: Your paper resembles paper D-I-1 just presented by Dr. Renner in that surprisingly good ion confinement is reported in both cases. I note, however, that in the former paper the favourable effects are ascribed to an electrostatic potential, while your communication does not mention that possibility.

K.UO: To explain the good confinement in Heliotron E, we do not need to introduce an electric potential. The good confinement obtained is the result of the Heliotron's field quality. Electric potential will give rise to further improvement in confinement.

CURRENTLESS PLASMA PRODUCTION AND HEATING IN THE TORSATRON URAGAN-3 BY RF WAVES

V.V. BAKAEV, S.P. BONDARENKO, V.V. BRONNIKOV, V.S. VOJTSENYA, M.P. VASIL'EV, A.Yu. VOLOSHKO, Yu.V. GUTAREV, A.G. DIKIJ, I.A. DIKIJ, Yu.K. KUZNETSOV, A.E. KULAGA, M.S. KULAK, V.B. KOROVIN, B.V. KRAVCHIN, S.S. KALINICHENKO, E.M. LATS'KO, A.P. LITVINOV, A.I. LYSOJVAN, Yu.K. MIRONOV, N.I. NAZAROV, G.P. OPALEVA, O.S. PAVLICHENKO, V.K. PASHNEV, V.V. PLYUSNIN, N.F. PEREPELKIN, N.P. PONOMARENKO, A.S. SLAVNYJ, A.I. SKIBENKO, S.I. SOLODOVCHENKO, K.N. STEPANOV, V.S. TARAN, V.T. TOLOK, V.M. TONKOPRYAD, I.P. FOMIN, O.M. SHVETS, A.F. SHTAN'
Institute of Physics and Technology,
Ukrainian Academy of Sciences, Khar'kov,
Union of Soviet Socialist Republics

Abstract

CURRENTLESS PLASMA PRODUCTION AND HEATING IN THE TORSATRON URAGAN-3 BY RF WAVES.

The paper describes experimental results for plasma production and heating in the Uragan-3 torsatron with a divertor by RF oscillations ($\omega \approx \omega_A$ and $\omega \approx \omega_{Bi}$) and gives results for net-current-free plasma equilibrium and divertor fluxes.

1. INTRODUCTION

The progress recently achieved in stellarator research is mainly attributable to experiments performed in net-current-free conditions by using powerful plasma heating [1]. An ever increasing number of research workers use an operation scenario where a target net-current-free plasma is created by means of electron cyclotron resonance (ECR) and is further heated by the injection of neutrals [2]. The use of ECR for plasma production imposes, however, certain limitations on the range of magnetic-field intensities and target plasma densities ($\omega_{pe} \leqslant \omega_{Be}$). It appears therefore to be more attractive to use Alfvén or ion cyclotron resonances which provide better opportunities for plasma production and heating [3, 4].

This paper reports on experimental results obtained for net-current-free plasma production and heating in Uragan-3 by using RF waves in specific conditions of the torsatron with a helical divertor.

TABLE I. MAIN PARAMETERS OF MAGNETIC SYSTEM

Confining magnetic field (T)	2.5
Major radius of helical winding (cm)	100
Minor mean radius of helical winding (cm)	27
ℓ-number	3
Number of field periods	9
Calculated radius of last closed magnetic surface (cm)	13.5
Calculated rotational transform at last magnetic surface, ι_h (a)	0.6
Useful duration of magnetic field (s)	0.6

2. EXPERIMENTAL ARRANGEMENT

Uragan-3 is intended for plasma heating and confinement studies in the magnetic field of a torsatron configuration, with special emphasis on helical divertor operation. A magnetic system consisting of an $\ell = 3$ helical winding and correcting and compensating windings is placed inside a large ($\approx$70 m^3) vacuum chamber. The main parameters of the magnetic system are listed in Table I. The chamber is evacuated by means of a titanium getter pump with a pumping speed of 6×10^4 $L \cdot s^{-1}$, down to a pressure of 3×10^{-7} torr.

The experimental arrangement also involves two RF generators tuned in the frequency range from 2 to 15 MHz, which have a power of up to 1 MW for a $\leqslant$ 50 ms pulse. The machine includes two loop antennas for RF power input designed for specific ranges of toroidal and poloidal wavenumbers. They are located inside the helical winding in the immediate vicinity of the calculated outermost magnetic surface.

The layout of the diagnostic equipment is shown in Fig.1.

3. RF SURFACE CONDITIONING

The large inner surface of the vacuum chamber ($\approx$76 m^2) and the presence of unbakeable magnetic-system elements in the stainless-steel enclosure inside the chamber required the use of a new method of conditioning these and the antenna surfaces. In addition, a method of power input by means of the antennas that were used subsequently for dense plasma production and heating had to be developed. To this end, it appeared convenient to use the excitation of fast magnetosonic (FMS) waves in a cut-off frequency range [3]. These waves were

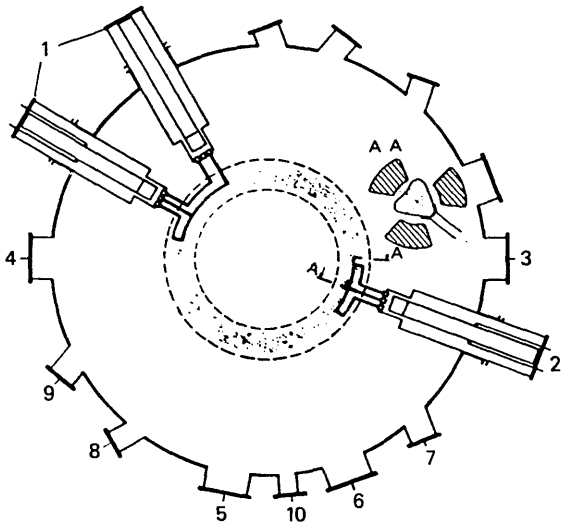

FIG.1. Arrangement of RF antennas and diagnostics in Uragan-3. 1,2 – RF antennas; 3 – 2 mm interferometer and superheterodyne radiometer; 4 – visible and UV spectroscopy; 5 – neutral-particle analyser, movable electric probe; 6 – 0.3 mm interferometer, 7 – VUV spectroscopy; 8 – laser scattering; 9 – soft-X-ray radiation detector; 10 – Fabry-Perot interferometer (λ = 8 mm).

excited in Uragan-3 by antenna excitation at 2.3–5.3 MHz for a magnetic field strength of 0.2–0.5 kG. With a steady magnetic field and continuous hydrogen admission ($\approx 10^{-4}$ torr), we obtained RF discharges of a duration of 50 ms and a maximum pulse frequency of up to 1 s^{-1}. The application of an RF kW pulse produced a plasma with a density of about 2×10^{12} cm^{-3} and an electron temperature of about 15 eV.

The mass-spectrometric analysis has shown that these discharges lead to effective production of H_2O molecules and hydrocarbons, thereby conditioning the surfaces interacting with the plasma. This method ensured rather clean (at least, for providing resonance RF heating) conditions in the chamber within 20 hours of RF conditioning after closing the chamber.

4. PLASMA PRODUCTION

The production of a sufficiently dense ($\geqslant 1 \times 10^{13}$ cm^{-3}) plasma by using Alfvén and ion cyclotron resonances without preliminary gas ionization encountered a number of difficulties. For given magnetic field strength and generator frequency,

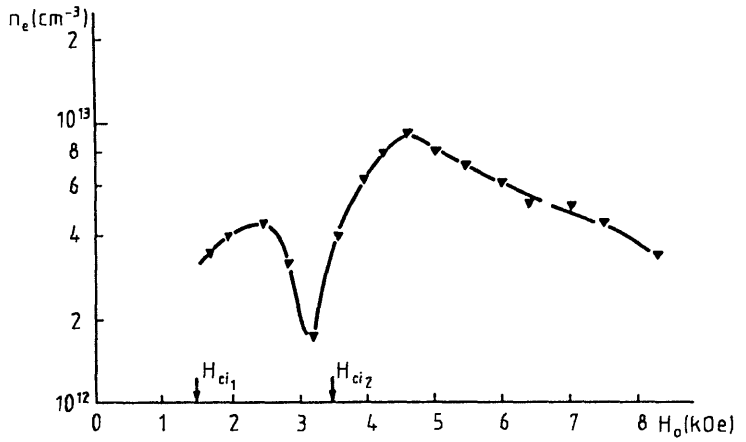

FIG.2. Average electron density versus magnetic-field intensity for RF frequencies f_1 = 2.3 MHz and f_2 = 5.3 MHz.

the density variation during the stage of plasma ionization and accumulation in a trap changes the conditions of wave excitation, propagation and absorption. This also involves variations of the loading resistance of the antenna and its potential. These difficulties were overcome by a proper choice of the antenna's toroidal and poloidal wavenumber spectra, which provided the 'mode relay race' for wave excitation at the stage of plasma density rise. Initially, to optimize the method of plasma production, we used continuous gas admission into the vacuum chamber.

Figure 2 shows the average plasma density (maximum during each RF pulse) versus the magnetic field strength. We see that the RF discharge is produced in a wide range of magnetic field strengths corresponding to the excitation of ion cyclotron (minimum B_φ) and Alfvén (with higher magnetic intensity) waves. The frequency rise shifts occurrence of a discharge towards the range of higher magnetic intensities. With one generator operating, the maximum radiated power (up to 500 kW) was limited by the maximum permissible RF voltage of the antenna during gas breakdown. Switching on the second generator with a time delay helped us to avoid no-load conditions for the second antenna and to increase the radiated power substantially (up to 1 MW).

The time evolution of the plasma parameters with two antennas in operation at different frequencies is shown in Fig.3. We see that the phase of gas ionization and plasma accumulation lasts for about 2 ms. We also note a monotonic increase in impurity line intensities during the RF pulse and a rapid decrease in both radiation temperature and fast charge-exchange atom flux after switching off the RF power. An additional spike of the H_α line intensity is due to radiative plasma recombination.

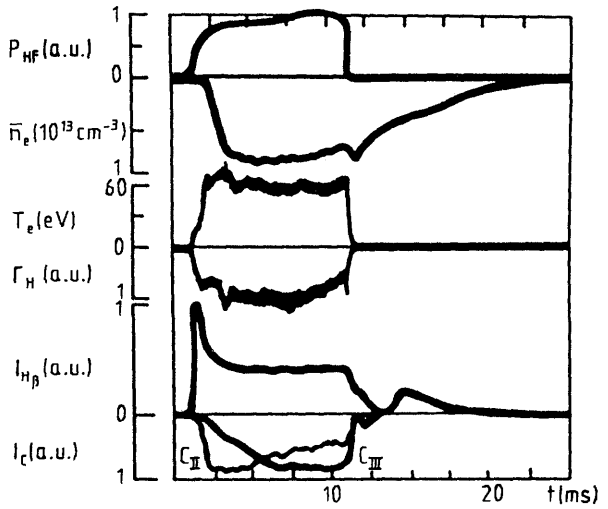

FIG.3. Time evolution of plasma parameters for RF frequencies f_1 = 2.3 MHz and f_2 = 5.3 MHz: absorbed power, electron density, flux of charge-exchange neutrals ($\mathcal{E}$ = 850 eV), intensity of H_α and carbon ion lines (B_φ = 4.8 kG).

In this set of experiments, for the $\lesssim$600 kW power supplied into the chamber, a plasma with an electron density of about 10^{13} cm^{-3} and electron and ion temperatures of 30 to 60 and 80 eV, respectively, was produced in a rather wide range of magnetic field values (2 kG $< B_\varphi <$ 10 kG).

The second set of experiments was performed to study the possibility of plasma production when both antennas are excited at about the same frequency ($f_1 = f_2$ = 5.3 MHz). Figure 4 shows the maximum electron density in the discharge versus the magnetic field strength, and Fig.5 illustrates the time evolution of plasma parameters for this case. For a magnetic field of B_φ = 5.2 kG and an initial hydrogen gas pressure of 1.4×10^{-4} torr, a plasma density of $\bar{n}_e \cong 2.5 \times 10^{13}$ cm^{-3} was obtained.

5. PLASMA EQUILIBRIUM

The plasma equilibrium studies were based on magnetic measurements using different external magnetic probes, i.e. diamagnetic loops, Rogowski coils and loops encircling the major torus axis. In the analysis of the experimental data we used a simple analytical model of plasma equilibrium in a stellarator [5], involving the assumptions of small toroidicity ($\rho/R \ll 1$) and slight asymmetry of the

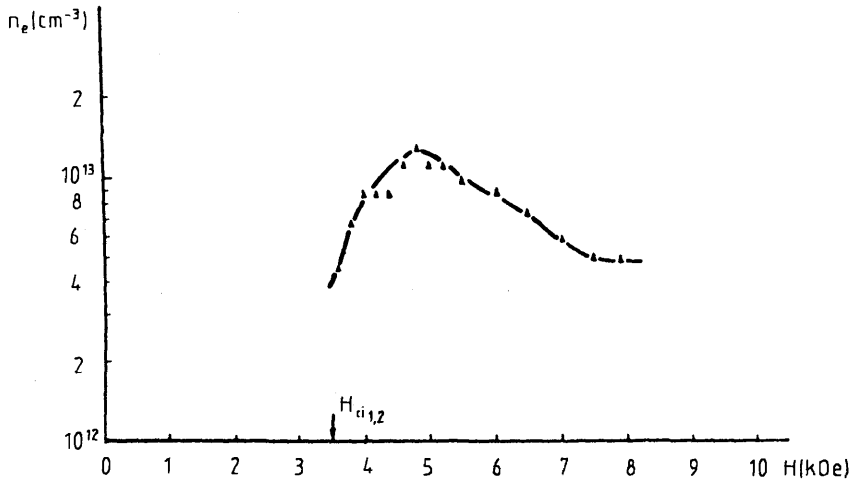

FIG.4. Average electron density versus magnetic intensity for $f_1 = f_2 = 5.3$ MHz.

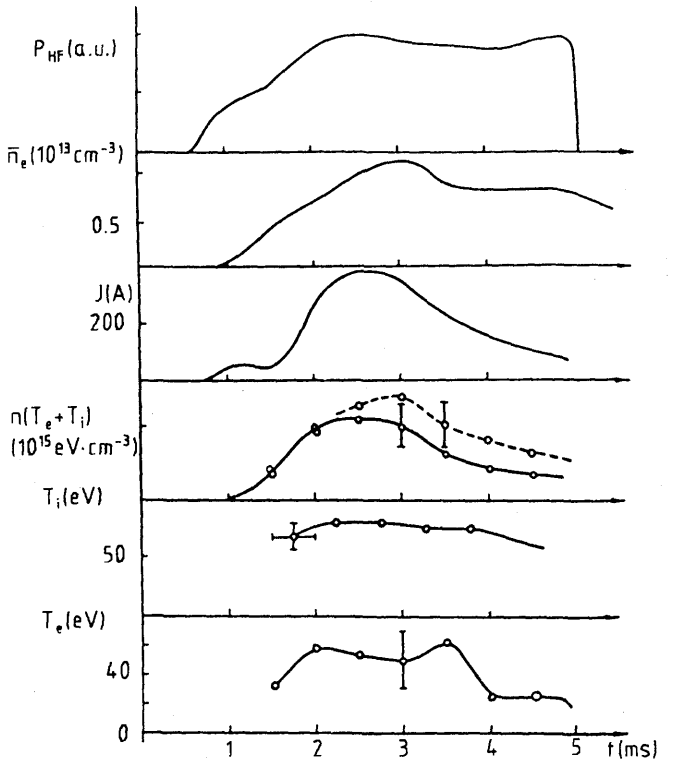

FIG.5. Time evolution of plasma parameters for $f_1 = f_2 = 5.3$ MHz: absorbed power, electron density, current in plasma and plasma pressure. (Solid line: ψ-winding; dotted line: $\bar{n}_e(\bar{T}_e + \bar{T}_i)$.)

magnetic surfaces ($\rho_{max} - \rho_{min} \ll \bar{\rho}$). It was also assumed that the magnetic configuration perturbations induced by the equilibrium currents are small. The experiment did not meet all these requirements well enough (particularly, the slight-asymmetry condition), a fact which is responsible for the approximate character of the numerical results obtained from the magnetic measurements.

The longitudinal magnetic flux variation due to plasma pressure and plasma current measured by a diamagnetic loop can be written as

$$\Delta\Phi = -\frac{4\pi^2 a^2 \bar{P}}{B_\varphi} + \frac{4\pi J_p^2}{c^2 B_\varphi} + \frac{4\pi^2}{cR}\int_0^a j_\varphi(\rho)\left[2\rho\int_0^\rho r\iota_h(r)dr + \rho^3\iota_h(\rho)\right]d\rho \quad (1)$$

where $\bar{P} = (2/a^2)\int_0^a P(\rho)\rho d\rho$ is the mean plasma pressure, $J_p = 2\pi\int_0^a j_\varphi(\rho)\rho d\rho$ is the plasma current, $\iota_h(\rho)$ is the stellarator angle of rotational transform, and B_φ is the longitudinal magnetic field.

The poloidal flux was measured by two loops (ψ-loops) [6] located outside the helical winding at an equal distance ρ_0 from the circular torus axis near the equatorial plane. The signal difference of the ψ-loops provided information on the magnitude of the dipole component of the longitudinal equilibrium current (the Pfirsch-Schlüter current):

$$j_{PS} = -\frac{2c}{\iota_h B_\varphi}\frac{\partial p}{\partial \rho}\cos\theta$$

The simplified expression for the poloidal flux variation has the form

$$\Delta\psi = 2\pi\rho_0 Rk\left\{-\frac{a^2 B_\varphi}{2\rho_0^2}\beta_0\alpha\int_0^1 \frac{x^{\alpha+1}}{\iota_h(x)}dx + B_\perp^j\right\} \quad (2)$$

where $B_\perp^j \approx (J_p/cR_0)\ln(8R/\rho_0)$ is the effective transverse field of the current $j_\varphi(\rho)$ on the measuring surface $\rho = \rho_0$, $x = \rho/a$, $\beta_0 = 8\pi p_0/(B_\varphi^2)$, $P = P_0(1-x^\alpha)$, k is a geometrical factor. Figure 6 shows the $nT = n(T_e + T_i)$ values obtained from $\Delta\Phi$ and $\Delta\psi$ measurements (assuming $\alpha = 3$). For comparison, the same figure shows $\bar{n}_e(\bar{T}_e + \bar{T}_i)$ data as derived from $\bar{n}_e\bar{T}_e$, $\bar{T}_i$ measurements. There is a fair agreement between the data, except for the initial stage when the time of pressure equalization on the magnetic surfaces is comparable with the duration of the initial stage.

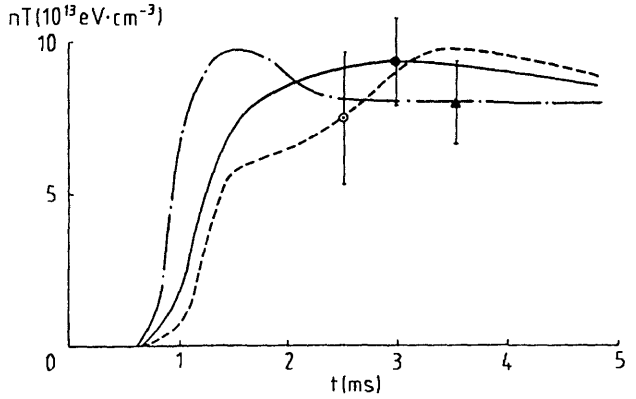

FIG. 6. Time evolution of plasma pressure: ——— *ψ-loop;* – · – · – · – *Φ-loop;* – – – – – $\bar{n}_e(\bar{T}_e + \bar{T}_i)$.

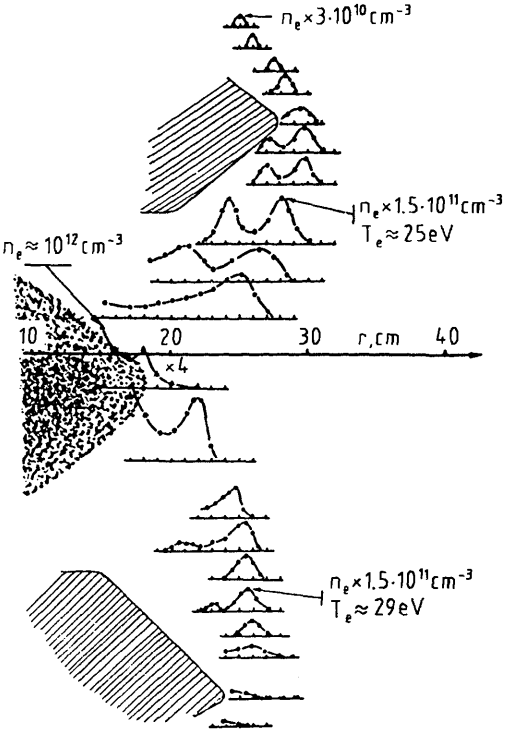

FIG. 7. Plasma density distribution in divertor fluxes.

6. PLASMA IN DIVERTOR FLUXES

The spatial distributions of the plasma fluxes escaping from the near-confinement volume were measured by a movable, double electric probe and several multilamellar probes located on the vacuum helical-winding enclosure, and the mean divertor flux density was measured by a microwave Fabry-Perot interferometer ($\lambda = 8$ mm). The measurements were performed for different RF frequencies ($f_1 = 2.3$ MHz, $f_2 = 5.2$ MHz), and at $B_\varphi = 4.5$ kG the mean plasma density in the containment volume was 8×10^{12} cm^{-3}. Figure 7 shows the results of the movable-probe measurements. We see that the plasma fluxes escaping from the confinement volume have two maxima converging and decreasing in magnitude with the distance from the confined-plasma area. The multilamellar-probe measurements have shown that, in accordance with magnetic-configuration calculations, the divertor fluxes, when occurring on the inner side of the torus, hit the helical-winding enclosures and bend around the winding sections on the outer side of the torus. The thickness of such a flux was about 1 cm and the mean plasma density across it was not higher than 3×10^{11} cm^{-3}. The electron and ion temperature measurements using, respectively, Langmuir probes and ion energy analysers with magnetic charge separation, have given $T_e = 35$ eV and $T_i = 60$ eV (68 ± 5 eV, as estimated from charge-exchange neutrals) at the periphery of the plasma confinement volume ($\rho = 8$ cm from the minor axis). The plasma density decreases along the divertor fluxes over typical distances of 10 to 15 cm in the plane of movable-probe measurements.

The general conclusions resulting from divertor-flux distribution measurements are as follows: the bulk of the divertor flux goes to the surface of the helical-winding enclosure that acts as a divertor plate, and the plasma target thickness in the divertor fluxes essentially varies in the minor-azimuth direction.

7. SUMMARY AND CONCLUSIONS

The experiments described in the Uragan-3 torsatron were mainly performed to develop a method of plasma production with RF power absorption in the frequency range of Alfvén and IC resonances. Simultaneous use of two antennas with specific toroidal and poloidal wavenumber spectra has allowed us to produce a plasma with a mean electron density of 2.5×10^{13} cm^{-3} in Uragan-3. In the operating volume, the antennas produce both longitudinal $\tilde{E}_\parallel$ (along the magnetic lines of force) and transverse $\tilde{E}_\perp$ electric fields. The interaction of these fields with electrons responsible for gas ionization may proceed in several stages, depending on the relationship between RF-field frequency and typical plasma frequency [4].

When $\omega > \omega_{Bi}$, the electrons may acquire the energy under the action of the longitudinal electric field of the antenna $\tilde{E}_\parallel$ until the condition $\omega \geqslant \omega_{pe}$ is fulfilled.

With further increase in the density, the antenna may excite electrostatic lower hybrid oscillations (initially forced, then natural ones). For $\omega > \sqrt{\omega_{pi}^2 + \omega_{Bi}^2}$, in the vicinity of the antenna, vortex electric fields $\tilde{E}_\perp$ exist, with amplitudes large enough for parametric lower hybrid instability excitation and electron heating to occur. For $\omega \geqslant \omega_A \sim v_A/a$, FMS waves propagating over the torus can be generated in the plasma. The electric-field amplitude of these waves is sufficient to impart a velocity of $v_\perp > v_s$ (v_s is the velocity of sound) to the electrons and to provide turbulent electron heating.

When $\omega < \omega_{Bi}$, the first stage at which electrons acquire their energy from the longitudinal electric field of the antenna, may be followed by the excitation, first, of a slow Alfvén wave, and then, as the plasma density increases, of an ordinary (electromagnetic) Alfvén wave.

With our antennas excited at closely spaced frequencies, the total power imparted to the plasma achieved 1.6 MW. Independently, the ultimate hydrogen plasma pressure under optimum conditions ($B_\varphi = 5.2$ kG) did not exceed 2.5×10^{15} eV · cm^{-3} ($\bar{\beta} = 0.6\%$). In deuterium experiments under optimum conditions ($B_\varphi = 8.6$ kG), the plasma pressure was not higher than 3×10^{15} eV · cm^{-3}. This implies that the global energy confinement time calculated on the assumption that the plasma volume is determined by the average radius of the last closed magnetic surface ($\bar{a} \approx 13$ cm), was within 0.17 ms. The estimates of possible energy losses due to ionization and charge-exchange processes, based on the measurements of atomic hydrogen density (from the H_α line intensity) and charge-exchange neutral fluxes, have demonstrated that these processes are not predominant in the plasma power balance.

This fact required accurate electron beam studies of the magnetic-configuration parameters of the machine. The measurements have shown that although the electron beam performs up to 200 revolutions in the near-axis region, rather long-lasting ($\geqslant$30 revolutions) beam confinement is detected in the volume with a mean radius of 6 to 7 cm, where the angle of rotational transform does not exceed 0.25. In this case, the neoclassical ion heat conduction χ_i gives the energy confinement time τ_E defined as $\tau_E = a^2/(6\chi_i)$ to be equal to 0.1 ms (for $\bar{n}_e = 1.5 \times 10^{13}$ cm^{-3}, $T_i \approx 200$ eV, $B_\varphi = 8.6$ kG, $a = 6.5$ cm, $\iota_h(a) = 0.25$), which is close to the observed value.

Thus, the experiments under discussion have shown that, with the excitation of FMS waves in the cut-off frequency range and of Alfvén waves by means of specially designed loop antennas, a rather dense net-current-free plasma can be produced in a torsatron, and large RF power can be delivered to this plasma. It is worth noting that the use of two generators provides a substantially wider operating range of the magnetic fields.

REFERENCES

[1] W VII-A TEAM, NI GROUP, in Controlled Fusion and Plasma Physics (Proc. 11th Europ. Conf. Aachen, 1983), Part 1 (1983) 191.
[2] MOTOJIMA, O., et al., in Heating in Toroidal Plasmas (Proc. 4th Int. Symp. Rome, 1984).
[3] ARSEN'EV, A.V., et al., in Plasma Physics and Controlled Nuclear Fusion Research (Proc. 9th Int. Conf. Baltimore, 1982), Vol.2, IAEA, Vienna (1983) 227.
[4] SHVETS, O.M., et al., in Heating in Toroidal Plasmas (Proc. 4th Int. Symp. Rome, 1984).
[5] SOLOV'EV, L.S., SHAFRANOV, V.D., Voprosy Teorii Plazmy, Moscow, Atomizdat 5 (1967) 3.
[6] KUZNETSOV, Yu.K., et al., Nucl. Fusion 23 (1983) 15.

DISCUSSION

M. SHIMADA: Your probe measurement showed two density peaks in the divertor. Can you explain this?

Yu.K. KUZNETSOV: We are unable at present to find a satisfactory explanation for this phenomenon.

J.D. CALLEN: You indicated concern about the quality of the outer magnetic surfaces in your experiment. What direct experimental measurements indicate that the quality of the magnetic surfaces is not good enough?

Yu.K. KUZNETSOV: Magnetic field measurements were performed using an electron beam. In the region $\rho \geqslant 7$ cm, electrons perform not more than 30 revolutions round the major radius of the torus. The method used does not permit measurement of the fine structure of the field, but it can reasonably be assumed that the magnetic surfaces have an island structure.

O. MOTOJIMA: Have you observed any toroidal current and, if so, what is its direction?

Yu.K. KUZNETSOV: We have measured the total current in the plasma using a Rogowski coil. It did not exceed 1 kA with the maximum RF power introduced into the plasma. We assume that this is a drag current caused by the asymmetry of RF wave excitation and absorption in the plasma.

FIRST RESULTS ON CURRENTLESS PLASMA PRODUCTION AND HEATING BY ECR WAVES IN THE L-2 STELLARATOR

E.D. ANDRYUKHINA, G.M. BATANOV, M.S. BEREZHETSKIJ, M.A. BLOKH, G.S. VORONOV, N.P. DONSKAYA, K.S. DYABILIN, S.V. KLADOV, L.M. KOVRIZHNYKH, L.V. KOLIK, N.F. LARIONOVA, A.I. MESHCHERYAKOV, A.V. NOVIKOVA, S.N. POPOV, A.V. SAPOZHNIKOV, K.A. SARKSYAN, I.S. SBITNIKOVA, A.D. SMIRNOVA, V.N. SUKHODOLSKIJ, A.E. PETROV, O.I. FEDYANIN, Yu.V. KHOLNOV, M.G. SHATS, I.S. SHPIGEL'
General Physics Institute,
Academy of Sciences of the USSR, Moscow

E.F. GIPPIUS, V.N. KOLESNIKOV, B.I. ILYUKHIN, A.V. PARAMONOV
P.N. Lebedev Physical Institute,
Academy of Sciences of the USSR, Moscow

A.G. LITVAK, O.B. SMOLYAKOVA, E.V. SUVOROV, A.A. FRAJMAN
Institute of Applied Physics,
Academy of Sciences of the USSR, Gorkij

Union of Soviet Socialist Republics

Abstract

FIRST RESULTS ON CURRENTLESS PLASMA PRODUCTION AND HEATING BY ECR WAVES IN THE L-2 STELLARATOR.

To produce and heat currentless plasma in the L-2 stellarator, extraordinary polarized ($\vec{E} \perp \vec{B}$) microwave radiation is utilized. The microwave power beam is directed into the vacuum vessel through a vertical port, which, because of the specific distribution of the magnetic field module in L-2, is equivalent to feeding from the strong-field side. At a beam power of 80 to 100 kW, a plasma with $T_e \approx 450-500$ eV, $T_i \approx 60$ eV, and $\bar{n}_e \approx 6 \times 10^{12} cm^{-3}$, and a total energy content of about 80 J is obtained; 30 to 50% of the microwave power is absorbed in the plasma. The absorption is shown to depend on n_e and to decrease for $n_e(0) \approx n_{cr}$. Collisionless heating of ions is recorded. Apparently, the observed broadening of the microwave spectrum scattered by the plasma hints at the appearance of some plasma instabilities resulting in the excitation of plasma oscillations.

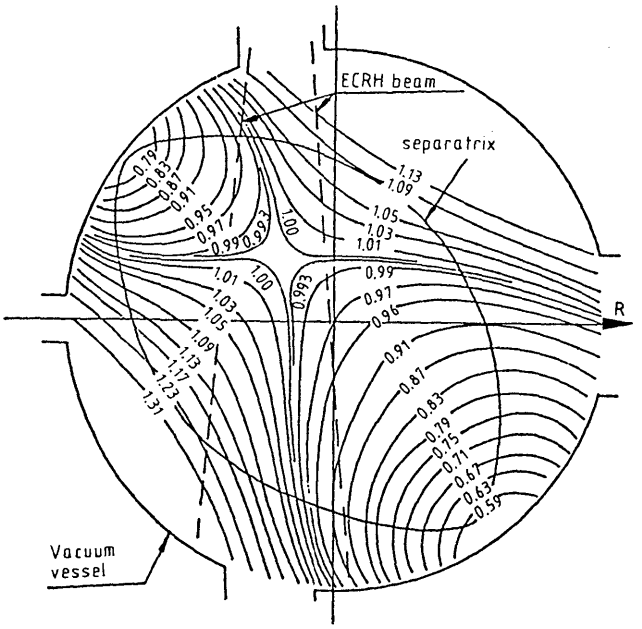

FIG.1. Distribution of magnetic field module in the cross-section of microwave power input.

1. In the L-2 stellarator (the main parameters of the machine are given in Ref.[1]), experiments were recently carried out on currentless plasma production and heating in the regime of electron cyclotron resonance at $\omega_0 = \omega_{He}$, where ω_0 is the microwave radiation frequency and ω_{He} is the electron gyrofrequency. Earlier, the results of such experiments in Heliotron-E [2, 3] and W-VIIA [4] were reported. In those works, the waveguide mode of the microwave power was used, with both polarizations present. In contrast to this situation, we used a Gaussian beam of extraordinary polarization ($\vec{E} \perp \vec{B}$) in order to study the efficiency of plasma heating in these conditions.

The specific distribution of the magnetic field module in the L-2 stellarator (Fig.1) allowed us to introduce the microwave power from the strong-field side through a vertical port, thus circumventing the cut-off layer and the region of upper hybrid resonance. In this geometry, however, the microwave beam refraction is somewhat higher, because of the skewness of the beam with respect to the density gradient.

2. In our experiments, we have used a gyrotron which yields microwave power of 200 kW at a wavelength of 10 mm in the H_{42} waveguide mode. To obtain an extraordinary wave, we use a specially designed mode converter. The beam is transported to the vacuum vessel via a quasi-optical catoptric system

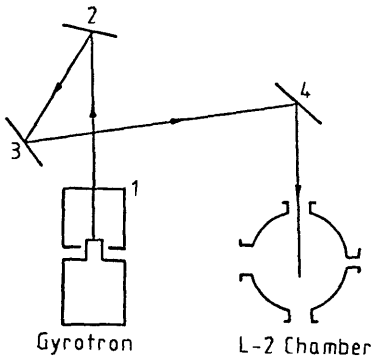

FIG.2. Scheme of quasi-optical catoptric system: 1–4 are the mirrors.

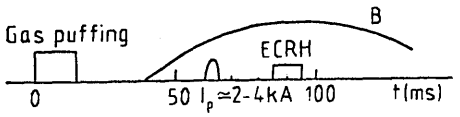

FIG.3. Scenario of ECRH experiments.

of four mirrors as shown in Fig.2. The last spherical mirror focuses the Gaussian beam into the vessel so that the beam diameter is 50 mm in the plane of the port, the beam divergence being ±6°. The power transported to the vessel was measured to be about 80 to 100 kW and to be practically fully polarized as an extraordinary wave.

3. The experiments were carried out with hydrogen at a magnetic field strength B_{res} such that the condition $\omega_0 = \omega_{He}$ was fulfilled at the centre of the plasma. The following experimental scenario was used (Fig.3): at the initial instant of time (80 to 90 ms before the heating pulse) hydrogen is puffed into the vessel, attaining a pressure of 5×10^{-5} torr; after 55 to 60 ms, a short (3 to 4 ms) inductive discharge is excited, thus producing a plasma density of $\bar{n}_e = (4-5) \times 10^{12}\text{cm}^{-3}$, which then decays to $(0.5-1) \times 10^{12}\text{cm}^{-3}$ at the moment when the microwave pulse is switched on. After switching on the microwave pulse, the electron density grows monotonically, reaching $\bar{n}_e = (5-7) \times 10^{12}\text{cm}^{-3}$ at the end of the pulse (the pulse duration is 7 to 9 ms).

The variation of the plasma parameters during the heating pulse is plotted in Fig.4. Two plasma regimes are possible, depending on the pre-ionization. In the scenario described above, the plasma density grows slowly (Fig.4a, solid line),

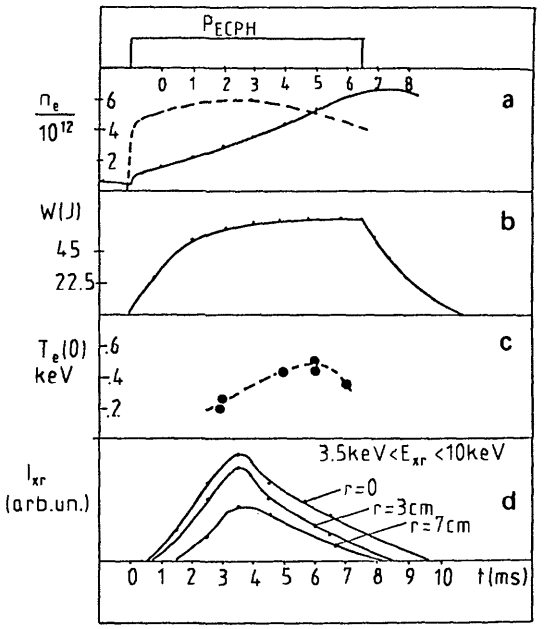

FIG.4. Time histories of plasma parameters.

the total plasma energy, $(3/2)\int n_e(T_e + T_i)dV)$ as determined by diamagnetic measurements also grows, attaining its maximum after 5 to 6 ms (Fig.4b), and the local electron temperature at the plasma centre increases up to a maximum value of about 500 eV at 5 to 6 ms and then decreases slightly (Fig.4c). On the other hand, if either no pre-ionization pulse is applied or the initial density before the heating pulse is $\bar{n}_e < 5 \times 10^{11} cm^{-3}$, the plasma density reaches a stationary level during 200 to 300 μs (Fig.4a, dashed line). In this case, however, the electron temperature is as low as 80 to 100 eV during the entire heating pulse. Thus, to achieve effective heating by extraordinary waves, a relatively slow growth of the plasma density has to be provided.

As is well known, the optical thickness of a plasma for extraordinary waves is [5] $\Gamma \approx T_e n_{cr}/n_e$, where $n_{cr} = \omega_0^2 m_e/(4\pi e^2)$, and m_e and e are electron mass and charge. Hence, at low temperatures but $n_{cr}/n_e \gg 1$, substantial absorption and heating of electrons can take place. With increasing density, the temperature growth rate decreases as $dT_e/dt \propto 1/n_e^2$. So, when the density approaches the critical value, the refraction increases, resulting in a decrease of microwave power in the resonance region. All this can lead to a decrease of the heating efficiency at the end of the heating pulse. When the density grows rapidly, the power released in the plasma is not sufficient for the radiation barrier to be overcome, because of

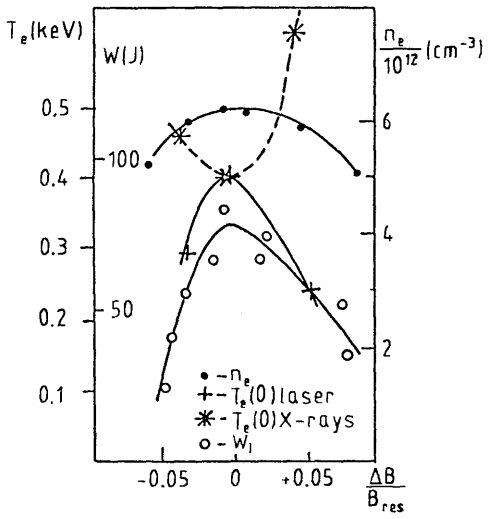

FIG.5. Dependences of plasma parameters on magnetic field strength: B_{res} is resonance field, $\Delta B = B - B_{res}$.

poor absorption and enhanced refraction. So, the electron temperature is fixed at 80 to 100 eV.

Figure 5 shows the dependence of plasma energy content and central electron temperature on the magnetic field. We see that $T_e(0)$ and the total plasma energy decrease drastically at $|\Delta B|/B_{res} = 3-5\%$.

4. In Fig.6, the measured profiles of electron temperature and density and of the radiative losses are shown. The electron temperature was measured at two points near the centre by Thomson scattering, but the electron density at the periphery was too low to be measured by the existing Thomson scattering devices. So, the electron temperature at $r > 4$ cm was found from the measured space-resolved intensities of the impurity spectral lines by using a numerical code. The electron density profile is defined by Abel inversion of the HCN laser interferometer data. The profile of the radiative losses is peaked at $r = 6-7$ cm.

The values of the energy stored in the plasma as obtained from integration of the profiles of Fig.6 and from diamagnetic measurements are both about 80 J. After switching off the heating, the plasma cools down during 2 to 3 ms, about 80% of the plasma energy being lost through radiation.

5. According to charge-exchange measurements, the energy distribution of the ions essentially differs from a Maxwellian one during the initial 4 to 5 ms of heating. Figure 7 shows the spectra of charge-exchange neutrals taken along the chords $r = 0$ and $r = 8$ cm at $\tau = 4.5-7.5$ ms (spectra 1 and 2) and along the chord

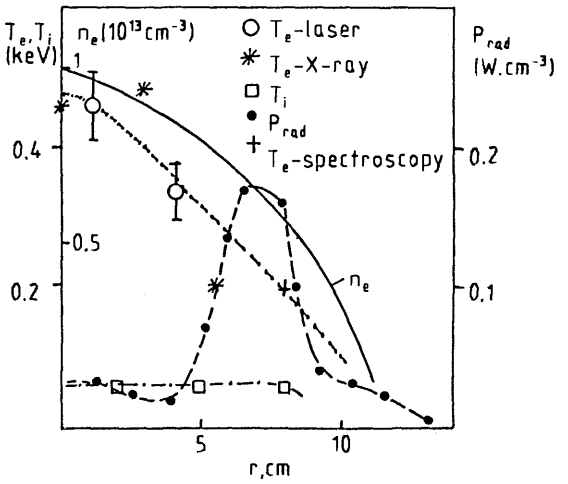

FIG.6. Profiles of plasma parameters.

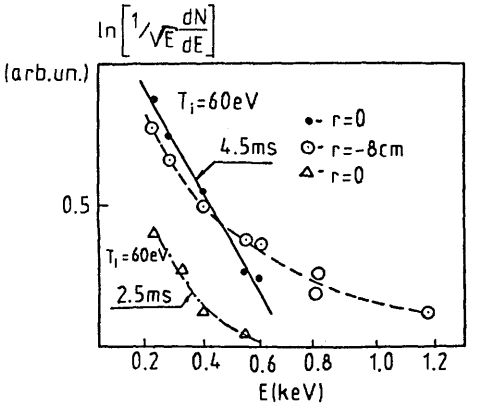

FIG.7. Energy spectra of charge-exchange neutrals.

r = 0 at τ = 1.5–3.5 ms (spectrum 3). The ion temperature derived from spectrum 1 in the energy range of 200–400 eV is T_i = 60 eV. But spectra 1 and 3 deviate strongly from Maxwellian ones. The ion 'temperature' as derived from spectrum 2 in the energy range of 400–1200 eV is 225 eV. This behaviour of charge-exchange spectra makes us suppose that during the initial heating stage, the energy is transferred to the ions by a collisionless mechanism, but at higher densities, the ions are heated and Maxwellized by Coulomb collisions. It should be mentioned that the ion temperature profile was found to be very flat (Fig.6).

The energy distributions of the electrons also exhibit deviations from the Maxwellian shape. These deviations were observed in the Thomson scattering spectra in the energy range $\mathscr{E} \leqslant 1$ keV and in the temporal behaviour of the soft-X-ray emission. They are most strongly pronounced during the initial phase of the heating pulse.

Figure 4d shows oscillograms of the X-ray emission in the energy range of 3.5–10 keV for three chords. The X-ray intensity is maximum at $\tau = 3$ ms although both electron temperature and density continue growing at this moment. This indicates that the electron distribution in energy is non-Maxwellian during the initial heating stage. Later on, the electrons become Maxwellized, because of the increased density. It is worth noting that the electron temperature as measured by a soft-X-ray spectrometer at a magnetic field out of resonance is much higher than that measured by Thomson scattering; the soft-X-ray spectra in these cases are strongly non-Maxwellian.

6. To reveal the reasons for the observed non-Maxwellian distributions, we have tried to measure the spectra of microwave power scattered by the plasma at frequencies near $f_0 \equiv \omega_0/2\pi$. For this purpose, a receiving horn was placed in a vertical port located at about 2.5 m from the heating beam along the torus. The scattering spectra at f_0 were measured by a pulsed spectral analyser. This device allowed the spectrum to be taken during 20 μs in the spectral range of $\Delta f = \pm 5$ MHz. The results obtained are presented in Fig.8. The spectrum taken at $\tau = 3$ ms (Fig.8a) is rather broadened and asymmetric while that at $\tau = 6$ ms is relatively narrow ($\Delta f = \pm 250$ kHz) and symmetric. Also broadened are the spectra measured under non-resonance conditions at $|\Delta B|/B_{res} = 3\%$ during the entire heating pulse (see Fig.8c, d). Although the analyser we used restricts measurements to low frequencies, we may assume that the observed broadening is due to scattering of the heating wave by oscillations excited in the plasma.

7. According to spectroscopic measurements performed in the visible and in vacuum ultra-violet regions, the main plasma impurities are carbon (0.5%) and oxygen (3%). The intensities of the observed spectral lines grow during the heating pulse, which can be explained by an increase in the electron density and, partly, by an increase in the concentration of the impurity ions.

A comparison of the radial profiles of the oxygen and carbon lines with results of numerical simulations indicated that the transport of impurities in ECRH can be described satisfactorily in the framework of neoclassical theory [6]. We note that a similar comparison for Ohmic heating [7] required the introduction of anomalous diffusivity much higher than the neoclassical one. In both cases, the impurities are in the Pfirsch-Schlüter regime of collisions.

8. The microwave power absorbed in the plasma, P_{ab}, was estimated from the derivatives of the diamagnetic signal at the moment when the microwave power was switched off. It was found that P_{ab} was 30 to 40 kW, the energy

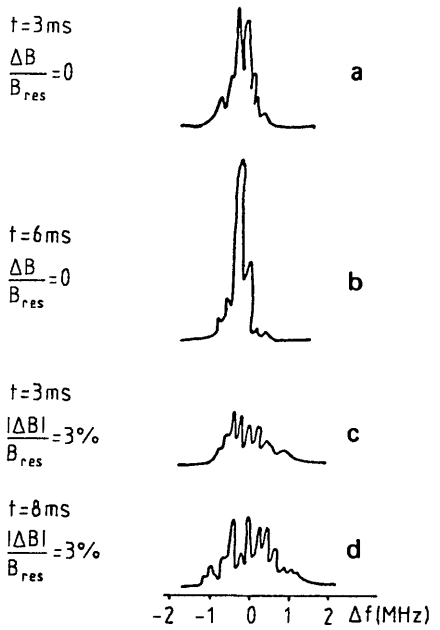

FIG.8. Spectra of scattered microwave power.

stored in the plasma being 60 to 80 J at the end of the heating pulse. So the energy confinement time can be estimated to be $\tau_E = W/P_{ab} = 2-2.5$ ms and the absorption efficiency is 30 to 50% at the end of the pulse.

CONCLUSIONS

(a) Using a microwave power of 80 to 100 kW in extraordinary polarization, currentless plasma was produced in the L-2 stellarator. The efficiency of microwave absorption was as high as 30 to 50%.

(b) In these conditions, the plasma parameters were: $T_e = 450-500$ eV, $T_i = 60$ eV, $\bar{n}_e = 6 \times 10^{12} cm^{-3}$, $W = 80$ J.

(c) The efficiency of absorption was found to depend on n_e; it decreases for $n_e(0) = n_{cr}$.

(d) The spectra of charge-exchange neutrals obtained indicate the presence of collisionless ion heating.

(e) Broadening of the spectra of microwave power scattered by the plasma suggests the development of some instabilities in the plasma, resulting in the excitation of plasma oscillations.

REFERENCES

[1] ANDRYUKHINA, E.D., BEREZHETSKIJ, M.S., GREBENSHCHIKOV, S.E., et al., L-2 Stellarator, P.N. Lebedev Physical Institute Preprint No.154, Moscow, 1977 (in Russian).

[2] UO, K., et al. Controlled Fusion and Plasma Physics (Proc. 10th Europ. Conf. Moscow, 1981), Vol.1 (Moscow, 1981) E-1.

[3] UO, K., in Heating in Toroidal Plasmas (Proc. 3rd Joint Grenoble-Varenna Int. Symp. Grenoble 1982), Vol.2, CEC, Brussels (1982) 667.

[4] WILHELM, R., in Plasma Physics and Controlled Fusion **26** 1A (1984) 259 (Invited papers of 11th Int. Conf. on Controlled Fusion and Plasma Physics, Aachen 1983).

[5] ALIKAEV, V.V., LITVAK, A.G., SUVOROV, E.V., FRAJMAN, A.A., High-frequency Plasma Heating, Gorkii, 1983 (in Russian).

[6] HIRSHMAN, S.P., SIGMAR, D.G., Nucl. Fusion **21** (1981) 1079.

[7] BLOKH, M.A., et al.,in Controlled Fusion and Plasma Physics (Proc. 11th Europ. Conf. Aachen 1983), Vol.7D, Part 1,215.

DISCUSSION

S.M. HAMBERGER: In L-2 you have $\iota = 1/2$ and $\iota = 1/3$ resonant surfaces inside the plasma. Do you see any evidence of MHD activity on these surfaces during ECRH?

L.M. KOVRIZHNYKH: We usually see MHD activity but we do not know what influence ECRH has on it.

L.A. BERRY: The ECH launching system on L-2 utilized the extraordinary mode launched from the high-field side of the fundamental resonance. This is expected to be more efficient than a mixed-mode launch from the low-field side. For many devices, the low-field launch is easier to implement. On the basis of your observations, is the additional complexity of the high-field launch compensated for by increased performance and/or efficiency?

L.M. KOVRIZHNYKH: We have not made a detailed study of the case in which the beam enters the chamber from the low-field side.

WAVE ABSORPTION AND TRANSPORT STUDIES ON ECR-HEATED STELLARATOR PLASMAS IN W VII-A

V. ERCKMANN, G. JANZEN, W. KASPAREK,
G. MÜLLER, E. RÄUCHLE, P.G. SCHÜLLER,
K. SCHWÖRER, M. THUMM, R. WILHELM
Institut für Plasmaforschung,
Universität Stuttgart, Stuttgart

W VII-A TEAM*
Max-Planck-Institut für Plasmaphysik,
Euratom-Association, Garching

Federal Republic of Germany

Abstract

WAVE ABSORPTION AND TRANSPORT STUDIES ON ECR-HEATED STELLARATOR PLASMAS IN W VII-A.

Ohmic heated current-free stellarator plasmas with attractive parameters (e.g. long mean free path conditions at $T_e \gtrsim 1.2$ keV and $n_e \approx 5 \times 10^{18}$ m^{-3} in deuterium) could be produced by irradiating intense, linearly polarized ECR waves into W VII-A. These waves ($f = 28$ GHz, $P \lesssim 200$ kW) were launched in O-mode orientation ($\vec{E} \parallel \vec{B}_0$, $\vec{k} \perp \vec{B}_0$) from the torus outside in the TE_{11} or HE_{11} mode. The localized power deposition results in a very narrow electron temperature profile, but it also allows profile shaping by choosing off-axis EC resonance. The total absorption agrees well with single-pass O-mode absorption, even at extreme power densities (absorbed power density ≈ 10 kW/cm^3) and at conditions of fully relativistic absorption ($k_\parallel/k < v_{th}/c$). In contrast to theoretical expectations, the reflection of the non-absorbed O-mode power in X-mode orientation did not improve the overall heating efficiency. The suspected reason for this is a local power absorption near the surface round the X-mode conversion layer caused by plasma density fluctuations. This idea is supported by the observation of wave decay spectra and correlated direct ion heating (appearance of high energy ions). Optimum confinement of the stellarator plasma in W VII-A is achieved at irrational ι-values. At these optimum conditions the electron energy transport in the ECRH-sustained plasma can be described by three main contributions: axisymmetric neoclassical transport in the central region, neoclassical losses due to the helical ripple at LMFP conditions in the intermediate zone, and anomalous losses ($\chi_{an} \propto 1/(n_e T_e^{0.6})$) dominating in the edge region.

---

* G. Cattanei, D. Dorst, A. Elsner, V. Erckmann, G. Grieger, P. Grigull, H. Hacker, H.J. Hartfuss, M.A. Hellberg, H. Jäckel, R. Jaenicke, J. Junker, M. Kick, H. Kroiss, G. Kuehner, H. Maassberg, C. Mahn, S. Marlier, G. Müller, W. Ohlendorf, F. Rau, H. Renner, H. Ringler, F. Sardei, M. Tutter, A. Weller, H. Wobig, E. Würsching, M. Zippe.

1. INTRODUCTION

Plasma heating by electron cyclotron resonance (ECRH) has been successfully tested in several plasma devices during the last few years. The main advantages of this high-frequency wave heating scheme are quasi-optical millimetre wave launching from simple open-ended circular waveguides, direct access to the plasma centre, localized power deposition (profile shaping), high heating efficiency, and the obvious absence of a direct impurity release, the latter being already verified in the MW range. This heating method is also of specific interest for a stellarator because ECRH provides the plasma build-up from a neutral gas as well as further heating to remarkable temperatures without the need of Ohmic heating [1–4].

ECRH experiments on the W VII-A Stellarator were performed at 28 GHz with a power of up to 200 kW and a pulse length of up to 40 ms. The frequency restricts the operation to plasma densities below the cut-off value of 10^{19} m^{-3} at a magnetic field of 1 T. Different wave launching systems were used to investigate the influence of RF beam divergence and polarization on the wave power deposition in order to find the optimum concept for larger scale ECRH applications in the future W VII-AS Modular Stellarator [5]. Concentrated and polarized RF beams allowed the highest values of electron temperature and plasma energy to be reached.

2. WAVE ABSORPTION AND PARAMETRIC DECAY

For reasons of accessibility to the plasma core by the RF wave, a linearly polarized microwave beam is launched in the equatorial plane of the torus from the outside, i.e. low field side, perpendicularly to the toroidal field. Only a wave polarized parallel to the magnetic field (ordinary polarization, O-mode) allows propagation towards the ECR layer in the plasma centre. Launching of the extraordinary mode (X-mode, $\vec{E} \perp \vec{B}_0$) results in strong reflections of the wave from the X-mode cut-off layer, and this was verified experimentally. The non-absorbed fraction of the incoming O-mode wave is reflected by a focusing polarization twist reflector mounted to the inner torus wall. The reflected wave penetrates the plasma in X-mode polarization and propagates towards the upper hybrid layer close to the outer plasma edge, where mode conversion to backward travelling and strongly damped electron Bernstein waves is predicted by theory [6]. This wave launching arrangement is shown schematically in Fig.1. Central electron temperatures of 1.2 keV at densities of 5×10^{18} m^{-3} were obtained with a pencil beam of 180 kW incident power emitted by a corrugated circular waveguide in the HE_{11} mode [7] and at a resonance field of 1 T on the magnetic axis.

The heating efficiency (η = absorbed power/incident power) is determined experimentally from the global plasma energy response to a fast (compared to the energy confinement time) reduction of the incident RF power [4, 8]; it is found

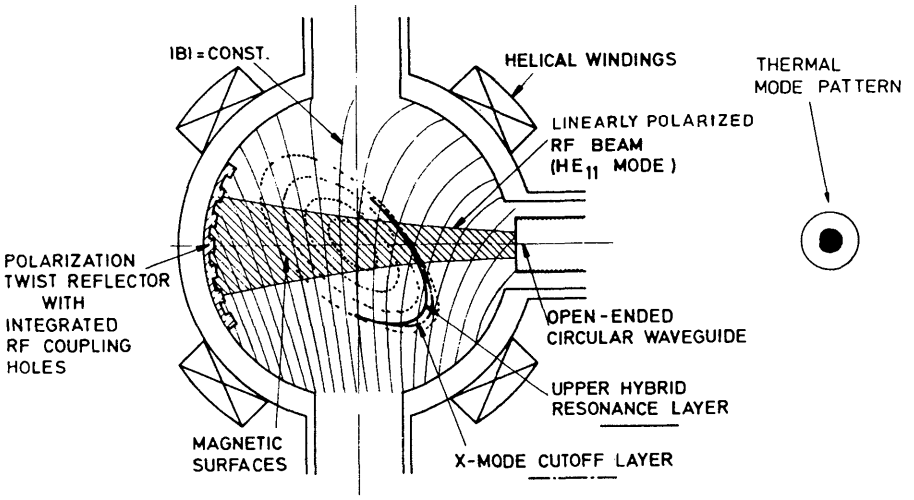

FIG.1. Stellarator plasma configuration, ECR wave-launching geometry and RF power distribution (thermographic paper burn pattern) of the linearly polarized HE_{11} mode at the antenna mouth.

to be in the range of $\eta = 0.3$ to 0.5. Measurements of the power density of the RF field reaching the polarization twist reflector indicate single-pass O-mode absorption of the same amount [9]. This value is also in agreement with the calculated O-mode absorption at electron temperatures mentioned above, which means that there is only little contribution of the X-mode absorption (via mode conversion to Bernstein waves) to the global plasma heating. A possible explanation of this fact is that the k-spectrum of the Bernstein waves is broadened by macroscopic fluctuations of the upper hybrid resonance layer or by parametric decay, which will lead to an absorption close to the plasma edge, where the energy is lost on a fast time scale. In the W VII-A experiments, parametric decay waves were identified. The low-frequency decay waves were detected by Langmuir probes at the plasma boundary showing a broad frequency spectrum with a sharp drop at a frequency of 230 MHz, which corresponds to the lower hybrid frequency close to the upper hybrid layer. The spectrum is shown in Fig.2(a). The high-frequency component of the decay spectrum was deduced from microwave emission measurements; a 10-channel superheterodyne detector with a tunable local oscillator served as spectrum analyser. Figure 2(b) shows the spectrum of the observed microwave radiation, which contains an upper and a lower sideband of the 28 GHz pump wave. The dominant lower sideband corresponds to the high-frequency decay component with a frequency range equal to the bandwidth of the low-frequency decay wave.

Simultaneously with the occurrence of wave decay, a highly energetic ion tail (E = 500 eV) is observed. Ion energy distributions measured by neutral

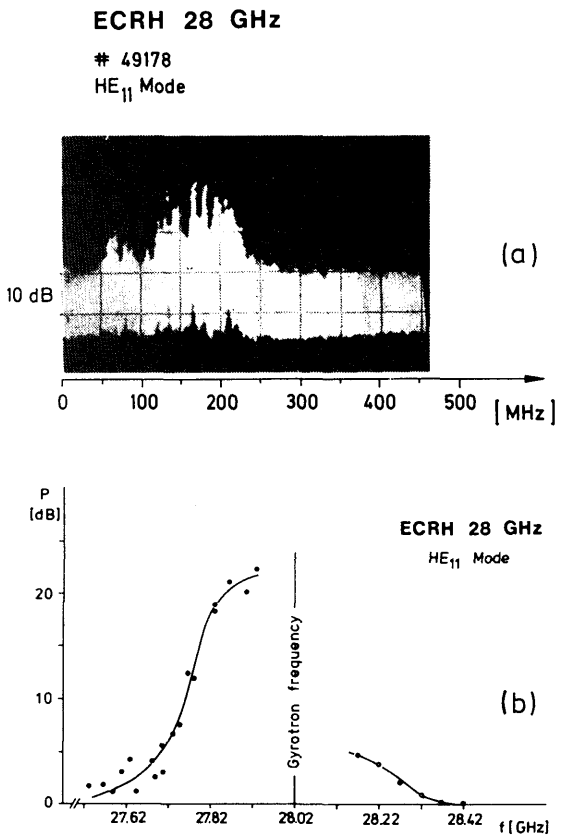

FIG.2. (a) Low-frequency decay spectrum detected by Langmuir probes. (b) High-frequency decay spectrum detected by a microwave heterodyne receiver.

particle diagnostics are shown in Fig.3. The flux of high energy ions is strongly correlated to the amplitude of the decay waves. This gives evidence of an energy transfer from the low-frequency decay waves to the ions. It follows from the energy conservation ($\omega_{pump} = \omega_{low} + \omega_{high}$) that the low-frequency waves may carry a maximum power of about 1 kW, which is sufficient to maintain the observed ion tails on the assumption of classical coupling to the ion bulk with temperatures of about 150 eV.

3. TEMPERATURE AND DENSITY PROFILES

ECRH has the inherent ability of tailoring the energy deposition profile by selecting different microwave beam cross-sections or by shifting the resonance

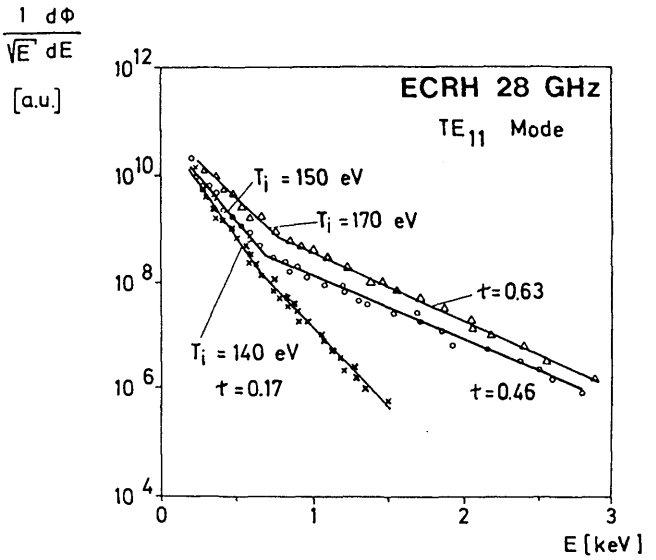

FIG.3. Ion energy distribution from charge-exchange flux measurements in discharges with different values of the rotational transform (TE_{11} irradiation).

zone out of the magnetic axis. The latter will result in a deposition of energy in an outer magnetic surface leading to edge heating of the plasma. Both methods were successfully tested in the experiment.

The microwave beam divergence was varied by changing the waveguide mode from TE_{02} [4] to TE_{11} (or HE_{11}) [10]. The influence of this change of beam power density is shown in Fig.4.

One recognizes the much more peaked temperature profile in the case of TE_{11} mode irradiation resulting in an almost doubled electron temperature on the plasma axis. The density profiles are similar in both cases. At a central density of 5×10^{18} m^{-3} (= 50% of the O-mode cut-off density) the effects of ray refraction are small. This was shown by measuring the transmitted power distribution of the wave at the polarization twist reflector surface. Similar results were obtained with the even more focused beam of the HE_{11} wave (near-field region). Here it should be noted that the RF power density in the plasma is further increased by a factor of about 1.5, approaching a value of 30 kW/cm^2 at ultimate conditions. Simultaneously, the beam divergence, measured as the mean deviation $k_{\parallel}/k$ from a ray perpendicular to the magnetic field, stays below v_{th}/c, which means that the O-mode absorption is due to relativistic resonance broadening. Nevertheless, the measured and calculated results for single-pass O-mode absorption agree well, even at these extreme conditions. Furthermore it can be stated that the plasma configuration with a power loss of less than 1 W/cm^3 is able to accept and distribute the large local power input of 10 kW/cm^3 without deterioration.

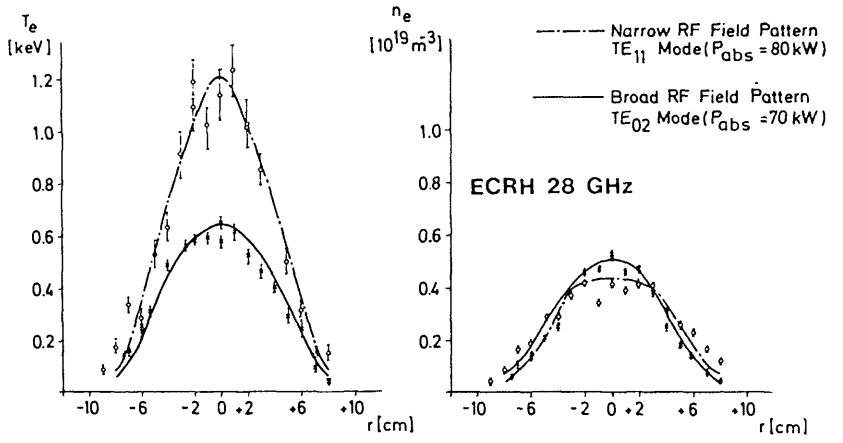

FIG.4. Comparison of measured and calculated profiles of T_e and n_e for unpolarized (TE_{02} mode) and polarized (TE_{11} mode) wave launching.

The highly concentrated input power of the HE_{11} wave also shows a shaping of the electron temperature profile by shifting the resonance zone away from the magnetic axis towards the plasma boundary. The resulting flat electron temperature profile is shown in Fig.5.

4. PLASMA TRANSPORT

Plasma confinement in the W VII-A stellarator strongly depends on the actual value of the rotational transform ι, as discussed in Paper No. IAEA-CN-44/D-I-1, in this volume. As a specific effect of the shearless $\ell = 2$ stellarator configuration, strong energy and particle outflow is observed at low-order rational ι-values (e.g. 1/3, 1/2, 2/3, ...), possibly due to ergodization of the flux surfaces. Optimum confinement, on the other hand, is achieved at a 'highly irrational ι-value' in the neighbourhood of a rational one. Plasma confinement at these optimum conditions was analysed by modelling the measured temperature and density profiles by 1-D transport calculations [3, 4, 8, 10]. In the numerical calculations the transport coefficients were assumed to be a sum of the following terms (e.g. electron heat conduction):

$$\chi_e = \chi_{e,\,nc} + \chi_{e,\,ripple} + \chi_{e,\,an}$$

where $\chi_{e,\,nc}$ is the neoclassical conductivity, as derived by Hinton and Hazeltine for an axisymmetric configuration [11]. $\chi_{e,\,ripple}$ describes the electron heat

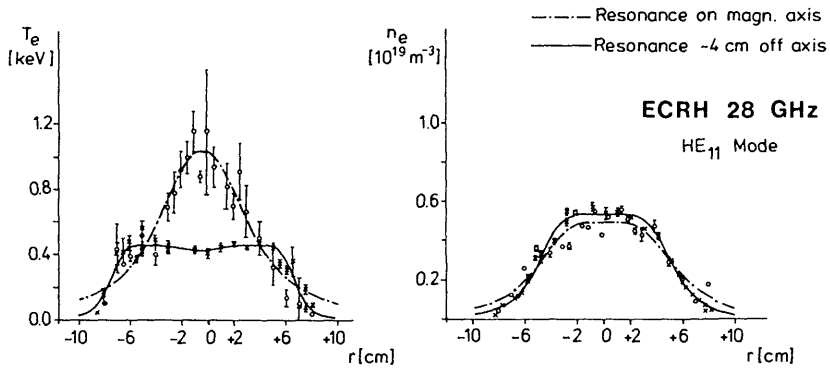

FIG.5. Comparison of measured T_e and n_e profiles for polarized wave launching (TE_{11} mode) with resonance on axis and with displaced resonance zone (inward shift by 4 cm, $B_0 = 0.98$ T).

transport due to the helically trapped particles according to Houlberg et al. [12]. Furthermore, an anomalous transport contribution was taken into account in the form: $\chi_{e,an} \propto 1/(n_e T_e^{0.6})$, as observed in Ohmic discharges in W VII-A.

The radial electron heating profile as a further input parameter was deduced from the measured transmitted RF power in combination with ray-tracing calculations. The resulting local heating power was then distributed across the flux surfaces crossing the area of local absorption. Evidence for the assumption of almost perfect transport parallel to $\vec{B}$ is given by the off-axis heating results, as can be seen in Fig.5. The ion energy transport was described by neoclassical, ripple and charge-exchange losses (the latter being calculated by a Monte Carlo procedure in the BALDUR code). As the ion heating term, the collisional power transfer P_{ei} due to Coulomb collisions was taken into account. The measured density profiles could be modelled with a diffusion coefficient containing an anomalous contribution $D_{an} \propto \chi_{e,an}$ and an atomic density influx at the plasma boundary. The measured radiation losses P_{rad} ($\approx$ (5–10) kW) were subtracted from the RF power input directly.

The most interesting results on the electron transport were obtained in the regime of low collisionality. At central electron temperatures above 1 keV, as achieved for the advanced TE_{11} and HE_{11} irradiation, the normalized mean free path (λ_t/R) exceeds the value at which the helical ripple transport should become significant. As a typical example, the resulting electron heat diffusivity and its individual contributions are shown as a function of the plasma radius in Fig.6 (the calculated values correspond to the TE_{11} case shown in Fig.4 and give the solid lines in the figure). According to the results shown in Fig.6, the radial power loss via the electron channel can be described by a nearly neoclassical transport in the plasma centre, a strong ripple contribution in the intermediate zone and by anomalous losses, which are dominant in the outer plasma regions.

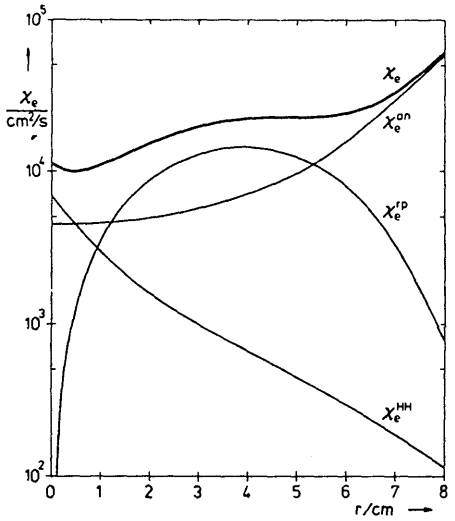

FIG.6. Radial profile of the transport coefficient χ_e (long mean free path conditions).

The calculated ion energy loss amounts to about 3–4 kW and is negligible for the overall energy balance. Nevertheless it should be noted that this value by far exceeds the collisional transfer P_{ei} for a pure deuterium plasma ($P_{ei} \approx 0.5$ kW). To simulate the observed ion temperature profile with a flat maximum of about 150 eV, an additional ion heating has to be assumed. The physical reasons for this additional ion heating are not yet clear. It may be attributed to direct RF ion heating (via low-frequency waves).

The transport coefficients derived from the stationary profile analysis still exhibit relatively large uncertainties. An improvement seems to be possible by measuring the dispersion of radially propagating heat waves, as first performed in tokamak transport studies [13]. In the tokamak case the heat pulses required are automatically generated by the internal sawtooth oscillations. They might be replaced by an appropriate RF power modulation for the ECR-heated stellarator plasma. This simultaneously gives the advantage of a free choice of pulse frequency, shape and amplitude. The latter would allow a linearized treatment of the heat diffusion equation at a sufficiently low degree of modulation. A first test of the modulation method has been started in the course of the 28 GHz experiments at W VII-A, using a rectangular pulse modulation of the gyrotron, as shown in an example in Fig.7. The time-dependent radial temperature response was obtained from ECE measurements at $2\omega_{ce}$. The ECE temperature measured at four radii on the high field side of the profile are also shown in the figure (the low field side EC emission is influenced by fast electrons [8]). Corresponding time-dependent 1-D transport calculations show quite similar results for the

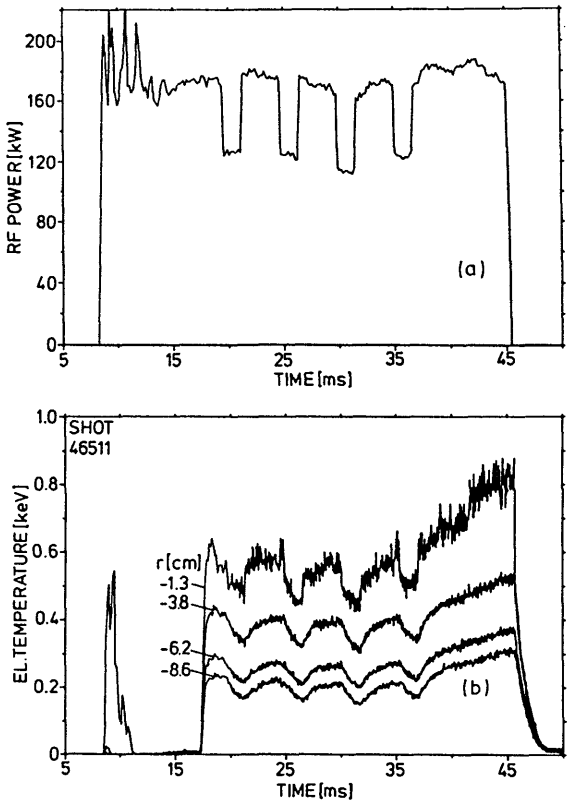

FIG. 7. Temporal behaviour of (a) modulated RF power and (b) electron temperature at four different radii measured by ECE.

temperature and density profiles, the latter being almost unaffected by the power modulation. Significant ECE signals, as shown in the figure, need a modulation amplitude, which is, however, at the limit for a simple linearized treatment of the problem. A more conclusive dispersion analysis at reduced modulation amplitudes is expected to be possible in the future ECRH experiments at 70 GHz with longer pulse duration, where the possibility of integrating measurements will exist.

5. CONCLUSIONS

At the W VII-A stellarator, plasma build-up and localized effective plasma heating were achieved by linearly polarized ECR wave irradiation. The waves were launched from the torus outside in the TE_{11} or HE_{11} mode, both in O-mode orientation. Direct absorption measurements in combination with ray tracing and

absorption calculations indicate that the absorbed power fraction (typically 50% at the optimum parameters) can be attributed to single-pass O-mode absorption. This also holds for the fully relativistic absorption (very narrow HE_{11} beam) and at extreme absorbed power densities ($\approx 10\,kW/cm^3$). The localized energy absorption allows shaping of the electron temperature profile. Reflection of the non-absorbed O-mode fraction as X-mode from an inside mirror did not improve the overall heating efficiency for the bulk plasma. The possible reason for this is the local absorption of generated Bernstein waves at the plasma edge caused by plasma turbulence. In addition to this process, wave decay was observed, the low-frequency component of which seems to give direct ion heating (ion tail formation).

Optimum energy and particle confinement in the almost shearless W VII-A stellarator occurs at an irrational ι-value close to a low-order rational one. For these conditions 1-D transport analysis showed the contributions to the radial transport: axisymmetric neoclassical transport seems to prevail in the central region; neoclassical losses due to the helical field ripple become important in the intermediate zone, when entering the long mean free path regime; and anomalous transport ($\chi_{e,an} \propto 1/(n_e T_e^{0.6})$) has to be assumed in the edge region.

REFERENCES

[1] ATKINSON, D.W., et al., "ECRH and neutral-injection experiments in the CLEO stellarator", Plasma Physics and Controlled Nuclear Fusion Research 1980 (Proc. 8th Int. Conf. Brussels, 1980), Vol.1, IAEA, Vienna (1981) 153.

[2] UO, K., et al., "Heliotron studies", Plasma Physics and Controlled Nuclear Fusion Research 1982 (Proc. 9th Int. Conf. Baltimore, 1982), Vol.2, IAEA, Vienna (1983) 209.

[3] RENNER, H., et al., Plasma Phys. Contr. Fusion **26** 1A (1984) 183 (Invited Papers of 11th Europ. Conf. Aachen, 1983).

[4] WILHELM, R., et al., Plasma Phys. Contr. Fusion **26** 1A (1984) 259 (Invited Papers of 11th Europ. Conf. Aachen, 1983).

[5] BROSSMANN, U., et al., "Concept of an advanced stellarator", Plasma Physics and Controlled Nuclear Fusion Research 1982 (Proc. 9th Int. Conf. Baltimore, 1982), Vol.3, IAEA, Vienna (1983) 141.

[6] STIX, T.H., Phys. Rev. Lett. **15** (1965) 878.

[7] THUMM, M., et al., in Heating in Toroidal Plasmas (Proc. 4th Int. Symp. Rome, 1984), Vol.2 (1984) 1461.

[8] WILHELM, R., et al., to be published in Plasma Phys. Contr. Fusion.

[9] SCHÜLLER, P.G., et al., in Proc. 4th Int. Workshop on ECE and ECRH, Frascati, 1984, Contributed Paper C-8, in press.

[10] ERCKMANN, V., et al., in Heating in Toroidal Plasmas (Proc. 4th Int. Symp. Rome, 1984), Vol.2 (1984) 846.

[11] HINTON, F.L., HAZELTINE, R.D., Rev. Mod. Phys. **48** (1975) 239.

[12] HOULBERG, W.A., et al., in Proc. 4th US Stellarator Workshop, Oak Ridge, 1983, p.77.

[13] SOLER, M., CALLEN, J.D., Nucl. Fusion **19** (1979) 703.

DISCUSSION

R.J.GOLDSTON: You showed very interesting data on the response of $T_e(r)$ to modulated RF power. I do not understand why you felt you could not analyse these data to learn about transport coefficients. There should be information both in the timing and in the amplitude of the response of the outer channels.

G. MÜLLER: We have analysed the electron cyclotron emission temperature response, and it does indeed provide information about the dispersion of the heat wave. In present conditions, however, the accuracy of the measurements in terms of noise is not sufficient to perform a reasonable Fourier analysis. The experiments must be seen as being proof-of-principle experiments with a view to future long-pulse application, in which the signal-to-noise ratio will be improved by small bandwidth detection.

A. Chian-Long CHIAN: Have you identified the low-frequency component of the wave decay process observed, and what is the influence of the decay process on the electron temperature?

G. MÜLLER: The low-frequency component has a quasi-continuous frequency spectrum up to the lower hybrid frequency. Since the k-spectrum cannot be measured, a mode analysis is not possible. Electron heating at the plasma edge cannot be excluded.

R.S. PEASE: Can you say why the various mechanisms proposed for electron thermal conduction dominate in different regions?

G. MÜLLER: The value of electron thermal conduction was derived from measured profiles and the heat source. In the plasma core (i.e. r = (2/3) a) this value agrees with the neoclassical value (including the helically trapped electron contribution). At the plasma edge, however, there seems to be an anomalous contribution to χ_e. It can be modelled by a scaling:

$$\chi_e = c \frac{1}{n_e} \frac{1}{T_e^{0.6}}$$

where c is fitted to the experimental result.

G. GRIEGER: I would just like to add that the anomalous transport coefficient was determined experimentally in OH discharges and that n and T are in the denominator $\chi_{e\,anomalous} \sim (1/n)T^{0.6}$. With the parameters achieved, this contribution is significant only at the plasma edge.

HIGH-CURRENT HIGH-BETA TOROIDAL PINCH EXPERIMENTS ON OHTE

T. TAMANO, W.D. BARD, T.N. CARLSTROM, C. CHU, B. CURWEN, R.K. FISHER, D.W. GRAUMANN, R.R. GOFORTH, G.L. JACKSON, R.J. LA HAYE, T. OHKAWA, M.J. SCHAFFER, M.T. SAITO, P.L. TAYLOR, T.S. TAYLOR
GA Technologies Inc.,
San Diego, California

D.F. REGISTER, S.E. WALKER
Phillips Petroleum Co.,
Bartlesville, Oklahoma

United States of America

Abstract

HIGH-CURRENT HIGH-BETA TOROIDAL PINCH EXPERIMENTS IN OHTE.

Toroidal pinch experiments have been carried out with a plasma current of up to 500 kA in the OHTE device. The empirical scalings previously obtained at the lower current level continue to hold at the high current level, indicating that plasma temperature increases linearly with plasma current. Poloidal beta values of about 20% have been achieved at each current level and Lawson parameters $n\tau$ around 10^{11} $cm^{-3} \cdot s$ have been obtained.

In the previous IAEA conference at Baltimore in 1982, the achievement of high density and high-β OHTE plasmas with plasma currents of up to 150 kA was reported [1]. The empirical scaling indicated that the electron temperature increased linearly with the plasma current. Since then, the plasma current was raised to the engineering design value of 500 kA and the plasma parameter range was greatly widened. This paper reports results of the high current experiments in the OHTE mode.

The OHTE device is a toroidal pinch device with $\ell = 3$ helical windings [2]. It is similar to a reversed field pinch (RFP) device, except that the helical fields produced by the windings provide additional magnetic shear near the plasma edge region where an ordinary RFP plasma cannot have as large magnetic shear as a minimum energy Taylor configuration does, due to the difficulty in maintaining large plasma current densities near the cold edge region in a practical device.

The present OHTE device [3] has a major radius of 124 cm, with the minor radii of the liner and the conducting shell being 18.7 cm and 20 cm, respectively. The device originally had an air-core Ohmic heating system, but it was replaced by a 5 V•s iron core system in the Fall of 1982 in order to efficiently increase the plasma current to 500 kA. The Ohmic heating system powered by a capacitor bank induced the plasma current. Typical non-sustained discharges without a flat-top current lasted for several milliseconds. However, sustained discharges with flat-top current for a few milliseconds were also produced at plasma current values up to about 300 kA.

One problem in establishing routine 500 kA operations was protection of the vacuum chamber wall from a large heat load. The Ohmic heating power for certain high current discharges exceeded 100 MW, although the discharge duration was less than 10 ms. The corresponding average wall loading was about 1 kW/cm^2 and the local wall loading was more than 20 kW/cm^2, enough to cause surface melting of the vacuum chamber, which consisted of 0.45-mm-thick stainless steel bellows with no limiter during the

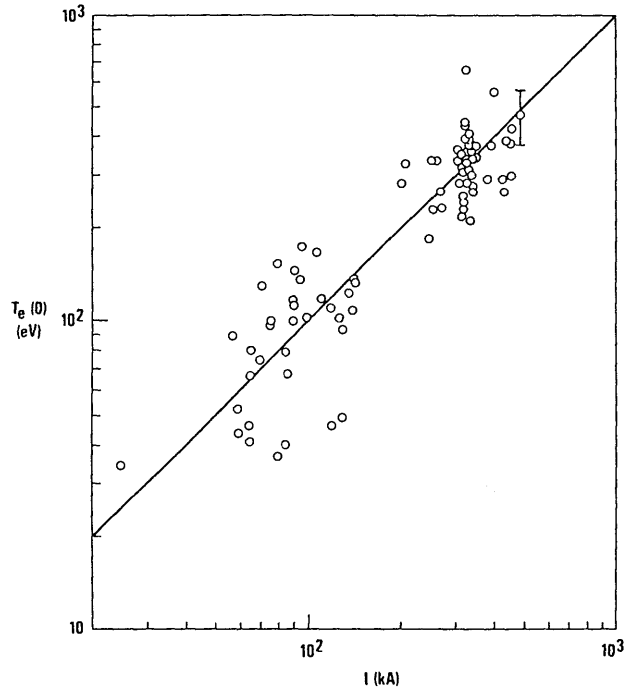

FIG. 1. Central electron temperature as a function of plasma current. The straight line corresponds to 1 eV/kA.

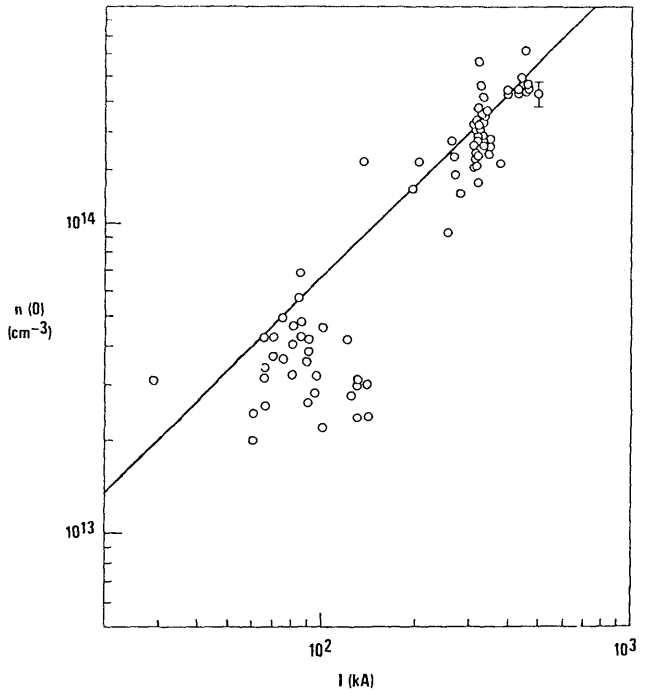

FIG.2. Central electron density as a function of plasma current. The straight line indicates $I/N_0 = 2 \times 10^{-14}$ *A · m.*

early operations with plasma current up to 300 kA. Later, partial protection was provided by covering about one-third of the stainless steel bellows by high density graphite, and 500 kA discharges were obtained. The corresponding average current density is 6.6 MA/m^2. Plasma characteristics with the partial protection were very good, but the chamber still suffered from melting in the areas not directly covered by the graphite. Based upon the good result with this use of a large amount of graphite in the chamber, the entire wall chamber is now covered by high density graphite and good discharges have been reproduced.

Central electron temperature and density were measured by a Thomson scattering system. Figure 1 shows electron temperature at a current peak as a function of plasma current. A typical uncertainty due to photon statistics is shown with the data point for the highest current. The electron temperature increases linearly with the plasma current, and electron temperature around 500 eV was observed. The rate coefficient is about 1 eV/kA as indicated by the solid line. With and without the graphite protection, essentially equal electron temperatures were obtained at a given current.

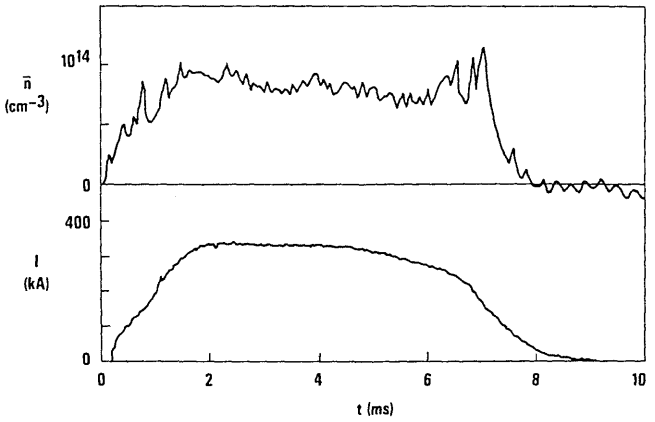

FIG.3. An example of time behaviour of plasma current (bottom) and line-averaged electron density (top).

Attainable central plasma density n(0) also increased linearly with plasma current as shown in Fig. 2. The solid line refers to $I/N_0 = 2 \times 10^{-14}$ A•m where N_0 is plasma line density. (Note that effective plasma radius $\bar{a}_p$ for the OHTE plasma is 15.3 cm and preliminary measurement indicates both temperature and density profiles are fairly flat inside $\bar{a}_p$.) This indicates that approximately the same poloidal beta β_p value was achieved at each current level, and the β_p value is about 20%. The central density exceeded 3×10^{14} cm^{-3} and the $\overline{nT}$ value of about 1.5×10^{14} keV•cm^{-3} was achieved.

Figure 3 illustrates an example of the time behavior of line-average plasma density $\bar{n}$ measured by an infra-red interferometer system. The plasma density initially increases as the plasma current increases and closely tracks the plasma current. This suggests a constant poloidal beta during the discharge, since the plasma temperature scales as the plasma current.

It should be noted that the "pump-out" phenomena often observed in various RFP devices and previously in OHTE are no longer evident. This may be attributed to the presence of the graphite covering a significant amount of the chamber wall. Possible explanations are that the graphite supplies a large amount of particles, or that hydrogen recycling on the graphite is large. This may also be related to reduction of metal impurities produced by plasma-wall interaction. In fact, spectroscopic measurement shows significant reduction of chromium lines. Bolometer measurements indicate that the ratio of radiation power to Ohmic heating power is typically less than 10% and at most 20% for the good discharges.

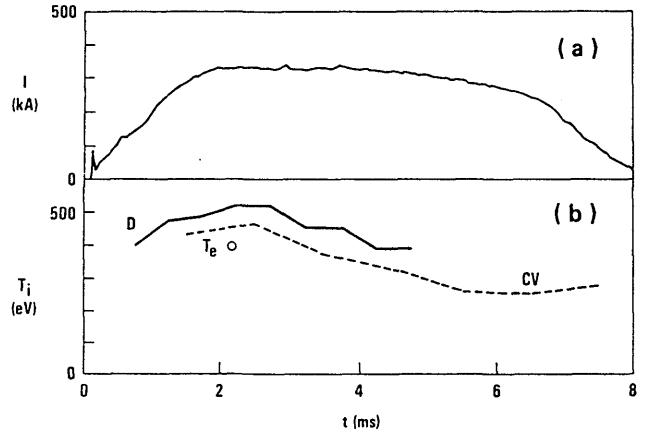

FIG.4. (a) Plasma current and (b) CV temperature inferred from Doppler broadening (broken line) and deuteron temperature inferred from neutron counting rate by a ^{3}He detector (solid line). Electron temperature is shown by an open circle.

Ion temperature was inferred from Doppler broadening measurement of impurity lines, especially CV (2271 Å), and from neutron measurement by a ^{3}He detector, as shown in Fig. 4. For high density plasmas the Doppler temperature late in the discharge was generally close to the central electron temperature; however, a Doppler temperature noticeably higher than the electron temperature was sometimes observed, particularly at lower density or at higher temperature. During the early phase of a discharge, values of the Doppler temperature greater than 1 keV were observed, and the Doppler temperature was found to increase approximately linearly with the magnetic field inside the plasma B, suggesting collisionless adiabatic compression of the plasma.

The neutron counting rate by the ^{3}He detector is consistent with thermonuclear origin. However, it should be noted that the thermonuclear neutron production rate is very sensitive to the deuterium temperature and density profiles used in the calculation and to the tail of the ion energy distribution.

Central electron temperature $T_e(0)$ and Lawson parameter $n\tau$ for the OHTE plasmas are plotted in Fig. 5. The Lawson parameter improved by more than two orders of magnitude as the temperature increased; that is, as the plasma current increased from 30 kA to 500 kA. An $n\tau$ value of about 10^{11} cm^{-3}•s was achieved. Using the temperature scaling $T \propto I$ and the definition of energy confinement time for an Ohmically heated plasma $\tau \equiv 3\ nT \times (\text{Volume})/RI^2$, where R is plasma resistance, one can show that the solid straight lines $T_e \propto \beta_p^{-4/5}\ (n\tau)^{2/5}$ in Fig. 5 correspond to constant β_p values of 0.1, 0.2 and 0.3 for $Z_{eff} = 2$, respectively.

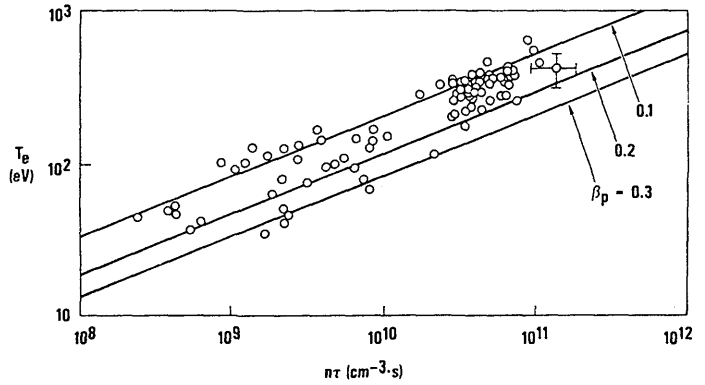

FIG.5. The nτ-T diagram for the OHTE discharges. Typical uncertainties due to photon statistics of the Thomson scattering measurements are shown with the highest nτ point.

Relative magnetic field fluctuations $\tilde{B}/B$ continue to scale as $S^{-1/2}$ at the high current with $S \simeq 10^4$, where S is the magnetic Reynolds number defined as the ratio of resistive decay time τ_R to Alfvén time τ_A [4].

In conclusion, the empirical scalings previously obtained at the low current level were confirmed at the high current (~500 kA) and the Lawson parameter greatly improved as expected. Good results were obtained with the use of a large amount of high density graphite protecting the chamber wall from a large heat load.

This work is supported by Phillips Petroleum Company and GA Technologies Inc. under Joint Research and Development Agreement (GA Reference No. 01341).

REFERENCES

[1] TAMANO, T., et al., "Pinch experiments in OHTE", Plasma Physics and Controlled Nuclear Fusion Research 1982 (Proc. 9th. Int. Conf., Baltimore, 1982), Vol.1, IAEA, Vienna (1983) 609.

[2] OHKAWA, T., CHU, M., CHU, C., SCHAFFER, M., Nucl. Fusion **20** (1980) 1164.

[3] GOFORTH, R.R., et al., Nucl. Instrum. Methods **207** (1983) 87.

[4] LA HAYE, R.J., GA Technologies Inc. Rep. GA-A 16945 (1982), to be published in Phys. Fluids.

DISCUSSION

R.S. PEASE: Among the very interesting results presented in your paper, the explanation of the rapidly increasing ion temperature as a compression effect helps resolve a long-standing problem of ion heating in reverse-field pinches (RFP) (see Spitzer, Nature (London), Jan. 1958). Can you say what the main differences of observation are between RFP and OHTE operation?

T. TAMANO: The results I have presented today all relate to OHTE mode. It is fair to say that the question of a comparison between OHTE and RFP modes is still open; we have recently been concentrating on OHTE mode operation, while RFP has not been given a proper chance. However, the trend is for the OHTE mode to yield higher energy density than RFP. For example, in our device the energy density for OHTE at a given plasma current is about three times higher than that for RFP, and our OHTE mode yields an energy density about five times higher than that in the similar-sized RFP devices in existence, unless better results are reported at this conference in later papers on RFP. Also, the more studies we perform, the clearer it becomes that edge confinement is playing an important role. Since the helical field is effective near the edge, it may not come as a surprise to find that the helical field does make a difference.

T.N. TODD: Do you believe that your lack of density pump-out is due to outgassing from the carbon with which you have now covered the inside of OHTE?

T. TAMANO: The neutron yield indicates that the majority of the plasma particles are deuterons rather than impurities. The pump-out phenomenon was also not observed with the metal (stainless steel) wall. However, the carbon wall certainly helped to provide a relatively large amount of particles, which the plasma can apparently tolerate.

H.A.B. BODIN: Can you say more about Z_{eff}? In particular, did you find that high values of T_e were generally obtained when Z_{eff} was high?

T. TAMANO: Z_{eff} as defined by the ratio of estimated plasma resistivity over Spitzer resistivity varies between 1 and 10. The higher current tends to give higher Z_{eff}. However, this aspect requires more detailed examination.

H.A.B. BODIN: Pinches have a history of non-thermal neutrons; can you say whether the neutrons you observed were thermal?

T. TAMANO: The neutron yield seems to be consistent with their being of thermonuclear origin if the Doppler temperature is compared with the deuteron temperature inferred from the neutron yield. Of course, it should be borne in mind that the Doppler temperature relates to perpendicular temperature and that parallel temperature is lower early in the discharge.

EXPERIMENTAL AND THEORETICAL STUDIES OF THE ZT-40M REVERSED-FIELD PINCH

D.A. BAKER, C.J. BUCHENAUER, L.C. BURKHARDT, E.J. CARAMANA, J.N. DiMARCO, J.N. DOWNING, R.M. ERICKSON, R.F. GRIBBLE, A. HABERSTICH, R.B. HOWELL, J.C. INGRAHAM, A.R. JACOBSON, K.A. KLARE, E.M. LITTLE, R.S. MASSEY, J.G. MELTON, G. MILLER, R.W. MOSES, C.P. MUNSON, J.A. PHILLIPS, M.M. PICKRELL, R.A. NEBEL, A.E. SCHOFIELD, K.F. SCHOENBERG, R.G. WATT, P.G. WEBER, D.M. WELDON, K.A. WERLEY, R.W. WILKINS, G.A. WURDEN
Los Alamos National Laboratory,
Los Alamos, New Mexico

D.D. SCHNACK, D.C. BAXTER
Science Applications Inc.,
La Jolla, California

A.Y. AYDEMIR, D.C. BARNES
Institute for Fusion Studies,
University of Texas, Austin, Texas

United States of America

Abstract

EXPERIMENTAL AND THEORETICAL STUDIES OF THE ZT-40M REVERSED-FIELD PINCH.

Modifications made to the Los Alamos ZT-40M reversed-field pinch (RFP) experiment, to increase the conducting shell's time constant and to reduce winding-induced field errors, resulted in 27 ms sustained discharges. The sustained RFP discharges, whose duration exceeded resistive diffusion estimates by an order of magnitude, and the successful demonstration of a new reactor-relevant startup mode, where plasma current is slowly increased *while in the RFP state,* have demonstrated a field regeneration or dynamo mechanism. The exploration of this mechanism to provide steady state current drive by low frequency field modulation (F-θ pumping) was examined and looks promising. Ohmic heating operation ($q<1$) of ZT-40M with short (2 ms) discharges at currents up to 0.4 MA has yielded electron temperatures of 500 eV with $T_i \cong T_e$ and poloidal betas of 10–20%. The use of pulsed discharge cleaning has significantly reduced initial density pumpout, improved particle confinement, and reduced impurity content. Under certain operation conditions, MHD modes, analogous to the tokamak's n = 1, m = 1 current-drive kink, have been identified and are in qualitative agreement with theoretical predictions. These results represent a significant contribution to the development of the RFP as a viable fusion reactor candidate.

1. INTRODUCTION

Since the 1982 IAEA meeting, significant experimental and theoretical advances have been made by the international reversed-field pinch (RFP) physics community. This paper

summarizes the experimental and theoretical work associated with the Los Alamos ZT-40M RFP experiment.

2. SUSTAINED DISCHARGE PERFORMANCE

ZT-40M uses a 0.4 mm thick Inconel toroidal vacuum vessel (liner) with a major radius of 1.14 m and a minor radius of 0.2 m, surrounded by a 2 cm thick conducting shell. In late 1982, ZT-40M was modified to increase the shell's vertical field time constant from 15 ms to 50 ms and to reduce the field errors caused by winding irregularities from a computed 6% to 2% of the maximum poloidal magnetic field[1]. The most striking result of these improvements was that RFP discharges were sustained for as long as 27 ms--over an order of magnitude longer than expected from resistive diffusion calculations[2]. This sustainment is believed to result from a field regeneration or dynamo process[3], and offers the potential for steady state operation (Section 5).

An extensive series of tests was run at sustained currents below 240 kA to determine how various plasma parameters scale with current. In the interval from 60 kA to 120 kA, the electron temperature on-axis (T_{eo}) scaled as $I_\phi^{0.56}$ and the average density ($\langle n_e \rangle$) as $I_\phi^{1.33}$. The resistivity on-axis, based on magnetic helicity balance[4], scaled as $I_\phi^{-0.85}$. When combined with the electron temperature data, the on-axis resistivity scales classically with temperature ($\eta \propto T_e^{-1.5}$). The product $T_{eo}\langle n_e \rangle$ scaled as I_ϕ^2, which implies constant poloidal beta (β_θ) operation within the range $0.1 \leq \beta_\theta \leq 0.2$.

The temporal behavior of density, temperature, resistivity and beta were roughly constant over the flat-topped current portion of the discharges studied. The favorable scaling of these parameters with current, however, deteriorated above 120 kA. It is postulated that this deterioration results from increased plasma-wall interactions at the higher currents due to uncorrected magnetic field errors at ports and gaps in the conducting shell[5].

3. HIGH CURRENT DISCHARGE PERFORMANCE

In order to minimize plasma-wall interactions and to protect the liner from damage, a series of "round-top" discharges was run in which the applied toroidal voltage was reversed soon after the attainment of peak plasma current. Using this operating mode, high current discharges up to 440 kA, with durations of approximately 2 ms, were achieved. The high current operation resulted in electron temperatures on-axis of 500 eV with $T_i \simeq T_e$ and poloidal betas of 10 to 20 percent.

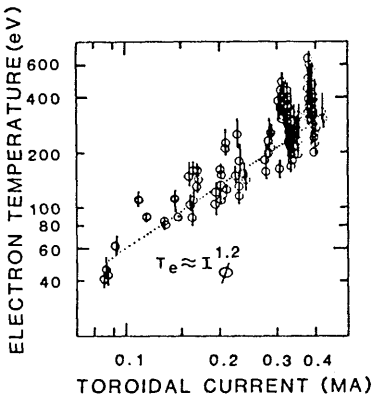

FIG.1. On-axis electron temperature as a function of current for round-top discharge operation.

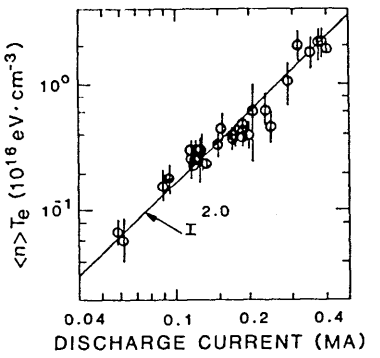

FIG.2. The product $T_{e0}\langle n_e \rangle$ versus current for round-top discharge operation.

Figure 1 shows the on-axis electron temperature as a function of current for round-top shots on a common F-Θ trajectory. Here, F and Θ are defined as the toroidal and poloidal magnetic field at the conducting shell divided by the mean toroidal magnetic field, respectively. The temperature scales as $I_\phi^{1.2}$ over the full range of current operation. Data scatter is the result of variations in the plasma density. That is, at a given plasma current, higher density operation results in lower electron temperatures and vice versa. The product $\langle n_e \rangle T_{eo}$ for these discharges is shown in Fig. 2. A least squares fit of the data confirms and extends the sustained discharge scaling results of constant β_θ operation up to 440 kA.

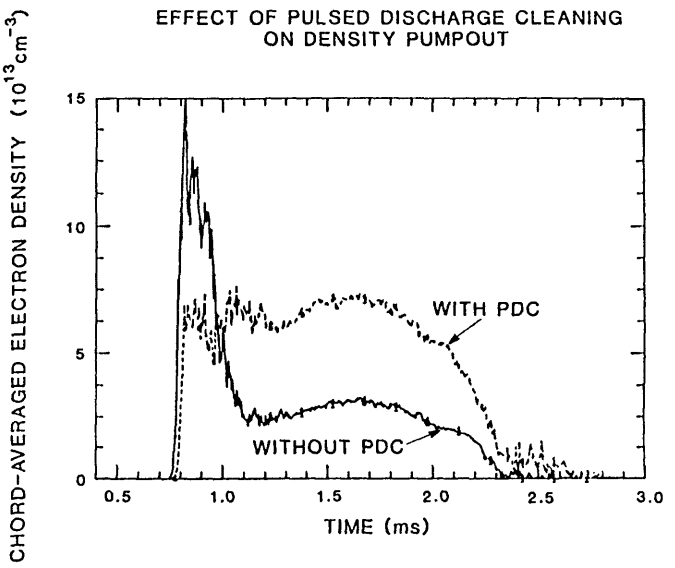

FIG.3. Temporal electron density behaviour with and without pulsed discharge cleaning (PDC).

The temporal behavior of the electron density for round-top discharges, with and without pulsed discharge cleaning (PDC), is shown in Fig. 3. Without PDC, the time dependence of the density for round-top discharges is similar to sustained discharges. There is an initial density peak that is set by the limits imposed on electrical breakdown of the discharge and burnthrough. The density then decays (pumps out) in time to a quasi-static value that is probably determined by a balance between the recycling of neutral gas from the wall and particle loss from the plasma. With PDC, however, the density pump-out can be essentially eliminated. The initial density peak is lowered because PDC allows running at a lower initial fill pressure, and at late times the density is higher due to a greater recycling rate and/or an improved particle confinement time. An estimate of the recycling time based on D_α radiation measurements indicates that although the recycling rate with PDC is somewhat higher, it is not enough to fully explain the higher density, and thus an improved particle confinement time is surmised. PDC also reduces plasma impurity content, as measured by Z_{eff}, by roughly a factor of two.

The most impressive confinement results for round-top discharges were obtained following 12 hours of continuous PDC with PDC operating between shots. For these discharges at

340 kA, the on-axis electron density was maintained at 10^{14} cm^{-3}, with an on-axis electron temperature of 330 eV, β_θ of 18%, $\langle n_e \rangle$ of 8×10^{13} cm^{-3}, and an estimated energy confinement time, including radiation losses, of 0.7 ms. These parameters yield an $\langle n \rangle \tau_e$ product of $5 \times 10^{10} cm^{-3}$-s with a confining magnetic field of only 0.3 T at the plasma edge.

4. SAWTOOTH OSCILLATIONS AND CONNECTION WITH MHD THEORY

A number of insights into the confinement physics of the RFP may be obtained from a general knowledge of tokamak behavior. The similarities between these two magnetic confinement approaches is evident in the experimental verification of RFP modes analogous to the tokamak's m = 1, n = 1 current-driven kink.

RFP theoretical studies have suggested the importance of tearing instabilities with poloidal mode number m=1 and toroidal mode numbers in the range n=5 to 20[6,7,8]. The nonlinear evolution of these instabilities was simulated and analysed in detail, and contrasted to the evolution of the m = 1 sawtooth mode in the tokamak[6]. It was concluded that sawtooth-like behavior should be present in the RFP. This behavior is experimentally observed in ZT-40M and is in qualitative agreement with theoretical predictions[7]. Detailed soft x-ray studies have recently shown that the RFP sawtooth oscillations have an m = 0, n = 0 structure[9], as well as an associated m = 1 precursor oscillation.

In summary, three-dimensional MHD simulations of the RFP have shown:

1. The nonlinear interaction of many m = 1 modes leading to a stochastic core.
2. Strong nonlinear beating of m = 1 modes to the m = 0 mode at the reversal surface for discharges with a high value of Θ, and a consequent outward spreading of the stochastic field region. High Θ refers to values greater than 1.5. During normal operation, ZT-40M runs with Θ values less than 1.5.
3. Indications that the maintenance of toroidal field reversal can be explained by the nonlinear evolution of multiple m = 1 resistive modes.
4. Long time-scale oscillatory behavior of the magnetic field configuration at high Θ and steady-state behavior at normal Θ[10]. This correlates with the experimentally observed large sawtooth oscillations at high values of Θ.

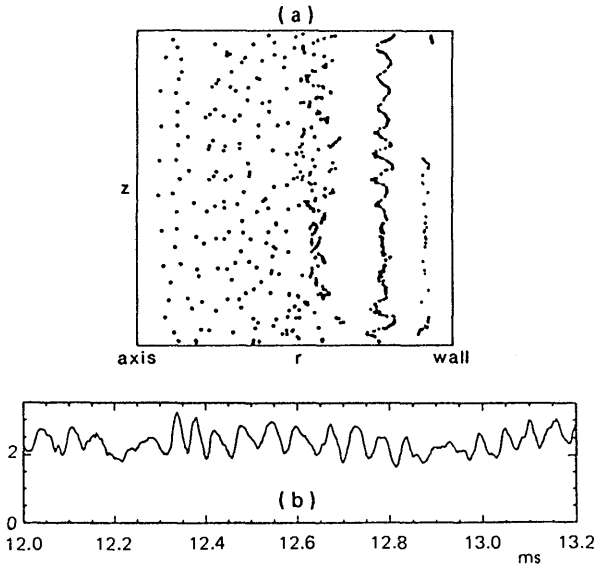

FIG.4. (a) Field line traces from non-linear 3-D MHD simulations of the RFP at normal Θ (r and z denote the radial and toroidal directions, respectively). (b) Soft X-ray data from an off-axis chord on ZT-40M.

These theoretical results suggest that energy confinement in the RFP at high Θ may come principally from the outer portion of the discharge. They may also explain the presence of very large sawtooth oscillations at high Θ since strong nonlinear beating to m = 0 modes can degrade the good confinement region.

Figure 4 is a comparison of nonlinear MHD simulations and soft x-ray data. Figure 4(a) shows field line traces in the r-z plane (r = radial, z = toroidal directions) taken from the 3D simulations. The central core is stochastic but the field line farther out oscillates in space and then develops a "flat" spot when the dominant m = 1 modes (m = 1, n = 10; m = 1, n = 11) lose phase coherence. Figure 4(b) shows the soft x-ray signal from one off-axis chord. Note that this signal shows a similar behavior in time, suggesting that the structure is rotating past the detector.

During normal Θ operation, soft x-ray measurements detect coherent m=1 oscillations. This experimental result implies that, at normal Θ, the core of the RFP may not be nearly as stochastic as the simulations would suggest, since a coherent structure is not likely to be present in a highly stochastic background.

5. RAMPED-CURRENT OPERATION

A new mode of ramped RFP startup has been demonstrated on ZT-40M[11]. In this mode, the plasma current is ramped to its final value on a very long time-scale after the RFP configuration is initially formed at low current. In contrast, during conventional startup, the peak toroidal plasma current is reached at about the time the toroidal field at the wall reverses. In comparison, the start up voltage and power requirements for ramping are considerably less and temporally more constant than for conventional startup.

After attaining peak current during a ramped discharge, T_{eo} and β_θ are at least as high as in a conventional discharge of comparable peak current, and the line-average density is actually higher. This allows lower fill pressure and consequently smaller density pumpout to occur for a given final current. In addition, the radiated power fraction for the ramped discharge at peak current is a factor of two higher than the conventional discharge. The net power lost, however, remains the same, which indicates that the nonradiative energy confinement time for ramped discharges exceeds those of comparable conventional discharges by a factor of two. This observation suggests that a trade off between radiation and other energy loss channels has occurred.

6. OSCILLATING FIELD CURRENT DRIVE

The RFP plasma dynamo or field regeneration mechanism may provide a technologically simple means of steady state current drive. With proper time-dependent programming of the toroidal and poloidal magnetic fields, it may be possible to sustain a mean toroidal plasma current even though the mean toroidal voltage is zero[12]. This current drive technique, termed Oscillating Field Current Drive or F-Θ pumping[13], is a consequence of the strong nonlinear plasma coupling between the toroidal and poloidal magnetic fields in the RFP.

The F-Θ pumping concept has been studied by computationally simulating the effect of audio-frequency oscillating voltage sources on the ZT-40M toroidal and poloidal field circuits. The simulation code assumes that, during modulation, the plasma remains in a quasi-relaxed state and that the modulation does not significantly degrade overall pinch performance.

The validity of these assumptions was confirmed by a series of modulation experiments on ZT-40M[14]. The measured plasma relaxation time (100 μs) was substantially shorter than the applied field modulation period (1 ms), and no obvious deleterious effects of field modulation were observed on overall

pinch performance, provided toroidal magnetic field reversal was adequately maintained. Although it is possible that phenomena such as enhanced plasma resistivity[4] could still affect RFP performance under full current drive operation, F-Θ pumping is a plausible candidate for RFP current drive.

7. CONCLUSIONS

The experimental and theoretical work summarized above makes a significant contribution to the field of RFP physics. The existence of a field regeneration or dynamo mechanism has been demonstrated, and its exploitation to provide steady state current drive looks promising. ZT-40M exhibits favorable plasma beta, temperature and density scaling up to the highest currents studied (0.4 MA). Finally, the demonstration of slow current ramping, which lowers the peak voltage and input power during startup, has important implications for future devices.

The strong effect of pulsed discharge cleaning on gas recycling, particle confinement and plasma impurity content demonstrates the importance of wall conditioning and protection in achieving good RFP discharge performance. These issues will continue to play an important role in the quest for even higher current operation.

REFERENCES

[1] MASSEY, R.S. et al., Preliminary Equilibrium and Field Error Studies on ZT-40M, Los Alamos Natl. Lab. Rep. LA-9567-MS (1983).
[2] CARAMANA, E.J., BAKER, D.A., Nucl. Fusion **24** (1984) 423.
[3] MOSES, R.W., "The physics of reversed-field pinch profile sustainment", Proc. Int. Conf. on Plasma Physics, Lausanne, 1984.
[4] SCHOENBERG, K.F., MOSES, R.W., HAGENSON, R.L., Phys. Fluids **27** (1984) 1671.
[5] HOWELL, R.B., VOGEL, H.F., Magnetic field perturbations due to a hole in a conducting wall on ZT-40M, J. Appl. Phys. **55** (1984).
[6] CARAMANA, E.J., NEBEL, R.A., SCHNACK, D.D., Phys. Fluids **26** (1983) 1305.
[7] WATT, R.G., NEBEL, R.A., Phys. Fluids **26** (1983) 1168.
[8] HUTCHINSON, I.H., MALACARNE, M., NOONAN, P., BROTHERTON-RATCLIFFE, D., Nucl. Fusion **24** (1984) 49.
[9] WURDEN, G.A., Phys. Fluids **27** (1984) 551.
[10] AYDEMIR, A.Y., BARNES, D.C., Phys. Rev. Lett. **52** (1984) 930.
[11] PHILLIPS, J.A., et al., Observations of Ramped Current Operation in ZT-40M, Los Alamos Natl. Lab. Rep. LA-10060-MS (1984).
[12] BEVIR, M.K., GRAY, J.W., in Proc. Reversed Field Pinch Theory Workshop, Los Alamos Natl Lab. Rep. LA-8944-C (1981) 176.
[13] SCHOENBERG, K.F., GRIBBLE, R.F., BAKER, D.A., Oscillating field current drive for reversed field pinch discharges, J. Appl. Phys. **55** (1984).
[14] SCHOENBERG, K.F., et al., Phys. Fluids **27** (1984) 548.

DISCUSSION

R.J. GOLDSTON: The Doppler-broadening measurements reported in Paper No. IAEA-CN-44/D-II-1 certainly cast doubt on the use of this technique for measuring ion temperature in pinches, since Dr. Tamano saw a two-component spectrum with one component at a temperature ten times lower than the other. How do you measure T_i, and what do you think of the reliability of Doppler measurements?

R.S. MASSEY: We use two methods to measure T_i: Doppler-broadening of C, N and O impurities, and a new technique for time-of-flight measurement of neutral-particle energies. The time-of-flight method, which we feel is more trustworthy than the Doppler technique, is also showing ion temperatures approximately equal to electron temperatures at times short compared to the equipartition time.

N.A. KRALL: Are there any experimental conditions, such as high density, etc., under which the dynamo effect is either eliminated or reduced?

R.S. MASSEY: If we operate with high impurity levels (as in impurity injection experiments) the resistivity can be so high that the dynamo cannot keep up. There is no problem under normal operating conditions.

H.A.B. BODIN: You said that metal impurities spoiled the confinement in flat-top pulses; on what data is this conclusion based?

R.S. MASSEY: With flat-top discharges, confinement at early times is comparable to that which I reported for round-top discharges. At later times we see a large increase in radiation from metal lines simultaneously with higher resistivity, somewhat lower B_θ, and a poorer confinement time.

J.B. TAYLOR: In the F-θ pumping mechanism there is a phase in which plasma is swept into the wall. There has always been concern that this would lead to contamination of the plasma by wall impurities. Have you considered this aspect in your simulations or estimates?

R.S. MASSEY: The simulations do not take this effect into account, but one of the reasons for doing the experiments was to see how important it is. Perhaps surprisingly, we saw no deleterious effects even at much higher modulation levels than are required for reactor steady-state drive. As long as reversal was maintained, the plasma did not seem to suffer from the modulation.

NEW RESULTS FROM HBTX1A REVERSED-FIELD PINCH

P.G. CAROLAN, B. ALPER, M.K. BEVIR, H.A.B. BODIN, C.A. BUNTING, D.R. BROTHERTON-RATCLIFFE*, H. AHMED**, D.E. EVANS, D. EVANS***, A.R. FIELD*, L. FIRTH, M.J. FORREST, C.G. GIMBLETT, N.C. HAWKES, I.H. HUTCHINSON+, M. MALACARNE, A. MANLEY*, A.A. NEWTON, P.G. NOONAN, A. PATEL*, N.J. PEACOCK, D.P. STOREY++, H. TSUI§, P.D. WILCOCK
Culham Laboratory,
(Euratom/UKAEA Fusion Association)
Abingdon, Oxfordshire,
United Kingdom

Abstract

NEW RESULTS FROM HBTX1A REVERSED-FIELD PINCH.

The electron temperature, previously reported as approximately 100 eV at peak current (200 kA), rises to approximately 350 eV at later times for flat-top operation. Neutral particle analyser measurements at peak current indicate $T_i \sim T_e$, which cannot be explained by electron-ion equipartition. With B_v and minor gap field error correction, the pulse length is increased from 5 to 14 ms; the resistivity, total radiation and impurity content are reduced, and τ_E increases. Dominant global modes with m = 0 and 1 of resistive MHD origin and localized activity in the core (which accounts for most of the power at high frequencies) occur throughout the discharge. The value of τ_E estimated from stochastic field line diffusion due to the m = 1 modes agrees with the observed value and can scale favourably with current.

1. INTRODUCTION

Results from HBTX1A [1] (major radius 80 cm, minor radius of graphite tile limiters 24 cm) operating with currents between 100 kA and 300 kA are presented. Unless stated, most data are for $p_0 \approx 3$ mtorr, $I_\phi \approx 200$ kA and $\Theta \approx 1.8$, usually with flat-tops of 2–5 ms. Measurements of $T_e(t)$ during the flat-top, of $T_e(r)$ (using a 24-chord surface barrier diode (SBD) array), of T_i (using a neutral particle analyser (NPA)) and of neutral density, n_0, are described. Total radiation and spectroscopic measurements yield values of the impurity content and Z_{eff}.

---

* Royal Holloway College, University of London, UK.
** University of Strathclyde, UK.
*** Imperial College of Science and Technology, University of London, UK.
+ Massachusetts Institute of Technology, Cambridge, MA, USA.
++ University of Hull, UK.
§ University of Manchester, Institute of Science and Technology, UK.

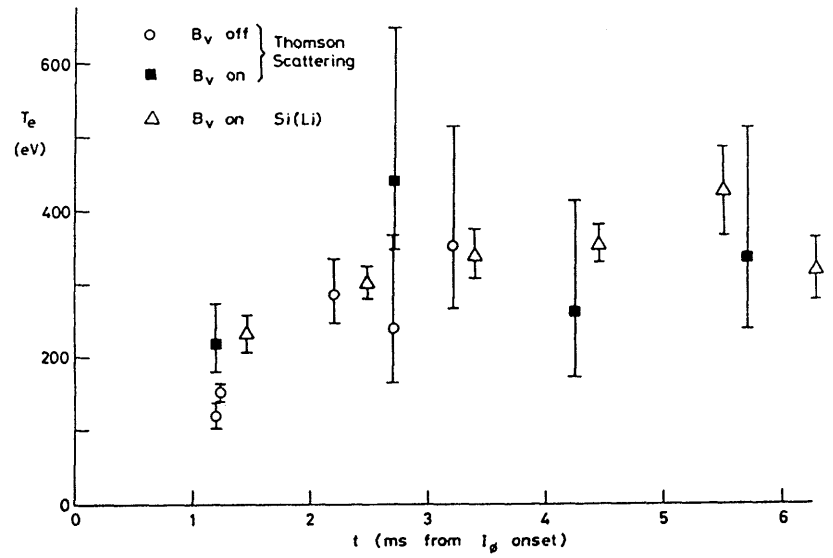

FIG. 1. Electron temperature, T_e, versus time measured by Thomson scattering and a Si(Li) detector (I_ϕ = 200 kA).

Operation with a steady vertical field (B_V) and minor gap field error correction gives pulses of 14 ms and lower resistivity, interpreted in terms of reduced impurity content and Z_{eff}. Magnetic and X-ray fluctuations [2, 3] reveal a wide range of modes; the origin of some of these and their contribution to transport and field generation are discussed.

2. PLASMA PARAMETERS: T_e, T_i AND n_0

At the time of peak current, the electron temperature (Thomson scattering and Si(Li) detector) and density (CO_2 interferometer) are 100 ± 30 eV and 2×10^{19} m^{-3} (line average) respectively. In discharges with density decreasing in time (approximately $(0.5-1.0) \times 10^{22}$ m^{-3}·s^{-1}) the temperature increases to 150–200 eV at 1 ms after peak current. This increase is consistent with the temperatures obtained from the resistivity using the value of Z_{eff} from radiation measurements [4]. Temperatures of up to 350 eV are obtained when $n \approx 10^{19}$ m^{-3} (see Fig. 1).

The electron temperature distribution is obtained from the SBD array, filtered to detect the C V resonant transition ($1s^2 - 1s2p$) at $h\nu \sim 300$ eV. Since C V is the dominant carbon ionization state over most of the plasma cross-section when

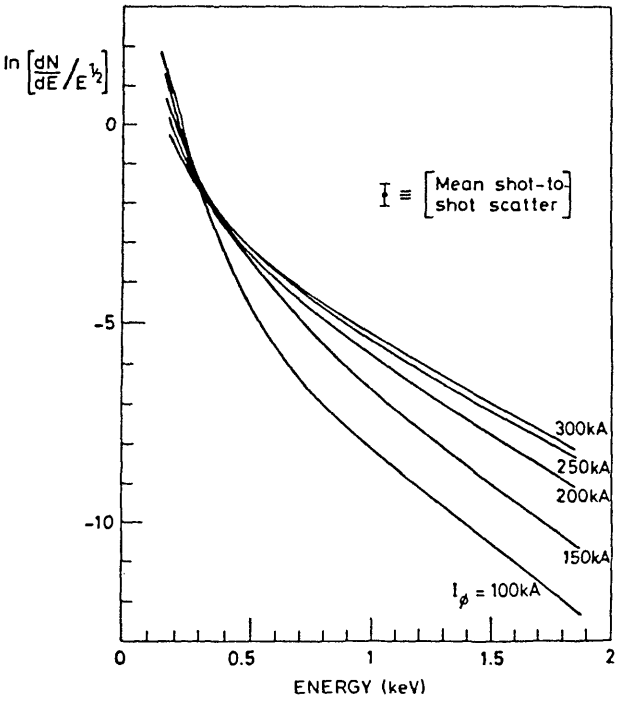

FIG.2. Neutral atom energy spectra emitted during the sustainment phase (1.6 ms integration time) for I_ϕ = 100–300 kA at 3 mtorr.

$20 \lesssim T_e \lesssim 200$ eV and as the line excitation rate is sensitive to T_e (e.g. $\propto T_e^4$ for T_e = 50–150 eV), the Abel-inverted SBD signals may be used to determine $T_e(r)$. A distribution of the form $T_e(r) \sim T_0\ (1 - (r/a)^5)$ is obtained. The flat profile indicates relatively fast thermal transport in the bulk of the plasma.

Neutral energy spectra from a 5-channel NPA (20 μs sampling time) are shown in Fig.2. The lower energy region (200–300 eV) of the spectra corresponds to T_i = 50–100 eV for I_ϕ = 100–300 kA respectively. These estimates contrast with those expected from ion heating by electron collisions, which yield $T_i \sim$ few eV. The thermalization time (about 1 ms) for the hotter ions (about 400 eV), corresponding to the higher energy spectral region (1.0–2.0 keV) in Fig.2, is longer than the time taken (<0.5 ms) to establish fully the spectrum from plasma initiation and is much longer than the time (about 100 μs) associated with the variations of the observed spectral gradient in this region. These results suggest that there are non-collisional ion heating mechanisms and non-thermal ions at energies approximately ten times the Maxwellian temperature.

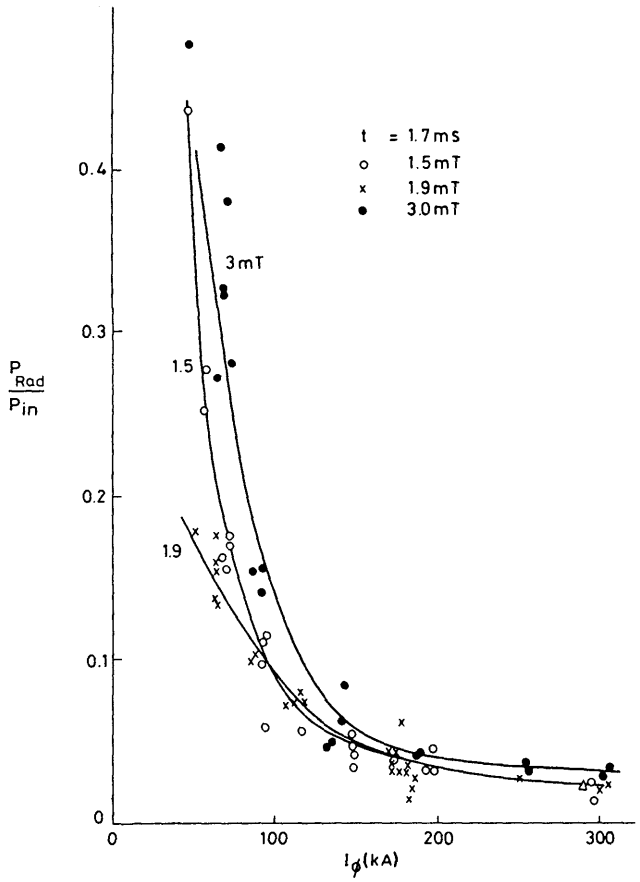

FIG. 3. Variation of total radiative power normalized to P_{OH} with plasma current and filling pressure.

The spatial distribution of the neutral density is measured by fluorescent scattering at both D_α (6561 Å) and D_β (4860 Å) wavelengths. Typically, $n_0 \approx 10^{18}$ m^{-3} and 5×10^{16} m^{-3} at approximately 4 cm inwards from the outer and inner plasma peripheries, respectively. The corresponding particle recycling times (at the edge) are 1 μs and 20 μs.

3. RADIATION AND IMPURITY MEASUREMENTS

Impurities are studied using a variety of spectroscopic instruments (20–7000 Å), a bolometer and the SBD array. A time-dependent coronal model is used to interpret the measurements, which are generally single-chord. At peak

current the main impurities found were carbon (1–2%), oxygen (about 2%) and iron (<0.1%). The radiated power losses are about 3% of the Ohmic input and the contribution to Z_{eff} is close to unity.

Plasma edge and core phenomena are investigated simultaneously by monitoring a range of impurity ion states (e.g. O II-O V and C II-C V) using a polychrometer (2000–4000 Å), because of the spatial localization of different ion states. Cross-correlation studies between the line intensities of different species (O II, O III, C II, C III) emitted from the outer regions show a close correlation between the behaviour of the two elements, but little with the C V core radiation. When T_e rises above 200 eV as n_e falls below about 10^{19} m^{-3} (see Section 2), the relative increase in Fe II radiation indicates that iron is the dominant impurity.

Figure 3 shows the radiated power as a function of Ohmic power for different values of p_0 and I_ϕ. Even for large I_ϕ/p_0 ratios, the radiated power is <50% of the total and falls to about 3% at 3 mtorr and I_ϕ = 200–300 kA. The radiated power remains constant during the sustainment phase even when n_e is decreasing, indicating progressive impurity build-up and increased Ohmic heating per particle.

4. EQUILIBRIUM WITH AND WITHOUT VERTICAL FIELD: FIELD ERRORS

The measured equilibrium shift, Δ, agrees with Shafranov's theory, evaluated using the measured magnetic field profile. It is relatively large, $\Delta/a \approx 0.1–0.15$ because of the tight aspect ratio ($R/a \approx 3$) compared with other reversed field pinch machines. As a consequence there is a large crescent-shaped vacuum region which reduces the plasma cross-sectional area by 20–30%, increases the average distance between the plasma and the stabilizing conducting boundaries at the liner and shell by ~15–30%, and concentrates plasma wall interactions on the outside.

A steady B_v (≈4.5 mT/100 kA) is applied outside the shell, chosen to give $\Delta \approx 0$ during the flat-top. This choice prevents breakdown at usual operating conditions, i.e. $p_0 < 3$ mtorr, $B_{\phi 0} \sim 0.05$ T. Satisfactory breakdown with B_v is found when $p_0 \gtrsim 3$ mtorr, $B_{\phi 0} \gtrsim 0.2$ T, but a large driven reversal is required to obtain the desired Θ. Optimum performance is obtained when the B_v error field at the minor gap, which is exacerbated by a large inward displacement during setting up, is also compensated with additional windings passively trimmed by pre-programming which reduce the gap flux from 1 mWb to ≲0.3 mWb in setting up and ≲0.1 mWb in the flat-top. Figure 4 shows the chord-integrated soft X-ray profile, measured using the SBD array, with and without B_v; the displacement is reduced from about 4 cm to a few mm. Centring is confirmed by edge coil measurements from 80 kA to 300 kA. With B_v and gap flux correction, the

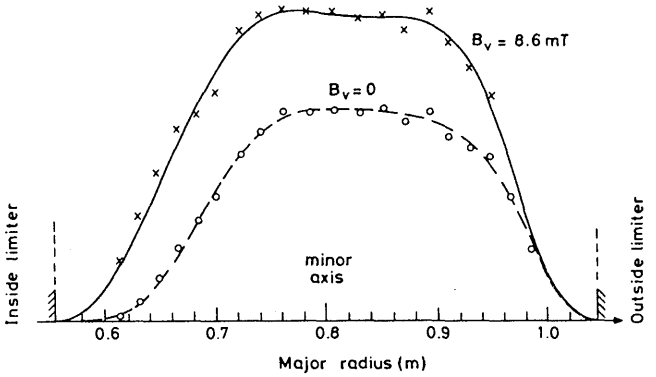

FIG. 4. Chord-integrated profiles from surface barrier diode array with and without B_v.

TABLE I. PLASMA PROPERTIES WITH AND WITHOUT B_v (200 kA)

	Normal	Centred
Displacement (cm)	3	±0.2
Plasma radius (cm)	21.5	24.5
Fluctuations, $\dot{B}$ (arb. units)	1	0.5
Resistivity ($\mu\Omega$·m)	3.5	1.7
Radiation, Fe 2599 Å (arb. units)	1	0.23
Bolometer power (MW)	0.6	0.3
Ohmic power (MW)	20	10

pulse length has been increased from 5 ms to 14 ms (close to the power supply and volt-seconds limits) using power crowbar on the I_ϕ and I_θ circuits. Parameters with and without B_v are given in Table I.

The average plasma resistivity (helicity model) during the flat-top is reduced from about 3.4 $\mu\Omega$·m to 1.7 $\mu\Omega$·m. This, with other data, suggests a two- to threefold increase in τ_E. The resistivity in long pulses, with compensation, appears to be insensitive to the filling pressure and the current, the value lying in the range 1.7 ± 0.3 $\mu\Omega$·m for p_0 = 3–8 mtorr and I_ϕ = 100–300 kA. The pressure independence, in contrast to measurements with short pulses (B_v = 0), on

HBTX1A [5] and elsewhere is thought to be associated with the observation that at long times the density is more a function of current ($n \propto I_\phi$) than of filling pressure and the plasma behaviour is more dependent on the radiation and impurity balance set-up in quasi-steady state than on the initial conditions. The apparent current independence also contrasts with results elsewhere and with those with no B_v on HBTX1A and short flat-tops [5] when the resistance (measured when $\dot{I}_\phi \sim 0$) was insensitive to current at high I_ϕ, but varied approximately as $I_\phi^{-3/2}$ at low I_ϕ and high p_0.

The operating range with B_v and gap correction is extended to higher pressures at higher currents, and at 300 kA long pulses are obtainable at 8 mtorr; previously, at $p_0 > 4$ mtorr, flat-tops could not be obtained. The reduction in resistivity and extended operating range are interpreted as being due to a reduction in the total radiated power by ~2, in the iron radiation by ~4–5 and in Z_{eff} by $\lesssim 2$ for similar densities. Time-resolved electron temperature measurements, with and without vertical field, are shown in Fig. 1.

5. MAGNETIC AND X-RAY FLUCTUATIONS

5.1. Mode classification

The different modes are summarized in Table II. The main features include global modes in the frequency range 4–20 kHz, with m = 1 and a wide toroidal mode spectrum centred about n = −8 (obtained from toroidal edge coil arrays). These modes are resonant inside the reversal surface. At least two independent m = 0 modes are observed. There is localized activity in the central regions (with long correlation lengths ($\gg \pi R/2$) toroidally (X-rays and C V-2271 Å) and short values (~3 cm) transversely (probes)), which contain comparable power to the global modes at lower frequencies but where most of the power is above 30 kHz. These dominant modes, with $\tilde{B}/B \sim 1$–2%, occur in all phases of the discharge, with larger amplitude (×5–10) during setting up. A large-amplitude ($\tilde{B}/B \sim 10\%$) m = 1, n = −3 mode appears only during termination when it dominates. The m = 0 mode on B_θ, corresponding to an oscillation of the toroidal current, correlates well with one of the m = 0 'X-ray' modes but, surprisingly, the m = 1 'X-ray' mode does not appear to be correlated well with the magnetic modes.

5.2. Origin of m = 1 modes and their role in transport and field generation

Estimates of the growth time from the frequency spectra suggest a resistive MHD origin; Δ' tearing mode calculations (based on measured field profiles) indicate that the most unstable mode has the observed helicity. The radial variation of the amplitude of the perturbed fields (from probes) is similar to

TABLE II. MODE CLASSIFICATION

	Magnetic fluctuations				X-ray fluctuations				
	m	n	$\frac{\tilde{B}}{\lvert B\rvert}$	Conditions of occurrence; comments		m	n	$\frac{\tilde{X}}{\lvert X\rvert}$	Conditions of occurrence; comments
Global:	1	−8	~1%	Universal. Occurs throughout the pulse. Resistive time-scales. Tearing mode-like properties.	Global:	1	$\gg 1$	~3%	Universal.
						0	0	~3%	Universal. Amplitude increases with θ, correlates well with B_θ mode.
	0	0	~0.5%	Universal. Fluctuations on I_ϕ. Non-linear from m = 1? Correlates with X-ray and m = 0 mode.		0	~1	~3%	Universal.
	0	~0	~1%	Universal. Consistent with tearing mode. Non-linear from m = 1?					
	1	−3	~2%	High-θ, sustainment phase. Possible ideal mode.					
	1	≈ 3	~10%	Termination.					
	1	−6	0.5%	Universal. Ideal kink, growth rate reduced by liner? (See text.)					
Local:	?	?	1%	Universal, but only in central regions. Dominant above 30 kHz; $\Lambda_T \sim 3$ cm.	Local:	?	?	<0.5%	Universal. Dominant above >30 kHz; $\Lambda_\phi \gg \pi R/2$.

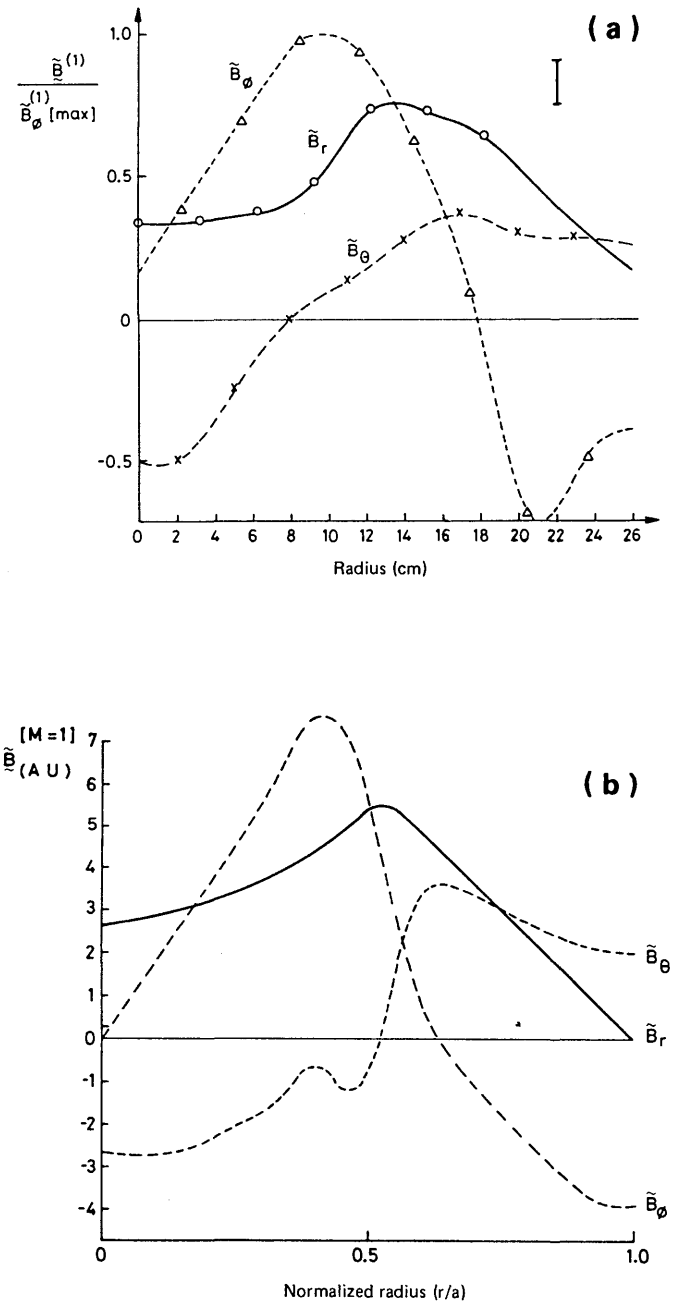

FIG.5. (a) Radial variation of perturbed magnetic field components for a global m = 1 mode, deduced from insertable magnetic probe data. (b) Theoretical m = 1 eigenfunctions calculated from tearing mode theory based on the measured field profiles.

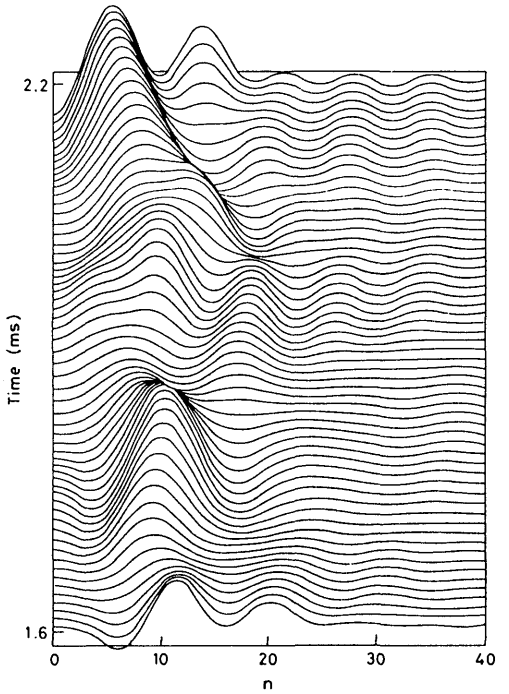

FIG. 6. Three-dimensional diagram illustrating the time evolution of the toroidal mode (n) spectrum (5–50 kHz).

the eigenfunctions calculated from linear tearing mode theory (Fig.5). This interpretation implies a continuously evolving structure in which a mode grows, reconnects non-linearly by profile modification, leading to the excitation of modes of other n, and so on. The temporal evolution of the n spectra [2] shown in Fig.6 supports this picture.

It can be shown [2] that the condition for magnetic island overlapping is satisfied if different helicities occur together, and the field lines will be stochastic out to the reversal surface. A measure of stochasticity is likely throughout the plasma, possibly with a contribution from m = 0 modes in the outer region.

The m = 1 modes can contribute directly to the transport and provide the stochastic fields required for the tangled discharge or non-local conductivity kinetic mechanisms (see Ref. [3]). The perpendicular energy diffusivity is estimated (for m = 1 modes) using measured quantities from the stochastic field line diffusion coefficient [2, 3], and yields $\tau_E \approx 50-100\ \mu s$, a value consistent with observation. It can be shown that τ_E varies approximately as $|\tilde{B}/B|^{-2}$ at the edge and when $|\tilde{B}/B|_{edge}$ varies as $S^{-1/2}$ (S is the magnetic Reynolds number) as observed

on OHTE and ETA BETA II, and if the mode structure remains the same (as is found on HBTX1A), the energy confinement time will vary as $\tau_E \propto S$, which scales favourably with I_ϕ and is qualitatively consistent with observations on several machines that $T_e \propto I_\phi$.

The m = 1 MHD activity could underlie reversed field generation through inverse reconnection or by an 'α-effect' (see Ref. [3]).

5.3. The possibility of operation without a thick shell

Improved positional control and reduction of field error would be obtained for operation without a thick shell if stability can be maintained. Consider the stability of a free surface plasma where a perfect shell gives marginal ideal stability at a radius r_m. A resistive shell at radius $r_s < r_m$ would 'release' an originally stable mode on a time of approximately the shell time constant, τ_s. Similarly, for a plasma surrounded by a liner at r_L (with $\tau_L \ll \tau_s$) and a shell, the instability time τ_i increases continuously from $\sim\tau_A$ to $\sim\tau_s$ as r_m moves from inside the plasma to outside the shell.

On HBTX1A, r_m is just outside the shell, with on-axis m = 1 modes at marginal stability. The m = 1, n ~ -6 kink mode (Table II) has been tentatively identified, for example by its radial structure, as an ideal mode with a growth time reduced by the liner to $\sim\tau_L$. This linear mode would grow indefinitely on simple theory, but is observed for times $\gg\tau_L$ with modest amplitude. This might be explained by plasma rotation, as evidenced by the observation that $\tilde{B}_r$ is temporarily $\pi/2$ out of phase with the other components, or because the equilibrium is evolving cyclically (see above). These considerations lend some support to the idea of stable operation without a shell.

6. CONCLUSIONS

(1) The rise in T_e after peak current to about 350 eV appears to be associated with a decreasing density and an increasing Z_{eff}, in accord with trends indentified by comparing results from different machines.

(2) The observation that $T_i (\sim T_e)$ is much higher than the value estimated from electron-ion equipartition suggests a collisionless ion heating mechanism.

(3) With B_v and minor gap field error correction, the pulse length increases from 5 to 14 ms and the resistivity falls by about 2, which is interpreted in terms of an associated reduction in the total radiation and Z_{eff}; τ_E increases.

(4) In normal conditions the main impurities (<0.1% Fe, 1–2% C, ~2% O) contribute ~1 to Z_{eff}, and the total radiated power is ~3% of the Ohmic power.

(5) Global m = 1 and m = 0 modes of resistive MHD origin and localized modes in the central regions (dominant at high frequencies) are observed. The

m = 1 modes can lead to field generation (dynamo) and also to stochastic fields; a value of energy confinement time from m = 1 activity is estimated which compares with that observed, and can scale favourably with current.

(6) The tentative identification of an ideal mode whose amplitude is limited and whose growth rate is determined by the liner indicates that shell-free operation may be possible.

REFERENCES

[1] BODIN, H.A.B., et al., "Results from the HBTX1A reversed field pinch experiment", Plasma Physics and Controlled Nuclear Fusion Research 1982 (Proc. 9th Int. Conf. Baltimore, 1982), Vol. 1, IAEA, Vienna (1983) 641.

[2] HUTCHINSON, I.H., MALACARNE, M., NOONAN, P., BROTHERTON-RATCLIFFE, D., Nucl. Fusion 24 (1984) 59.

[3] BODIN, H.A.B., in Proc. Int. Conf. on Plasma Physics, Lausanne, 1983, Vol. 2.

[4] BUNTING, C.A., CAROLAN, P.G., MUIR, D.G., in Proc. 11th Europ. Conf. on Controlled Nuclear Fusion and Plasma Physics, Aachen, 1983, Part 1 (1983) 157.

[5] HUTCHINSON, I.H., ibid., p. 151.

DISCUSSION

D.B. NELSON: What is the cause of the sudden drop in loop voltage near the end of the discharge?

P.G. CAROLAN: This is due to the deliberate shorting of the power crowbar circuit to allow for gradual rundown of current which helps to avoid liner damage. It is also used to prevent iron core saturation that leads to large field errors at the shell gaps.

H.R. GRIEM: What is the physical mechanism of the ion heating observed? I would be interested to know what the time dependence is and how the temperatures obtained depend on the charges and masses of the ions.

P.G. CAROLAN: We have not identified the ion heating mechanism but we observe coherent behaviour in the high-energy neutral-particle analyser channels with approximately 100 μs characteristic time in the fluctuation behaviour.

The spectral profile of the thermalized ions is fairly constant during sustainment. Doppler-broadening measurements of the charge-exchange portions of the deuterium Balmer lines (D_α and D_β) give $T_i \gtrsim 100$ eV, while O VI gives $T_i \sim 280$ eV. We have no further information on other ion species at present.

S. ORTOLANI: Were you able to vary the density-versus-time behaviour, and did Z_{eff} vary with density?

P.G. CAROLAN: Generally, the density decreases with time during the sustainment phase. Since the radiation power remains fairly constant, the impurity concentration should increase, which indicates that Z_{eff} depends inversely on the density.

3D MHD STUDIES OF DYNAMIC PROCESSES IN THE REVERSED-FIELD PINCH

T. SATO, K. KUSANO
Institute for Fusion Theory,
Hiroshima University,
Hiroshima, Japan

Abstract

3D MHD STUDIES OF DYNAMIC PROCESSES IN THE REVERSED-FIELD PINCH.

A causal mechanism for the self-reversal process in the reversed-field pinch (RFP) is proposed. The mechanism is based on non-linear reconnection driven by a single helical kink instability. As a result of non-linear deformation by the kink instability, radial magnetic fields are generated, which are conveyed by axial plasma flows induced by the kink instability and eventually reconnected at the encounter points of the flows. Consequently, the radial fields are converted to reversed and normal toroidal fields in the outer and inner regions, respectively, and a reversed-field-pinch configuration is realized. Magnetohydrodynamic simulations have clearly confirmed the validity of the proposed reversal mechanism.

1. INTRODUCTION

The aim of this paper is to detect the causal mechanism leading to self-reversal of the toroidal field in the reversed-field pinch (RFP). Taylor's theory [1] states that field reversal is a minimum-energy state. Since this theory is a steady-state theory, the dynamic process leading to the minimum-energy state cannot be specified. Not only for reasons of theoretical interest in physics but also in view of finding some ingenious method of sustaining the reversal configuration it is important to discover the self-reversal process in RFP.

Three mechanisms have thus far been proposed: the m = 1 kink instability model, the turbulent dynamo model and the tangled-discharge model [2]. In this classification, the present mechanism belongs to the m = 1 kink instability model. The main contribution of the present paper is, however, to give a self-consistent explanation of how field reversal evolves starting from an m = 1 kink instability and to give a quantitative proof of the proposed mechanism by means of a 3D MHD simulation.

The previous explanation [2] was that a reversed toroidal field could be produced by the solenoidal effect of the helical distortion of the current-carrying plasma column. This effect can certainly generate a reversed field outside the plasma column (i.e. outside the limiter), but not inside the plasma column (inside the limiter) unless inward diffusion is invoked. The present model proposes a new mechanism which generates a reversed toroidal field inside the plasma.

2. NON-LINEARLY DRIVEN RECONNECTION MODEL

As far as the plasma freezes the magnetic field, indeed, no topological change occurs in the magnetic field in the plasma. Therefore, no reversed-field configuration is realized. To produce a topological change in the magnetic field in the plasma, reconnection is inevitable. An ideal kink instability itself cannot lead to any topological change. We thus consider the question of non-linear kink mode development and whether a magnetic configuration subject to reconnection can be realized non-linearly or not.

In this respect, the plasma flow is of paramount importance. We examine the flow pattern in the axial cross-section of a cylindrical plane. The flow pattern induced by a single helicity kink mode is illustrated in Fig. 1a for one fundamental wavelength. The azimuthal (θ) and radial (r) magnetic fluxes are redistributed by this plasma flow. Without loss of generality, we may assume that the non-linear m = 1 poloidal flux, ψ (r, θ, z), is given by

$$\psi\,(r, \theta, z) = \psi_0 + \psi_1 \cos(\theta - 2\pi z/L) \tag{1}$$

Thus, the poloidal and radial fields are given by

$$B_\theta\,(r, \theta, z) = \partial\psi_0\,(r)/\partial r \tag{2}$$

$$B_r\,(r, \theta, z) = -\psi_1 \sin(\theta - 2\pi z/L)/r \tag{3}$$

Since the flow and the perpendicular magnetic fields are known, we are now able to evaluate whether reconnection can be driven non-linearly or not. We recall here that driven reconnection is triggered at an encounter point of two plasma flows conveying anti-parallel fields [3]. Examining Fig. 1a, we find that the A–O line (z = 0 and $\theta = \pi$) is the only candidate region where non-linear reconnection can take place. We then consider the axial distribution of the azimuthal and radial fields, $B_\theta(r, \pi, z)$ and $B_r(r, \pi, z)$, conveyed by the encountering flows. From Eqs (2) and (3), we see that the encountering flows convey parallel B_θ and anti-parallel B_r (see Fig. 1b). Thus, it is expected that the flows induced by the kink instability drive reconnection for radial fields on the A–O line. Once reconnection is driven there, the radial fluxes are transformed to a pair of positive and negative axial fluxes as can be seen from Fig. 2. From the topological consideration it is concluded that a reversed axial field is generated in the outer region and a normal field in the inner region of the plasma column.

In short, the proposed theoretical model predicts that (1) a single helicity kink mode can lead to self-reversal, (2) the keys to self-reversal are the axial plasma flows induced directly by the kink instability and the radial magnetic fields produced by the non-linear distortion due to the kink instability, and (3) the essential physical process leading to self-reversal is non-linearly driven reconnection.

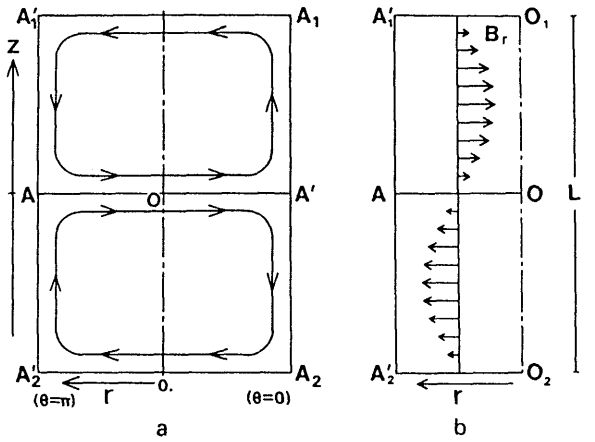

FIG. 1. Plasma flow pattern in the θ-z plane induced by an m = 1 helical kink instability (a) and axial distribution of radial fields produced by non-linear deformation due to kink instability (b).

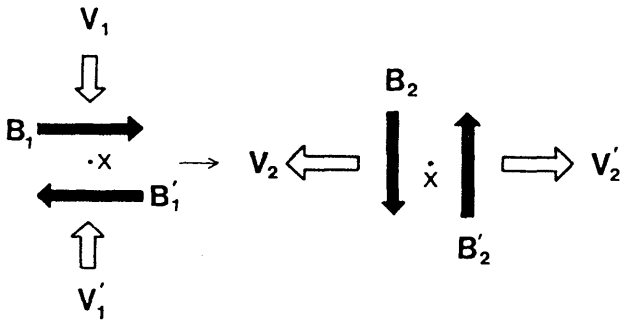

FIG. 2. Schematic diagram showing that driven reconnection transforms magnetic into perpendicular flux.

3. MHD SIMULATION

To prove the validity of the proposed model, we have carried out a magneto-hydrodynamic (MHD) simulation for cylindrical geometry. In the radial direction, the plasma is bounded by a conducting wall, and a periodicity condition is imposed in the axial direction. In the first place, starting from a uniform axial field configuration, the current set-up phase is simulated by applying a certain amount of poloidal flux from the wall. When a near-equilibrium state is established, a single helicity mode perturbation is applied. It is observed that a reversed axial

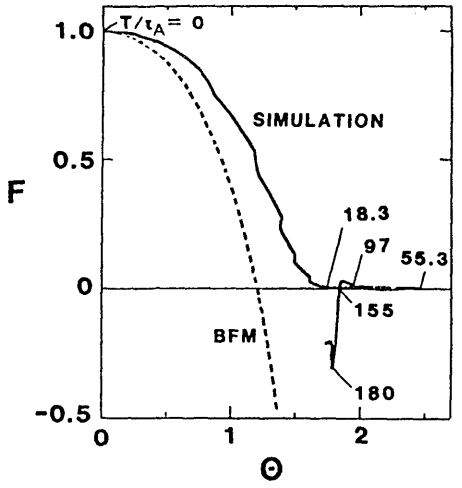

FIG. 3. F-Θ diagram obtained by MHD simulation for m = 1 helical kink instability. Note that field reversal has occurred.

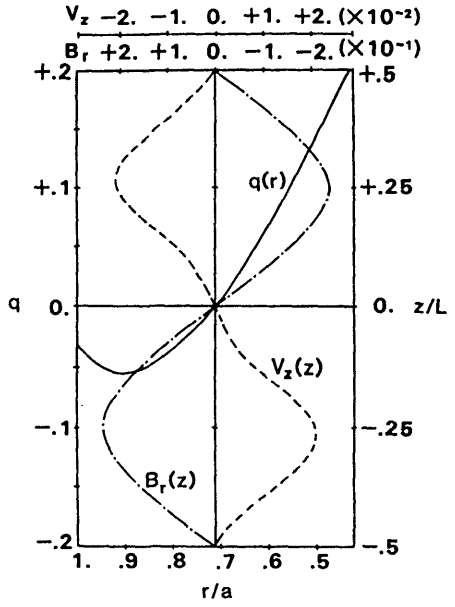

FIG. 4. Radial q-profile (solid line), the axial profiles of radial field (dot-dash) and axial plasma flow (dashed).

field is spontaneously generated in the outer region. The F-θ diagram of this run is shown in Fig. 3. Note that the perturbation is applied at $T = 97\tau_A$.

Figure 4 is a composite figure which shows the radial distribution of the q-profile, along with the axial distributions of the radial magnetic field and the axial plasma flow at a radial position, where the q-profile reverses its sign. As was theoretically predicted (see Fig. 2), the axial flows convey anti-parallel radial magnetic fields so that they become reconnected at the encounter point; consequently, reversed axial fields are generated.

Note the experimental result in our companion paper [4].

ACKNOWLEDGEMENT

This work was supported by a grant-in-aid from the Ministry of Education, Science and Culture of Japan.

REFERENCES

[1] TAYLOR, J.B., Phys. Rev. Lett. **33** (1974) 1139.
[2] BODIN, H.A.B., NEWTON, A.A., Nucl. Fusion **20** (1980) 1255.
[3] SATO, T., HAYASHI, T.,Phys. Fluids **22** (1979) 1189.
[4] YOSHIDA, Z., et al., Paper No. IAEA-CN-44/D-II-4-2, this volume, p.467.

MHD BEHAVIOUR OF A REVERSED-FIELD PINCH PLASMA IN THE SETTING-UP PHASE

Z. YOSHIDA, N. INOUE, H. YAMADA, S. HAMAGUCHI*,
K. ITAMI, N. SUZUKI, K. HATTORI, Y. KAMADA,
K. OKANO, J. MORIKAWA, H. NIHEI, K. MIYAMOTO*,
T. UCHIDA**
Department of Nuclear Engineering, University of Tokyo,
Tokyo

T. SATO
Institute for Fusion Theory, Hiroshima University,
Hiroshima

Japan

Abstract

MHD BEHAVIOUR OF A REVERSED-FIELD PINCH PLASMA IN THE SETTING-UP PHASE.

Magnetohydrodynamic phenomena in the setting-up phase of reversed-field pinches (RFPs) are studied both experimentally and theoretically. The experimental observation shows that, in the setting-up phase, a negative flux is generated by the coherent dynamics of a global helical mode rather than by turbulent or statistical behaviour. The experiment is consistent with a non-linear reconnection model.

1. INTRODUCTION

The dynamics of reversed-field pinchs (RFPs) is of great interest both experimentally and theoretically. Phenomenological RFP dynamics affects our understanding of global plasma dynamics: under certain conditions a plasma spontaneously reaches mechanical equilibrium, before its ultimate relaxation to thermodynamical equilibrium. A pronounced form of self-organized mechanical equilibria is the RFP state, where the magnetic-field distribution shows a distinct preference to profiles around the Bessel function state. Much theoretical research work has been devoted to this subject in order to find a self-consistent interpretation of this self-organization; see, e.g. Refs [1–4]. Theoretical models have been also introduced to provide explicit descriptions of the governing causal

---

* Department of Physics, University of Tokyo, Japan.

** Present address: Institute of Plasma Physics, Nagoya University, Nagoya, Japan.

dynamical mechanism leading to the RFP state, although some questions have been left open [5]. This paper describes the MHD behaviour of RFP plasmas in the setting-up phase in order to reveal the self-reversal mechanism.

2. ULTRA-LOW-q DISCHARGE

The series of TORIUT devices has been used to study MHD phenomena in the low-safety-factor (q) regime of toroidal discharges [6]. The currently operating device TORIUT-5 is a small tokamak-type toroidal system that can operate in the ultra-low-q regime ($q < 1$). The main parameters are as follows: $a = 0.13$ m, $R = 0.38$ m. The liner is made of 4 mm thick stainless steel, and there is no conducting shell. The toroidal plasma current is activated by an iron-core transformer with a core flux of 0.1 V·s (loop voltage < 100 V).

The toroidal magnetic flux is controlled by a couple of independent poloidal winding systems, one of which is an ordinary toroidal-field coil system providing a positive bias field. The other system is installed in a closer position to the plasma and produces a negative flux, which we refer to as an active flux conserver (AFC). The AFC current is driven by a waveform-controllable power supply. The temporal behaviour of the total toroidal flux in the plasma can be controlled by the superposition of positive and negative fluxes. In the usual operation, the activation of the AFC current is essentially passive by induction due to the flux pinch in the plasma, and the current is actively sustained by low-voltage capacitor bank energy.

TORIUT-5 produces ultra-low-q discharges, where the toroidal magnetic field in the peripheral region is almost reversed. When the AFC circuit is activated by being matched to its passive reaction on the plasma, the discharge trajectory in the F-Θ plane goes down along the BFM curve. Unfortunately, no quiescent period could be realized in TORIUT-5, because of the technical reason that the poloidal-flux swing is insufficient. Here, however, we are mainly interested in the MHD phenomena during the setting-up phase, and the basic problem is the self-reversal mechanism. In the next section, we describe the experimentally observed dynamics in the setting-up phase.

3. SETTING-UP DYNAMICS

The MHD activities in the setting-up phase were studied by a Fourier analysis of the magnetic-probe signals. The dependence of the MHD spectrum on the Reynolds number was studied by examining different gases (H, He, N, Ar); see Fig.1. For a relatively large magnetic Reynolds number $S(= \tau_D/\tau_A)$, i.e. in a hydrogen discharge, the MHD spectrum has a continuous turbulent structure (power spectrum density $\propto f^{-2}$) with some harmonic peaks. As S is decreased by using heavier gases, the coherence of the MHD activity increases, and the spectrum

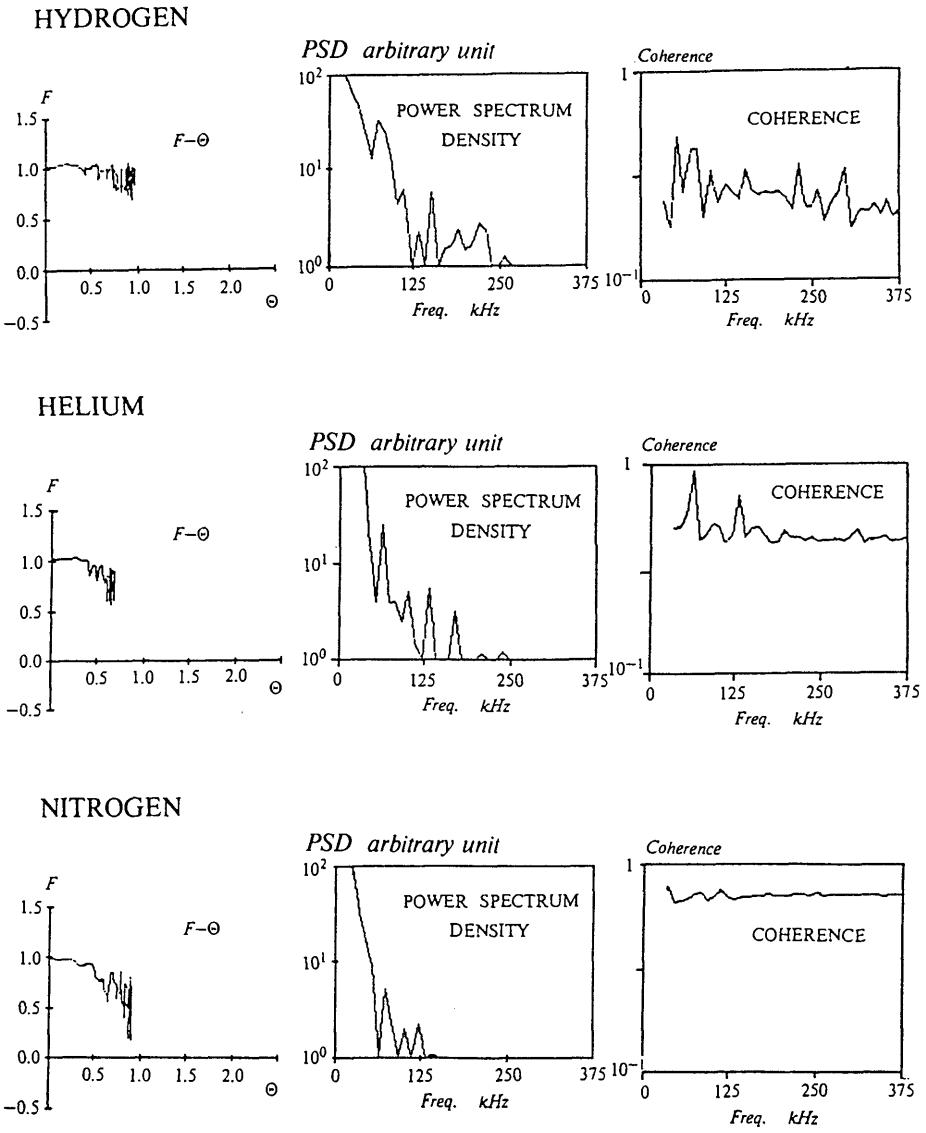

FIG.1. F-Θ plots,PSD(f) of poloidal field $\widetilde{B_\theta}$ and $coh^2(f)$ of $\widetilde{B_\theta}$ and $\widetilde{B_T}$, for ultra-low-q discharges with H, He and N.

shifts to the lower-frequency side. In less turbulent discharges with small S, we find an increasingly efficient generation of negative flux, i.e. F reaches smaller values; see Fig.2. The poloidal mode number of the dominant activity is 1, and the toroidal mode number increases as the plasma current rises. This coherent activity is considered to be responsible for the generation of the reversed field.

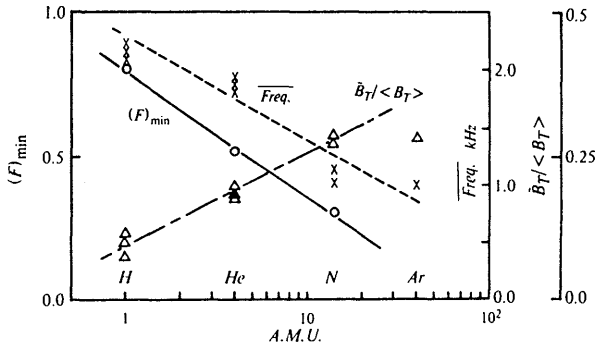

FIG.2. Field-reversal ratio F obtained for equal poloidal-flux swing as function of m_i. Magnetic Reynolds number S is roughly proportional to $m_i^{-1/2}$. Also plotted is frequency and $\tilde{B}_T/\langle B_T\rangle$ of dominant coherent fluctuation.

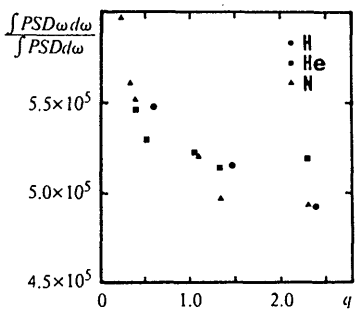

FIG.3. Averaged frequency $\int PSD\,\omega d\omega/\int PSD d\omega$ [kHz] of electron density fluctuation as function of q. Integrals are calculated over 470–750 kHz range.

Since the mode activity for small S shows high coherence between $\tilde{B}_T$ and $\tilde{B}_\theta$ (Fig.1), stochastic behaviour of the field lines or non-linear mode coupling does not play an essential role in the setting-up dynamics.

The non-MHD high-frequency regime of electron density fluctuation, $\tilde{n}_e$, has less significance for the setting-up phenomenon. Figure 3 shows PSD-averaged frequencies of $\tilde{n}_e$, for different q and different gases, detected by the 90° scattering of a 4 mm microwave. Changing the gas does not influence the $\tilde{n}_e$ spectrum although it strongly affects the self-reversal phenomenon. It was shown that the high-frequency component of $\tilde{n}_e$ is stabilized by conserving the toroidal flux by AFC.

The experimental observations are consistent with a non-linear reconnection model. Key features of this model are global plasma circulation with streamlines along the magnetic surface inverse to those of the helical kink mode (we call this

a double-helix-type circulation) and subsequent magnetic reconnection on a helical plane whose topology is the same as that of the kink mode. This circulation is induced by a single helical kink mode. We refer the reader to Refs [7, 8] for a detailed study of the model and numerical simulation results by which it is supported.

4. EXPERIMENTS ON REPUTE-1 RFP

Similar MHD characteristics in the setting-up phase were observed in the first experiments on the REPUTE-1 RFP, which started operation in August 1984. The main parameters of the device are as follows: $a = 0.2$ m, $R = 0.82$ m, iron core flux = 1.6 V·s. REPUTE-1 has a thin shell with poloidal and toroidal cuts. Its skin time for vertical-field penetration is 1 ms. The equilibrium field is controlled by external coil systems; the toroidal flux is provided by a reversible, PFN-controlled coil current. Up to 200 kA, RFP discharges have been tested by 0.5 ms and 1 ms setting-up operations. The discharge duration is around 2 ms without Ohmic-heating current crowbar.

The Fourier spectra of MHD activity in the setting-up phase are close to the data in TORIUT-5. Fluctuation in the toroidal field $\tilde{B}_T$ inside the wall has a coherent structure near the reversal period; $\mathrm{coh}(\omega)$ (i.e. the coherence of a function of frequency) is typically greater than 0.1 over the range of $\omega \leqslant 300$ kHz for $\tilde{B}_T$ measured at two points with $\delta\phi = 60°$ in the toroidal direction.

5. CONCLUSIONS

The self-organization of the RFP state has been shown to pass through a transient phase where the coherent dynamics of an $m = 1$ helical MHD mode plays an essential role by giving rise to the flux pinch phenomenon. This experimental observation supports our non-linear reconnection model for the setting-up phase; its implication, for optimizing the setting-up operation, is that the Reynolds number should be better kept small in the startup phase.

REFERENCES

[1] TAYLOR, J.B., Phys. Rev. Lett. **33** (1974) 1139.
[2] MONTGOMERY, D., TURNER, L., VAHALA, G., Phys. Fluids **21** (1978) 757.
[3] BHATTACHARJEE, A., DEWAR, R.L., Phys. Fluids **25** (1982) 887.
[4] YOSHIDA, Z., UCHIDA, T., INOUE, N., Phys. Fluids **27** (1984) 1785.
[5] BODIN, H.A.B., NEWTON, A.A., Nucl. Fusion **20** (1980) 1255.
[6] YOSHIDA, Z., et al., in Plasma Physics and Controlled Nuclear Fusion Research 1982 (Proc. 9th Int. Conf. Baltimore, 1982), Vol.3, IAEA, Vienna (1983) 273.
[7] SATO, T., KUSANO, K., HAYASHI, T., Research Rep. HIFT-71 (1983).
[8] KUSANO, K., SATO, T., Research Rep. HIFT-83 (1983).

DISCUSSION

ON PAPERS IAEA-CN-44/D-II-4-1 AND D-II-4-2

A.A. NEWTON: In the TORIUT experiment, is the toroidal equilibrium controlled by a time-dependent vertical field?

N. INOUE: The vertical field of TORIUT-5 was pre-programmed.

C.G. GIMBLETT: What is the fluctuation level required in your self-reversal model, and does the model have anything to say about sustainment as opposed to setting-up of reversal?

T. SATO (IFT, Hiroshima): The model itself does not require any critical fluctuation level. The model says that the reversal rate can be higher for higher amplitude. As long as the driving flow associated with m = 1 modes is higher than the diffusion speed, reversal is achieved. (The nature of driven reconnection is such that this takes place.)

In Paper No. IAEA-CN-44/D-II-4-1, I was concerned with the setting-up phase. Simulation results indicate, however, that the reversal configuration would be sustained essentially by the same mechanism, i.e. by (linear) superposition of the contributions of the excited modes. Thus, turbulence may not be the essential process. The sustainment process is now being studied in our high-resolution simulation.

REVERSED-FIELD PINCH EXPERIMENT ON TPE-1R(M)

Y. HIRANO, Y. KONDOH*, Y. MAEJIMA, Y. NOGI**,
K. OGAWA, M. SATO**, T. SHIMADA, Y. YAGI,
H. YOSHIMURA**
Electrotechnical Laboratory,
Sakura-mura, Niihari-gun, Ibaraki, Japan

Abstract

REVERSED-FIELD PINCH EXPERIMENT ON TPE-1R(M).

Recent experimental results from the reversed-field-pinch experiment TPE-1R(M) are described and discussed. The device has a metal-walled toroidal bellows linear (R/a = 0.5 m/0.09 m) with limiters made of SUS 316L and is operated at a plasma current of up to 140 kA. Reversed-field configurations are set up by self-reversal and B_ϕ control. In current pulses of over 1 ms duration produced with power crowbar, the steady, improved-stability phases last 0.5 ms (in contrast to 0.3 ms without power crowbar). In these sustainment phases the more accurate transport physics of RFP can be discussed with various kinds of plasma parameter measurements. Especially, new results come from ion temperature measurements: both neutral-particle energy analysis (charge-exchange measurements, deuterium ion temperature) and the spectroscopic measurement of the Doppler broadening of the C V 2271 Å line (carbon-V ion temperature) show the same value within experimental errors, which is also the same value as, or a little higher than, the electron temperature on the axis found by Thomson scattering; moreover, the time behaviour is nearly identical ($T_i \approx 300$ eV at $\hat{I}_p \approx 60$ kA, $T_i \approx 700$ eV at $\hat{I}_p \approx 100$ kA and $T_i \propto I_p$). Soft-X-ray emission from the central region of the plasma measured with surface barrier diodes is observed when sawtooth oscillations and electron temperature variations in the central region ($\Delta T_e/T_e \approx 0.1-0.2$) in the sustainment phase are monitored. – The partially relaxed state model (PRSM) has been introduced to represent the RFP equilibrium configuration with finite β-values dominated by various dominant (m, n) tearing modes. The relaxation states of RFP in TPE-1R(M) are discussed according to this model.

1. INTRODUCTION

This paper describes and discusses new results of the reversed-field pinch experiment on TPE-1R(M). The device has a metal-walled toroidal bellows liner (R/a = 0.5 m/0.09 m) with limiters made of SUS 316L and is operated at a plasma current of up to 140 kA. Reversed-field configurations are set up by

---

* Department of Electronic Engineering, Gunma University, Kiryu, Gunma, Japan.
** Department of Physics, College of Science and Technology, Nihon University, Kanda-Surugadai, Chiyoda-ku, Tokyo, Japan.

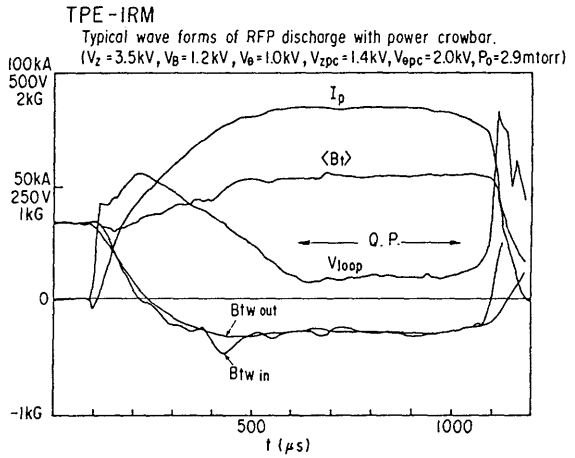

FIG. 1. Typical wave forms of RFP discharge with power crowbar; plasma current (I_p), toroidal field flux inside liner ($\langle B_t \rangle$), toroidal field at the wall ($B_{tw\ in}$ and $B_{tw\ out}$; inside and outside liner) and toroidal loop voltage (V_{loop}).

self-reversal and B_ϕ control (optimum operation with constant-θ mode in TPE-1R(M)) [1].

In current pulses of over 1 ms duration produced with power crowbar, the steady, improved-stability phases are sustained for 0.5 ms (in contrast to 0.3 ms without power crowbar). Typical waveforms of the plasma current (I_p), the toroidal field flux inside the liner ($\langle B_t \rangle$), the toroidal field at the wall (B_{twin} and B_{twout}: inside and outside the liner), and the toroidal loop voltage (V_{loop}) are shown in Fig.1; the time variations of F and θ values are given in Fig.2. Experiments without power crowbar are described in Ref.[1], which reports the plasma parameters and discusses various kinds of parameter scaling.

The experiments with power crowbar aim at the realization of a steady state in a stable RFP configuration and at a more accurate discussion of the RFP transport physics. These experiments have been performed successfully; the RFP configuration and the toroidal flux are sustained as long as the plasma current is maintained until it is disrupted by loss of equilibrium, and then the previous results on plasma parameters and scaling as observed at the current top [1] are reconfirmed in the current flat top of the present experiment.

In Section 2, the main results of plasma parameter measurements are described. New results from ion temperature measurements are reported; both neutral-particle energy analysis (charge-exchange deuterium ion temperature) and Doppler broadening of the C V 2271 Å line (carbon-V ion temperature) yield the same value within the experimental error, which is also the same as, or a little higher than, the electron temperature on the axis as measured by

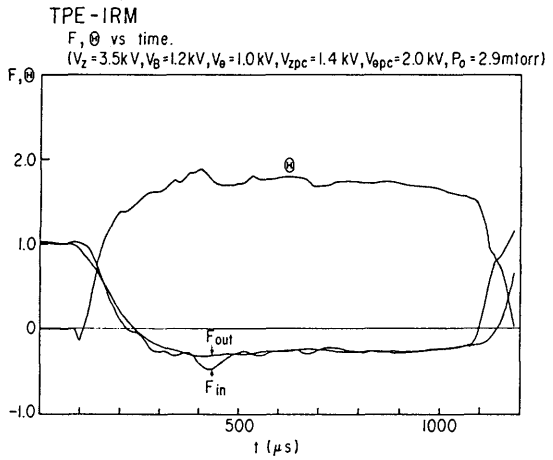

FIG.2. Time evolution of F and θ in the same discharge as Fig.1.

Thomson scattering ($T_i \approx 300$ eV at $\hat{I}_p \approx 60$ kA, $T_i \approx 700$ eV at $\hat{I}_p \approx 100$ kA and $T_i \propto I_p$). Soft-X-ray emission measured by surface barrier diodes is observed by monitoring the sawtooth oscillations and the electron temperature variations in the central region ($\Delta T_e/T_e \approx 0.1-0.2$) in the sustainment phase.

In Section 3, the partially relaxed state model (PRSM) is presented to describe the RFP equilibrium configuration with finite β-values dominated by various dominant (m, n) tearing modes. The relaxation states of RFP in TPE-1R(M) are discussed in the frame work of this model.

The paper concludes with a discussion of the main results obtained in Section 4.

2. PLASMA PARAMETER MEASUREMENTS

Typical waveforms and the F-θ behaviour of a discharge with power crowbar are shown in Figs 1 and 2, respectively. The plasma behaviour in the setting-up phase is the same in the previous cases without power crowbar (constant-θ mode, by control). In the sustainment phase, the F and θ values are approximately constant. The toroidal loop voltage, V_{loop}, goes down during the setting-up phase and is maintained at a constant value in the sustainment phase until about 100 μs before the current disruption. The dependence of V_{loop} on the plasma current in the flat top phase is shown in Fig.3. The loop voltages are approximately proportional to $I_p^{-1/2}$. Dynamo motion (sawtooth oscillations) in the setting-up and sustainment phases is observed by monitoring of soft-X-ray emission.

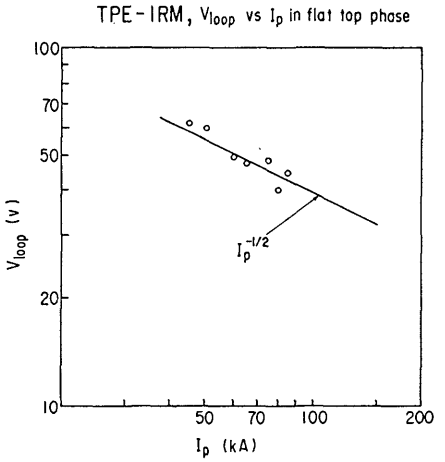

FIG.3. Dependence of toroidal loop voltage on plasma current in sustainment phase.

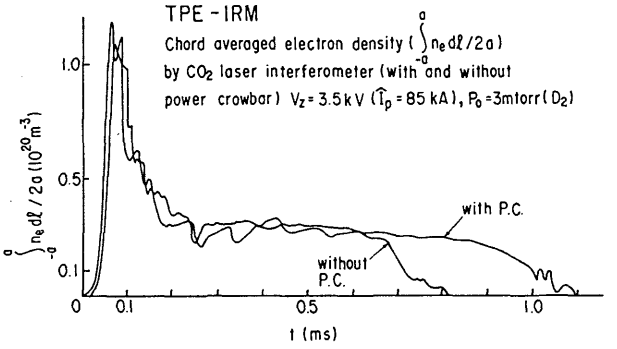

FIG.4. Chord-averaged electron density ($\int_{-a}^{a} n_e d\ell/2a$) found by CO_2 laser interferometer with and without power crowbar.

The plasma parameter measurements were carried out through the whole current pulse in the range of 1.8 to 4 mtorr of initial deuterium gas pressure and 40 to 120 kA of plasma current.

2.1. Electron density

The electron density was measured by a CO_2 interferometer at 10.6 μm. The chord-averaged electron density ($\int_{-a}^{a} n_e d\ell/2a$) along a vertical minor diameter of the torus is shown in Fig.4. The average electron density initially has a peak at 0.1 ms after discharge initiation and then decays rapidly. After pump-out,

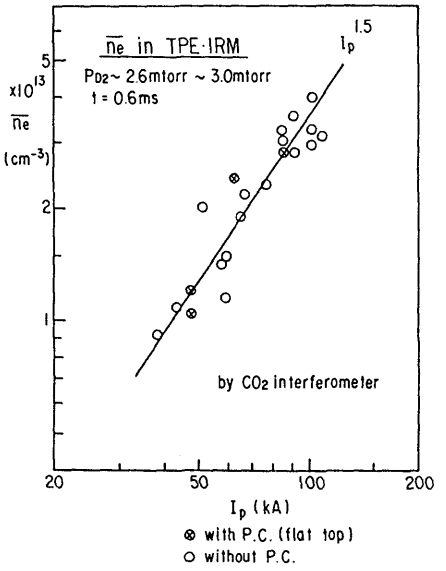

FIG.5. Dependence of average electron density ($\bar{n}_e$) on plasma current, with and without power crowbar.

the electron density reaches a steady state and remains constant until about 0.1 ms before plasma current termination. In Fig.5 the dependence of the average electron density ($\bar{n}_e$) on the plasma current in the steady state (t = 0.6 ms) is shown. We see that $\bar{n}_e$ increases with the plasma current ($I_p^{1.5}$ scaling).

The density starts decaying when the current decreases, which coincides with a rise in the toroidal loop voltage.

2.2. Plasma temperatures

The electron temperature on the axis, T_{e0}, has been measured by Thomson scattering. Figure 6 is an example of the time evolution of T_{e0}. T_{e0} is maintained constant in the sustainment phase, and the previous scaling of T_{e0} with I_p is reconfirmed.

Two methods of ion temperature measurement are used on TPE-1R(M): a neutral-particle energy analyser system (deuterium ion temperature) and a spectroscopic system measuring the Doppler broadening of an impurity line (impurity ion temperature). The number of photons disturbing the measurement is a key factor in the former method. It was found, after careful tests, that the effect of the photons can be reduced, except for the start-up phase of the discharge.

The temperatures of the deuterium ions (in the central plasma region) as measured by the neutral-particle energy analyser are shown in Fig.7 (circles).

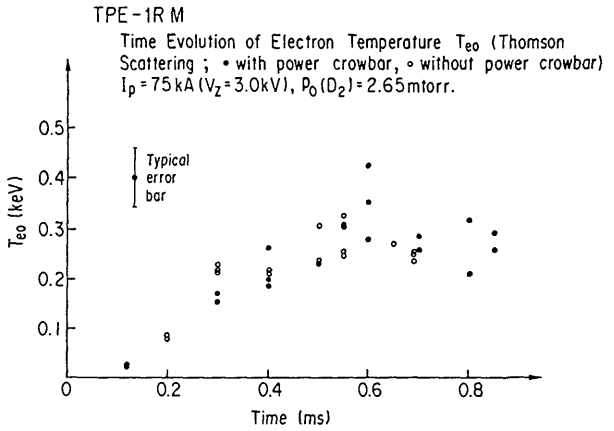

FIG. 6. Time evolution of electron temperature, T_{e0} (Thomson scattering) on the axis.

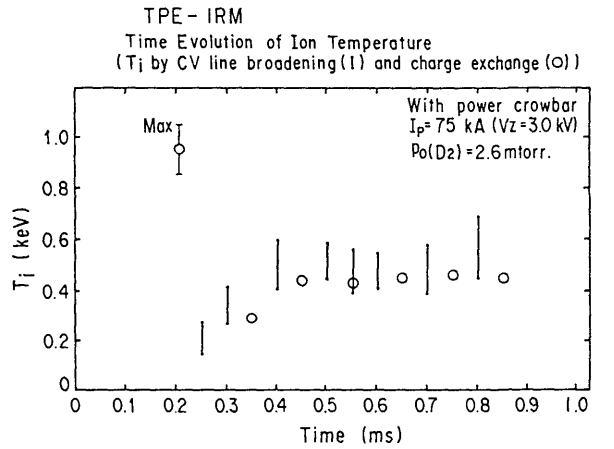

FIG. 7. Time evolution of ion temperature by C V line broadening and charge exchange, with power crowbar.

The vertical error bar arises from an ambiguity in the Maxwellian fitting. The temperature rises with increasing I_p and is maintained constant in the sustainment phase.

The Doppler broadening data of the CV 2270.9 Å line are taken simultaneously with the neutral-particle measurement. A half-value width of about 2.5 Å is seen when a second-order line of 2270.9 Å is observed. The temperature of the C V ions is obtained from the Gaussian fitting of the wavelength scanning signals, which are normalized by the total intensity of 2270.9 Å. The intensity changes by about 30% over all the shots. Both temperatures are plotted in the

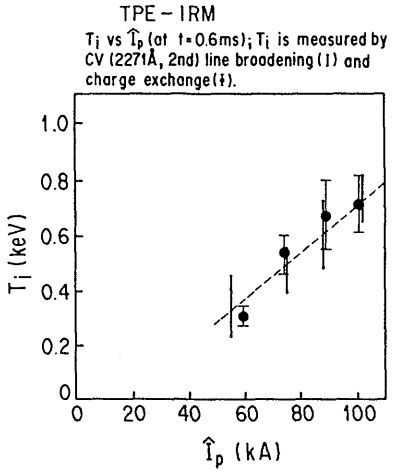

FIG.8. Dependence of ion temperature (line broadening and charge exchange) on plasma current.

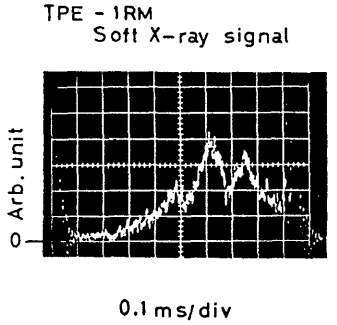

FIG.9. Typical trace of soft-X-ray emission by surface barrier diode ($h\nu \gtrsim 600$ eV); $\hat{I}_p$ = 75 kA, p_0 (D_2) = 2.65 mtorr.

same figure (Fig.7). Their time evolutions have similar waveforms, except for the fact that the Doppler temperature rises earlier (by about 0.1 ms). Both maximum temperatures agree within the experimental error. With power crowbar the temperature does not drop, but rises in the sustainment phase.

Figure 8 shows the dependence of the temperature on $\hat{I}_p$ (t = 0.6 ms), ($T_i \propto \hat{I}_p$ scaling) with two measuring systems.

2.3. Soft X-rays

A surface barrier diode has been used to measure the soft-X-ray emission ($h\nu \gtrsim 600$ eV). A typical trace is shown in Fig.9. In this figure, the characteristic

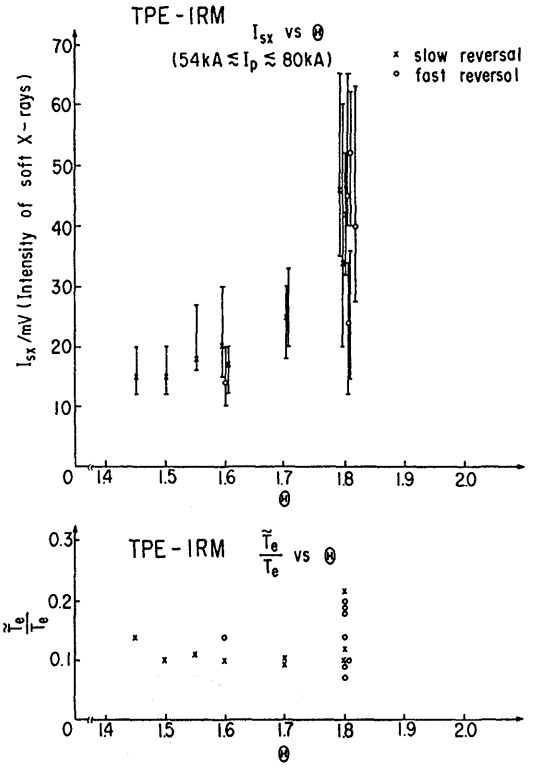

FIG. 10. Dependence of intensity (I_{sx}) of soft-X-ray emission and electron temperature fluctuation ($\Delta T_e/T_e$) on θ-value.

sawtooth oscillations in both setting-up and sustainment phases indicate the existence of relaxation oscillations (dynamo mechanism). It is suggested that these soft X-rays are mainly emitted from the central plasma region. The detected signal intensity, I_{sx}, is proportional to I_p^7 for I_p = 60 kA–120 kA and also proportional to T_e^5, if we use $I_p \propto T_e$. This dependence is reasonably comprehensible if a Maxwellian energy distribution is assumed. These signals can be used to monitor the electron temperature variation. In Fig. 10 the upper diagram shows how the soft-X-ray signals depend on the θ-value. If the θ-value is above 1.6, the signal rises, as was also observed in other machines, e.g. in the ZT-40 M experiment [2]. The lower diagram of Fig. 10 shows the dependence of the electron temperature fluctuation on the θ-value in the sustainment phase, deduced by assuming a Maxwellian energy distribution.

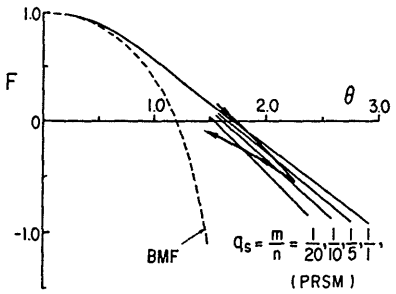

FIG.11. F-θ curves of marginally stable configurations with respect to Suydam criterion in four cases of dominant modes with (m, n) = (1,1), (1,5), (1,10) and (1,20). Dashed line shows F-θ curve of BFM. Bold line with arrows qualitatively shows experimental F-θ curve in TPE-1R(M); aspect ratio = 5.56.

3. PARTIALLY RELAXED MINIMUM ENERGY STATES

The partially relaxed state model (PRSM) has been introduced to represent RFP equilibrium configurations with finite β-values dominated by various (m, n) modes [3]. The equilibrium equation can be written as

$$\vec{j} = \frac{\lambda(\chi)}{\mu_0}\vec{B} + \frac{\nabla\omega \times \nabla}{\vec{B}\cdot\nabla\omega} \qquad (1)$$

where $\lambda(\chi) = [\lambda_0 1 - (\chi/\chi_w)]$. Here, χ is the helical flux defined by $\chi = q_s(\psi - \psi_0) - \phi$, χ_w is χ at the conducting wall, ψ and ϕ are the poloidal and toroidal magnetic fluxes, respectively, ω is the poloidal angle which increases by 2π after each circuit, and $q_s = m/n$ for the mode number (m, n) of the tearing mode. By numerical computation, the equilibrium configuration of partially relaxed states with finite-β values dominated by various (m, n) modes is obtained. Figure 11 shows F-θ curves of marginally stable configurations with respect to the Suydam criterion in four cases of dominant modes with (m, n) = (1,1), 1,5), (1,10), and (1,20). An experimental F-θ curve in TPE-1R(M) is also shown qualitatively by a bold line with arrows. It is found that the finite-β effect yields a noticeable shift of the F-θ curves, for the same dominant modes of the β = 0 cases, towards higher values. The F-θ curve of the partially relaxed state by the dominant m = 1 mode with a higher n number is closer to that of the BFM, which is considered to be the fully relaxed state, as is shown in Fig.11. The experimental F-θ curve in Fig.11 suggests that the RFP plasma in TPE-1R(M) has the tendency to relax towards more advanced, partially relaxed states dominated by m = 1 tearing modes with higher n numbers. Numerical results for dominant modes m = 1 and various numbers of n show that the partially relaxed states by the lower-n

dominant modes have profiles of current densities which concentrate more pronouncedly towards the magnetic axis. This suggests that the RFP configurations in the earlier phase of the relaxation process should have current density profiles concentrating more distinctly towards the magnetic axis. This also suggests that, if the current densities concentrate more strongly towards the magnetic axis by such a transport process of Ohmic heating near the axis during the sustainment phase, the RFP configuration, consequently, comes back to a state with higher θ-values in the earlier phase of the relaxation process dominated by the tearing modes. The state returning to the earlier phase would again undergo a relaxation by a tearing mode with higher n number so as to approach the more advanced relaxed states. This consideration might be related to experimental observation of the F-θ trajectory with soft-X-ray sawtooth oscillations (probably, with m = 1 and high-n magnetic disturbances) in the sustainment phase.

4. DISCUSSIONS AND CONCLUSION

An RFP confinement experiment on TPE-1R(M) with power crowbar has been carried out, and the steady, improved-stability phases are sustained for 0.5 ms until current disruption caused by the loss of equilibrium. TPE-1R(M) has no external coil to control the equilibrium. In later times of the sustainment phase, the toroidal drift is accelerated towards the outer wall, and the plasma touches the limiters about 0.1 ms before the disruption. This causes a rapid cooling of the plasma periphery, and a current concentration at the centre; finally, the plasma current is disrupted by instabilities. These phenomena occur in 0.1 ms; they are observed from an enhancement of the impurity line radiation, e.g. the Fe line, a rise in the toroidal loop voltage and a noticeable plasma current decay at about 0.1 to 0.2 ms before current disruption.

Previous results on plasma parameters and scaling observed at the current top are reconfirmed in the sustainment phase. Typical figures in the sustainment phase: (i) high current density, $\langle j_\phi \rangle \approx 3.5$ MA$\cdot$m^{-2} for $I_p = 90$ kA; (ii) relatively low density, $\langle n_e \rangle = 3 \times 10^{19}$ m^{-3} for $I_p = 90$ kA; (iii) large streaming parameter, $\xi = 0.15$–0.2; (iv) low magnetic field, $B \approx 2B_0 \approx 0.4$ T; (v) S-number = $(1-2) \times 10^5$; (vi) T_{e0} (laser scattering) ≈ 400 eV $< T_e$ (soft-X-ray energy analysis) ≈ 770 eV, $T_{e0} \approx 100$ eV, for $I_p = 90$ kA; (vii) high T_i (D ion and C V ion) ≈ 700 eV for $I_p = 90$ kA; (viii) $Z_{eff} = 3$–5, $\tau_E = 0.1$–0.2 ms, $\tau_{eq} = 7$ ms $> \tau_{exp}$, $E < E_c \approx 50$ V$\cdot$m^{-1}, and scalings $T_e \propto I_p$, neo $\propto I_p$, $\bar{n}_e \propto I_p^{1.5}$, $V_{loop} \propto I_p^{-1/2}$, $T_i \propto I_p$ and $\tau_E, \tau_p \propto I_p^{3/2}$. Typical F/$\theta$ values are $-0.25/1.6$.

High ion temperatures are observed both with deuterium ions and C V ions. The problem of whether such high-temperature ions constitute the bulk of the plasma or not remains to be solved. Experimental data obtained so far are no evidence that these ions might be a high-energy tail. The density of the cold atoms (D_2) has been estimated by charge exchange and D_α 6503^0 resonance

scattering measurements: $n_0 \lesssim 10^{14}$ m^{-3}. It should also be noted that the spatial distributions, the heating mechanism, and the transport phenomena might differ from each other for deuterium ions and C V ions. Since the electron/ion energy equilibration time is $\tau_{eq} = 6-7$ ms ($\tau_{exp} \approx 1$ ms), these high ion temperatures cannot be explained by Ohmic heating alone. This anomalous ion heating seems to be a mechanism similar to that observed in Alcator [4], in which ion plasma waves excited in a low-density discharge interact strongly with the bulk of the ions. We have no information on the plasma oscillations driven by the current in the present experiments, and also it is rather difficult to explain quantitatively the energy balance between the constituents in the plasma, in terms of these plasma waves. To explain the energy balance in plasmas with such high ion temperatures we might want to introduce a thermalization due to some kind of mass motion in the plasma caused by MHD activities.

Soft-X-ray emission measured by surface barrier diodes were observed when sawtooth oscillations and electron temperature variations in the central region during the sustainment phase are monitored.

A new partially relaxed state model (PRSM) was introduced to describe the RFP equilibrium configuration with finite β-values dominated by various (m, n) tearing modes. The relaxation states of RFP in TPE-1R(M) were discussed in the framework of this model; however, the experimental data accumulated so far are not sufficient for a resonable discussion of the subject.

ACKNOWLEDGEMENTS

It is a pleasure to acknowledge K. Hattori, of Tokyo University, for carrying out the soft-X-ray measurements.

This work was supported by the Atomic Energy Bureau, Science and Technology Agency, Prime Minister's Office, Japan. The authors are grateful to all persons concerned for supporting this research work.

REFERENCES

[1] OGAWA, K., et al., in Plasma Physics and Controlled Nuclear Fusion Research (Proc. 9th Int. Conf. Baltimore, 1982), Vol.1, IAEA, Vienna (1983) 575;
HIRANO, Y., et al., Nucl. Fusion 22 (1982) 1613.

[2] WATT, R.G., NEBEL, R.A., Phys. Fluids 26 (1983) 1168.

[3] KONDOH, Y., et al., to be printed in J. Phys. Soc. Japan 53 No.10 (1984).

[4] OOMENS, A.A.M., et al., Phys. Rev. Lett. 36 (1976) 255.

REVERSED-FIELD PINCH PLASMAS WITH CURRENT FLAT-TOP IN ETA-BETA II

V. ANTONI, M. BASSAN, A. BUFFA, S. COSTA,
L. GIUDICOTTI, W. GROSSMANN*, S. MARTINI,
S. ORTOLANI, R. PACCAGNELLA, M.E. PUIATTI,
P. SCARIN, M. VALISA, E. ZILLI
Istituto Gas Ionizzati del Consiglio Nazionale delle Ricerche,
Associazione Euratom-CNR,
Padua, Italy

Abstract

REVERSED-FIELD PINCH PLASMAS WITH CURRENT FLAT-TOP IN ETA-BETA II.

Flat-top current pulses of approximately 2 ms have been obtained in ETA-BETA II. In these conditions, reversed field pinch configurations are maintained at $\Theta \geqslant 2$ and $\beta_\theta \approx 0.1$, and the heating phase is prolonged as compared to the decaying current operation. These discharges at $I_\phi \approx 100$ kA are characterized by plasma resistances $\gtrsim 0.6$ mΩ, fluctuation amplitudes $\cong 2\%$ with dominant modes $m = 0.1$; $n/m \approx -10$; and $Z_{eff} \approx 2$. It is found that increasing the density does not cool the discharge, but the confinement improves and β increases until the high density limit is reached. The steady state discharges are discussed in terms of an empirical model for the field profiles from which the q-limits of the configuration are derived and a comparison with the tokamak is drawn. Discharges at $I_\phi \gtrsim 200$ kA show an encouraging scaling corresponding to plasma resistances $\gtrsim 0.25$ mΩ and lower fluctuation amplitudes.

1. INTRODUCTION

The ETA-BETA II toroidal experiment (a = 12.5 cm, R = 65 cm) has operated in the past with currents $\leqslant 250$ kA decaying in time for pulses $\lesssim 2$ ms [1, 2]. The reversed-field pinch (RFP) configurations obtained with this mode of operation were characterized by relatively high densities ($\lesssim 10^{20}$ m^{-3}), low resistance ($Z_{eff} \approx 1$) [2] and high values ($\geqslant 2$) of the pinch parameter $\Theta = B_\theta(a)/\langle B_\phi \rangle$. With the installation of a new power crowbar bank, current flat-top conditions have recently been obtained, and we present here the results obtained at $\cong 100$ kA.

In Section 2 we discuss the resistance and temperature measurements, the density limits and behaviour of the magnetic field fluctuations, comparing flat-top and decaying current regimes. The properties of the discharges as a function of the time variation of density are discussed in Section 3. The filling density, wall

---

* On leave from Courant Institute of Mathematical Sciences, New York University, New York, USA.

conditions and gas puffing all enter into determination of the actual density, and the discharges are characterized in terms of the time evolution of the I/N parameter and the corresponding values of β_θ. The properties of the discharges as a function of Θ are presented in Section 4. An empirical fit of the experimentally measured profiles is used to discuss the q-limits of the plasma and leads to a comparison with tokamaks. A recently developed transport model for stationary profiles in an RFP is discussed; clear distinctions between tokamak and RFP ion transport result. Preliminary results at higher plasma currents ($\gtrsim$200 kA) are presented in Section 5.

2. COMPARISON OF FLAT-TOP AND DECAYING CURRENT

Measurements at various current amplitudes have been made with decaying current pulses [3]. For these discharges we have observed an almost linear increase of the temperature with plasma current, a decrease of the magnetic field fluctuation amplitude with current, and Z_{eff} is close to unity independent of current [3].

Flat-top operation now allows measurement of the plasma parameters in quasi-steady state conditions. Figure 1 gives examples of the waveforms. The pinch parameter Θ is $\gtrsim$2 and is fairly constant during pulses lasting $\approx$2 ms.

The toroidal component of the magnetic field fluctuations, measured with a set of external probes and normalized to the total field at the wall, is about 2% during the flat-top; the dominant poloidal modes are m = 0 and m = 1 (almost 80% of the total power spectrum). The correlation length along the toroidal direction is $<2\pi R/18$, and a maximum is found along a helical path with $n/m \approx -10$. The presence of both low and high filling density limits [1, 2] is confirmed for flat-top discharges; radiation losses are dominant at high density and high frequency ($\geqslant$25 kHz); magnetic fluctuations increase at low densities.

An important question in RFPs is whether the sustainment of the configuration in time is associated with an increased resistivity [4, 5]. To illustrate this point, the results of temperature and resistivity measurements are presented below. The results versus time for both decaying and flat-top current are shown in Fig. 2, which shows that sustaining the current results in heating the electrons to $\approx$100 eV on the axis. During the early phase of the discharge there is no significant difference in the temperature-versus-time behaviour; the flat-top operation prolongs the heating phase slightly until a quasi-steady state is reached. Temperature measurements have been made simultaneously at two radial positions (r = 0 and r = 7 cm) and indicate a rather broad temperature profile (see Fig.2(d)). From the measured line-of-sight average density (Fig.2(e)) and assuming a parabolic profile for the density we find $\beta_\theta \approx 0.1$ during the quasi-steady state phase.

The on-axis conductivity temperature is obtained from the voltage and current measurements through a current density form factor $J_\phi(0)/\langle J_\phi \rangle = 4$.

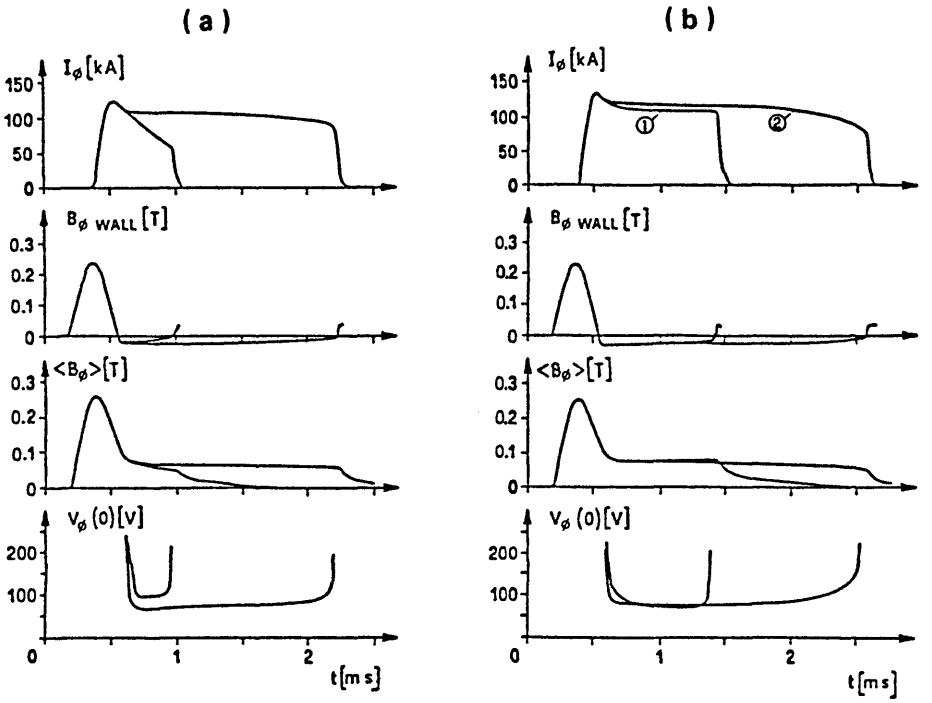

FIG. 1. Time behaviour of plasma current I_ϕ, toroidal magnetic field at the wall $B_{\phi\,\mathrm{wall}}$, average toroidal magnetic field $\langle B_\phi \rangle$ and toroidal voltage on the axis $V_\phi(0)$. (a) Comparison of flat-top and passive crowbar operation. (b) Comparison of different active crowbar modes of operation: in curve① only the current is sustained and in curve ② both current and toroidal field at the wall are controlled.

For both the active and passive operations it is found that $T_\sigma(0) < T_e(0)$, corresponding to a resistance anomaly factor approximately equal to 2. Previous measurements for decaying current discharges [3, 4] have usually given closer agreement between electron temperature and conductivity temperature corresponding to $Z_{eff} \approx 1$. This difference may be due to a small fraction of a new impurity measured in the XUV spectrum (lines have been found in the range $\lambda \approx 40$–60 Å, probably Cl VIII). There are, however, no substantial differences between the cases of decaying and sustained current, and the spectrum emitted by the plasma is also similar. The result, which is peculiar to these recent measurements, is the new emission below 100 Å which was never observed in the past [2, 6].

Multichord measurements of the D_β line, shown in Fig.3, indicate that during the formation of the configuration with $I_\phi \approx 100$ kA the deuterium emission is not symmetric with respect to the central chord, suggesting a significant outward shift ($\lesssim 1$ cm) of the plasma. During the flat-top the two outermost chords give

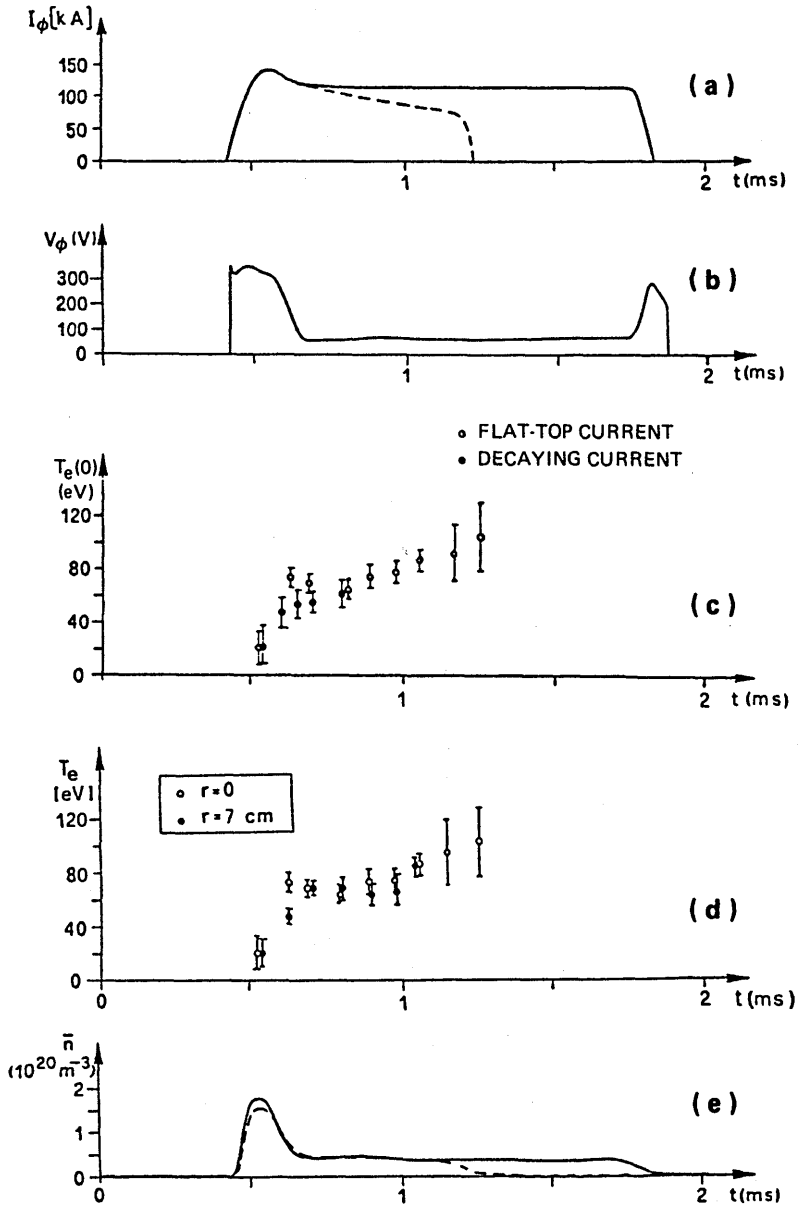

FIG. 2. Time evolution of (a) plasma current; (b) loop voltage; (c), (d) electron temperature; (e) line-of-sight electron density. Solid lines: flat-top operation. Dashed lines: decaying current operation.

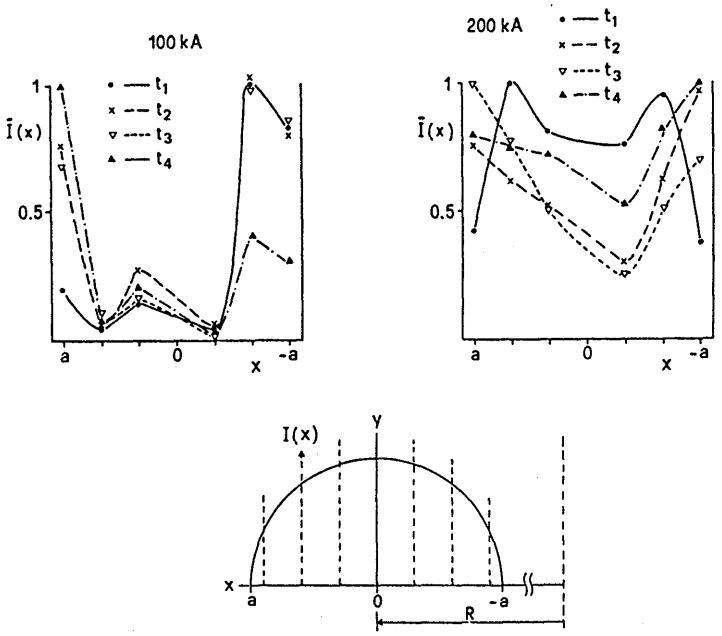

FIG. 3. Multichord measurements of the D_β emission at four times during the current pulse: at the setting-up phase (t_1), at about current peak (t_2), during the flat-top (t_3), and before termination (t_4).

the most intense signals; this behaviour is consistent with a peripheral neutral gas density layer about 1 cm thick. Somewhat different behaviour of the D_β emission has been measured for discharges at $\cong$200 kA, in which case, also shown in Fig.3, the observed emission during formation is larger from the central chords, suggesting the presence of a symmetric skin current layer. During the flat-top the measured emission is hollow, which is consistent with a symmetric deuterium layer in the outer cm of the vacuum vessel. The density of the neutrals in this layer is estimated to be $\approx 10^{19}$ m^{-3}, which corresponds to a fraction $\leqslant 10^{-3}$ of the total plasma particles.

3. PROPERTIES OF THE DISCHARGE WITH DIFFERENT DENSITY-VERSUS-TIME BEHAVIOUR

Gas puffing, together with the filling density and wall effects, produces different density-versus-time behaviour. We observe that the discharges with the higher densities also have the higher β. This means that increasing the density does not cool the discharge giving the same plasma energy, but the confinement improves and the plasma energy and β increase.

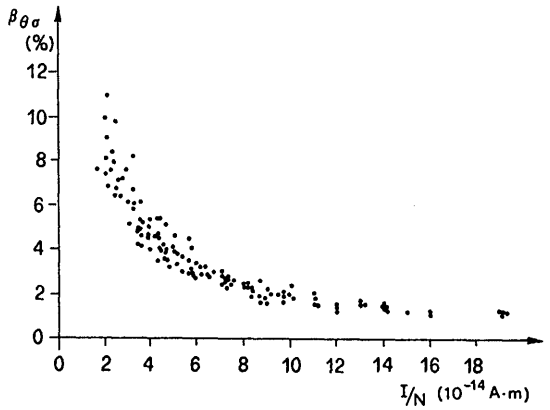

FIG. 4. Poloidal beta computed from conductivity temperature $\beta_{\theta\sigma}$ versus the I/N parameter from a large number of discharges.

Figure 4 shows the dependence of $\beta_{\theta\sigma}$ on I/N as deduced from a large number of discharges. The values of $\beta_{\theta\sigma}$ reported in the figure are computed using the conductivity temperature and therefore represent a lower limit for β_θ. The data appear to confirm a previous suggestion [4, 7] that it is extremely important to operate at as high a density as possible in order to obtain high β and good confinement conditions. The data reported in Fig.4 refer to discharges which, within 10%, have the same current ($\approx$100 kA) and the diagram therefore shows that β_θ is proportional to the plasma density (i.e. $T_\sigma/I \approx$ const). This trend is confirmed by discharges at currents $\geqslant$200 kA and indicates that β_θ increases with density until the high density limit is reached at $I/N \approx 10^{-14}$ A·m [7, 8].

Moreover, it is found that by increasing the density (i.e. decreasing I/N) the high frequency ($\geqslant$25 kHz) fluctuation amplitude decreases. The density dependence of the experimental streaming parameter ξ (derived from the conductivity temperature) is quite similar to the density dependence of the fluctuations, and an almost linear relationship of the high frequency fluctuations on ξ is deduced.

4. PROPERTIES OF THE DISCHARGE AS A FUNCTION OF THETA

The RFP configuration has been described as a plasma state corresponding to a minimum of the magnetic energy [9]. In particular, for a $\beta = 0$ plasma surrounded by a perfectly conducting cylindrical wall, the minimum energy magnetic configuration is described by the Bessel function model (BFM), $B = B_0 (0, J_1(\mu r), J_0(\mu r))$, where $\mu = \mu_0 \vec{J} \cdot \vec{B}/B^2 =$ const and $\mu a = 2\Theta \leqslant 3.11$. The $\mu =$ const condition requires a large parallel current density in the outer

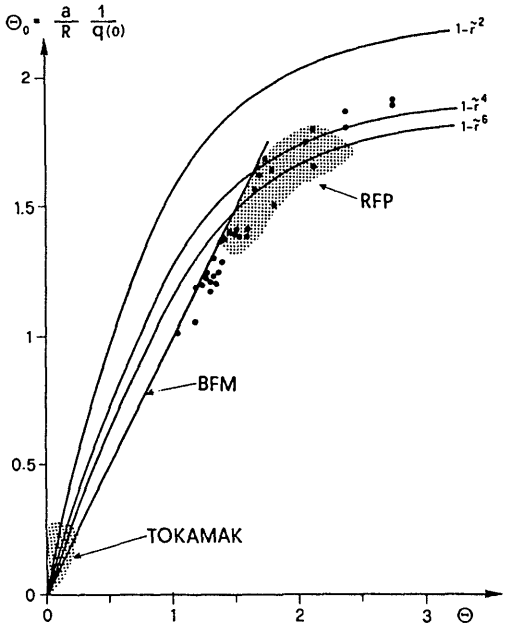

FIG.5. Diagram of Θ_0 versus Θ from experimental data (dots) and for various μ profiles (solid lines).

region of the plasma where it is known that a low-temperature, high-resistivity, low current density region exists. Furthermore, the experimental β is small ($\cong$0.1) but finite, giving rise to a small current density perpendicular to the magnetic field. More realistic configurations can be generated by considering a $\mu \neq$ const profile [10], satisfying the boundary conditions $\mu(a) \approx 0$, $J(a) \approx 0$, of the form $\mu = \mu(0)[1 - (r/a)^{\alpha}]$. This, together with $\nabla p \neq 0$, completely specifies the magnetic field distribution.

The range of Θ values for an RFP is experimentally quite large, and results have been reported with $\Theta \approx 1.5$–3 [10–12]. However, the central region of the RFP configuration, which can be characterized by the parameter $\Theta_0 = \mu(0)a/2 = (a/R)(1/q(0))$, is less variable. To illustrate this, experimental data for Θ_0 versus Θ [5, 10] are shown in Fig.5 along with curves computed with $\beta = 0$ and various μ profiles. It is seen that the total current and Θ are not limited to $\Theta \leqslant 1.6$, as the BFM would impose [9].

However, Θ_0 appears limited to $\leqslant 2$, experimentally, and this can be thought of as a lower limit on the pitch or on q on-axis since:

$$P(0) = Rq(0) = \frac{2B(0)}{\mu_0 J(0)} = \frac{2}{\mu(0)} = \frac{a}{\Theta_0}$$

The condition $\Theta_0 < 2$ implies that $q(0) > \frac{1}{2}\, a/R$, whereas for a tokamak the condition $q(0) \approx 1$ corresponds to $\Theta_0 \approx a/R$ and hence,

$$\frac{q(0)^{TOK}}{q(0)^{RFP}} \approx 2R/a$$

A low value of the pitch or of q on the axis corresponds to a high current density on the axis; this seems limited to $J(0) < 4B(0)/(\mu_0 a)$, but in any case it can be substantially larger than in the tokamak, typically by a factor 2(R/a).

Considering a μ profile of the form $1 - (r/a)^{\alpha}$, it can be shown [5] that the transition from a q-profile monotonically increasing with radius (tokamak) to a q-profile monotonically decreasing with radius (RFP) occurs with profiles which have a minimum q. It is known that unstable global modes exist in configurations with a pitch minimum [13]. It is interesting that our model provides a continuous transition from tokamak to RFP without requiring toroidal effects [9].

It is observed experimentally that the magnetic field distribution is a function of Θ [10–12] and that a Θ = const discharge can be maintained for times significantly longer than the resistive diffusion time which in ETA-BETA II is < 1 ms. On the other hand, it is well known that, to maintain a steady state RFP profile, some mechanism is necessary which regenerates the magnetic field in the presence of ordinary field diffusion. One can then consider a modified Ohm's law including an additional electric field which drives the currents necessary to sustain the magnetic configuration [5]. This electric field is usually referred to as a dynamo electric field which may be generated in the plasma through instabilities and/or turbulence. Ohm's law is then written as:

$$\vec{E}_i + \vec{E}_D = \eta \vec{J}$$

where $\vec{E}_i$ is the induced electric field satisfying the stationary condition which implies $E_{i\theta} = 0$ and E_{iz} = const.

A calculation corresponding to typical ETA-BETA II parameters [5] shows that, in the outer region, the internally generated electric field is large and comparable to the induced one. This is a general feature which is related to the sustainment of the large azimuthal current, J_θ, in the region of the field reversal.

The stationary condition corresponds to a resistance enhancement factor which is typically about 2 [4, 5]. Thus the power necessary to sustain a stationary RFP is about twice the classical Ohmic heating power.

Once the stationary distributions of the electric field and current density are known, the plasma power balance can be computed and, assuming that the dominant energy loss is due to heat transport, the heat conduction coefficient consistent with a stationary profile can be derived [5]. It is interesting to write explicitly the expression for the heat conductivity in the central region; for a

parabolic temperature profile in particular, the on-axis value normalized to the classical ion value has the form:

$$\tilde{\chi}(0) \cong \frac{0.2}{\sqrt{A}} \frac{\Theta_0^2}{\beta_0^2}$$

where A is the mass number and β_0 is the on-axis β.

It is seen quite generally that for a deuterium pinch characterized by $\Theta_0 \approx 1.5$, $\beta_0 \approx 0.1$,

$$\tilde{\chi}(0) \approx 30$$

On the other hand, the maximum β which would be possible if the heat losses were due to classical ion transport, i.e. with $\tilde{\chi}(0) = 1$, would be

$$\beta_0^{\mathrm{cl,RFP}} \cong \Theta_0 \sqrt{\frac{0.2}{\sqrt{A}}} \approx 0.6$$

which is far beyond the tearing mode stability limit [14].

These simple considerations can be used for comparison with the ohmically heated tokamak where, taking into account the neoclassical correction, one finds:

$$\tilde{\chi}(0) \cong \frac{0.2}{\sqrt{A\epsilon}} \frac{\Theta_0^4}{\beta_0^2}$$

where $\epsilon = a/R$ is the inverse toroidal aspect ratio. In tokamaks the global heat conduction is not far from the neoclassical ion value, but this corresponds to a β limit given by:

$$\beta_0^{\mathrm{cl,TOK}} \approx \Theta_0^2 \sqrt{\frac{0.2}{\sqrt{A\epsilon}}} \approx 0.5\,\Theta_0^2 \approx 0.5\,\epsilon^2 \approx 0.05$$

Thus in the RFP the transport would approach the classical limit for very high β values ($\approx$0.5); with the present experimental β values ($\approx$0.1) it is typically $\chi = 30$. In the tokamak, however, the classical ion transport limits β to a lower value ($\approx$0.05), which is also close to the ideal MHD limit [15].

Recent theoretical work [16, 17] suggests that the experimentally observed RFP β-limit may be due to resistive instability-induced turbulent transport; the characteristic time-scale being $\tau_R \propto a^2 T_e^{3/2}$. More general considerations of the density limits and scaling laws [7] have suggested that β should be constant since $T = 1.56 \times 10^{11}\, \beta_\theta\, II/N$, where, experimentally, T varies linearly with I for the

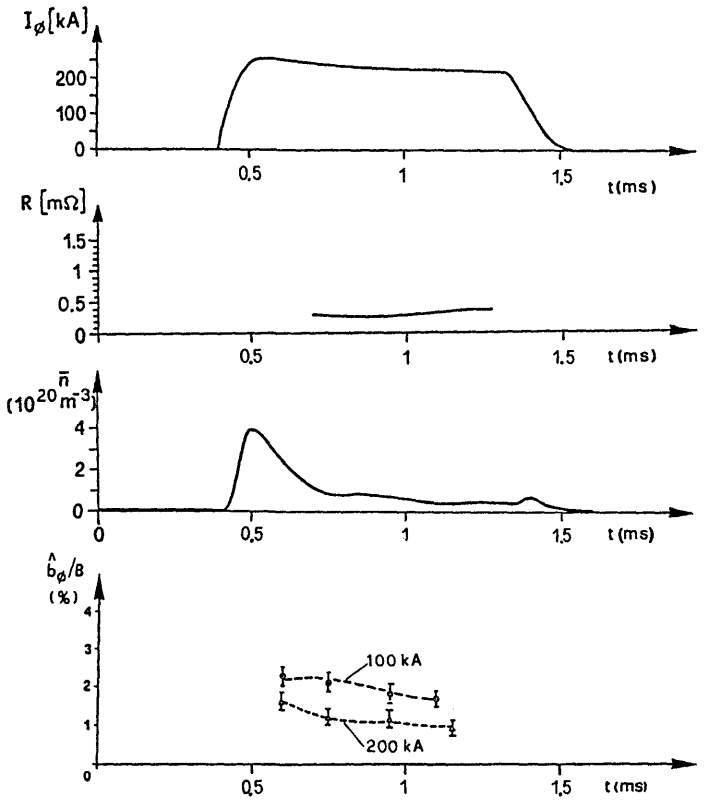

FIG. 6. Plasma current I_ϕ, resistance R, and line-of-sight electron density $\bar{n}$, for a high current discharge together with the time evolution of the magnetic field fluctuation amplitude for 100 kA and 200 kA discharges.

constant I/N operation characteristic of both RFPs and tokamaks [7, 18]. Correspondingly the energy confinement time-scales as $\tau_E \propto a^2 T^{3/2}$, which is consistent with the assumption of classical behaviour modulo a factor which depends on the value of β.

5. DISCHARGES AT I ≅ 200 kA

Only a limited number of experiments have been carried out under high current flat-top conditions. Figure 6 gives an example of the waveforms and shows that a substantially lower plasma resistance is obtained, although the conditions at this current level have not yet been optimized and operation at higher densities should be possible.

The plasma resistance is $\geqslant 0.25$ mΩ, corresponding to conductivity temperatures on the axis of $\cong 80$ eV. This must be compared with resistances $\gtrsim 0.6$ mΩ and $T_\sigma(0) \approx 45$ eV obtained typically at $I_\phi \cong 100$ kA. The magnetic field fluctuations measured for these high current discharges are compared in Fig.6 with the results obtained at $\cong 100$ kA. During the flat-top the amplitude is about constant at a value $\sim 1\%$ for the 200 kA discharges, and the results are consistent with the dependence $\hat{b}/B \propto I^{-1}$ previously found [3, 4].

6. CONCLUSIONS

RFP discharges with current flat-top have been studied in ETA-BETA II. RFP plasma configurations are maintained for times $\geqslant 2$ ms at const $\theta \geqslant 2$ and with $\beta_\theta \approx 0.1$. Sustaining the current prolongs the heating phase and at $I_\phi \approx 100$ kA the electron temperature reaches ≈ 100 eV on the axis. Both for flat-top and decaying current discharges $Z_{eff} \approx 2$ is found, corresponding to a new impurity (probably Cl) whose line emission is observed in the XUV spectrum.

The study of discharges with different plasma densities has shown that the higher values of β_θ correspond to the higher densities. This is found from a large number of discharges at ≈ 100 kA as well as from higher current discharges and shows that $\beta_\theta \propto N$ until the high density limit is reached at $I/N \cong 10^{-14}$ A·m. The higher densities also correspond to the lower amplitudes of the magnetic field fluctuations. The variation of the profiles with Θ has been presented in terms of the parameter $\Theta_0 = (a/R)(1/q_0)$ and the q-limits of RFP configurations have been discussed together with a comparison with tokamaks. A steady state model has been presented which indicates that the ETA-BETA II discharges, characterized by $\Theta_0 \approx 1.5$ and $\beta_0 \approx 0.1$, correspond to heat transport typically 30 times the classical ion value. The transport model also allows a clear comparison of the β-limits in tokamaks and RFPs.

Discharges at $I \geqslant 200$ kA show an encouraging scaling with lower plasma resistances $\geqslant 0.25$ mΩ and lower fluctuation amplitudes $\sim 1\%$.

ACKNOWLEDGEMENTS

The valuable collaboration of the ETA-BETA II technical staff is gratefully acknowledged. The authors also wish to thank Drs G. Flor and N. Guarino for co-operation on the data acquisition and analysis system, and Dr. G. Tondello for continuous support in the spectroscopic diagnostics.

REFERENCES

[1] BUFFA, A., et al., "ETA-BETA II: Reversed-field pinch plasmas with improved confinement", Plasma Physics and Controlled Nuclear Fusion Research 1980 (Proc. 8th Int. Conf. Brussels, 1980), Vol.2, IAEA, Vienna (1981) 275.
[2] ANTONI, V., et al., "Studies on high-density RFP plasmas in the ETA-BETA II experiment", Plasma Physics and Controlled Nuclear Fusion Research 1982 (Proc. 9th Int. Conf. Baltimore, 1982), Vol.1, IAEA, Vienna (1983) 619.
[3] ANTONI, V., et al., in Controlled Fusion and Plasma Physics (Proc. 11th Europ. Conf. Aachen, 1983), Vol.7D, Part 1 (1983) 143.
[4] ANTONI, V., RFP Experiments at Various Plasma Currents on the ETA-BETA II Device, Istituto Gas Ionizzati, Padua, Rep. IGI 83/03 (1983).
[5] ORTOLANI, S., Stationary Reversed Field Pinch Profiles, Istituto Gas Ionizzati, Padua, Rep. IGI 84/06 (1984).
[6] ORTOLANI, S., PUIATTI, M.E., SCARIN, P., TONDELLO, G., "Spectroscopic observations of a reversed field pinch: ETA-BETA II", to be published in Plasma Phys. Contr. Fusion.
[7] ORTOLANI, S., ROSTAGNI, G., Nucl. Instrum. Methods **207** (1983) 35.
[8] COSTA, S., DeANGELIS, R., ORTOLANI, S., PUIATTI, M.E., Nucl. Fusion **22** (1982) 1301.
[9] TAYLOR, J.B., "Relaxation of toroidal discharges to stable states and generation of reverse magnetic fields", Plasma Physics and Controlled Nuclear Fusion Research 1974 (Proc. 5th Int. Conf. Tokyo, 1974), Vol.1, IAEA, Vienna (1975) 161.
[10] ORTOLANI, S., "Equilibrium and stability properties of reversed field pinch configurations", Course on Mirror-Based and Field-Reversed Approaches to Magnetic Fusion, Varenna, 1983.
[11] ANTONI, V., MARTINI, S., ORTOLANI, S., PACCAGNELLA, R., "Properties of the fluctuating and mean magnetic field as a function of Θ in RFP", ibid.
[12] ORTOLANI, S., PACCAGNELLA, R., ZILLI, E., in Proc. Int. Conf. Plasma Physics, Lausanne, 1984, P12-4 150.
[13] ROBINSON, D.C., Plasma Phys. **13** (1971) 439.
[14] ROBINSON, D.C., Nucl. Fusion **18** (1978) 939.
[15] Proc. 2nd European Tokamak Programme Workshop, Saulx-les-Chantreaux, 1983.
[16] CONNOR, J.W., TAYLOR, J.B., Resistive Fluid Turbulence and Energy Confinement, Culham Rep. CLM-P714 (1984).
[17] CONNOR, J.W., TAYLOR, J.B., Paper No. IAEA-CN-44/E-I-2, these Proceedings, Vol.2.
[18] PERKINS, F.W., HULSE, R.A., On the Murakami Density Limit in Tokamaks and Reversed Field Pinches, Princeton Univ. Rep. PPPL-2087 (1984).

DISCUSSION

N.A. KRALL: Did your estimated $\tilde{\chi}$ change between the low-current and high-current cases?

S. ORTOLANI: No, because β is approximately constant as the current increases and therefore, unless the profiles change, the estimate of $\tilde{\chi}$ is independent of current.

N.A. KRALL: This was despite the reduced fluctuation level?

S. ORTOLANI: Yes, because $\tilde{\chi}$ is normalized to the classical ion conduction, i.e. the transport losses scale with temperature and size as the classical ion diffusion times a multiplication factor which is independent of current and which we have estimated to be ≈30. This scaling is consistent with the decrease observed in the fluctuations with current.

R.S. PEASE: Did you make any measurements of the important magnetic field details in the outer region when comparing flat-top with decaying current?

S. ORTOLANI: We measured the magnetic field profiles in detail only with decaying current and found that the current density in the outer region is small and becomes zero near the wall. This also explains why, although θ can vary in a wide range between 1.5 and 3, $\theta_0 = (a/R)(1/q_0)$ does not and is typically $\theta \approx 1.5$. With our experimental distributions, there is very little reversal of the toroidal current density in the outer region, or even none at all. We do not see significant differences between flat-top and decaying-current operation, and therefore the above characteristics should apply to both the flat-top and the decaying current cases.

SPHEROMAK STUDIES ON CTX

T.R. JARBOE, C.W. BARNES, I. HENINS, H.W. HOIDA,
S.O. KNOX, R.K. LINFORD, G.J. MARKLIN, D.A. PLATTS,
A.G. SGRO, A.R. SHERWOOD, B.L. WRIGHT
Los Alamos National Laboratory,
Los Alamos, New Mexico

A.A. MIRIN, D.E. SHUMAKER
National Magnetic Energy Computer Center,
Lawrence Livermore National Laboratory,
Livermore, California

United States of America

Abstract

SPHEROMAK STUDIES ON CTX.

Recent experimental results are reported of spheromaks generated by a magnetized coaxial plasma source in the CTX experiment, and related theoretical studies are presented. The injection of magnetic helicity by the source has been shown to determine the formation and refluxing of the spheromak. Spheromaks have been sustained at nearly constant density and magnetic field for over ten magnetic energy lifetimes. Impurity radiation problems have been overcome, and electron temperatures of over 100 eV (measured by multipoint Thomson scattering) achieved. Energy balance analysis and additional diagnostics have provided information on the confinement properties of the spheromaks. The mode structures associated with different oscillations seen during sustained operation and during the configuration decay have been identified. The modes are well understood by MHD theory, and numerical simulations are used to show that an n = 2 distortion appears when a non-uniform resistivity is present.

A spheromak is a compact toroidal magnetic confinement configuration having comparable toroidal and poloidal magnetic fields and having no material linking the hole in the torus. Some potential reactor advantages of this confinement concept are simply connected fusion blanket and coil structures, high power density, small size, and magnetic field sustainment using dc power. Results reported here are steps toward the goals of understanding the confinement and stability properties of spheromaks and of sustaining spheromaks using dc power.

A magnetized, coaxial Marshall gun is used to form the spheromaks [1]. Plasma and magnetic fields are injected into an oblate-shaped flux conserver. The spheromak is formed by the relaxation of the injected fields towards a minimum-energy state, determined by the amount of magnetic helicity supplied

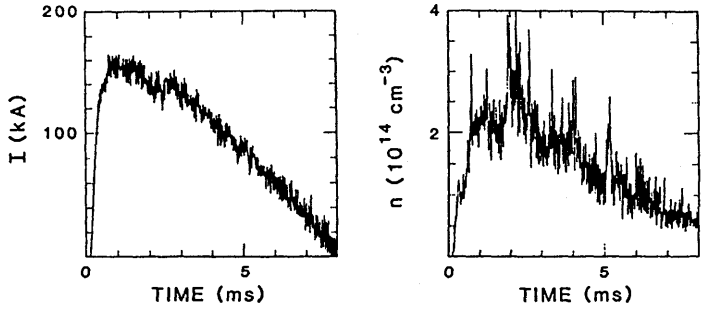

FIG.1. Toroidal current and diameter-averaged density as a function of time for a sustained spheromak. The density variations are caused by the rotating n = 1 mode discussed in the text. The toroidal current is calculated (using an equilibrium model) from local surface currents measured in the flux conserver. The fluctuations on the current are not real but come from variations in the local currents induced by the n = 1 mode. The steady state current decrease after 1 ms is due to a decrease in the helicity injection rate.

and the geometry of the flux conserver. The helicity flows from the source at the rate of $2V\Phi_p$ (where V is the voltage on the electrodes and Φ_p is the magnetizing flux of the source) and decays on a resistive diffusion time scale in the spheromak. Assuming a constant resistive decay time, and that 100% of the helicity from the source is absorbed by the spheromak, the field strengths of the spheromak are predicted by helicity balance to within 20% over a wide range of operating conditions.

There are two types of operating conditions for CTX, depending upon the duration of the helicity injection time. Sustainment is achieved by injecting plasma and magnetic helicity for times long compared to the characteristic magnetic energy decay time (τ_{B2}) of the spheromak. Magnetic field and electron density measurements show that under this condition spheromaks are generated early in time and "sustained" against resistive decay by source currents and fluxes which are only a fraction of the currents and fluxes in the spheromak [1]. So far, T_e for sustained spheromaks is only 20-30 eV at B $\simeq$ 2.5 kG and $n_e \simeq 1 \times 10^{14}$ cm^{-3}. Recently, the injection time has been increased from the previous 2 ms to over 10 ms. The amount of time that the spheromak can be sustained is now limited by the flux loss time of the passive flux conserver. This suggests the possibility of steady state sustainment by operating the source continuously and by actively supplying the spheromak equilibrium fields with external coils. Figure 1 shows the toroidal current and diameter-averaged density of a spheromak sustained for over 5 ms.

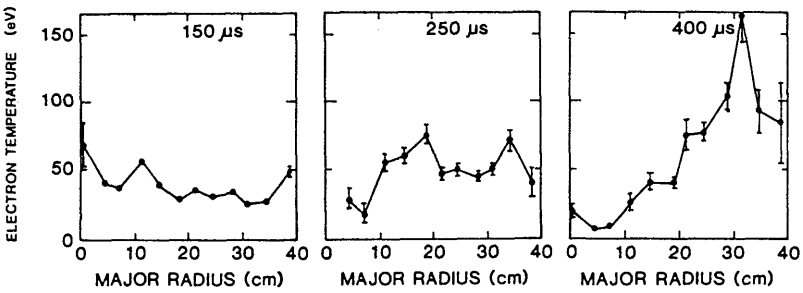

FIG.2. Electron temperature versus radius at three different times for a decaying spheromak. The flux conserver radius is 40 cm.

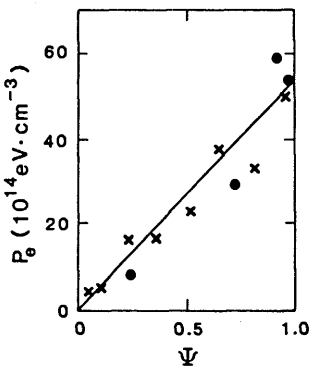

FIG.3. Electron pressure P_e versus normalized poloidal flux Ψ from one discharge. Ψ = 0 at the flux conserver and Ψ = 1 at the magnetic axis. The x s are from Thomson scattering data positions that are at smaller radii than that of the magnetic axis. The solid circles are from radii larger than that of the magnetic axis.

In the second type of operation, the helicity injection time is shorter than τ_B2, and decaying spheromaks are studied. In one set of operating conditions in CTX, the helicity injection time is 0.06 ms (about a resistive tearing time), and the time for the spheromak to tear free from the source is about another 0.1 ms. Under these conditions 100-eV spheromaks are obtained in an 80-cm-diameter, 40-cm-long flux conserver constructed from 12-mm-diameter rods in a welded mesh design [2]. A hydrogen pressure of 30 mtorr is present in the vacuum tank which contains the flux conserver. Using a multipoint Thomson scattering instrument, full radial electron temperature and density profiles (12 points) are measured on a single discharge. By the end of the formation time, 0.16 ms, the electron temperature profile is fairly flat

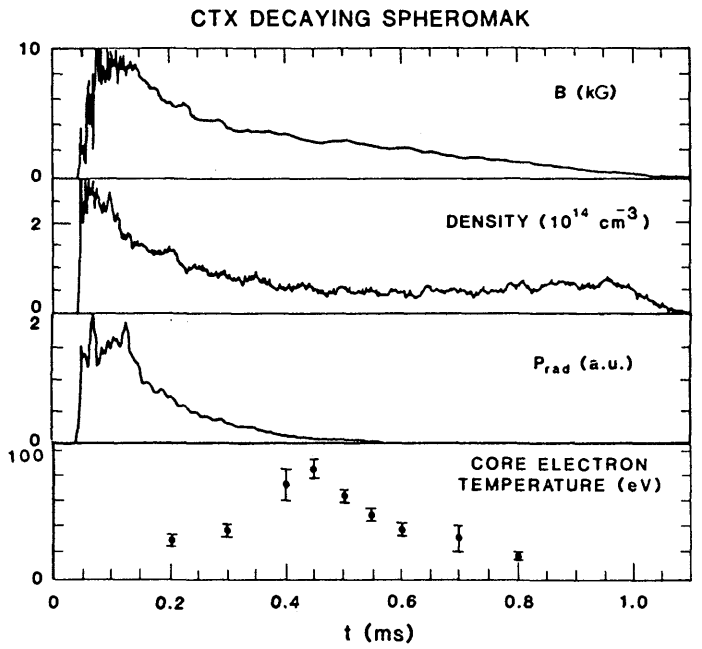

FIG.4. The poloidal magnetic field at the geometric center of the spheromak (B); the diameter-averaged density; the diameter-averaged power radiated (P_{rad}), and the core electron temperature versus time for a decaying spheromak. The magnetic field is deduced (assuming a minimum energy model) from probe measurements on the geometric axis 7 cm from the end wall of the flux conserver. The density is from interferometry, the radiation is from bolometry, and the temperature is from Thomson scattering.

around 30 eV (Fig. 2). Subsequently, the radial temperature profiles show initial rapid heating on the outer flux surfaces. This is consistent with the results of a 1 1/2-D transport code where the off-center temperature peaks are due to the current profile and ohmic heating peaking off center and to the density being lower on the outer flux surfaces [3]. In the experiment, two peaks of the temperature rise and move toward the magnetic axis as time progresses, coalescing into a single-peaked > 100-eV temperature at or near the magnetic axis. The electron pressure (P_e) vs. radius can be calculated from the multipoint Thomson scattering data. The poloidal flux (Ψ) vs. radius can be estimated using analytic models [4]. Thus P_e vs. Ψ can be deduced. As shown in Fig. 3, P_e increases monotonically with Ψ. Assuming $P \propto \Psi^{\alpha}$, α varies from shot to shot in the range of 1/2 to 2. The value of the magnetic field at the geometric center (B) at the time of the 100 eV temperature is 2 - 3 kG. While the temperature is

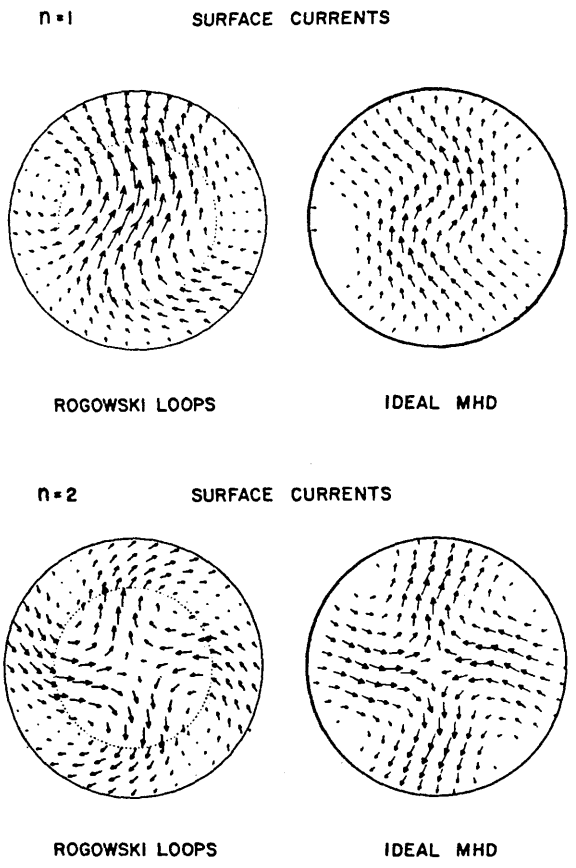

FIG.5. Experimentally derived surface currents in the flux conserver compared with those calculated from a 2D linearized stability code. The reconstruction of the perturbed current pattern from Rogowski loop data is aided by the rotation of the modes and by the assumption that there are no oscillating currents between the plasma and the flux conserver.

rising, the diameter-averaged density (n) drops from 2-3 x $10^{14}cm^{-3}$ to 2-9 x $10^{13}cm^{-3}$. The impurity radiation (P_r) drops even more dramatically, showing a decrease in the fractional concentration of impurities. Figure 4 shows n, B, P_r from a single discharge and the core temperature (T_c) averaged from many discharges vs. time. T_c is the average of the temperatures measured in the range r = 21 - 35 cm. At the time of peak temperature, $\langle\beta\rangle_{vol} \simeq 8\text{-}10\%$ and $n\tau_E \simeq 4 \times 10^9 cm^{-3}s$ are observed. The density remains constant thereafter, while the magnetic field and T_e decay to zero at about 1 ms. Energy balance modeling [5] shows that by the time of peak temperature, particle replacement power and

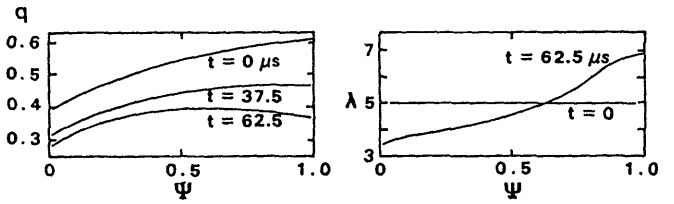

FIG.6. The parameters q and λ versus poloidal flux Ψ. $\lambda = \mu_0 Rj/B$. R is the radius of the flux conserver.

thermal conduction losses are the principal components of the energy loss. The analysis indicates that the impurities are "pumping out" as opposed to "burning through". Observations of OV and OVI radiation from different chords with VUV spectrometers show that oxygen impurities leave the outer flux surfaces more rapidly than the inner. Assuming no oxygen recycling occurs, the oxygen particle confinement time near the magnetic axis is ~ 0.1 ms and on the outer flux surfaces is about a factor of two lower. After the density plateau is reached, the particle confinement time of the hydrogen is measured using Lyman α and H_α radiation, and values of 0.1 - 0.2 ms are obtained. These times are (within the accuracy of the measurements) equal to the characteristic decay time of the density toward the plateau value.

Long-wavelength, low-frequency (10-25 kHz) oscillations are observed on magnetic, density and spectroscopic diagnostics in both the sustained and decaying spheromaks. The mode structure of the rotating distortion which causes the oscillations is determined by measuring the current pattern in the mesh flux conserver. An n = 1 mode is observed during sustainment and an n = 2 mode is observed during the decay. A 2D-linearized stability code shows that if j/B is uniform across the flux surfaces ("Taylor state") the spheromak is stable; if j/B is larger on the outer flux surfaces (currents are driven there in the sustained operation) the n = 1 kink mode becomes unstable; if j/B is smaller on the outer flux surfaces (e.g. because of the more resistive outer edge in a decaying spheromak) the n = 2 kink mode becomes unstable. The stability code shows the n = 1 mode becoming unstable when q is above 1.0 everywhere and the n = 2 mode becoming unstable when q is below 0.5 everywhere. The measured surface current patterns agree with those computed by the stability code (Fig. 5). The connection between the oscillations and the j/B profiles is strengthened by the experimental observation that a small amount of current driven in the decaying spheromak (presumably making j/B more uniform) suppresses the

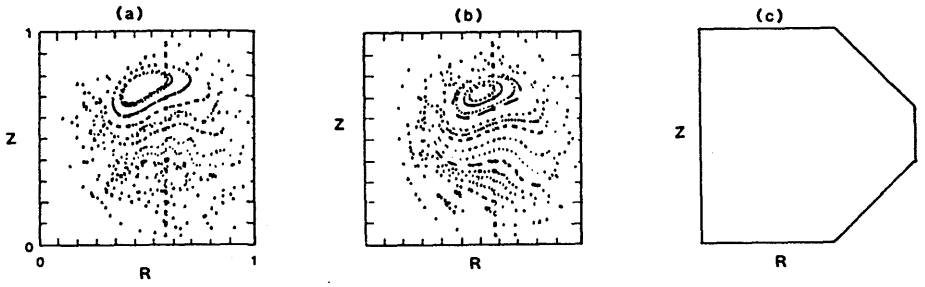

FIG. 7. (a) Magnetic flux puncture plot at $t = 22\tau_A$; (b) at $t = 64\tau_A$. (c) Flux conserver cross-section used in the experiment.

oscillations. The MHD calculations do not predict rotation; however, in the experiment both modes rotate. The rotational velocity of the n = 1 mode is proportional to the voltage on the source, suggesting that the rotation may be driven by an $\vec{E} \times \vec{B}$ effect associated with the source. The rotational velocity of the n = 2 mode may be due to electron diamagnetic drift. The suggested sources of the rotation have been tested by changing the directions of the poloidal and toroidal fields, and the results agree with the hypotheses.

The evolution of a toroidally symmetric spheromak through the diffusion phase is numerically simulated with the "1-1/2D" transport code MINERVA [6]. In such a code the plasma inertia is neglected and the plasma evolves through a sequence of quasi-equilibria. All thermodynamic variables are assumed to be constant on a flux surface, and the diffusion of these variables across the flux surfaces is computed. The resistivity profile in this calculation is $\eta = \eta_0(1+\varepsilon-\Psi)$, where $\Psi = 0$ at the boundary and $\Psi = 1$ at the magnetic axis. The parameters η_0 and ε are chosen so that the temperature implied if η were classical resistivity with $z_{eff} = 1$ is 4.5 eV at the boundary and 23 eV at the magnetic axis. A resistivity profile is required because if η were constant in space, the spheromak fields would simply decay self-similarly. In the initial state the q(r) profile at the z midplane increases monotonically from 0.4 at the boundary to 0.6 at the magnetic axis. Diffusion causes the q(r) profile to become flat (causing low shear) over the 30-40% of the plasma closest to the magnetic axis, as shown in Fig. 6.

Two-dimensional linear stability codes are used to check the stability of the equilibria during the diffusion phase. Both an ideal [7] and a resistive [8] code are used. The equilibria are found by both codes to become unstable to the

n = 2 mode when q on the magnetic axis drops below 0.5, at t = 37.5 μs (Fig. 6), and that the growth time is less than the diffusion time. The growth times calculated by both codes agree to within a factor of two, so that the mode is a resistively modified ideal mode.

The dynamical evolution of this unstable equilibrium is calculated with the 3D resistive MHD code TEMCO [8]. This code is initialized with the unstable equilibrium at 62.5 μs and the n = 2 unstable perturbation. For the calculation reported on here, only the n = 0 and n = 2 modes are included, but the additions of n = 4 are in progress. For this simulation, $S = \tau_R/\tau_A = \mu_o RB/\eta\sqrt{\mu_o \rho} = 10^4$, where R is the flux conserver radius and B is at the geometric center. Both η and ρ are uniform. The 3D magnetic field is input to the TUBE [9,10] code, which outputs puncture plots in a given poloidal plane. The puncture plot in Fig. 7a shows that the unstable perturbation grows and the magnetic axis moves nearer the boundary. Eventually the displacement saturates as the plasma relaxes into a three-dimensional equilibrium. Figure 7b shows a puncture plot later in time when the plasma position has shifted down and to the right. Figure 7c shows the geometry of the experiment.

These numerical calculations demonstrate that a resistivity profile drives the spheromak away from the toroidally symmetric minimum energy state to a new three-dimensional equilibrium having n = 2 toroidal variation. Although the n = 2 distortion observed in the decaying spheromak experiment is found in the calculation, the rotation is not found. This is because neither the electron pressure nor the Hall term is used in Ohm's law.

REFERENCES

[1] JARBOE, T.R., et al., Phys. Rev. Lett. **51** (1983) 39.

[2] JARBOE, T.R., et al., Phys. Fluids **27** (1984) 13.

[3] SHUMAKER, D.E., BOYD, J.K., AUERBACH, S.P., McNAMARA, B., J. Comput. Phys. **45** (1982) 266.

[4] BARNES, C.W., et al., Nucl. Fusion **24** (1984) 267.

[5] BARNES, C.W., et al., Los Alamos Natl Lab. Rep. LA-UR-84-3667 (1984), submitted to Nucl. Fusion.

[6] SGRO, A.G., SPENCER, R.L., LILLIEQUIST, C., "Quasistatic evolution of compact toroids", in Proc. 10th Conf. Numerical Simulation of Plasmas, San Diego, 1983.

[7] MARKLIN, G.J., MHD Stability of the Spheromak, PhD Thesis, Univ. of Maryland, Rep. PL 83-039, 1983.

[8] MIRIN, A.A., KILLEEN, J., "Nonlinear 3D MHD calculations of resistive instabilities in reversed field pinches", Proc. US/Japan Workshop on 3D MHD Studies for Magnetically Confined Plasmas, Hiroshima, 1983.

[9] O'NEILL, N.J., MIRIN, A.A., TUBE, a Field Line Integrator Code, LIBRIS Abstract P81, NMFECC, Lawrence Livermore Natl Lab. Rep. (1982).
[10] KILLEEN, J., et al., Lawrence Livermore Natl Lab. Rep. UCRL-50161 (1967).

DISCUSSION

R.S. PEASE: In the sustained case, what is the voltage on the Marshall gun, and how does the current flow from the gun into the spheromak?

T.R. JARBOE: In the stustained case the voltage on the gun or source is about 1 kV. In the simple axially symmetric picture, the current flows from the anode along magnetic field lines that connect with the source, around the outside of the spheromak, through its geometric centre, and then back to the cathode. (The inner electrode is the cathode.) The amount of flux that connects to the source has been as low as 5% of the spheromak's poloidal flux. Of course, some non-axisymmetric motion, probably associated with the n = 1 mode, is necessary for the relaxation which converts the injected toroidal flux (associated with the injected current) into the fields of the spheromak.

THEORETICAL STUDIES OF FIELD-REVERSED CONFIGURATIONS (FRC) AND EXPERIMENTAL STUDY OF THE FRC DURING TRANSLATION

R.E. SIEMON, W.T. ARMSTRONG, R.E. CHRIEN,
P.L. KLINGNER, R.K. LINFORD, K.F. McKENNA,
D.J. REJ, J.L. SCHWARZMEIER, A. SGRO, E.G. SHERWOOD,
R.L. SPENCER, M. TUSZEWSKI
Los Alamos National Laboratory,
Los Alamos, New Mexico

N.T. GLADD
Jaycor, San Diego, California

D.S. HARNED
New York University, New York, N.Y.

D. SHUMAKER
Lawrence Livermore National Laboratory,
Livermore, California

C.E. SEYLER
Cornell University, Ithaca, N.Y.

United States of America

Abstract

THEORETICAL STUDIES OF FIELD-REVERSED CONFIGURATIONS (FRC) AND EXPERIMENTAL STUDY OF THE FRC DURING TRANSLATION.

Theoretical studies of FRC stability and transport are summarized. Finite Larmor radius theories are shown to be unreliable for explaining the experimentally observed stability to tilting. Control of the n=2 rotational instability has been demonstrated in two-dimensional hybrid code simulations, and the stability appears to be described within MHD if the nearly square equilibria that result from quadrupole fields are taken into account. Simulations of the lower hybrid drift instability in parameter regimes relevant to experiments show good agreement with a non-local theory of the instability. A 1.5-dimensional transport code shows agreement with the energy confinement time but disagreement with the flux loss time observed in FRX-C. The process of FRC translation in which the plasma is formed, translated into a DC solenoid and trapped by magnetic mirrors, has been studied in the FRX-C/T experiment. Efficient transfer of particles, energy and internal magnetic flux are observed with no enhancement of loss processes over in-situ FRC experiments. The axial velocity of the FRC can be estimated reasonably well with a simple model based on conservation of energy. Internal magnetic field probing during translation shows the expected structure of poloidal field and a complex distribution of generally weak toroidal fields. Measurements of radiated power indicate that radiation is a small fraction of the total plasma power loss (typically 8%). Translation has facilitated scaling studies of confinement over a wider range of

parameters than were achieved by in-situ FRX-C experiments. For example, the variable x_s, the ratio of the separatrix radius to the metal wall radius, has been increased to about 0.7 by allowing the FRC to expand during translation. In all cases, particle confinement times agree within a factor of two with predictions by models that assume a lower hybrid drift resistivity. However, for the conditions studied there are indications that the experimental scaling departs in functional form from that predicted theoretically.

I. INTRODUCTION

The FRC is an elongated prolate compact toroid which contains mainly poloidal magnetic fields. (Evidence for relatively small toroidal magnetic fields in translated FRCs is presented in the experimental section of this paper.) The equilibrium of such an object is characterized by very high beta within the separatrix volume and strong field line curvature at the ends of the prolate configuration. As a result of the high beta, steep density gradients near the separatrix appear to drive anomalous particle transport. The strong field line curvature results in MHD predictions of a tilting instability which is not observed experimentally.

Progress on the difficult theoretical analysis needed for these highly kinetic configurations is presented in Section II. In Section III experimental studies of FRC translation are described. The compact toroid can be translated[1] as a self-contained structure along a cylinder by means of a gradient in a solenoidal guide field. This property permits a linear reactor arrangement in which plasma formation and heating can be separated from the nuclear blanket region. The engineering simplifications achieved by this separation of functions, and the high-beta nature of the FRC, offer the potential for an economical reactor with small unit power and high power density.

II. THEORETICAL STUDIES

A finite Larmor radius (FLR) treatment of the tilting instability for FRCs has been completed. It is shown on two accounts that such a treatment is inadequate. First, the FLR terms become infinite at the field null of the magnetic axis due to a breakdown of the small Larmor radius assumption. The singular terms can be arbitrarily cut off or smoothed near the field null, but then the resulting growth rate strongly reflects that arbitrary cut-off or smoothing. Second, numerical computations using realistic parameters show that the magnetic moments of the ions are very poorly conserved at the tips of the flux surfaces in FRC equilibria; thus any theory that assumes the magnetic moments of the ions are conserved is suspect. Therefore, FLR theories cannot be used reliably to explain the observed stability to tilting of FRC experiments. A fully kinetic, nonlocal stability analysis must be performed, and that work is in progress.

The quadrupole stabilization of the n=2 rotational instability in FRCs has been studied with a 2-dimensional hybrid code and by means of the MHD model. The hybrid simulations demonstrate that the mode is suppressed when the quadrupole field is sufficiently strong[2]. The MHD model of Ishimura[3], without mode coupling, predicts stabilization of the rotational instability when the quadrupole field is at a magnitude comparable to values required for stabilization in the hybrid simulations. However, when mode coupling is included in the MHD model of Ishimura, it becomes virtually impossible to obtain stability. The key to reconciling these two theories is to examine the equilibrium states studied in each one. In Ref.[3] it was assumed that the plasma was nearly circular, while the hybrid simulations showed that the plasma was strongly deformed into a square shape. By using Bernoulli's law it can be shown that there are two equilibrium states for a rotating FRC in a quadrupole field: (1) nearly circular equilibria with multipole field nulls on the plasma surface, and (2) nearly square equilibria without field nulls on the plasma surface, i.e. cusp-like equilibria[4]. Hence, the two calculations use different equilibrium states, and agreement is not to be expected. In experiments, equilibria similar to type 2, the kind obtained in the hybrid simulation, are observed. If the MHD calculation of Ref.[3] is re-examined to estimate the effect of using a different equilibrium state, it can be shown that the cusp equilibrium is expected to be more stable.

The lower hybrid drift (LHD) instability is thought to play an important role in determining anomalous transport in FRCs. We have compared the simulated linear phase of LHD modes with a nonlocal theory that was previously developed for the linear theta pinch. The instability is found to persist into low drift (weakly inhomogeneous plasma) regimes that have not been previously accessed by simulation but which are relevant to experiments. In all instances, there is clear evidence that the plasma is unstable in the spatial region predicted to be most unstable by the nonlocal theory. In terms of growth rates, the simulated fluctuating electric field is Fourier-decomposed and compared, harmonic by harmonic, with theoretically predicted growth rates. Not only is the quantitative comparison good (within a factor of two for the most rapidly growing modes), but there is qualitative agreement as to the shapes of the eigenfunctions for modes with $k_{\perp}\rho_e \sim 1$, which are the most rapidly growing. We find similar results for moderate, low and very low drift parameters. We have also determined that the fluctuating electric field can be represented as a superposition of theoretical eigenmodes in the vicinity of the maximum in the drift parameter.

Transport in FRCs is being studied with a 1.5-dimensional transport code that employs flux surface coordinates and finite elements[5]. The transport calculation consists of the simultaneous solution of three 1-dimensional transport equations

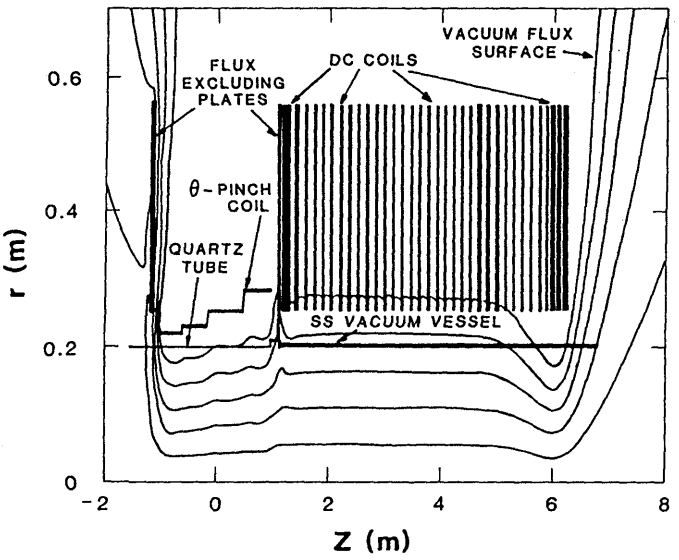

FIG.1. Configuration of FRX-C/T for translation experiments. Note disparity between r and z length scales.

for the ion density, electron entropy and ion entropy. The physical processes that are modelled by this calculation are: classical transport, Joule heating, collisional transfer of energy between ions and electrons, radiation cooling of electrons due to impurities, and anomalous transport based on a local theory for LHD resistivity given by the wave-energy bound. When the simulation is done for a case representing FRX-C, the energy confinement time is in approximate agreement, but the particle confinement time is larger than observed experimentally. The most obvious difference between the simulation and the experiment is that the theory predicts a slower rate of poloidal magnetic flux loss than is observed. As noted elsewhere[6], this is because the effective collision frequency for LHD resistivity is largest near the separatrix where the current is high, and LHD does not affect the resistivity at the magnetic axis that controls flux loss.

III. EXPERIMENTAL STUDY OF TRANSLATION

A. Experimental Configuration and General Observations

Translation is initiated by the magnetic field gradient produced in a stepwise-tapered theta-pinch coil which varies in radius from 22 cm to 28 cm as shown in Fig. 1. The FRC enters a dc solenoid that has a flux-conserving stainless steel vacuum vessel. The conducting boundary changes abruptly in radius from

28 cm to 20 cm across the 15-cm insulating gap separating the theta pinch from the translation region with no apparent detrimental effects on the translation process. Additional FRC acceleration is often provided by using a vacuum dc guide field, B_o, which is smaller than the vacuum field generated by the theta pinch. Vacuum field lines representing this condition are shown in Fig. 1. Diagnostics include axial arrays of infrared interferometers (6 locations) and external magnetic probes (53 locations), an end-on framing camera, side-on VUV and visible monochromators, a side-on radiation calorimeter, and occasionally internal magnetic probes.

With a few exceptions noted below, data were obtained using a fast-acting valve to form a localized deuterium gas distribution in the theta pinch equivalent to 5-mtorr pressure. With static fill at 20-mtorr pressure (one of the standard conditions for in situ FRX-C experiments[7]) the elongated FRC tended to bifurcate and to display a short lifetime, apparently as a result of the different formation conditions and axial acceleration process. Additional experiments are needed to clarify the translation behavior at higher pressure.

The FRCs formed at 5 mtorr were generally robust in their ability to translate intact and reflect from magnetic mirrors. No significant losses of particles or internal poloidal flux resulted from these processes. The measured loss rates of particles, flux and energy following formation are not enhanced over rates measured for similar stationary FRCs. Quadrupole fields were not utilized in the translation chamber, and the characteristic n=2 rotational mode of instability was usually observed late in time. Helical quadrupoles[8] are planned in future experiments.

B. Dynamics of Translation

The FRCs move out of the source 10-25 μs following formation in a manner consistent with the finite inertia of the plasma and the applied field gradient. The observed acceleration to speeds v_z of about 0.3 to 1.0 times the ion thermal speed agrees with approximate analytic models or predictions from a 2-D MHD code[9] modified to treat translation. As shown in Fig. 2, the larger translational speeds are obtained at reduced magnetic guide fields, B_o. As the FRC moves into a reduced B_o it expands, and temperature measured by pressure balance indicates that the FRC cools in approximate agreement with reversible adiabatic theory[10]. An estimate of the translational speed, shown as the dashed line on Fig. 2, is obtained by equating the kinetic energy of translation to the changes of thermal and magnetic energy that occur as a result of the adiabatic expansion: $(1/2)m_i v_z^2=(5/2)k\Delta T$ where m_i is the ion mass, k is Boltzmann's constant and ΔT is the change of ion plus electron temperature resulting from the adiabatic expansion. The estimate is reasonably accurate even though the FRC is assumed to be an elongated equilibrium object undergoing reversible adiabatic expansion, while in fact it is

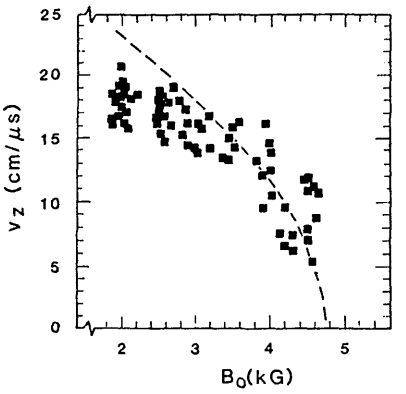

FIG.2. Peak axial velocity v_z of the center of the FRC separatrix volume versus the vacuum dc guide field. Data points represent discharges with fixed source conditions: $\bar{n} \cong 1.6 \times 10^{15}$ cm^{-3}; $T_e + T_i \cong 500$ eV; $r_s \cong 11$ cm. The curve is derived with an analytic model.

rapidly accelerated to speeds comparable to the ion thermal speed in magnetic field gradients with gradient lengths less than or comparable to the FRC length.

The FRCs propagate 5 m and reflect from a downstream mirror with mirror ratio R_M of either 1.8, 2.5 or 5.3. Reflection of the full particle inventory is observed when the vacuum dc mirror field exceeds approximately 1.2 times the maximum Θ-pinch vacuum B-field. For R_M of 1.8 or 2.5 the plasma remains nearly unchanged (except for v_z) immediately following the reflection, whereas at $R_M = 5.3$ the plasma length approximately doubles and an increase in the pressure balance temperature of up to 30% is observed. For all mirror ratios, the magnitude of v_z following reflection is reduced by approximately 30%. The slower-moving FRCs propagate back to the mirror formed by the crowbarred Θ-pinch field where they reflect and lose another 50% of their translational energy. In this manner the FRCs are readily trapped in the translation region without active mirrors.

The axial kinetic energy lost as a result of the reflection has not yet been accounted for, and the question needs further experimental and theoretical work. The observed change in kinetic energy during a reflection is less than 20% of the FRC thermal energy. Possibly the reflection process excites one or more types of internal plasma oscillations such as shear Alfvén waves. Such oscillations if generated in the initial acceleration process might explain the discrepancy in Fig. 2 between observed and predicted v_z, and might be related to the presence of toroidal fields reported in the next section. It has been observed at Osaka University that in some cases the translational energy is rapidly thermalized during FRC trapping[8], but except for the R_M=5.3 case we do not observe a measurable heating effect.

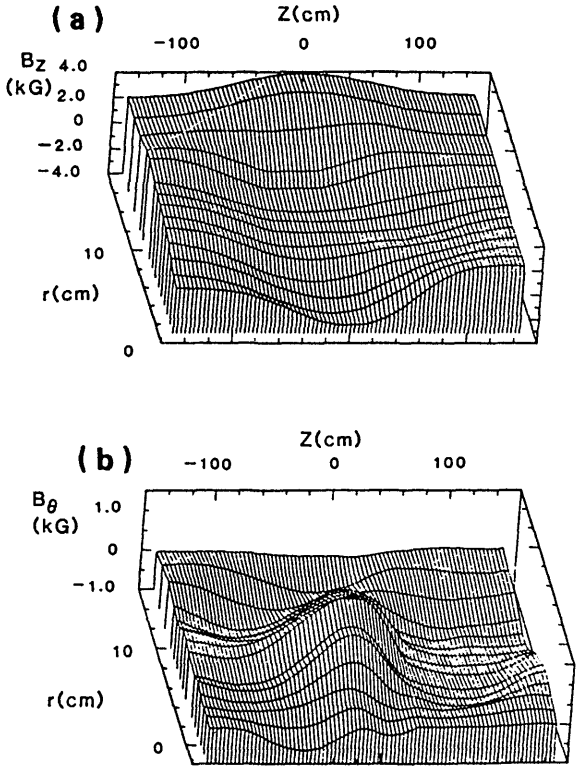

FIG.3. Internal magnetic profiles of (a) B_z and (b) B_θ obtained by translating the FRC past a probe array.

C. Internal Probing Measurements

The magnetic field structure of translating FRCs[11] is studied using a radial array of probes aligned to measure either $B_z(r)$ or $B_\Theta(r)$. Data from internal probes are subject to numerous qualifications. Estimates of the time for the probe surface to reach its boiling temperature, or the characteristic time for cooling of the plasma in contact with the probe by electron thermal conduction, are comparable to the transit time of the FRC past the probe. For the data in Fig. 3 the perturbing effect of the probe array was reduced to the extent possible by expanding the FRCs into a 2-kG guide field. Thus the FRC energy density and transit time past the probe are minimized.

Typical profiles of $B_z(r,z)$ in Fig. 3a and $B_\Theta(r,z)$ in Fig. 3b are obtained from two similar FRCs which have $x_s = 0.7$, $\bar{n} = 0.6\times10^{15}$ cm^{-3}, $T_i + T_e = 375$ eV, $\ell \simeq 250$ cm, and $v_z = 18$ cm/μs, where ℓ is the length of the separatrix. The observed distribution and magnitude of B_z are consistent with the general

features expected for a high-beta FRC equilibrium[12], and the profiles are reasonably symmetric about the axial midplane. The poloidal flux Φ_p from internal probes is 520 ± 30 kG-cm^2, in agreement with a diffuse-profile estimate (500 kG-cm^2) based on external measurements. These results give added credence to the use of internal magnetic probes. The field reversal depth (-3.2 kG) at the separatrix corresponds to $\beta_s = \beta(r_s) = 0.3 \pm 0.1$, which is lower than that reported for FRCs with smaller x_s ($\beta_s = 0.6$ at $x_s = 0.4$)[13]. The radial profile of B_z is nearly flat in the vicinity of the field null; however, steeper profiles were observed under other conditions.

The $B_\Theta(r,z)$ profile shows a radially and axially oscillating structure which differs from shot to shot. The rms B_Θ, defined as the square root of $\int dz \int B_\Theta^2 r dr / \int dz \int r dr$ where the integrals are over the separatrix volume, is 0.16 ± 0.08 of B_w (averaged over all shots), where B_w is the B_z external to the FRC equal to $B_0/(1-x_s^2)$. The observed toroidal field energy is 2% of the plasma thermal energy (1 → 7% for all shots) and is 6% of the poloidal field energy (3 → 30% for all shots). The net toroidal flux Φ_T (400 kG-cm^2 in Fig. 3b) varies widely due to the fluctuating nature of B_Θ, but is typically four times Φ_p. The sign of Φ_T is usually in the left-handed sense relative to the direction of ejection from the conical source. The generation of net toroidal flux is believed to be caused by the magnetic field gradient used to accelerate the FRC during translation ($\dot{B}_\Theta(t=0) = \vec{B} \cdot \nabla u_{e\Theta}$ where u_e is the electron fluid velocity) and by peaking of the electron fluid rotation outside the field null[14].

D. Radiated Power Measurements

The total power radiated by the translating FRC, as it traverses the z = 3.6 m axial position, is determined using a calorimeter[15] with a risetime of 0.9 μs. A 6.3-μm-thick gold foil, with a 0.7-μm-thick back surface layer of high emissivity CuO, is heated by the incident plasma radiation, and the resulting foil temperature increase is measured by sensing the infrared emission from the CuO surface with a LN-cooled HgCdTe detector. The calibrated system sensitivity is 1.9 mJ·cm^{-2}/°C or 13.6 mJ·cm^{-2}/volt. Figure 4 shows a typical data trace where three successive passes (beginning at t ≈ 30, 60 and 120 μs) of the FRC through the calorimeter field of view can be identified. Assuming that the plasma radiation is uniform through the FRC cross-section and time-independent during a transit, the total power radiated is $(2\pi^2/\Omega)\int F r_s v_z dt$, where F is the incident flux of energy on the foil and Ω is the solid angle. Averaged over a number of representative 5-mtorr discharges, the radiated power during the first pass of the FRC (before reflection from the end mirror) is 6.1 ± 1.6 MW. This result, combined with independent measurements of energy and particle confinement, implies that plasma radiation accounts for 8±2% of the total plasma power loss and 14±4% of the power loss by processes other than particle

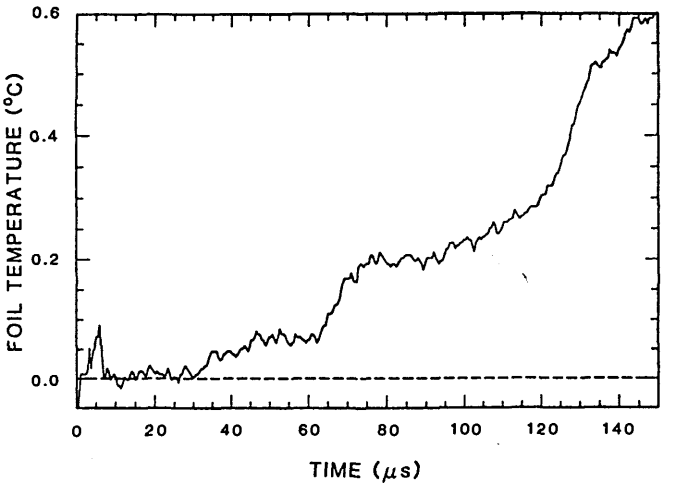

FIG.4. Calorimeter data obtained at z = 3.6 m in the translation chamber for 5 mtorr, R_M = 2.5, and B_0 = 2.5 kG. Each incremental increase of temperature represents passage of the FRC by the calorimeter field of view.

transport. Accordingly, thermal conduction appears to represent an energy loss mechanism significantly larger than radiation.

The radiated power was also measured using a static fill of deuterium seeded with oxygen or silane gases. For either impurity a least-squares fit to the data of power radiated vs. concentration implies an upper bound of 0.6 ± 0.3 % for the intrinsic impurity concentration. Simultaneous measurements of OVII (162.3 nm) radiation during oxygen seeding imply an intrinsic oxygen concentration of (0.6 ± 0.2) %. Thus the data suggest that oxygen can account for the majority of the radiated power in the absence of impurity seeding.

E. Confinement Scaling

The translated FRC plasma has a range of equilibrium parameters that results from variations in the formation process. The range of parameters is increased as a consequence of controllable plasma expansion with reduced B_o. Future experiments are planned to further increase the parameter regime by means of Z-preionization and a larger-diameter theta-pinch source. For the present operation at 5 mtorr, the translated FRCs have lengths $\ell \simeq 130\text{-}280$ cm, $x_s \simeq 0.4\text{-}0.7$, total temperatures $T \simeq 150\text{-}700$ eV, and peak densities $n_M \simeq (0.5\text{-}1.5)\times10^{15}$ cm^{-3}. The closed-flux and energy confinement times are inferred to be $\tau_\phi \simeq 40\text{-}200$ μs and $\tau_E \simeq 30\text{-}120$ μs, respectively. The particle confinement times are in the range $\tau_N \simeq 80\text{-}250$ μs. For a data base of 60 discharges, the observed τ_N have been compared with calculated values τ_{Nc} based on a

TABLE I. PARTICLE CONFINEMENT SCALING $\tau_N \cong \ell^a x_s^b n_M^c T^d$

	a	b	c	d
Theory (τ_{Nc})	0.6	3.4	0.5	−0.2
FRX-C/T (τ_N)	0.2 ± 0.4	1.4 ± 0.8	0.5 ± 0.3	0.4 ± 0.3
TRX-1	0	2.2	0.6	~0

model[16] with LHD resistivity. The magnitudes are in reasonable agreement (τ_N/τ_{Nc} = 1.3 ± 0.5) but a difference in scaling is observed. A chi-square routine is used to estimate the various exponents in a scaling of the form $\ell^a x_s^b n_M^c T^d$. The results are given in Table I, which includes a similar scaling from the TRX-1 device[17]. The large uncertainties in the exponents of the experimental data are due to correlations between ℓ, x_s, n_M and T as B_o varies. Table I suggests a more favorable temperature scaling and weaker dependences on x_s and ℓ for the experimental data than for the calculation.

Translation dynamics (with or without static gas fill) do not alter appreciably the FRC confinement. One exception is for the *mirror ratio* R_M=5.5 where a degradation of τ_ϕ and τ_E is observed after reflection.

Values of $n\tau_E$ up to 10^{11} $cm^{-3}s$ at T ≈ 0.7 keV and n ≈ 10^{15} cm^{-3} have been achieved. The values obtained on FRX-C without translation ranged from $n\tau_E \approx 7\times10^{10}$ $cm^{-3}s$, T ≈ 0.8 keV, n ≈ 2×10^{15} cm^{-3} at 5 mtorr to $n\tau_E \approx 4\times10^{11}$ $cm^{-3}s$, T ≈ 0.2 keV, n ≈ 5×10^{15} cm^{-3} at 20 mtorr. Therefore, for the same 5 mtorr pressure in the source, the confinement of translated FRCs in FRX-C/T somewhat exceeds the confinement for similar plasmas without translation.

REFERENCES

[1] ALIKHANOV, S.G., et al., "Three-dimensional plasma compression in a Z-pinch liner system – transport and compression of a compact torus by a quasi-spherical liner", Plasma Physics and Controlled Nuclear Fusion Research 1982 (Proc. 9th Int. Conf. Baltimore, 1982), Vol.3, IAEA, Vienna (1983) 319.

[2] HARNED, D.S., Phys. Fluids **27** (1984) 554.

[3] ISHIMURA, T., to be published in Phys. Fluids.

[4] SPENCER, R.L., TUSZEWSKI, M., submitted to Phys. Fluids.

[5] SHUMAKER, D.E., et al., J. Comput. Phys. **45** (1982) 266.

[6] HOFFMAN, A.L., MILROY, R.D., STEINHAUER, L.C., Appl. Phys. Lett. **41** (1982) 31.

[7] SIEMON, R.E., et al., "Experimental studies of field-reversed configuration confinement in FRX-C", Plasma Physics and Controlled Nuclear Fusion Research 1982 (Proc. 9th Int. Conf. Baltimore, 1982), Vol.2, IAEA, Vienna (1983) 283.

[8] TANJYO, M., et al., Paper No. IAEA-CN-44/D-III-2-2, these Proceedings, Vol. 2.
[9] MILROY, R.D., BRACKBILL, J.U., Phys. Fluids **25** (1982) 775.
[10] SPENCER, R.L., TUSZEWSKI, M., LINFORD, R.K., Phys. Fluids **26** (1983) 1564.
[11] ES'KOV, A.G., et al., in Controlled Fusion and Plasma Physics (Proc. 10th Europ. Conf. Moscow, 1981) L-5.
[12] HEWETT, D.W., SPENCER, R.L., Phys. Fluids **26** (1983) 1299.
[13] TUSZEWSKI, M., Plasma Phys. **26** (1984) 991.
[14] HEWETT, D.W., Nucl. Fusion **24** (1984) 349.
[15] INGRAHAM, J.C., MILLER, G., Rev. Sci. Instrum. **54** (1983) 673.
[16] TUSZEWSKI, M., LINFORD, R.K., Phys. Fluids **25** (1982) 765.
[17] STEINHAUER, L.C., MILROY, R.D., SLOUGH, J.T., submitted to Phys. Fluids.

STABILIZATION AND TRANSLATION OF A PLASMA WITH FIELD-REVERSED CONFIGURATION

M. TANJYO, S. OKADA, Y. ITO, M. KAKO, S. OHI,
S. GOTO, T. ISHIMURA, H. ITÔ
Plasma Physics Laboratory,
Osaka University, Osaka

Y. NOGI, S. SHIMAMURA, T. IKAWA, S. HAMADA
College of Science and Technology,
Nihon University, Tokyo

Japan

Abstract

STABILIZATION AND TRANSLATION OF A PLASMA WITH FIELD-REVERSED CONFIGURATION.

A theoretical analysis and its experimental test are carried out on multipole-field suppression of the $n = 2$ rotational instability. The theoretical analysis based on the MHD approximation gives a stability criterion for quadrupole field, $B_s \geqslant B_{sc} = \frac{1}{2} r_s |\Omega| \sqrt{\mu_0 \rho_0}$, where r_s, ρ_0, and Ω are the radius, the mass density and the rotational angular velocity of the plasma column, respectively, B_s is the field strength at $r = r_s$ without a plasma column present, B_{sc} is its threshold, and μ_0 is the vacuum permeability. The experiments show that the experimental stability threshold obeys the scaling $r_s|\Omega| \sqrt{\rho_0}$, but is about 25 to 30% of the theoretical value. The $n = 2$ rotational instability is also suppressed by using helical quadrupole fields produced by the helical winding. For a perturbation uniform in the z-direction, the stabilization effect of the helical field is not uniform along the z-axis so that there is always a region in the plasma column where the stabilization effect is large. Therefore, the rotational instability is considered to be more effectively suppressed by using a helical field. Experiments show that the stabilization threshold current J supplied to the helical winding decreases with the pitch angle α ($= 2\pi/L$; L is the pitch length of the winding). Typically, the current J in $\alpha = 6$ is less than a fifth of that in $\alpha = 0$ (straight quadrupole field). – To examine the possibility of extending the lifetime of a field-reversed-configuration (FRC) plasma by increasing the ratio x_s of the plasma radius to the conducting-wall radius, experiments are carried out on the translation of the FRC plasma from the formation region into the confinement region (metal vessel) with mirror field. The ratio x_s increases up to 0.7 and the lifetime of the translated plasma is 80 μs, while the ratio x_s and the lifetime are 0.4 and 30 μs, respectively, when the FRC plasma is confined in the formation region.

1. INTRODUCTION

Suppression of rotational instability and reduction of particle diffusion loss are necessary to improve the lifetime of plasmas with field-reversed configuration (FRC).

The suppression of the n = 2 rotational instability was accomplished by imposing a quadrupole field on the FRC plasma produced by the PIACE apparatus at Osaka University; first results were reported at the IAEA Baltimore Conference 1982 [1]. In this paper, a theoretical analysis of the multipole-field suppression effect and experiments undertaken to test the theoretical predictions are reported. Furthermore, we report the NUCTE experiments at Nihon University on the suppression effect of the helical field which was found to be more effective than the quadrupole field.

An increase of the ratio x_s of plasma radius to wall radius has been known to be a promising method of reducing the particle diffusion loss [2]. For this purpose, experiments were carried out on the translation of an FRC plasma from the formation to the confinement region with low external field on the OCT apparatus at Osaka University. The first results showed that the FRC plasma was translated without any serious particle and energy losses and the ratio x_s increased up to 0.7.

2. SUPPRESSION OF n = 2 ROTATIONAL INSTABILITY

2.1. Theoretical analysis of multipole-field suppression of instability

We consider an infinitely long, high-β plasma column of radius r_s rotating about its axis of symmetry with an angular velocity Ω. The plasma column may be subject to an n = 2 rotational instability and undergo an elliptical deformation. When, however, a multipole field is imposed on the plasma column, the deformation is suppressed because the multipole field, which does not penetrate into the plasma column, exerts a higher magnetic pressure on the bulging-out part of the boundary surface of the plasma column. On the basis of these considerations, linearized MHD equations for the perturbation with an azimuthal mode number n (>0) are written in the frame rotating with the plasma column. When the plasma mass density ρ_0 and the phase velocity a of the magnetoacoustic wave in the plasma are constant, the equations are solved analytically. For $|\Omega r_s/a| \ll 1$, the displacement $\vec{\xi}_s$ of a plasma element on the boundary surface and the change $\delta p_{T,s}$ in the total pressure (the sum of plasma and magnetic pressures) that is 'felt' by the plasma element are given by

$$\frac{\xi_{s,r}}{r_s} = \frac{c}{2}\exp[i(n\theta - \hat{\omega}\Omega t)] + \text{c.c.} \tag{1}$$

$$\frac{\xi_{s,\theta}}{r_s} = i\frac{c}{2}\exp[i(n\theta - \hat{\omega}\Omega t)] + \text{c.c.} \tag{2}$$

$$\delta p_{T,s} = \frac{1}{2}\rho_0 r_s^2 \Omega^2 \left(\frac{\hat{\omega}^2}{n} + \frac{2\hat{\omega}}{n} + 1\right)\frac{2\xi_{s,r}}{r_s} \tag{3}$$

where $\hat{\omega}$ is the angular frequency normalized by Ω, $\frac{1}{2}\rho_0 r_s^2 \Omega^2$ the centrifugal pressure on the boundary surface, and c an arbitrary constant; c.c. stands for 'complex conjugate' of the preceding term.

Since the magnetic pressure of the external axial field is uniform on the boundary surface as long as the deformation is uniform in the z-direction, the axial field is useless in suppressing the deformation. We consider a multipole field of order 2m whose strength is B_s at $r = r_s$. In the presence of the plasma column, the z-component A_z of the vector potential of the field is given by

$$A_z(r, \theta, t) = -\frac{r_s B_s}{m}\left[\left(\frac{r}{r_s}\right)^m - \left(\frac{r_s}{r}\right)^m\right]\cos[m(\theta + \Omega t)] \tag{4}$$

where $\theta + \Omega t$ is the deflection angle in the laboratory system. The change δA_z in the vector potential due to the deformation given by Eqs (1) and (2) should satisfy the equation

$$A_z(r_s + \xi_{s,r}, \theta + \xi_{s,\theta}/r_s, t) + \delta A_z(r_s + \xi_{s,r}, \theta + \xi_{s,\theta}/r_s, t) = \text{const} \tag{5}$$

because the resultant vector potential $A_z + \delta A_z$ should also be constant on the distorted boundary surface. Assuming the displacement $\vec{\xi}_s$ to be small, we expand the first term on the left-hand side of Eq.(5) in terms of $\xi_{s,r}$ and $\xi_{s,\theta}$, neglect the terms of order higher than two and approximate the second term as $\delta A_z(r_s, \theta)$. Then, $\delta A_z(r, \theta)$ which is equal to the value of $\delta A_z(r_s, \theta)$ on the unperturbed boundary surface is obtained by solving by Laplace equation. From the obtained vector potential $A_z + \delta A_z$, we calculate the magnetic pressure of the multipole field on the deformed boundary surface. It consists of several components and the component proportional to the radial displacement $\xi_{s,r}$ is given by

$$\delta p_{M,0} = \frac{B_s^2}{2\mu_0}[\max(n, m) - 1]\frac{4\xi_{s,r}}{r_s} \tag{6}$$

where $B_s^2/(2\mu_0)$ is the magnetic pressure of the multipole field.

The pressure balance condition on the boundary surface implies that $\delta p_{T,s} = \delta p_{M,0}$ so that we obtain the frequency $\hat{\omega}$ as

$$\hat{\omega} = -1 \pm \{1 - n + 2n[\max(n, m) - 1]A\}^{\frac{1}{2}} \tag{7}$$

$$A = \frac{B_s^2}{\mu_0 \rho_0 r_s^2 \Omega^2} \tag{8}$$

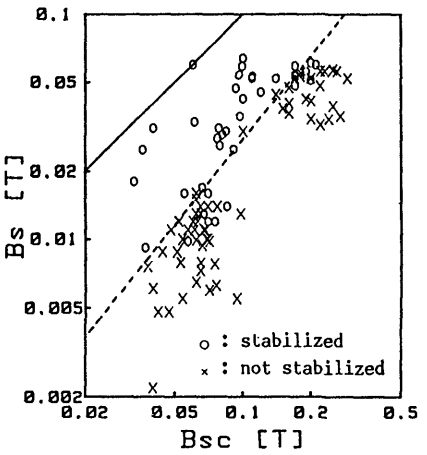

FIG.1. Experimental results for scaling of stability threshold: B_{sc} stands for $\frac{1}{2} r_s|\Omega|\sqrt{\mu_0\rho_0}$ as calculated from experimental data and B_s is the field strength at $r = r_s$. Broken and solid lines represent experimental and theoretical thresholds, respectively.

and the stability criterion

$$A \geqslant A_c = \frac{n-1}{2[\max(n,m)-1]} \tag{9}$$

For n = 2, the stability criterion can be rewritten as

$$B_s \geqslant B_{s,c} = \frac{1}{2\sqrt{m-1}}\, r_s|\Omega|\sqrt{\mu_0\rho_0} \tag{10}$$

As we have already mentioned, the magnetic pressure of the multipole field has components other than $\delta p_{M,0}$ which affect the stability criterion. However, the discussion of these extra components is so complicated that we restrict ourselves here to pointing out that the criterion for n = 2 and m = 2 (quadrupole field) might be substantially different when the effects of other components are taken into account. A detailed discussion is given in Ref.[3].

2.2. Experimental scaling of stability threshold

Since we obtained the first results of quadrupole-field (m = 2) suppression of the n = 2 rotational instability, we have been carrying out experiments to examine the theoretical stability criterion over a wide range of plasma parameters (r_s = 2.5–3.5 cm, plasma length ℓ_s = 40–90 cm, $\bar{n}_e = (2–6) \times 10^{15}$ cm^{-3}, T_e = 80–150 eV, T_i = 300–500 eV) by using the PIACE apparatus. The experimental results are summarized in Fig.1, where the abscissa shows

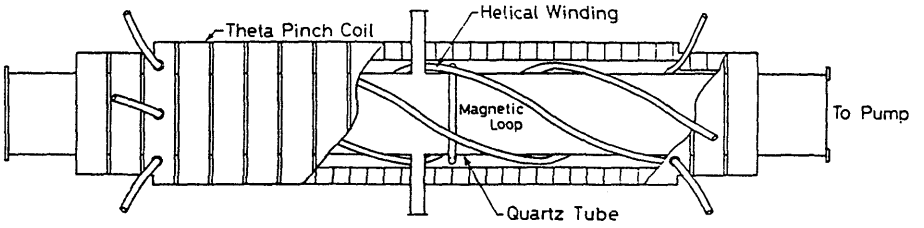

FIG.2. Schematic of NUCTE-1 with helical quadrupole windings.

$B_{sc} = \frac{1}{2} r_s |\Omega| \sqrt{\mu_0 \rho_0}$, which is calculated from the experimental data on r_s, Ω and $\bar{n}_e$ and the ordinate is the field strength at $r = r_s$. The rotational angular velocity Ω was not measured directly but inferred from the angular frequency of the oscillation appearing on the interferometer signal of the cross-plasma integrated electron density, assuming that the angular velocity of the perturbation is $-\Omega$ in the frame moving with the plasma column. The broken and solid lines show the experimental and the theoretical stability threshold, respectively. The experimental stability threshold is between 25 and 30% of the theoretical value.

2.3. Helical-field suppression of n = 2 rotational instability

As was already mentioned, the multipole field exerts a higher magnetic pressure on the bulging-out part of the deformed boundary surface of the plasma column, and this part is pushed back so as to recover equilibrium. When, however, the bulging-out part is in the weak-field region which is near the line cusp formed between two adjacent straight conductors for the multipole field, the magnetic pressure on the bulging-out part is not sufficient to push it back and, if the growth rate γ of the instability is large, the instability grows before the bulging-out part reaches the strong-field region so that the multipole field cannot suppress the instability. The critical growth rate γ_c is estimated to be about $2m|\Omega|/\pi$, from the excursion time in the weak-field region. Since the rotational angular velocity Ω of the plasma column and the growth rate γ of the instability are different in every FRC device and, even in the same device, depend on the experimental conditions, we cannot expect γ to be always smaller than γ_c and the instability to be suppressed by the multipole field.

This difficulty can be removed by using a helical multipole field produced by twisted conductors. Along the ridge of the bulging-out part of the deformed plasma column, weak- and strong-field regions appear alternately. As the stabilizing effect in the strong-field region extends into the weak-field region along the magnetic lines of force of the axial field in the plasma column, the plasma column is expected to be stabilized.

This idea was confirmed experimentally by using NUCTE-1 (Nihon University), a schematic diagram of which is shown in Fig.2. It is constructed from a 2-m-long

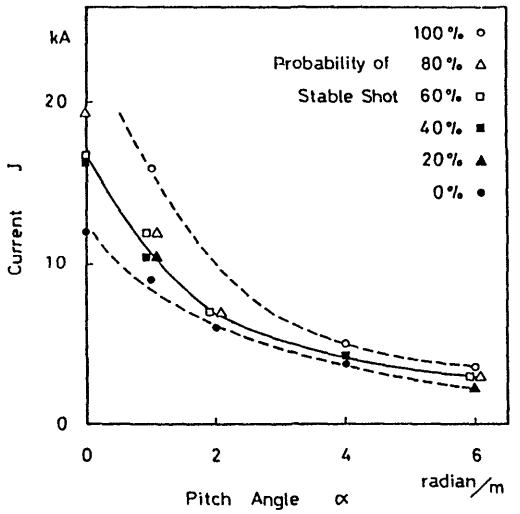

FIG.3. Stabilizing current J_s versus pitch angle α: solid line shows line on which probability to obtain a stable plasma is 50%. Upper broken line is boundary above which plasma is stable; and lower broken line that below which it is unstable.

theta pinch coil, a 12-cm-diameter quartz tube and a set of helical quadrupole windings. The pitch angle of the winding α ($= 2\pi/L$; L is the pitch length of the winding) is changed from 0 to 6, where $\alpha = 0$ corresponds to the straight quadrupole field. The plasma parameters t = 10 μs after the main compression bank has been fired are: $n_e = 2.5 \times 10^{15}$ cm^{-3}, $T_e = 100$ eV, $T_i \cong 200$ eV, $r_s = 2.2$ cm, and $\ell_s \approx 100$ cm. In this case, the rotational instability appears at t = 30–35 μs. The threshold field strength B_{sc} for the straight quadrupole field is 0.12–0.14 T, and the current J_{sc} which is necessary to feed the winding is 38–48 kA. Experimental results are shown in Fig.3, where the stabilizing current J is plotted as a function of the pitch angle α. As some shots are stable and some unstable in the same experimental conditions, the probability of a stable shot to occur is used as a parameter in the figure. The current J for which half of the shots are stable is about 0.4 J_{sc} for $\alpha = 0$ and about 0.1 J_{sc} for $\alpha = 6$.

The present experimental result that the stabilizing current decreases with the pitch angle α demonstrates the effectiveness of the helical multipole field in suppressing the instability.

3. TRANSLATION OF FRC PLASMA INTO MIRROR FIELDS

To examine the possibility of extending the lifetime of the FRC plasma by increasing the ratio x_s of plasma radius r_s to conducting-wall radius r_w, experi-

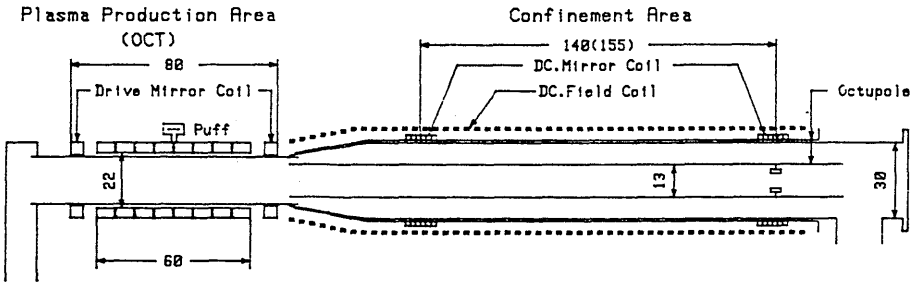

FIG.4. Schematic of OCT. Large-bore vessel (30 cm i.d.) and small-bore vessel (13 cm i.d.) are shown.

ments aiming at the translation of the FRC plasma into the mirror fields were carried out by using the OCT device [4]. As is shown in Fig.4, the device consists of the formation and the confinement regions. The FRC plasma is produced in the formation region by the field-reversed-theta-pinch method. The main compression coil is 60 cm long and has an inner diameter of 22 cm. When the currents flowing in the main coil and the subsidiary coils are adjusted so that the compression field forms a mirror field, the FRC plasma is confined in the formation region for 25 to 30 μs. The plasma is a hydrogen plasma with the following parameters: $r_s = 5$ cm, $x_s = 0.4$, $\ell_s = 40$ cm, $n_e = 5 \times 10^{15}$ cm^{-3} and $\overline{T}$ ($= \overline{T_i + T_e}$) = 230 eV, where $\overline{T}$ is inferred from pressure balance between the plasma and the magnetic field.

In the translation experiments, the currents are adjusted so that the compression field is flat on the right-hand side in the formation region. Then, the FRC plasma is ejected from the formation region with a velocity of 2×10^7 cm$\cdot$s^{-1}.

3.1. Experiment with large-bore vessel

In this experiment, the metal cylinder of 13 cm inner diameter (i.d.) in the confinement region is removed. The FRC plasma is injected into the mirror field generated in a stainless-steel vessel of 30 cm i.d. and 0.5 cm thickness. The distance between the two mirror points is 140 cm and the field strength B_{DC} of the mirror field varies between 0.1 and 0.2 T. The overall behaviour of the FRC plasma was monitored by measuring the magnetic field outside of the plasma by magnetic probes set at intervals of 20 cm. The line-integrated density $\overline{n_e \ell}$ in the midplane was measured by using a He-Ne laser interferometer.

The front mirror field was adjusted so that it allows the injected plasma to enter the confinement region at high speed but stops the plasma that is reflected at the rear mirror point at a velocity that is one third of the incident one. At $t = 40$ μs after formation, for the case of $B_{DC} = 0.13$ T, the plasma

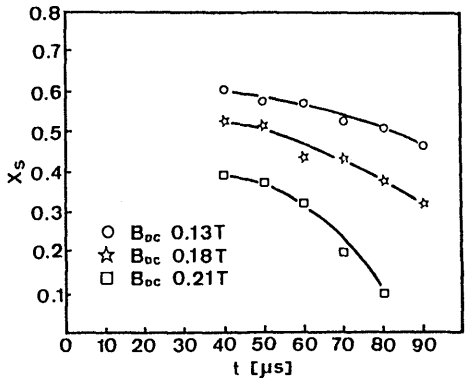

FIG.5. Time histories of x_s (= separatrix radius/wall radius) for B_{DC} = 0.13, 0.18 and 0.21 T of plasma translated into large-bore (30 cm i.d.) metal vessel.

parameters are: r_s = 9 cm, x_s = 0.6, ℓ_s = 90–100 cm, $n_e = 4 \times 10^{14}$ cm^{-3}, and $\bar{T}$ = 180 eV. From these data, the total particle inventory N and the trapped flux ϕ_i are estimated to be 60 to 70% of the values of the source plasma, while the temperature $\bar{T}$ is 70 to 80% of the value holding for the source plasma. Therefore, no serious loss of particle, energy and trapped flux occurs during the injection phase. The time histories of the ratio x_s for the field strength B_{DC} = 0.13 T, 0.18 T, and 0.21 T are shown in Fig.5. As is seen from this figure, the plasma lifetime is the longer the larger the ratio x_s and, for B_{DC} = 0.13 T, the plasma survives longer than 100 μs after its formation.

3.2. Experiment with small-bore vessel

To investigate the confinement properties of an FRC plasma with high values of x_s and high electron density n_e, it was injected into a conducting cylinder of 13 cm i.d. which serves as a flux conserver. The distance between the mirror coils was extended up to 155 cm, and an octopole field was imposed to suppress the n = 2 plasma deformation. The ratio x_s was 0.7 at its maximum and n_e was (1.5–2) $\times 10^{15}$ cm^{-3}. A typical example for time histories of x_s, ℓ_s, n_e and $\bar{T}$ for B_{DC} = 0.25 T is shown in Fig.6. As is seen from this figure, x_s is kept constant from 40 to 75 μs. To keep x_s constant, the thickness of the metal cylinder was chosen so that the external magnetic flux ϕ_e inside the vessel was diffusing out during the presence of the plasma and its decay rate nearly matched the decay rate of ϕ_i. The decay time $\tau_{\phi e}$ of the external flux ϕ_e is 210 μs and 18% of ϕ_e is lost before 75 μs. Around 80 μs, x_s, N, the trapped flux ϕ_i and the plasma energy E_p begin to decay rapidly. The decay times, τ_N, $\tau_{\phi i}$, τ_T and τ_{Ep}, during the constant-x_s phase are inferred from the obtained data as 100 μs, 150 μs, 200 μs and 70 μs, respectively. The thermal energy loss time τ_E' and the

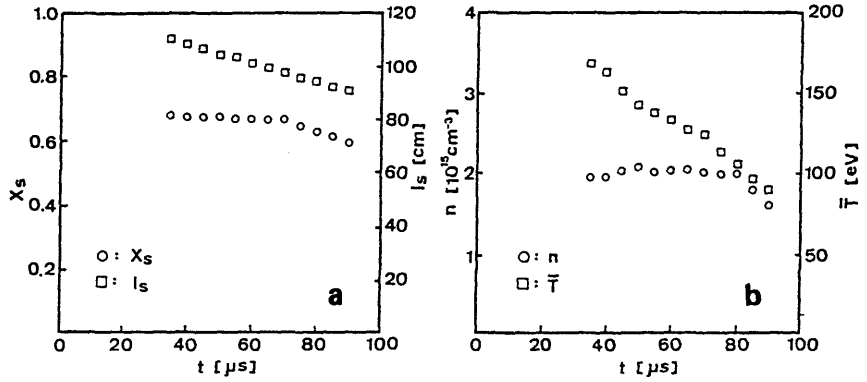

FIG.6. Time histories of a) x_s (= separatrix radius/wall radius) and ℓ_s (plasma length) and b) n and $\bar{T}$ (= $\overline{T_i + T_e}$) for B_{DC} = 0.25 T of plasma translated into small-bore (13 cm i.d.) metal vessel.

energy confinement time τ_E, which are defined by $1/\tau'_E = 5/(3\tau_T) + 2/(3\tau_N) - 5\alpha/(3\tau_{\phi e})$, $1/\tau_E = 5/(3\tau_{Ep}) - 5\alpha/(3\tau_{\phi e})$ and $\alpha = 8(1-x_s^2)/5(2-x_s^2)$, are 100 μs and 50 μs, respectively. As to the particle confinement time τ_N, the experimental confinement time of 100 μs at $x_s = 0.66$ is twice as large as the confinement time 43 μs which is derived from the R^2/ρ_i scaling [5] by using the plasma parameters at 50 μs on the assumption of $T_i = T_e = T/2$. Since the R^2/ρ_i scaling is obtained from experiments where $x_s \approx 0.4$, the longer experimental confinement time may be attributed to the larger value of x_s in the present experiment.

4. CONCLUSIONS

On the basis of the MHD approximation, a theoretical analysis is carried out on the multipole-field suppression effect of the rotational instability excited in a high-β plasma column. For the n = 2 mode, the field strength at the stability threshold is given by $\frac{1}{2}(m-1)^{1/2} r_s|\Omega|\sqrt{\mu_0 \rho_0}$. The experiment carried out to test the scaling $r_s|\Omega|\sqrt{\rho_0}$ of the stability threshold for the quadrupole field (m = 2) shows that the experimental threshold obeys the scaling fairly well but the experimental threshold is about 25 to 30% of the theoretical value.

It was also shown experimentally that helical quadrupole fields are effective in suppressing the n = 2 rotational instability. Furthermore, the stabilizing current J decreases with the pitch angle α of the helical winding so that helical-field stabilization seems to be advantageous.

The FRC plasma translation experiments were carried out using the OCT device. The FRC plasma was translated from the formation region into the mirror-field confinement region generated in the metal vessel. The translation

process was nearly isothermal, as was expected, and the particle, energy, and trapped-flux losses were 20 to 30% during the translation phase. In a typical example where an FRC plasma of $x_s = 0.66$, $n_e = 2 \times 10^{15}$ cm^{-3} and $\overline{T} = 180$ eV was confined in a vessel of 13 cm i.d., it was shown that the particle confinement time τ_N and the energy confinement time τ_E was 100 μs and 50 μs, respectively.

ACKNOWLEDGEMENT

This work was partly supported by the Scientific Research Fund of the Ministry of Education, Science and Culture of Japan.

REFERENCES

[1] MINATO, T., et al., in Plasma Physics and Controlled Nuclear Fusion Research 1982 (Proc. 9th Int. Conf. Baltimore, 1982), Vol.2, IAEA, Vienna (1982) 303.
[2] TUSZEWSKI, M., LINFORD, R.K., Phys. Fluids **255** (1982) 765.
[3] ISHIMURA, T., to appear in Phys. Fluids **278** (1984).
[4] OHI, S., et al., to appear in Compact Toroid Research (Proc. 6th US-Japan Symp. Princeton, 1984).
[5] Mc KENNA, A.F., et al., Phys. Rev. Lett. **50** (1983) 1787.

DISCUSSION

ON PAPERS IAEA-CN-44/D-III-2-1 AND D-III-2-2

M. YAMADA: In the $n\tau_E$-T diagram for the translation experiment shown in your oral presentation, the data points seem to be somewhat lower than the value obtained in the earlier experiments without translation. If this is so, is it due to a reduction in n_e or τ_E? Or can you say that neither value changes during or after translation?

R.E. SIEMON: The data for our scaling studies were taken with 5 mtorr initial pressure. In fact, the $n\tau_E$ value is at best somewhat higher than in previous experiments at 5 mtorr without translation. Higher values of $n\tau_E \approx 4 \times 10^{11}$ cm^{-3}·s previously reported correspond to higher density (about 5×10^{15} cm^{-3}) and comparable energy confinement time (80 μs). The values do not appear to be influenced by the translation process as such.

C.K. CHU: In all these devices, is beta practically 1 and, if so, is that where the (5/2)NkT for the total energy comes from?

R.E. SIEMON: Yes, measurements show that volume-averaged beta is close to the value for an elongated equilibrium with purely poloidal fields for which $\langle\beta\rangle = 1 - x_s^2/2$. For such an equilibrium one can show that the sum of all energy, both magnetic and thermal, inside a metal cylinder is given by the expression $E = (5/2)NkT + (B_v^2/2\mu_0)V$, where N is the total number of ions; $T = T_e + T_i$; V is the volume of the cylinder; and B_v is the vacuum field in the absence of plasma.

H.P. FURTH: Stabilization of the n = 2 mode by means of a straight quadrupole field has the disadvantage that the closure of the magnetic field lines is destroyed in the process of resistive diffusion. Stabilization by a stellarator field has the incidental advantage that closed magnetic surfaces can exist. A weak toroidal field is generated by the helical windings, thus providing a kind of high-β prolate spheromak. A study of the MHD stability of this configuration, with the option of an added internal toroidal field, might be of considerable interest.

INITIAL RESULTS FROM S-1 SPHEROMAK*

M. YAMADA, R. ELLIS Jr., H.P. FURTH, G. HART,
A. JANOS, S. JARDIN, F. LEVINTON, D. MEYERHOFER,
M. MIMURA**, C.H. NAM, S. PAUL, A. SPERDUTI,
S. Von GOELER, F. WYSOCKI, P. YOUNG
Plasma Physics Laboratory,
Princeton University,
Princeton, New Jersey,
United States of America

Abstract

INITIAL RESULTS FROM S-1 SPHEROMAK.

The primary objectives of the S-1 experiment are investigations of the confinement and MHD stability properties of a spheromak configuration with loose-fitting conductor walls, supported by an external magnetic field. The formation scheme is based on inductive transfer of toroidal and poloidal magnetic fluxes from a flux core and does not require the use of electrodes. This formation technique, which was tested earlier in the Proto S-1 devices, has now been verified in S-1. In addition, a figure-eight-coil stabilizing system has been found to dramatically improve the gross stability of the plasma. In this paper, initial S-1 results are summarized, together with a brief description of future compression experiments.

1. INTRODUCTION

The spheromak, a type of compact toroid with internal toroidal field and non-linked coil structure, allows for a simple wall and blanket topology [1]. These features ease engineering requirements and add potential flexibility to reactor operation by permitting translation and compression. The S-1 spheromak experiment is designed to investigate plasma stabilization by loose-fitting conductors and coils, allowing adiabatic compression of the plasma for further heating. Plasmas are produced by an electrodeless inductive technique [2, 3].

The S-1 device was completed and started full operation in September 1983. As is shown in Fig. 1, the major components of the S-1 device are the flux core, vacuum vessel, equilibrium field coils and power system to energize the flux core. The plasma formation is based on inductive transfer of toroidal and poloidal magnetic flux from the flux core into a surrounding plasma [3]. If the two coil currents are timed so that the formed plasma approaches the Taylor minimum-energy state, a spheromak configuration is created with major radius of 45–65 cm.

---

* Supported by US DOE Contract DE-AC02-76-CHO-3073.

** On leave from Osaka City University, Japan.

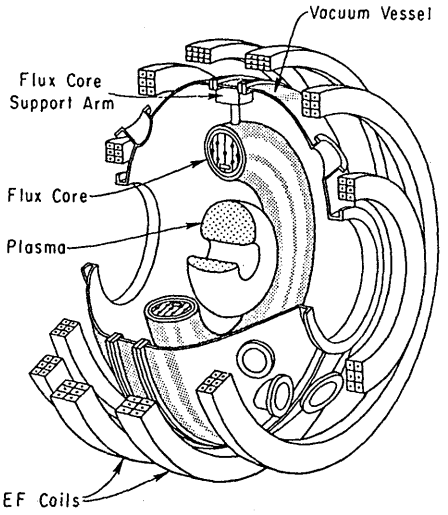

FIG. 1. Schematic diagram of S-1 device.

The flux core is the technically most challenging component of S-1. The poloidal and toroidal field windings are shown in Fig. 1. The flux core has a major radius of 1 m and a minor radius of 0.19 m; it also contains an equilibrium field winding. The Inconel cover of the flux core, which prevents outgassing, must be thin enough to allow the flux to penetrate in a short time, creating a difficult fabrication problem. The first flux core liner for S-1 had an average thickness of 0.25 mm. Earlier difficulties with the flux core liner have been corrected, and base pressures of 5×10^{-8} to 2×10^{-7} torr are regularly obtained.

The quasi-steady equilibrium field (EF) is produced by a set of coils mounted on the vacuum vessel domes and two turns located inside the flux core. These coils can be connected in different combinations to yield the following values of the field index at R = 55 m: Mode A, n = −0.2; Mode B, −0.06; Mode C, +0.1; Mode D, +0.8; Mode E, +0.7. The EF coils are powered by two large DC generators.

2. INITIAL OPERATION WITHOUT STABILIZING COILS

S-1 has been operated for one year (firing about 9000 plasma shots) without passive stabilizing coils (Figure-eight coil system). Spheromaks were formed on time-scales of 0.1, 0.2, 0.5, and 0.8 ms with various equilibrium fields (Modes A, B, C and D).

In this early operation, spheromak plasmas were created with toroidal currents up to 350 kA and with typical configuration lifetimes of about 0.5 ms. In most discharges, the plasma was unstable against gross MHD modes, such as shift/tilt instabilities.

Two representative discharge modes have been investigated mainly to date: detached discharge (Type P), in which the spheromak plasma completely pinches off (detaches) from the flux core, 0.2 ms after the start of the discharge, and linked discharge (Type L), in which the spheromak plasma is formed (also at 0.2 ms) with part of the outer flux lines linked to the flux core. In detached discharges the separatrix of the spheromak moves away from the flux core to an inner radial position; in linked discharges it remains linked around the flux core.

In detached discharges, the PF bank is crowbarred after the plasma detaches from the core. Data from magnetic probes and framing camera show that the spheromak shifts rapidly (within 0.1 ms) after the formation [4]. The shifting velocity of the magnetic axis (in R) is measured to be about $(0.5 - 1.0) \times 10^6$ cm·s^{-1}. The direction of the shift motion is quite random and is considered to be related to slight non-uniformities during formation.

In linked discharges, the PF bank is crowbarred before the plasma completely detaches from the core and the formed spheromak is observed to reside in an equilibrium position for a longer time. A typical spheromak configuration appears 0.2 ms after the plasma discharge, and lasts more than 0.5 ms. However, it has been found that, to keep the spheromak plasma in a proper position, 80–85% of poloidal flux has to be linked to the flux core or vacuum vessel walls in most discharges. In these linked discharges, the plasma electron densities are from 0.6 to 4×10^{14} cm^{-3} for H_2 and He fill pressures of 1–10 mtorr. Peak electron temperatures of up to 45 eV have been measured by a movable single-point Thomson scattering system [5] for $I_p \lesssim 200$ kA.

In Fig.2, the basic parameters of the plasma in the absence of figure-eight coils are shown as functions of time. Shown from the top of the figure are the raw data from the toroidal field B_t near the magnetic axis measured by internal coils, average electron density n_e measured by CO_2 laser interferometer, and n_e, T_e measured by a Thomson scattering system. Immediately after the magnetic axis detaches from the flux-core (30 to 50 μs), the electron temperature reaches its maximum value ($25 \lesssim T_e \lesssim 45$ eV), then quickly falls to 5 to 10 eV while the plasma collides with the flux core or the vessel wall. The beta value of the plasma core reaches about $10\% \pm 3\%$.

3. OBSERVATION OF FLUX CONVERSION IN S-1

One of the significant results to date is the observation of flux conversion between the toroidal and poloidal fluxes of the S-1 spheromak during and after the formation of the plasma [6]. The degree of constancy of I/Φ (the ratio of

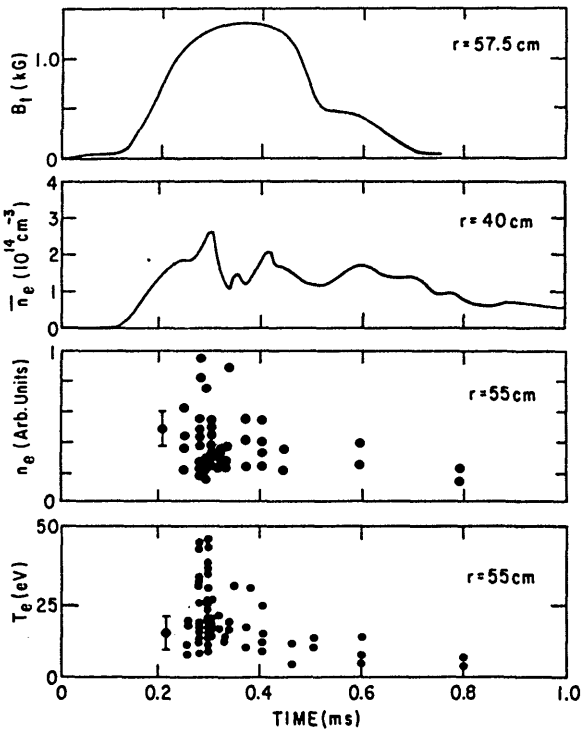

FIG.2. Time evolution of plasma parameters in absence of figure-eight coil system. From top: toroidal field at R = 57.5 cm (nearly magnetic axis) of mid-plane, average electron density (R = 40 cm, −40 ⩽ Z ⩽ 40 cm), local density n_e (at R = 55 cm, Z = 0) and local electron temperature T_e (R = 55 cm, Z = 0) are depicted as function of time.

toroidal plasma current to toroidal plasma flux), the relaxation oscillations, and the associated precursor oscillations have also been observed. Relaxation to a minimum energy state is an important mechanism in S-1 spheromak plasmas and is achieved by either abrupt flux conversion during equilibrium or quiet continuous conversion during formation. The plasma seeks a state such that the 'pinch parameter' ratio of poloidal flux (toroidal current) to toroidal flux is a constant, independent of initial conditions, as shown in Fig.3. Flux conversion can occur in either direction. This process may offer an opportunity for steady-state inductive maintenance of the S-1 spheromak, similar to F – θ pumping [7] in a reversed-field pinch.

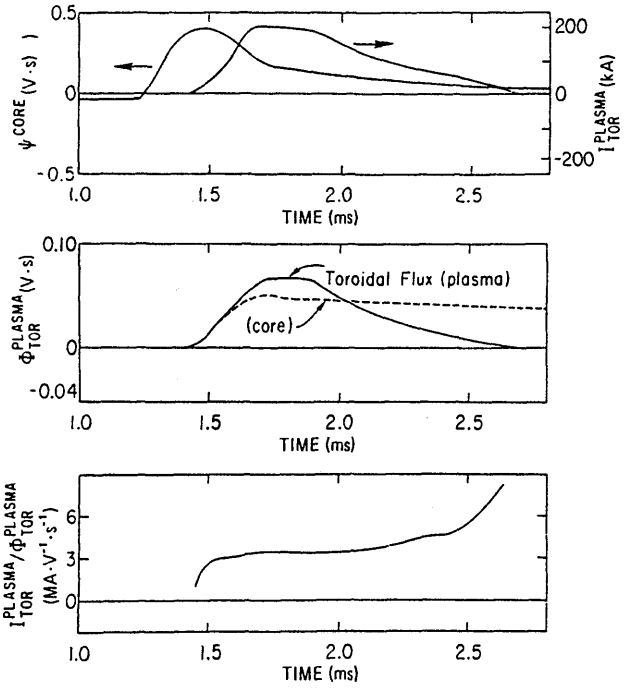

FIG.3. Time evolution of poloidal (top) and toroidal (centre) fluxes and ratio of toroidal plasma current to flux (bottom) in long-lived linked discharge. ψ^{core} is the total poloidal flux linking the core. The toroidal flux in the formed plasma is 40% greater than that originally in the core.

4. INVESTIGATION OF A STABLE SPHEROMAK WITH FIGURE-EIGHT COILS

According to MHD theory, in the absence of a passive stabilizer, the spheromak plasma is predicted to by unstable to at least one of the rigid-body modes in any type of EF field: either the tilt, shift, or vertical instability. Initially, S-1 has been operated in the equilibrium field (EF) Modes A, B, C and (primarily) D. In Mode D, an equilibrium field is of the mirror machine type, where the field index $n_i = (r_0/B_{EF})(dB_{EF}/dr)$ is 1.1 at $r_0 = 60$ cm. In Modes B, C, and D the movement of the plasma in the midplane due to the shift instability was anticipated and was observed in most of the discharges.

To stabilize the gross MHD modes, a figure-eight coil system (named according to its eddy current pattern) was designed, based on theoretical studies [8] and the results of the Proto-S-1 devices [9] and has recently been installed

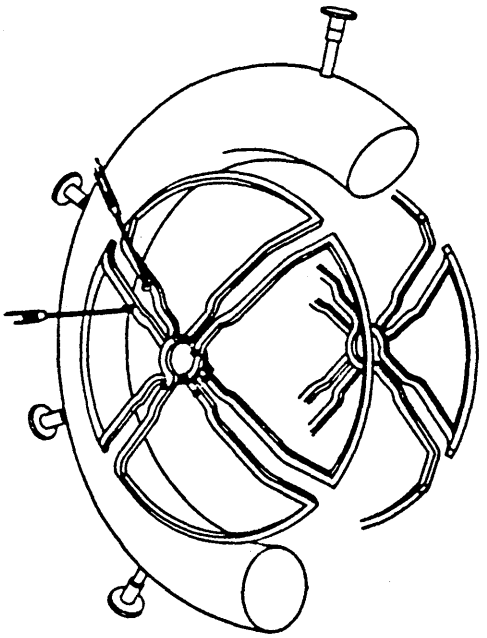

FIG.4. Schematic diagram of figure-eight coil system installed on S-1 device.

in S-1. The first figure-eight coil system was designed primarily to stabilize shift modes of a plasma with major radius of 45–65 cm. As is shown in Fig.4, 2 pairs of butterfly-shaped figure-eight coils were installed on each side of the midplane of the flux core so that the cross points of the coil bar are 60 cm ($\cong 1.5\ a_{plasma}$) away from the mid-plane. The major radius of the coil system plane is 75 cm. The present passive coil system is made of (2 cm × 3 cm cross-section) oxygen-free copper bars.

The installation of the figure-eight system made a dramatic change in the stability features of the formed spheromak plasma. The left-hand side of Fig.5 shows the time evolution of the radial profile of the B_z field (i.e. the z-component of the poloidal field, where the z-axis is the major symmetry axis) for a plasma shot taken without the stabilizing system. Immediately after the plasma is formed, it starts shifting in the $z = 0$ midplane with a speed of $(0.2–0.5) \times 10^6$ cm·s^{-1}. With the figure-eight system installed, the spheromak is now kept in a stable equilibrium position for more than a half millisecond, an order-of-magnitude

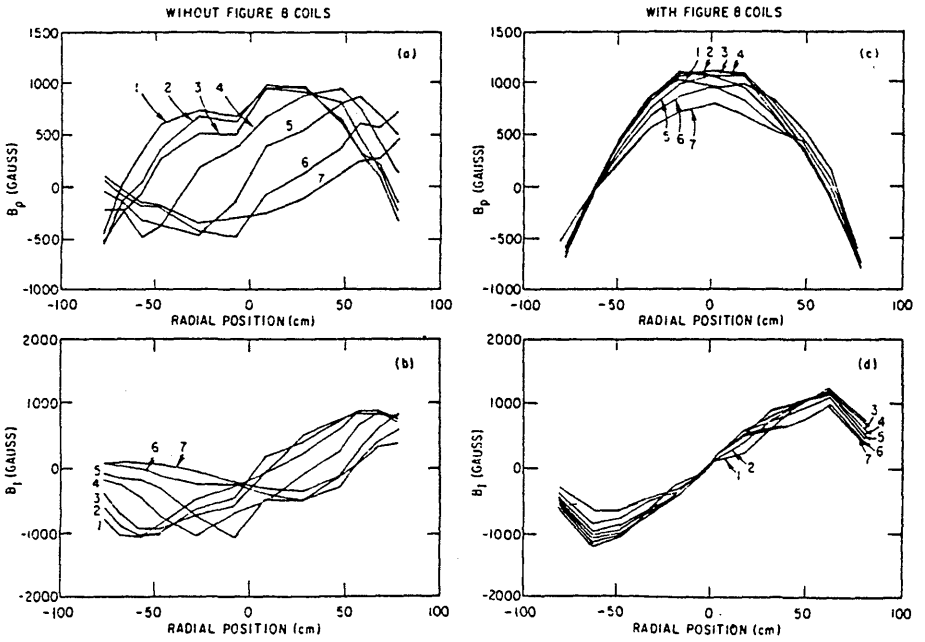

FIG.5. Evolution of radial profile of internal magnetic field taken between 0.3 ms and 0.6 ms after initiation of discharges (curves 1–7 are taken every 0.05 ms interval during this time). (a) and (b) refer to toroidal (B_t) and poloidal (B_z) field in the absence of figure-eight coils and (c), (d) to B_t, B_z with the installed figure-eight coils.

improvement in the duration of the stable quiescent period. As is seen in Fig.5, the plasma has a characteristic spheromak configuration [1], with a low current density (flux hole) in the vicinity of the major axis.

So far, gross MHD-stable spheromaks have been obtained with up to 80–85% of the poloidal flux pinched off from the flux-core, with significant improvement from the previous (Type L, Type P) discharges without figure-eight coils. With the stabilizing coils, the spheromak discharges became so reproducible that the time evolution of the global magnetic field structure can be mapped out on the basis of internal magnetic probe data of 40 consecutive discharges. In particular, a cross-section of the plasma in a chosen toroidal plane can be traced by scanning a radial arm probe in the z-direction; grid sizes of the sampling are 7.5–15 cm. Figure 6 presents the time evolution of poloidal flux plots taken 0.2, 0.3, 0.4, 0.5 ms after the start of the discharges. In this case, the figure-eight coil system is always outside the separatrix of the formed spheromak during the entire period, excluding effects of line tying. This figure verifies the formation of a stable

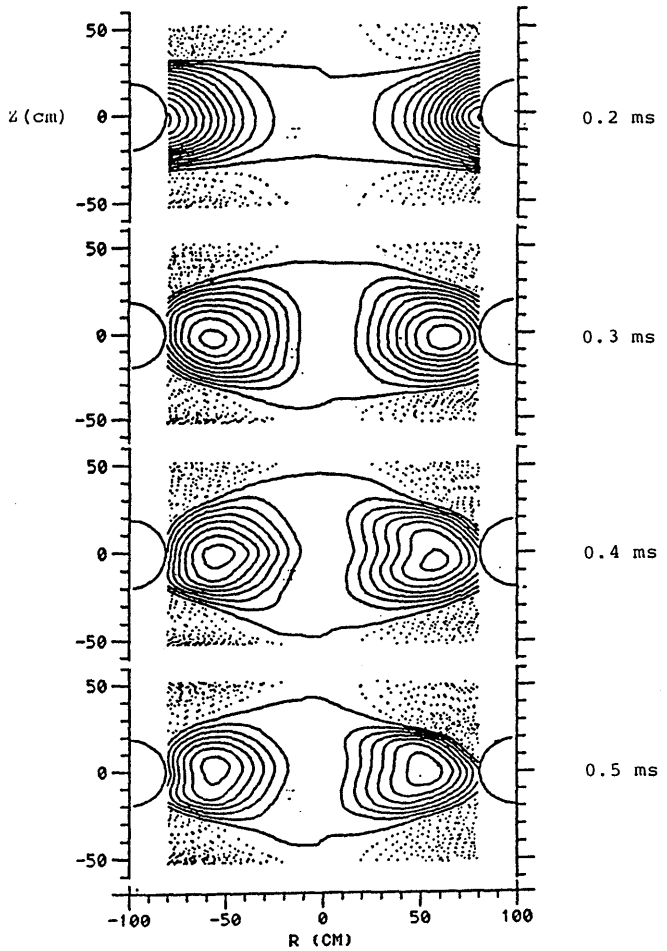

FIG. 6. Time evolution of poloidal magnetic flux plots obtained by internal magnetic probe data from 40 consecutive reproducible shots. The probe is scanned through -52.5 cm $< Z <$ 52.5 cm, and -77.5 cm $< R <$ 77.5 cm. Separatrices of spheromak configuration are shown by outermost solid lines around plasmas.

spheromak configuration by the S-1 induction scheme. Although no other pronounced MHD activities have been detected, a more detailed study of q-profile, shear, and deviation from the minimum energy state will be reported in the near future.

An investigation of spheromak transport with the stabilizer coils has just been initiated with various diagnostics. Spectroscopic data show that the plasma

contains O, C, Ni and Fe, and it appears that the created plasmas are impurity-dominated after one month of operation in this mode; it is difficult to identify other energy loss mechanism than radiative losses at this point. Major improvements of the vacuum condition are underway.

5. IMPROVEMENT OF PLASMA PARAMETERS BY COMPRESSION

A compressional heating experiment is under consideration for S-1, with a radial compression factor of about 2.5. If the spheromak is magnetically compressed [10] with a radial scale factor C, for adiabatic compression ($\tau_C \ll \tau_E$ and τ_N), the plasma parameters are expected to increase as: $n_e \propto C^3$, $T \propto C^2$, $B \propto C^2$, and $\beta \propto C$, $j \propto C^3$, relative drift velocity $u/u_{th} \propto C^{-2}$, and magnetic Reynolds number $S \propto C^{5/2}$. Alternatively, if RFP scaling holds during the compression, the plasma parameters will be controlled by the physical mechanisms that hold β constant. If one assumes that particle 'pump-out' is a dominant process in keeping β constant, RFP scaling would then suggest $n \propto C^2$, $T_e \propto C^2$, $n\tau_E \propto C^3$, $j \propto C^3$, and $S \propto C^3$. Thus, for a compression of 2.5, a significant increase in n_e, T, $n\tau_E$, and S might be achieved. On the other hand, if particles are conserved and thermal losses are dominant, β = constant scaling would yield $n \propto C^3$, $T \propto C$, $n\tau_E \propto C^{5/2}$, and $S \propto C$. In both cases, a sizeable increase in T and n_e and an order-of-magnitude increase in $n\tau_E$ would be achieved. Spheromak stability against tilting could be maintained during the compression by passive coils. This experiment would be an important step for the translation/compression reactor scheme and would contribute to the knowledge of spheromak heating, stability, size scaling, collisionality scaling, and β-limits.

REFERENCES

[1] BUSSAC, M.N., et al., in Plasma Physics and Controlled Nuclear Fusion Research 1978 (Proc. 7th Int. Conf. Innsbruck, 1978), Vol. 3, IAEA, Vienna (1979) 249; FURTH, H.P., J. Vac. Sci. Technol. **18** (1982) 1073.

[2] JARDIN, S.C., PARK, W., Phys. Fluids **24** (1981) 679; LUI, H.C., et al., Phys. Fluids **24** (1981) 673.

[3] YAMADA, M., et al., Phys. Rev. Lett. **46** (1981) 188.

[4] PAUL, S., et al., in Compact Toroids (Proc. 6th Symp. Princeton, New Jersey, 1984) (to appear).

[5] HART, G., McNEILL, D., ibid.

[6] JANOŠ, A., ibid.

[7] SCHOENBERG, K.F. et al., Nucl. Fusion **22** (1982) 1433.

[8] JARDIN, S.C., CHRISTENSEN, V., Nucl. Fusion **21** (1981) 1665; SATO, T., HAYASHI, T., Phys. Rev. Lett. **50** (1983) 38.

[9] YAMADA, M., et al., in Plasma Physics and Controlled Nuclear Fusion Research 1982 (Proc. 9th Int. Conf. Baltimore, 1982),Vol. 2, IAEA, Vienna (1983) 265; MUNSON, C., PhD Thesis, Princeton Univ. (1983).
[10] KATSURAI, M., YAMADA, M., Nucl. Fusion 22 (1982) 1407.

DISCUSSION

H. FLEISCHMANN: I was very interested to hear about your important work on tilt stabilization using a figure-8 coil. Do you have any indication as to how far you can compress your rings further away from that coil and how you could move the rings axially as envisioned in a moving-ring reactor?

M. YAMADA: The data I have presented today were obtained very recently. We are investigating optimum plasma positions with respect to two types of figure-8 coil system which we have constructed. Later we shall also be testing the 'saddle-coil system' that I described at the Baltimore Conference (see Ref.[9] cited in the paper), which is compatible with axial translation of compressed plasmas.

J.B. TAYLOR: You have shown data on the constancy in time of the ratio I/Φ. Have you any data on the constancy of the local quantity j/B in time or space, i.e. on the quantity $\mu(v)$?

M. YAMADA: No, before we installed the figure-8 coils the plasma discharges were unstable, and consistent local measurements were not possible. But now that the plasma has become stable, we will be able to investigate the $\mu(v)$ profile of the S-1 spheromak in detail. I should add, however, that data obtained in the Proto S-1 device have shown that the q-profile of the plasma was relatively flat up to the plasma edge, i.e. in rough agreement with the $\mu \cong$ const spheromak configuration.

RECENT ADVANCES IN CONFINEMENT AND HEATING PHYSICS ON EBT-S*

L.A. BERRY, F.W. BAITY, D.B. BATCHELOR, F.M. BIENIOSEK, T.S. BIGELOW, J.A. COBBLE, R.J. COLCHIN, W.A. DAVIS, J.C. GLOWIENKA, J.R. GOYER, G.R. HASTE, D.L. HILLIS, S. HIROE, H.D. KIMREY, L.W. OWEN, T.L. OWENS, R.K. RICHARDS, L. SOLENSTEN, D.W. SWAIN, N.A. UCKAN, T. UCKAN, J.B. WILGEN
Oak Ridge National Laboratory,
Oak Ridge, Tennessee,
United States of America

Abstract

RECENT ADVANCES IN CONFINEMENT AND HEATING PHYSICS ON EBT-S.

Recent advances in experimental diagnostic capability and electron cyclotron heating (ECH) theory for the ELMO Bumpy Torus (EBT) have led to the development of a new picture of the electron heating and confinement. The diagnostic improvements include an improved, radially scanning Thomson scattering system, a new spectroscopic technique for measuring T_e using Al ion line ratios, and soft X-ray and microwave interferometer measurements of plasma properties in the high magnetic field 'throat' region. The results indicate that the electron distribution ($E \leqslant 2$ keV) has two components: a cold isotropic collisional component ($n_c \approx 0.7 \times 10^{12}$ cm^{-3}, $T_c \approx 80$ eV), and a warmer, collisionless, anisotropic tail component ($n_w/n_c \leqslant 0.3$, $T_w \approx 600$ eV). This result is in qualitative agreement with Fokker-Planck calculations of ECH in EBT, which indicate that most of the microwave power is absorbed by the warm tail electrons and that up to 50% of the absorbed power may be carried immediately to the walls by particles on unconfined drift orbits. A new closed bumpy field line device in the form of a square (ELMO Bumpy Square (EBS)) is proposed, which is predicted to have significantly better confinement properties than EBT.

The EBT is a closed line configuration with a bumpy toroidal magnetic field. Single particle confinement and plasma equilibrium are established by the poloidal, magnetic gradient drifts which are associated with the bumpy fields. Stability is established by the presence of relativistic electron rings [1,2]. ECH is used for both ring and toroidal plasma heating. The magnetic field structure is shown in more detail in Fig. 1 where the field lines are shown for one of the twenty-four sectors on the EBT-S device, which has a major radius of 1.54 m and a clear bore radius through the mirror throat of 0.11 m. The mirror ratio on axis is about 1.9 and the device is typically operated with a mean toroidal field of 1 T. Also shown are the fundamental resonant surfaces (B = 1 T) that correspond to the 28-GHz ECH power,

* Research sponsored by the Office of Fusion Energy, US Department of Energy, under contract No. DE-AC05-84OR-21400 with the Martin Marietta Energy Systems Inc.

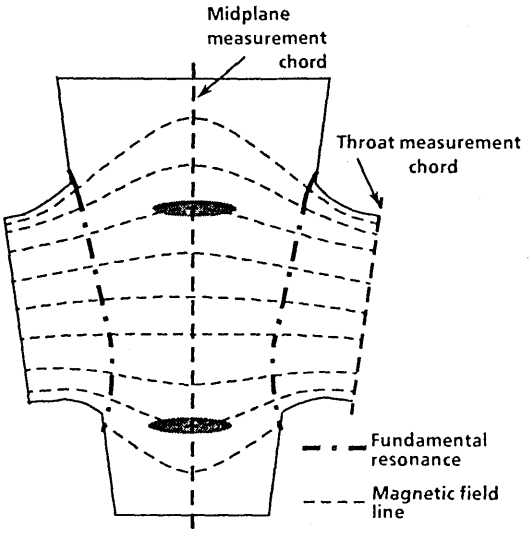

FIG. 1. Plan view of the magnetic configuration for one of 24 identical EBT-S sectors. Location of the hot electron ring is indicated schematically by the shaded areas.

and the approximate location of the hot electron ring. The ring is localized in the volume where the second harmonic resonance surface is parallel to the magnetic field lines.

The detailed mechanism by which ECH power is absorbed at these surfaces, when coupled with the single particle confinement characteristics of the configuration, has a dominant role in establishing the characteristics of the EBT plasma. Earlier measurements were consistent with the notion that the plasma was dominated by two components: (1) an isotropic toroidal plasma heated by ECH at the fundamental resonance and (2) the relativistic electron ring heated at the second harmonic surface (with a radius of 12 cm in the midplane). The toroidal plasma had characteristic parameters of $n \sim 10^{12}/cm^3$ and $Te \sim 700$ eV with an applied microwave power of 150 kW [3]. The density and temperature were measured by a microwave interferometer and soft X-ray spectrometer respectively. Plasma densities were sufficiently low that reliable Thomson scattering data were difficult to obtain.

During the past year, improved diagnostic measurements coupled with a more detailed understanding of ECH physics have led to the identification of a more complex structure for the lower energy component ($E < 2000$ eV) of the electron distribution function. The present understanding is consistent with the existence of an isotropic toroidal plasma with a temperature of 50–100 eV (depending on microwave power) and a mirror-trapped tail with temperatures in the 400–800 eV range (again depending on conditions) with a density of 10–30% of the colder component. This tail is created by preferential absorption of the ECH power into moderately energetic particles.

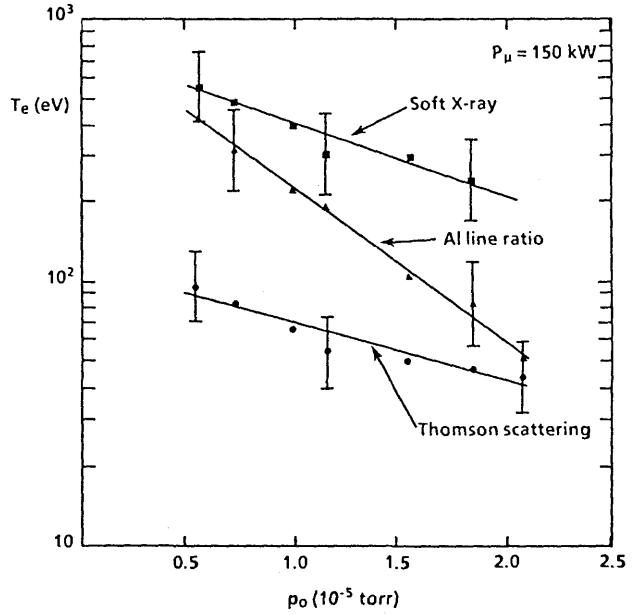

FIG.2. Midplane electron 'temperature' measurements as determined by soft X-ray, Al line ratio, and Thomson scattering techniques.

As will be discussed later, one consequence of this process is that, for the present EBT-S device,ECH is inefficient, with about 50% of the energy which is absorbed by the plasma being lost rather quickly. Several new EBT configurations have been developed which provide improved particle confinement without the necessity for increasing the magnetic aspect ratio. One of these, the EBS, is particularly attractive because it can be tested by reconfiguring the present device. For this device, these ECH losses should be reduced by a factor of about four, and there is the potential for an order of magnitude improvement in plasma parameters.

In the remainder of this paper, the data which support the hypothesis put forth in the preceding paragraph will be presented and correspondence with a theoretical model will be established. Of particular importance are: (1) improved Thomson scattering data and analysis, (2) a line ratio technique based on the intensity of lines which are emitted from different excited states of AlIII, (3) comparison of soft X-ray and microwave interferometer data from the throat (made through a split mirror coil) and midplane regions of the plasma, and (4) behavior of the tail component with various heating configurations. The paper will conclude with a brief description of the EBS configuration.

Fig. 2 illustrates the characteristic variation of electron temperature as measured by Thomson scattering,soft X-rays and the Al line ratio as a function of fill gas pressure for a microwave power of

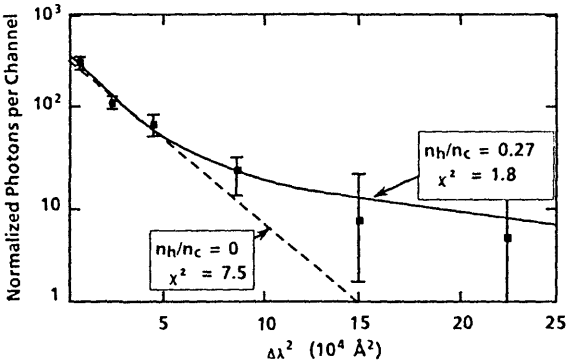

FIG. 3. Number of Thomson-scattered photons per channel versus $(\Delta\lambda)^2$*, summed over 10 laser shots.*

150 kW. All three measurements were made along the midplane chord as shown in Fig. 2. The pressure range is limited by plasma stability: at low pressure there is insufficient cold plasma to stabilize the ring against the hot electron interchange mode and at high pressure there is insufficient ring beta (density) to stabilize the core plasma against simple interchanges. The underlying statistical errors in data and possible systematic errors in interpretation are such that the differences between the measurements are significant.

At high pressure the Thomson scattering and Al line ratio data are closest to each other. As the pressure is lowered, the Al line ratio temperature moves toward the soft X-ray value.

Each of the three measurements tends to be sensitive to a different energy of electrons. The Thomson scattering is most sensitive to low energy electrons(less than 300 – 400 eV) because for 100 – 200 eV temperatures the distribution function weighting dominates, while the soft X-ray system is only sensitive to photons with E > 400 eV. The line ratio technique tends to respond to the average energy. Based on the data and these observations, it is reasonable to examine the possibility that the electron distribution is non-Maxwellian with a low energy component which can be characterized by the laser scattering data and a high energy component which corresponds to the soft X-ray measurements.

The spectrum of Thomson-scattered photons obtained by summing ten laser shots is shown in Fig. 3. When the data are fitted by a single-temperature Maxwellian with two parameters, n and T, an unnormalized chi-square of 7.5 results. If a second component is added and the data fit with three parameters, n_c, n_w, and T_c with the tail temperature given by soft X-ray measurements, a significantly better fit is obtained with a chi-square of 1.8. Thus, from a purely analytic point of view, the Thomson scattering data are consistent with a bi-Maxwellian distribution function in the range of E < 2 keV. In addition, the density of the tail obtained in this fashion varies systematically with machine parameters in the manner expected from the measurements shown in Fig. 2: it is largest at low pressures and

vanishes for high pressures. However, both known experimental random error and the possibility of systematic errors in the data analysis process are such that obtaining a good estimate of the warm plasma density is not possible.

Soft X-ray measurements in the high field throat region of the plasma show that the tail population is mirror-trapped in the midplane. A comparison of total line-average electron density in two regions, normalized to path length (i.e. $1/B^{1/2}$), suggests that the electron density is constant along a field line. However, the soft X-ray measurements yield quite different results. The temperature inferred from the soft X-ray spectrum is reduced by up to 40%, and the intensity of the emission is much lower, typically a factor of $4-10$. This verifies that the tail is dominated by mirror-trapped electrons. In parallel with the measurements, a more detailed assessment of ECH physics has been made [4]. High energy passing electrons are heated preferentially because the ECH absorption is sufficiently strong to significantly reduce the amplitude of the extraordinary wave before it reaches the cold plasma resonance. In the absence of particle losses, a high energy tail would form which is localized around the pitch angle for which particles turn just past the resonant zone, $v_\parallel/v \approx 0.6$. However, for slightly larger pitch angles, $v_\parallel/v \approx 0.7$, i.e. the angle at which particles change from being trapped to passing, single particle confinement is poor. In the absence of ambipolar electric fields, there are no closed drift orbits. Because the ECH creates high energy electrons, the ambipolar field can only partially mitigate the problem. Fokker-Planck calculations which model the ECH and particle confinement physics suggest that about 50% of the absorbed power is lost due to poor confinement of stronger heated transitional particles.

The correlation of the electron tail with ECH was demonstrated by varying the locations at which microwave power is applied. Typically ECH is launched into the midplane in nearly every cavity. Even those cavities which are not directly heated receive a significant amount of power as a result of the transmission of ordinary mode waves from adjacent cavities. When the power from three adjacent cavities was shut off and soft X-ray measurements were made in the middle cavity, it was found that the intensity dropped by over two orders of magnitude even though gross plasma parameters were not affected by more than 10%. This behavior proves that the tail is driven by local ECH in agreement with the model.

In addition to significantly reducing the ECH heating efficiency, the relatively poor single particle confinement also results in inefficient ring formation relative to simple mirrors [5] and is thought to be correlated with the ambipolar field structure. Thus, finding configurations with improved confinement without the need for increased aspect ratio is vital. Several new configurations have in fact been developed which achieve the desired end [6]. Of these the EBS can most easily be implemented for evaluating the effect of improved particle confinement. The bumpy square in general uses a combination of straight bumpy sections on the sides to provide equilibrium and relatively high field corners to give improved particle confinement. Improved confinement results from localizing the toroidal curvature in regions of high magnetic field and thus reducing the vertical drift

which is associated with toroidal gradients, since the vertical drift velocity (and hence the single particle orbit shifts) are inversely proportional to B_T ($v_d \sim 1/B_T$). The important parameter is the global mirror ratio M_G, defined as the ratio of the maximum field in the corners to the minimum axial field on the sides. Drift orbit centering is found to improve as $M_G^{3/2}$ [7]. The same calculations which show a loss of 50% for the absorbed ECH power indicate a factor of 4–5 improvement for the comparable square with a global mirror ratio of about 4.

As a result of this improved confinement, smaller reactor configurations are possible. The bumpy square, as well as several of the other new configurations, shows a reduction in projected reactor size of about 2 m to about 15 m major radius from the earlier values of 30–35 m. It is expected that the reactor size will continue to drop with further development.

In summary, as a result of better measurements and more refined models, our understanding of EBT physics has been substantially advanced. These studies have identified the need for improved single particle confinement as the most important direction for advancing the EBT concept. A number of new EBT configurations have been developed which address this issue. Among these the EBS is most promising for near term investigation.

REFERENCES

[1] DANDL, R.A., et al., "Plasma confinement and heating in the ELMO Bumpy Torus (EBT)", Plasma Physics and Controlled Nuclear Fusion Research 1974 (Proc. 5th. Int. Conf. Tokyo, 1974), Vol.2, IAEA, Vienna (1975) 141.

[2] SPONG, D.A., EL NADI, A.M., HIROE, S., Profile effects on EBT stability boundaries, Bull. Am. Phys. Soc. 28 (1983) 1.

[3] HILLIS, D.L., et al., Electron confinement studies on the EBT-S Bumpy Torus experiment using soft X-ray techniques, Phys. Fluids 26 (1983) 3.

[4] HEDRICK, C.L., et al., Paper No. IAEA-CN-44/D-IV-4, these Proceedings, Vol.2.

[5] DANDL, R.A., EASON, H.O., ENGLAND, A.C., SPROTT, J.C., Nucl. Fusion 13 (1973) 693.

[6] Proc. Workshop on Advanced EBT Configurations (830758), Rancho Santa Fe (1983).

[7] UCKAN, N.A., et al., ELMO Bumpy Square, Oak Ridge Natl Lab. Rep. ORNL TM 9110 (1984).

CHARACTERISTICS OF HIGH-DENSITY AND HIGH-TEMPERATURE PLASMAS IN THE NAGOYA BUMPY TORUS

M. FUJIWARA, T. KAMIMURA, M. HOSOKAWA,
T. SHOJI, H. IGUCHI, H. SANUKI, K. TAKASUGI,
F. TSUBOI, H. TSUCHIDATE, K. KADOTA, K. SATO,
K. TSUCHIDA, A. TSUSHIMA*, H. IKEGAMI
Institute of Plasma Physics,
Nagoya University,
Nagoya, Japan

Abstract

CHARACTERISTICS OF HIGH-DENSITY AND HIGH-TEMPERATURE PLASMAS IN THE NAGOYA BUMPY TORUS.

Experimental studies are made on heating and confinement of plasmas in the Nagoya Bumpy Torus (NBT-1M). ECH-heated plasmas ($n_e \approx 10^{12}$ cm^{-3}, $T_e \approx 100$ eV) in the bumpy torus are stably confined by the closed drift surface due to ∇B and $\vec{E} \times \vec{B}$ drift although the ring beta is lower than the theoretically required value. The electron energy confinement and the profile of ambipolar potential observed experimentally cannot be explained by the conventional neoclassical theory. Heating and confinement of high-density and high-temperature plasmas ($n \cong 10^{13}$ cm^{-3}, $T_i \cong 150$–500 eV) are examined by the use of high-power ICH. The plasma potential changes from a negative well to a positive hill with increasing ion temperature. The ion energy transport is still dominated by the charge-exchange loss.

1. INTRODUCTION

The bumpy torus, which consists of a set of toroidally linked magnetic mirrors, is considered to be one of the promising candidates for a fusion reactor because of its advantages such as (i) possible steady-state operation, (ii) stable confinement of a high-β plasma, and (iii) easy maintenance and good accessibility, resulting from the simple structure of the magnetic coil system. MHD stability is guaranteed by the local magnetic well owing to the high-β, energetic electron plasma ring produced by the electron cyclotron heating. The confinement of the plasma particles is mainly achieved by the closed drift surface in the vacuum magnetic field configuration. The plasma confinement is greatly improved by a nested potential surface through $\vec{E}_r \times \vec{B}$ poloidal drift.

---

* Present address: Department of Electronic Engineering, Tohoku University, Sendai 980, Japan.

The NBT-1M bumpy torus consists of 24 simple mirror sectors (mirror ratio 2.4 at the magnetic axis, B_{max} at midplane axis 1.0 T, major radius 1.4 m, average plasma minor radius 7 cm). ECH microwave sources: 8.5 GHz/20 kW/cw, 18 GHz/45 kW/cw and 28 GHz/200 kW/100 ms (available in 1984). RF sources for plasma production and heating in the ion cyclotron frequency range: 7–28 MHz/500 kW/10 ms [1].

2. ECH BUMPY TORUS PLASMAS

The basic characteristics of ECH bumpy torus plasmas are studied by using an 18 GHz microwave which heats the toroidal plasma electrons and simultaneously produces hot-electron ring plasmas. As is well known, there are three distinct modes of operation called C (collisional), T (toroidal) and M (mirror) modes, depending on the ambient gas pressure and the intensity of the hot-electron ring. In the intermediate range of operating ambient gas pressure (T-mode), a hot-electron plasma builds up in the midplane of each mirror sector encircling the toroidal core plasma. In this mode, the plasma potential surfaces form closed nested toroidal surfaces which correspond to magnetic surfaces in tokamak and stellarator configurations.

(a) The hot electron ring plasma: The temperature of the hot electron ring measured by an NaI scintillator is 230 keV, which is scaled by $\rho/L = 0.05$ [2] (here, ρ is the hot-electron Larmor radius and L is the characteristic scale length of the mirror field). As is shown in Fig. 1(a), the ring intensity increases linearly with the microwave input power, and the maximum beta value β_h is estimated to be 3–6% from energy spectrum analysis and the photon number of the hard-X-ray measurements. This value is also consistent with the direct measurement of the magnetic field strength at the ring position by Zeemann splitting of Li beam probing [3]. As is shown in Fig. 1(b), the measurement by radial scanning of hard-X-ray telescope shows the profile to be ring-shaped; its peak coincides with $\omega_\mu = 2\omega_{ce}$, where ω_μ is the input microwave frequency. The ring width is 2–3 cm. The value of β_h is considered to be lower than the theoretically required $\beta_{hc} \approx 2(\triangle/R_c)$ [4] (10–20% in NBT-1M), but the plasma does not show any macroscopic unstable modes such as an interchange instability.

(b) Toroidal core plasma: The plasma density n_e is $5 \times (10^{11}–10^{12})$ cm^{-3} and the radial profile measured by Li beam probing (4 keV neutral Li beam) has the shape of a bell whose centre is located close to the mod B axis.

The plasma potential, which plays a key role in plasma confinement in a bumpy torus configuration, is measured by a heavy-ion beam probe. The results of two-dimensional measurements show that the plasma potential in an ECH bumpy torus plasma is a negative well with a depth of $\phi_w \approx 150$ V and with equipotential surfaces which are almost concentric with the mod B surfaces (Fig. 2(a)). The outermost closed potential surface is located at the second

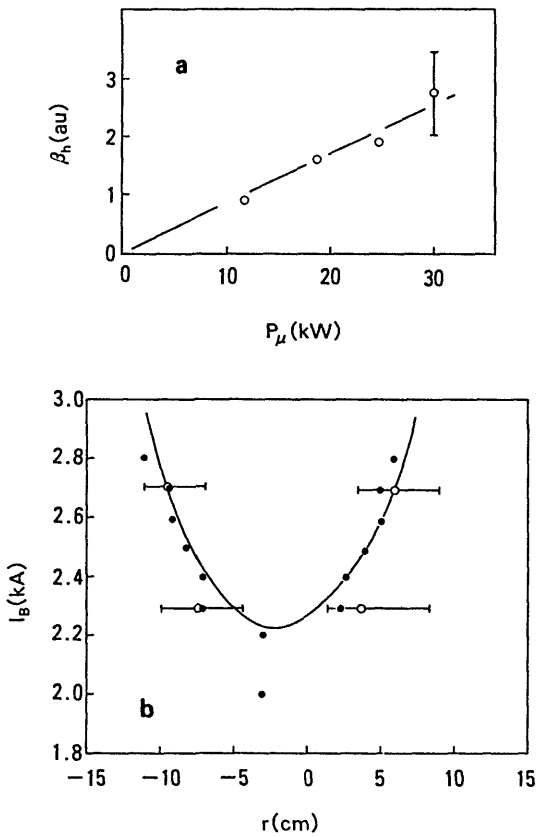

FIG.1. (a) Dependence of ring intensity on microwave input power. Ring temperature and density are estimated from hard-X-ray measurements.

(b) Relation between ring position measured by hard-X-ray telescope and magnetic field strength. Ring positions coincide with $\omega_\mu = 2\omega_{ce}$.

harmonic of the electron cyclotron resonance ($\omega_\mu = 2\omega_{ce}$), just where the hot electron ring exists (Fig.2(b)).

Several methods were used to measure the electron temperature, i.e. soft X-rays, visible spectroscopy for the line ratio of singlet and triplet lines of helium atoms introduced as impurities, plasma conductivity, as well as Thomson scattering. The electron temperature T_e is estimated to be 50–100 eV.

Measurements of density fluctuations in the low-frequency range ($f < 100$ kHz) by a frequency spectrum analysis of the H_α line emitted from the plasma were carried out to study the detailed structure of bumpy torus plasmas and to estimate the anomalous transport from the fluctuation level $\tilde{n}/n$ and its correlation time.

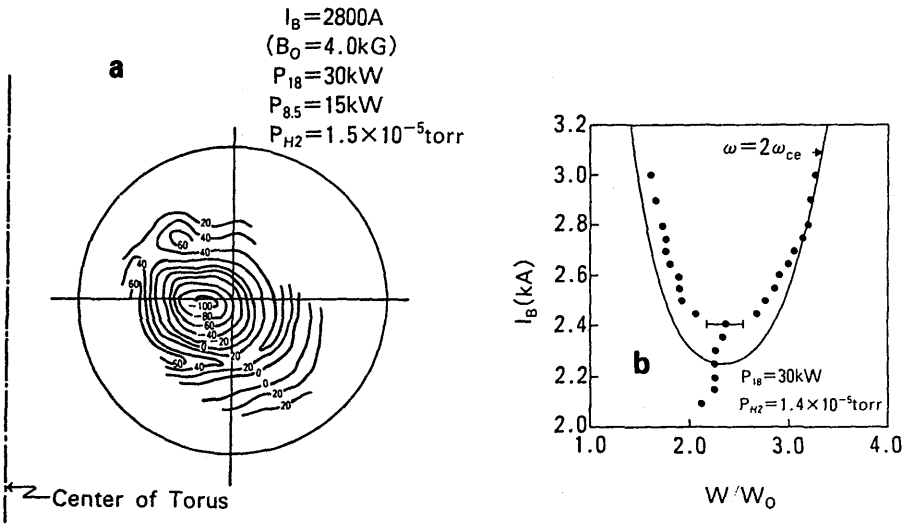

FIG.2. (a) Two-dimensional display of equipotential surfaces measured by heavy-ion beam probe. (b) Spatial positions of potential rim versus coil current I_B measured along vertical scanning line of heavy-ion beam probe. Abscissa shows normalized ion beam energy w/w_0, where w_0 is energy of primary beam which directly reaches energy analyser. Solid line also corresponds to $\omega_\mu = 2\omega_{ce}$ zone.

Two kinds of fluctuations were observed. The first one is in the very low frequency range below 10 kHz and is localized in the surface plasma located outside the hot-electron rings. This fluctuation correlates over a very long distance along the field line in the same phase and seems to be a flute mode. The second one, in the 50–80 kHz range, exists inside the toroidal core plasma, and the amplitude is suppressed down to a quite low level at the high-β hot-electron annulus. This fluctuation is identified to be a drift wave from mode analysis (poloidal mode m = 2) and an estimation of the phase velocity, including the Doppler effect due to $\vec{E}_r \times \vec{B}$ rotation. In the NBT-1M plasma, the rate of net input power to the hot electron ring plasmas and to the toroidal core plasma are 10% and 10–15% of the total output power from the microwave source, respectively. A much greater amount of microwave power, 30–40%, is exhausted in the poorly confined surface plasma. The electron energy confinement time τ_{Ee} is evaluated to be τ_{Ee} = 0.3–0.5 ms, which is two to three times shorter than the particle confinement time τ_p = 1–2 ms estimated from neutral density measurements. Transport due to fluctuations is not the dominant effect, because the confinement time estimated from $|\tilde{n}/n|^2 \tau_{cor}$, where τ_{cor} is the correlation time of the fluctuations, is 10–30 ms.

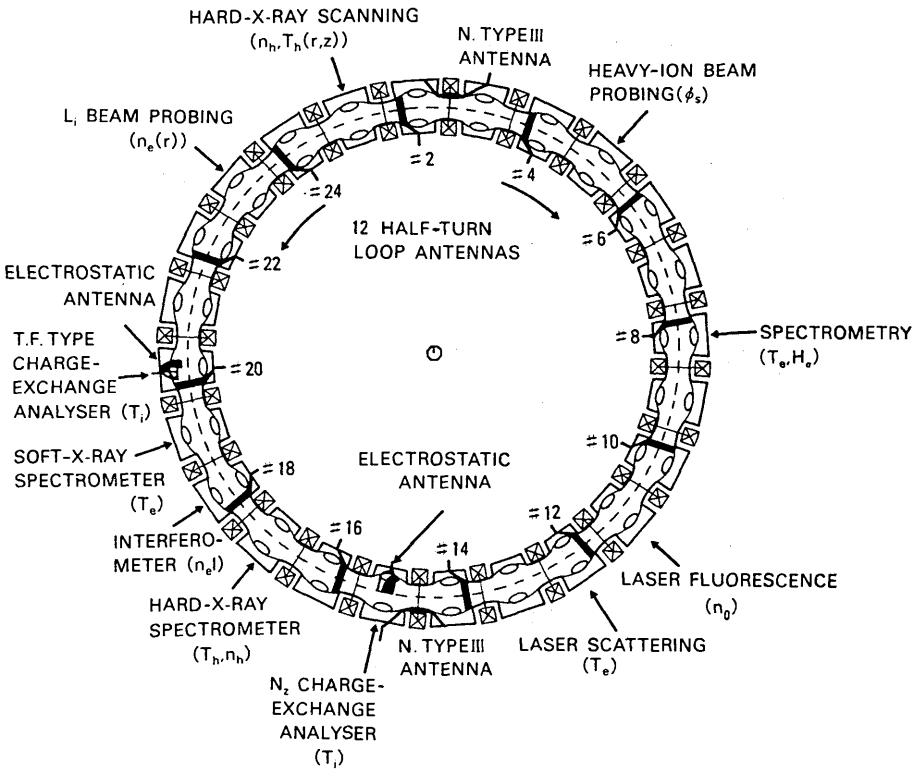

FIG.3. Schematic cut view of RF antennas arrangement and diagnostic instruments in NBT-1M device.

The observed results on radial profiles such as $n_e(r)$ or $\phi(r)$ indicate that the bumpy torus plasma is stably confined without touching the wall although the ring beta β_h is less than the required critical value for MHD stability. The confinement times τ_{Ee} and τ_p, which are shorter than the values predicted by neoclassical transport theory by a factor of three to five [5], can be explained by direct losses or $\vec{E} \times \vec{B}$ convection, which comes from the subtle but essential difference among the n(r), ϕ(r) and mod B surfaces.

3. ICH BUMPY TORUS PLASMAS

Studies on plasma confinement in the high-temperature, high-density regime are carried out by using high-power ion cyclotron heating. A schematic cut view of the NBT-1M apparatus in this operation is shown in Fig.3.

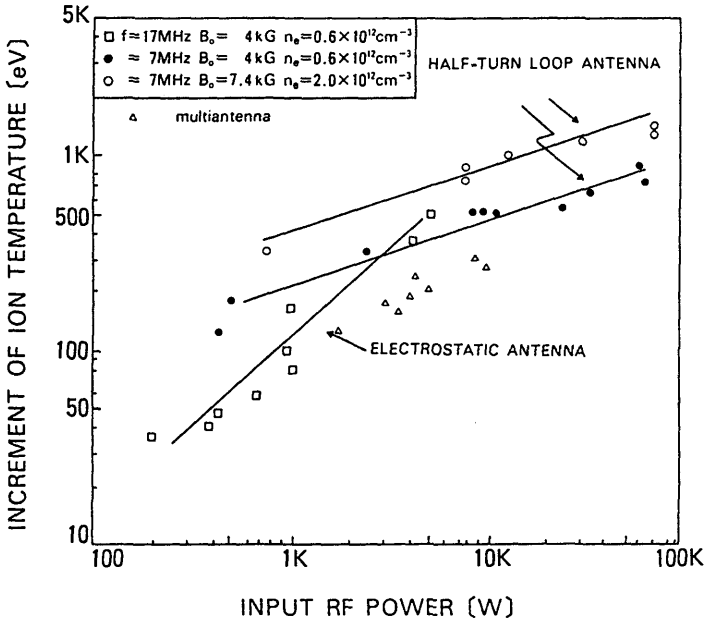

FIG.4. Increase in ion temperature versus the RF input power. Triangular points show results of ion heating by 12 antennas.

(a) ICH in a single-cavity plasma: Ion cyclotron (slow-wave) and ion Bernstein wave heating were applied to the plasma in one mirror sector described in Section 2, using a half-turn coil placed near the mirror throats and an electrostatic antenna at the midplane [6]. The increase in ion temperature observed by energy analysis of fast neutral atoms from the plasma is shown in Fig.4.

The RF power deposit was mainly to the perpendicular energy of ions that were well confined in the mirror geometry, and the heating wave was observed to be heavily damped within the antenna cavity. Furthermore, the plasma density is still so low that the rather high-density neutrals determine the energy confinement through charge-exchange processes since the ion-ion pitch angle scattering time is longer than the charge-exchange time. Therefore, the heating was rather localized in the cavity where the antenna was mounted.

(b) ICH by multi-antennas: To heat ions of the toroidal core plasma effectively, RF power is delivered into 12 half-turn antennas arranged uniformly around the torus. All antennas are installed near the mirror throats.

The increase in ion temperature is also plotted against the equivalent input power/one mirror sector (Fig.4). The ion energy confinement time τ_{Ei} is roughly explained by the charge-exchange loss time.

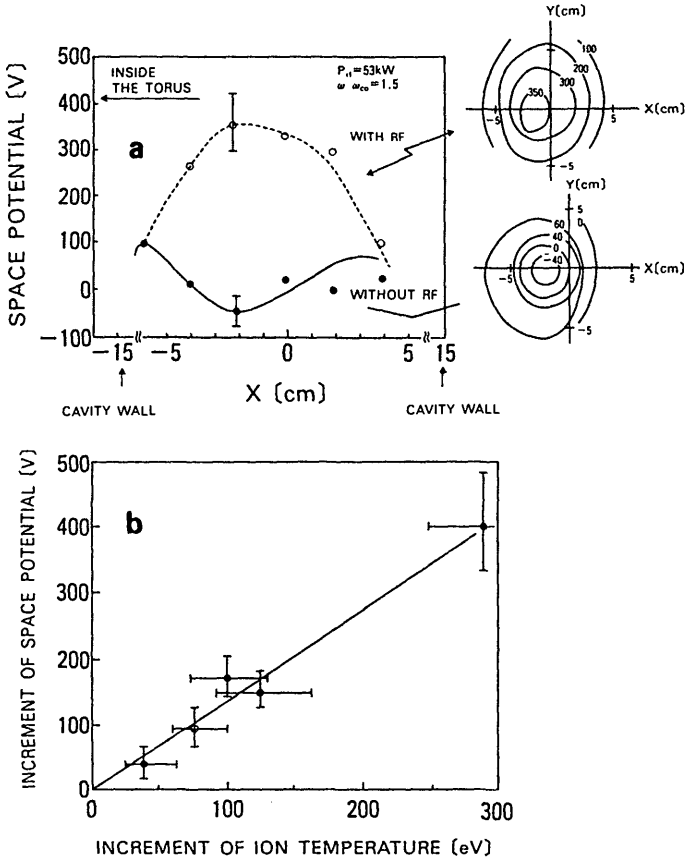

FIG.5. (a) Effect of ion heating on radial electrostatic potential profile measured by heavy-ion beam probing. X and Y are horizontal and vertical axes at midplane, respectively.

(b) Increment of plasma potential at plasma axis as a function of increase in ion temperature.

The important result of this experiment is the substantial change in ambipolar potential due to the increase in ion temperature. Conventional neoclassical theory predicts that the potential well becomes deeper when the ions are heated, so the theory contradicts the experimental results, which show potential profile changes from a negative well in the case of $T_e > T_i$ without RF to a positive hill in the case of $T_i > T_e$ with RF (Fig.5).

(c) ICH on an RF-produced dense plasma: The ion cyclotron heating is also applied to a high-density plasma produced by high-power RF waves (9 MHz, 250 kW, 10 ms) launched from Nagoya Type III coils. The increase in plasma

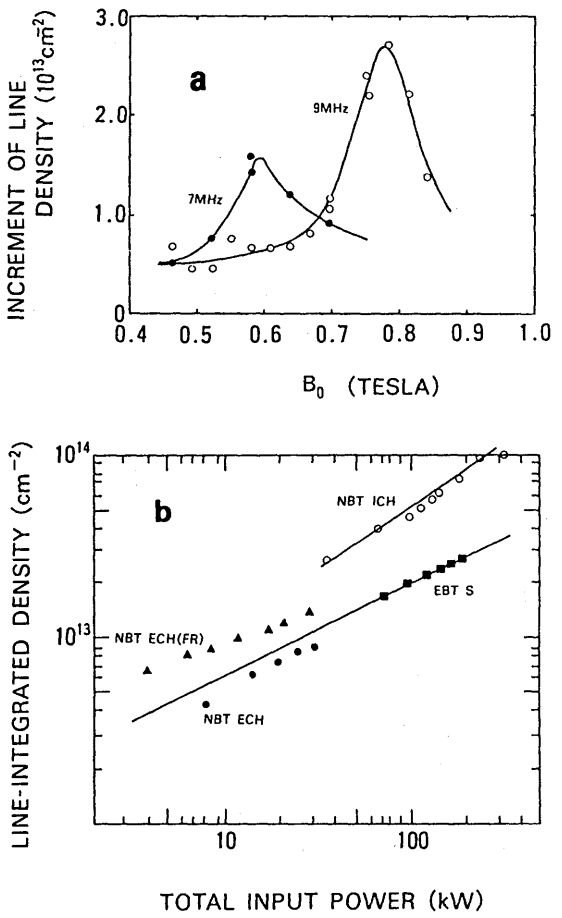

FIG. 6. (a) Increase in line density by application of 90 kW RF power on Type III coil versus magnetic field strength on axis at midplane B_0.

(b) Dependence of plasma density on input power including ECH and ICH power.

density depends on the RF frequency, the input power, and the amount and the timing of controlled gas puffing. The maximum density ($n \approx 10^{13}$ cm^{-3}) is obtained under the condition that $\omega_{RF}/\omega_{ci0} \approx 0.8$, where ω_{ci0} is the ion cyclotron frequency on the axis in the midplane (Fig.6). Ion heating on such a high-density plasma by using 12 half-turn antennas (17 MHz) raises T_i up to 150–500 eV, which is measured by Doppler broadening of the C III line and by an energy analysis of fast neutrals emitted from the plasma.

REFERENCES

[1] FUJIWARA, M., et al., IPP-Nagoya Research Rep. IPPJ-579 (1982).
[2] UCKAN, N.A., Phys. Fluids **25** (1982) 2381.
[3] MATSUNAGA, K., KADOTA, K., FUJIWARA, M., FUJITA, J., Jpn. J. Appl. Phys. **20** (1981) L713.
[4] SPONG, D.A., in EBT Stability Theory (Proc. Workshop Oak Ridge, Tennessee, 1981) 33.
[5] HASTINGS, D.E., KAMIMURA, T., Nucl. Fusion **24** (1984) 473.
[6] SHOJI, T., et al., in Heating in Toroidal Plasmas (Proc. 4th Int. Symp. Rome, 1984) C24.

DISCUSSION

R.H. COHEN: Have you included the effect of azimuthal electric fields – for example, those due to heating asymmetry or to the response to the magnetic configuration – in your transport calculations?

M. FUJIWARA: No azimuthal electric field is included in our calculation. In fact, we have observed that potential profiles are different from mod B surfaces, so we need to examine the transport calculation, taking into account the E_θ observed experimentally.

NON-HYDRODYNAMIC MODEL OF PLASMA FOCUS STRUCTURE

V.S. IMSHENNIK
Institute of Theoretical and Experimental Physics, Moscow

N.M. ZUEVA, O.V. LOKUTSIEVSKIJ, M.S. MIKHAJLOVA
M.V. Keldysh Institute of Applied Mathematics,
Academy of Sciences, Moscow

Union of Soviet Socialist Republics

Abstract

NON-HYDRODYNAMIC MODEL OF PLASMA FOCUS STRUCTURE.

Experimental and theoretical plasma focus study has resulted in the necessity of creating a non-hydrodynamic plasma focus structure model (MKHD model). This model describes the final stage of plasma focus, which starts immediately after maximum plasma compression. It is related to a very limited space near the neck of the sausage instability. The MKHD model is two-dimensional, axially symmetric and collisionless with respect to the ions and magnetohydrodynamic with respect to the electrons; it accounts for the pinch instability of the sausage type (m = 0 mode). The MKHD model, first of all, explains the long time of the plasma focus existence and non-thermonuclear peculiarities in the neutron yield.– The MKHD model is solved numerically for a cylindrical region of 2 mm radius and 3 mm height, which contains the neck of the sausage instability. The initial and boundary conditions are formulated in accordance with the experiments and the results of computations in the 2D MHD model. A non-stationary process of plasma focus dynamics is studied numerically for a relatively long time – about 20 ns; this time is, in principle, not restricted. The computations show that the external edge of the neck expands rather slowly (at a speed that is lower than the thermal ion velocity, by an order of magnitude), and the magnetic field energy is converted to the kinetic energy of the chaotic ion motion (which is doubled for the time of computation). A 'supra-thermal' tail (with the deuterium ion energy higher than 10 keV) forms slowly at the ion distribution function; this tail determines a substantial part of the total neutron yield. The formation of stable vortices, which actually determine the structure of the plasma flow during the developed non-hydrodynamic stage of the plasma focus, is also found in the computations. These properties of the development of the sausage instability, as found in the numerical experiment with the MKHD plasma focus model, are in qualitative agreement with the behaviour of an instability of the same type in the MHD models of the Z-pinch.

It has been shown within the framework of a 2D MHD model [1] that the applicability conditions of the MHD approximation to the ion plasma component are violated at the sausage instability neck. Formally, the MHD model results in a disruption of the neck with the following properties: $R_{min} \to 0$, $n_{max} \to \infty$, $\Pi = n_{max} \times R_{mm}^2 = \text{const}$ ([1] and references therein). The MKHD model was developed and some numerical experiments on its basis were described in

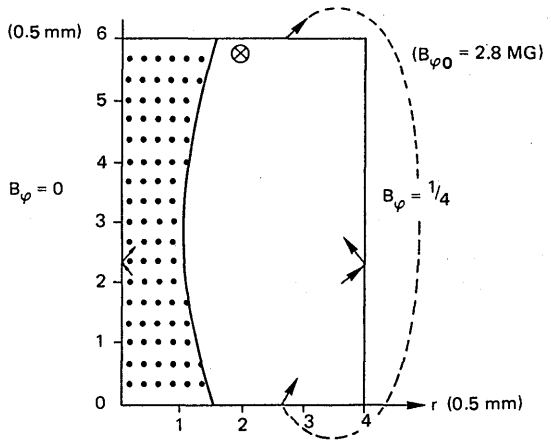

FIG.1. Region of computations, initial and boundary conditions.

Refs [2, 3]. The solution of the plasma focus dynamics problem is repeated in this paper, but with a considerably increased amount of ion macroparticles. We denote the charge and the mass of a deuterium ion by e_d and m_d, respectively, and the weight of a macroparticle by q. The amount of macroparticles in Ref. [3] was k = 5648 (each i-th macroparticle has a charge of qe_d and a mass of qm_d, and it looks like a thin ring around the plasma focus axis with cylindrical co-ordinates r_i, z_i). In the last run of computations we succeeded in obtaining k = 22 592. At each node of the difference mesh (r, z), at the initial instant of time, there were 32 macroparticles imitating a flat Maxwellian distribution (the velocities of the macroparticles in the azimuthal direction were equal to zero). A comparison with the previous computations, where the amount of macroparticles was four times less, has shown satisfactory coincidence of results, at least in the macroscopic values of the MKHD model: v_r and v_z are the radial and axial components, respectively, of the plasma velocity; B_φ is the azimuthal component of the magnetic field; n is the density of ions and electrons (under the condition of quasi-neutrality); T_e is the electron temperature; E_r, E_z are the radial and axial components of the electric field, respectively. All these quantities are the functions of three variables: r, z and t.

The region of computations, the initial conditions, as well as the boundary conditions of periodicity in the z-direction, and those of reflection in the r-direction are shown in Fig.1. Physically, the most important boundary condition is the prescription, in relative units, $B_\varphi = 1/4$ at the external boundary, r = 4. This condition corresponds to a direct current of $J_0 = 0.7$ MA. A system of units with $R_0 = 0.5$ mm, $I_0 = 0.7$ MA and $n_0 = 3 \times 10^{19}$ cm^{-3} as its basic parameters is adopted in the problem. In particular, $r_0 = z_0 = 0.5$ mm, $t_0 = 0.63 \times 10^{-9}$ s,

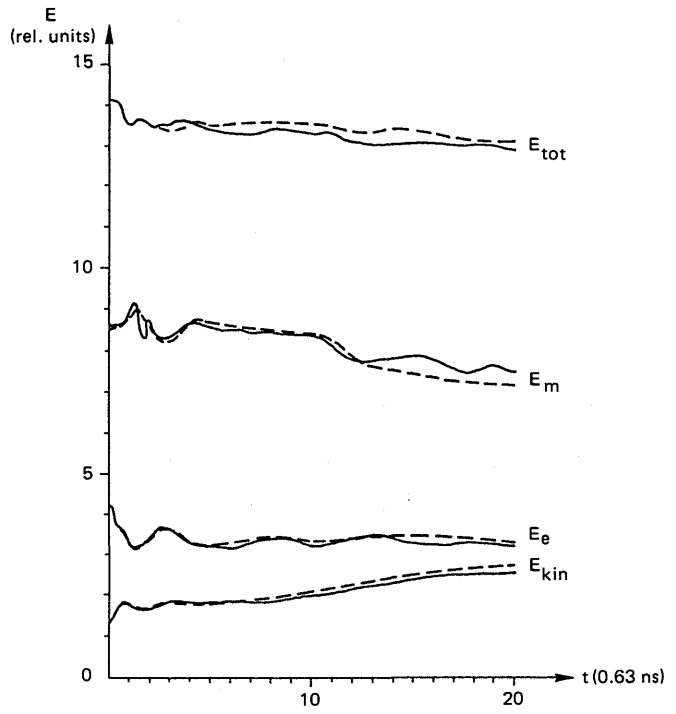

FIG.2. Energies versus time.

$v_0 = 7.9 \times 10^7$ cm·s^{-1}, $B_\varphi = 2.8 \times 10^6$ G, $n_0 = 3 \times 10^{19}$ cm^{-3}, etc. The initial position of the external neck edge is shown in Fig.1 by a solid trace. The macroparticles are located at the indicated nodes of the mesh on the left-hand side of this line. The integral energies (in relative units) of the plasma focus versus time are shown in Fig.2. The dashed traces correspond to computations with an amount of macroparticles that has been decreased by four times, from Ref. [3]. We may say that good agreement of the results is achieved. For a given problem (with the selected boundary conditions), the total energy, $E_{tot} = E_m + E_e + E_{kin}$, should be constant. Actually, it is conserved with an accuracy of 10%, which characterizes (integrally) the error in the difference method. The magnetic energy, E_m, decreases, to a certain degree, in time, the kinetic energy of ion motion, E_{kin}, rises noticeably, and the thermal energy of the electrons, E_e, is approximately conserved. A rather effective process of conversion of magnetic energy to kinetic energy for the chaotic (turbulent) motion of the collisionless ion plasma component takes place. In this case, a fraction of the ions (less than 10%) acquires rather high (suprathermal) velocities directed towards the cathode (positive direction of the z-axis).

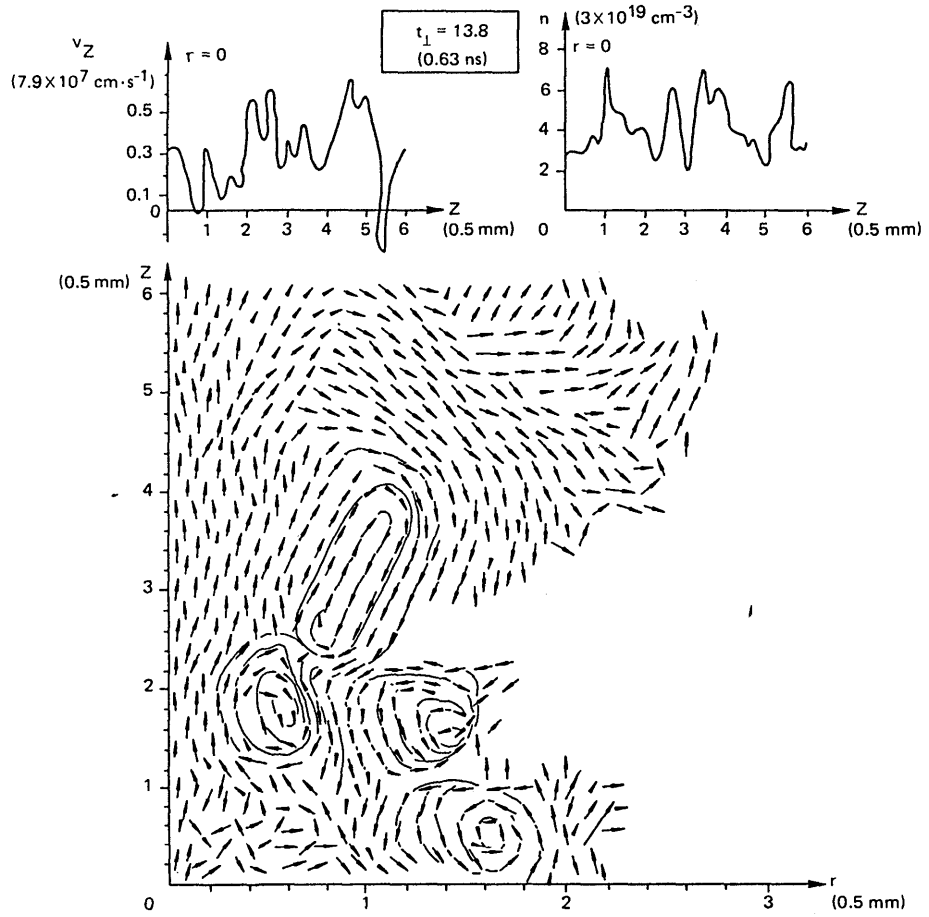

FIG.3. Velocity field in (r, z) plane for t_1 = 13.8.

The velocity fields in the r, z-plane are shown in Figs 3 and 5 (the arrows show the direction and the magnitude of the velocity vector). Figure 3 refers to the time t_1 = 13.8, Fig.5 to t_2 = 20 (in units of t_0 = 0.63 ns). These figures demonstrate the plasma vortices developed in the sausage instability neck. The smallest radius of the neck ('puncture') appears between two vortices of opposite rotation. Near the axis, the vortices are converted into a flow from the anode to the cathode (v_z = 0). The main vortex in the middle of the region is stable at the transition from time t_1 to time t_2. We also see that the characteristic magnitudes of the plasma velocities at this transition rise substantially (near the axis, in particular). The profiles of v_z (r = 0, z) and n (r = 0, z) for the same instants of time are given in Figs 3 and 5, besides the velocity field. They demonstrate the

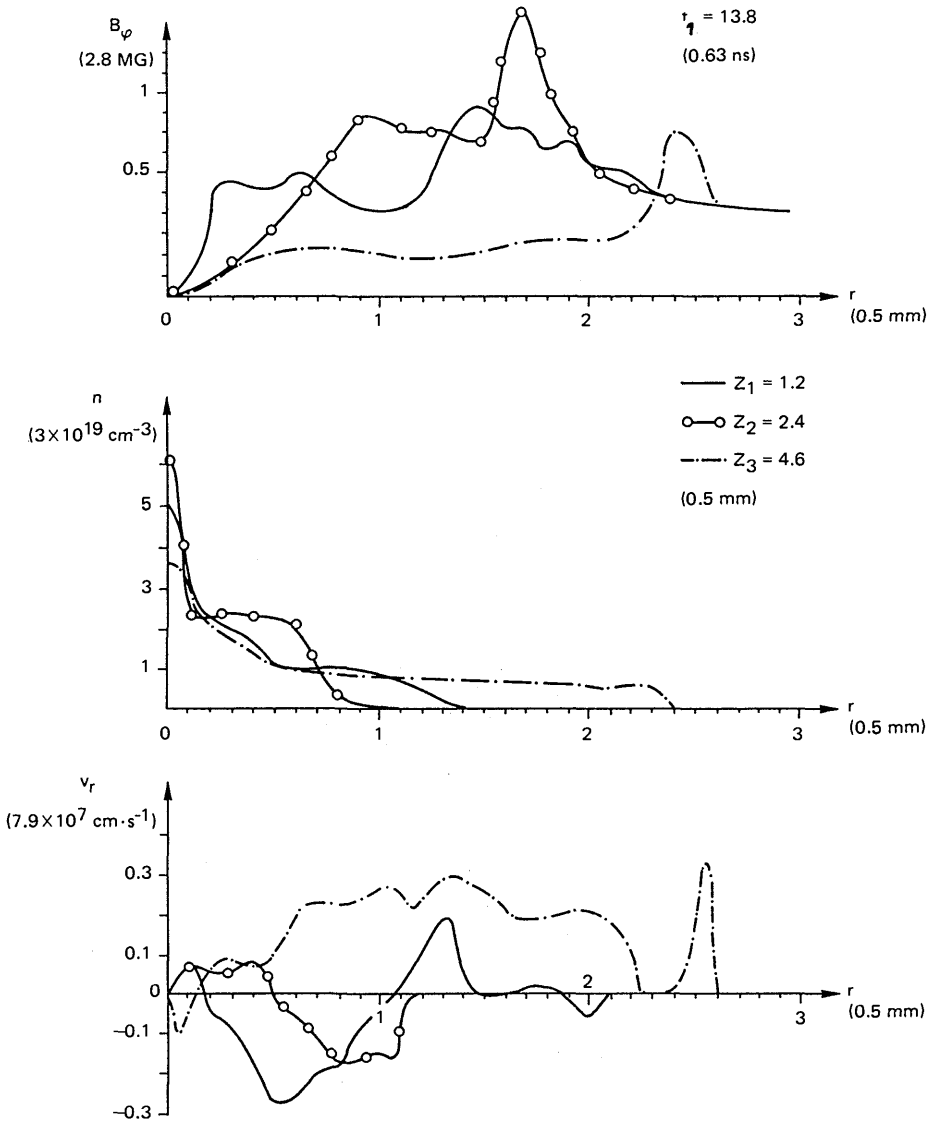

FIG.4. B_φ, n and v_r versus r for t_1 = 13.8.

properties of a vortex: high velocity, together with a low density at the most developed stage of the vortex, at a time of $t_2 = 20$. At last, the characteristics of the radial plasma focus structure, i.e. B_φ (r, z = z_j) profiles, n (r, z = z_j) profiles and v_r (r, z = z_j) profiles, where $z_1 = 1.2$, $z_2 = 2.4$ and $z_3 = 4.6$ determine the selected cross-sections of the computational region with respect to the Z-coordinate (j = 1, 2, 3), are given in Fig.4, corresponding to a time of $t_1 = 13.8$.

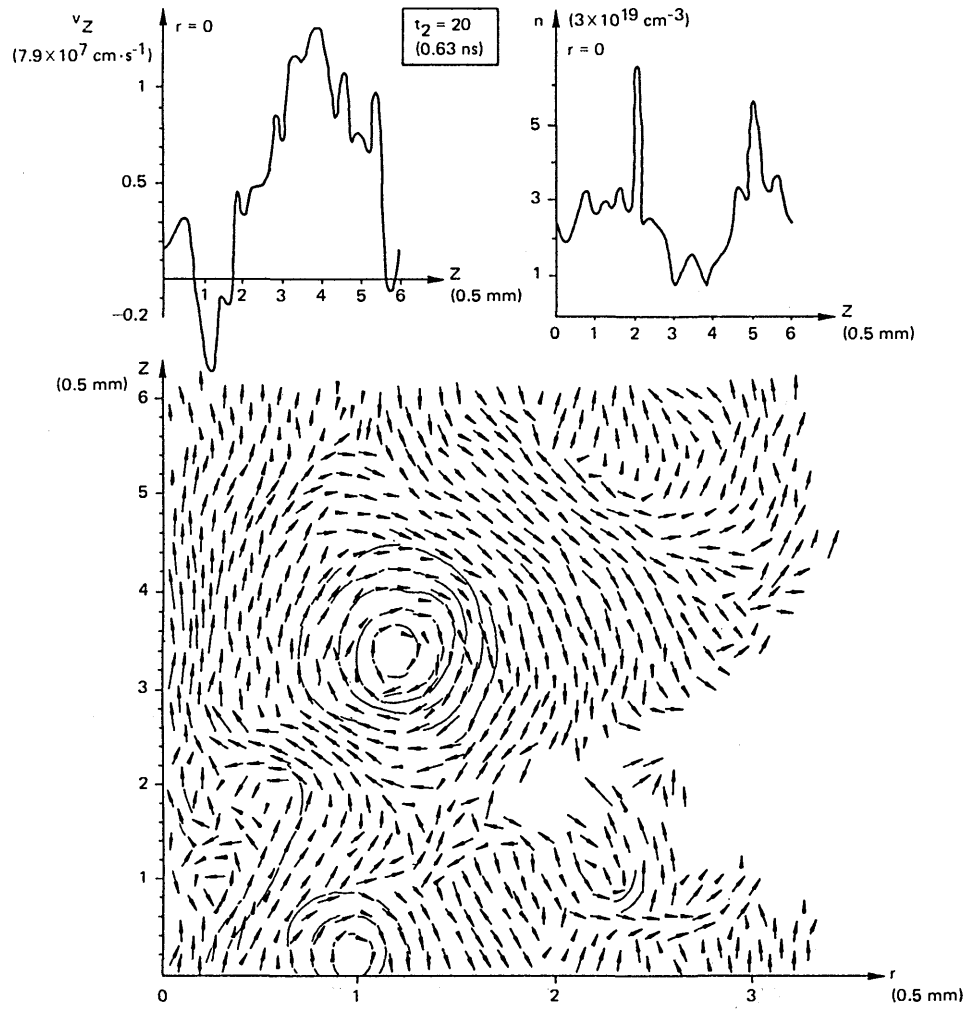

FIG.5. Velocity field in (r, z) plane for $t_2 = 20$.

The place of 'puncture' approximately corresponds to j = 2, the place of 'brow' corresponds to j = 1 and to j = 3; note that the 'brow' at j = 3 is the largest. The magnetic field B_φ and the radial velocity v_r have a complicated (turbulent) structure. The magnetic field penetrates deep into the plasma, limiting a small, dense plasma 'pinch' near the axis with n = 3–5 from a rarefied outer 'corona' with n = 1. At the place of a 'puncture' (j = 2) and at a small 'brow' (j = 1), the velocity averaged over the radius is considerably smaller than its amplitude as if magnetosonic waves were propagating through the plasma. At another 'brow'

(j = 2), $\bar{v}_r \approx 10^7$ cm·s^{-1}; meanwhile, the average macroscopic velocity has reached $\bar{w} \approx 10^8$ cm·s^{-1}, by this time. Note that there is a steep rise at r ≈ 0.2 on the graph of $B_\varphi(r)$ for $z_1 = 1.2$. This corresponds to an overturning of the $B_\varphi(r)$ profile due to a two-dimensional Hall effect. It is important to emphasize that the vortex plasma motion as developed in the MKHD simulation is in qualitative agreement with the vortices in the non-linear stage of instability development, m = 0, in the MHD models of the Z-pinch [4]. There it has been interpreted as a new quasi-stationary state of the Z-pinch, turned inside out. We also emphasize that the condition for collisionless ion motion to occur is well fulfilled up to the end of the computation.

Let us briefly note some difficulties in the MKHD plasma focus model: 1) insufficient feasibility of the simplest boundary conditions assumed (between rare MKHD plasma and dense MHD plasma); 2) complicated problem of the real significance of the azimuthal direction, in which in the MKHD model even the initial velocities $w_\varphi \neq 0$ are not taken into account; 3) complexity and incompleteness of the existing difference method, especially near the axis; 4) doubtful adequacy of a continuous description of the blurred plasma/vacuum boundary; 5) necessity of self-consistent account for the anomalous plasma conductivity (we use $\sigma_e = 10^{-2}\ \sigma_\perp$, where $\sigma_\perp$ is the classical conductivity across the magnetic field).

Undoubtedly the MKHD model describes, however, the most complicated stage of the experimental plasma focus to a sufficient accuracy and, in addition, includes great opportunities for development and modification that have not been made use of so far. On the other hand, the MHD model is found to be completely inadequate for the real conditions of the problem under discussion.

REFERENCES

[1] D'YACHENKO, V.F., IMSHENNIK, V.S., Two-Dimensional Magnetohydrodynamic Model of the Plasma Focus in the Z-Pinch, Voprosy Teorii Plazmy, Issue 8, Atomizdat, Moscow (1974) (in Russian).

[2] ZUEVA, N.M., IMSHENNIK, V.S., LOKUTSIEVSKIJ, O.V., MIKHAJLOVA, M.S., Model of Non-Hydrodynamical Stage in the Plasma Focus (Neck in the Z-Pinch), Prepr. No.73, Institute of Appl. Math. USSR, Moscow (1975) (in Russian).

[3] (a) IMSHENNIK, V.S., Non-Hydrodynamic Model of Plasma Focus (to appear).
(b) ZUEVA, N.M., IMSHENNIK, V.S., LOKUTSIEVSKIJ, O.V., MIKHAILOVA, M.S., Numerical Study of Plasma Focus with a Non-Hydrodynamical Model, in Two-Dimensional Numerical Plasma Models, M.V. Keldysh Institute of Appl. Math., Moscow (1979) (in Russian).

[4] (a) GERLAKH, N.I., ZUEVA, N.M., SOLOV'EV, L.S., MHD Instability Development in the Z-Pinch, Prepr. No.83, M.V. Keldysh Institute of Appl. Math. (1979) (in Russian).
(b) ZUEVA, N.M., SOLOV'EV, L.S., Non-Linear Development of MHD Instability, Prepr. IAE-3300/1 (1980) (in Russian.)

CORRELATION BETWEEN CHARGED-PARTICLE BEAMS AND NEUTRON EMISSION IN A DENSE PLASMA FOCUS

K. HIRANO, T. YAMAMOTO, K. SHIMODA,
K. KOBAYASHI
Department of Electronic Engineering,
Gunma University, Kiryu, Gunma

M. YOKOYAMA, Y. YAMAMOTO, A. KISODA, Y. YAMADA,
Y. KITAGAWA, M. YAMANAKA, C. YAMANAKA
Institute of Laser Engineering, Osaka University,
Suita, Osaka

Japan

Abstract

CORRELATION BETWEEN CHARGED-PARTICLE BEAMS AND NEUTRON EMISSION IN A DENSE PLASMA FOCUS.

The neutron production mechanism is investigated through a time correlation between the plasma dynamics, including the distribution of the magnetic field, the electron density, the emission of X-rays, charged-particle beams and neutrons in a plasma focus discharge. A method was developed to obtain the time-resolved azimuthal field distribution, using polarimetry and moiré schlieren technique. The experimental results show that in the low-pressure mode, high-energy deuterons and protons are generated by the plasma diode, because of the disruption of the pinched column, and the diode is produced from radiative cooling by high-Z impurities. Also, neutrons are generated by a beam target model in which deuterons below 80 keV can contribute. In the high-pressure mode, deuterons below 50 keV contribute to the neutron emission, but it is not so clear as to be explained by a simple beam target model.

1. INTRODUCTION

The plasma focus is not only a suitable device for detailed studies of fundamental plasma physics, but also one of the complementary fusion devices lying between a low-β tokamak and a high-compression inertial-fusion device.

The plasma focus device emits intense bursts of neutrons, X-rays and charged-particle beams. This fact makes the plasma focus one of the most efficient pulsed neutron, X-ray or charged-particle beam sources. Moreover, recent developments of the plasma focus, both theoretically and experimentally, seem to suggest the possibility of a break-even reactor [1]. However, even the burst mechanism has not been fully understood, in spite of investigations from various points of view.

In the present paper, the neutron production mechanism is investigated through a time correlation between the plasma dynamics, including the distribution of the discharge current and emission of X-rays, charged-particle beams and neutrons. Though the neutron yield Y_n is always scaled, as to $Y_n = I_p^{3.3-4}$, where I_p is the plasma current, a reliable method of measuring the current without disturbing the plasma has hardly ever been proposed. In this work, a polarimetric technique using Faraday rotation was employed. To measure the angle, a wedge made of quartz and preparing parallel fringes beforehand has been developed [2]. Deflection of the probe light by the gradient of the electron density, ∇n_e, also causes a rather substantial fringe shift. To solve this problem, ∇n_e is observed by a moiré schlieren technique and is used in the course of polarimetric data processing.

2. APPARATUS

Two Mather-type plasma focus devices, A [3] and B [2], are used in the present paper. Device A was operated at 30 kV for a stored energy of 18 kJ at 1.5 torr D_2 (low-pressure mode) and at 5 torr D_2 (high-pressure mode), respectively. A capacitor bank of 4×1.06 μF was used to energize device B. For device A, high-energy deuterons and protons were measured by nuclear activation techniques [4]. Radioactivity induced in graphite, aluminium and copper targets provided the deuteron intensity, energy spectrum and angular distribution. The deuteron energy was analysed by using a stack of ten aluminium foils. High-energy protons were also measured by cellulose nitrate particle track detectors. The data were analysed by using the computer MELCOM-COSMO 700II.

For device B, the measurement of the spatial distribution of the magnetic field due to the collapsing plasma was carried out by a polarimetric technique. To observe the macroscopic plasma behaviour, a moiré-schlieren technique in the streak mode was employed. We had background fringes every 180° of the Faraday rotation angle by the quartz wedge. To increase the number of fringes, levorotatory and dextrorotatory quartzes were combined. When a Faraday rotation by a time-varying magnetized plasma is superposed on the background fringes, we could detect the Faraday rotation by the plasma as shift in the background fringe with time. The Faraday rotation angle and the moiré-schlieren pattern were simultaneously recorded by an image camera through the slits in the streak mode. Time-resolved measurement of the ion and electron beams produced in the focused plasma was carried out by a Thomson parabola analyser and a Cherenkov detector with rise-times of 2.3 and 0.3 ns, respectively.

The time-varying voltage across the electrode was observed by a resistive divider.

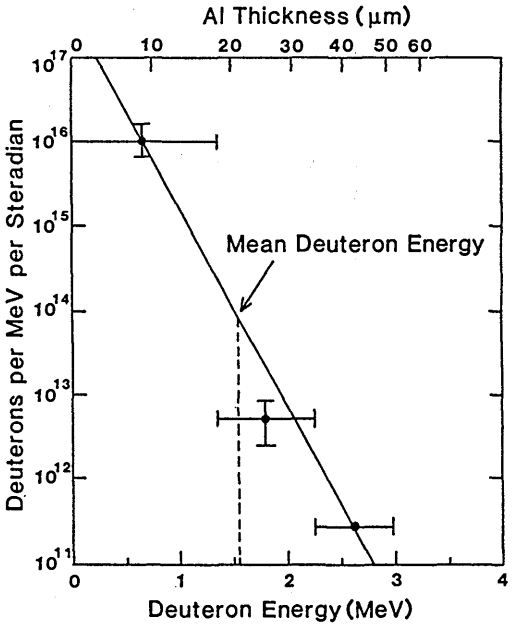

FIG.1. Deuteron energy spectrum measured by aluminium foil stack.

3. RESULTS AND DISCUSSION

Figure 1, which was obtained by device A, shows the deuteron energy spectrum with a deuterium filling gas pressure of 1.5 torr D_2 (low-pressure mode) for 30 kV/18 kJ focus operation. In the low-pressure D_2 mode, the main energy was up to 2 MeV and the high-energy tail reached from 2 MeV to more than 3 MeV. The ratio of the $^{12}C(d,n)\,^{13}N$ and $^{27}Al(d,n)\,^{28}Al$ reactions determined the mean deuteron energy as 1.5 MeV for 1.5 torr D_2 and 1.4 MeV for 5 torr D_2, respectively, as is shown in Fig.2.

For a hydrogen filling gas pressure of 4.2 torr (low-pressure mode), the proton energy spectrum was obtained by using a CN film track detection technique as is shown in Fig.3. The spectrum consisted of an exponentially decreasing component and a high-energy tail of up to 2 MeV for 30 kV/18 kJ operation. The experimental equations for the proton energy spectrum can be written as follows:

$$\frac{dn}{dE_p} = 10^9 \exp(-8.8\,E_p) \qquad (E_p \leq 1\ \text{MeV})$$

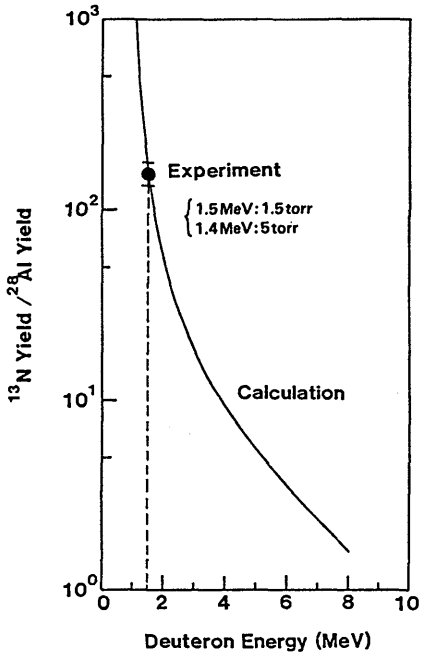

FIG.2. Mean deuteron energy obtained from $^{12}C(d,n)^{13}N$ and $^{27}Al(d,n)^{28}Al$ ratio.

and

$$\frac{dn}{dE_p} = 3 \times 10^5 \exp(-0.9\, E_p) \qquad (E_p \gtrsim 1 \text{ MeV})$$

The mean proton energy was lower than 1 MeV. The angular distribution of the protons was obtained by analysing the latent track images in the CN films. The high-energy protons of energies exceeding 800 keV concentrated in a cone angle of 10° around the axis.

The angular distribution of the deuterons showed a single peak on the axis at 1.5 torr D_2, while the distribution at 5 torr D_2 had two peaks at 10° and 60°, which may be due to the azimuthal rotation of the deuterons about the axis.

The location of the places of ion generation was measured by using two ion pinhole cameras located in the radial and axial directions. The pinhole was made of 2 mm thick lead, and the film was Kodak CN 85. The film on the Z-axis was filtered by 17 μm thick aluminium. The axial location of the deuteron image at 3 mm on top of the anode agreed with that of the pinched-column disruption recorded by holographic interferograms. The pinhole images in both radial and

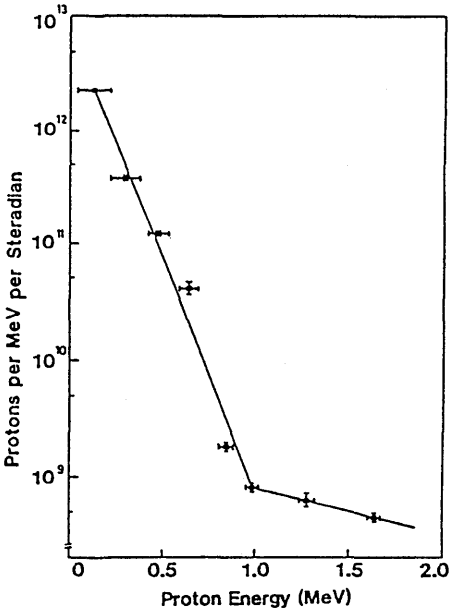

FIG.3. Proton energy spectrum measured by CN film.

axial directions showed that deuterons were generated from a multiple filament-like source.

The high-energy electron beam was also observed by detecting the hard X-rays due to electron bombardment of the inner electrode. By an Si PIN detector with a 1 mm thick layer of lead, the high-energy (>300 keV) electron beam was observed at 4.0 torr H_2 under 30 kV/18 kJ operation. The electron beam pulse width was 10 ns.

The ion temperature, T_i, was obtained by measuring the D-D/D-^{3}He reaction ratio. In operating a molecular mixture of D_2 and ^{3}He in the high-pressure mode, T_i of 5.0 keV is estimated on the assumption that a thermonuclear model can be used. In the low-pressure mode operation, a plasma directional energy E_d of 74 keV is estimated if the validity of a beam target model is assumed.

The neutron energy spectrum was measured by a TOF method using a scintillation detector, and the absolute yield was estimated by an Ag and Dy activation method combined with counter. The maximum neutron emission was 2×10^9 neutrons per shot. The location of the neutron source was directly determined by a neutron pinhole camera and a scintillation detector. Figures 4 and 5 show the axial and radial intensity distributions of the neutron emission. Figure 6 shows an isointensity contour display of the neutron source on top of the focus anode. It is seen that the highest density of neutrons is located up to 2 cm above the anode tip with a maximum radius of 0.5 cm, and the emission is

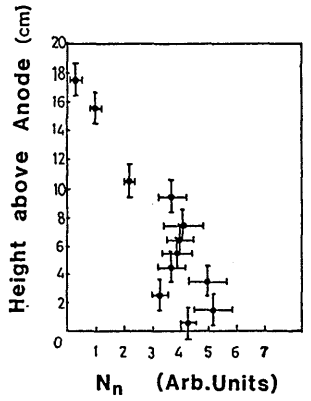

FIG.4. Axial intensity distribution of neutron emission.

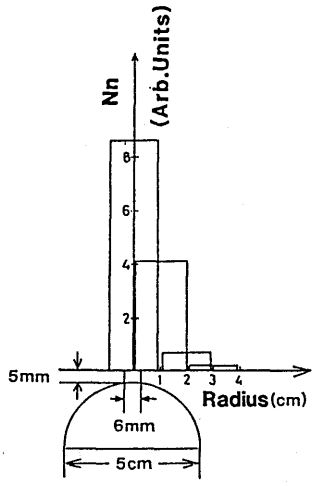

FIG.5. Radial intensity distribution of neutron emission.

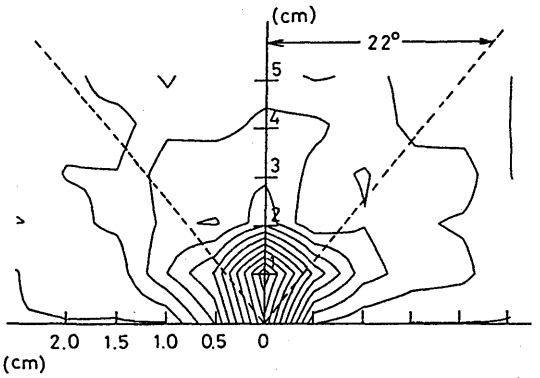

FIG.6. Isointensity contour display of neutron source by using double collimators.

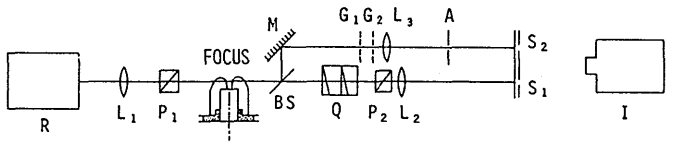

FIG.7. Optical alignment of polarimetric and moiré schlieren technique. R: ruby laser; L_1 to L_3: lenses; P_1, P_2: polarizers; M: full mirror; BS: beam splitter; Q: quartz wedge; G_1, G_2: ronchi gratings; A: aperture; S_1, S_2: slits; I: image converter camera.

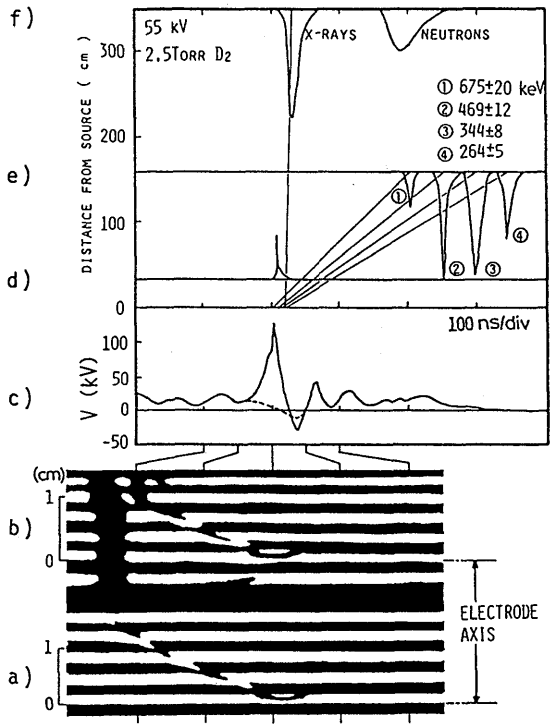

FIG.8. (a) Example of polarimetry in streak mode, (b) moiré schlieren, (c) voltage across electrode, (d) electron beam, (e) time and distance plots of energy-analysed deuteron beams, (f) X-rays and neutrons.

within a cone angle of 44° ± 10°, where the top of the cone is located at the anode tip.

The optical alignment of the polarimetry and the moiré schlieren technique for device B is shown in Fig.7. A typical example for the time correlation among the dynamic behaviour of the plasma, the voltage spike and the emissions is shown in Figs 8(a) to (f). As is shown in Fig. 8(c), the onset of the voltage spike appears faster than the other signals. In some shots, we had no voltage spikes, as

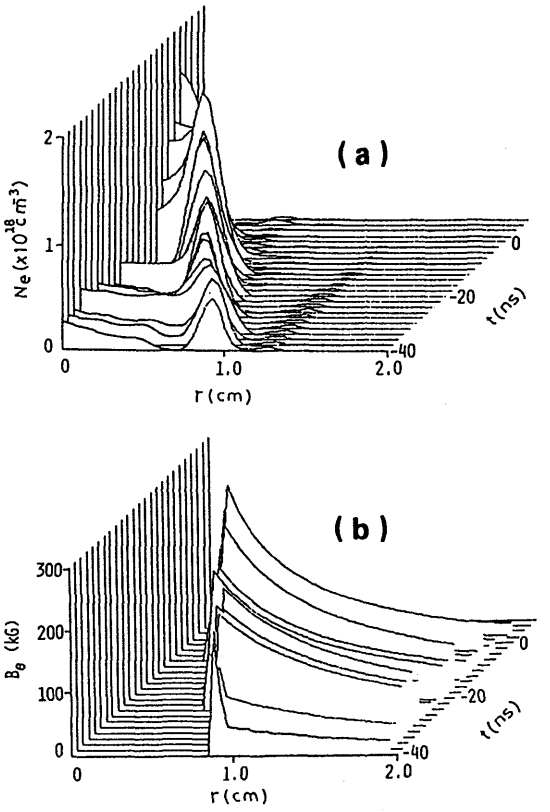

FIG. 9. (a) Time-resolved spatial distribution of electron density calculated by using Fig. 8(b). (b) Time-resolved spatial distribution of azimuthal magnetic field calculated by using Figs 8(a) and (b).

is shown by the dotted line in Fig. 8(c). The point at which it is determined whether or not a spike will appear occurs during the collapse phase of the current sheet. In such shots, no X-rays, neutrons, electron or ion beams are generated. The disruption of the plasma column occurs in the upward slope of the voltage spike, and the peak comes after the disruption. Just after the voltage peak, the electron signal which consists of an extremely steep and narrow component and a rather broad component appears, as is shown in Fig. 8(d). Peaks of energy-analysed ion beams observed in the downstream direction appear around the sharp peak of the electron signal as is shown in Fig. 8(e). These are concentrated in an interval of 20 ns. Nearly at the end of the interval which is after the disruption of the plasma column a peak of hard-X-ray signals is observed as is shown in Fig. 8(f). The peak of the neutron signal drops in the interval which is formed by the energy-analysed

ion peaks mentioned above if we assume a neutron energy of 2.45 MeV. The deuteron energy was found to be distributed from 100 keV to nearly 2 MeV with an FWHM less than 20 ns. Even in discharges which did not produce X-rays or neutrons, a growth of the m = 0 instability was observed by framing interferometry. Neutrons were only emitted when voltage spike and beams were generated. This means that the growth of the m = 0 instability, i.e. a rapid change in plasma inductance, is not directly correlated with the voltage spike.

The time- and space-resolved electron density, $n_e(r,t)$, and the azimuthal magnetic field, $B_\theta(r,t)$, can be obtained from Figs 8(a) and (b) by Abel inversion, on the assumption of axisymmetry. The calculated results are shown in Figs 9(a) and (b), respectively. The time zero refers to the maximum pinch of the plasma. The profile of the collapsing plasma shown in Fig. 9(a) is quite similar to that provided by the interferometric results, but the electron density peak (1.6×10^{18} cm^{-3}) is approximately five times lower than that resulting from interferometry, which overestimates the electron density by nearly a factor of five, because of the deflection caused by ∇n_e. At maximum pinch, we see that the value of $B_\theta(r,t)$ is approximately 210 kG.

After the disruption, by the m = 0 instability, the plasma cannot be studied by optical means such as interferometry, moiré schlieren technique or polarimetry. If we assume an anomalous resistivity by field anihilation in the focus phase, which was proposed by Gary [5], as $\eta^* = \mu_0 L^2/\tau$, the resistance R is estimated to be 0.4Ω for τ = 10 ns and current channel of 1 cm length. This resistance is sufficient to generate a voltage with a peak of about 100 kV.

4. SUMMARY

In conclusion, we may say that the experimental results show that in the low-pressure mode, high-energy deuterons and protons are generated by a plasma diode due to the disruption of the plasma column, and the diode is produced by radiative cooling due to high-Z impurities. Also, neutrons are generated according to a beam target model in which deuterons below 80 keV can contribute. In the high-pressure mode, deuterons below 50 keV contribute to the neutron emission but this is not so clear to explain by a simple beam target model.

The generation of electron and ion beams concentrates in an interval of 20 ns around the voltage spike peak. The peak of the hard-X-ray signal is observed after the disruption of the plasma column.

m = 0 instabilities are observed even if voltage spike and emission of charged-particle beams, X-rays and neutrons do not occur. The acceleration of the charged-particle beam is not generated by a rapid change in plasma inductance, but by an abrupt rise in the plasma resistivity.

REFERENCES

[1] HEROLD, H., HAYD, A., in Plasma Focus Research (Proc. 3rd Int. Workshop, Stuttgart, 1983), IPF-83-6 (1983) 131.
[2] HIRANO, K., et al., in Controlled Fusion and Plasma Physics (Proc. 11th Europ. Conf. Aachen, 1983), Vol.1 (1983) 551.
[3] YOKOYAMA, M., KITAGAWA, Y., YAMADA, Y., YAMANAKA, C., HIRANO, K., in Plasma Physics and Controlled Nuclear Fusion Research 1980 (Proc. 8th Int. Conf. Brussels, 1980), Vol.2, IAEA, Vienna (1981) 187.
[4] YOKOYAMA, M., et al., in Plasma Physics and Controlled Nuclear Fusion Research 1982 (Proc. 9th Int. Conf. Baltimore, 1982), Vol.2, IAEA, Vienna (1983) 415.
[5] GARY, S.P., Phys. Fluids **17** (1974) 2135.

TWO PHASES OF NEUTRON PRODUCTION IN THE POSEIDON PLASMA FOCUS*

H. HEROLD, L. BERTALOT, K. HIRANO**,
U. JÄGER, H.J. KAEPPELER, M. SADOWSKI+,
H. SCHMIDT, R. SCHMIDT, M. SHAKHATRE, A. SHYAM++
Institut für Plasmaforschung,
Universität Stuttgart

G. BÖCKLE, K. MATL, N. WENZEL, R. WOLF,
R. BÄTZNER, H. HINSCH, K. HÜBNER
Institut für Angewandte Physik,
Universität Heidelberg

Federal Republic of Germany

Abstract

TWO PHASES OF NEUTRON PRODUCTION IN THE POSEIDON PLASMA FOCUS.

Various measurements performed in the 280 kJ, 60 kV operational mode of the Poseidon plasma focus confirm that at high pinch currents (≈1 MA) there exist two phases of suprathermal neutron production. In the pinch phase, the neutron emission from a macroscopically smooth, relatively quiet thermal ($T_i \approx 1-0.4$ keV) plasma column is very likely caused by accelerated deuterons (≲400 keV) trapped for up to 100 ns in the pinch by gyro-motion and relaxation. MHD calculations suggest that the acceleration may be due to MHD instability-induced reconfiguration process, leading to current filamentation and high B_z-fields. Filaments, particularly a central filament, were observed in soft X-ray pictures. Indications for B_z-fields ($B_z \leqslant 0.3\ B_{\varphi max}$) were deduced from the directions of the reaction proton trajectories. The rather irreproducible strong neutron production in the second phase is associated with m = 0 pinch break-ups and with fast deuterons accelerated mainly in the axial direction.

1. INTRODUCTION

Studies have been performed concerning turbulence, non-equilibrium phenomena, ion acceleration and neutron production in the Poseidon plasma focus. The measurements were carried out at 280 kJ, 60 kV, with a hollow anode,

* Work supported by the Deutsche Forschungsgemeinschaft.

** Fellow of the A. v. Humboldt Stiftung, on leave from Gunma University, Kiryu, Japan.

+ Fellow of the A. v. Humboldt Stiftung, on leave from Institute for Nuclear Studies, Świerk, Poland.

++ On leave from Bhabha Atomic Research Centre, Trombay, India.

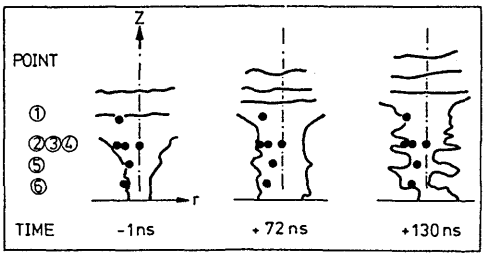

	z[mm]	r[mm]
①	43	10
②	28	11
③	28	7
④	28	0
⑤	19	5
⑥	10	8

FIG. 1. Observation positions for laser light scattering. Focus contours are taken from Schlieren pictures.

mostly in the neutron optimized regime (5 mbar) with pinch currents of about 1 MA and neutron yields up to 10^{11}. In this operational mode, the Poseidon focus exhibits two distinctly separated phases of strong neutron production with different plasma dynamical characteristics [1]. The pinch phase from maximum compression until m = 0 instability onset is characterized by a rather smooth compressed plasma column, whereas the second or late phase is dominated by m = 0 pinch break-ups and possibly by post-m = 0 macroturbulence phenomena.

2. LASER LIGHT SCATTERING

Laser light scattering experiments were performed at six different positions in the focus pinch plasma (Fig.1). Both k-spectra and ω-spectra were measured simultaneously. The incident beam of the ruby laser (Δt = 25 ns) and the scattering k-vectors were oriented in a plane perpendicular to the z-axis. The observation volume had a typical diameter of 2 mm. The diagnostic system consisted of 11 S(k) elements positioned at $10°-120°$ and one $S(\omega)$ element at 45°. The scattering signals from each channel were integrated (Δt = 12 ns) and digitalized. Both S(k) and $S(\omega)$ diagnostics were calibrated absolutely by Rayleigh scattering in CO_2.

At every observation point, scattering spectra were observed which can be interpreted according to the Salpeter approximation by scattering in thermal plasmas (Fig.2 gives examples). Electron densities and temperatures were evaluated from k-spectra or, by absolute calibration, from ω-spectra; ion temperatures were evaluated from ω-spectra.

Figures 3 and 4 show the time development of plasma parameters on the axis. The temperatures and the density are characterized by a significant rise near maximum compression with $T_{i,max} \approx 1$ keV, $T_{e,max} \approx 600$ eV (12 ns time-integrated) and by axially peaked radial profiles. During the pinch phase these values drop considerably, the radial temperature profiles become flat and n_e shows a hollow profile. After pinch break-up, T_i and n_e again attain maxima,

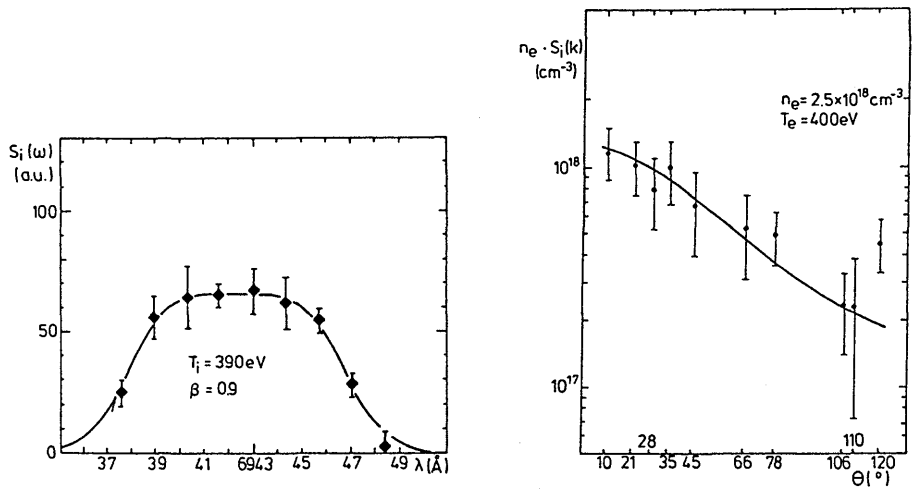

FIG.2. ω- and k-spectra, fitted according to the Salpeter approximation. The polychromator has a linear dispersion of 1.35 Å/channel.

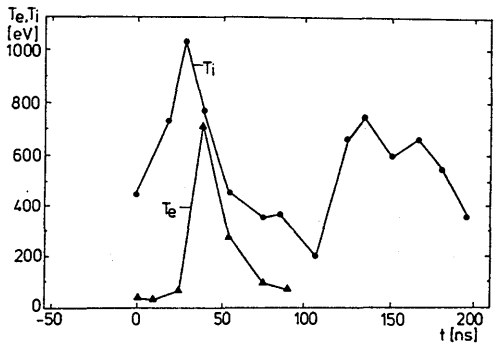

FIG.3. Time development of plasma temperatures at position 4 (on axis), determined by laser light scattering. Each point represents the average of different discharges with similar scattering time. t = 0 maximum compression.

but only at the axis with $T_{i,max} \approx 700$ eV. A preliminary analysis shows a second maximum of the electron temperature in the late phase, with values up to ≈500 eV in outer observation points.

Different classes of spectra with deviations from thermal scattering were observed. Some ω-spectra at position 1.3 and 5 show a narrow peak at the ruby line with enhancement factors S/S_{th} up to 7 or peaks shifted toward long wavelengths enhanced by a factor ≲2 over a bell-shaped basis. Several interpretations seem possible. For example, such spectra may be due to scattering in a

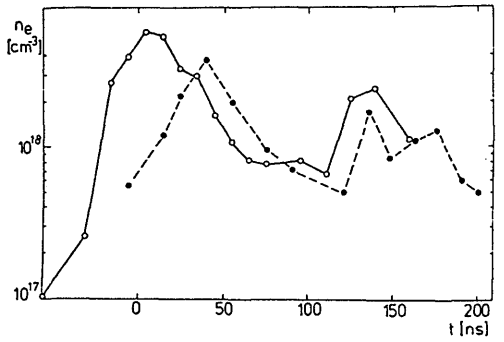

FIG.4. Time development of scattering (●) and interferometric (○) electron density at position 4. Each point represents the average of different discharges with similar scattering time. Interferometric data are space-integrated across the scattering volume.

thermal deuterium plasma contaminated with copper. Another class includes k-spectra having only signals at small angles as well as k-spectra that can be fitted following the Salpeter theory but show enhanced scattering at small angles with enhancement factors of typically 2 to 15. These types occur preferentially during the rise of the second neutron pulse in off-axis regions of the pinch plasma. They coincide with the second peak in temperatures and density. With increasing radius of the observation position, the number of such events grows. Spectra of these types were also detected by former light scattering measurements at the plasma focus devices in Frascati [2] and Heidelberg. The spectra may be interpreted assuming scattering in a non-thermal plasma, but a preliminary analysis of simultaneously performed interferometric measurements shows that density gradients in the scattering volume may affect the results.

3. NEUTRON, REACTION PROTON AND DEUTERON EMISSION PROPERTIES

The source structure, the time-resolved flux anisotropy and the time correlations of neutron emission to other radiations have been studied for different filling pressures. The results were completed by measurements of reaction protons and fast deuterons, particularly by analysing spectra and source structures. Particle track detectors were used for detecting reaction protons and deuterons; scintillator-multiplier systems with 2 ns time resolution were used for time-resolved measurements.

3.1. Time correlations

Figure 5 shows the double-humped neutron signal, time-correlated to fast deuteron, hard X-ray and fast electron emission for a typical shot at 5 mbar. The ion signals were obtained with a magnetic spectrometer, end-on, and the electron signals with a Čerenkov detector. The results reveal that coincident with both neutron pulses there appear pulses (or pulse trains) of fast deuterons, again coincident with mostly single pulses of hard X-rays and fast electrons. Hence, at least two main time-separated ($\Delta t \approx 200$ ns) acceleration phases for deuterons and electrons occur. The spectrum of the pinch phase deuterons ranges to about 400 keV, whereas the late phase ions (pulse(s) at $t \gtrsim 200$ ns) have a broader energy distribution from $E_d \approx 200$ keV (lower detection limit) to $E_d \approx 1.5$ MeV and irreproducibly also to higher energies of up to 4–5 MeV. It is interesting to note that the neutron emission begins regularly up to ≈80 ns before the maximum pinch compression, a fact also observed in Ref. [3].

3.2. Neutron and proton source structure

A neutron pinhole equipped with a detecting array (8 X 8) of scintillators was used to determine the time development of the source in single shots. The space resolution was about 2 cm at the source. With reaction proton pinhole cameras, far better spatial resolution (≈3 mm) could be achieved, although only in time-integrated pictures. The deviation of the proton trajectories by the focus magnetic fields and the correction for the proton images were analysed mathematically. Figure 6 shows typical z-distributions (r-integrated) of neutrons. The results reveal that the source of the first neutron pulse extends over a rather small z-region from $z \approx -2$ cm to $z \approx +6$ cm ($z = 0$: anode end). Whereas this source stays approximately spatially fixed, the source of the second neutron pulse grows in the +z direction roughly synchronous with the front of the dense plasma taken from interferograms and extends over the whole length (about 12–14 cm) of the neutron-emitting region.

About 50% of the proton pictures show a radial shift of the source (Fig.7) particularly in the vicinity of the anode, which is not present in neutron images. According to ion optical calculations, such shifts can only be caused by axial B-fields in the pinch. From the amplitude of the radial shift a $B_z \lesssim 0.3\ B_{\varphi max}$ is deduced. A purely azimuthal B-field produces essentially only an axial shift of $\Delta z \approx 2$ cm for the present focus parameters. Spontaneously occurring B_z-fields were also detected in the Frascati MJ plasma focus by Faraday rotation measurements [4].

3.3. Reaction proton spectra and angular proton distribution

Reaction proton spectra in different angles θ to the z-axis have been measured, applying Cr39 films and 54-step Al filters [5]. To interpret the results

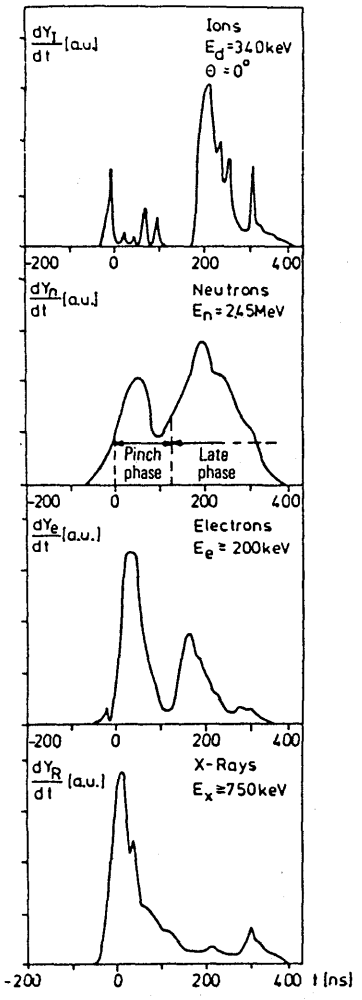

FIG.5. Time-correlated signals of fast ions, neutrons, electrons and hard X-rays. t = 0: maximum compression. $W_0 = 280$ kJ; $p_0 = 2$ mbar, D_2.

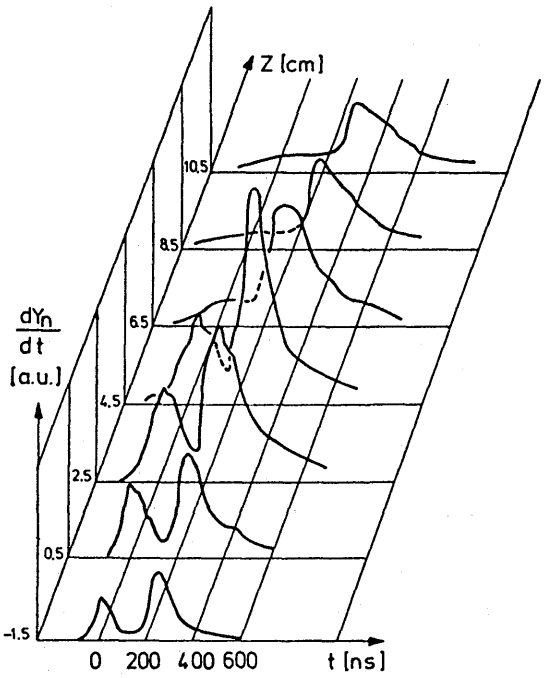

FIG.6. Axially resolved (r-integrated) time development of neutron emission, taken with neutron pinhole from a single shot. Resolution $\Delta z = 2$ cm; $W_0 = 280$ kJ; $p_0 = 5$mbar, D_2.

a new model was developed, henceforth called the 'gyrating particle model' (GPM), the essence of which is the determination of fast deuteron trajectories in a model focus plasma with $T_e(r_{pl}(z,t); z_{pl}(t); t)$ and $n_{e,i}(r_{pl}(z,t); z_{pl}(t); t)$ approximated to experimental results. Energy losses of the deuterons by elastic collisions $dE_d/dx = f(E_d, n_e, T_e)$ and fusion collisions ($\sigma_f(E_d, \vartheta_{d-n})$) are taken into account by superimposed Monte Carlo treatments. Arbitrary conditions for the initial

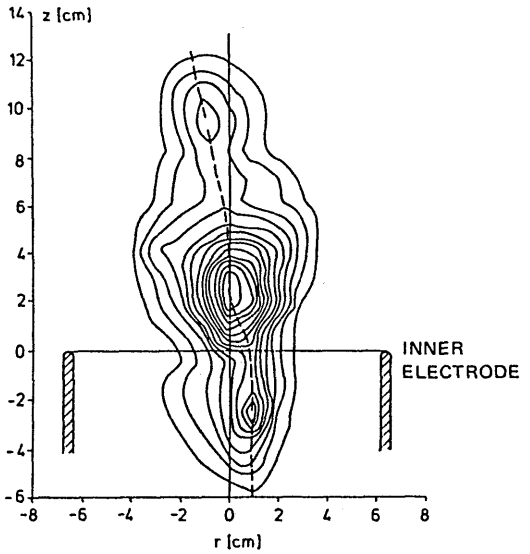

FIG.7. Pinhole picture of reaction proton source, uncorrected for beam deviation by focus magnetic fields. Contours are lines of constant proton density on the film. $W_0 = 280$ kJ; $p_0 = 5$ mbar, D_2.

fast deuterons (source location, spectrum, angular distribution) and the current density j(r,z,t) can be chosen.

Figure 8 shows typical spectra taken in different directions θ from a single shot. These spectra may be compared with the results of the GPM, Fig.9, which give the spectral position of the proton line together with the spectral width (FWHM) as a function of θ. An initial energy distribution of the fast deuterons denoted as a pseudo-temperature distribution T_i^* (see Fig.9) was assumed. Inspection of about 200 spectra suggests that the experimentally obtained spectral shapes (time-integrated) are essentially determined by the superposition of two main lines: (1) a quasi-thermal line, well described by the GPM, and (2) a main axial beam target line. In the example, (2) can be identified at about 3.7 MeV ($\theta = 28°$ in Fig.8). A component with higher energy (4.1 MeV) is also visible. In 5 mbar neutron-optimized shots mainly the quasi-thermal emission is dominant, and the total FWHM becomes quite large, as seen in Fig.8. At lower pressures (2 mbar), on the other hand, the axial beam target appearance of the spectra prevails. From time-resolved flux anisotropy measurements [5] it must be concluded that the quasi-thermal line belongs to the first neutron pulse, and the axial beam target line(s) to the second pulse. In lower energy PF devices with late single-pulse neutron emission, the neutron spectra exhibit a somewhat modified general beam target character [6].

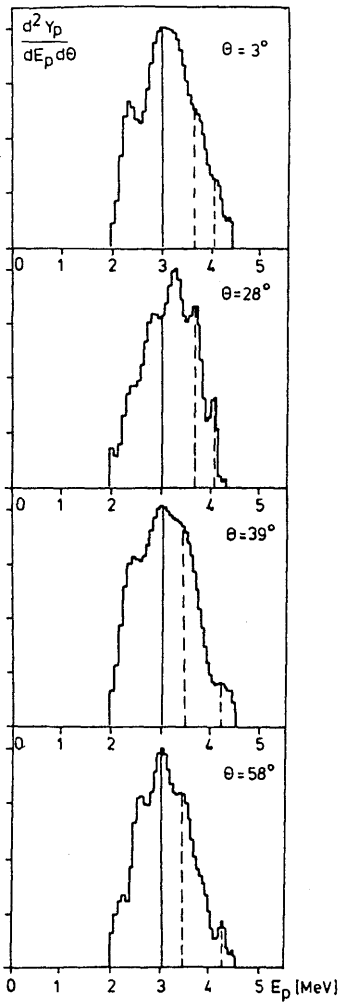

FIG.8. Reaction proton spectra from a single shot for four angles of observation θ (θ = 0 end on). E_p is proton energy; $W_0 = 280$ kJ; $p_0 = 5$ mbar, D_2; total neutron yield 5.4×10^{10}.

From the GPM calculations it turns out that the fast deuterons are 'trapped' for some time in the focus pinch owing to their gyro-motion and relaxation. The ratio of the trapping time to the axial transit time is about 2 to 3 for T_i^* of some 50 keV. This is compatible with the duration of the first neutron pulse of about 100 ns (FWHM 50 ns). The GPM is further checked by measuring the angular distribution of the total reaction proton emission. Agreement is quite good (Fig.10). Since the calculated distributions are dependent on the amount of the pinch current I_p, experimental values of I_p can be determined.

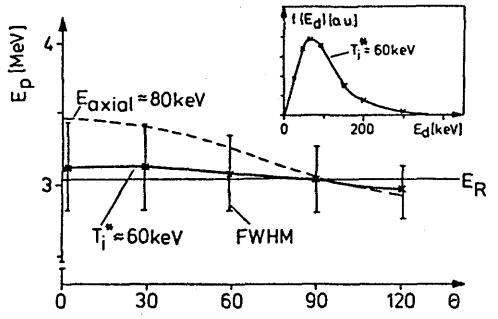

FIG.9. Energy of reaction proton line and FWHM of spectra for different directions of observation θ (θ = 0 end on; θ = 90° side on), calculated with the gyrating particle model. The insert gives the chosen initial energy distribution T_i^* of fast deuterons. E_{axial} is the position of the proton line for an axial beam target process with $E_d \approx 80$ keV. E_R is proton reaction energy.

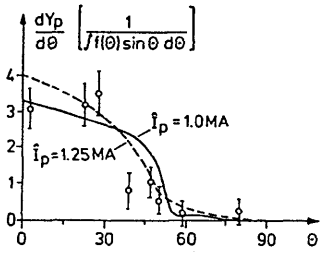

FIG.10. Angular distribution of reaction proton emission. (○) experimental. (---) calculated with the gyrating particle model for different amounts of maximum total pinch current I_p.

4. FINE STRUCTURE OF THE FOCUS PINCH

The fine structure of the focus was investigated with soft X-ray pinhole cameras. Distinct, axially oriented, continuous filaments were observed in time-integrated pictures. Figure 11 shows the existence of an almost regularly occurring central filament and of some peripherally filamentary structures in the neutron-optimized (5 mbar) regime. Time-resolved measurements with scintillators in the image plane and first framing pictures with a gated channel plate showed that the filamentation exists in the pinch phase. The lifetime of the central filament is found to be from $t \approx -20$ ns to $t \approx +50$ ns. It appears well before maximum compression. At lower and higher filling pressures the central filament dominates and has either a diffuse (2 mbar) or a narrow high-intensity appearance. The origin of the filaments and their physical nature (temperature? density? impurities?) are not yet clear. The theory explains the formation of the

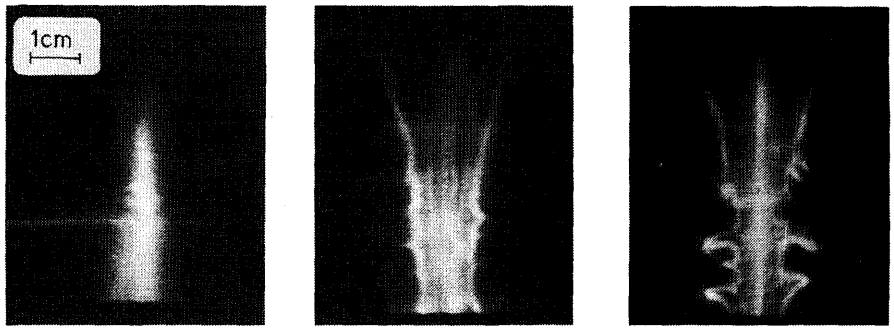

FIG.11. Soft X-ray pictures, time-integrated, side on, for three filling pressures. Pinhole diameter 200 μm; Be filter 10 μm; $W_0 = 280$ kJ.

central filament in the case calculated in Ref. [7] by an increased turbulent interaction of the collapsing plasma sheath front arriving at the axis. In addition, the central filament should carry the relativistic electrons observed.

5. DISCUSSION

We have shown that at high energy level and with high pinch current, at least for Poseidon conditions, a first phase of strong fusion reactivity becomes important in the plasma focus. This phase manifests itself in a pre-m = 0 neutron pulse of high intensity (≈500 times over thermal), in a considerable change of the general features of the reaction product spectra, and in a decrease in neutron fluence anisotropy compared to low energy focus results. It is interesting that in this phase the pinch column has a macroscopically quiet outer boundary; it also has a bulk ion and electron temperature and density not much different from low energy foci. Laser scattering does not indicate strong microturbulence in central plasma regions during the pinch phase, but shows non-thermal spectra associated with pinch break-up. It is important that the lifetime of the pinch phase grows with the pinch current approximately with $I_p^{3/2}$ [1].

More detailed measurements have shown that there is an accelerating mechanism in the pinch phase which creates quite reproducibly fast deuterons with energies up to 400 keV and with an exponential rise of intensity toward lower energy. The deuterons are trapped for some time (up to 100 ns) in the pinch column by gyromotion and relaxation. The features of the associated neutron and proton emission are well described by a GPM if a near-thermal distribution of the fast ions with T_i^* of about 50–100 keV is assumed.

According to theoretical predictions, based on a newly developed four-fluid, hybrid REDUCE/FORTRAN code, the acceleration of the ions is caused by a reconfiguration process in the pinch [8]. For high pinch currents, m = 2 and m = 4 instabilities should occur early in the pinch phase and lead to current filamentation with helical structures. Strong electric fields of up to about 600 kV/cm are associated with these phenomena and cause the acceleration of ions and electrons. First indications for such events may be the occurrence of distinct axially oriented long-living filaments in X-ray pictures of the pinch and distortions in reaction proton trajectories, pointing to the existence of rather strong axial magnetic fields.

The second phase of strong but irreproducible neutron emission is associated with pinch break-up(s) and possibly with post-m = 0 macroturbulence phenomena. Measurements of time-resolved flux anisotropy, of proton and deuteron spectra and the increasing length of the neutron source in this phase show that the fast deuterons have a dominant axial energy component. Their reaction mechanism may be described by an axial beam target model. The mechanism of the deuteron acceleration in this phase in not yet ascertained. Shot-to-shot scaling of the second-phase neutron yield shows that a high yield is not only an effect of increased source volume but also of increased neutron emission density varying from $1 \times 10^9 \text{cm}^{-1}$ to $1.2 \times 10^{10} \text{cm}^{-1}$. The particular features of the m = 0 break-up(s) (growth, sequence, current path) may thus be responsible for the yield variations.

REFERENCES

[1] HEROLD, H., et al., "Investigation of the neutron production phases of a large plasma focus device", Plasma Physics and Controlled Nuclear Fusion Research 1982 (Proc. 9th Int. Conf. Baltimore, (1982), Vol.2, IAEA, Vienna (1983) 405.

[2] EHRHARDT, J., KIRCHESCH, P., HÜBNER, K., RAGER, P.R., Phys. Lett. **89A** (1982) 285.

[3] KIES, W., Dissertation, Univ. of Düsseldorf, 1982.

[4] RAGER, J.P., in Controlled Fusion and Plasma Physics (Proc. 10th Europ. Conf. Moscow, 1981), Vol.2 (1981) 71.

[5] HEROLD, H., et al., Controlled Fusion and Plasma Physics (Proc. 11th Europ. Conf. Aachen, 1983), Vol.1 (1983) 477.

[6] DEUTSCH, R., HEROLD, H., KAEPPELER, H.J., SCHMIDT, H., Inst. für Plasmaforschung, Stuttgart, Rep. IPF-82-10 (1982).

[7] KAEPPELER, H.J., HAYD, A., MAURER, M., MEINKE, P., Inst. für Plasmaforschung, Stuttgart, Rep. IPF-83-2 (1983).

[8] HAYD, A., KAEPPELER, H.J., MAURER, M., MEINKE, P., in Proc. Int. Conf. Plasma Physics, Lausanne, 1984, Vol.1 (1984) 166.

NEUTRON, ION AND X-RAY EMISSION FROM A 360 kJ PLASMA FOCUS DEVICE

A. JERZYKIEWICZ, M. BIELIK, L. JAKUBOWSKI,
Z. JANKOWICZ, K. KOCIĘCKA, J. KUCIŃSKI,
E. RYDYGIER, M. SADOWSKI, J. ŻEBROWSKI
Institute for Nuclear Studies, Świerk

M. BOROWIECKI, S. CZEKAJ, S. DENUS,
A. KASPERCZUK, M. PADUCH, T. PISARCZYK,
W. SKRZECZANOWSKI
Institute of Plasma Physics and Laser Microfusion, Warsaw

Poland

Abstract

NEUTRON, ION AND X-RAY EMISSION FROM A 360 kJ PLASMA FOCUS DEVICE.

The results of investigations with a new 360 kJ plasma focus facility are presented. Time-integrated and time-resolved neutron, X-ray and ion measurements are presented for various experimental conditions. The relations between pinch dynamics and radiation processes are discussed.

1. EXPERIMENTAL CONDITIONS

A new 360 kJ plasma focus (PF) device was supplied by a condenser bank divided into four units of 70 μF capacity. Measurements were performed for the experimental conditions described here [1, 2] and, in addition, for 210 μF, 35 kV and 40 kV. Most of the results were collected at 126 kJ and 171 kJ energy levels. Two sets of cylindrical electrodes 30 cm long were examined. The inner electrode was 100 mm in diameter and the outer one was 150 mm or 225 mm. An alumina insulator 8 cm long had the same outer diameter as the inner electrode. A voltage pulse opening the Pockel's cell for ruby-laser shadowgraphy was recorded with other time-resolved observations. To define the time relation between the maximum compression and the development of a PF recorded on shadowgrams, the laser pulse and a plasma image were recorded by a streak camera.

2. INVESTIGATION OF NEUTRON RADIATION

The neutron yield was estimated by the silver activation method. Two GM counters were placed perpendicular to the z-axis at a distance of 1.2 m and 3 m.

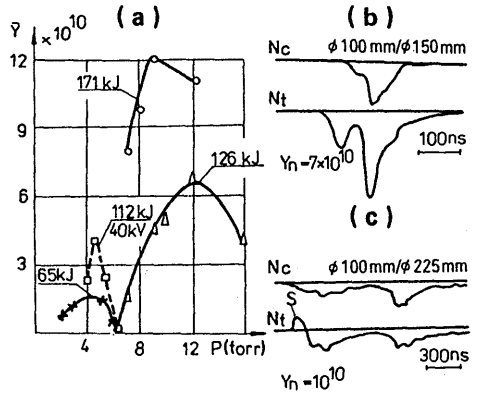

FIG.1. Results of neutron measurements. (a) Mean neutron yield as a function of deuterium pressure; solid line – 100 mm/150 mm φ electrodes; dashed line – 100 mm/225 mm φ electrodes. (b), (c) Neutron emission versus time; N_c = with and N_t = without collimator. (b) 12 torr, 40 keV, 168 kJ. (c) 6 torr, 32 kV, 143 kJ. S is the correlation signal.

For the 100 mm/150 mm φ electrodes, the neutron yield depended only on the energy stored and the deuterium pressure. The charging voltage in the range 21.5–40 kV did not influence the optimized neutron yield for a constant energy level. The mean value of the optimized neutron yield was proportional to $E^{2.1}$, $I^{3.2}_{max}$ and I^4_{pp} up to the 170 kJ level. Above 170 kJ the neutron yield decreased rapidly for this set of electrodes. Two types of discharge were observed. The first could be described by means of the snowplough model. For the second type of discharge the voltage on the condensers and on the collector was shifted about 90° in relation to the current, and the load seemed to be inductive. The neutron yield did not depend significantly on the type of discharge at 35 kV and 171 kJ, and was lower for the second type of discharge at 30 kV and 126 kJ. When the device was equipped with 100 mm/225 mm φ electrodes, the measured neutron yields were lower and increased with charging voltage for a constant energy level. Only at 40 kV, 112 kJ, was the maximum neutron output equal to the value calculated from the scaling law $Y \propto I^4_{pp}$. When this set of electrodes was used for $E > 120$ kJ, the neutron yield did not increase. Examples of characteristics of the mean neutron yield as a function of pressure are shown in Fig.1(a).

Time-resolved neutron measurements were made by means of two shielded scintillator-photomultiplier (PMT) detectors placed perpendicular to the z-axis at a distance of 2.4 m and 1.8 m. The first detector observed the whole vacuum chamber and the second (equipped with a collimator) observed a 10 × 10 cm^2 pinch region close to the inner electrode. The observations for 100 mm/150 mm φ electrodes can be summarized as follows. The neutron emission starts at the

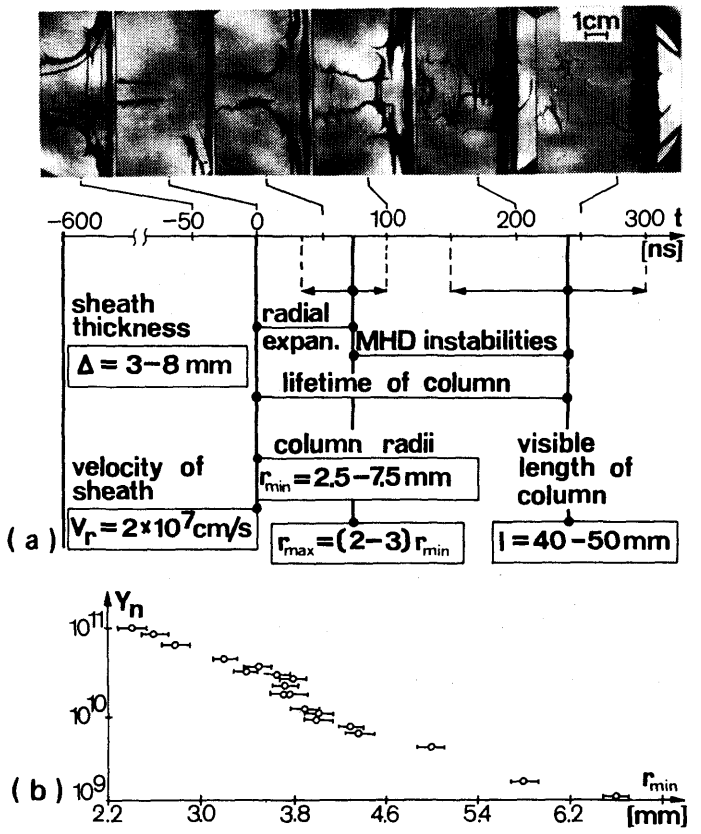

FIG.2. Results of plasma focus discharge measurements obtained by shadowgraphy.

beginning of or during maximum compression. Up to three maxima on the neutron pulse are measured without the collimator (Fig.1(b)). The first peak occurs (on 50% of the data) 20–80 ns after the start of emission; the main maximum appears 95–215 ns after the start of emission. A third weak maximum occurring 130–300 ns later is probably caused by scattered neutrons. Only the main and the third maxima are recorded with collimator (Fig.1(b)) and 50% without collimator. During the first pulse the neutron-emitting zone is probably localized inside the anode. The FWHM is usually 85–250 ns. With 100 mm/225 mm ϕ electrodes, long-lasting (>1 μs) neutron pulses were observed. A typical neutron pulse had two maxima shifted by 300–500 ns. The neutron emission between the maxima was several times lower than inside the maxima (Fig.1(c)). The start of emission was delayed to maximum compression for about 80–90 ns and correlated with the growth of MHD instabilities.

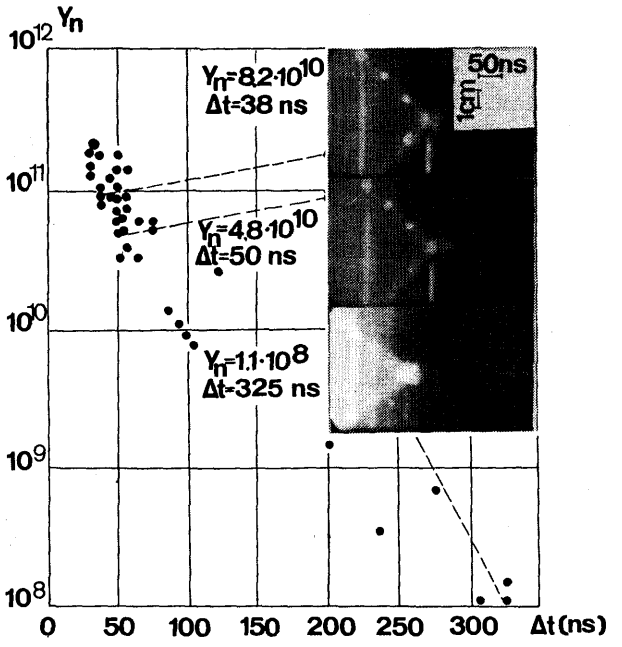

FIG.3. Neutron yield versus time distance between two 'compressions' for pressures of 6–13.5 torr.

Pinch-forming and decay processes were investigated with a four-frame shadowgraph (2 ns exposure time and 50 ns frame-to-frame shift). A course of this phase is shown in Fig.2(a). By comparing measured parameters and neutron yields for the discharges investigated, a number of correlations were found. A high neutron yield was accompanied by a relatively narrow and homogeneous plasma sheath, minimum pinch radius, the shortest time of radial expansion, and minimum time of pinch decay. Because the pinch decay depends on r_{min}, the last parameter was recognized as essential for correlation. The relation between a neutron yield and the minimum pinch radius is shown in Fig.2(b). Correlations of neutron yields and macroscopic plasma parameters, as found in the PF-360 device, were analogous with those obtained with PF-150 [3]. In some discharges with 100 mm/225 mm ϕ electrodes an anomalous plasma sheath structure was observed. These discharges were characterized by a 'delaminated' plasma sheath in the collapse phase and often by a low neutron yield.

To study relations between plasma dynamics and radiation, a streak optical camera (KSK-2 type) was used. Photographs were taken for the $\lambda > 6900$ Å wavelength in the plane z = 7 mm (to the anode) through a 200 μm slit. Two bright zones were usually recorded after maximum compression. The first zone

(well correlated with shadowgrams) appeared at the time of maximum compression and existed for about 30 ns in the case of high neutron yield. The second zone had no correspondence in the shadowgrams. It seems that the streak photographs can be interpreted as records of the radial motion of a cylindrical shock wave driven by a magnetic piston. This wave implodes on the PF axis, reflects from it, and expands radially up to a new reflection from the magnetic piston, which leads to a subsequent compression. Balancing gas-kinetic pressure behind the shock wave and the magnetic piston determines the scale and duration of the radial expansion. Fast balancing of the pressure causes a short time of expansion, which is facilitated by high magnetic field gradients. In such a case a narrow well-formed plasma sheath should be observed in correlation with a high neutron production. The neutron yield versus the time shift between the two zones is shown in Fig.3.

3. INVESTIGATION OF X-RAY EMISSIONS

Integral measurements of X-ray emissions were performed with a stereoscopic set of two pinhole cameras. Gas pressure inside the cameras was kept at $10^{-2}-10$ torr. Using pinholes of different diameters and absorption filters, a series of X-ray pictures was taken for PF discharges realized at various initial pressures and charging voltages.

The X-ray pinhole pictures revealed a filamentary structure in the pinch column similar to that observed with the Poseidon facility [4]. The appearance of a continuous filament during the pinch phase is shown in Fig.4(a). In some cases two or three filaments were observed. Taking into account the absorption of X-rays by the working gas (distance from focus to film 96 cm; operating pressure 9 torr, D_2) and that of a 1.5 μm Al filter, it can be estimated that the minimum energy of the X-rays recorded was about 700 eV and maximum energy was below 3 keV, because no picture was recorded on the second emulsion layer. Usually, the central filament becomes more distinct with an increase in initial voltage and energy. With high enough pinch current (>0.8 MA in this case) the filamentary structure of a pinch can be observed within a whole operational regime of the facility.

To study the chronology of an X-ray emission, various filter-scintillator-PMT sets were used. Time-resolved X-ray signals were observed for different electrodes and various experimental conditions (some examples are given in Fig.4(b)). With 100 mm/150 mm ϕ electrodes, all the soft (<6 keV) and hard (>7 keV) X-ray signals reveal two maxima. Time shift for the soft X-ray peaks is on average equal to 60 ns, while that for hard X-rays is about 75 ns. An averaged FWHM value of a double soft X-ray signal at p = 7 torr D_2 and V = 30 kV is 100 ns, while that for hard X-rays is 130 ns. This value decreases with increased operating pressure and charging voltage. With the larger 100 mm/225 mm ϕ electrodes,

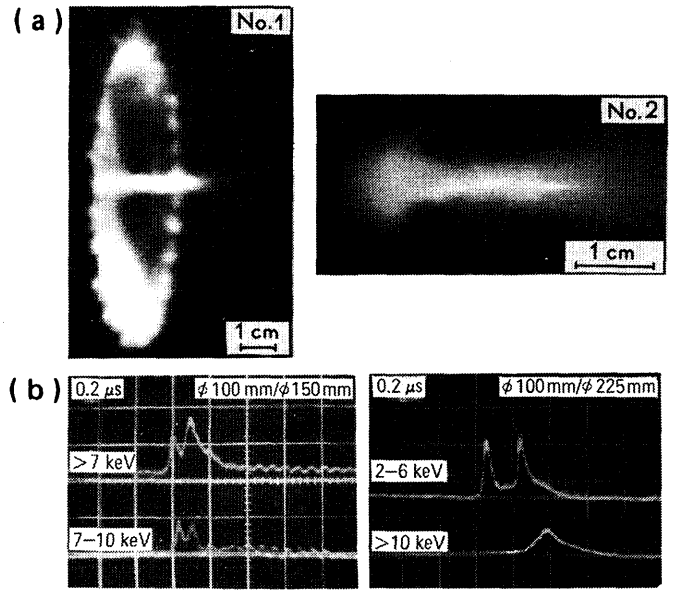

FIG.4. (a) X-ray pinhole images taken with two side-on cameras (No.1 – 280 μm φ pinhole + 10 μm Be filter; No.2 – 200 μm φ pinhole + 1.5 μm Al filter), showing a filamentary structure in the pinch column. Conditions: p = 9 torr, D_2; V = 35 kV; E = 171 kJ. (b) Time-resolved X-ray signals recorded with various filter-scintillator sets for two shots performed with different external electrodes. Conditions: p = 7 torr, D_2; V = 30 kV; E = 126 kJ.

two peaks are observed for soft (2–6 keV) X-rays only. Hard (>10 keV) X-rays reveal a single maximum delayed by 70–90 ns in relation to the second soft X-ray peak. An averaged FWHM value of the first soft X-ray peak in that case is 50 ns, that of a second soft X-ray peak is 100 ns, and that of hard X-rays 160 ns. The shape of hard X-ray signals did not change much within the energy range studied. Simultaneous time correlation measurements showed that neutron emission starts during the first soft X-ray pulse.

4. INVESTIGATION OF ION BEAM EMISSION

To study ion emission (in comparison with previous investigations on the smaller PF-20 facility [5]), an ion pinhole camera equipped with cellulose nitrate (CN) films was used. The ion camera was adjusted along the z-axis and placed 265 mm away. The effective length of the camera could be changed by special inserts or extension tubes, and camera volume was pumped out differentially by

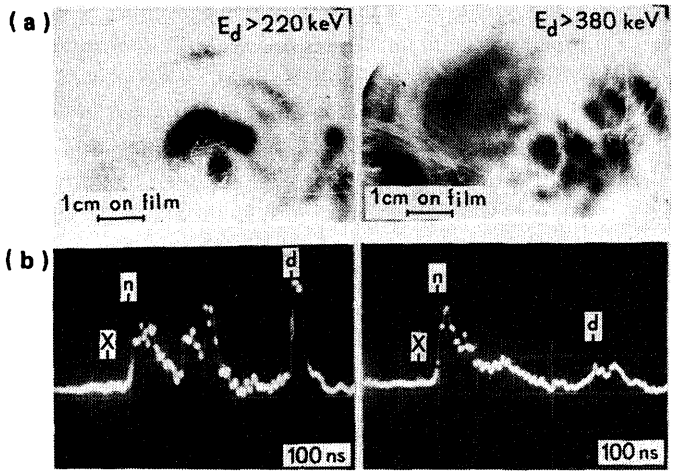

FIG.5. (a) Ions photographed along the z-axis by a pinhole camera and cellulose nitrate films covered with various Al foils, showing high energy deuteron beams. Conditions: p = 4 torr, D_2; C = 210 μF; V = 35 kV; E = 128 kJ; shot 0426/08 – $Y_n = 2.6 \times 10^{10}$; shot 0426/13 – $Y_n = 6.9 \times 10^{10}$.
(b) Time-resolved signals recorded by a scintillator detector placed on the z-axis at the ion pinhole image plane, about 100 cm from a focus. X – hard X-rays; n – neutrons; d – deuterons. Conditions: p = 12 torr, D_2; C = 280 μF; V = 35 kV; E = 171 kJ; shot 0612/22 – Y_n = = 1.2 × 10^{11}; shot 0613/09 – $Y_n = 1.3 \times 10^{11}$.

an auxiliary vacuum stand. Using Al foil filters of various thicknesses, it was found that, among low-energy (>40 keV) deuterium beams, microbeams of high-energy (>80 keV) deuterons are emitted. Some examples of ion pinhole photographs are shown in Fig.5(a).

With the PF-360 facility's initial energies of 126 and 170 kJ, it was observed that, in the system optimized from the point of view of neutron emission, an increase in energy and discharge current value does not cause a great increase in emission of high energy deuterons. In agreement with observations on other large PF facilities [6], the number of deuterons in the beams of energy >80 keV was found to the CN approximately independent of the initial energy of the discharges. At a distance between electrodes and pinhole of 265 mm and a distance from a pinhole to the film of 537 mm, about 10^9 deuterons of energy >80 keV were recorded on the 20 cm^2 surface of the detector. Simultaneous measurements with different filters showed that among these deuterons there were 7.3×10^8 deuterons of energy >380 keV. Also in agreement with results from other large facilities [6], the maximal energy of deuteron beams observed on the PF-360 facility was lower than that on smaller PF devices, and amounts to several hundreds of keV (instead of 3–5 MeV).

We investigated the dynamics of the ion emission by means of a 78-cm-long pinhole camera equipped with a set of thin plastic scintillators (placed at the ion pinhole image plane) and fast photomultipliers. Some examples of time-resolved signals are shown in Fig.5(b). Provided that the fast deuterons are emitted from the PF region simultaneously with relativistic electron beams and hard X-rays, time-of-flight analysis of the observed deuteron signals can be performed. However, the recorded deuteron pulses reveal a complex structure, and the energy can be found with a relatively large jitter. The individual spikes of the FWHM < 10 ns can be identified by the deuteron microbeams emitted from different micro-sources [7].

REFERENCES

[1] JERZYKIEWICZ, A., et al., in Controlled Fusion and Plasma Physics (Proc. 11th Europ. Conf. Aachen, 1983), Part 1 (1983) 485.
[2] JERZYKIEWICZ, A., et al., in Proc. 3rd Int. Workshop on Plasma Focus Research, Stuttgart, 1983, Inst. für Plasmaforschung, Stuttgart, Rep. IPF-83-6 (1983) 17.
[3] CZEKAJ, S., et al., in Controlled Fusion and Plasma Physics (Proc. 11th Europ. Conf. Aachen, 1983), Part 1 (1983) 469.
[4] SADOWSKI, M., HEROLD, H., SCHMIDT, H., SHAKHATRE, M., Phys. Lett. **105A** (1984) 117.
[5] SADOWSKI, M., et al., in Proc. 3rd Int. Workshop on Plasma Focus Research, Stuttgart, 1983, Inst. für Plasmaforschung, Stuttgart, Rep. IPF-83-6 (1983) 39.
[6] HEROLD, H., et al., in Controlled Fusion and Plasma Physics (Proc. 11th Europ. Conf. Aachen, 1983), Part 1 (1983) 477.
[7] SADOWSKI, M., SCHMIDT, H., HEROLD, H., Phys. Lett. **83A** (1981) 435.

DISCUSSION

ON PAPERS IAEA-CN-44/D-III-6-1 to D-III-6-4

S. MERCURIO: Could you tell me whether any of the groups whose work you are reporting on has considered the possible formation of electrical double layers in their plasma focus devices?

S. DENUS: This possibility is not discussed in any of the four papers I have presented. However, the physical mechanism of ion and electron acceleration in the plasma focus is still not clear and the models at present in existence do not describe the experimental data well. I believe that the double-layer formation mechanism could also be taken into account.

LIFETIME SCALING OF FIELD-REVERSED CONFIGURATIONS*

A.L. HOFFMAN, D.G. HARDING, R.D. MILROY,
J.T. SLOUGH, L.C. STEINHAUER, G.C. VLASES
Mathematical Sciences Northwest Inc.,
Bellevue, Washington,
United States of America

Abstract

LIFETIME SCALING OF FIELD-REVERSED CONFIGURATIONS.

Field-reversed configurations are elongated compact toroidal plasmas confined solely by poloidal fields. Their particle lifetimes have been described by analytical models assuming a lower hybrid drift (LHD)-governed anomalous resistivity. While these models have correctly predicted the observed particle lifetimes, they do not correctly reproduce the measured flux lifetimes. Moreover, the predicted particle lifetimes, for present small experiments, depend more on open than closed field line confinement and therefore comparisons with theory are not very accurate in illuminating the true nature of the closed field line confinement. Measurements on the TRX field reversed theta pinch display flux decay rates which imply a more spatially uniform resistivity than predicted by the LHD model. The detailed measurements over a wide range of conditions also suggest a much weaker dependence on open field line confinement. A parameter $s = \Delta r_{FL}/\rho_{i0}$, where Δr_{FL} is an equivalent poloidal flux layer thickness and ρ_{i0} is the ion gyroradius in the external field, has been shown to be the relevant parameter for examining the contribution of open field line effects. In the presence of drift parameter-related microinstabilities, s must be greater than 3 for closed field line confinement to dominate. For present experiments, s rarely exceeds 2. For large s, where the closed field line confinement will truly dominate, the particle confinement is predicted to approach an s^4 dependence for an LHD-governed resistivity.

Considerable advances have been made in the past several years in the generation of field-reversed configurations (FRC) by using programmed formation methods [1,2], and in the stabilization of the previously lifetime-terminating n=2 rotational instability through the application of multipole fields [3,4]. Attention has therefor been focused on measuring the transport limited lifetime. Some agreement has been found with models based on diffusion coefficients given by the wave energy bound of the lower hybrid drift (LHD) micro-instability [5]. A semi-empirical particle lifetime scaling, $\tau_N \propto R^2/\rho_{io}$, has also been postulated, where R is the FRC major radius (radius of the field null) and ρ_{io} is the ion gyroradius in the external magnetic field. It has since been realized that an important scaling paramater, for both stability and lifetime

* Supported by the US Department of Energy.

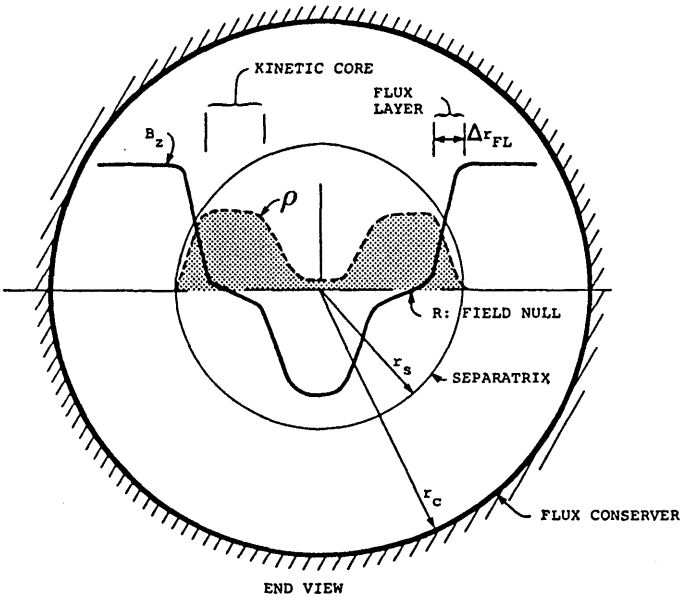

FIG. 1. Thin flux layer model of field-reversed configuration.

scaling, is not R/ρ_{io} but rather a normalized flux layer thickness to gyroradius ratio defined as

$$s \equiv \Delta r_{FL}/\rho_{io} = \int_R^{r_s} \frac{r\,dr}{r_s \rho_i} \qquad [1]$$

where ρ_i is the local ion gyroradius and $r_s = 2^{1/2}R$ is the separatrix radius. An end view of an FRC density and magnetic field profile is sketched on Fig. 1 with the flux layer, Δr_{FL} indicated. For a given size FRC this flux layer thickness is obviously related to the amount of poloidal flux, and thus to the average plasma beta.

In the absence of a toroidal field, the strong poloidal field line tension at the FRC ends is only resisted by plasma pressure, and results in a high average plasma beta. For an elongated FRC in a cylindrical flux conserver of radius r_c, this average beta can becalculated, independent of field profile, as $\langle\beta\rangle = 1 - x_s^2/2$ where $x_s \equiv r_s/r_c$ [6]. The relationship between s and $\langle\beta\rangle$, or the amount of poloidal flux ϕ_p, can conveniently be written as $s = \langle\phi_i\rangle R/2^{3/2}\rho_{io}$ where $\langle\phi_i\rangle = \phi_p/\pi R^2 B_e$ is the poloidal flux normalized to the external field B_e and the area inside the major radius. For a rigid rotor

profile, which is characteristic of present experiments, $\langle \phi_i \rangle \approx 0.62 x_s$ and a convenient approximation has been used for s:

$$s = \frac{x_s}{5}\left[\frac{R}{\rho_{io}}\right] \quad \text{[RIGID ROTOR PROFILE]} \qquad [2]$$

In these present experiments with $R \leq 7$cm and $x_s < 0.6$, there are very few internal gyroradii, and s is always less than 2.5. This produces very steep density gradients near the separatrix, and the particle lifetime would be expected to be strongly influenced by the open field line confinement.

Since FRC particle confinement has been noted to be shorter than classical and to be related to the ratio of pressure scale length ℓ_n to gyroradius ρ_i, resistivity models have been proposed based on the high growth rate LHD instability. In saturation at a normalized electric field energy ϵ_F, the LHD instability results in an effective collision frequency given by [7]

$$\nu_{AN} \approx \left[\frac{\pi m_e}{2m_i}\right]^{1/2}\left[\frac{\omega_{pe}^2}{\omega_{ce}}\right]\left[\frac{v_{De}}{v_i}\right]^2 \epsilon_F \qquad [3]$$

The drift parameter (v_{De}/v_i) is the ratio of electron drift speed to ion thermal speed, and is equal to $\ell_n/2\rho_i$. Assuming saturation at the wave energy bound, $\epsilon_F \approx \omega_{ce}^2/2\omega_{pe}^2$, the LHD anomalous particle diffusion coefficient, $D_{AN} = \beta 4\pi \nu_{AN}/2\omega_{pe}^2$ has the numerical value

$$D_{AN} = 5\left[\frac{T(keV)}{B(T)}\right]\left[\frac{\rho_i}{\ell_n}\right]^2 \quad m^2/s \qquad [4]$$

This is a Bohm-like diffusion coefficient, reduced by the normalized square of the gradient scale length. It implies a particle confinement time of approximately $R\ell_n/D_{AN}$ proportional to $R(\ell_n/\rho_i)^3/T^{1/2}$.

Simple quasi-steady models have been derived for the particle confinement time when the resistivity is much higher near the separatrix than at the magnetic null, and the flux loss rate is low [5]. This is predicted to occur for present experiments where the anomalous resistivity is at least several times higher than classical. The models also assume uniform, although unequal, electron and ion temperatures. For the limiting case where the FRC is large enough that the internal confinement time, represented as $\tau_\perp \propto s^4$, is large compared to the open field line confinement time $\tau_\parallel$, the density at the separatrix is low and the profiles assume a thin flux layer

TABLE I. EXPERIMENTAL FRC LIFETIME MEASUREMENTS AND THIN FLUX LAYER PREDICTIONS

	CASE	P_o (mtorr)	T_i (eV)	T_e (eV)	x_s	ℓ_s (cm)	s	$s_o/3$	w	τ_{TFL} (μs)	τ_N (μs)	τ_ϕ (μs)	τ_E (μs)
TRX-1	r_c = 12.5cm	15	250	150	.4	80	1.0	.18	.98	40	60	60	45
	B_e = 8.0kG				.55	70	1.9	.46	.95	93	130	120	70
TRX-2	r_c = 12.0cm	10	350	150	.4	40	1.2	.22	.86	30	40	43	30
	B_e = 12.0kG	6	550	175	.3	37	0.6	.08	.81	11	17	21	11

(TFL) distribution as shown on Fig. 1. A simple expression can then be written for the particle confinement time [8]:

$$\tau_{TFL} = 2.8\frac{\langle\beta\rangle}{\left[1+T_e/T_i\right]B(T)}\left[\frac{R}{\rho_{io}}\right]\left[w + s_o/3\right]^3 \ \mu s \qquad [5]$$

$$w = 0.87\left[1 + T_e/T_i\right]^{1/8}\left[\frac{B(T)\ell_s(m)}{T_i^{1/2}(keV)}\right]^{1/4} \qquad [6]$$

$$s_o = 0.27x_s^2\left[R/\rho_{io}\right] \qquad [7]$$

$\tau_{\parallel} = \ell_s/2v_i$ where ℓ_s is the FRC separatrix length; w is the ratio of open field line scale length to ρ_{io} and is proportional to $(\tau_{\parallel}/\tau_{\perp})^{1/4}$ [5,8]. It has the numerical value shown above and is approximately equal to unity for both present conditions and for reactor extrapolations. s_o is the appropriate value for s for the type of sharp boundary profile indicated on Figure 1 (where $\langle\phi_i\rangle = 0.75x_s^2$). In the LHD model the particle confinement is affected equally by the effective closed field line density scale length $s_o/3$ and the open field line density scale length w.

Experimental measurements of the particle lifetime τ_N, poloidal flux lifetime τ_ϕ, and plasma energy lifetime τ_E are shown on Table I for operation in the TRX field reversed theta pinch. TRX is a 1-m long, 20-cm diameter (plasma tube ID), theta pinch operated at 10 kV (TRX-2) to 30 kV (TRX-1) azimuthal voltages [9]. TRX-2 is a three-turn modification of TRX-1 which was built to demonstrate lower voltage FRC formation in a regime where radial shock heating is ineffective and Ohmic and axial shock heating must be relied upon [10]. An improved electrical efficiency allowed for the achievement of higher magnetic fields, and the data shown on Table I attests to the ability to form FRCs under these conditions. Based on the utilization of new programmed formation techniques [1,2], it was possible to operate reproducibly at high reverse bias fields and thus produce large separatrix radii r_s up to 7 cm (at the lower confinement fields). However, even for the largest x_s condition, $s_o/3$ is still much less than w, and Eqs (5), (6) and (7) imply a $(R/\rho_{io})\ell_s^{3/4}$-type scaling.

The lifetimes listed on Table I for each experimental condition are the averages over a great many individual experiments. The particle lifetimes are compared with the LHD-TFL model predictions even though the assumptions made in deriving the TFL model do not apply for the present rigid rotor-type profiles. Detailed one-dimensional numerical and quasi-steady analytic calculations show that the TFL calculated particle lifetimes do not vary by more than 20 percent from the more accurately calculated lifetimes even for the present small-s conditions [11]. Unfortunately, due to the strong dependence on open field line confinement of the LHD model for small s,

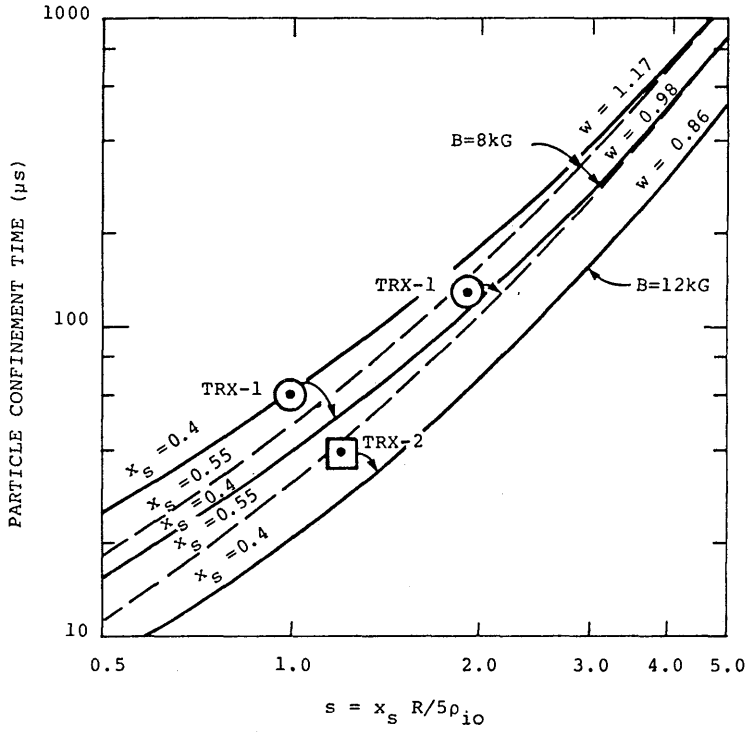

FIG. 2. Experimental measurements and thin flux layer model calculations of particle confinement time.

the calculated TFL lifetime is very insensitive to the magnitude of the coefficient (to about the one-fourth power) in the expression for anomalous collision frequency. It is thus not possible to say if the reasonable agreement shown on Table I between the measured and predicted particle lifetimes is due to the lower hybrid drift, or some other drift-related micro-instability. A localized LHD resistivity would imply long flux lifetimes, $\tau_\phi >> \tau_N$, at electron temperatures over 100 eV, but these have only been seen in one larger high-temperature experiment [12]. The energy lifetime τ_E, expressed simply as the rate of decay of the total plasma energy without considering magnetic field compression or decompression work, is also noted to be always within a factor of two of the flux and particle lifetimes.

Although it cannot yet be said if the LHD instability is dominant, any anomalous resistivity with a drift parameter scaling of the type given by Eq. (4) will yield the same type of TFL scaling. It is thus instructive to plot the TFL confinement time versus the experimental s parameter. This is done on Fig. 2 for the conditions given on Table I, and the

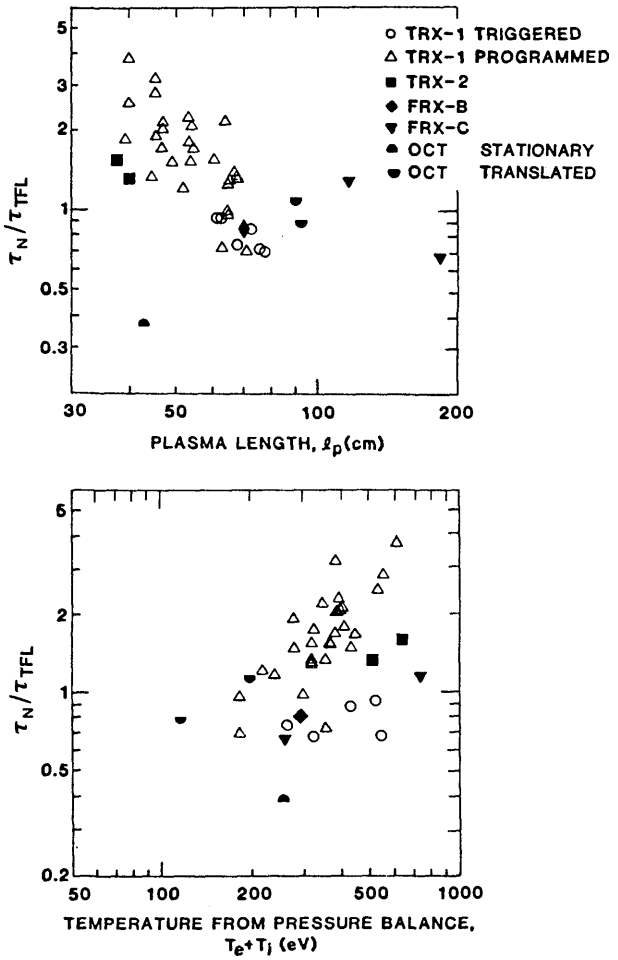

FIG.3. Comparison of experimental particle lifetimes with thin flux layer model length and temperature scaling.

experimental measurements are also noted. The change from a linear to quadratic (and eventually quartic) dependence on s, and the reduced dependence on w at larger s, is clearly seen. The w = 1.17 curves correspond to the same conditions as TRX-1, with twice as long a separatrix length ℓ_s. Eventually the two sets of B = 8 kG curves would coalesce, but there is seen to be some small dependence on axial confinement even for moderate s. The w = 0.86 curve has a lower asymptotic value because the magnetic field is higher. The dependence on magnetic field given by Eq.(5) is really a $T^{-1/2}$ dependence (since $\rho_i \propto T^{1/2}/B$). This unfavorable temperature scaling is due to the Bohm-like nature of the wave energy bound saturated LHD diffusion.

The data shown on Table I and Fig. 2 appear to support a $\tau_N \propto f(s)$ scaling, but it cannot be determined whether the LHD resistivity model is correct, or even what is the actual dependence on temperature and magnetic field beyond that contained in ρ_{io}. The relevance of LHD resistivity can be examined by comparing individual data points with the TFL-LHD predictions for as wide a range of experimental conditions as possible. This is done on Fig. 3 as a function of both separatrix length and total electron plus ion temperature. There is a clear tendency for the confinement to be better than predicted at shorter lengths, which implies a weaker than predicted dependence on open field line confinement. A uniform resistivity profile, which is more consistant with the noted close equivalence of flux and particle lifetimes, does not yield the strong dependence on w given by Eq. (5) since the assumed resistivity does not increase rapidly near the separatrix as the density drops. In fact, open field line effects then become unimportant for $s > w$ [2]. However, the lack of strong lifetime scaling with w may just imply a more nearly constant value of w set by other effects such as large kinetic orbits.

The lack of agreement shown on Fig. 3 of the higher temperature data with LHD predictions is encouraging since, without the $1/B$ or $1/T^{1/2}$ dependence, the s dependence of Eq. (5) is highly favorable for scaling to small reactor sizes. However, some of this disagreement with the TFL predictions may also be related to the same lack of dependence on w, since the open field line confinement time in the TFL model was assumed proportional to $\ell_s/T_i^{1/2}$. The higher-temperature experimental conditions were achieved by operating at lower deuterium fill pressures, which tended to also produce shorter FRCs.

It has been shown that the TFL-LHD model gives good agreement with experimental particle lifetime measurements for the nominal operating conditions, $\ell_s \approx 70$ cm and $T_e+T_i = 300$-500 eV, of TRX. However, the lack of differentiation between flux and particle lifetimes, and the lack of correct temperature scaling, cast doubt on both the spatial dependence and scaling magnitude of the resistivity. Experiments at larger values of s (such that $s_o >> 3$) are clearly called for to elucidate the true closed field line scaling of FRCs.

REFERENCES

[1] BELIKOV, V.V., et al., "Suppression of losses in a compact torus with programmed shaping of the magnetic structure", Plasma Physics and Controlled Nuclear Fusion Research 1982 (Proc. 9th Int. Conf. Baltimore, 1982), Vol. 2, IAEA, Vienna (1983) 343.

[2] SLOUGH, J.T., HOFFMAN, A.L., MILROY, R.D., HARDING, D.G., STEINHAUER, L.C., "Flux and particle lifetime measurements in field reversed configurations", in preparation.

[3] MINATO, T., et al., "Experimental studies on confinement of field-reversed-configuration plasma", Plasma Physics and Controlled Nuclear Fusion Research 1982 (Proc. 9th Int. Conf. Baltimore, 1982), Vol. 2, IAEA, Vienna (1983) 303.
[4] HOFFMAN, A.L., SLOUGH, J.T., HARDING, D.G., Phys. Fluids **26** (1983) 1626.
[5] TUSZEWSKI, M., LINFORD, R.K., Phys. Fluids **25** (1982) 765.
[6] ARMSTRONG, W.T., LINFORD, R.K., LIPSON, J., PLATTS, D.A., SHERWOOD, E.G., Phys. Fluids **24** (1981) 2068.
[7] LIEWER, P.C., DAVIDSON, R.C., Nucl. Fusion **17** (1977) 85.
[8] HOFFMAN, A.L., MILROY, R.D., Phys. Fluids **26** (1983) 3170.
[9] ARMSTRONG, W.T., HARDING, D.G., CRAWFORD, E.A., HOFFMAN, A.L., Phys. Fluids **25** (1982) 2121.
[10] STEINHAUER, L.C., Phys. Fluids **26** (1983) 254.
[11] STEINHAUER, L.C., MILROY, R.D., SLOUGH, J.T., "A model for inferring transport rates from observed confinement times in field-reversed configurations", in preparation.
[12] TUSZEWSKI, M., et al., Phys. Fluids **25** (1982) 1696.

Z-PINCH FUSION RESEARCH

J.D. SETHIAN, K.A. GERBER, A.E. ROBSON,
A.W. DeSILVA*
Naval Research Laboratory,
Washington, D.C.

J.E. HAMMEL, D.W. SCUDDER, J.S. SHLACHTER
Los Alamos National Laboratory,
Los Alamos, New Mexico

United States of America

Abstract

Z-PINCH FUSION RESEARCH.

Two independent United States Laboratories, the Los Alamos National Laboratory and the Naval Research Laboratory, are studying the dense z-pinch as a potential fusion power source. These efforts are motivated by the results of a recent Los Alamos study concluding that if a straight, high density pinch could be maintained for 2 μs, it could produce 4.4 MJ of fusion energy for an input of 140 kJ. At Los Alamos, the pinch is formed along a pre-ionized channel created by a laser pulse and then ohmically heated to kV temperatures. In this gas-embedded pinch the temperature is limited by accretion of surrounding gas into the pinch channel. This accretion has been verified with a Moire-Schlieren technique, and the observed results are consistent with a two-stage model. Two methods of controlling this accretion, the use of D_2 fibres and a wall-limiting technique, are being investigated. At the Naval Research Laboratory, the pinch is formed inside 200 μm inner diameter quartz capillaries filled with D_2. This fixes the total number of pinch particles and hence is expected to eliminate the accretion. The wall material plasma that appears between the pinch and wall is expected to be kept cold by radiation and therefore to shunt only a small fraction of the pinch current. In experiments without the capillary, electron temperatures exceeding 1 kV were achieved and a simple magnetic loop detected the axial magnetic field produced by an m = 1 instability. When the pinch was formed inside the capillary filled with D_2 at 1 atm, no axial field was detected, suggesting that the instability had been suppressed. Based on this concept, a fusion reactor design study has been started in which the pinch is repetitively formed in a vortex of cold water. The design makes extensive use of existing pressurized water fission reactor technology and produces 500 MW(th) for an input of 17 MW(e).

---

* Sachs/Freeman Associates, Bowie, MD, and University of Maryland, College Park, MD, USA.

I. INTRODUCTION

The dense linear z-pinch has been considered as a basis for a very simple and compact fusion system since the earliest days of CTR. The current renewed interest is due partly to the significant advances made in pulsed power technology and partly to a recent Los Alamos Study [1] which concluded that if a straight pinch, 10 cm long, and ~ 30 μm radius, could be maintained at a density of ~ 10^{22} ions/cm^3 for 2 μs, it would produce 4.4 MJ of fusion energy per pulse for the relatively modest input of 140 kJ per pulse.

Early attempts to achieve high density z-pinches by implosion produced hollow pressure profiles which resulted in disruptive m=0 (interchange) instabilities. These instabilities are not found in the gas-embedded pinch, which is formed from a very narrow spark channel (typically 100-200 μm) and thus near an interchange stable profile. (While this configuration is subject to an m=1 instability which turns the linear pinch into a helix, this is a geometrical re-arrangement and is not necessarily disruptive.) It has been proposed that the pinch could be kept at its initially small radius by following a prescribed current waveform [2] that is within the capabilities of modern pulsed power technology. However, the gas-embedded pinch is prone to a rapid accretion of the surrounding gas during the early stages of formation, which increases the line density N and, since the Bennett relation I^2=4 NkT applies, prevents the attainment of high temperatures. It is believed that if this accretion could be contained, the z-pinch could become a truly viable alternative fusion system.

II. LOS ALAMOS PROGRAM

We have studied the laser-initiated gas-embedded z-pinch for three years and have approached or achieved many of the reactor study conditions. These include: (a) initiation laser beam channels of less than 30 μm radius; (b) z-pinch channels less than 50 μm radius and with a density of 3×10^{20}cm^{-3}, (c) a plasma ohmically heated to 1000 eV, and (d) demonstration of an interchange stable configuration. Detailed discussions of these experiments have been given in previous papers[2,3]. The work presented here is concerned primarily with aspects of the accretion.

The pinch channel was designed with a neodyminum laser. Approximately 50-100 ns later, the pinch was driven by a 600 kV Marx generator capable of delivering 300 kA at a rate of 4 kA/ns. A Moire-Schlieren technique[3] utilizing a

1 ns low coherence N_2 laser provided evidence for a monotonic increase in plasma inventory in the gas-embedded pinch. At a fill pressure of 11.1 psia, the average line density increased by 1×10^{28} cm/s for the first 50 ns of the discharge. Additionally, the plasma radius increased at a rate of 10^6cm/s. These data are self-consistent with a model of a central plasma channel that incorporates new plasma from the surrounding neutral gas. Using a two-foil scintillator-photomultiplier diagnostic[4], we found the plasma temperatures to peak at approximately 1000 eV, persist for 10-20 ns, and occur within 20 ns after the start of the current flow. Our accretion model, based on the observed increase in line density, the measured plasma current, and the assumption of Spitzer resistivity, predicted this observed temperature signature.

There are several mechanisms which couple the plasma channel to the neutral gas. We have estimated the relative importance of these processes on the observed accretion with the aid of the MANIAC code and the assistance of Lindemuth[5]. Radiation transport is not treated in the code; thus it is assumed the plasma is optically thin. Simple analytical calculations of the bremsstrahlung emission by the plasma core, coupled with the Kramer absorption law, have provided us with an estimate for the direct ionization of the neutral halo region by radiation. These calculations suggest that the accretion cannot be accounted for by absorption of bremsstrahlung, but is instead due to a two-stage process in which the core, through radiation, heat conduction or a shock, raises the neutral gas ionization fraction by a small amount, e.g. $< 0.01\%$. Because this ionization has increased the conductivity of the basically neutral region, the E-field will provide Ohmic heating to the neutral gas, thereby raising its temperature and further increasing the ionization fraction. This two-step process then leads to the observed accretion without need for the previously held notion of core-driven full ionization because the driver for the accretion is the external current source.

While work is continuing on gas-embedded z-pinches, we are also actively examining the feasibility of line density limiting schemes. This effort is in part motivated by the two-stage ionization/accretion model results because we believe it will be difficult to reduce the initial shock that is launched into the neutral gas. Our approaches to limiting the line density fall into two categories: wall-limiting and solid D_2 fibers. The wall-limiting scheme eliminates accretion by filling a small diameter (~ 500 μm) tube with an acceptable quantity of gas and allowing all of the fill to become ionized. In order to accurately initiate the pinch inside such

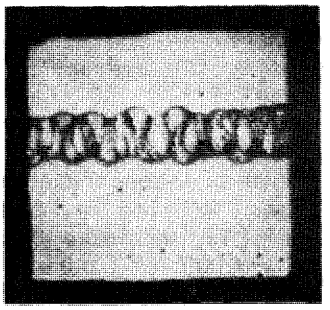

FIG. 1. Schlieren photograph of plasma channel in a 0.5 cm radius graded chamber. The walls of the chamber define the top and bottom of the illuminated area. A grading ring is at the right-hand edge.

a tube we have recently installed a 12 Joule, Q-switched Nd-glass laser which operates in a single transverse mode. By focusing this beam through a 2.0 meter focal length positive lens, we can easily exceed the threshold for optical breakdown in 3 atmospheres of hydrogen. Schlieren photographs of these laser-produced plasmas reveal narrow channels with sub-100 μm diameters and lengths of many centimeters. As the characteristic laser spot size for these experiments is approximately 600 μm, we believe these narrow plasma channels are indicative of laser self-focusing. The first wall-limiting pinch experiments using this laser have been performed in a 0.5 cm radius chamber. We installed grading rings along the chamber in order to maintain an axially uniform E-field. Figure 1 shows a Schlieren photograph of such a pinch channel. Similar results are obtained in 1.5 mm inner radius polycarbonate cylinders with no grading rings. Experiments with sub-millimeter cylinders and x-ray diagnostics are now being prepared.

The solid fiber approach is to pass the current through D_2 fibers 30-50 μm diameter. As the fiber is immersed in vacuum, the amount of fiber material determines N. The technology required is only a slight extrapolation from the work of Jarboe[6], and we are presently designing the necessary generating apparatus. One promising possible initiation technique is to use the fiber as an optical waveguide for the self-focusing laser channels.

III. NRL PROGRAM

The NRL approach is based on the wall-limiting concept and forms the pinch inside a small, 200 μm inside-diameter quartz capillary filled with deuterium. Again the idea is to fix the

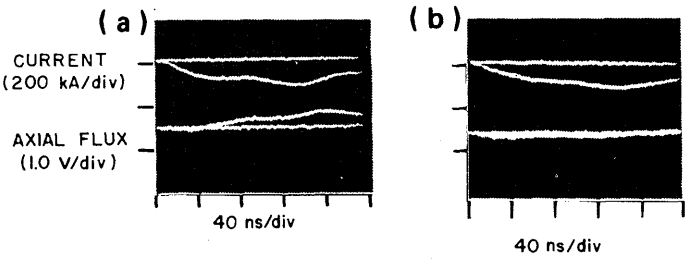

FIG.2. Axial current and axial flux signals of (a) the gas-embedded pinch and (b) the pinch formed in a 200 μm inside diameter capillary.

line density. We also plan to exceed that current rise rate necessary to maintain a constant radius, and thus expect the pinch to contract and undergo both compressional as well as Ohmic heating. This contraction will, of course, produce a wall plasma between the pinch and wall, but we expect this "corona" to be kept cold by radiation and hence be too resistive to shunt an appreciable fraction of the pinch current. We also expect this dense corona to substantially retard the m=1 instability[7].

We have produced both gas-embedded and capillary pinches in deuterium at 1 atmosphere. Using a 3.5 Ohm, 100 ns pulse line we obtained pinch currents of 100 kA rising at a rate of 6 kA/ns. The gas-embedded pinch was designed with tungsten pins placed in the electrodes. As in the Los Alamos experiments, streak photographs showed this type of pinch to expand rapidly with a velocity of 10^6 cm/s, and soft x-ray detectors showed the electron temperature to rise and fall in 20 ns with a peak at 950 eV. Both of these observations are manifestations of the accretion. The 950 eV is too high to be accounted for by classical processes alone, suggesting the pinch was anomalously resistive. As the drift velocity was estimated to be about four times the sound speed, it seems the most likely cause was the ion acoustic instability. Figure 2a shows oscilloscope traces of the pinch current and the signal from a simple one-turn loop oriented to detect the axial flux produced by the m=1 instability. At t=80 ns, when streak photographs show the pinch radius to be 0.1 cm, we calculate n, the number of turns of the helical plasma, to be only 0.4. This implies that the pinch has not wound up into a helix with wavelength $\lambda = 4\ r$ as predicted by theory[7] and observed in other experiments[8], but rather has adopted a "twist" with wavelength $\lambda = 125\ r$. This may be because the rate of rise of current in our experiments was an order of magnitude greater than that in Ref. [8].

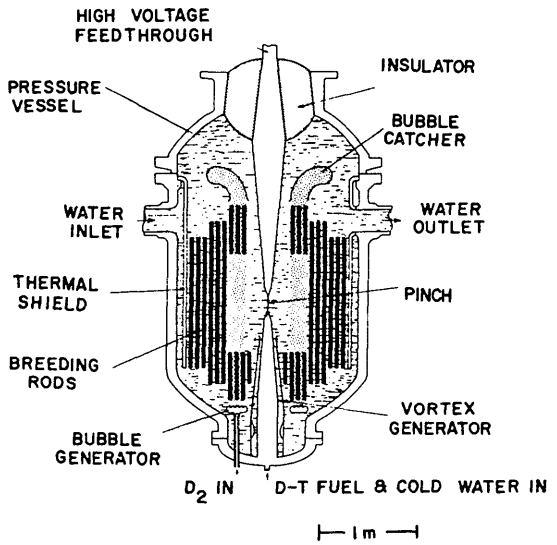

FIG. 3. Conceptualized pressurized water z-pinch reactor.

When the pinch was formed inside the capillary, we observed virtually the same axial current as in the gas-embedded pinch but no axial flux (Figure 2b). From this we conclude that the instability had indeed been suppressed and the current path remained axial. What we cannot conclude from this data is whether or not the plasma actually contracted away from the wall: 100 kA may not be enough to pinch the plasma if it is anomalously heated. The Bennet temperature for these conditions is about 900 eV and the total neutron yield was predicted to be $\sim 10^6$, which was below our detector threshold. Experiments at higher currents (400 kA), which should produce significant neutron yields, are under development.

NRL is developing a fusion reactor concept based on the z-pinch, as shown in Fig. 3. It is proposed to form the 100 μm radius pinch repetitively in a vortex of water pressurized to about 100 atmospheres, which would also be the pinch pressure. Axial flow of the water provides a continuously replaceable first wall and removes the heat. The design is intended to exploit the technology of pressurized water fission reactors, including the use of fuel rods to breed tritium. Based on the Los Alamos figure of 4.4 MJ nuclear yield per cycle, the pinch, if operated at 120 Hz, would

produce about 500 MW_{th}. It is proposed to power the pinch from a 60 Hz supply which would be compressed into a train of bipolar pulses, each of 2 μs duration, by means of non-linear magnetic elements. This eliminates the need for repetitive switches, which are a principal drawback of pulsed systems. The rapid repetition rate would ensure that the thermal stresses were essentially steady state.

IV. SUMMARY

Although the linear z-pinch is one of the oldest plasma confinement geometries, its development into a practical fusion system is still in its infancy. Nevertheless, both the pinch physics and the engineering appear to be quite favorable, and they suggest that this could become a very attractive uncoventional approach to fusion.

REFERENCES

[1] HAGENSON, R.L., TAI, A.S., KRAKOWSKI, R.A., MOSES, R.W., Nucl. Fusion **21** (1981) 1351.
[2] HAMMEL, J.E., SCUDDER, D.W., SHLACHTER, J.S., Nucl. Instrum. Methods **207** (1983) 161.
[3] SHLACHTER, J.S., Los Alamos Natl Lab. Rep. LA-9333-T (1982).
[4] JAHODA, F.C., LITTLE, E.M., QUINN, W.E., SAWYER, G.A., STRATTON, T.F., Phys. Rev. **119** (1960) 843.
[5] LINDEMUTH, I.R., BROWNELL, J.H., OLIPHANT, T.A., WEISS, D.L., J. Appl. Phys. **53** (1982) 1415.
[6] JARBOE, T.R., BAKER, W.R., Rev. Sci. Instrum. **45** (1974) 43.
[7] MANHEIMER, W.H., LAMPE, M., BORIS, J.P., Phys. Fluids **16** (1973) 1126.
[8] DANGOR, A.E., FAVRE DOMINQUEZ, M.B., LEE, S., KAHAN, E., Phys. Rev. **A27** (1983) 2751.

DRIFT INSTABILITIES AND THE DYNAMO EFFECT IN THE REVERSED-FIELD PINCH

N.T. GLADD, N.A. KRALL
JAYCOR, San Diego, California

R.W. MOSES, A.R. JACOBSON
Los Alamos National Laboratory,
Los Alamos, New Mexico

United States of America

Abstract

DRIFT INSTABILITIES AND THE DYNAMO EFFECT IN THE REVERSED-FIELD PINCH.

Current-driven drift modes are shown to have potentially a strong influence on both the confinement of the plasma configuration and the dynamo sustainment of the magnetic configuration in the reversed-field pinch (RFP). A transport model is developed based on the fluctuating radial magnetic fields produced by this mode which could produce a low level of magnetic stochasticity. A kinetic model of the dynamo effect is presented in which stochastically wandering electrons are found to sustain poloidal currents. Results are presented which explain the key anomalies observed in RFP behaviour (particularly the slow current decay) in terms of such electron dynamics.

1. INTRODUCTION AND CONCLUSIONS

The RFP is a toroidal axisymmetric device in which the primary confinement field, B_θ, is poloidal, generated by a toroidal current flowing in the plasma. This current implies a possible source of instabilities which could affect transport of particles and energy. However, if the instability produces fluctuating radial magnetic fields, it could also be the source of magnetic stochasticity, which has been suggested as a possible mechanism for the dynamo effect observed in RFP experiments.

In this paper we develop both the theory of instabilities which drive radial magnetic fluctuations and the theory of magnetic sustainment produced by radial transport of electrons. The stability calculation is based on the current-driven drift wave; the dynamo calculation is general in that any source of adequate radial electron transport can drive the proposed mechanism. We conclude that the current-driven drift wave is a likely source of turbulence in RFP, and that the proposed dynamo mechanism is both plausible and consistent with observed confinement properties of RFP.

In Section 2 we investigate the stability of RFP to current-driven drift modes, including the effects of beta, shear and collisionality, and estimate the magnetic fluctuation level, transport and stochasticity to be expected from these modes. In Section 3 we develop a model of the dynamo effect based on the presence of magnetic stochasticity.

2. CURRENT-DRIVEN DRIFT WAVES: STABILITY AND TRANSPORT

The RFP is characterized by a strong field-aligned current which is almost certainly its dominant source of free energy. This parallel current can lead to the unstable coupling of various drift waves, either through the coupling of accelerated and decelerated Alfvén waves [1-3] or through the coupling of accelerated sound waves and decelerated Alfvén waves [4,5]. We focus here on this latter class of modes, the current-driven drift waves (CDDW).

Because of the strong current, CDDW are unstable in the presence of a sheared magnetic field, even without lowest level toroidal effects. It is important, however, to include other characteristic features of RFP--strong current, strong magnetic shear, finite plasma beta, and strong collisional effects. We examine the CDDW in such a parametric environment.

The governing equations for CDDW consist of two coupled second-order differential equations, with coefficients asymmetric with respect to a mode rational surface [5]. The great complexity of these governing equations makes analytical analysis impractical. Therefore we resort to numerical shooting methods to analyse the linear stability of these modes.

In brief summary, we find that the effect of the current is to destabilize the longest wavelength universal mode (CDDW). Magnetic shear is stabilizing and affects the critical current for exciting the CDDW. Strictly speaking, a slab model analysis is not adequate to treat the strong shear characterizing reversed field pinches, $L_N/L_S \sim 1$, but values as large as $L_N/L_S \sim 0.2$ may be safely examined to give an indication of the threshold current. Another very important parameter is the plasma beta. Electromagnetic effects strongly couple the universal modes to Alfvénic modes, and in the specific case of CDDW the coupling is such as to significantly enhance the growth rates. The destabilizing influence of magnetic shear is illustrated in Fig. 1 where the critical current required to excite long-wavelength CDDW is given as a function of shear for several values of beta.

Another important factor affecting the growth of CDDW is the plasma collisionality which may be substantial in an RFP environment. The collisionality model is also important since simple number-conserving models are suspect because of the strong parallel current. To this end, we have developed momentum- as well as number-conserving collisional models. The

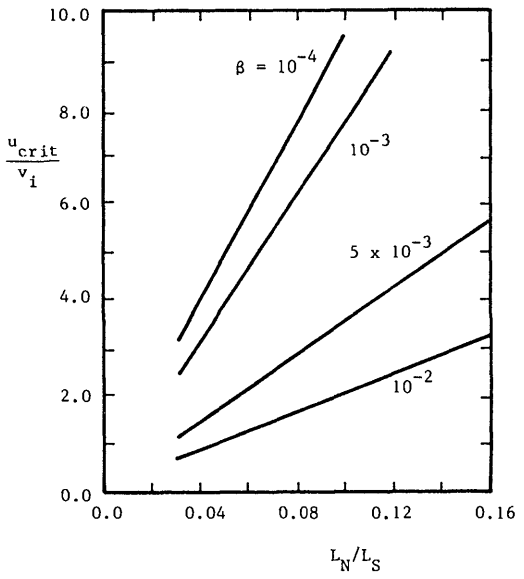

FIG. 1. Dependence of critical current on shear for different plasma β, with ν = 0 and $k_y \rho_i = 0.1$.

effect of collisionality is stabilizing in some regimes and destabilizing in others. We show the effect of collisionality on the critical current for long-wavelength CDDW in Fig. 2 for a low-beta, weakly sheared tokamak-like case and a higher beta, more strongly sheared RFP case.

These modes are fully electromagnetic, $\delta B \gtrsim \delta E$, and the dominant transport is due to flow along perturbed magnetic field lines. This effect allows a particle to cover a radial distance $v_{Th} \delta B_r / \omega B_o$ in an oscillation time ω^{-1}. Assuming that the bulk diffusion is ambipolar, the radial flux produced by this mode is

$$nV_x = n(T_e/m_i)^{1/2}(\omega_{ci}/\omega)(a_i/a)(\delta B_r/B_o)^2$$

If the mode saturates at an energy comparable to that of the drifts which drive it, the mode will have an energy $\simeq (c^2/a^2\omega_p^2)\ (B_o^2/8\pi) \simeq 5 \times 10^{-5}\ (B_o^2/8\pi)$ for ZT-40M parameters.

Even this low level will substantially influence transport, leading to a confinement time $\tau \simeq 10^{-16}\ na_j^2/B$, where a_j is the width of the current channel. This gives $\tau \simeq 0.2$ ms for a typical example.

Just as important as confinement is the fact that this effect produces both an ambipolar electric potential $\simeq T_e$ and

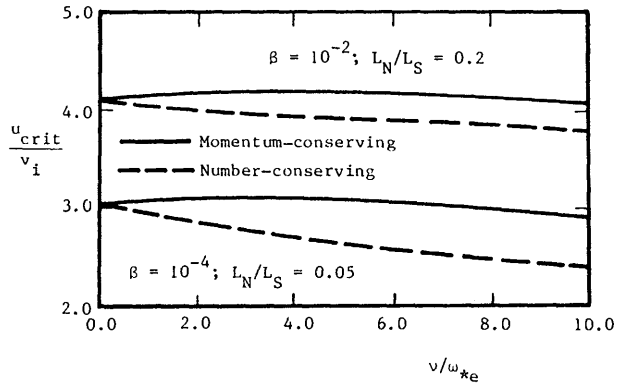

FIG. 2. Marginal stability curves comparing critical current with collisionality for two different collision models, with $k_y\rho_i = 0.1$.

a radial wandering of electrons, with excursion distances proportional to their velocity. This sort of radial excursion is an essential feature of models of the dynamo effect observed in RFP, as detailed in the next section.[1]

3. NONLOCAL RESISTIVITY AND THE DYNAMO EFFECT

The model of nonlocal plasma resistivity proposed by Jacobson and Moses [6] incorporates the concept of magnetic field line stochasticity discussed by many other authors [7-9]. To avoid the complexity of having trapped particles, this model is presented in slab geometry with $\beta = 0$, so that $B = |\underset{\sim}{B}|$ is approximately uniform in space. The magnetic axis of the cylindrical model becomes the $x = 0$ plane of the slab model. The plasma boundary is now at $x = \pm a$. As in the case of the cylinder, the driving electric field is $\langle\underset{\sim}{E}\rangle = E_0\hat{z}$, where $\hat{z}$ is the unit vector in the z direction. It is assumed that $\langle\underset{\sim}{B}\rangle$ satisfies a force-free model, $\nabla x\langle\underset{\sim}{B}\rangle = \mu(r)\langle\underset{\sim}{B}\rangle$. If μ were a constant, the solution would be $\langle B_z(x)\rangle = B_0\cos\mu x$, $\langle B_y(x)\rangle = B_0\sin\mu x$. In this model, μ is allowed to be a function of x to obtain self-consistent currents and fields.

It is postulated that stochasticity is introduced by field fluctuations $\delta\underset{\sim}{B}(\underset{\sim}{r},t)$ that randomly move field lines across the plasma. Following Rosenbluth et al. [7], a field line diffusivity, D_F, is introduced such that a particle

[1] In fact, the same level of δB used above to estimate the confinement time gives a stochasticity level (defined in Section 3) of $\lambda_0 D_F/a^2 \lesssim 0.1$, which is consistent with the experiment.

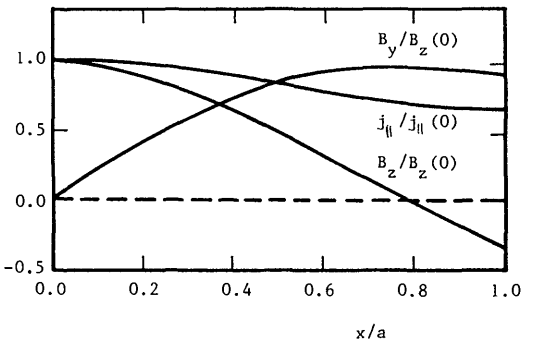

FIG. 3. Magnetic field components and parallel current density versus x, normalized to 1 at x = 0, with $\lambda_0 D_F/a^2 = 0.05$.

following a field line a distance ℓ will undergo a mean square excursion in the x direction,

$$\langle(\Delta x)^2\rangle \simeq 2\ell D_F \tag{1}$$

The plasma is treated by a Lorentz model where only electron-ion scattering is considered. For simplicity, it is assumed that electron guiding centers move along field lines, and the electron magnetic moment does not change between collisions. Unlike the Spitzer model [10], the total momentum imparted to all electrons in a volume element by the electric field does not equal the momentum lost by electrons to collisions in the same volume element. For example, electrons near the x = 0 plane gain momentum faster than it is scattered away:

$$\eta_{\|}\langle J_z(0)\rangle < \langle E_z(0)\rangle \tag{2}$$

This happens because the mean-free path of an electron, λ, may be large enough to move the electron over significant portions of the plasma between collisions:

$$2\lambda D_F \sim a^2 \tag{3}$$

An electron may be accelerated in a region of high parallel field, $E_{\|}$, and move out of that region before it has a chance to scatter. Correspondingly, electrons may enter a region such as the reversal layer, $x = x_r$, where they lose more momentum to scattering than is gained from electric fields:

$$\eta_{\|}\langle J_y(x_r)\rangle > \langle E_y(x_r)\rangle = 0 \tag{4}$$

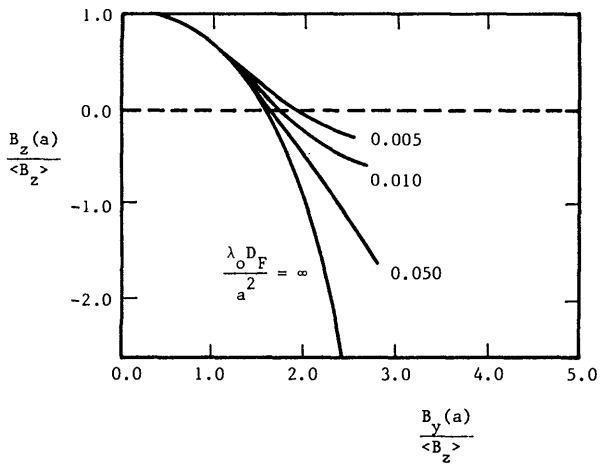

FIG.4. $B_z(a)/\langle B_z \rangle$ *versus* $B_y(a)/\langle B_z \rangle$ *for various* $\lambda_0 D_F/a^2$.

If the inequalities in Eqs (2) and (4) are correct, there is a possibility for a kinetic RFP profile sustainment mechanism.

A detailed description of the nonlocal resistivity is given in Ref. [6] and is beyond the scope of this paper. The key conclusions are given in Figs 3 and 4. A Boltzmann equation for electrons in a stochastic RFP was developed and a self-consistent example with field reversal was computed using ZT-40M temperature, density and confinement time data. The results shown in Fig. 3 indicate that field reversal can be maintained with a nonlocal resistivity. The level of stochasticity is described by $\lambda_o D_F/a^2 = 0.05$,[2] where λ_o is the mean-free path for 90° scattering of electrons with the speed $v_o = (2kT/m_e)^{1/2}$. These data were obtained for ZT-40M parameters at a current of $I_z \simeq 100$ kA [11]. Since λ scales as $\lambda = \lambda_o(v/v_o)^4$, the high speed electrons are far more effective than thermal electrons in carrying current to the reversal layer. This allows λ_o to be much smaller than indicated by Eq. (3).

Figure 4 illustrates how the reversal depends on $\lambda_o D_F/a^2$. Although the information available to estimate $\lambda_o D_F/a^2$ is subject to many approximations [6], the model is quite insensitive to the precise value of $\lambda_o D_F/a^2$.

Although field line stochasticity is sufficient to drive this RFP model, it is not necessary. It is necessary that electrons wander stochastically through the plasma whether or

[2] Comparable to that obtained in the previous section.

not field lines do. There may be instances in which perpendicular transport of electrons drives an RFP in the presence of good flux surfaces. This result, coupled with calculations of instabilities such as the CDDW which predict radial transport of electrons, suggests that the proposed dynamo model applies in a wide variety of practical situations.

ACKNOWLEDGMENT

This work was supported by the U.S. Department of Energy.

REFERENCES

[1] CHU, M. S., CHU, C., Bull. Am. Phys. Soc. 22 (1977) 1110.
[2] KRALL, N. A., GLADD, N. T., Bull. Am. Phys. Soc. 27 (1982) 1033.
[3] CHU, C., BARD, W., MOORE, R., LEE, Y. C., GA Technologies Report GA-A17484 (1984).
[4] NISHIKAWA, K. I., ITOH, K., TUDA, T., TERASHIMA, T., J. Phys. Soc. Japan 51 (1982) 1606.
[5] GLADD, N. T., KRALL, N. A., JAYCOR Report J530-83-150 (1983).
[6] JACOBSON, A. R., MOSES, R. W., Phys. Rev. A 29 (1984) 3335.
[7] ROSENBLUTH, M. N., et al., Nucl. Fusion 6 (1966) 297.
[8] RECHESTER, A. B., ROSENBLUTH, M. N., Phys. Rev. Lett. 40 (1978) 38.
[9] RUSBRIDGE, M. G., Plasma Phys. 19 (1977) 499.
[10] SPITZER, L., Physics of Fully Ionized Gases, Wiley, New York (1962).
[11] BAKER, D. A., et al., "Experimental and Theoretical Studies of the ZT-40M Reversed Field Pinch," this conference paper no. IAEA-CN-44/D-II-2.

COUPLED TRANSPORT AND HEATING IN EBT AND EBS*

C.L. HEDRICK, D.B. BATCHELOR, G.L. CHEN,
R.C. GOLDFINGER, D.E. HASTINGS, E.F. JAEGER,
D.K. LEE, L.W. OWEN, D.A. SPONG, J.S. TOLLIVER,
N.A. UCKAN
Oak Ridge National Laboratory,
Oak Ridge, Tennessee

N.A. KRALL, S. HAMASAKI, J. SPERLING
JAYCOR, San Diego, California

United States of America

Abstract

COUPLED TRANSPORT AND HEATING IN EBT AND EBS.

In ELMO Bumpy Torus (EBT) and EBT-like devices, hot electron rings form at the edge of the warm core plasma. As early as 1975 it was recognized that microwave heating, which plays such a significant role in electron dynamics, should be incorporated into transport models. Recent theoretical microwave heating and transport studies suggest that this is critical for explaining EBT experiments. In particular, descriptions of the electron distribution as a sum of only two distributions (i.e. one for the core and one for the rings) are inadequate for understanding either the heating or the losses in any depth. In this paper the interplay of heating and transport from a kinetic standpoint is discussed and phenomena associated with the microwave heating at the fundamental and second harmonic of the electron cyclotron frequency are pointed out. These phenomena for the EBT magnetic configuration are compared and contrasted with those for a variant of the standard EBT – the ELMO Bumpy Square (EBS).

1. INTRODUCTION

The non-Maxwellian character of the electron distribution function in ELMO Bumpy Torus (EBT) is intimately connected with fundamental and second harmonic electron cyclotron heating (ECH). These two types of ECH affect different parts of velocity and configuration space, which in turn have differing single-particle orbit and loss characteristics. Thus, it is natural to divide the discussion of transport and heating into two parts: fundamental ECH and second harmonic ECH. The body of this paper consists of three sections: heating and losses associated with fundamental ECH in EBT; heating and losses asssociated with second harmonic ECH in EBT; and, finally, comparison of these phenomena in EBT and the ELMO Bumpy Square (EBS).

* Research sponsored by the Office of Fusion Energy, US Department of Energy, under Contract No. DE-AC05-84OR 21400 with Martin Marietta Energy Systems Inc.

2. FUNDAMENTAL ECH

The elementary notion of fundamental heating is that strong resonance heating occurs at spatial positions for which the microwave frequency ω is equal to the local electron cyclotron frequency Ω_e. (In standard EBT operation the resonant surface is approximately orthogonal to the field lines and located nearer the coil planes than the midplanes.) When the Doppler effect is included, the condition for fundamental cyclotron resonance becomes

$$V_{\parallel}^{res}(s) = [\omega - \Omega_e(s)]/k_{\parallel}(s) \tag{1}$$

where $V_{\parallel}^{res}(s)$ is the parallel velocity necessary for resonance at location s along the field line and $k_{\parallel}(s)$ is the real part of the parallel wave number at s. As an extraordinary mode wave approaches the (unshifted) fundamental resonance from the high magnetic field side, absorption begins, and wave power starts to decrease where the Doppler-shifted resonance is a few times the thermal speed.

The wave power profile along a field line may be estimated from

$$P_{\mu}(\Omega_e/\omega) = P_{00}\exp\left\{-\int_{s(\Omega_e/\omega)}^{\infty} ds'\, 2k_i\left[\frac{\Omega_e}{\omega}(s')\right]\right\} \tag{2}$$

Here $k_i(\Omega_e/\omega)$ is the imaginary part of the wave vector obtained by solving the dispersion relation for extraordinary waves. Using a linear approximation for the dependence of the magnetic field on s near resonance, we find that most of the power is absorbed before reaching the unshifted resonance. For example, using a magnetic scale length of 20 cm and an electron temperature of 300 eV, we find that 90% of the power is absorbed before the wave is 0.8 cm from the unshifted resonance [$\delta \equiv \Omega_e(s)/\omega - 1 = 0.04$].

The importance of this observation is that only particles with comparatively large $V_{\parallel}$ are strongly heated (i.e. those which reach regions where P_{μ} is large). To make contact with variables commonly used to describe single-particle drift motion (and associated losses), we use μ-conservation to rewrite Eq. (1) as

$$\epsilon^{res} = \frac{1}{2} mc^2 \frac{\delta^2}{n_{\parallel}^2}/[1 - r(1+\delta)(1-\zeta^2)] \tag{3}$$

where the resonant energy ϵ^{res} and the parallel index of refraction $n_{\parallel}$ are functions of $\delta \equiv \Omega_e(s)/\omega - 1$. The quantities $r \equiv \omega/\Omega_{e0}$ and $\zeta^{\parallel} \equiv (V_{\parallel}/V)_0$ are measured in the midplane. We see from Eq. (3) that

the minimum resonant energy is obtained for passing particles ($\zeta = 1$) and that the resonant energy increases for lower values of ζ (e.g. for those trapped particles which cross the unshifted resonant surface). We conclude that if the bulk electron distribution in EBT were a Maxwellian with $T_e = 300$ eV most of the power would be absorbed by passing particles with energy above approximately $3/2T_e$ and by barely trapped particles with energy above approximately $6T_e$.

We see that there is considerable velocity space structure in the microwave heating operator. This comes about not only through the explicit velocity dependence but also because of the velocity dependence of the spatial location of the Doppler-shifted resonance and the strong spatial variation in wave power density due to heavy damping. Of course particles with $\zeta < (1 - 1/r)^{1/2}$ (i.e. particles that turn before reaching resonance) are not heated at all.

The primary effect of fundamental extraordinary mode heating is to increase the electron's perpendicular energy at the resonance location. Parallel heating comes about only through μ-conservation as the particle moves to lower magnetic field. Therefore, μ tends to decrease as the heating progresses, passing particles become trapped, and trapped particles turn ever closer to the midplane, until electric field profile effects effectively shut off the heating. For the particles that are resonant at large values of δ, where the wave electric field is large, the heating is quite rapid. We can estimate the average heating rate as

$$\frac{\Delta\epsilon_\perp}{\Delta t} = \left(\frac{1}{\tau}\frac{\pi e^2 E_+^2}{2m\Omega_e}\frac{L}{V_\parallel}\right)_{s^{res}}$$

where $\epsilon_\perp$ is the perpendicular electron energy, E_+ is the amplitude of the right circular component of the field, L is the magnetic field scale, τ is the transit time between successive passes through resonance, and s^{res} is the location of the Doppler-shifted resonance. Using parameters appropriate for EBT-S with 100 kW of ECH power [giving the asymptotic value for $E_+ \cong 3 \times 10^7$ (eV/cm)], one obtains $\Delta\epsilon_\perp/\Delta t \simeq 3 \times 10^7$ eV/s. On the other hand, particles in the bulk of the distribution ($\epsilon \lesssim T_e$) can only be heated by collisions with those energetic particles that are directly heated by the microwaves.

We now turn to loss processes associated with the region of velocity space primarily affected by fundamental ECH[1]. At energies high enough that $\vec{E} \times \vec{B}$ drifts are subdominant, transitional particle drift orbits are poorly centered in the standard EBT magnetic configuration [2]. In the absence of scattering, many of the particles would drift to the wall. Thus, the effect of fundamental ECH in the standard EBT magnetic configuration is to drive particles into a region of velocity space (loss wedge) where they are poorly confined.

Thus, one is tempted to model the loss processes in a manner similar to that employed for loss cones in mirror machines. However, for low and modest energies, the drift times are sufficiently long and the scattering by Coulomb collisions and (especially) microwaves is so rapid that the loss processes tend to be diffusive in character. That is, a single particle is scattered on and off a poorly confined drift orbit many times before reaching the wall. Even so, the diffusive loss processes tend to be large in the transitional regions of velocity space.

To take into account the spatial diffusion due to scattering by microwaves as well as Coulomb collisions, it is convenient (as in ordinary neoclassical theory) to subdivide the processes into nonresonant and resonant diffusion. By ordinary neoclassical theory we include formulations [1,3-7] that allow for determination of the distribution function rather than just macroscopic moments (e.g. density and temperature). These formulations take the form $\partial f/\partial t = C(f) + \nabla \cdot (\tilde{D}\nabla f) = 0$. Taking moments of $\tilde{D}$ with an assumed form for f (e.g. a Maxwellian) yields the various macroscopic transport coefficients.

Nonresonant diffusion is dominant at low energies, where $\vec{E} \times \vec{B}$ drifts dominate single-particle orbit behavior. For these low energies, the new feature encountered in that microwave scattering is far more localized in pitch angle than is Coulomb scattering. Numerical calculations of nonresonant transport due to pitch angle scattering in the large electric field limit (i.e. low energy) have been performed. Even when the scattering rate due to microwaves is much larger than the Coulomb scattering rate, the nonresonant transport is only changed by approximately a factor of 2 — because of the localization of the fundamental ECH scattering in pitch angle space.

At higher energies, where resonant diffusion becomes important, including microwave scattering in addition to Coulomb scattering is relatively simple since only the scattering rates near resonance are important. This allows one to carry over previously developed neoclassical results [6-8] by the simple process of replacing the Coulomb collision frequency by the sum of the Coulomb and microwave scattering frequencies. The formal expressions for "plateau" diffusion in EBT (independent of scattering frequency) are unchanged. However, plateau diffusion extends to higher energy because microwave scattering does not decrease as rapidly with energy as does Coulomb scattering.

For sufficiently high energies, plateau diffusion is replaced by "banana" diffusion, which is larger than neoclassical diffusion by the ratio $(1 + \nu_m/\nu_c)$, where ν_m is the microwave scattering rate and ν_c is the Coulomb scattering rate. For energies where banana diffusion would formally apply, the distinction between diffusive losses and losses due to particles drifting directly to the wall becomes blurred. In particular, the usual transport ansatz that the losses do not significantly modify the shape of the lowest-order distribution function is no longer tenable for these high energies.

To ascertain the joint effect of fundamental ECH and diffusive and direct losses, Fokker-Planck calculations (in ϵ and μ) have been carried out numerically. Because of the aforementioned blurring between diffusive and direct losses, various simplified models of the loss processes have been used. Although detailed differences occur for the shape of the electron distribution function, the various models all lead to the conclusion that approximately 50% of the power absorbed at the fundamental in EBT-I/S is rapidly lost due to scattering into regions of velocity space with poorly confined single-particle orbits.

3. SECOND HARMONIC ECH

It has long been observed experimentally that the radial ambipolar potential profile is linked to the heating geometry [9]. For example, the peak of the potential occurs approximately at the radial position where second harmonic heating is strongest. In this region of minor radius, one expects [4] not only that the high energy (hundreds of keV) hot electron rings form but also that an electron population intermediate in energy to the bulk and ring characteristic energies will form. This intermediate energy (e.g. 1/2 to tens of keV) population will differ primarily from the hot electron ring population in that its loss rates will be much higher. (It will also tend to be spread more in radius — particularly at its lowest energies.)

The large loss rates for this intermediate population of electrons suggest that it could dominate formation of the electrostatic potentials. This can be seen by assuming that the losses are diffusive in character so that if this population has density n_W and temperature T_W then its contribution to the radial particle flux is

$$\Gamma_W = -D_W\left[\nabla n_W - n_W \frac{|e|\nabla\phi}{T_W} + \left(\eta \frac{n_W}{T_W}\right)\nabla T_W\right] \qquad (4)$$

where D_W is a generalization of the neoclassical diffusion coefficient that includes microwave (and any other scattering process) in addition to Coulomb scattering. The dimensionless quantity η is the ratio of the off-diagonal transport coefficient to D_W ($\eta \gtrsim 1$).

If D_W is large compared to the (lower-energy) bulk electron and ion transport coefficients, then charge conservation ($\Gamma_e = \Gamma_i$) can only occur if the factor multiplying D_W in Eq. (4) is relatively small. If we regard n_W and T_W as fixed (i.e. constantly replenished by second harmonic heating), then the smallness of this factor implies

$$|e|\nabla\phi \cong \eta\nabla T_W + T_W\nabla \ln n_W \qquad (5)$$

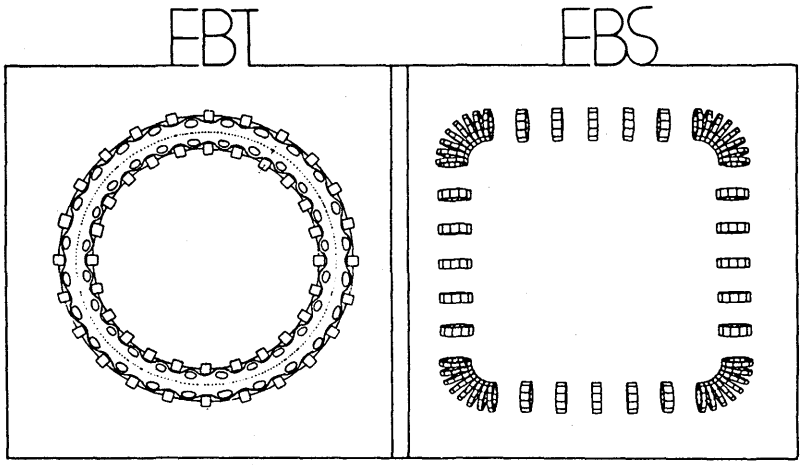

FIG. 1. Comparison of standard EBT and EBS configurations. The toroidal effects on particle drifts in the EBS are greatly reduced by increasing the ratio of the 'corner' magnetic field to the bumpy field of the sides.

This expression for $\nabla\phi$ implies that the profile of ϕ will follow, approximately, the radial profiles to T_W and n_W. These simple analytic arguments for potential formation have been validated numerically by more elaborate, radially resolved transport calculations.

Another feature of the experimentally observed potential is that it is asymmetric in poloidal angle [9]. The lowest-order feature is that the radial potential peak is highest nearest the major axis. Because single-particle orbits are shifted toward the major axis [the shift increasing with $(V_{\parallel}/V)_0$ for trapped particles], one would expect the intermediate population of electrons to have somewhat higher density and temperature nearest the major axis. Equation (5) would then predict that the potential has a similar asymmetry.

The low-energy bulk population of particles is quite sensitive to the electric field because its drift motion is dominated by $\vec{E} \times \vec{B}$. Monte Carlo calculations of the losses for this group of particles indicate that asymmetric potentials can increase the losses by one to two orders of magnitude [10].

4. ELMO BUMPY SQUARE

Virtually since the inception of the EBT program, variants of the basic EBT magnetic configuration have been considered in an attempt to reduce drift-orbit-induced losses of the types described in the previous sections. An interesting variant is the ELMO Bumpy Square (EBS), illustrated in Fig. 1. The EBS, like many EBT

variants, improves single-particle confinement of transitional and passing particles. The central idea, validated by detailed numerical calculations [2], underlying the orbit improvement is that the toroidal effects are concentrated in high-B "corners" (segment of toroidal solenoids). As in any EBT variant, the vertical drift produced by toroidal curvature must be augmented by rotary drift provided by bumpiness. (Non-closed-field-line toroidal devices use rotational transform to achieve this augmentation.) In EBS the vertical drift (inversely proportional to B_{corner}) is reduced relative to the rotary drift produced by bumpiness. By increasing the ratio of B_{corner} to B_{side}, the drift orbits of passing and transitional particles become better-centered about the minor axis of the device. Trapped particles, which do not enter the corners at all, have drift surfaces that are concentric to the minor axis.

There are still some transitional and passing particles that are poorly confined, but the fraction of pitch angle space with poor orbits is greatly reduced. In addition, the region of poorest confinement (transitional particles) is moved to higher values of $(V_{\parallel}/V)_0$. These effects, together with the greater geometric separation between fundamental resonance surfaces and regions where transitional particles spend considerable time, greatly reduce the type of loss discussed in Section 2. The various Fokker-Planck calculations discussed in Section 2 indicate an order of magnitude reduction in this class of loss.

Formation of the hot electron rings has been observed experimentally to be facilitated by axisymmetric mirror cells as in EBS [11]. The more symmetric orbits of EBS would lead to a more symmetric intermediate energy population (associated with second harmonic ECH). This in turn would lead to more symmetric ambipolar potentials.

In addition to the order-of-magnitude improvement associated with symmetric potentials indicated by Monte Carlo calculations for EBT-I/S, numerical calculations comparing EBT and EBS with symmetric potentials indicate an order-of-magnitude improvement in lifetime for EBS [2].

Theoretical comparisons of EBT and EBS equilibrium and macrostability properties indicate no substantial differences (aside from better centering of the plasma) [2,12]. This, coupled with the very substantial reduction in the losses discussed herein, makes the EBS a very attractive alternative to the basic EBT magnetic configuration.

REFERENCES

[1] DANDL, R. A. et al., Research Program for Plasma Confinement and Heating in ELMO Bumpy Torus Devices, Oak Ridge National Laboratory Report ORNL-TM-4941 (June 1975).

[2] UCKAN, N. A. et al., ELMO Bumpy Square, Oak Ridge National Laboratory Report ORNL/TM-9110.

[3] JAEGER, E. F., HEDRICK, C. L., and TOLLIVER, J. S., A Kinetic Transport Model for the ELMO Bumpy Torus, Oak Ridge National Laboratory Report ORNL/TM-6313 (May 1978).
[4] TOLLIVER, J. S., JAEGER, E. F., and HEDRICK, C. L., in EBT Ring Physics (Proc. Workshop, December 3-5, 1979, Oak Ridge, Tennessee, ORNL CONF-79/228 (1980).
[5] JAEGER, E. F., HEDRICK, C. L., and SPONG, D. A., Nucl. Fusion 19 (1979) 1627.
[6] HASTINGS, D. E., JAEGER, E. F., HEDRICK, C. L., TOLLIVER, J. S., Phys. Fluids 26 (1983) 1516.
[7] TOLLIVER, J. S., JAEGER, E. F., HASTINGS, D. E., and HEDRICK, C. L., Phys. Fluids 26 (1983) 1391.
[8] HEDRICK, C. L., et al., in Plasma Physics and Controlled Nuclear Fusion 1982," Vol. II (Proc. Ninth Int. Conf.) 613.
[9] BERRY, L. A. et al., "Recent Advances in Confinement and Heating Physics in EBT-S," paper IAEA-CN-44/D-III-4 this conference.
[10] TOLLIVER, J. S. and HEDRICK, C. L., "Monte Carlo Estimates of Transport Rates in an EBT with Asymmetric Potential Profiles," submitted to Phys. Fluids.
[11] DANDL, R. A. et al., "The ELMO Bumpy Torus Experiment," Oak Ridge National Laboratory Report ORNL-TM-3694 (November 1971).
[12] SPONG, D. A., HEDRICK, C. L., and VAN DAM, J. W.,, "Ballooning Modes in the ELMO Bumpy Square Configuration Using the Generalized Kinetic Energy Principle," to be submitted to Phys. Fluids.

IMPURITY TRANSPORT IN THE WENDELSTEIN VII-A STELLARATOR

W VII-A TEAM: G. CATTANEI, D. DORST, A. ELSNER, V. ERCKMANN, G. GRIEGER, P. GRIGULL, H. HACKER, H.J. HARTFUSS, H. JÄCKEL, R. JAENICKE, J. JUNKER, M. KICK, H. KROISS, G. KUEHNER, H. MAASSBERG, C. MAHN, S. MARLIER, G. MÜLLER, W. OHLENDORF, F. RAU, H. RENNER, H. RINGLER, F. SARDEI, M. TUTTER, A. WELLER, H. WOBIG, E. WÜRSCHING, M. ZIPPE

NI GROUP: K. FREUDENBERGER, G.G. LISTER, W. OTT, F.-P. PENNINGSFELD, E. SPETH

Max-Planck-Institut für Plasmaphysik,
Euratom-Association, Garching,
Federal Republic of Germany

Abstract

IMPURITY TRANSPORT IN THE WENDELSTEIN VII-A STELLARATOR.

The impurity transport in typical net current-free neutral beam heated plasmas in the W VII-A Stellarator is modelled by a 1-D impurity transport and radiation code. The evolution of the total radiation in time and space deduced from soft X-ray and bolometer measurements can be fairly well simulated by the code. Experimentally, oxygen was found to give the main contribution to the radiation losses. In the calculations an influx of cold oxygen desorbed from the walls in the order of $(10^{13} - 10^{14})$ $cm^{-2} \cdot s^{-1}$ and a rate of fast-injected oxygen corresponding to a 1% impurity content of the neutral beams in combination with neoclassical impurity transport led to a quantitative agreement between simulation and observed radiation. The transport of Al trace impurities injected by the laser blow-off technique was experimentally studied by soft X-ray measurements using a differential method allowing the time evolution of Al XII and Al XIII radial profiles to be extracted. These are compared with code predictions together with additional spectroscopic measurements. The main features of the impurity transport can be explained by neoclassical predictions. Some details, however, seem to require some additional anomalous transport. This may be due to a distortion of the magnetic configuration round resonant magnetic surfaces induced either by pressure-driven currents or some drift or fluctuations on the current of different coil systems.

1. INTRODUCTION

Plasma with $\beta(0) \lesssim 1\%$ can be confined by external magnetic fields in Wendelstein VII-A (R = 200 cm, a = 10 cm, l = 2, m = 5 helical windings). After build-up of an ohmically heated target, plasma neutral beam heating is applied (27 kV, H^0, 3–4 beam lines each with a power of 200–350 kW, almost perpendicular injection). The transition to currentless operation is achieved by controlled

reduction of the plasma current during the NI startup phase. During the current ramp the helical field is increased in order to keep the total rotational transform at the plasma edge constant [1]. $t(a) \approx 0.46$ has been used for the experiments. Under these conditions, regimes with good confinement properties ($\tau_p \approx 100$ ms) have been found. Typically this phase can be maintained for about 100–150 ms; after this time, radiation losses from accumulated impurities, also increased by the increased electron density, have increased so much that they lead to a significant decay of the electron temperature. Therefore the impurity problems are partly linked with good particle confinement [2]. There are also strong impurity sources in W VII-A because of the small plasma radius and the almost perpendicular neutral beam injection. Plasma/wall interaction, especially of fast injected hydrogen (up to 50% shine-through and 10–30% orbit losses), probably causes a high rate of desorption (O, C) and sputtering (Fe, Cr, Mo). In particular, beam impurities (O, C) can contribute because they are trapped more efficiently than fast hydrogen neutrals. Moreover, during changes of magnetic configuration, when the plasma current is decreased, increased plasma/wall interaction is observed.

The dominant part of the radiation losses in the plasma centre (up to 80%) consists of line radiation from He- and H-like oxygen impurities [1].

The one-dimensional simulation code for impurity transport and radiation, SITAR [3], has been used to describe the total radiation observed by soft X-ray and bolometer measurements as well as line radiation from oxygen and aluminium, the latter being injected as a tracer impurity.

Four different types of plasma discharges have been studied in particular: discharges with relatively low density and narrow density profiles (without gas puff) are compared with high density discharges characterized by significantly broader density profiles (with steady gas flow), which are expected to have a beneficial influence on the retardation of the central impurity density build-up.

A second comparison was made between experiments corresponding to 'co' and 'counter' neutral beam injection.

2. IMPURITY DIAGNOSTICS

Total radiation measurements were performed with a ten-channel bolometer system and a soft X-ray camera with 30 surface barrier diodes which are sensitive to radiation $\gtrsim 400$ eV. The radiances of various resonance lines along a chord through the plasma centre were recorded by a flat crystal spectrometer operating between 7 and 20Å and a grazing incidence spectrometer. Another VUV spectrometer supplied with a rotating mirror can also provide radial scans of resonance radiation from lower ionization states. Generally, however, the radiation originating near the plasma edge shows significant asymmetries which do not allow the measurements to be compared with 1-D transport calculations. Radial and time-resolved data on the combined radiation power from Al XII and Al XIII resonance lines are

derived from soft X-ray measurements using a 50 μm Be filter which, compared to the case without filter, attenuates the radiation by a factor of about 100, whereas the Al radiation at about 7 Å is only reduced by a factor of about 5. Typically, a 10–30% increase of the filtered X-radiation was observed when Al was injected into the plasma in tolerable doses by laser blow-off. Taking the difference between similar shots with and without Al injection after Abel inversion, the local power sum of Al XII and Al XIII can be evaluated. To correct for small n_e, T_e and Z_{eff} deviation of the shots taken for subtraction, HCN-laser interferometer signals and T_e and Z_{eff} measurements from X-continuum radiation were used. Oxygen continuum radiation has been assumed to be responsible for producing the radiation without Al injection.

3. IMPURITY TRANSPORT CODE

The code takes into account both neoclassical and anomalous impurity transport. The classical, Pfirsch-Schlüter and plateau fluxes corresponding to collisions of the impurity ions with the background plasma have been taken from Ref.[4]. The Pfirsch-Schlüter fluxes, including the interaction of impurity ions in different charge states, have been evaluated using the formalism given in Ref.[5] with the modification proposed in Ref.[6] to account for the mixed collisionality of background and impurity ions. For typical W VII-A experimental conditions, it has been found that the Pfirsch-Schlüter fluxes due to impurity-background collisions are in close agreement with the expression given in Ref.[4]. The classical fluxes due to impurity-impurity collisions are taken from Ref.[7]. The corresponding Pfirsch-Schlüter fluxes could be represented without loss of accuracy by using a simplified expression which differs from the classical impurity-impurity fluxes by the same factor of $2q^2$ as that for the impurity-background fluxes given in Ref.[4]. Therefore, to save computing time, the expression

$$\Gamma_z^{add} = \sum_{z' \neq z} \frac{\rho_{z'}^2}{\tau_{z'z}} \frac{1}{\sqrt{2}} \frac{z'}{z} (0.5 + q^2)$$

$$\times \left[\frac{\partial n_{z'}}{\partial r} - \frac{n_{z'} z'}{n_z z} \frac{\partial n_z}{\partial r} - \frac{1}{4} \left(\frac{z'}{z} - 1 \right) \frac{z_{z'}}{T} \frac{\partial T}{\partial r} \right]$$

was used for the neoclassical fluxes due to impurity-impurity collisions in addition to the fluxes given in Ref.[4].

Particularly in the case when oxygen concentrations exceed about 1%, this term leads to a considerable increase in the transport fluxes. They were separated

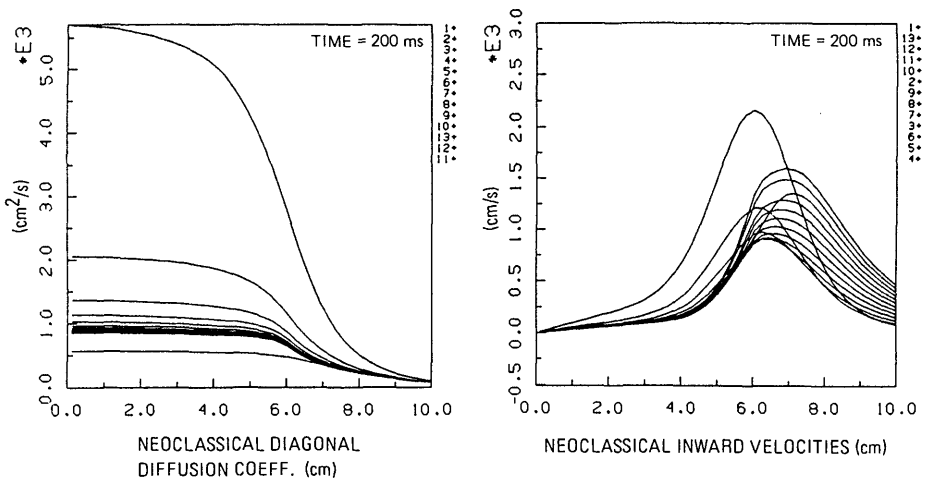

FIG.1. Calculated radial distribution of neoclassical diffusion coefficient and inward velocity (sum of classical, Pfirsch-Schlüter and plateau terms) for a particular time (200 ms) of a high density discharge.

into a diffusive and a convective term ($\Gamma_z = -D \cdot \partial n_z/\partial r - v n_z$). The anomalous transport, if it applies, is also modelled this way, with D and v equal for all charge states. Figure 1 gives an example of the calculated neoclassical diffusion coefficients and convective velocities for various Al charge states. For typical density and temperature profiles in W VII-A the velocity is generally inward.

The source term of neutral beam injected impurities was calculated by a Monte Carlo beam injection code [8]. Charge-exchange recombination of impurity ions with injected hydrogen neutrals is included. The excitation rate coefficients are taken in the form given in Ref.[9]. Because of the appreciable change of plasma parameters during typical W VII-A discharges, the time variations of temperature and density profiles are taken into account.

4. RESULTS FOR Al LASER BLOW-OFF EXPERIMENTS

Figure 2(a) shows the evolution of the spatial distribution of the radiation power density of Al XII and Al XIII after laser blow-off ($\sim 3 \times 10^{16}$ Al atoms). At the beginning, a peak of Al density is formed at about 5 cm as indicated by the hollow radiation profiles. After 10–15 ms a transition to peaked Al density profiles occurs. In Fig.2(b) a code calculation is presented which simulates the measured intensity quite well. For this particular high density discharge, hollow

plasma density profiles are maintained by strong gas feed during the Al penetration phase. The relatively small neoclassical diffusion coefficient in the plasma centre of about 500 $cm^2 \cdot s^{-1}$ in combination with a small outward convection velocity therefore implies a relatively slow transport to the plasma centre. To simulate the faster increase of the central radiation and the accelerated transition to peaked profiles, an additional anomalous diffusion coefficient in the order of (2000–3000) $cm^2 \cdot s^{-1}$ had to be added at particular radial ranges. This rather local deviation from neoclassical transport may possibly be caused by magnetic island formation near the plasma centre. This hypothesis is based on investigations of the dependence of energy and particle confinement on external rotational transform and residual current [1, 10, 11]. Moreover, for typical discharges, relatively flat temperature and density profiles are always observed around the plasma centre.

The decay of the Al radiation intensity is almost entirely caused by the electron temperature reduction at the end of the discharge. This is illustrated in Fig.2(c), (d), where the Al density corresponding to the calculation of the radiation intensity (Fig.2(b)) is plotted. The measurement is thus consistent with only negligible losses of Al ions during the entire duration of the discharge. In the plasma centre even a steady increase of the Al density can be observed, which seems to be an effect of the neoclassical inward velocity in combination with the continuous steepening of the plasma density in the plasma centre.

The characteristic time behaviour of the line-integrated intensities from three different ionization states (Al X (333 Å), Al XI (550 Å), Al XII (7.76 Å)) are also in good agreement with the calculation, as is seen from comparison of Fig.3(a) (experimental data) with Fig.3(b) (code calculation).

For Al transport in the low density discharges, which always show fairly peaked plasma density profiles, a good agreement is obtained between the experimentally observed Al radiation and code predictions based only on neoclassical transport. In the comparison of 'co' and 'counter' experiments, no significant difference has been found in their behaviour. Potential modifications of the impurity fluxes caused by the different momentum transfer of 'co' and 'counter' neutral beam injection are apparently very small owing to the nearly perpendicular injection. Moreover, no toroidal rotation and no significant difference of the basic plasma parameters are observed.

By varying the Al injection time, sudden redistributions of the Al ion density occurring within short time intervals (some ms) could be detected. This is particularly evident during the existence of hollow Al radial profiles with steep gradients. Qualitatively, this behaviour was modelled by anomalous transport fluxes which shift Al impurities outward, flattening the Al density peak of about 5 cm. This effect seems to be correlated with small modulations of the plasma pressure observed during maximum energy content. The structure of the magnetic surfaces may be affected by critical values of pressure-driven currents which can produce localized magnetic islands at rational t-values.

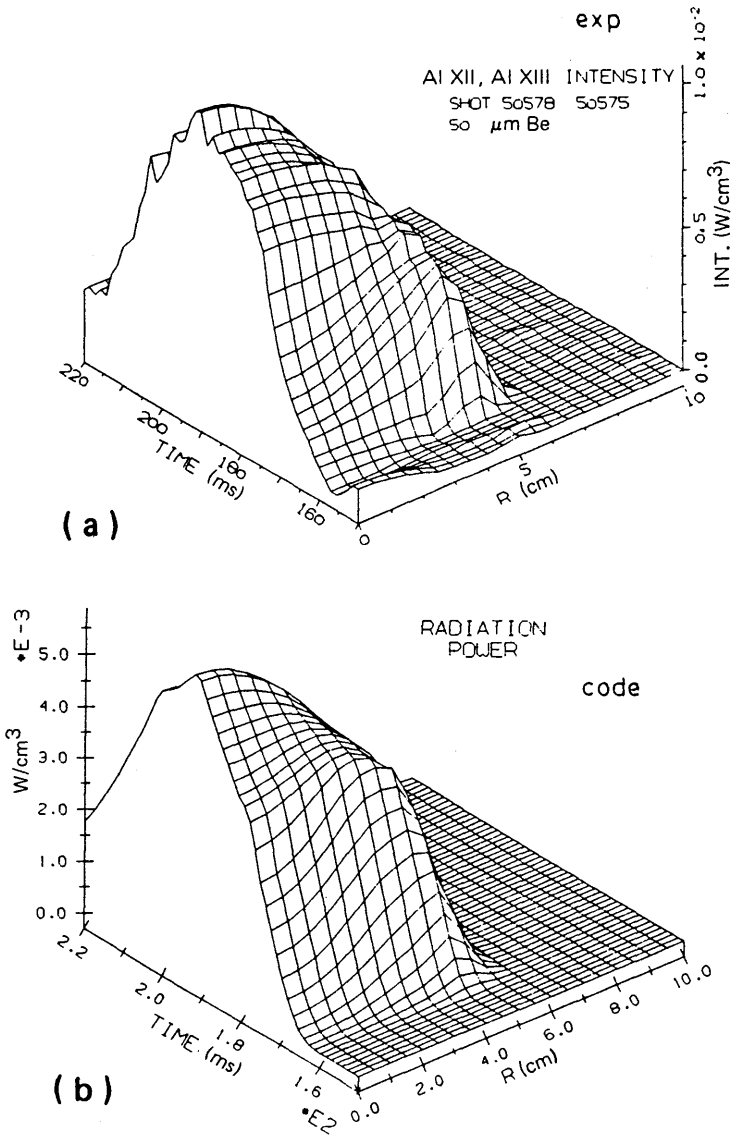

FIG.2. (a) Evolution of Al XII and Al XIII radiation power from soft X-ray measurements after Al injection into a high density discharge. (b) Code simulation of (a).

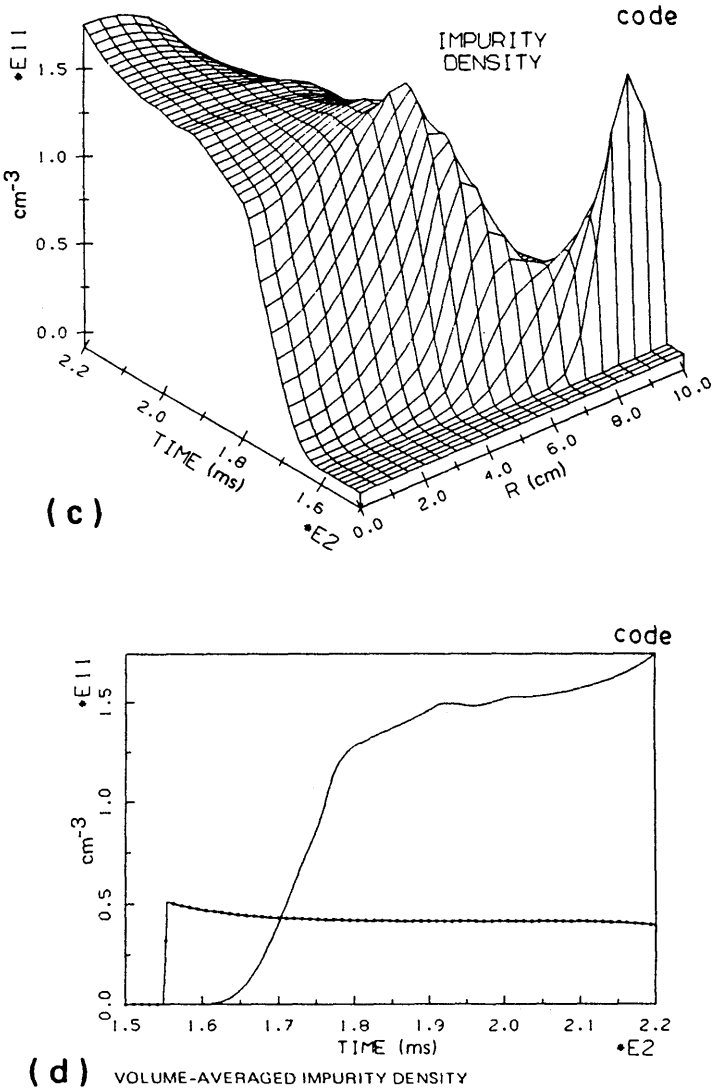

(FIG.2 cont.) (c) Evolution of Al ion density. (d) Central and volume-averaged Al ion density, as predicted by the code.

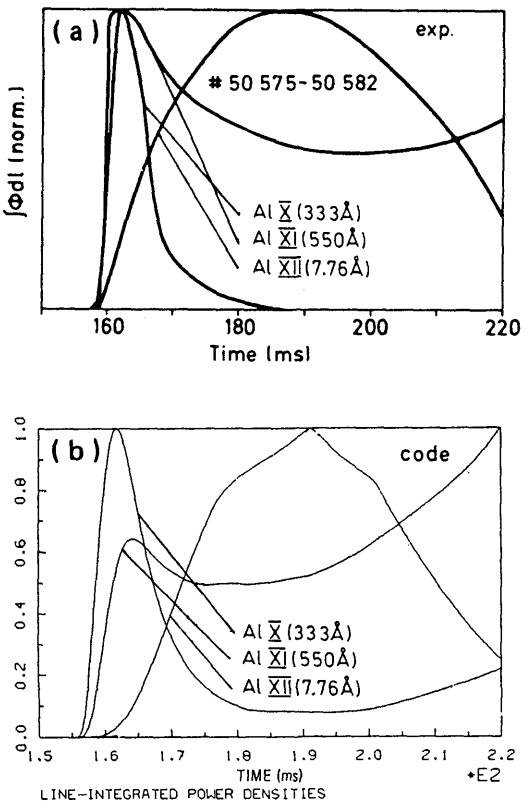

FIG.3. (a) Experimentally observed line-integrated intensities of three Al resonance lines for the case shown in Fig.2. (b) Code simulation.

5. SIMULATION OF TOTAL RADIATION

To check the transport terms with a different impurity species for the same discharges investigated with Al tracer impurities, the total radiation losses were also calculated by summation over the relevant resonance lines. In Fig.4 the local soft X-ray radiation (Fig.4(a)) is compared with a simulation (Fig.4(b)) based on neoclassical transport and the same anomalous term already used in Fig.2. The need to include additional anomalous transport is not very strong. Almost all oxygen calculations with neoclassical transport led to good agreement with the measurements.

In Fig. 4(c), (d) the measured brightnesses of individual resonance lines (O V–O VIII) are compared with the code calculations. For radiation from outside the hot plasma core (O V, O VI), good agreement may not be expected owing to asymmetric distribution of impurity sources.

In this calculation a 1% oxygen content in the neutral beams ($\sim 3 \times 10^{18} s^{-1}$) and an influx of $3 \times 10^{13} cm^{-2} \cdot s^{-1}$ from the walls ($\sim 2.8 \times 10^{18} s^{-1}$) can explain the observed central radiation power. These two impurity sources contribute to almost equal parts. Z_{eff} (Fig.4(e)), derived experimentally from soft X-ray continuum, reaches a value of about 1.8, corresponding to an oxygen concentration of about 2.2% of the electron density.

The low density discharges (without gas-puff during neutral injection) are characterized by significantly higher central radiation losses with Z_{eff} up to 4.5 and n_0/n_e increasing up to 7%. The oxygen influx from the walls has to be increased up to $8 \times 10^{13} cm^{-2} \cdot s^{-1}$ ($\hat{=} 7.5 \times 10^{18} s^{-1}$) in the calculations. In this case 1% beam impurities contribute to only 15% of the central impurity content.

6. SUMMARY AND CONCLUSIONS

The main features of the impurity transport in W VII-A seem to be consistent with neoclassical predictions. Localized additional anomalous transport during particular short time intervals improves the agreement of code calculations with the experimental data for certain types of discharges. These regions of increased impurity transport may be caused by modifications either of the t-profile (change of the residual current distribution) or of t(a) (modulations of the helical field). Simulations with Al and O impurities provide a consistent description of the transport.

The analysis of the total radiation in discharges with and without additional D gas feed indicates a reduction of the impurity radiation level in the plasma centre due to broad plasma density profiles. This is to be expected with neoclassical transport theory because of the flat inward convection velocity in the plasma centre. Aluminium injection experiments also show a higher central Al density for discharges without gas-puff. The penetration of impurities to the plasma centre

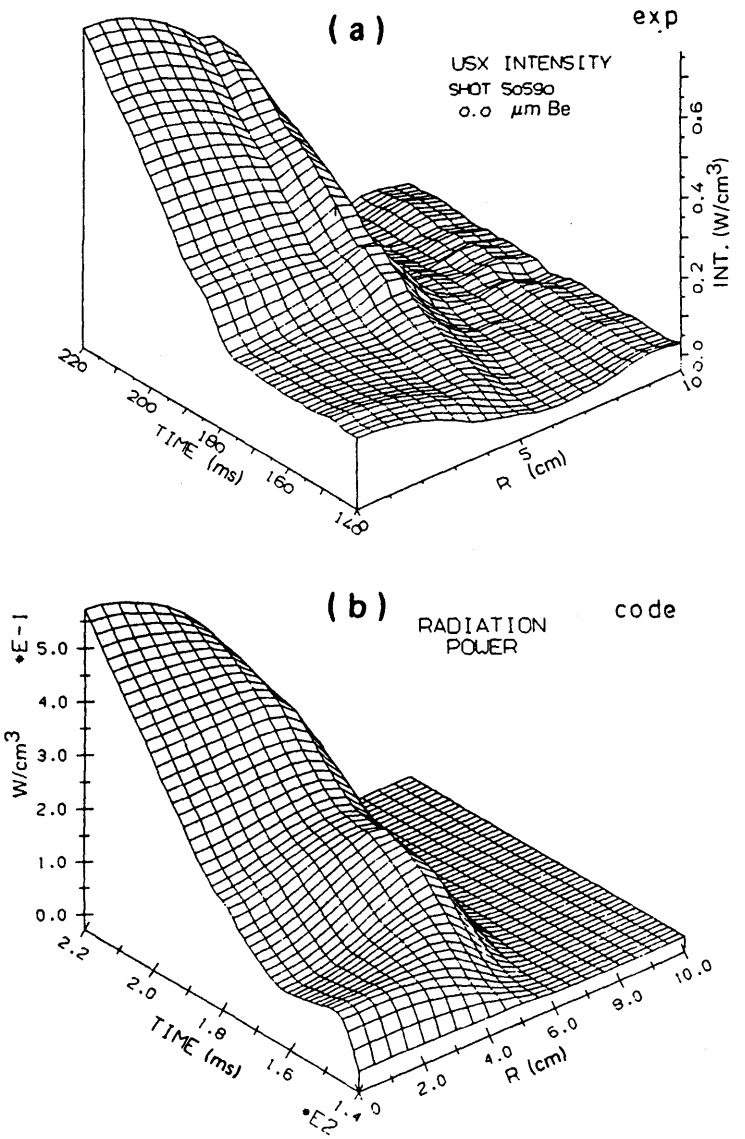

FIG. 4. (a) Soft X-ray radiation ($E \gtrsim 400$ eV) for the same experimental conditions as in Figs 2 and 3. (b) Code simulation of soft X-ray radiation with oxygen.

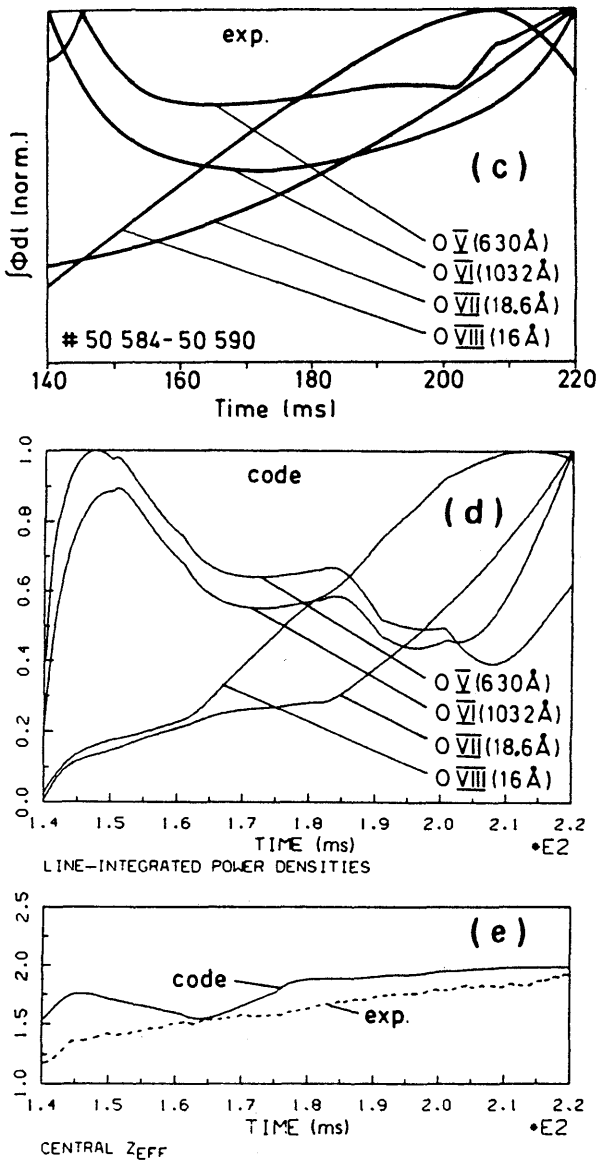

(FIG.4 cont.) (c, d, e) Comparison with simulation of line-integrated intensities from four resonance lines and Z_{eff}.

can be studied by the laser blow-off technique. The characteristic behaviour of different discharge types, as expected from neoclassical theory, seems to be masked by contributions of anomalous transport. A dependence of neutral beam induced transport from toroidal momentum transfer could not be observed, probably owing to the almost perpendicular neutral beam injection.

REFERENCES

[1] CATTANEI, G., et al., "Neutral injection heating in the Wendelstein VII-A Stellarator", Plasma Physics and Controlled Nuclear Fusion Research 1982 (Proc. 9th Int. Conf. Baltimore, 1982), Vol.2, IAEA, Vienna (1983) 241.
[2] W VII-A TEAM, NI GROUP, in Controlled Fusion and Plasma Physics (Proc. 11th Europ. Conf. Aachen, 1983), Part 1 (1983) 195.
[3] SARDEI, F., WELLER, A., in preparation.
[4] TFR GROUP, Nucl. Fusion **22** (1982) 1173.
[5] HIRSHMAN, S.P., Phys. Fluids **20** (1977) 589.
[6] HAWRYLUK, R.J., SUCKEWER, S., HIRSHMAN, S.P., Nucl. Fusion **19** (1979) 607.
[7] HIRSHMAN, S.P., Oak Ridge Natl Lab. Rep. ORNL/TM-6481 (1978).
[8] LISTER, G.G., OTT, W., SPETH, E., in Heating in Toroidal Plasmas (Proc. Joint Grenoble-Varenna Int. Symp. Grenoble, 1982), Vol.2 (1982) 813.
[9] KATO, T., Inst. for Plasma Physics, Nagoya Univ., Rep. IPPJ-AM-2 (1977).
[10] RENNER, H., et al., Paper No. IAEA-CN-44/D-I-1, these Proceedings, Vol.2.
[11] UO, K., et al., Paper No. IAEA-CN-44/D-I-2, these Proceedings, Vol.2.

Z-PINCH EXPERIMENTS AND THEORY

M.G. HAINES, A.E. DANGOR, A. FOLKIERSKI,
P. BALDOCK, W.G. BESSELL, D.J. BOND,
C.D. CHALLIS, P. CHOI, M. COPPINS,
M.B. FAVRE-DOMINGUEZ, D.A. HAMMER*,
E.L. LINDMAN**, J.R. LIU+, G. NAVE,
O.G. PARFENOV++, G. RICKARD, J. WESTLAKE
The Blackett Laboratory,
Imperial College of Science and Technology,
London, United Kingdom

Abstract

Z-PINCH EXPERIMENTS AND THEORY.

A Z-pinch satisfying Lawson conditions under pressure balance with end-losses has a coincidental advantage that the ion Larmor radius is comparable in magnitude to the pinch radius, possibly giving enhanced stability. Progress is reported on three experimental approaches to achieving a dense Z-pinch; a compression-pinch, a laser-initiated gas-embedded pinch, and a gas-puff pinch. The compression-pinch with T = 250 eV, $\omega_i \tau_{ii} > 1$, $n = 2 \times 10^{17}$ cm^{-3}, and $a_i/a \cong 0.2$, appears to be anomalously stable during the whole discharge time, which is from 4 to 20 e-folding MHD growth times. Theoretical progress has been made in including (a) the Hall effect and (b) a kinetic treatment of large ion Larmor orbits for the m = 0 instability. In a laser-initiated gas-embedded pinch the use of preheat gives a stable pinch of constant radius which suddenly evolves into an expanding helical configuration. A 1-D MHD simulation of the radially symmetric phase shows good agreement with experiment. The gas-puff pinch has negligible Larmor radius stabilization and produces localized hot spots on axis associated with an m = 0 instability. A 2-D particle ion and electron fluid simulation is developed to indicate how ion beams can be generated in this instability.

1. INTRODUCTION

It has been shown [1] that a Z-pinch in radial pressure equilibrium and with conduction losses to the electrodes balanced by Ohmic heating can satisfy the Lawson criterion. Such a pinch requires about 1 MA current and a line density of $\sim 5 \times 10^{18}$ m^{-1}, so that coincidentally the ratio of the ion Larmor radius to the pinch radius is approximately 0.3. Conventional MHD theory needs modification for finite Larmor radius (FLR) effects, and enhanced stability is expected. At

---

* Cornell University, Ithaca, NY, USA.
** Los Alamos National Laboratory, Los Alamos, NM, USA.
\+ Changsha Institute, China.
++ Krasnoyarsk University, Krasnoyarsk, USSR.

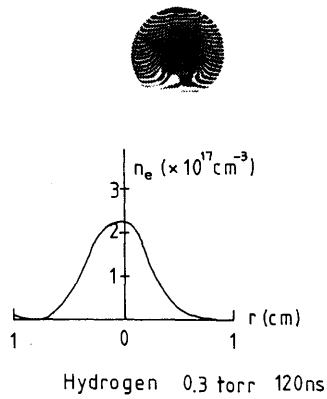

FIG. 1. Holographic interferogram of compression-pinch and electron density profile.

Imperial College, experimental and theoretical work is being done on the generation, heating and stability of Z-pinches. Three experiments are in progress: (i) a compression-pinch where the plasma is heated by a cylindrical converging shock, (ii) a gas-embedded pinch where a small plasma channel is formed in high pressure gas and subsequently Joule-heated under pressure balance, and (iii) a gas-puff pinch where a preformed hollow cylindrical gas shell implodes onto the axis.

Theoretical work complements the experimental programme. In particular, linear stability with large ion Larmor radius and Hall effects is being studied; the non-linear evolution of the m = 0 instability using an ion kinetic model is being simulated, and 1-D fluid codes model the principal experimental features.

2. THE COMPRESSIONAL Z-PINCH

This apparatus and early experiments on it were reported in 1978 [1, 2]. A 3-Ohm pulse-forming line gives a current of up to 150 kA with rise-time 50 ns and duration 200 ns. The quartz pinch tube is 5 cm long with 2 cm diameter. Pre-ionization is by UV from an adjacent coaxial discharge. Optical streak end-on and side-on photography shows no bounce after the initial collapse, and there is no gross instability either during the initial 200 ns before current reversal or, subsequently, in cases when further plasma shells form at the wall and collapse onto the pinch. Figure 1 shows a typical end-on double transit interferogram and the associated $n_e(r)$ taken with hydrogen at 300 mtorr filling pressure at t = 120 ns, after which time the formation of the second plasma shell at the wall begins. The measured pinch line density ($\sim 10^{19}$ m^{-1}), together with the Bennett relation, gives $T \cong 250$ eV. The observed radius of the discharge is $a \approx$

$\approx 4 \times 10^{-3}$ m and the ion thermal velocity v_i is $\sim 2.5 \times 10^5$ ms^{-1}, so that the MHD instability growth time $\tau_s = a/v_i$ is ~20 ns. The time to pinch is ~70 ns, and current reversal occurs at 200 ns. Thus, for at least $6\tau_s$, the discharge appears stable, during which time the amplitude of an instability should have grown fifty-fold. This enhanced stability may be due to FLR effects. The value of a_i/a is approximately 0.2 if the effective magnetic field is taken as half the maximum spatial value, and $\omega_i \tau_{ii}$ is $\gg 1$.

3. LARGE ION LARMOR RADIUS STABILITY

This theoretical study is motivated by the possibility that MHD instability growth rates may be greatly reduced by large ion Larmor radius effects. At present only the m = 0 mode is under consideration.

Two effects are significant: first, ion kinetic effects, and second, the Hall term, which arises as an extra term on the right-hand side of Ohm's law:

$$\vec{E} + \vec{u} \wedge \vec{B} = \frac{\vec{j} \wedge \vec{B}}{n_e}$$

We have studied Hall fluid instabilities (in which the second effect alone is included) by means of a linearized initial value code [3] in which both the ions and the electrons are treated as fluids. In contrast to previous studies (e.g. Ref. [4]), incompressibility is not assumed. The actual time evolution of an initial arbitrary perturbation, applied to a given equilibrium, is followed. After a few growth times the fastest growing mode dominates and the growth rate converges. This method has been previously applied to MHD instabilities in tokamaks [5]. We find that for a Bennett equilibrium the Hall effect actually destabilizes the fastest growing MHD mode. For a second equilibrium, the growth rate of the fastest growing MHD mode is reduced but new modes with higher growth rates and spatial structure strikingly dissimilar to the MHD modes are found.

The code has been modified to include the ion kinetic effects, which should exert a strong stabilizing effect. The fluid description of the ions has been replaced by an ensemble of particles. By integrating the perturbed fields along unperturbed ion trajectories, the first-order ion distribution function can be obtained from the linearized Vlasov equation:

$$\frac{df_1}{dt'} = -\frac{e}{m_i}(\vec{E}_1 + \vec{v} \wedge \vec{B}_1) \nabla_v f_0$$

Here d/dt' is the total time derivative following an unperturbed ion trajectory. The field advancing routine is retained from the Hall fluid code, and the electrons

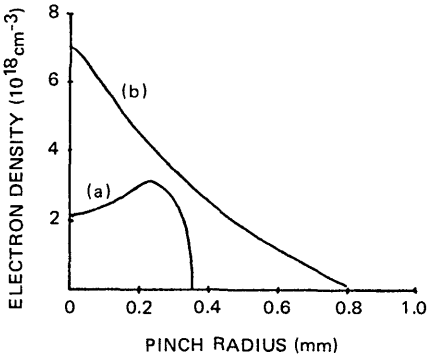

FIG. 2. Electron density profiles for the gas-embedded pinch at 0.33 atm H_2: (a) during preheat phase, 52 ns after laser initiation; (b) during main current, stable phase, 25 ns after commencement of main current.

are still treated as a cold fluid. This particle-fluid code is currently being tested and it is hoped that results will be available soon.

4. THE GAS-EMBEDDED PINCH

Here [6] a 2 J, 10 ns ruby pulse is used to initiate a narrow plasma filament in hydrogen at pressures of 0.2 to 2 atm. A preheat current (~6 kA for 60 ns) is then applied during which the channel expands with a velocity of 10^4 m/s owing to pressure imbalance. Interferometry shows that at this time the number density has a minimum on axis.

When the main current is applied, with initial $d\ell/dt \cong 1.5 \times 10^{12}$ A · s^{-1} (rising to 45 kA in 30 ns), the plasma conditions are such that heating occurs under pressure balance. The radius is constant at 400 μm with the $n_e(r)$ profile now peaked on axis, as shown in Fig. 2. The pinch column is stable for 20–40 ns, corresponding to 2–0.2 atmospheres filling pressure; it then suddenly forms an internal helical configuration which expands radially and meets the enhanced neutral number density layer at the edge of the plasma region. This thin layer is formed during the pre-pulse and has a density of about three times the filling density. After formation it expands at the same speed as the initial channel. Table I gives some plasma parameters for the stable, constant radius phase and for the later helix formation. We note that the duration of the stable phase is shorter at higher filling pressure and appears to be unrelated to MHD growth times. The calculated growth time of an m = 1 MHD instability [7] fits well with the observed expansion rate of the helix. Here, values of T_e are derived from the Bennett equilibrium. Stabilizing effects due to neutral gas [8] inertia are not observed.

TABLE I. PLASMA PARAMETERS FOR THE GAS-EMBEDDED PINCH

	Pressure	0.33 atm	1.00 atm
Constant radius phase	Temperature, T_e (eV)	34	19
	Duration of stable phase, τ_s(ns)	40	15
	Ion Hall parameter, $\omega_i\tau_{ii}$	0.1	0.22
Growth of helix	Observed growth time, r/ṙ (ns)	12.2	8.1
	Calculated τ_{MHD}, m = 1 (ns)	8.1	8.0

$\omega_i\tau_{ii}$ values are $\ll 1$ during the stable phase, so that FLR effects cannot be responsible for enhanced stability, in contrast to the compression experiment.

5. 1-D SIMULATION OF GAS-EMBEDDED PINCH

A fluid simulation including ionization effects shows in Fig.3(b) the formation of a high neutral density shell surrounding the plasma region. The shell produces a shock wave which expands into the neutral gas with a velocity of about 10^4 m/s. Within this shell the plasma current is also annular, showing a pronounced skin effect enhanced by the greater conductivity and temperature (Fig.3(a)) associated with the Ohmic heating. The ion temperature exceeds the electron temperature in the shocked gas. The simulation shows an increasing electron line density during the preheating phase and a minimum electron density on axis. During the main current, the magnetic field confines and compresses the plasma, thus preventing significant further ionization and causing the electron density to peak on axis. The plasma pressure exceeds the magnetic pressure, which leads to radial oscillations.

6. THE GAS-PUFF PINCH

This apparatus was described at Aachen in 1983 [9]. An annular supersonic jet of gas (either 50 mm or 30 mm in diameter, about 5 mm thick) is injected between two electrodes 2 cm apart. A 9 μF, 30 kV capacitor is then triggered, giving a peak current of 300 kA and a quarter-period of 1 μs. The pinch occurs just after current maximum, and a pulse of X-rays occurs simultaneously. The

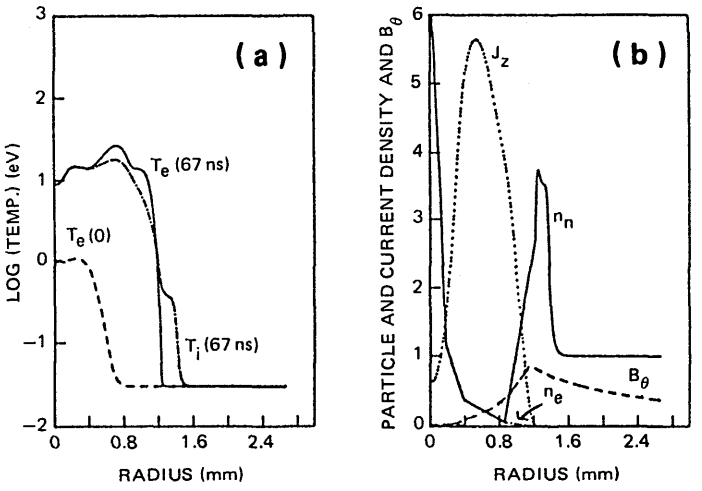

FIG. 3. 1-D simulation of gas-embedded pinch at 0.33 atm H_2: (a) Log T_e (eV) after laser initiations; log T_e (eV) and log T_i (eV) after main current compression at 67 ns. (b) Current density J_z, magnetic field B_θ, ion and neutral density n_n, and electron density n_e (in units of the filling density), at 67 ns, with current at 50 kA (the main current commences at 50 ns).

hard X-ray signal (1.5–20 keV) lasts about 20 ns; the XUV signal lasts some 100 ns. Pinhole photography (time-integrated) shows a series of hot spots. Hard X-rays (>10 keV) are emitted from the anode, which indicates that energetic electron beams are present. Energetic ions travelling towards the cathode have been detected with a Faraday cup.

The experiment has been operated with argon, CO_2, neon and nitrogen; spatially resolved X-ray spectra between 10 Å and 100 Å have been studied, using a 5 m grazing incidence grating spectrograph. Up to 10 J of soft X-rays are emitted. In argon, Ar XI–Ar XV have been observed in hot spots, with Ar IX and Ar X in the surrounding plasma. In CO_2, carbon lines give 80 eV and 10^{24} m^{-3}, while oxygen gives 130 eV and 10^{27} m^{-3}. The discrepancy may be due to carbon and oxygen emitting at different times in different places. Less reliable estimates in neon give 200 eV and 10^{27} m^{-3}. The latter estimates are based on satellite line-intensity ratios.

7. SIMULATION OF ION BEAM FORMATION AT AN m = 0 INSTABILITY

The mechanism for particle acceleration in Z-pinches and plasma focus experiments has been a long-standing problem. Recently a new mechanism for ion beam generation has been proposed [10] in which axial singular ions interact

with the neck of an m = 0 unstable pinch and are accelerated, the axial momentum being redistributed in off-axis ions. A 2-D hybrid code has been constructed to demonstrate such a process in a self-consistent calculation.

The ions are simulated as collisionless particles and the electrons form a cold, charge-neutralizing background fluid. Electron inertia in the electron momentum equation is included in such a way that the collisionless skin depth can be artificially enlarged [11]. The displacement current is dropped from Maxwell's equations. In this way the high frequencies associated with e.m. waves are eliminated, allowing an investigation of ion kinetic effects for several radial ion transit times.

The programme also successfully includes an external vacuum region and the collisionless sheath at the plasma/vacuum interface, enabling the inductive fields in the vacuum to be correctly coupled to the plasma.

The computational method employed in the code contains elements of methods at present in use elsewhere, i.e. the 'direct implicit fluid' [12] and ('implicit fluid' [13] techniques. The implicitness appears in the electric field solution, where the value of the electric field depends on the present values of the magnetic field and the sources, i.e. the current and the number density. This occurs because the displacement current is eliminated. The direct side of the calculation allows for a correction of the sources in the electric field solution, using moment equations derived from the ion equations of motion.

REFERENCES

[1] HAINES, M.G., Physica Scr. T2/2 (1982) 380.
[2] CHOI, P., et al., "Z-pinches of intense energy density driven by high-voltage storage lines", Plasma Physics and Controlled Nuclear Fusion Research 1978 (Proc. 7th Int. Conf. Innsbruck, 1978), Vol. 2, IAEA, Vienna (1979) 69.
[3] COPPINS, M., BOND, D.J., HAINES, M.G., to be published in Phys. Fluids.
[4] SCHAFER, U., J. Plasma Phys. **29** (1983) 1.
[5] SYKES, A., WESSON, J.A., Nucl. Fusion **14** (1974) 645; BATEMAN, G., SCHNEIDER, W., GROSSMAN, W., Nucl. Fusion **14** (1974) 669.
[6] DANGOR, A.E., et al., Phys. Rev. **A27** (1983) 2751.
[7] KRUSKAL, M., SCHWARZSCHILD, M., Proc. R. Soc. (London), Ser. A, **223** (1954) 348.
[8] MANHEIMER, W.M., et al., Phys. Fluids **16** (1973) 1126.
[9] CHALLIS, C.D., et al., in Controlled Fusion and Plasma Physics (Proc. 11th Europ. Conf. Aachen, 1983), Vol. 7D, Part 1 (1983) 555.
[10] HAINES, M.G., Nucl. Instrum. Methods **207** (1983) 179.
[11] LINDMAN, E.L., RICKARD, G., HAINES, M.G., in Controlled Fusion and Plasma Physics (Proc. 11th Europ. Conf. Aachen, 1983), Vol. 7D, Part 2 (1983) 351.
[12] LANGDON, A.B., et al., J. Comput. Phys. **51** (1983) 107.
[13] NIELSON, C., et al., Methods Comput. Phys. **16** (1976) 367.

SHEAR STABILIZING EXPERIMENT OF GUN-SPHEROMAK PLASMA (CTCC-I)*

M. NAGATA, Y. HONDA, K. IKEGAMI**, M. NISHIKAWA,
A. OZAKI, N. SATOMI, T. UYAMA, K. WATANABE
Course of Electromagnetic Energy Engineering,
Faculty of Engineering, Osaka University,
Yamada-oka, Suita, Osaka, Japan

Abstract

SHEAR STABILIZING EXPERIMENT OF GUN-SPHEROMAK PLASMA (CTCC-I).

In a gun-spheromak experiment (CTCC-I), the plasma is cleaned of impurities by titanium coating on the flux conserver (FC) wall, becomes active and sometimes suffers from disruptive termination. To overcome the disruptive instability, it is tried to insert a central conductor along the geometric axis of the FC, which is expected to have a higher magnetic shear configuration. Results demonstrate a suppression of the disruptive instability, but a rather weak instability remains, the so-called stepwise instability. – Magnetic-field measurements show spatial differences in the field decay, probably due to an inhomogeneity in the plasma resistivity. The equilibrium configuration of CT is hence interpreted as one that changes into a configuration with a rather peaked current profile, resulting in the stepwise instability. OV line (2781 Å) radiation and the average density show a sawtooth and a stepwise waveform, respectively. – Moreover, the change in the plasma behaviour is examined by using conductors with different diameters. The results show that larger diameters of the conductor make the plasma more stable.

1. INTRODUCTION

Compact-torus research is a fundamental study of magnetic-confinement plasmas aiming at the design of an inexpensive nuclear fusion reactor. Its purpose is to achieve stably confined toroidal plasmas in magnetic fields produced without toroidal magnetic coils.

In the early stages of research, the plasma was apparently stable and decayed exponentially with a lifetime of 0.2 ms, which was interpreted as a radiation-loss-dominated process [1, 2]. In our CTCC-I experiment (Fig.1), using a magnetized co-axial gun and a drum-type flux conserver, this stage has been cleared by titanium coating on the flux conserver wall surface [3, 4]. The plasma has really become 'active' in this experiment, but sometimes suffered from disruptive terminations. The plasma lifetime, in some cases, reached up to a little less than 1 ms.

* Supported by a grant-in-aid for fusion research from Ministry of Education.

** Present address: Mitsubishi Electric Corporation, Chiyoda-ku, Tokyo, Japan.

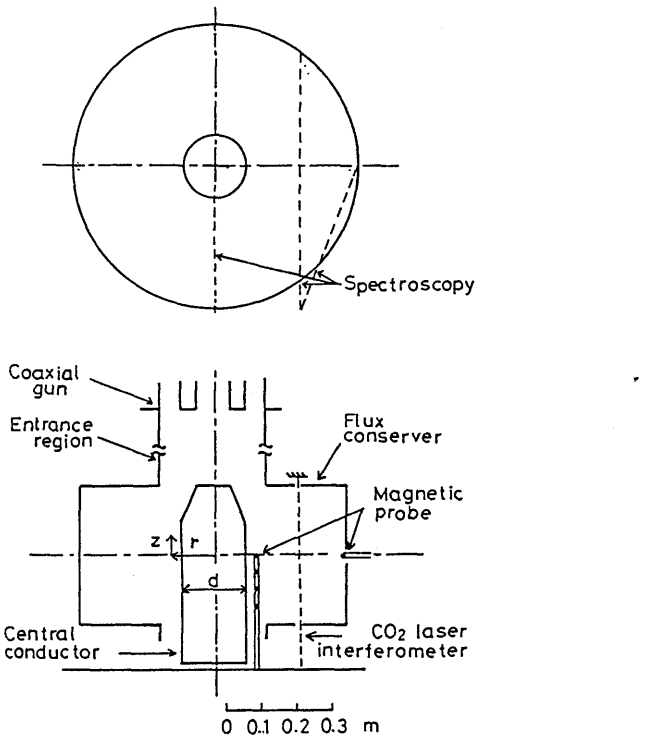

FIG.1. Schematic diagram of CTCC-I experiment, illustrating arrangement of diagnostics.

In our first attempt to suppress the disruptive instability we changed the magnetic-field profile by inserting a conducting cylinder along the geometric axis of the conserver, which was expected to provide a higher magnetic shear [5]. In fact, the plasma was observed to show no disruptive termination but instead displayed a behaviour of stepwise decay [6]. The result suggests the suppression of the disruptive instability, but, apparently, a rather weak instability remained.

The stepwise instability was studied by measuring the magnetic-field fluctuations and the impurity line radiation and also by examining the change in plasma behaviour in the flux conserver geometries each of which had a different central-conductor diameter. The results show that larger cylinder diameters make the plasma more stable.

2. EXPERIMENTAL APPARATUS AND MEASUREMENTS

In the CTCC-I experiments, spheromak-type compact toroids (CTs) were produced by a magnetized co-axial gun. The experimental arrangements are in

detail described elsewhere [1–3]. An FC-D1 flux conserver was first applied with a central conductor of 0.18 m diameter so as to increase the magnetic shear over the plasma region. After the FC-D1, central conductors of 0.03 m and 0.12 m diameter were applied to study the magnetic-shear stabilizing effect in greater detail. In these experiments, for impurity control, Ti-coating was applied to the FC and the vacuum chamber wall. The base pressure was 2×10^{-8} torr before the discharge.

The temporal variation of the CT magnetic field was monitored by a magnetic probe located 2 cm from the FC wall in the midplane.

The average electron density was measured by a CO_2 laser interferometer along the line of sight through the magnetic axis and in parallel to the geometric axis of the torus.

The behaviour of the impurity line radiation (O, C, Ti, Cu) from the periphery and the central part in the midplane of the CT was measured simultaneously by using two spectrometers. To compare the phases of the sawtooth signal of the O V line (2781 Å) at various plasma radii, the line of sight was scanned from the magnetic axis to the CT periphery.

Furthermore, a spectral analysis of the poloidal-magnetic-field signals was performed by simultaneous measurements of eight magnetic probes set along the toroidal and poloidal field lines.

3. RESULTS

3.1. Results without central conductor

After applying the Ti-coating to the FC wall, the electron temperature and the lifetime of the CT plasma were increased up to 20–40 eV and 0.7–0.8 ms, respectively [4]. In the same conditions, however, a plasma disruption was found to occur at a rate of 30%. Figure 2 shows typical waveforms of electron density, $\bar{n}_e$, monitor magnetic field, B_p, and O V line intensity, I_{OV}, observed in the discharge, where (a) and (b) have a major disruption until 0.5 ms (D-mode) and (c) has an intermittently occurring instability, named stepwise instability, with a sawtooth waveform of I_{OV} (SW-mode).

In case (a) of the D-mode, B_p decreases rather linearly during 0.3 ms with irregular oscillations from the start in the early phase, and n_e shows a pump-out. In case (b), B_p decreases rapidly during 0.3–0.5 ms after a short stable period, accompanied by intense magnetic fluctuations, and $\bar{n}_e$ first remains constant and then decreases rapidly, as is shown in this figure. The characteristic features of the SW-mode are described in the following section in somewhat greater detail. In this figure, the instants of time when the stepwise instability occurs are designated by t_1, t_2, t_3, t_4, (see Table I).

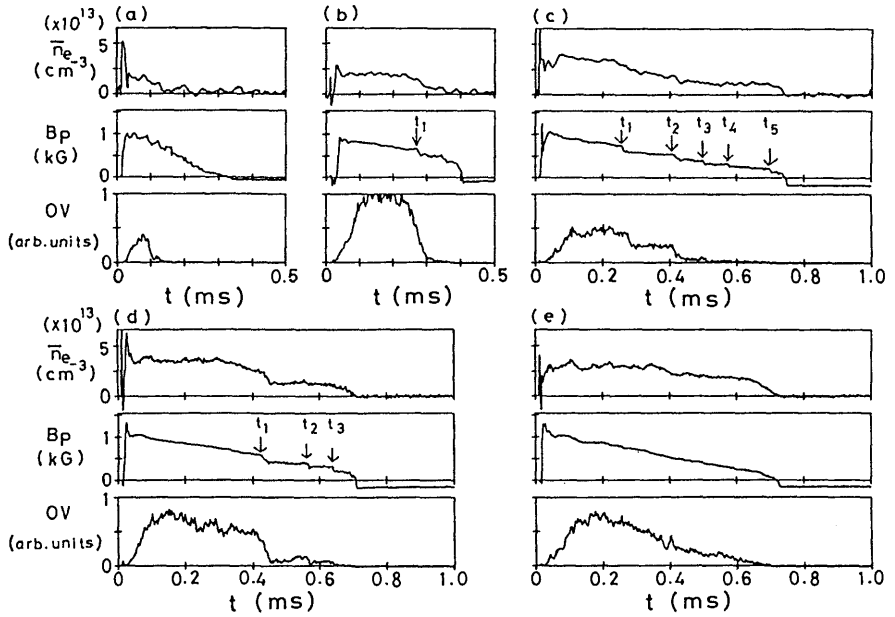

FIG.2. Typical waveforms of $\bar{n}_e$, B_p and O V line (2781 Å) intensity $I_{O\,V}$. (a)–(c) and (d)–(e) are obtained with no central conductor and with central conductor of 0.12 m diameter, respectively. Shots are classified into three kinds of mode: D-mode [(a), (b)], SW-mode [(c), (d)], S-mode [(e)].

TABLE I. PERCENTAGES OF OCCURRENCE OF THREE MODE TYPES (D-, SW-, AND S-MODES) FOR VARIOUS CENTRAL-CONDUCTOR DIAMETERS AND APPEARANCE TIME OF STEPWISE INSTABILITY (t_1, t_2-t_1)

	Total number of shots	D-mode (%)	SW-mode (%)	S-mode (%)	$[t_1]$ (μs)	$[t_2-t_1]$ (μs)
d = 0	100	30	70	0	268 ± 75	169 ± 44
d = 0.03 m	52	7	91	2	323 ± 60	187 ± 37
d = 0.12 m	45	0	82	18	390 ± 80	163 ± 65
d = 0.18 m (FC-D1)	140	0	86	14	372 ± 51	150 ± 34

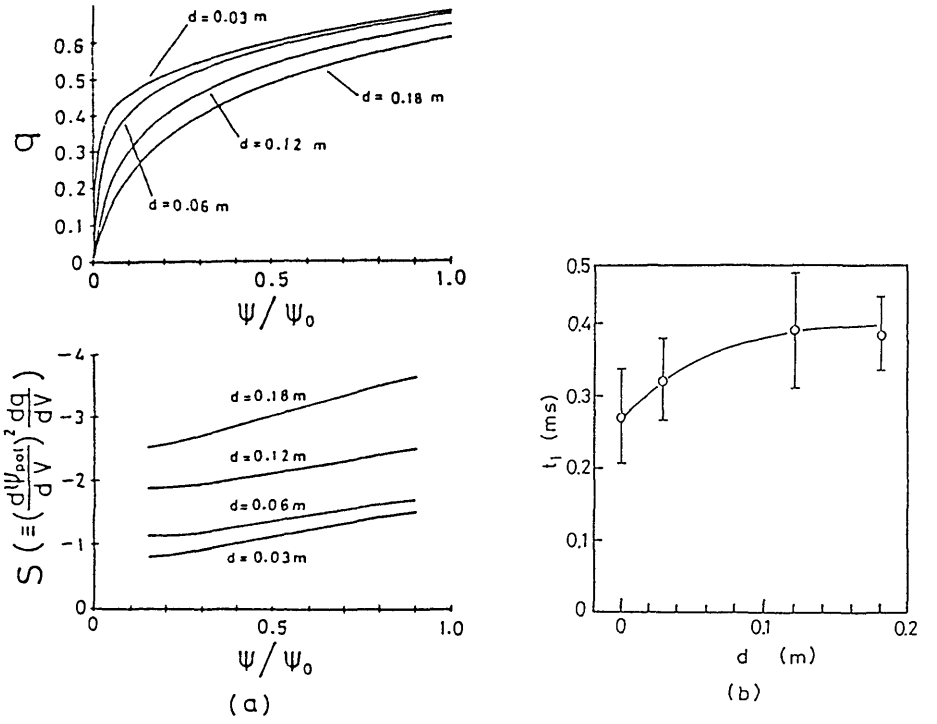

FIG.3. (a) Safety factor q and magnetic shear S versus normalized flux function ψ/ψ_0 for various diameters of central conductor; (b) appearance time t_1 of first stepwise event versus central-conductor diameter.

3.2. Application of a central conductor

The introduction of a central conductor increases the magnetic shear over the plasma confinement region, whose profile is altered by changing the diameter of the central conductor.

Figure 3(a) shows the safety factor, q, and the magnetic shear, S, versus a normalized flux function, $\tilde{\psi} = \psi/\psi_0$, estimated on the basis of a force-free Bessel function model which assumes rot $\vec{B} = \lambda\vec{B}$, where ψ_0 is the flux function at the magnetic axis and λ is constant over the plasma in the FC. The figure shows that the magnetic shear becomes larger over the plasma as the diameter of the central conductor is increased.

To study experimentally the effect of shear stabilization on plasma confinement, we have used three kinds of central conductor with diameters of 0.03, 0.12 and 0.18 m. The experimental data obtained in the same operating conditions are classified into three types, from the viewpoint of plasma confinement: the D-mode, the SW-mode and the S-mode, as was done before. In the SW-mode

case, B_p shows an intermittent stepwise 'down' behaviour in the course of resistive decay without disruption. I_{OV} shows a kind of sawtooth waveform, similar to the soft-X-ray signals detected in tokamak discharges, although the repetition of sawteeth is only a few times here. Smooth ramps and rapid 'downs' of I_{OV} sawteeth correspond to stable decays and stepwise 'downs' of B_p, respectively. The S-mode shows a stable behaviour of B_p and I_{OV} without fluctuations, having a long lifetime of over 0.7 ms.

Typical waveforms of $\bar{n}_e$, B_p and I_{OV}, observed in the discharge with a central conductor of 0.12 m diameter, are shown in Figs 2(d) and (e). The former shows an SW-mode and the latter an S-mode.

Table I gives the percentage of occurrence of the three types observed and the averages of both t_1 and t_2-t_1 for each of the four cases. It is shown in Fig. 3(b) that the average of t_1 increases with increasing central-conductor diameter.

From these data, we have found two effects of introducing a central conductor. The first effect is the suppression of disruptions occurring up to 0.5 ms without central conductor, and the second effect is the prolongation of t_1 or the complete suppression of the stepwise instability, in extreme cases.

3.3. Features of stepwise instability

(a) Behaviour of magnetic-field decay

The typical behaviour of $B_{p,\,out}$ as monitored in the outside plasma near the FC wall is a stepwise decay consisting of a smooth decay phase and a stepwise 'down'. The decay constant for the smooth decay phase is typically 0.6–0.8 ms. This value is somewhat larger than that estimated from the Spitzer resistivity of 20–30 eV electron temperature, on the assumption of $Z_{eff} = 1$. On the other hand, $B_{p,\,in}$ in the inside plasma near the central conductor rather shows an exponential decay with small humps at the times corresponding to the stepwise 'down' of $B_{p,\,out}$. We find a little difference between the two signals, as is shown in Figs 4(a) and (b).

Figure 4(c) shows the ratio, R, of $B_{p,\,out}$ and $B_{p,\,in}$. This ratio first decreases gradually and suddenly again assumes its initial value, R_0 of the upper dotted line; later, it even decreases below the lower dotted line, R_c, in the figure. This phenomenon occurs at the time of the stepwise event. R_0 is probably the value attained at the instant of a stable CT configuration formed initially, and R_c represents a kind of critical value for the CT stability. This behaviour repeats a few times. If the resistivity of the plasma were constant in space, the magnetic field profile would show a self-similar decay, i.e. R would be constant. In CTCC-I, the results indicate that, during the smooth decay phase, the equilibrium configuration of CT tends to be modified in time because of the spatial inhomogeneity of the plasma resistivity and results in the occurrence of a stepwise instability.

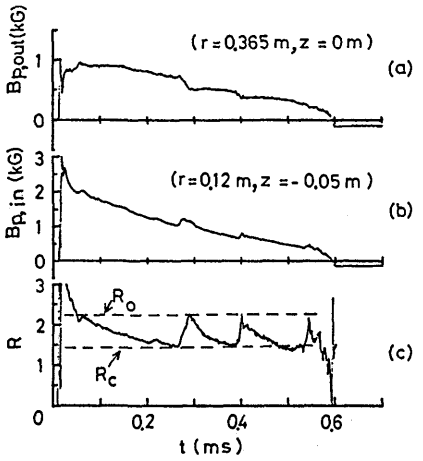

FIG.4. (a) Typical poloidal magnetic field $B_{p,\,out}$ measured near flux conserver wall; (b) typical poloidal magnetic field $B_{p,\,in}$ measured near central conductor wall; (c) temporal evolution of ratio R of $B_{p,\,in}$ and $B_{p,\,out}$. R_0 is value attained at instant of stable CT configuration formed initially, R_c is a kind of critical value for instability.

(b) Mode analysis of magnetic fluctuations

Two sets of eight magnetic probe coils are used to obtain the toroidal and poloidal mode numbers of the instability. Figure 5 shows the temporal evolution of the spectral intensity of the poloidal (a) and the toroidal (b) modes. As to the poloidal mode, the m = 1 mode is clearly dominant and also the m = 0 mode is stronger than the m = 2, 3 and 4 modes.

As to the toroidal mode, each mode among n = 2, 3 and 4 is found. The n = 0 mode is seen especially at the instant when B_p goes down stepwise. The most dominant toroidal mode is not identified clearly because our CT plasma has many resonant surface of $n > 2$ if m = 1 is fixed, and many modes can become unstable.

(c) Electron density and impurity radiation

Figure 6(a) shows the temporal evolution of $\bar{n}_e$ after Ti- coating. $\bar{n}_e$ remains almost constant in time, except for the stepwise-'down' associated with that of B_p, while results observed before Ti-coating show that $\bar{n}_e$ increases with time in the early phase, up to $(0.8–2.0) \times 10^{14}$ cm^{-3}. The behaviour of $\bar{n}_e$ reveals that wall recycling is an important process, on account of $\bar{n}_e$ remaining constant during the smooth decay phase. On the other hand, the density decrease of 30–60%, which

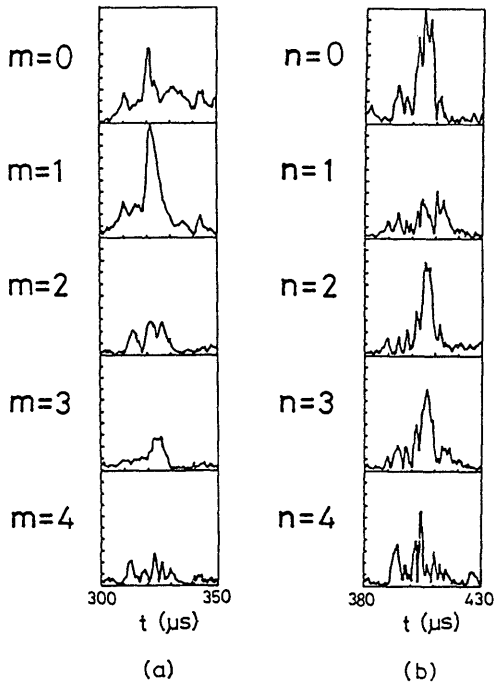

FIG.5. Spectral densities of poloidal (a) and toroidal (b) modes for stepwise instability.

is caused by the stepwise instability, indicates that the particle loss to the FC wall is significant, which is also confirmed by spectroscopic measurements.

In the confinement phase, the O II, O III and O IV impurities are 'burnt through' during 0.1–0.2 ms, and the radiation from O V becomes dominant as is shown in Fig. 6(b). From this fact, the electron temperature is estimated to be 20–30 eV, on the basis of the corona model.

The temporal evolution of the O V line (2781 Å) shows a kind of sawtooth waveform. The signals of the O II, O III and Ti II radiation show sawtooth phases opposite to those of the O V radiation. From these data, the electron temperature is considered to increase in time, because of Ohmic heating, during the smooth decay phase of B_p, and to decrease rapidly, owing to the instability. On the other hand, the plasma particles and the thermal energy are transported from the plasma core region to the plasma periphery or to the FC wall, because of the instability, and the impurity and the hydrogen are then sputtered out from the FC wall and ionized. As a result, reversed-phase sawtooth signals from low-charge ion radiation are observed.

The O V line radiation is measured through various chords and is compared with that observed through the chord along the magnetic axis by the other spectrometer used as a monitor. Results show that the sawtooth signals of the O V line behave in phase spatially over the plasma volume.

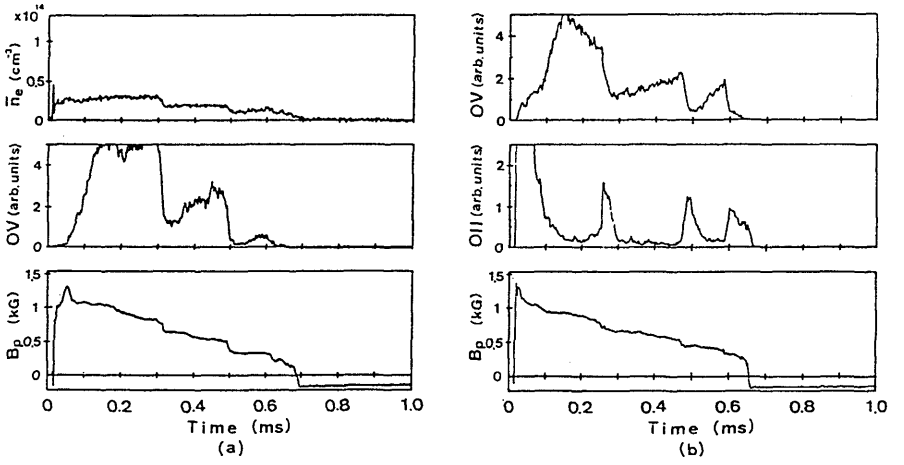

FIG.6. (a) Temporal evolution of average electron density; (b) temporal evolution of O V (2781 Å) and O II (4415 Å) line intensities.

4. DISCUSSION

In CTCC-I, the application of a central conductor suppresses disruptions which have often been observed in the FC run without such a conductor. The disruptions (D-mode) can be grouped into two types as is shown in Figs 2(a) and (b). The former type terminates disruptively without forming a stable configuration, but no disruption of this type is observed in the FC with central conductor. This observation indicates that the central conductor is effective in establishing a stable CT configuration. In the latter type, the CT plasma looks stable during 0.2–0.3 ms after plasma injection, but then an anomalous particle loss is caused by the growth of the instability, and when $\bar{n}_e$ drops down below a critical level of about $\bar{n}_e = 1 \times 10^{13}$ cm^{-3}, disruptive termination occurs. The local beta value, β_0, on the magnetic axis of our CT-plasma is 5–7%, which is apparently above the critical value estimated from the ideal-MHD stability (Mercier and ballooning modes) calculation for the plasma in the FC without central conductor. We think that these pressure-driven instabilities are a possible candidate for the anomalous particle loss. The application of a central conductor increases the magnetic shear in the plasma core capable of controlling the instabilities of these modes.

The characteristics of the stepwise instability have been investigated in the FC-D1 experiment. Our plasma settles down to a stable CT configuration in the early phase after injection, but changes to an unstable state in the resistive decay phase. This instability does not give rise to a disruption but results in the release of particles and thermal energy (density pump-out and rapid decrease of O V radiation). After that, the plasma relaxes back to a stable state.

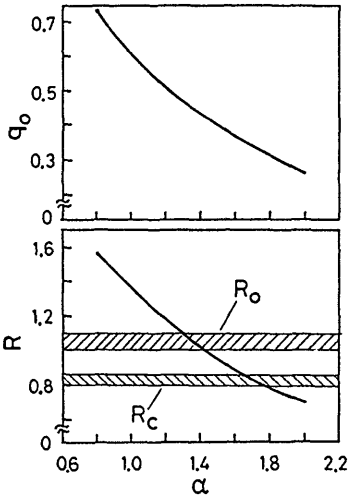

FIG. 7. Ratio $R \equiv B_{p,\,in}/B_{p,\,out}$ and safety factor on magnetic axis (q_0) as functions of current peaking parameter α. Solid lines are deduced from calculation. One shaded area, R_0, represents R experimentally obtained at early time of smooth decay phase or just after stepwise instability, and the other shaded area, R_c, represents R just before occurrence of instability.

The equilibrium configurations in our FC are dominantly determined by the current profile, but only little dependent on the pressure profile. We have studied the equilibrium for FC-D1 calculated by solving the Grad-Shafranov equation, assuming that

$$\Pi' = A(\tilde{\psi})^{\alpha}\, e^{(1-\tilde{\psi})(\alpha-1)}$$
$$p' = 0$$

The parameter α is a measure of the current profile, which becomes more pronouncedly peaked as α increases.

The ratio $R = B_{p,\,in}\,(r = 0.12\ m,\ z = -0.1\ m)/B_{p,\,out}\,(r = 0.335\ m,\ z = 0\ m)$ is compared with the calculation, as is shown in Fig. 7. The initial value R_0 is small (20%) compared with $R = 1.36$ for the force-free minimum energy state ($\alpha = 1$). When R decreases from R_0 to the critical value, R_c, the stepwise instability occurs. The decrease in R observed in our experiments can be explained by this assumption of current peaking, and we think that this critical level will depend on the magnetic shear.

The characteristics of this stepwise instability are the following:

(1) The instability is derived from current peaking.
(2) Mode analysis results are $m = 1$ for the poloidal mode and $n = 0, 2, 3, 4$ for the toroidal mode.

(3) The O V sawtooth is in phase spatially, which suggests that the instability occurs globally.

At present, we are making an effort to control the stepwise instability so as to improve the confinement of CT plasma.

REFERENCES

[1] WATANABE, K., et al., J. Phys. Soc. Jpn. **50** (1981) 1823.
[2] WATANABE, K., et al., in Plasma Physics and Controlled Nuclear Fusion Research 1982 (Proc. 9th Int. Conf. Baltimore, 1982), Vol.2, IAEA, Vienna (1983) 311.
[3] UYAMA, T., et al., in Compact Toroids (Proc. 4th US-Japan Workshop Osaka University, 1982), Osaka, Japan (1982) 1.
[4] SATOMI, N., et al., ibid., p.44.
[5] OKABAYASHI, M., TODD, A.M.M., Nucl. Fusion **20** (1980) 571.
[6] WATANABE, K., et al., in Compact Toroids (Proc. 5th US-Japan Workshop Princeton University, 1984), Princeton, USA (1984).

CHAIRMEN OF SESSIONS

Volume 2

Session E-I	P.H. RUTHERFORD	USA
Session E-II	L.M. KOVRIZHNYKH	USSR
Session C-I	D.D. RYUTOV	USSR
Session C-II	S. MIYOSHI	Japan
Session D-I	L.A. BERRY	USA
Session D-II	T. UCHIDA	Japan
Session D-III	R.J. BICKERTON	CEC/JET

SECRETARIAT OF THE CONFERENCE

Scientific Secretaries:	M. LEISER A.A. SHURYGIN	Division of Research and Laboratories, IAEA
Administrative Secretary:	Gertrude SEILER	Division of External Relations, IAEA
Editors:	J.W. WEIL Miriam LEWIS	Division of Publications, IAEA
Records Officer:	H. ORMEROD	Division of Languages, IAEA

HOW TO ORDER IAEA PUBLICATIONS

An exclusive sales agent for IAEA publications, to whom all orders and inquiries should be addressed, has been appointed in the following country:

UNITED STATES OF AMERICA UNIPUB, P.O. Box 433, Murray Hill Station, New York, NY 10157

In the following countries IAEA publications may be purchased from the sales agents or booksellers listed or through your major local booksellers. Payment can be made in local currency or with UNESCO coupons.

ARGENTINA	Comisión Nacional de Energía Atomica, Avenida del Libertador 8250, RA-1429 Buenos Aires
AUSTRALIA	Hunter Publications, 58 A Gipps Street, Collingwood, Victoria 3066
BELGIUM	Service Courrier UNESCO, 202, Avenue du Roi, B-1060 Brussels
CHILE	Comisión Chilena de Energía Nuclear, Venta de Publicaciones Amunategui 95, Casilla 188-D, Santiago
CZECHOSLOVAKIA	S.N.T.L., Mikulandska 4, CS-116 86 Praha 1 Alfa, Publishers, Hurbanovo námestie 3, CS-815 89 Bratislava
FRANCE	Office International de Documentation et Librairie, 48, rue Gay-Lussac, F-75240 Paris Cedex 05
HUNGARY	Kultura, Hungarian Foreign Trading Company P.O. Box 149, H-1389 Budapest 62
INDIA	Oxford Book and Stationery Co., 17, Park Street, Calcutta-700 016 Oxford Book and Stationery Co., Scindia House, New Delhi-110 001
ISRAEL	Heiliger and Co., Ltd., Scientific and Medical Books, 3, Nathan Strauss Street, Jerusalem 94227
ITALY	Libreria Scientifica, Dott. Lucio de Biasio "aeiou", Via Meravigli 16, I-20123 Milan
JAPAN	Maruzen Company, Ltd., P.O. Box 5050, 100-31 Tokyo International
NETHERLANDS	Martinus Nijhoff B.V., Booksellers, Lange Voorhout 9-11, P.O. Box 269, NL-2501 The Hague
PAKISTAN	Mirza Book Agency, 65, Shahrah Quaid-e-Azam, P.O. Box 729, Lahore 3
POLAND	Ars Polona-Ruch, Centrala Handlu Zagranicznego, Krakowskie Przedmiescie 7, PL-00-068 Warsaw
ROMANIA	Ilexim, P.O. Box 136-137, Bucarest
SOUTH AFRICA	Van Schaik Bookstore (Pty) Ltd., P.O. Box 724, Pretoria 0001
SPAIN	Diaz de Santos, Lagasca 95, E-28006 Madrid Diaz de Santos, Balmes 417, E-08022 Barcelona
SWEDEN	AB Fritzes Kungl. Hovbokhandel, Fredsgatan 2, P.O. Box 16356, S-103 27 Stockholm
UNITED KINGDOM	Her Majesty's Stationery Office, Publications Centre, Agency Section 51 Nine Elms Lane, London SW8 5DR
U.S.S.R.	Mezhdunarodnaya Kniga, Smolenskaya-Sennaya 32-34, Moscow G-200
YUGOSLAVIA	Jugoslovenska Knjiga, Terazije 27, P.O. Box 36, YU-11001 Belgrade

---

Orders from countries where sales agents have not yet been appointed and requests for information should be addressed directly to:

Division of Publications
International Atomic Energy Agency
Wagramerstrasse 5, P.O. Box 100, A-1400 Vienna, Austria

85-01173

INTERNATIONAL
ATOMIC ENERGY AGENCY
VIENNA, 1985

SUBJECT GROUP: III
Physics/Plasma Physics, Fusion
PRICE: Austrian Schillings 1300,–